PREPRINTS
2ND INTERNATIONAL WORKSHOP ON
WAVE HINDCASTING AND FORECASTING

VANCOUVER, B.C.
APRIL 25-28, 1989

This Workshop was supported by the
Federal Panel on Energy R&D

Published by:

Environment Canada
Atmospheric Environment Service
4905 Dufferin Street
Downsview, Ontario
M3H 5T4

ACKNOWLEDGEMENTS

The organizers are indebted to many people who provided valuable assistance in the planning and conduct of the workshop. We would like to thank the sponsors, in particular the federal Panel on Energy Research and Development, who provided most of the financial assistance for the workshop. The Canadian Meteorological and Oceanographic Society and the American Meteorological Society also assisted by carrying notices of the workshop in their Bulletins. The committee would also like to thank all those who submitted papers for the workshop program, and those who served as chairmen for the various sessions. Special thanks are due to Krystyna Czaja who assisted in the assembly and production of this preprint volume.

Cover: Photograph taken by Deborah S. Hutton of Oakville, Ontario, from a Soviet passenger liner in a storm in the north Atlantic. The ship was delayed two days enroute from Europe to New York by the weather conditions.

WORKSHOP ORGANIZING COMMITTEE

Val R. Swail, Chairman
Atmospheric Environment Service

Ross D. Brown
Atmospheric Environment Service

David Szabo
Mobil Research and Development Corp.

Langley R. Muir
Office of Energy Research and Development

J. Ron Wilson
Marine Environmental Data Service

John F. Garrett
Institute of Ocean Sciences

Kirk Johnstone
Atmospheric Environment Service

WORKSHOP SPONSORS

Environment Canada - Atmospheric Environment Service

Panel on Energy Research and Development

Canada Oil and Gas Lands Administration

Canadian Meteorological and Oceanographic Society

AUTHOR INDEX

abstract only - full paper not available
* abstract only - if received in time, full paper will appear at back of book

TABLE OF CONTENTS

FIELD EVALUATION OF NDBC DIRECTIONAL WAVE DATA

David B. Gilhousen

National Data Buoy Center
Stennis Space Center, Mississippi

Since 1987, the National Data Buoy Center (NDBC) has deployed buoys at eight locations with capability to measure directional wave data. Several comparisons were performed to assess the quality of data. These included comparisons of wave spectra from standard nondirectional systems with those produced by the directional system on the same buoy. Another comparison was conducted of directional wave spectra for a pair of directional wave buoys located within a few miles of each other in the Gulf of Mexico. Both these comparisons produced favorable results. Finally, wind directions were compared with wave directions at frequencies above 0.20 Hz under certain restricted wind conditions. In addition to further validating the wave data, these results will be used to improve a monitoring algorithm that flags suspicious wind or wave data.

A number of computer graphic displays were produced to examine these data. These graphics were animated to show how the spectra changes when winds increase or shift direction.

1. INTRODUCTION

In 1983, the National Data Buoy Center (NDBC) initiated development of a Directional Wave Analyzer (DAIA) system. This system for pitch-roll buoys is based on the methods of Longuet-Higgins (1963) and experience from earlier NDBC wave measurement experiments. The DWA sensors consist of a Datawell "Hippy 40" heave, pitch, roll sensor and a two-axis magnetometer to measure hull orientation. The DWA transmits partially processed data through the GOES satellite to the National Weather Service Telecommunications Gateway where real-time messages are transmitted each hour. Data are also processed at NDBC where they are monitored and edited for archival at the National Oceanographic Data Center. The theory and approach used in the DWA system is given by Steele et al. (1985) and a description of the data products is given by Lang (1986).

Figure 1 shows DWA deployment locations, station numbers, water depths, and deployment intervals. All deployments have been funded by other U.S. government agencies, such as the U.S. Army Corps of Engineers (USCOE) and elements of the U.S. Navy. The systems have been installed on 3-meter discus hulls at all stations, except for 46025 where a 10-meter discus hull is used (Steele, 1988), and 42007 where a 12-meter discus hull is used.

Directional wave data are thought to be of excellent quality because of extensive verifications and calibrations (Steele et al., 1985).

These include predeployment tests of the Hippy 40 by displacing and rotating the sensor to verify measured heave, pitch, and roll. Numerical simulations of Hippy 40 and magnetometer outputs are fed to each DWA microprocessor to verify the calculated results. Algorithms correct the azimuth angles for induced as well as fixed magnetic fields in each hull. Shoreside processing adjusts the spectrum for hull-mooring response.

In order to document the quality of DWA data, field intercomparisons were performed similar to those performed for wind data (Gilhousen, 1987). First, DWA displacement spectrum and significant wave heights were compared with measurements made by NDBC's standard one-dimensional system on the same buoy. Second, two buoys measuring DWA data were moored within 3.5 miles of each other off the entrance to Mobile Bay, Alabama. Wave directions were then compared in the portion of the spectrum which would be unaffected by water depth. Third, high frequency wave directions were compared with wind directions under certain restricted wind conditions. In addition to further validating the wave data, this study was performed to improve a monitoring algorithm that flags suspicious wind or wave data. Finally, a number of animated computer graphic displays were produced to see if the spectra changes observed appear reasonable when winds increase or shift directions.

2. INTRABUOY COMPARISONS

A DWA system has been operating in a 10-meter discus buoy at station 46025 off southern California since January 1986. A standard one-dimensional wave-measuring system, called the WDA, was also installed on the same buoy.

Therefore, the measured wave energy could be compared between two systems. The mean difference in significant wave height for 729 hourly observations during May 1988 was 0.01 meter. The standard deviation of the differences was 0.08 meter. However, an interesting difference between the significant wave heights does exist. Figure 2 shows that the heights from the DWA system are systemically slightly higher than the heights from the WDA system in heights more than 2.0 meters. Causes of these differences are not known and are being investigated. However, these differences are considerably less than the 10-15% variations of significant wave height due to sampling variability for finite record lengths (Donelan and Pierson, 1983) and are thus of little practical consequence.

Two correlation coefficients were calculated each hour. A correlation coefficient was calculated between all nondirectional spectra based on DWA wave heave motion, $C_{11}(f)_{DWA}$, and the same spectra measured by the WDA system, $C_{11}(f)_{DWA}$, for f(Hz) between 0.03 and 0.35 Hz. A second

correlation was computed between $C_{11}(f)_{DWA}$ and the nondirectional spectra based on DWA wave slope motion, $C_{11S}(f)$ (Steele and Lang, 1988). Figure 3 shows the frequency distributions of these correlation coefficients for May 1988. Spectra measurements are highly correlated and have similar frequency distributions. Thus, the DWA system is producing spectra with the same shapes and peaks as the WDA system. Also, since C_{11S} is well correlated with C_{11}, it could be used as a quality control tool.

3. INTERBUOY COMPARISONS

In 1988, the USCOE funded a DWA station, identified as buoy station 42016, approximately 3.5 miles NE of another USCOE-funded DWA station, 42015. These stations are located at the entrance to Mobile Bay, Alabama (see Figure 4), to study the effects of an underwater mound produced by dredging. The mound, located southeast of 42016, reduces the water depth to 30 feet, so waves with a frequency of less than 0.29 Hz would be depth-limited. However, wave directions in frequencies above 0.29 Hz should agree well.

To determine how well these directions agreed, DWA data from 42015 and 42016 were analyzed for a period immediately after 42016's deployment, April 25-May 31, 1988. DWA systems produced two measurements of wave direction at each frequency, the mean wave direction, $\alpha_1(f)$, and the principal wave direction, $\alpha_2(f)$. Because α_1 has greater continuity in time and frequency, α_1 was chosen for data analysis. A mean α_1 for the frequencies 0.30-0.35 Hz was calculated for both buoys and these directions were then compared under two conditions. First, there had to be adequate wave energy in this band. The criteria that C_{11}(0.32 Hz) must be greater than 0.03 m^2/Hz was chosen after examining the data. Second, events where wave directions were rapidly changing were eliminated. More specifically, cases were removed if α_1 changed by more than 20° per hour at either buoy. This reduced the chance that legitimate discontinuities in the wave field between the buoys due to rapidly changing winds would affect the comparison. Of the 888 possible cases, 306 met these criteria. The mean wave direction difference was only - 1.3° and the standard deviation of differences was 10.02°. Figure 5 is a histogram showing these wave direction differences along with a fitted normal curve. Figure 6 shows a scatterplot of those wave directions. Most of the waves originated from the open Gulf and, therefore, had a long fetch. The few large differences in wave direction were associated with northeasterly wave directions with a limited fetch.

In order to assess the significance of these statistics, a similar comparison was made for wind data. Comparable stratification conditions were chosen. The wind speed had to exceed 1.5 m/s and cases

featuring hourly speed changes greater than 2.5 m/s or direction changes greater than 30 degrees were eliminated. Figure 7 is a histogram showing these wind direction differences between 42015 and 42016. The mean difference is 1.5 degrees with a standard deviation of 8.45 degrees. These statistics show that wave direction differences between adjacent buoys are about the same magnitude as the wind direction differences. Thus, the DWA produces consistent results in the field and wave directions from adjacent buoys agree as well as wind directions from the same buoys.

4. WIND-WAVE COMPARISONS

Additional validation was performed by comparing high frequency wave directions with wind directions under certain restricted wind conditions. The wave direction at 0.35 Hz was chosen because high frequency waves respond most quickly to changes in wind direction. Average wind speed and direction over the last 3 hours were used for this comparison. This reduces the hour-to-hour variability due to the small (8.0-minute) sampling period of our hourly winds. Also, the wave direction is better correlated to the wind direction observed an hour or two ago than to the present direction. In order to consider cases with ample wind and wave energy, we included just those cases where the wind speed was greater than 7 m/s and C_{11}(0.35 Hz) was greater than 0.03 m^2/Hz. Finally, cases were eliminated if the wind direction changed by more than 30 degrees in the last 2 hours to give the sea time to respond to changing wind direction.

This comparison was performed for data collected during January 1988 at buoy station 44006. Figure 8 shows the location of 44006. This station and time period were chosen because of a large number of high wind episodes. Figure 9 shows a histogram of wave-wind direction differences for the 306 cases that met the above criteria. Good agreement between the two directions was observed, with a mean difference of only 1.1°. The distribution is approximately normal with a standard deviation of 11.4°. Therefore, the difference between wind and wave direction is comparable to those obtained between two adjacent buoys recording wave directions. The DWA measurement system is totally independent of the wind measurement system, so this comparison provides some indication of the accuracy of the DWA system. Furthermore, NDBC is developing a monitoring algorithm based on this comparison. This algorithm will be executed regularly to aid detection of failing DWA or wind measurement systems.

A scatterplot of the wind versus wave directions shown in Figure 10 reveals several interesting biases. When the wind blew from the southwest, the wave directions were more southerly than the wind. When the wind blew from the northwest, the wave directions were more

northerly than the wind. No such bias is apparent in easterly winds. Because this buoy is located only 10 miles from the coastline which is oriented approximately north-south, wave refraction and fetch effects are a possible cause of these biases. The month of December 1987 was chosen because the winds blew from a greater variety of directions than in January 1988,

5. ANIMATION OF DIRECTIONAL WAVE DATA

Computer graphic displays of selected DWA data were animated to show how the spectra changes when winds increase or shift direction. Figure 11 shows a plot of $C_{11}(f)$ and $C_{11S}(f)$ versus frequency on the lower graph and $\alpha_2(f)$ versus frequency on the upper graph. The solid horizontal line on the upper graph gives the wind direction. The solid vertical line on the lower graph is the inflection point on the Pierson-Moskowitz spectrum based on the current wind speed. Energy in frequencies above this line mainly result from the local wind as opposed to swell.

Figure 11 depicts the spectrum at a single time, 1800 UTC on January 7, 1988, at buoy station 44006. A spectral peak is present in the range 0.14-0.16 Hz with wave directions 15°-39°, in approximate agreement with the wind direction, 34°, averaged over the last 3 hours. Over the course of the next 3 hours, the wind shifted to approximately 70°. Figure 12 depicts the spectrum 6 hours later at 0000 UTC on January 8, 1988. Though the significant wave height has only dropped 0.2 meter, a much broader spectrum is observed. The waves with frequencies from 0.14-0.19 Hz are still moving in the original direction of 35°. However, α_1 and α_2 for spectral peaks at successively higher frequencies are getting closer to the current wind direction of 72°. From an animated sequence of such plots, it appeared that small spectral peaks would emerge with frequencies greater than 0.25 Hz and with wave directions slightly more adjusted to the wind direction. These small peaks would rapidly propagate to lower frequencies, thereby gradually adjusting the wave direction of the spectral peak. Several other cases of 30°-60° wind shifts were animated with similar results.

Young, et al. (1987), modeled changes in spectra which result from wind shifts of 30°-180°. They found that for wind shifts 60° or less the wind-sea direction adjusts smoothly, but that for larger shifts a second independent wind-sea spectrum is generated in the new wind direction. In order to validate these results, several cases featuring large wind shifts were investigated.

Figure 13 is a plot of the DWA data from buoy station 42014 at 0500 UTC on March 8, 1987. The spectral peak at 0.12 Hz appears to be swell, with the peak at 0.15-0.16 Hz the wind-driven sea. Between 0700

and 1000 UTC, the wind shifts from 50° to 260°–270°. Figure 14 shows the DWA plot at 1100 UTC. It shows that the waves associated with the old wind direction at 0.14 Hz are greatly diminished, while a new spectral peak aligned with the wind emerges at 0.25 Hz. Thus, these data support the results of Young, et al.

6. PROBLEM SPECTRA

During the passage of several tropical cyclones at 42016 and 41008, a problem surfaced concerning low frequency wave directions. Sporadically, low frequency waves would be shown to come from nearby land, 180 degrees out of phase with the directions at the same frequency from previous hours. Figure 15 shows an example of obviously bad data. Both α_1 and α_2 at the frequency with the most energy, 0.10 Hz, are coming from the west (260°) while the higher frequency energy comes from the east. Given the position of 41008, it is impossible for these large swells to be produced with only 22 miles of fetch.

Perhaps steep or breaking waves at these shallow water sites are causing the buoy not to follow the surface of the water. This violates the assumptions underlying the measurement theory, and the final measurements became contaminated. Only about 20 hourly observations out of approximately 20,000 have these problems. However, these observations were archived before the problem was identified. In the future, an algorithm will be added to make sure that swell does not come from directions of limited fetch.

7. CONCLUSIONS

A field intercomparison of DWA data with a WDA system shows mean significant wave height differences of 0.01 meter and standard deviations of 0.08 meter. Comparisons with a collocated DWA buoy, and wind directions show mean directional differences of about 1° and standard deviations of about 10°. Wave directions at adjacent buoys compare about as well as the wind directions under certain conditions. Spectral changes during wind shifts appear to confirm the results of Young, et al. (1987). A few cases of bad directional swell data were noted with steep waves in shallow water, and an algorithm will be added to prevent such data from being archived.

Overall, these initial comparisons place confidence in the quality of DWA directional wave data. These data are expected to have considerable value for marine forecasts as well as scientific studies, such as wave modeling.

about as well as the wind directions under certain conditions. Spectral changes during wind shifts appear to confirm the results of Young, et al. (1987). A few cases of bad directional swell data were noted with steep waves in shallow water, and an algorithm will be added to prevent such data from being archived.

Overall, these initial comparisons place confidence in the quality of DWA directional wave data. These data are expected to have considerable value for marine forecasts as well as scientific studies, such as wave modeling.

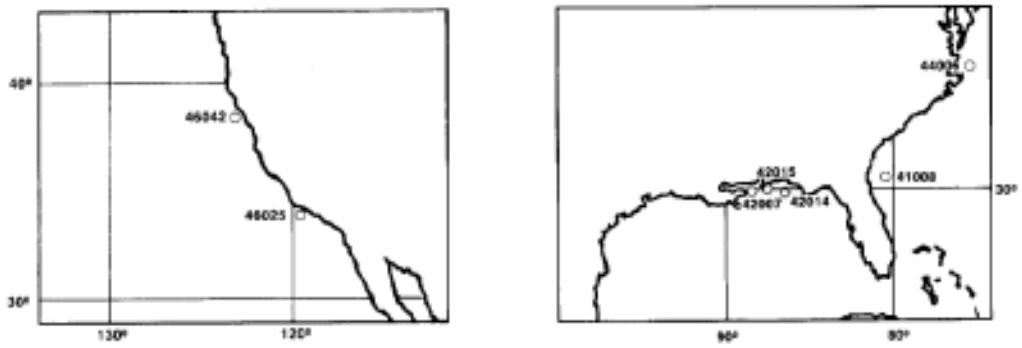

DEPLOYMENT #	USER	HULL	STATION #	LOCATION	LATITUDE/ LONGITUDE	WATER DEPTH (M)	MOORING TYPE	DEPLOYMENT INTERVAL
1	NCEL	10D04	46025	27 nmi SE Port Hueneme, CA	33°44'48" N 119°04'06" W	839	Inverse Catenary	1/22/86 Present
2	NDBC	3D12	42014	80 nmi south of Pensacola, FL	29°15'42" N 87°25'53" W	1005	Inverse Catenary (Heavy)	1/27/87 4/21/87
3			42015	5 nmi south of Dauphin Island, AL	30°08'56" N 88°10'02" W	17	All Chain (Light)	4/22/87 7/14/87
4	COE				30°08'56" N 88°10'06" W	16	All Chain (Heavy)	7/20/87 Present
5		3D14	46042	Mouth of Monterey Bay, CA	36°46'31" N 122°12'32" W	581	Inverse Catenary (Light)	6/17/87 8/10/87
6					36°45'54" N 122°13'29" W	640	Inverse Catenary (Heavy)	9/02/87 Present
7		3D15	44006	10 nmi east of Duck Pier, NC	36°14'20" N 75°32'42" W	26	All Chain (Heavy)	9/12/87 3/11/88
8			41008	Near St. Marys Inlet, GA	30°43'48" N 81°04'48" W	20	All Chain (Heavy)	3/15/88 Present
9			42007	OTP	30°05'24" N 88°46'12" W	13	All Chain (Heavy)	8/29/88 Present

Figure 1. Locations of buoys measuring DWA data. The station identifier appears near the station circle. The water depth, deployment, and recovery dates appear in the table.

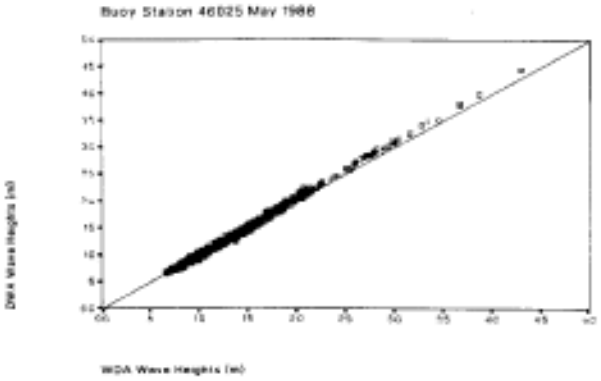

Figure 2. Significant wave heights measured by a DWA system versus those measured by a WDA system on the same buoy.

Figure 3. A population pyramid comparing frequency distributions for two correlations. The distribution on the right shows the correlations between C_{11} of the DWA system with those measured by the WDA system at the same buoy and the same hour. The distribution on the left shows similar correlations between C_{11} and $C_{11\delta}$.

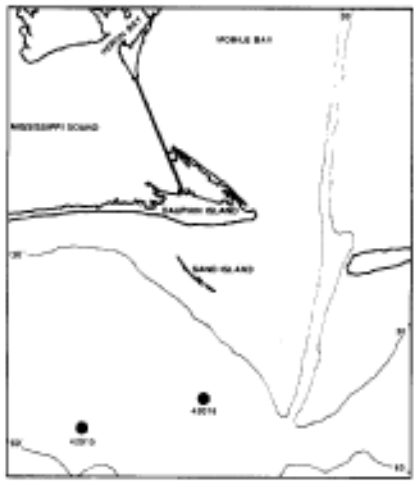

Figure 4. Map showing the location of buoy stations 42015 and 42016.

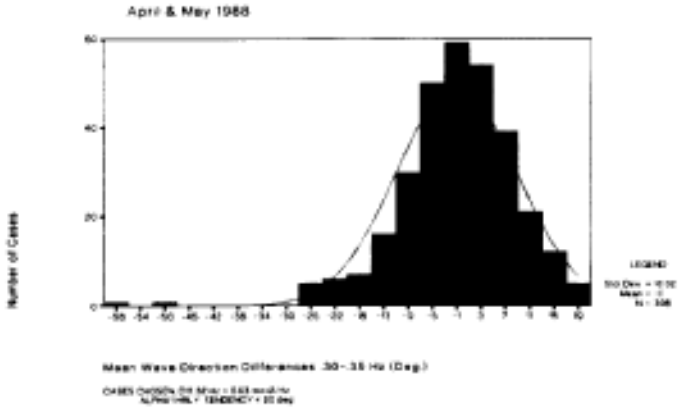

Figure 5. Wave direction differences between buoy station 42015 and 42016. See text for details.

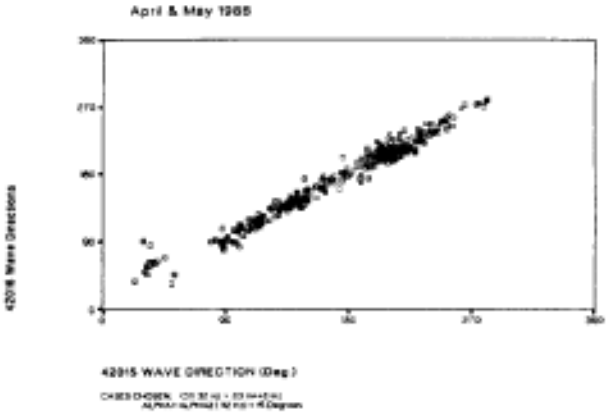

Figure 6. Scatterplot of 42015 versus 42016 wave directions. See text for details.

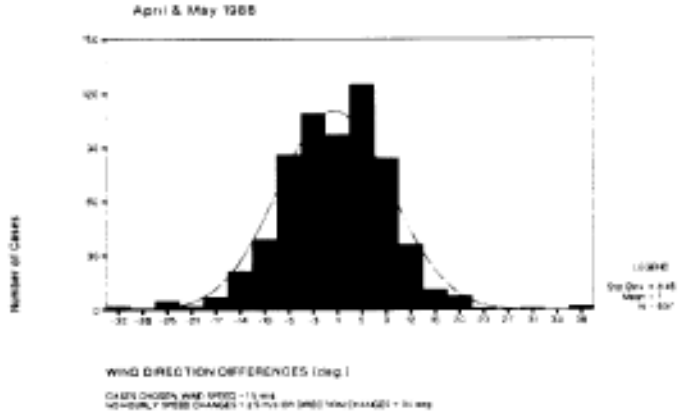

Figure 7. Wind direction differences between 42015 and 42016.

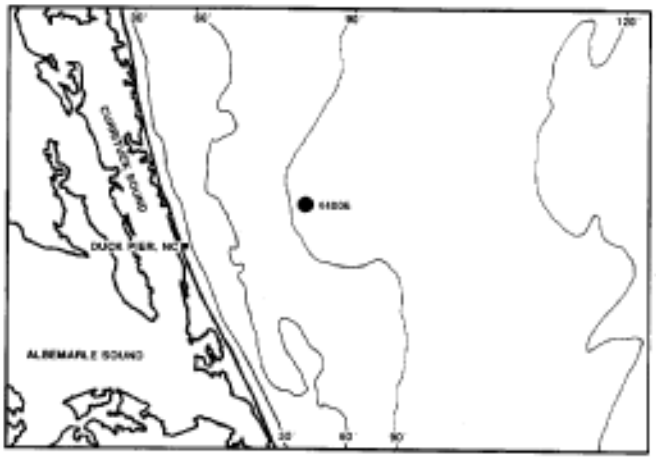

Figure 8. Map showing the location of buoy station 44006.

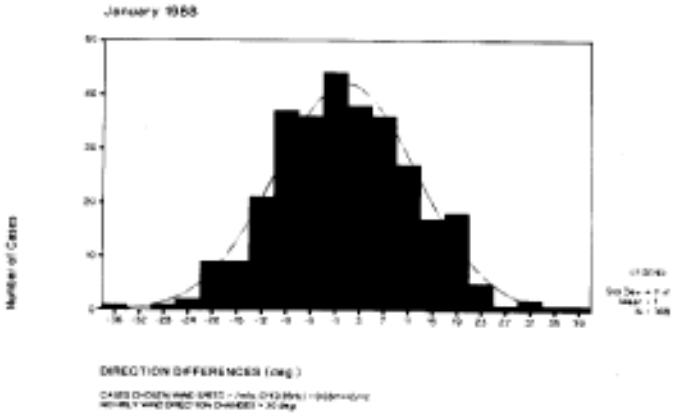

Figure 9. Wave-wind direction differences at station 44006 during January 1988. See text for details.

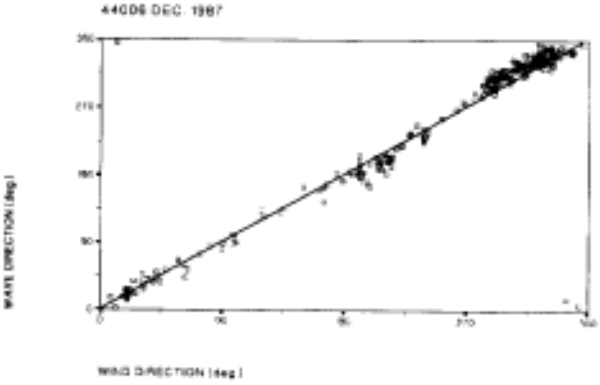

Figure 10. Scatterplot of wind versus wave directions.

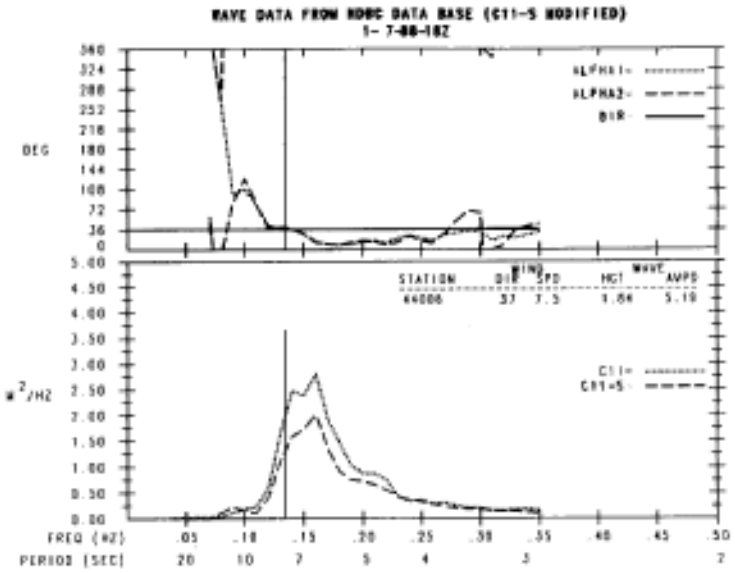

Figure 11. Plots of spectral density and wave direction versus frequency for a single time. See text for details.

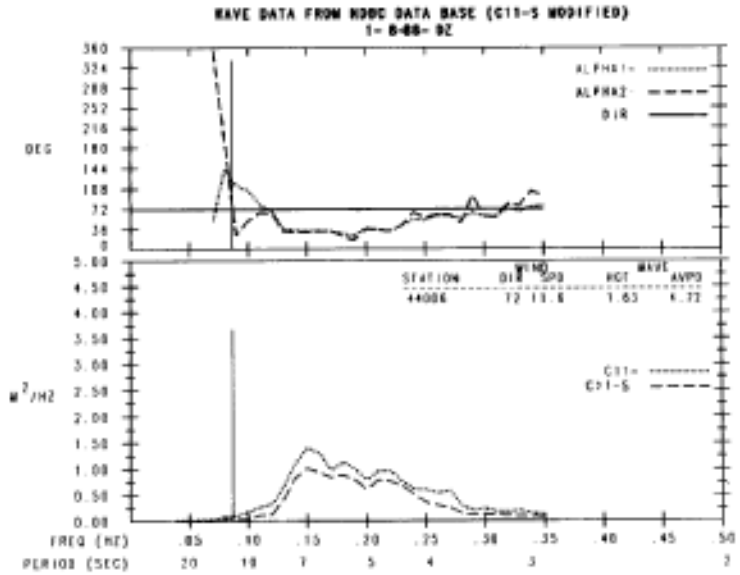

Figure 12. Same as Figure 10, but for a time 6-hours later after a 35° wind shift.

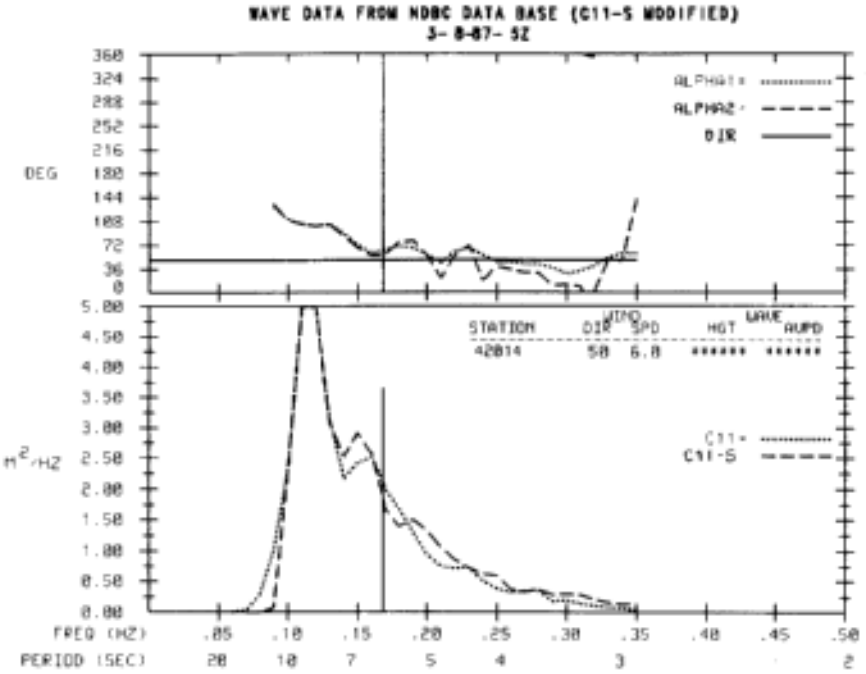

Figure 14. Same as Figure 12, but at 1100 UTC after a 160° wind shift.

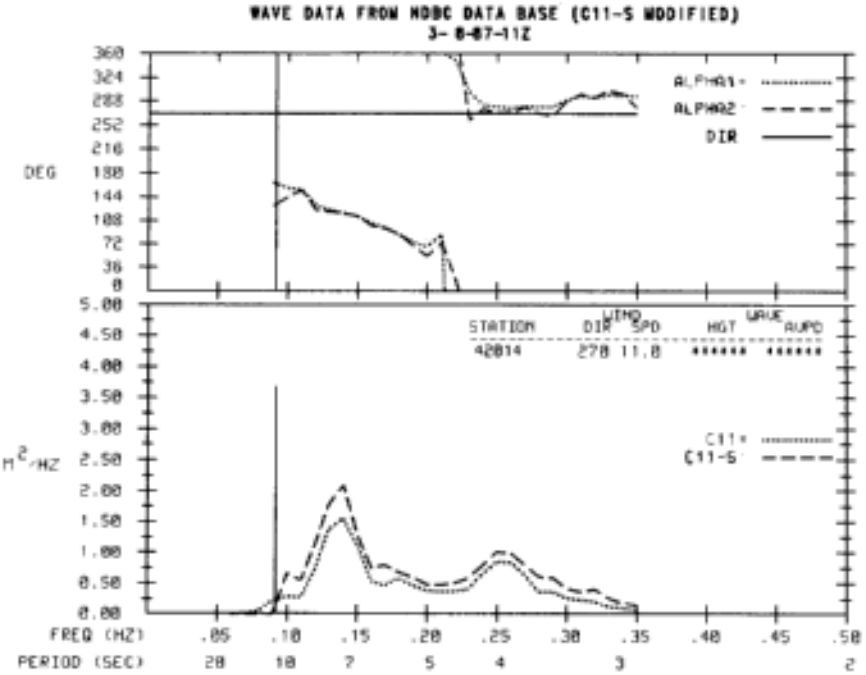

Figure 13. Same as Figure 10, but for buoy station 42014 at 0500 UTC on March 3, 1987.

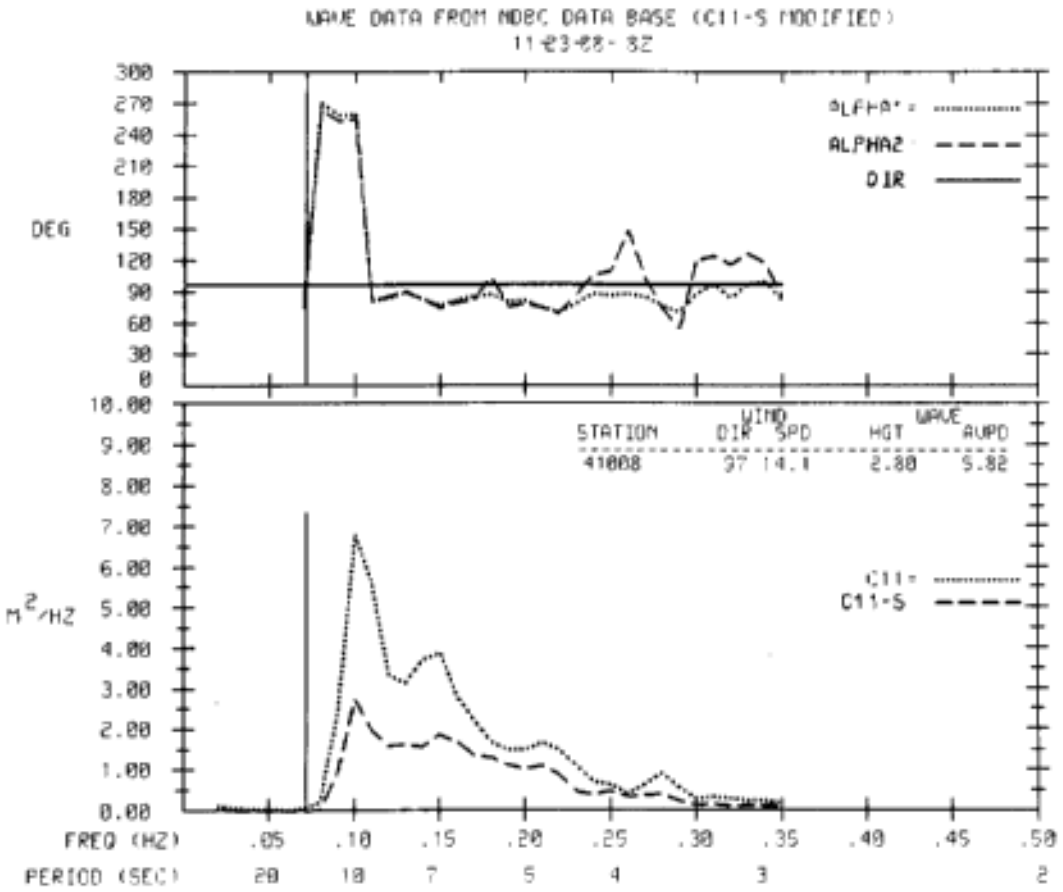

Figure 15. Same as Figure 13, but for buoy station 41008 at 0800 UTC on November 23, 1988.

8. REFERENCES

Donelan, M. and W. J. Pierson, 1973: The Sampling Variability of Estimates of Wind-Generated Gravity Waves, *Journal of Geophysical Research*, 88, 4381-4392.

Gilhousen, D.B., 1987: A Field Evaluation of NDBC Moored Buoy Winds. *J. Atmos. Ocean. Tech.*, 4, 94-104.

Lang, N., 1986: NDBC Wave Data Products - Present and Future. *Proceedings Marine Data Systems International Symposium*, New Orleans, Marine Technology Society, 54-58.

Longuet-Higgins, M.S., D.E. Cartwright, and N.O. Smith, 1963: Observations of the directional spectrum of sea waves using the motions of a floating buoy. *Ocean Wave Spectra*. Prentice Hall, New York.

Steele, K.E., J.C. Lau, and Y.L. Hsu, 1985: Theory and Application of Calibration Techniques for an NDBC Directional Wave Measurements Buoy. *IEEE Journal of Oceanic Engineering*, OE-10 No. 4, 382,-396.

Steele, K.E. and N. Lang, 1988: Samples of NDBC Directional Wave Data. *Preprints 4th Conference on Meteorology and Oceanography of the Coastal Zone*, Anaheim, Amer. Meteor. Soc., 50-57.

Young, I.R., S. Hasselmann, and K. Hasselmann, 1987: Computations of the Response of a Wave Spectrum to a Sudden Change in Wind Direction. *J. Phys. Oceanogr.*, 17, 1317-1338.

ON THE RELATIONSHIPS BETWEEN FETCH, WAVE AGE AND WIND STRESS COEFFICIENT AS REVEALED BY THE CASP (CANADIAN ATLANTIC STORMS PROGRAM) WIND AND WAVE DATA

M.L. Khandekar

Atmospheric Environment Service
Downsview, Ontario.

1. INTRODUCTION

The Canadian Atlantic Storms Program (CASP) was an intensive observational program aimed at studying the evolution of winter storms that affect the Canadian Atlantic provinces. A large amount of meteorological and oceanographical data was collected during the CASP field project (15 January - 15 March, 1986) over the Scotian Shelf and the Grand Banks area of the Canadian Atlantic. In conjunction with the data collection and analysis program, two spectral ocean wave models were run in an operational mode to generate sea-state analysis and forecast over the Canadian Atlantic. Both the wave models were driven by winds obtainable from the operational weather prediction model of the Canadian Meteorological Centre (CMC) in Montreal. In addition, one of the models was also driven, in tandem, by winds based on a 'man-machine mix' procedure; this allowed an examination of the impact of wind specification on the model performance.

In this paper, the observed wind and wave data collected at three deep-water regions (see Figure 1) in the Canadian Atlantic were analyzed for selected storm periods to obtain relationships between various non-dimensionalzied parameters like wind stress coefficient (commonly known as the drag coefficient), wave age and fetch. These relationships were further examined in the light of theoretical relationships developed recently by Wu (1985). The model generated wind and wave products were evaluated against the observed data by calculating error parameters like Root Mean Square (RMS) error, Scatter Index (SI) etc., the model products were further analyzed in the context of theoretical relationships (developed by Wu) among the various parameters. Finally, the utility of this study for operational wave analysis and modelling is discussed.

2. THE MODELS

The two spectral wave models used in the study are identified as the ODGP and the WAVAD models. The ODGP (Ocean Data Gathering Program) model is a first generation model developed by Cardone et al (1976) and is based on the well-known spectral energy balance equation in which each spectral component is assumed to grow independent of all other components in accordance with an essentially linear input source function until the energy of each spectral component approaches its

limiting 'saturation' level. The Pierson-Moskowitz (P-M) spectrum is used to model transition from the growing sea to the fully developed sea. The ODGP model uses 24 direction bands and 15 frequency bands to express the energy spectrum at any given point. The ODGP model operates over a nested grid covering the northwest Atlantic; the coarse grid of the model has a spacing of 1.25° latitude by 2.5° longitude while the nested fine grid covering the Canadian Atlantic Shelf region has half the spacing of the coarse grid. More details on the model physics are available in a report by MacLaren Plansearch Ltd. (1985) prepared for the Atmospheric Environment Service.

During the CASP field project, the ODGP model was driven by boundary layer winds extracted from the lowest active level of the CMC weather prediction model. The lowest level was set at σ=0.998 where σ is the ratio p/p_s, p being the pressure at the level in question and p_s is the sea-level pressure. In a standard atmosphere, the level σ=0.998 corresponds to approximately 17m above the sea-level. The ODGP model was also driven by winds generated by a 'man-machine mix' procedure in which the north Atlantic surface weather charts were reanalyzed based on latest ship weather reports and then digitized. The boundary-layer model of Cardone (1969) was then applied to generate effective neutral winds at 20m level above the ocean surface. The ODGP model products obtained using the two wind fields were identified as ODGP-CMC and ODGP-OPR respectively.

The WAVAD is a second generation spectral wave model applicable to arbitrary water depths and has been developed by Resio as an extension of his deep-water model (Resio,1981). The WAVAD model uses a new theory of equilibrium spectral shapes in waters of arbitrary depths; these equilibrium shapes are maintained by a mechanism which provides a strong flux of energy towards high frequencies where it is lost due to wave breaking. A dynamic balance between wind input and nonlinear flux dominates the shape of the spectrum and controls energy level and energy loss in waves propagating to water depths of 10m or less. The bottom friction is considered as a free parameter in the model and is included only for long period swell waves with little or no wind. For the duration of the CASP field project, the WAVAD model was operated on a coarse grid (2° latitude by 2° longitude) covering the northwest Atlantic and two nested grids covering the Canadian Atlantic Shelf region. More details on the WAVAD model are available in a report by NORDCO Ltd. (1986) prepared for the Atmospheric Environment Service. The WAVAD model was driven by CMC winds during the CASP field project.

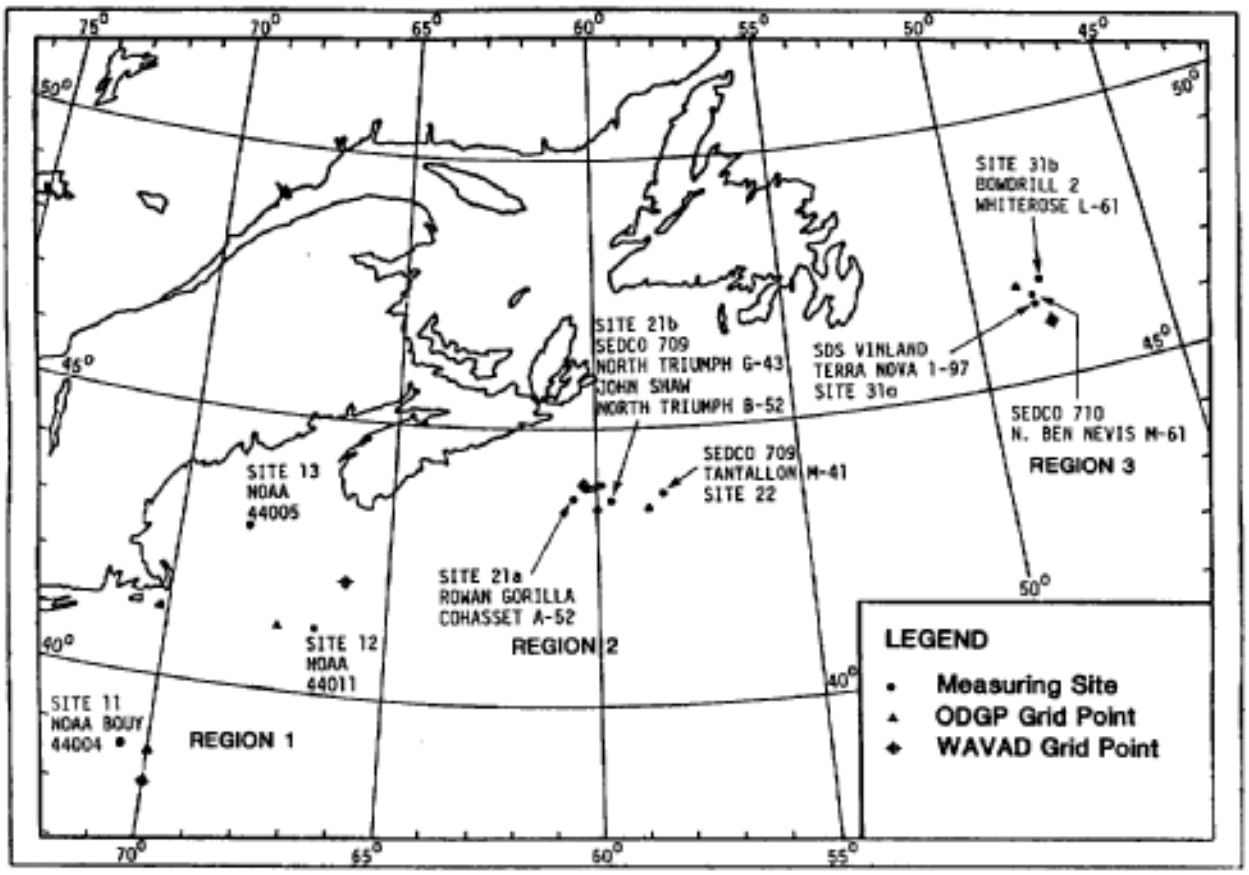

Figure 1: The CASP study area showing the various measuring sites and grid point locations over the three deep-water regions.

3. ANALYSIS OF OBSERVED DATA

As mentioned before, wind and wave data were measured and archived at three deep-water regions (of Figure 1) in the Canadian Atlantic during the two months of the CASP field project. During this period (15 January–15 March 1986) as many as 16 storm cases were recorded which were identified as Intensive Observing Periods (IOP). We have selected two IOP in this study for which the storm tracks are shown in Figure 2 .

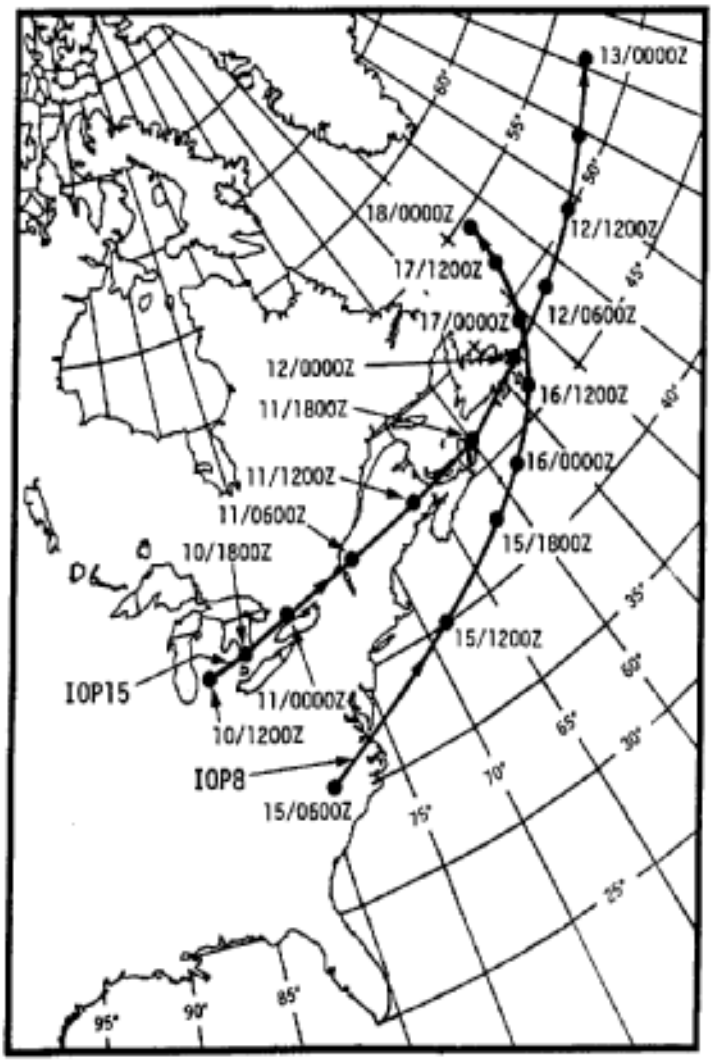

Figure 2: The storm tracks for two selected IOP (Intensive Observing Periods) during the CASP field project.
IOP8: 15-18 February 1986; IOP15: 10-13 March 1986

For these two storm periods, values of wind speed, wave height and wave period as recorded at the sites 11, 21a and 21b were used to obtain the following nondimensional parameters:

1. Drag coefficient = C_D. In this study, we have considered the variation of drag coefficient with wind speed as proposed by Wu(1980). According to Wu's formula the drag coefficient variation is expressed as:

$$C_D = \begin{cases} 1.2875 \times 10^{-3} & \text{for wind speed } U < 7.5 \text{ ms}^{-1} \\ (0.8+0.065U) \times 10^{-3} & \text{for } U \geq 7.5 \text{ ms}^{-1} \end{cases}$$

The above expression provides a linear increase in drag coefficient with wind speed.

2. Fetch = gL/U^2. Here g is the gravitational acceleration, L is the over-water fetch and U is the wind speed. The value of L was estimated at each of the three recording sites from the six-hourly surface weather charts available for the duration of the two storm periods.

3. Wave age = c/U_*. Here c is the phase speed of the dominant wave and U_* is the friction velocity defined as $U_* = U\sqrt{C_D}$. The phase speed c was calculated from the ratio L/T where L is expressed using the deep-water wave phase speed formula so that L (meters) $\approx 1.56T^2$ (seconds). Using the measured values of the peak period for T, the wave age was calculated at the three recording sites, 11, 21a and 21b respectively. Since the values of the peak period were not available at the Grand Banks site (31a), that site was not included in the calculations.

Having obtained the values of three nondimensionalized parameters, these parameters were plotted against each other to determine the relationships amongst them. Three sets of plots are presented in Figure 3 , showing variations of drag coefficient vs. wave age, wave age vs. fetch and drag coefficient vs. fetch respectively. The plots are drawn separately for site 11 (a deep-water location with water depth over 2800m) and for sites 21a and 21b together (both sites located on the Scotian Shelf with water depths between 50 and 100m).

The variations of the three non-dimensionalized parameters as displayed in Figure 3 have been theorized in a recent study by Wu (1985) who has developed the following two equations connecting the three variables:

$$C_D = k/\ln[(gL/U^2)2/3(0.14/C_D)] \quad (1)$$

$$c/U_* = (0.05/\sqrt{C_D})(gL/U^2)^{0.3} \quad (2)$$

Here k is the von Karman constant and the remaining symbols have already been defined. From these two equations, an expression involving the drag coefficient (C_D) and the wave age (c/U_*) can be developed. The top panel of Figure 3 shows a logarithmic variation between the drag coefficient and the wave age as conjectured by Wu. The solid lines in the two scatter plots of the top panel represent the nonlinear regression curves obtained using least square fit to the data points showing the variation of drag coefficient with wave age. The mathematical form of the nonlinear regression curve is given by $y=\alpha+\beta\gamma^{\bar{x}}$ where α, β and γ are the coefficients to be determined; the nonlinear parameter γ is determined by an iterative technique, while the parameters α and β are computed by the standard least square equations. For the two scatter plots of the top panel in Figure 3 , the following regression equations were obtained:

$$C_D = 0.00124+0.00133\ (0.944)^{c/U_*} \text{ for site 11}$$

$$C_D = 0.00129+0.00154\ (0.944)^{c/U_*} \text{ for site 21} \quad (3)$$

Equation (3) suggests a logarithmic variation between C_D and c/U_*. From equations (1) and (2) it is possible to develop a formula

relating the drag coefficient and the wave age, which would be comparable to equation (3). Thus, the observed wind and wave data over the Canadian Atlantic can be reasonably well described by theoretical and empirical relationships developed by Wu. It may be noted here that in a recent study by Geernaert et al. (1987), a power law of the form $C_D=A(c/U_*)^B$ was used to investigate the relationship between the measured values of the drag coefficient and related wind and wave data.

4. ANALYSIS OF MODEL DATA

The wind and wave products generated by the two models (ODGP and WAVAD) were evaluated against the measured data at sites 11, 12, 21a 21b and 31a (see Figure 1) respectively. The model products generated at the grid points closet to these sites were used and all available data for the two storm periods were used. The model products were evaluated quantitatively using error parameters like RMS error, Scatter Index etc. The evaluation was made for the model products generated at analysis time (zero-hour forecast) as well as at 12- and 24-hour forcast times. Table I shows the various error parameters calculated in respect of three model products namely ODGP-CMC, ODGP-OPR and WAVAD respectively.

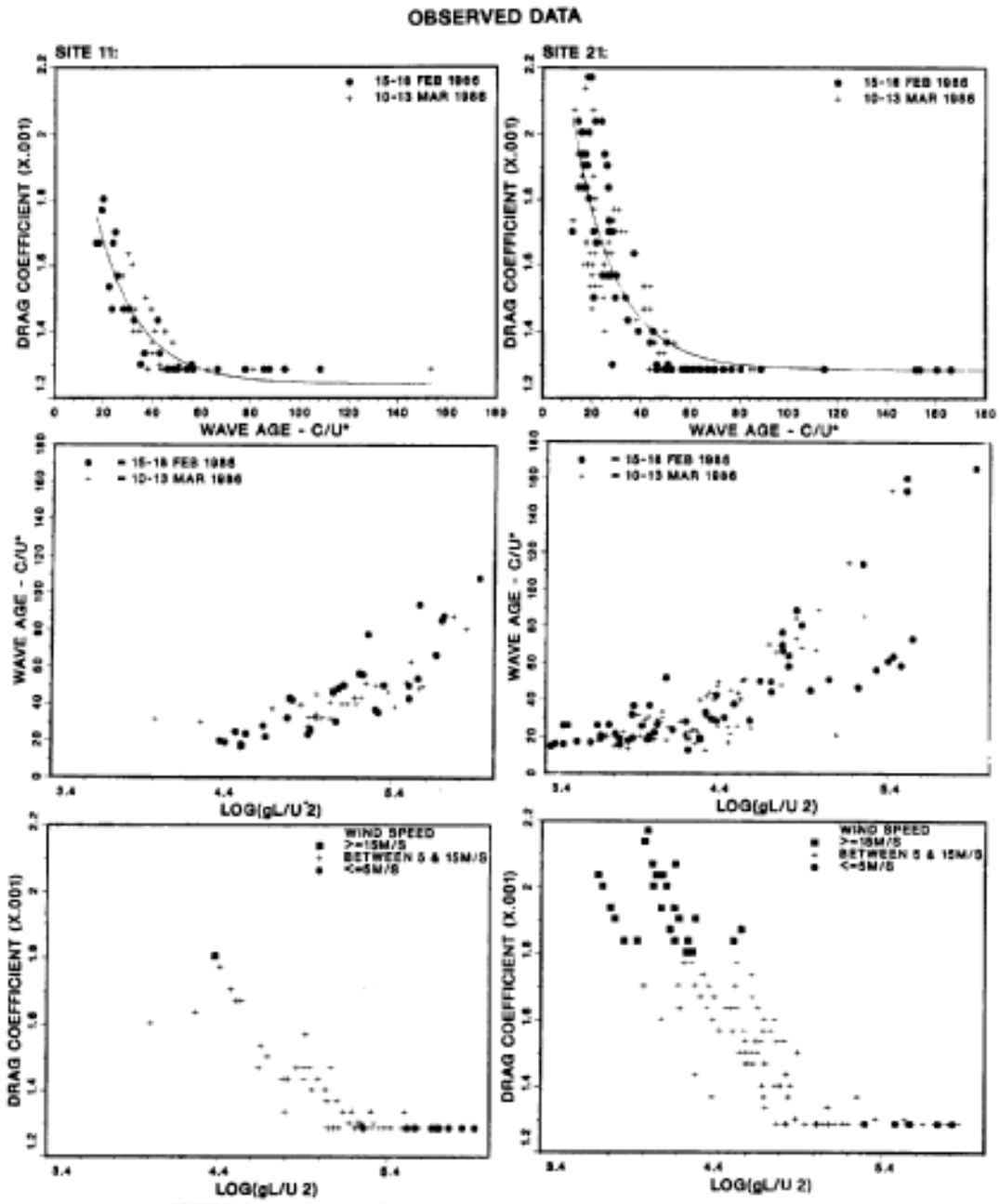

FIGURE 3: Scatter plots of drag coefficient vs wave age (top panel), wave age vs. fetch (middle panel) and drag coefficient vs. fetch (bottom panel) at sites 11 and 21 based on observed wind and wave data for two CASP storms.

TABLE I A statistical evaluation of wave models based on selected CASP storms

SUMMARY OF ERROR STATISTICS

Model	Parameter	WIND SPPED (Knots) Forecast Time 00hr	12	24	WAVE HEIGHT (Metres) Forecast Time 00hr	12	24	PEAK PERIODS (Seconds) Forecast Time 00hr	12	24
ODGP-CMC	RMSE	6.8	8.0	9.3	1.36	1.41	1.53	1.66	1.68	1.83
	ME	2.0	4.0	4.9	0.72	0.81	0.99	0.35	0.34	0.56
	SI	32	38	44	46	48	52	20	20	22
	r	0.81	0.78	0.72	0.82	0.82	0.81	0.56	0.54	0.49
	N	144	144	144	144	144	144	112	112	112
ODGP-OPR	RMSE	6.0	10.1	9.8	0.89	1.00	1.13	1.82	1.79	2.00
	ME	-0.4	1.4	1.8	0.11	0.13	0.17	-0.45	-0.35	-0.51
	SI	29	48	47	30	34	38	21	21	23
	r	0.83	0.60	0.64	0.87	0.84	0.81	0.54	0.54	0.52
	N	144	144	144	144	144	144	112	112	112
WAVAD	RMSE	6.1	7.1	9.7	1.12	1.30	1.37	2.49	2.47	2.37
	ME	-0.8	0.8	1.7	0.21	0.37	0.45	-0.86	-0.78	-0.48
	SI	30	35	47	36	42	44	29	29	28
	r	0.82	0.75	0.61	0.84	0.80	0.77	0.40	0.38	0.39
	N	112	112	112	112	112	112	112	112	112

RMSE = Root Mean Square Error = $\sqrt{1/N\Sigma(\text{Model}-\text{Observed})^2}$

ME = Mean Error (Bias) = $1/N\,\Sigma(\text{Model}-\text{Observed})$

SI = Scatter Index = RMSE x 100/Mean Observed value

r = linear correlation coefficient between model and observed value

N = number of data points

The Table reveals several interesting features of the wave model evaluation. The model ODGP-OPR provides the best error statistics in respect of wave height thus indicating that improved wind specification (through a 'man-machine mix' procedure) generates improved wave products in an analysis as well as in a forecast mode The error statistics in respect of wave period, however, does not show a similar improvement for ODGP-OPR; this may be due to the fact only two storm cases are considered here. The error statistics based on the complete 2-month CASP dataset (see MacLaren Plansearch Ltd., 1987) demonstrate clearly the improvement in wave products when improved wind specification is used to drive the ODGP model. The ODGP-CMC and the WAVAD model products are both obtained using essentially the same wind input namely, the CMC winds. (The WAVAD model uses a special interpolation scheme to generate winds for its doubly-nested grid); hence the difference in the error statistics for these two model products could be attributed to the differences in the model physics. For the two storm periods, the WAVAD model generates wave heights which show an improvement of up to ten percent or more over the corresponding wave heights generated by the ODGP-CMC. However, the peak period generated by the WAVAD model appears to be underestimated and weakly correlated with the observed values of the peak period during the two storm periods.

The model wind and wave products were further analyzed to investigate the relationship between the drag coefficient and the wave age. The drag coefficient values were calculated using the model wind speeds and Wu's formula as discussed earlier. The values of wave age were calculated using the values of the peak period generated by the models. In Figure 4 are shown the scatter plots of drag coefficient vs. wave age for the three model products namely ODGP-CMC, ODGP-OPR and WAVAD respectively. These scatter plots can be compared with the scatter plots in the top panel of Figure 3 which are obtained using observed data. In general, both the ODGP model products appear to depict a similar relationship between the drag coefficient and the wave age as that depicted by the observed data. The scatter plots for the WAVAD model (bottom panel of Figure 4) appear to suggest that the peak period is improperly modelled by the WAVAD. The present WAVAD model code does not have an algorithm to select a dominant period based on the maximum spectral energy; such an algorithm, according to Dr. Resio (personal communication), would provide an improved specification for the peak period.

5. CONCLUDING REMARKS

The observed wind and wave data collected during selected CASP storms over the Canadian Atlantic appear to support the theoretical relationships between the drag coefficient, wave age and fetch as

proposed by Wu(1985). An evaluation of the model products reveals that improved wind specification can provide improved model products in analysis as well as in forecast modes. The second generation WAVAD model appears to provide an improvement over the first generation ODGP model when both the models are driven by identical wind fields.

6. REFERENCES

Cardone, V.J., W.J. Pierson and E.G. Ward, 1976: Hindcasting the directional spectra of hurricane generated winds. J. Petroleum Technology, 28, 385-394.

Geernaert G. L., S.E. Larsen and F. Hansen, 1987: Measurements of the wind stress, heat flux and turbulent intensity during storm conditions over the North Sea. J. Geophy. Research, 92, C12, 13127-13139.

MacLaren Plansearch Ltd. 1985: Evaluation of the Spectral Ocean Wave Model (SOWM) for supporting real-time wave forecasting in the Canadian east coast offshore. Final Report prepared by MacLaren Plansearch Ltd. Halifax, Nova Scotia, January 1985, 159 pp + Appendices.

MacLaren Plansearch Ltd. 1987: Ocean wave model Intercomparison study for the duration of the Canadian Atlantic Storms Program (CASP) field project. Final Report prepared by MacLaren Plansearch Ltd., Halifax Nova Scotia, March 1987.

Nordco Ltd. 1986:: Wave forecast operational test during the Canadian Atlantic Storms Program (CASP) field project. Final report prepared by NORDCO Ltd. St. Johns, Newfoundland. NORDCO No. 297-85G, October 1986.

Resio, D.T., 1981: The estimation of wind-wave generation in a discrete spectral wave model. J. Physical Oceanography, 11, 510-525.

Wu, J., 1980: Wind-stress coefficients over sea surface near neutral conditions - A revisit. J. Physical Oceanography, 10, 717-740.

Wu, J., 1985: Parameterization of wind-stress coefficients over water surfaces. J.Geophy. Research, 90, C5, 9060-9072

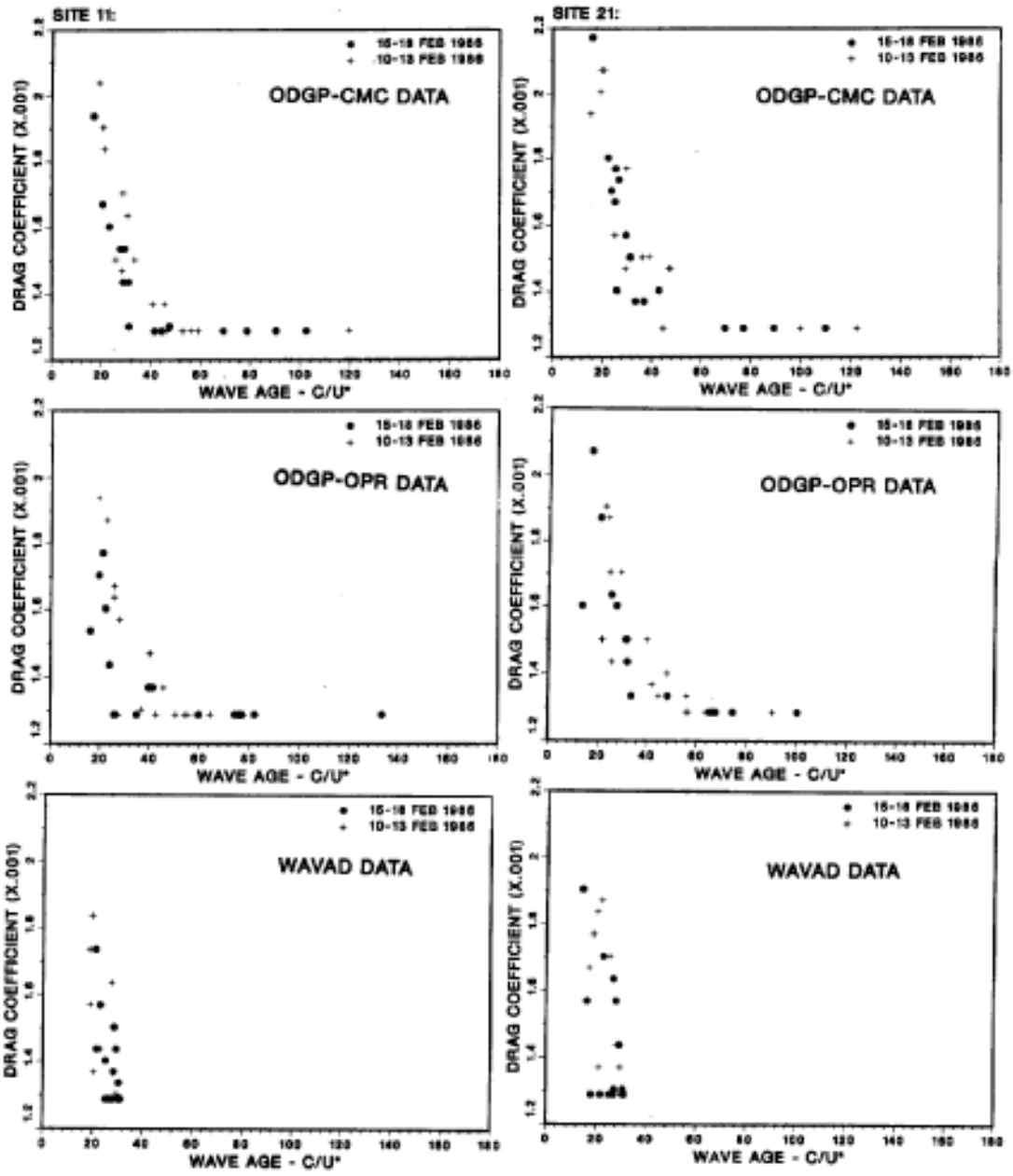

FIGURE 4: Scatter plots of drag coefficient vs. wave age based on wind and wave products generated by three models namely ODGP-CMC, ODGP-OPR and WAVAD.

DIRECTIONAL SPECTRA OF WAVES DURING CASP

Diane Masson

Institute of Ocean Sciences
Sidney, B.C.

ABSTRACT

During the Canadian Atlantic Storms Program, or CASP, an array of wave buoys was deployed along a 30 km line offshore from Martinique Beach, N.S. The array consisted of three directional buoys and six nondirectional buoys in water depths from 22m to 100m. Data collected by the three directional buoys (Datawell "Wavec" pitch/roll) are analyzed using the Maximum Likelihood Method (MLM). Several characteristics of the directional spectra are examined under various conditions, including turning winds.

WAVE DIRECTIONAL SPECTRA IN MIXED SEAS

[1]I.K. Tsanis and [2]M.A. Donelan

[1]Department of Civil Engineering
McMaster University
Hamilton, Ontario

[2]National Water Research Institute
Burlington, Ontario

ABSTRACT

Air-water interaction experiments were undertaken during a three year period (1985-1987) at the National Water Research Institute's (NWRI) Waves Tower on Lake Ontario for the "Deep Water Wave Breaking and Wave-Turbulence Interaction" project. A part of this experiment was to investigate wave directional spectra under different environmental conditions, i.e., fetch, wind direction (fetch gradient) and wind speed. The wave direction sensor was an array of six capacitance gauges arranged at the apices and centre of a pentagon. The principal method of analysis is the Maximum Likelihood Method (MLM) using the elevation data directly. For comparison with traditional floating buoy wave sensors, the gauge data is used to compute local slopes and curvatures and to construct the directional distributions that would be observed by pitch-roll-heave and cloverleaf buoys. The directional discrimination of these three methods is compared using test data with plane waves from various directions. The root-mean square spread for a mixed wind-sea and counter-swell case is compared for the three methods.

1. INTRODUCTION

Much of the information on directional spectra of wind waves and swell has been gathered from moored buoys. Most wave directional buoys measure pitch, roll and heave (eg. Hasselmann et al. 1980), but a few attempts to observe higher derivatives of the surface slope have been attempted (eg. Mitsuyasu et al. 1975). The resulting directional resolution of these methods is not very much better than the expected rms spread of wind seas and may be totally inadequate for distinguishing more than one swell component in a frequency bin or delineating the skewed distribution that may occur in rapidly turning winds or the appearance of double peaks (Phillips, 1957) in response to resonant wind forcing.

The Maximum Likelihood Method (MLM) has much greater resolving power (Jefferys, 1981 & 1986) but the resulting resolution (window) is dependent on the data (Pawka, 1983), and the observed directional distributions will be somewhat distorted. An efficient correction

procedure to the MLM has been derived (Krogstad et al., 1988), but we have not implemented this in the results presented below.

The data were collected from a fixed tower in Lake Ontario, (Tsanis & Donelan, 1987). The National Water Research Institute's Waves Tower is in 12 m of water, 1.1 km off the beach at the west end of Lake Ontario. In the Tower's location the shoreline is straight and the bottom slope is gentle. The annual water level variation is less than 0. 5 m. The location of the tower makes possible fetches from 1.1 km for west winds up to 300 km for east winds. Finally, every year Lake Ontario sees a number of wind episodes with speeds in excess of 15 m/s.

Capacitance type wave staffs are used as sensing elements to provide information for the water surface elevation changes, eg. Oakley et al. (1977). The wave staffs are teflon-coated wires 6 m in length with an overall diameter of 4.8 mm. Six wave staffs are arranged in a pentagon with one at the center (the distance between the wave staff at the center and the others is 0.25 m) and are held taut with rubber shock cords (490 N tension). The array is symmetrical resulting in smaller azimuthal differences in directional sensitivity and its size is appropriate for the wave periods of interest, i.e., 0.6 to 8.0 seconds. The wave staffs had a very stable linear calibration during the experimental period and were cleaned almost every week from any impurities and algae that had accumulated on them.

The wave staff data, after proper filtration and amplification, are digitized on the tower and transmitted via a system of modems, a microcomputer and an underwater cable to the data acquisition system in another microcomputer in a trailer on shore. The data are digitized at 20 Hz and the length of the different episodes are at least 80 minutes to ensure adequate wave statistics.

In the following sections we outline the methodology of the three analysis methods (section 2), explore the response of each method to mixed seas (section 3) and compare the observed spreading distribution for a case in which a strongly forced wind sea propagates against decaying swell (section 4).

2. OUTLINE OF METHODS

The three directional spectral methods used in the present work are briefly described.

(a) **Pitch-Roll Buoy**, eg. Longuet-Higgins (1964). The directional spectra can be determined by the information yielded by the motion of a buoy. The vertical displacement and angles of pitching and rolling of the buoy, can provide information on the water surface elevation $\zeta(x,y,t)$ and its slopes $\zeta_x(x,y,t)$ and $\zeta_y(x,y,t)$ in x and y directions,

respectively. In our study the elevation and the slopes are measured by using the information from all six wave staffs. The elevation of the wave staff at the center of the pentagon $\zeta_3(0,0,t)$ is used and the rest of the wave staffs are used for evaluating the slopes as follows

$$\zeta_x(0,0,t) = \frac{\partial \zeta}{\partial x}(0,0,t) = \frac{1}{2}\left[\frac{\zeta_1 - \zeta_3}{r(1,1)} + \frac{2\zeta_3 - (\zeta_5+\zeta_6)}{r(1,5)}\right] \quad (1)$$

$$\zeta_y(0,0,t) = \frac{\partial \zeta}{\partial y}(0,0,t) = \frac{1}{2}\left[\frac{\zeta_2 - \zeta_4}{2r(2,2)} + \frac{\zeta_5 - \zeta_6}{2r(2,5)}\right] \quad (2)$$

where r(i,j) are the coordinates of the wave staffs (i=1,2 for the x and y coordinate, respectively, and j=1,6 for the wave staffs). Figure 1 shows the wave staff array, the numbering of the wave staffs and the coordinate system orientation.

(b) **Cloverleaf Buoy**, eg. Cartwright and Smith (1964) & Mitsuyasu et al. (1975). The directional spectra can be determined by the information yielded by the motion of a cloverleaf buoy. The cloverleaf buoy measures the vertical acceleration ζtt, the slopes $\zeta x, \zeta y$, and curvatures $\zeta xx, \zeta yy, \zeta xy$ of the wave surface $\zeta(x,y,t)$. In our study, a second order polynomial

$$\zeta(x,y,t) = a_1(t) + a_2(t) + a_3(t)y + a_4(t)x^2 + a_5(t)y^2 + a_6(t)xy \quad (3)$$

is used to describe the water surface. Using Eq. (3) for the six wave staffs yields a system of six linear equations with six unknown coefficients $a_i(t)$, i=1,6. The system of equations is solved and the coefficients $a_i(t)$, i=1,6 are evaluated. The coefficients represent the elevation, slopes and curvatures of the water surface at the point (x,y)=(0,0), i.e.,

$$a_i(t) = \zeta(0,0,t) \quad (4\alpha)$$

$$a_2(t) = \zeta_x(0,0,t) = \frac{\partial \zeta}{\partial x}(0,0,t) \quad (4b)$$

$$a_3(t) = \zeta_y(0,0,t) = \frac{\partial \zeta}{\partial y}(0,0,t) \quad (4c)$$

$$2a_4(t) = \zeta_{xx}(0,0,t) = \frac{\partial^2 \zeta}{\partial x^2}(0,0,t) \quad (4d)$$

$$2a_5(t) = \zeta_{yy}(0,0,t) = \frac{\partial^2 \zeta}{\partial y^2}(0,0,t) \quad (4e)$$

$$a_6(t) = \zeta_{xy}(0.0,t) = \frac{\partial^2 \zeta}{\partial x \partial y}(0.0,t) \qquad (4f)$$

(c) **Maximum Likelihood Method** (MLM),eg. Capon (1969) & Jefferys et al. (1981). According to the Maximum Likelihood Method the energy incident from direction Θ is evaluated by minimizing the influence from all the other components. The minimization uses standard Lagrangian theory and leads to an estimate of the energy in the plane wave

$$E(\omega_k,\Theta) = [\chi^{*T}(\omega_k,\Theta) C^{-1}(\omega_k) \chi(\omega_k,\Theta)]^{-1} \qquad (5)$$

where k is the frequency index and $C^{-1}(\omega_k)$ is the inverse of the cross spectral density matrix. In terms of the energy spectrum $E(\omega_k,\Theta)$ from directions Θ_i in the frequency band near ω_k, the cross spectral density matrix is given by:

$$C(\omega_k) = \sum_{i=1}^{N} \chi(\omega_k,\theta_i)\, \chi^{*T}(\omega_k,\theta_i)\, E(\omega_k,\theta_i) \qquad (6)$$

where $\chi(\omega_k,\Theta_i)$ is the complex phase lag between the jth sensor and the origin for a wave of frequency ω_k approaching from direction Θ_i.

The cross spectra between the elevations, slopes and or curvatures needed for the computation of the directional spectra using the above techniques, make use of the following values:
Number of wave staffs = 6
Number of directions = 72
Sampling rate = 20 Hz
Spectral analysis = FFT method
Number of samples in data block/FFT = 4096
Number of blocks = 24
Frequency interval 8 X 20 / 4096 = 0.039 Hz
(averaging every 8 intervals is performed for spectral smoothing)

3. DIRECTIONAL DISCRIMINATION IN MIXED SEAS

Fig. 2 shows the normalized (to peak) angular distribution of wave energy $E(\Theta)$ for plane waves of 0.10 m amplitude at three frequencies, 0.154, 0.583 and 1.013 Hz from different angles, 60°, 300° and 180°, respectively. The numbers, in the upper right corner in these plots indicate the frequency and in the bottom left corner the frequency index. The dashed, dash-dotted and solid lines represent the directional estimates based on the pitch-roll buoy, cloverleaf buoy and the MLM techniques, respectively. A perspective plot of the previous case, for all angles (0° - 360°) and frequencies (0.037 -

1.40 Hz) based on the above techniques (on the same scale) is shown in Fig. 3 . Close inspection of the spreading of the wave energy reveals the following: (a) the directional spread calculated by means of the pitch-roll and the cloverleaf buoy equivalent techniques are independent of frequency and (b) the directional spectra evaluated via the MLM technique are frequency dependent. At low frequencies the spreading is wider than at high frequencies. This is a direct consequence of the nonlinearity of the MLM technique.

The angular distribution of wave energy based on the pitch-roll buoy technique is wider than the corresponding one based on the cloverleaf buoy technique, and both are wider than the corresponding one based on the MLM. A test on the angular discrimination of the above techniques for plane waves at frequency 0.662 Hz, is shown in Fig. 4 . Fig. 4a shows the angular distribution of wave energy for three plane waves at 50°, 60° and 70°, Fig. 4b for plane waves at 30° and 90°, Fig. 4c for plane waves at 20° and 100° and Fig. 4d for plane waves at 130° and 350°. The plane waves are 10° apart in Fig. 4a , 60° apart in Fig. 4b , 80° apart in Fig. 4c and 140° apart in Fig. 4d . The pitch-roll buoy technique begins to resolve the plane waves when they are 140° apart while the cloverleaf buoy technique begins to resolve plane waves when they are 80° apart. The MLM has the greatest resolving power as indicated in Fig. 4a , where it is able to resolve waves even when they are only 10° apart.

4. COMPARISON OF MEASURED SPECTRAL WIDTHS

During the extensive observational period (October to December in three successive years) we captured a few occasions of multiple seas. Lake Ontario is about 300 km long

and so it is generally subject to the influence of only one meteorological system at a time. However when a strong easterly (long fetch) blow was followed by a rapid shift to the prevailing westerlies, we observed a growing offshore wind sea propagating counter to the residual swell from the east. The most interesting of these events is depicted in 3-D (Fig. 5) and 2-D (Fig. 6) representations of the pitch-roll, cloverleaf and MLM calculations. In addition to these Fig. 6 includes a $\mathrm{sech}^2\beta(\Theta-\Theta_p)$ fit to the directional estimates, where Θ_p is the angle at the peak of the distribution and β is a spreading parameter. The swell with relatively narrow spread is shown at 60° and the wind sea (somewhat broader) is centered at 215°. Figs. 5 and 6a show the directional spreads from the MLM, pitch-roll and cloverleaf equivalent calculations of the swell. The cloverleaf fails completely for these long waves probably because the quantization error (2.5 mm) in surface elevation means

that curvature errors of 200% or more occur randomly for these long waves. On the other hand similar slope errors are only about 10% so the pitch-roll equivalent calculation does not fail as badly, but it is still more than twice as wide as the MLM.

The spreading at the peak of the wind sea is shown in Fig. 6b . Here all methods appear to work and the cloverleaf and MLM are nearly in agreement, although the cloverleaf is still somewhat wider. The pitch-roll buoy is considerably wider.

An overall look at the root-mean square spread for the swell and the wind-sea case of Fig. 5 . is given in Fig. 7 . The mean square spread is given by the definite integral $\int_{-\pi}^{+\pi}(\theta-\theta_c)^2 E(\omega_k,\theta)d\theta$

normalized by the area under the spectrum $\int_{-\pi}^{+\pi} E(\omega_k,\theta)d\theta$

where Θ_c is the angle at the centroid of the distribution. For the wind-sea above the peak the cloverleaf and MLM are in close agreement. On the other hand the pitch-roll spreads are appreciably wider and only reach agreement with the other methods for the rather wide distribution beyond twice the peak frequency.

5. ACKNOWLEDGEMENTS

The authors gratefully acknowledge the use of the MLM code provided by E.R. Jefferys, and support by the Panel for Energy Research and Development under project 62123.

6. REFERENCES

Capon, J., 1969. High-resolution frequency-wavenumber spectrum analysis, Proc. IEEE, 57, 1408-1418.

Cartwright, D.E. and N.D. Smith, 1964. Buoy techniques for obtaining directional wave spectra. Buoy Technology, Washington, D.C., Marine Tech. Soc., 112-121.

Hasselmann, D.E., Dunckel, M & J.A. Ewing, 1980: Directional wave spectra observed during JONSWAP 1973. J. Phys. Oceanogr., 10, 1264-1280.

Jefferys, E.R., Wateham, G.T., Ramsden N.A. and M.J. Platts, 1981: Measuring directional spectra with the MLM", Proc. Directional Wave Spectra Applications Conference, University of California, Berkley, California, 203-219.

Jefferys, E.R., 1986: Comparison of three methods for calculation of directional spectra, Proc. 5th International Offshore Mechanics and Arctic Engineering Symposium, Tokyo, Japan, Vol 1, 45-50.

Krogstad, H.E., Gordon, R.L. and M.C. Miller, 1988: High-resolution directional spectra from horizontally mounted acoustic doppler current meters", J. Atm. & Ocea. Tech., Vol. 5, 340-352.

Longuet-Higgins, M.S., D.E. Cartwright and N.D. Smith, 1963: Observations of the directional spectrum of sea waves using the motions of a floating buoy", Ocean Wave Spectra, Prentice-Hall, New Jersey, 111-132.

Mitsuyasu, H., F. Tasai, T. Sabara, S. Mizuno, M. Okusu, T. Honda and K. Rikiishi , 1975: Observation of the directional spectrum of ocean waves using a clover-leaf buoy", J. of Phys. Oceanogr., 5(4), 169-181.

Oakley, O.H. and J.B. Lozow, 1977: Directional Spectra Measurement by Small Arrays, Proc. Offshore Technology Conference, Houston, Paper No. OTC 27459 155-166. Pawka, S.S., 1983: Island shadows in wave directional spectra. J. Geophys. Res., 88, 2579-2591.

Phillips, O.M. 1957 On the generation of waves by turbulent wind. J. Fluid Mech., 2. 417-445.

Tsanis, I.K. and Donelan, M.A., 1987, "The WAVES Programme on the CCIW Research Tower", National Water Research Institute (NWRI) Report, No. 87-65, Research and Applications Branch, Canada Centre for Inland Waters.

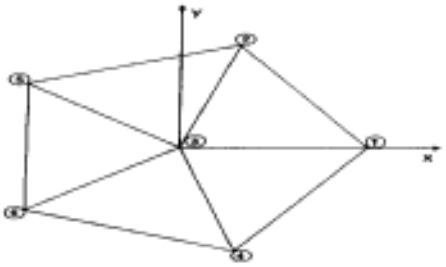

Fig. 1 The wave staff array

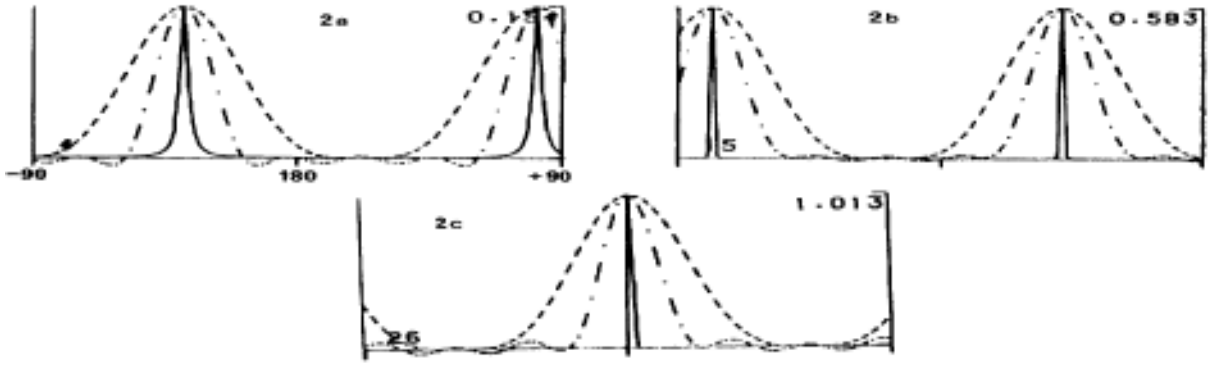

Fig. 2 2-D presentation of plane waves from different angles at different frequencies. ---------- Pitch-roll buoy; ---------- Cloverleaf buoy; ——— MLM

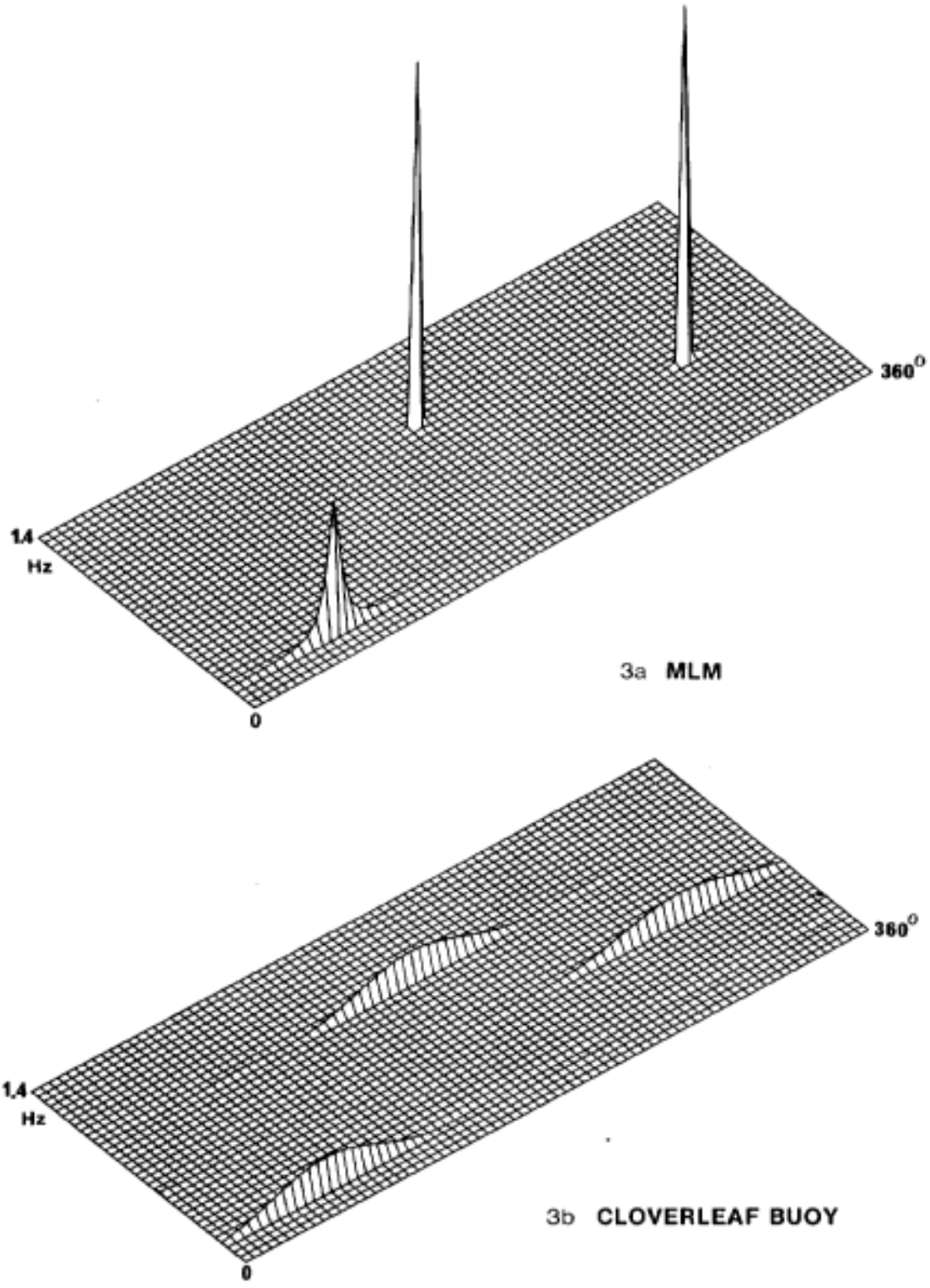

Fig. 3 3-D presentation of plane waves from different angles at different frequencies.

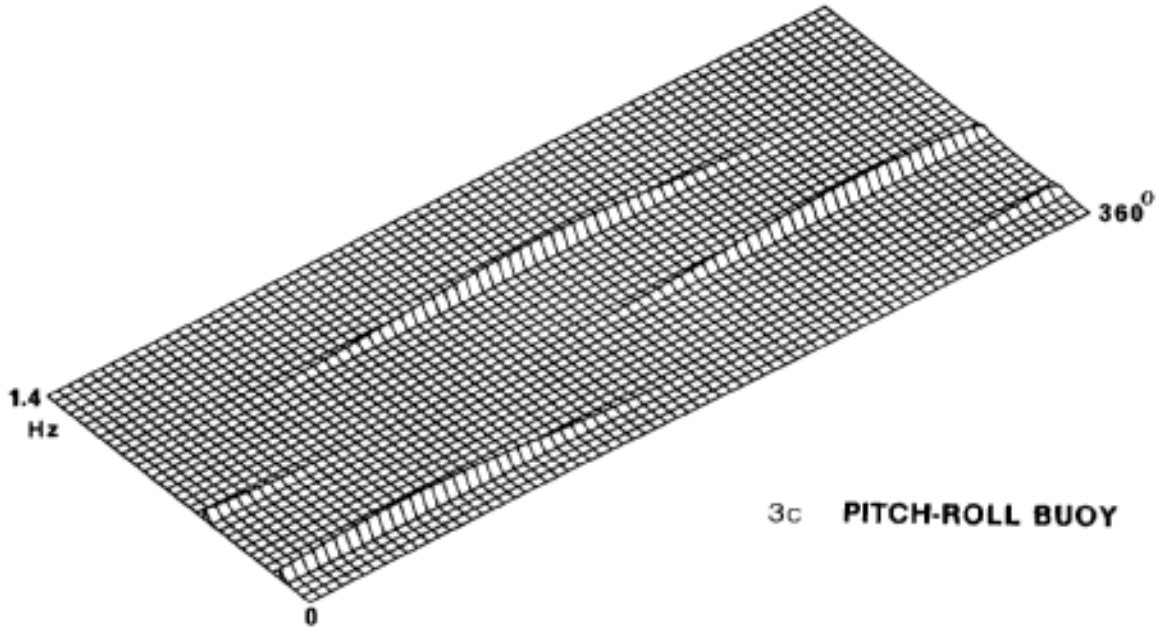

Fig. 3 3-D presentation of plane waves from different angles at different frequencies.

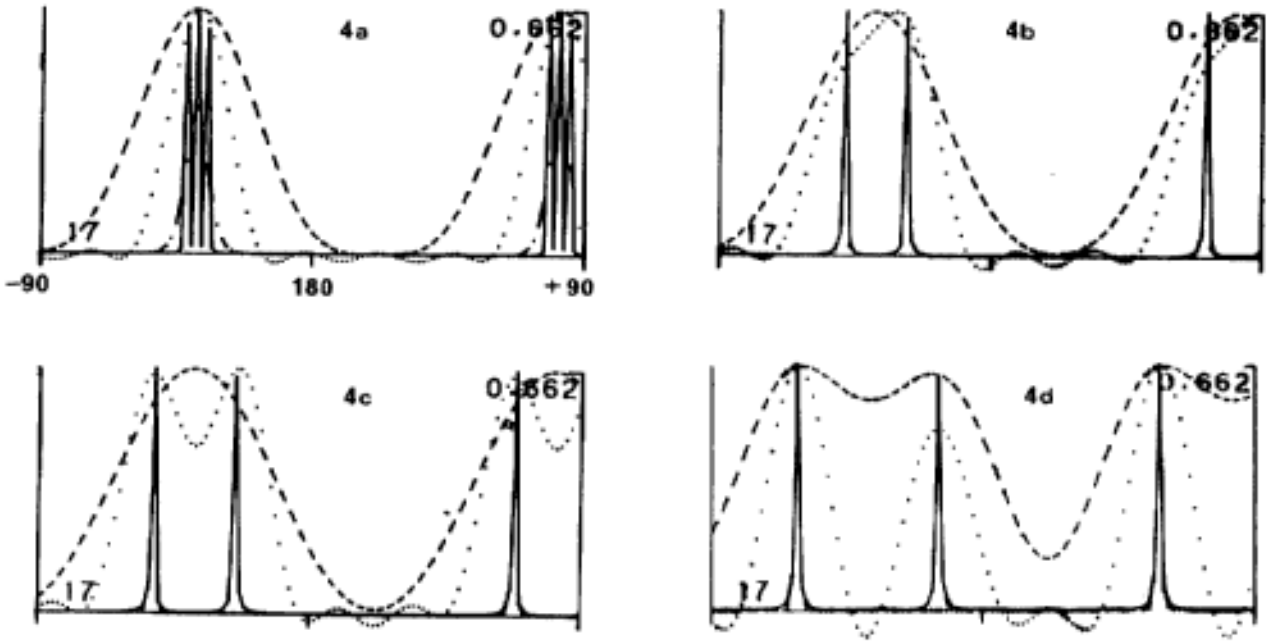

Fig. 4 Test of angular discrimination of different techniques.
---- Pitch-roll buoy; ..... Cloverleaf buoy; —— MLM

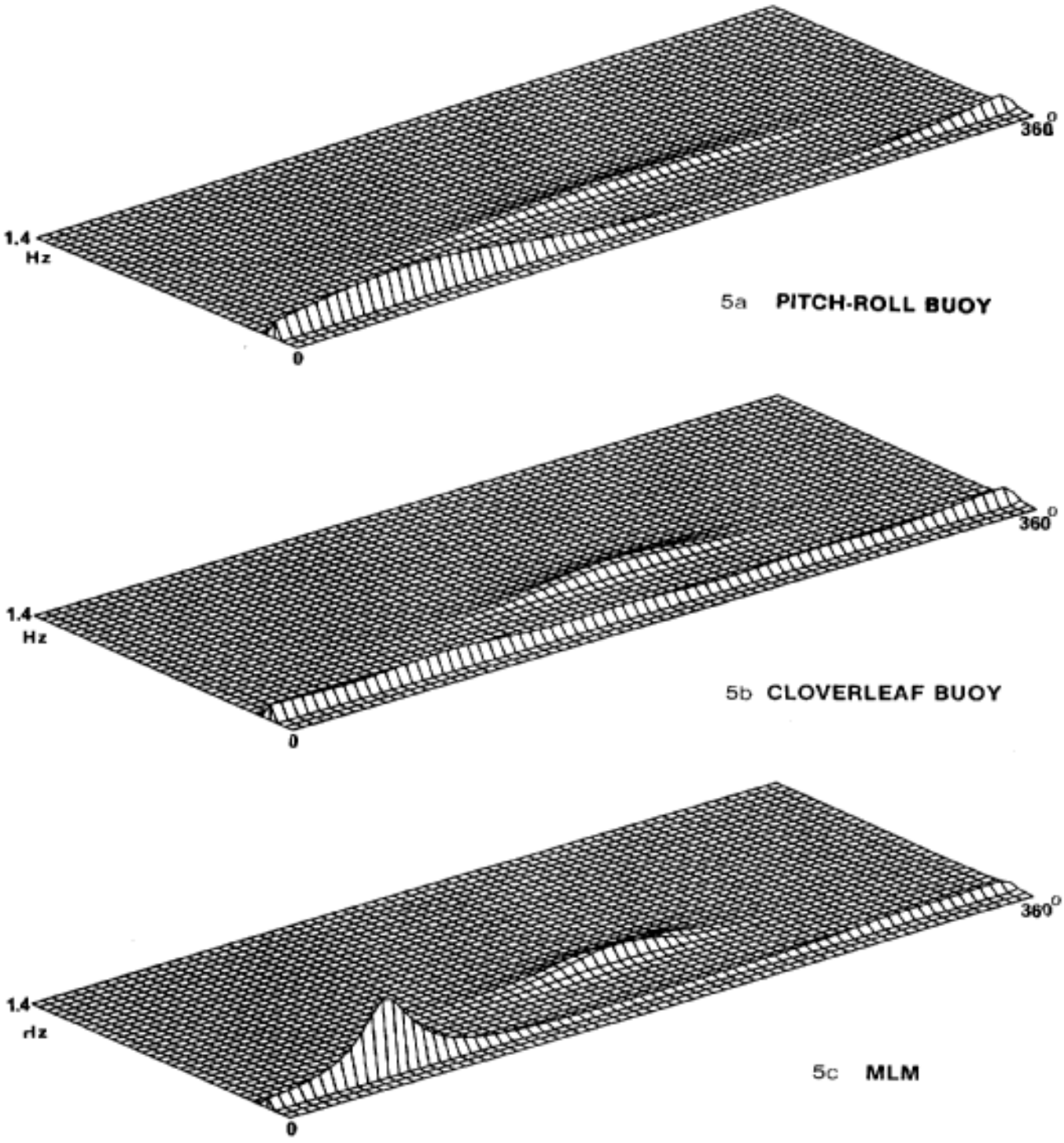

Fig. 5 3-D presentation of wave directional spectra in an offshore wind with an onshore swell.

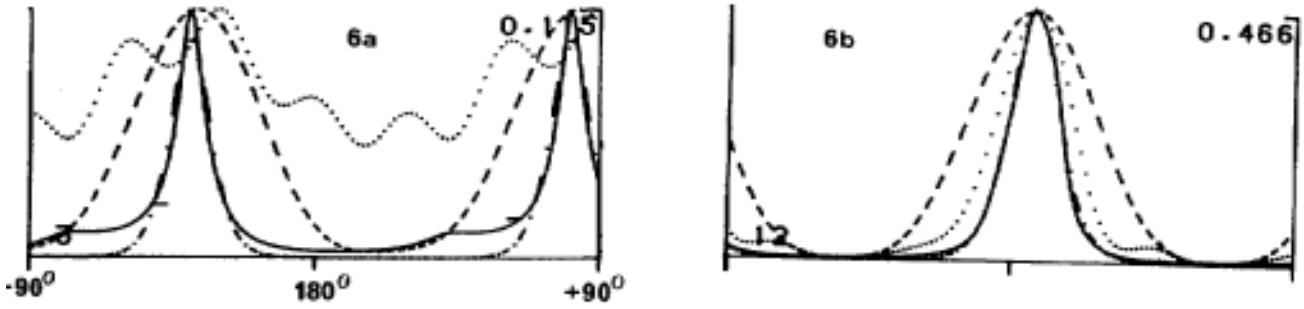

Fig. 6 2-D presentation of wave directional spectra in an offshore wind with an onshore swell. (----- Pitch-roll buoy; ..... Cloverleaf buoy; ——— MLM)

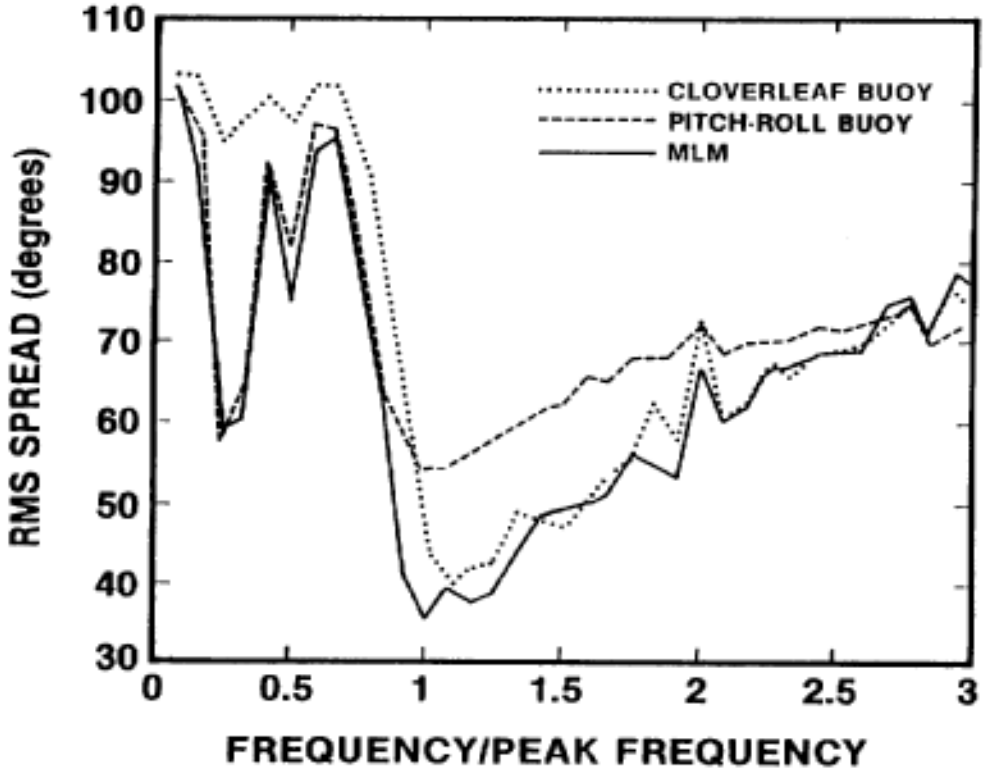

Fig. 7 Frequency dependance of RMS spread of the mixed sea of Fig. 5.

Joint Long Term Description of Environmental Parameters for Structural Response Calculation

Elzbieta M. Bittier-Gregersen and Sverre Haver

A.S Veritas Research, P.O.Box 300, N-1322 Hφvik, Norway
Statoil, P.O.Box 300, N-4001 Stavanger, Norway

ABSTRACT

A joint distribution function is proposed for the long term simultaneous description of wind, waves and current. The model is based on experience gained from measurements and/or hindcast data from the Norwegian Continental Shelf. It should therefore be regarded as an empirical model. However, to a certain extent, it agrees qualitatively with the underlying physics. The joint distribution is intended for application in response prediction of offshore structures where the mechanical behaviour is of a linear nature, and the hydrodynamic load function can be linearized with a reasonable degree of accuracy. Under these restrictions the study is limited to the following environmental parameters: 1-hour mean wind speed, wind direction, current speed, current direction, significant wave height, peak period and main wave direction. The joint environmental model is fitted to instrumental (1980-1.985) and hindcast (19551985) data from Haltenbanken.

1. INTRODUCTION

The overall objective of the design of a marine structure is to ensure that the structure can resist all foreseen loads with an adequate degree of safety against failure. That means to demonstrate that the load effects satisfy specified resistance criteria. In this connection the most important load processes, wind, waves and current, are assumed to be fully (or nearly fully) correlated. Thus, the design load effects are traditionally calculated by combining worst cases of wind, waves and current and multiply the results with a proper load coefficient. The assumption of full correlation is most probably rather conservative and it may result in an unnecessary overestimation of the design loads.

In order to indicate the degree of conservatism, the design loads should also be calculated using a consistent simultaneous description of wind, waves and current. Unfortunately, very few data bases of reliable measurements are available for such a purpose. On the other hand, concerning wind and waves, reliable hindcast data represent an adequate data source for establishing a proper description of these quantities, especially if some simultaneous measurements are available for calibration purposes. There is still a limited number of

simultaneous current data. Measured current data are Usually of a rather short duration and the hindcast technique regarding total Current is presently not very reliable. In spite of all difficulties, however, several authors have indicated the possible gains by a more consistent handling of joint occurrence of wind, waves and Current, see e.g. Gordon, R.L. (1982), Gordon, R.L. et al. (1985), E & P Forum (1985). As it was shown in 1985 at the E & P Forum meeting, in some cases, the forces on structures may be reduced from 5 to 40% by accounting for joint occurrence.

Herein a joint long term distribution of wind, waves and current is deduced bearing in mind a stochastic response analysis of fixed offshore structures, which, additionally are dominated by the linear/linearized wave induced loads. The model is fitted to measurements (1980-1985) and hindcast data (1955-1985) from Haltenbanken of Mid-Norway. The joint description of wind and wave characteristics is assumed to be of a reasonably good accuracy, while the current model is simple and should primarily be used for sensitivity studies.

2. STOCHASTIC RESPONSE ANALYSIS OF FIXED PLATFORMS SIMULTANEOUSLY EXPOSED TO WIND, WAVES AND CURRENT

When developing a joint probabilistic description of the environmental processes, it is important, first of all, to identify the class/classes of structures it is meant to be applied to. The method adopted for the calculation of design load effects, and so the environmental model will depend very much on the properties of structures under consideration.

Herein, emphasis is given to fixed offshore structures, i.e. structures that are exposed to rather small motions. These structures are not exposed to any drift force and the wind induced response is very well described by a quasi-static approach. It is, furthermore, reasonable to assume that, within a stationary situation, the wind and wave induced responses are statistically independent. The present formulation is especially meant to be applied to deep water structures for which dynamics may be important. Such structures will be dominated by the wave induced response and results of a reasonable accuracy can often be obtained by linearizing the hydrodynamic load functions, i.e. making a frequency domain analysis. However, it should be noted that the adopted linearization procedure may vary for different purposes.

A possible formulation of a stochastic response analysis of a dynamic fixed platform is discussed into some detail in Bitner-Gregersen and Haver (1988). Herein we will merely sum up the main steps of this procedure. The resulting response process is assumed to be given by

$$X'(t) = X'_1(t) + X'_2(t) \qquad (1)$$

where $X'_1(t)$ is the wind induced response and $X'2(t)$ is resulting hydrodynamic (waves and current) response. Both $X'_1(t)$ and $X'2(t)$ are rapidly fluctuating processes with slowly varying properties. Accordingly, for short time periods, the resulting process is conveniently written

$$X'_1(t) = X_1(t) + X_2(t) + \bar{x}_1 + \bar{x}_2 \quad (2)$$

where now $X_1(t)$ and $X_2(t)$ both are zero mean stationary stochastic processes $\bar{x}_1$ is the response due to the constant mean wind and $\bar{x}_2$ is the mean hydrodynamic response due to a constant current. Since the turbulent wind is much less than the mean wind, the contribution due to the square term of the turbulent wind speed is neglected. Accordingly, it is reasonable to model $X_1(t)$ and $X_2(t)$ as zero mean independent Gaussian stochastic processes. Consequently, $X(t)=X'(t)-\bar{x}_1-\bar{x}_2$ is also a zero mean Gaussian process. The distribution of the primary crest height of $X(t)$, Y_x, is reasonably well modelled by the Rayleigh distribution, i.e.:

$$F_{Y_X}(y) = 1 - \exp\left[-\frac{1}{2}\left(\frac{y}{\sigma_X}\right)^2\right] \quad (3)$$

where the resulting variance, σ^2_x, is given by

$$\sigma_X^2 = \sigma_{X_1}^2 + \sigma_{X_2}^2 \quad (4)$$

The short term probability of exceeding the value y' is then

$$P(Y_X > y' \mid environment) = P(Y_X > y' - \bar{x}_1 - \bar{x}_2 \mid environment) = \exp\left[-\frac{(y' - \bar{x}_1 - \bar{x}_2)^2}{2(\sigma_{X_1}^2 + \sigma_{X_2}^2)}\right] \quad (5)$$

A short term sea state is assumed to be characterized by;

* 1-hour mean wind speed, u
* wind direction, Θ
* current velocity profile, $v(z)$
* current direction assumed to be collinear with the wind direction
* significant wave height, h_{mo}
* spectral peak period, t_p
* main wave direction, assumed to equal the wind direction.

$\bar{x}_1$ can be calculated for a given mean wind speed and direction, possibly by introducing a proper admittance function, Davenport

(1977). The fluctuating part of the wind induced response is to the first approximation proportional to the turbulent wind speed, $X_1(t) \approx k_1 U_T(t)$, where k_1 is a proper coefficient. The response variance is thus given by

$$\sigma_{X_1}^2 \approx k_1^2 \sigma_{U_T}^2 \tag{6}$$

The variance of the turbulent wind, $\sigma_{U_T}^2$, is proportional to the mean wind speed squared and will of course also depend on wind direction, i.e.:

$$\sigma_{X_1}^2 \approx k_2^2 u^2 = \sigma_{X_1}^2(u,\theta) \tag{7}$$

where k_2 denotes coefficient.

$\bar{x}_2$ is only a function of $v(z)$ and the direction and can be determined when the current field is given. The wave spectrum, $S_{\Xi\Xi}(f)$, is assumed to be a function of the significant wave height and the spectral peak period. The response spectrum, $S_{X_2X_2}(f)$, is then given

$$S_{X_2X_2}(f;h_{mo},t_p,v(z),\theta) = \int_{\psi} |h_{\Xi X_2}(f;\theta+\psi,v(z))|^2 S_{\Xi\Xi}(f,\psi;h_{mo},t_p,\theta)\,d\psi \tag{8}$$

where h_{mo}, t_p, θ are the primary wave characteristics, $v(z)$ is the current field, ψ describes the wave energy spreading around the main wave direction, θ, and $|h_{\Xi X_2}(\,)|$ is the transfer function.

The variance, $\sigma_{X_2}^2$ is now obtained by integrating over the response spectrum, i.e.:

$$\sigma_{X_2}^2 = \int_0^{\infty} S_{X_2X_2}(f;h_{mo},t_p,v(z),\theta)\,df = \sigma_{X_2}^2(h_{mo},t_p,v(z),\theta) \tag{9}$$

It is seen in (8) that the transfer function, $|h_{\Xi X_2}(\,)|$, is a function of the current field. Accordingly, it is convenient from a practical point of view if the current can be described in terms of a limited number of possible profiles, $v_k(z)=v_k$.

Expressed as a conditional probability, the short term probability of exceedance is now written

$$Q_{\underset{X}{Y}}(y|h_{mo},t_p,u,v,\theta)=1-F_{\underset{X}{Y}}(y|h_{mo},t_p,u,v_k,\theta)=\exp\left[-\frac{1}{2}\frac{(y-\bar{x}_1(u,\theta)-\bar{x}_2(v_k,\theta))^2}{\sigma^2_{X_1}(u,\theta)+\sigma^2_{X_2}(h_{mo},t_p,v_k,\theta)}\right] \quad (10)$$

The long term probability of exceedance is now approximately given by

$$Q_{\underset{X}{Y}}(y)=\frac{1}{\bar{\nu}^+_o}\int\int\int\int\int\nu^+_0(h_{mo},t_p,v,\theta)\cdot Q_{\underset{X}{Y}}(y|h_{mo},t_p,u,v,\theta)\cdot f_{H_{mo}T_pVU\Theta}(h_{mo},t_p,v,u\theta)dh_{mo}dt_pdvdud\theta \quad (11)$$

The mean zero-crossing frequency $\bar{\nu}^+_o$ is given by

$$\bar{\nu}^+_0=\int\int\int\int\nu^+_0(h_{mo},t_p,v,\theta)\cdot f_{H_{mo}T_pV\Theta}(h_{mo},t_p,v,\theta)dh_{mo}dt_pdvd\theta \quad (12)$$

where ν^+_0 is the expected zero-up-crossing frequency for a stationary sea state.

The equations above are valid under the assumption that the resulting zero mean process, $X(t)$, is dominated by the hydrodynamic response. Consequently, the zero up-crossing frequency is assumed to be very well modelled by the zero up-crossing frequency of the hydrodynamic response process, $\nu^+_o(h_{mo},t_p,v,\theta)$. If the wind induced part, $X_1(t)$, becomes comparable to $X_2(t)$, the above equations should be modified.

When applying Eq.(11) in practice both V and θ should be considered as discrete variables in order to keep the number of transfer functions on a reasonable level. In view of this, the present formulation is recommended herein;

$$Q_{\underset{X}{Y}}(y)=\frac{1}{\bar{\nu}^+_o}\sum_{i=1}^{imax}p_\Theta(\theta_i)\int\int\sum_{k=1}^{kmax}\nu^+_o(h_{mo},t_p,v_k,\theta_i)\cdot p_{V|H_{mo}}(v_k|h_{mo}) \quad (13)$$

$$\cdot f_{U|H_{mo}}(u|h_{mo})Q_{\underset{X}{Y}}(y|h_{mo},t_p,u,v_k,\theta_i)du\cdot f_{H_{mo}T_p|\Theta}(h_{mo},t_p|\theta_i)dh_{mo}dt_p$$

3. JOINT DESCRIPTION OF ENVIRONMENTAL PARAMETERS

There is no theoretical preference when it comes to deciding on probabilistic models for the various conditional density functions of the environmental parameters included in Eq,(13). The actual choices are therefore to be made on an empirical basis. The recommended distributions and fitting procedures are discussed in Bitner-Gregersen and Haver (1988). Herein only the main results of the study are presented. The joint model is fitted to data from Haltenbanken at a position 65°0'N, 7°36'E.

Conditional Distribution of Wind

The Haltenbanken area has rather complex meteorological conditions being influenced by several phenomena such as frontal cyclones, small cyclones which may develop over the ocean in outbreaks of cold arctic air misses in the rear of the frontal cyclones, local monsoon regimes, and the high mountains. Measurements of the wind speed at the area show that Haltenbanken represents the part of the Norwegian Continental Shelf with the overall highest wind speeds (Haaland, 1978). A considerable percentage of the observations correspond to southwest wind. The large portion of winds front SE, i.e. mainly offshore, is also present.

30 years hindcast wind data prepared by the Norwegian Meteorological Institute (Reistad et al. (1986)), from a period 1955-1985, have been chosen for the present analysis. The data represent 1-hour average wind speed 10m above sea level and for the present applications they are most probably of a reasonable accuracy, Haver (1986).

It is assumed that the conditional long term distribution of the 1-hour average wind speed, U, given H_{mo} follows a two-parameter Weibull probability function

$$f(u\,|h_{mo}) = k\frac{u^{k-1}}{U_c{}^{k}}\exp\left[-\left(\frac{u}{U_c}\right)^{k}\right] \qquad (14)$$

where the parameters U_c (scale parameter) and k (slope parameter) are functions of h_{mo}. The choice of a 2-parameter Weibull model is supported by the empirical distribution functions, Bitner-Gregersen and Haver (1988). The data have been divided into a coastal directional sector $22.5° < \theta < 202.5°$ and an open sea directional sector $\theta < 22.5°$ or $\theta > 202.5°$. For each class of the significant wave height including a sufficient number of observations a two-parameter Weibull distribution has been fitted to the data by the equal weight least squares technique. The evaluated parameters k and U_c are plotted versus h_{mo} in Figure 1 .

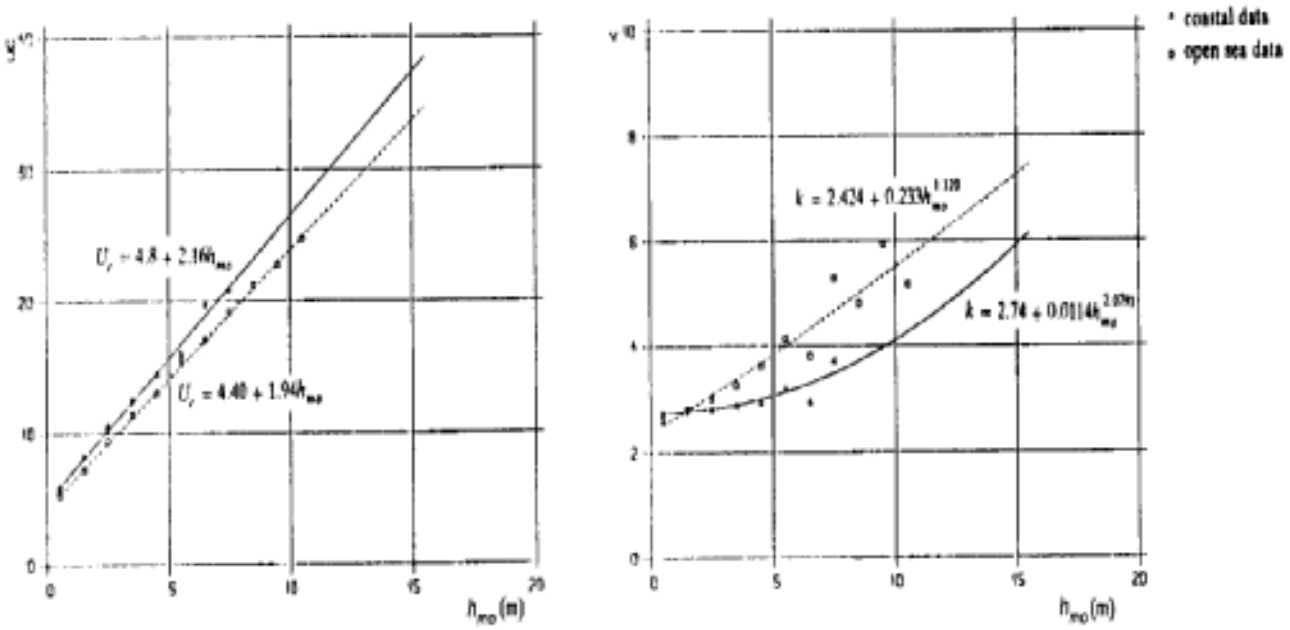

Figure 1 The scale and slope parameters as functions of h_{mo}.

The density function and distribution of the wind speed for the open sea sector, i.e. θ<22.5° and θ>202.5°, obtained from the model are compared with the data in Figure 2 . A reasonable good fit is observed, especially when considered in view of the relative importance of the wind induced loads. The model overestimates extreme wind speeds.

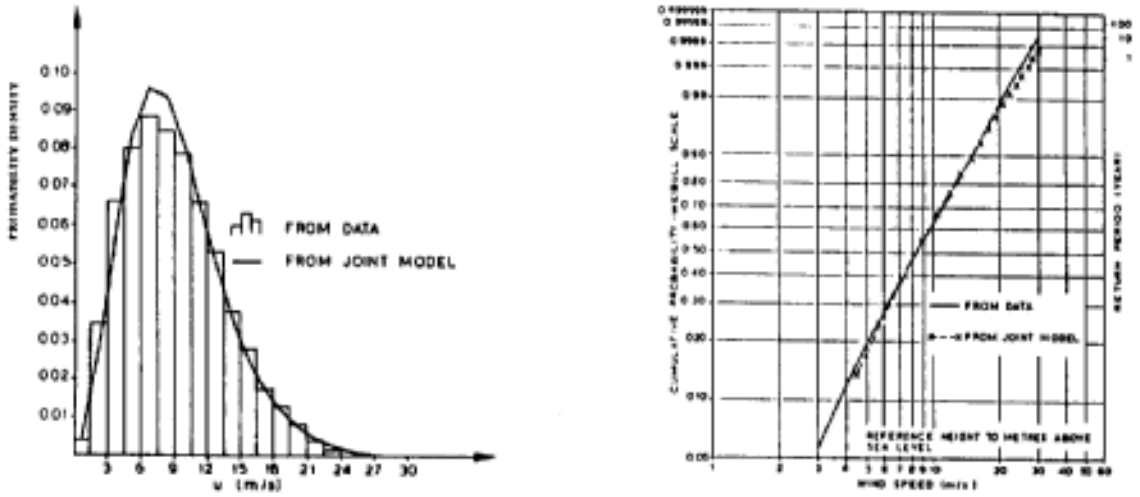

Figure 2 The probability density and distribution function of the wind speed for the open sea sector.

when considered in view of the relative importance of the wind induced loads. The model overestimates extreme wind speeds.

Wave Conditions

The wave climate which is closely related to the wind conditions is severe at the Haltenbanken area. The highest waves will most likely come from a southwesterly-westerly direction but also winds from north-northwest have a long fetch and may build up severe seas. Another feature of the Haltenbanken wave climate is the presence of swell since this area is openly exposed to waves generated by North Atlantic cyclones.

The actual measurements were registered by directional ODAS buoys for a period 1980-1985 within the ODAP project (Ocean Data Acquisition Project), Faanes & Torsethaugen, (1986). 20 minutes records were taken every 3rd hour and separated into the following directional sectors: N, NE, E, SE, S, SW, W, NW.

Data simulated by the hindcast model operated by the Norwegian Meteorological Institute, Eide et al. (1985), Reistad et al. (1986), show that the measuring period 1980-1985 is not representative for the wave climate at Haltenbanken. The years-1980-1985 are more severe than the typical long term wave climate for the area. The marginal distribution of H_{mo}, seems to be more sensitive to climatological changes than the conditional distribution of the peak period, Bitner-Gregersen and Haver (1988), and for some directions it should be corrected by a climatic bias, e.g. as suggested by Torsethaugen et al. (1984). The present analysis does not, however, include this correction.

Based on analysis of wave data around the Norwegian Continental Shelf, Bitner-Gregersen and Mathisen (1988), it is suggested to approximate a long term distribution of H_{mo} and T_p as follows

$$f(h_{mo}, t_p) = f(h_{mo}) \cdot f(t_p \mid h_{mo}) \qquad (15)$$

The marginal distribution of H_{mo}, $f(h_{mo})$, is assumed to be well described by a three parameter Weibull distribution

$$f(h_{mo}) = \frac{\beta}{\alpha}\left(\frac{h_{mo}-\gamma}{\alpha}\right)^{\beta-1} \exp\left[-\left(\frac{h_{mo}-\gamma}{\alpha}\right)^{\beta}\right] \qquad (16)$$

where α = scale parameter, β = slope parameter, and γ location parameter. The conditional distribution of T_p given H_{mo} is modelled by a log-normal distribution

$$f(t_p \mid h_{mo}) = \frac{1}{\sqrt{2\pi}\sigma t_p} \exp\left[-\frac{(\ln t_p - \mu)^2}{2\sigma^2}\right] \qquad (17)$$

where $\mu = E(\ln T_p)$, $\sigma^2 = Var(\ln T_p)$. The following continuous functions are fitted to the empirical estimates of μ and σ^2:

$$\mu = \alpha_1 + \alpha_2 h_{mo}^{\beta} \quad (18)$$

$$\sigma^2 = a_1 e^{-b_1 h_{mo}} + a_2 e^{-b_2 h_{mo}} \quad (19)$$

The parameters α_1, α_2, ß, a_1, a_2, b_1 and b_2 as well as α, β and γ are site specific and have to be determined from existing data.

The distribution (15) has been fitted to the nondirectional data and the measurements for all 8 directional sectors. The parameters α, β, and γ for the marginal distribution of H_{mo} have been evaluated by the least squared method (see Table 1) after the data have been plotted on the Weibull paper according to the Gumbel plotting position, Gumbel (1958). The data follow the three-parameter Weibull distribution reasonably well for the sea as well as coastal directions, e.g. Figure 3 .

Table 1 The Weibull parameters of the marginal distribution of the significant wave height

Directional sector	Probability of direction	Weibull parameters α	β	γ
N	0.2154	1,282	0.990	1.008
NE	0.0755	0,925	0.878	1.102
E	0.0373	1,386	1.092	1.097
SE	0.0184	2,611	2.201	0.348
S	0.0210	2,978	2.449	0.127
SW	0.2724	2,692	1.464	0.596
W	0.2204	1,843	1.085	0.894
NW	0.1396	1,441	1.036	0.922
all directions	1.0000	2,154	1.273	0.763

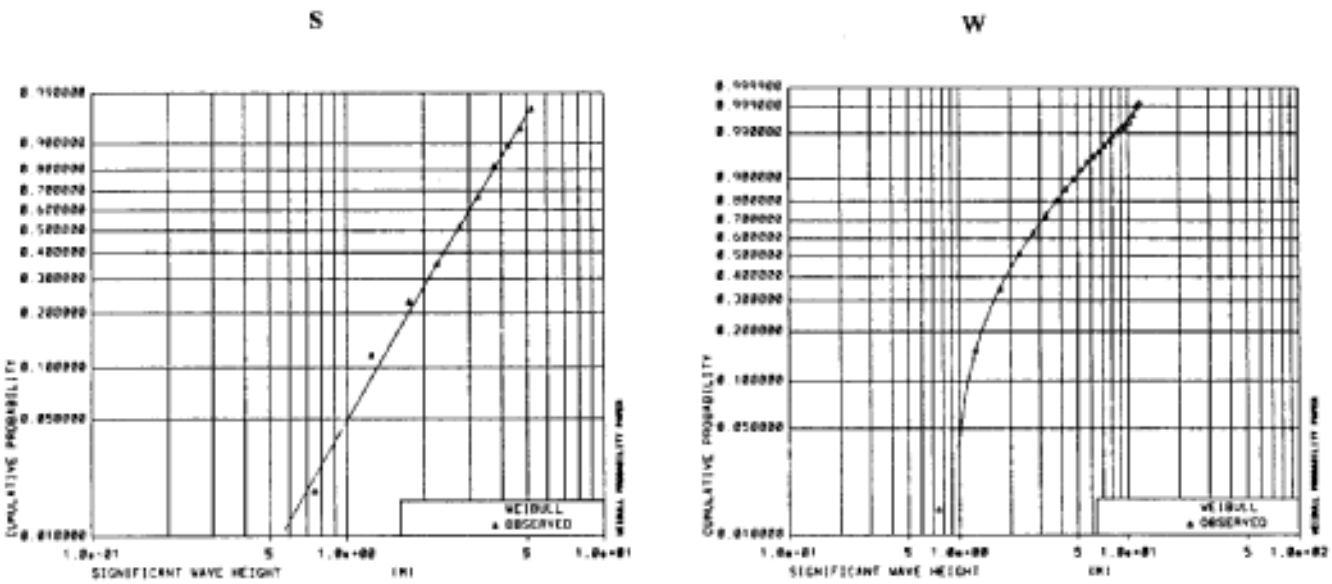

Figure 3 The marginal distribution of significant wave height S and W directions.

For each class of the significant wave height including a sufficient number of observations, μ and σ^2 have been estimated. Continuous functions fitted to these estimates by a multiple nonlinear regression are given in Table 2 , see also Figures 4 and 5 . For the present data it has been convenient to assume b_1=0.0. In order to avoid negative values of σ^2 an "empirical" asymptote σ^2=0.005 has been introduced in the fit. By introducing this lower limit a reasonable fit is obtained for the continuous functions of $\sigma^2(h_{mo})$ also for the directions with a limited number of data (e.g.,E, SE), where, additionally effects of combined seas become important. The present fit should be regarded as subjective since for some directions reasonable results are obtained only if the empirical values for some of the h_{mo} classes are omitted and the asymptote for σ^2 is introduced.

The adequacy of the joint $f(h_{mo},t_p)$ has been tested. Thus the conditional mean values and standard deviations of significant wave height given T_p have been evaluated from the fitted model and compared with the corresponding empirical values. A satisfactory good fit is observed for the mean value and standard deviation for the open sea sector as well as the coastal directions (see Figures 6 and 7) The discrepancies between the model and the data observed for high t_p are most probably caused by problems in accounting properly for swell dominated tail regions.

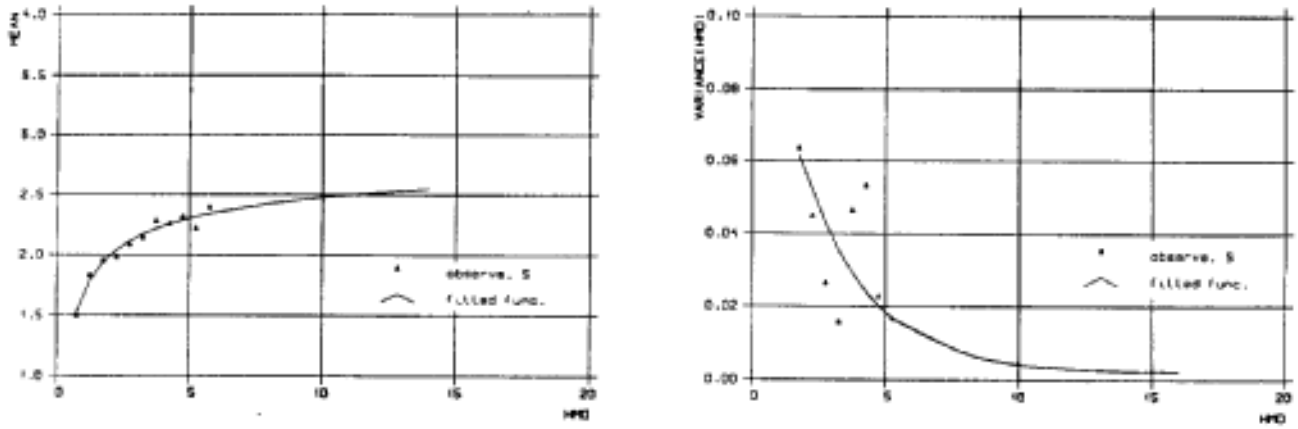

Figure 4 The peak period mean μ and variance σ^2 as a function of h_{mo} for S.

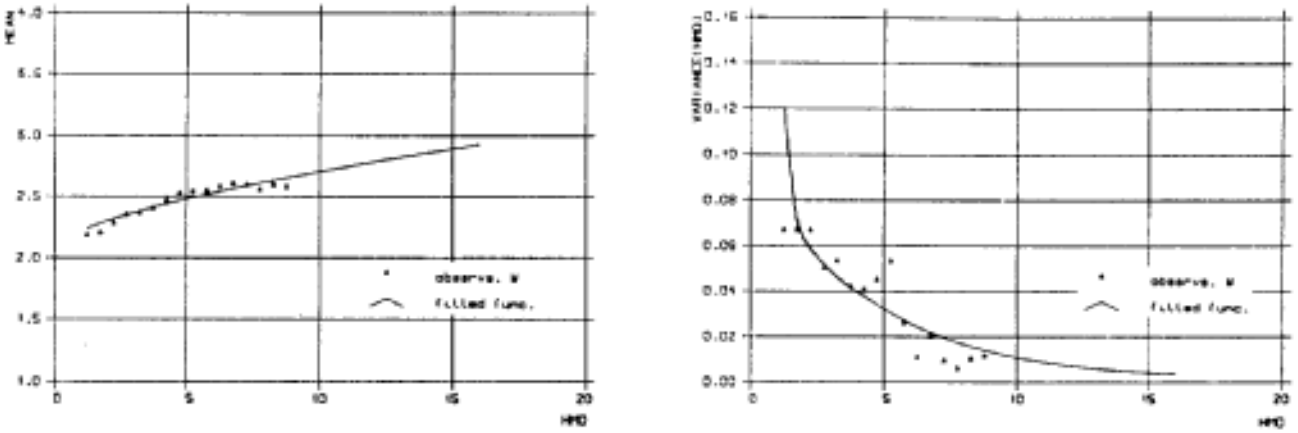

Figure 5 The peak period mean μ and variance σ^2 as a function of h_{mo} for W.

Table 2 The parameters of the conditional distribution of the wave period						
Directional sector	μ			σ^2		
	$\alpha 1$	$\alpha 2$	ß	a1	a2	b2
N	1.7667	0.2817	0.5115	0.0126	0.10330	.7415
NE	-0.5298	2.2439	0.1657	0.0107	0.21110	.8969
E	7.5800	-6.1028	-0.0878	0.0024	0.05170	.1857
SE	4.0513	-2.5116	-0.1904	0.0042	0.06070	.3640
S	3.0825	-1.4087	-0.3682	0.0020	0.12560	.4074
SW	2.1550	0.0634	0.9252	0.0012	0.12020	.2696
W	2.0809	0.1396	0.6501	0.0012	0.09920	.2335
NW	1.3585	0.6298	0.3389	0.0045	0.06930	.4793
all directions	1.9307	0.1607	0.6898	0.0012	0.11610	0.2721

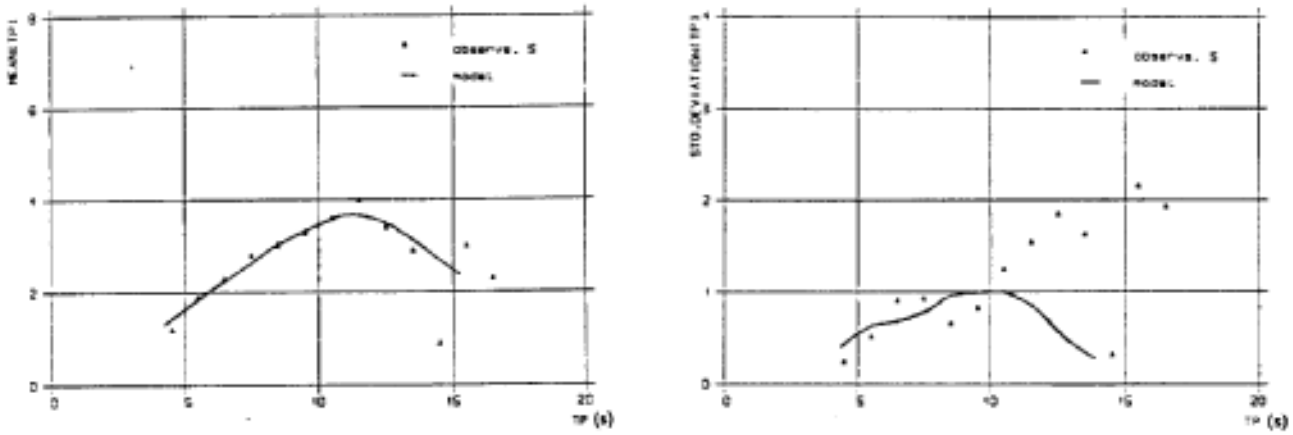

Figure 6 The conditional mean and standard deviation of H_{mo} given T_p for S.

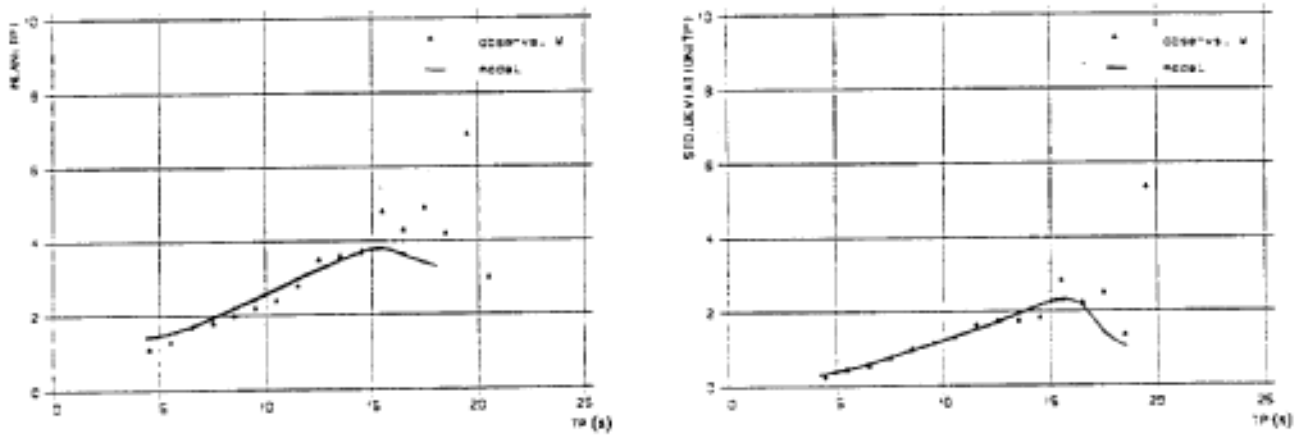

Figure 7 The conditional mean and standard deviation of H_{mo} given T_p for W.

Current Field

The typical current pattern is characterized by a clockwise vortex around the Haltenbanken plateau, Orvik et al. (1985). The total current being the resulting effect of several processes is divided into two subfields: a wind- and wave-induced current field (dependent on the actual weather conditions) and a residual current (independent of the actual weather conditions), which herein also includes the tidal current. The velocity amplitude associated with the tidal current is typically of the order of 0.1m/s.

Long term current measurements adopted as basis for the present description have been made during the years 1980-84 at 6 depth levels, Olsen and Jenkins (1986). The measuring procedure aims at an estimate of the 10min. mean velocity at each depth level every hour.

The residual current is herein modelled as a constant current speed all through the water column. In order to reduce the number of

transfer functions that have to be calculated, the residual current is modelled as a discrete variable with only four possible realizations, Table 3 . The actual realizations and the corresponding probabilities are selected by considering the empirical distribution functions for depth levels of 100, 175 and 265 m, Olsen and Jenkins (1986).

Table 3 Probabilistic model for the residual current (herein including the tidal current) $V_c^{(r)}$.

$v^{(r)}$ (m/s)	$P_{V_c^{(r)}}(v^{(r)})$ (m/s)
0.00 (>0.06)	0.1000
0.10 (0.06-0.20)	0.8000
0.30 (0.20-0.40)	0.0999
0.45 (>0.40)	0.0001

The wind induced current is assumed to be correlated to the wave height. However, in order to reduce the number of needed transfer functions, this current component is also described by a discrete variable with only four possible realizations, Table 4 . The wind induced current is usually determined as a certain percentage of the wind speed. Herein it is assumed to be related to the significant wave height. The actual realizations corresponding to intervals of the significant wave height and the associated probabilities are given in Table 4 . Three sets of current velocities correspond to a current speed equal to 0.75%, 1.5%, and 2.5% of the mean wind speed. The profile is assumed to be of a slab type and the depth of the profile is assumed to equal 50 m no matter of wind speed/wave height.

Table 4 Probabilistic description of the wind induced current, $V_c^{(w)}$

Significant wave height (m/s)	Wind speed (m/s)	Current speed (m/s)			Proba-bility
		I 0.75%	II 1.5%	III 2.5%	
2 (0-4)	8	0.06	0.12	0.20	0.82
6 (4-8)	15	0.11	0.23	0.38	0.17
10 (8-12)	22	0.17	0.33	0.55	0.0098
14 (>12)	29	0.22	0.44	0.73	0.00002

For a given set of the wind induced current, the random resulting current constitutes of a total of 16 possible profiles. As an illustration, the possible profiles are shown in Figure 8 when the wind induced component is characterized by the second set of values, i.e. current speed is 1.5% of the wind speed. The probability of occurrence associated with each profile is also given at the figure.

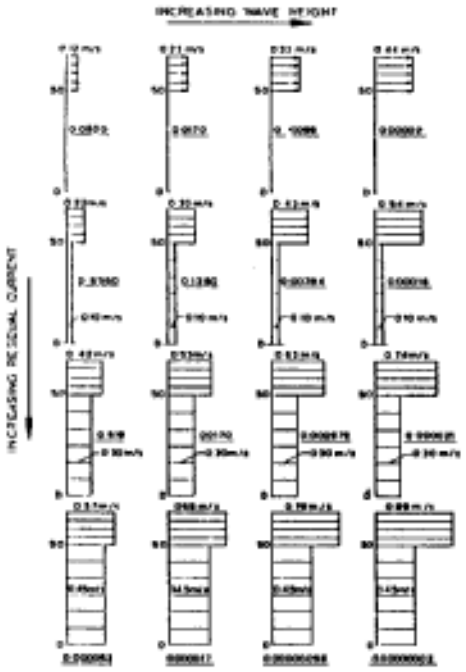

Figure 8 Possible current profiles within the frame of the adopted model.

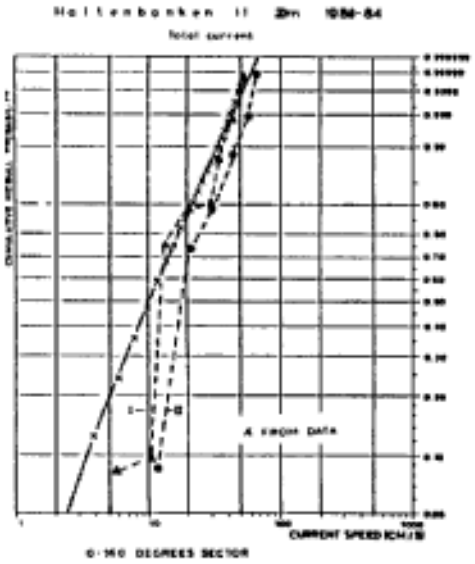

Figure 9 Distribution functions for the total current obtained from the present model compared to the empirical distribution function for the set I and II (see Table 4).

It is not obvious which of the included sets of wind induced currents that provide the best result. The distribution functions corresponding to the first (0.75%) and second (1.5%) set of values for the wind induced current have been compared to the empirical distribution for 2m and 20m. Herein the results for 20m are only presented, see Figure 9 . Based on this it is recommended that the wind induced current is modelled as a slab model with a velocity equal to 0.75% of the wind speed.

4. CONCLUSIONS

The present joint long term distribution of wind, waves and currents should be regarded as the first attempt of modelling simultaneous environmental conditions for Haltenbanken. Emphasis is given to the wave description since the model is meant to be applied to fixed marine structures assumed to be dominated by the wave loads.

The wave model seems to be well approximated by a 3-parameter Weibull distribution for H_{mo} and log-normal distribution for T_p given H_{mo} for all directions. The adequacy of the fitted joint model is of a reasonable accuracy, especially for the open sea directions which are the most important for the structural response calculations. The main uncertainties are related to the description of swell dominated seas. If these show to be very important, then the model should be updated at a later stage. The fitted model gives most probably, conservative values of the 100-year wave height for the following sectors: N, E,

SW, W and NW as it does not take into consideration climatological variations of the Haltenbanken wave climate. This should be accounted for in a final developed model.

A 2-parameter Weibull distribution seems to be a proper model for the conditional distribution of the wind speed U_{10} given H_{mo}, especially when considered in view of the relative importance of the wind induced loads for fixed marine Structures.

A very simple discrete model is suggested for the current field. However, it is expected to reproduce the relative frequency of various ranges of current speeds with a reasonable accuracy. The model seems furthermore to be ,I useful tool for indicating the effect of simultaneous description of waves and current for the considered structures.

ACKNOWLEDGEMENT

This paper has been prepared within the research program "Reliability of Marine Structures", which is sponsored b), Veritas Research, Saga Petroleum, Statoil, and Conoco. Permission to publish these results is gratefully acknowledged. The opinions expressed herein are those of the authors and should not be construed is reflecting the views of these companies.

5. REFERENCES

[1] Bitner-Gregersen, E.M. and J.Mathisen, "Uncertainties in Statistical Models for Wind, Waves and Current", *A.S Veritas Research Report No.88-2007, 9th February, 1988*.

[2] Bitner-Gregersen, F.M. and S.Haver, "Joint Long Term Description of Environmental Parameters for Structural Response Calculations", *A.S Veritas Research Report No.88-2016, 19th May, 1988*.

[3] Davenport, A.G., "The Prediction of the Response of Structures to Gusty Wind" *Proc. Safety of Structures, Norwegian Institute of Technology, 1977*.

[4] Eide, I,.I., et al., "Database av Beregnede Vind og Bϕlgepirametre for Nordsjϕen, Norskhavet og Barentshavet, Hver 6 Time for Arene 19-5-5 81", *Report DNMI, Oslo/Bergen 1985*.

[5] E&P FORUM, Workshop, "The Application of Joint Probability of Metocean Phenomena in the Oil Industry's Structural Design Work", *London, Nov. 1985*.

[6] Faanes, T. and K.Torsethaugen, "Analysis of Wave Data from Haltenbanken 1974 -1985. Summary Report 1985", *ODAP Report No.59.0006, 15th May, 1985*.

[7] Gumbel, E.J., "Statistics of Extremes", *Columbia Univ. Press. New York, 1958*.

[8] Haver, S., "On the Adequacy of the Norwegian Hindcast Database for Statfjord, Tromsøflaket, Ekofisk and Haltenbanken", *Statoil Report, 21st August 1986*.

[9] Haaland, L., "Bidrag tit Beskrivelse av Klimaet paa Kontinentalsokkelen", *Scientific Report No.18, 1978, DNMI*.

[10] Orvik, et al., "Analysis of Current and Hydrographic Data, Intensive survey, Haltenbanken-Trænabanken 1984" *ODAP Report No. 61, Trondheim, 1985*.

[11] Olsen and Jenkins, "Analysis of Current Data", *ODAP Report 1986*.

[12] Reistad, M. et al. "Maritimt Klima - Atlas for den Norske Kontinentalsokkel og Tilgrensende Havomrader", *DNMI Report, Bergen 1987*.

[13] Torsethaugen, K., et al., "Characteristica for Extreme Sea-States on the Norwegian Continental Shelf", *Report STF60 A84123, Norwegian Hydrodynamic Lab., Trondheim, 1984*.

THEORETICAL AND PRACTICAL CONSIDERATIONS IN FIRST-, SECOND-, AND THIRD-GENERATION WAVE MODELS

[1]Donald T. Resio and [2]Will Perrie

[1]Offshore & Coastal Technologies, Inc. (OCTI)
911 Clay Street, Vicksburg, Mississippi 39180 U.S.A.

[2]Physical and Chemical Sciences Scotia-Fundy Region
Dept. of Fisheries and Oceans, Bedford Institute of Oceanography
Dartmouth, Nova Scotia B2Y 4A2 CANADA

ABSTRACT

Over the last year, substantial progress has been made in understanding nonlinear energy transfers in a wave spectrum (Resio and Perrie, 1989a, 1989b, 1989c; Perrie and Resio, 1989a, 1989b). Calculations based, not on parameterizations, but on an improved version of the complete Boltzmann integral, have yielded some very interesting results. Based on these results, first-, second-, and third-generation wave models are reviewed in terms of expected accuracies in four situations: fetch-limited wave growth, duration-limited wave growth, turning winds, and the transition from sea to swell. These accuracies are examined in terms of wave heights, peak wave periods, mean wave directions, and spectral shapes.

It would appear from the primary results shown here that a modified third-generation model could be programmed to be as efficient as (or perhaps even more efficient than) first- or second-generation wave models with substantial increase in accuracy. Thus, results given in this paper are very pertinent to hindcast models, operational forecasting, and the interpretation of satellite wind and wave data.

1. INTRODUCTION

During the past several years a new generation (third) of spectral wave models has emerged as a potential tool for practical wave hindcasting and forecasting. Three important questions in the application of these models have not as yet been addressed in much depth:

a. What are the significant theoretical differences among various generation wave models?

b. Are there differences in the expected performance of the various generation wave models that have actual practical consequence in different applications?

c. What are the necessary computer demands inherent in the use of various generation wave models?

Although we have never been entirely certain as to what exact definitions are correct for various generation wave models. Table 1

puts forth some simple descriptions which will at least categorize the terms first-, second-, and third-generation wave models as used in this paper. The purpose of this paper is to investigate, at least in a preliminary fashion, the answers to the three questions previously posed.

Table 1

CATEGORIZATION OF VARIOUS GENERATION WAVE MODELS

Model	Treatment of Source Terms	Constraints
First-Generation	o wind input only o breaking implicit in spectral constraints	o Pierson-Moskowitz spectrum
Second-Generation	o wind input and nonlinear wave-wave interaction source terms o breaking assumed implicit in spectral constraints	o dynamic balance exists between all source terms in region above spectral peak o various spectral forms (JONSWAP, f^{-4}, etc.)
Third-Generation	o explicit representations of wind input, nonlinear wave-wave interactions, and wave breaking	o constrains spectral shape at frequencies about twice the frequency of the spectral peak and higher

2. THEORETICAL CONSIDERATIONS

The general, deep-water form for the evolution of energy densities in a spectrum is

$$\frac{\partial E(f,\theta)}{\partial t} = \vec{c}_g(f,\theta)\,\vec{\nabla} E(f,\theta) + \sum_{\kappa=1}^{n} S_\kappa(f,\theta)$$

where $E(f,\Theta)$ is the energy density in a directional spectral band located at frequency f and propagation direction Θ, $\vec{c}_n(f,\theta)$ is the group velocity vector for this bands $S_K(f,\Theta)$ is a source term representing a net exchange of energy into or out of this band, and n is an integer denoting the number of source terms considered significant.

Figure 1 shows the idealized evolution of a wind-generated sea in the three generations of models being considered here. As can be seen there, the second- and third-generation models appear essentially identical, while the first-generation model is distinctly different. The reason for this lies in the source terms and constraints controlling the spectral shapes in these models.

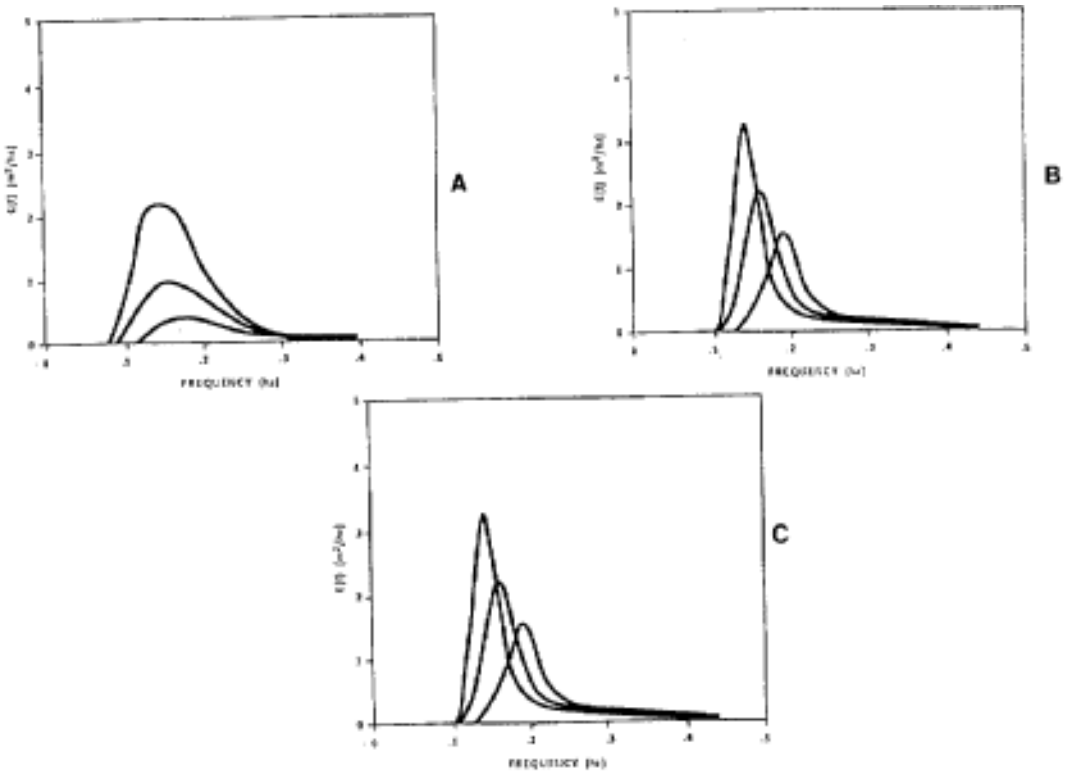

Figure 1. Evolution of wave spectra in 1st-, 2nd-, and 3rd-generation wave models.

There are three primary source terms which are included either implicitly or explicitly in most deep-water spectral wave models: wind input, nonlinear wave-wave interactions, and wave breaking.

In first-generation wave models, the wind input is generally of the form

$$(1) \qquad S_{in}^{1}(f,\theta) = A(f,\theta) + B(f,\theta)\, E(f,\theta)$$

where the superscript denotes the model generation and $A(f,\Theta)$ and $B(f,\Theta)$ represent separate linear and exponential wind input mechanisms. For examples of these one can refer to Bunting (1970) and Inoue (1967). In most second- and third-generation models the "$A(f,\Theta)$" term is neglected as very small; thus, we have

$$(2) \qquad S_{in}^{2}(f,\theta) = S_{in}^{3}(f,\theta) = B(f,\theta)\, E(f,\theta)$$

where a typical form for $B(f,\Theta)$ is

$$(3) \qquad B(f,\theta) = \max\left[0,\ 0.25\ \frac{\rho_a}{\rho_w}\ \omega\left(\frac{28u_*}{c(f)}\cos\phi - 1\right)\right]$$

where ρ_a and ρ_w are the densities of air and water, respectively, $c(f)$ is phase velocity, u_* is the friction velocity, and ϕ is the angle between the wave component at angle Θ and the wind direction.

In second-generation models, the parameterization of the nonlinear source terms are of the form

$$S_{NL}^2 = S_{NL}(f/f_p, \theta/\theta_o)$$

where f_p is the frequency of the spectral peak and Θ_0 is the mean wave direction. In third-generation models a sort of "diffusion operator" approach to parameterization is used. This approach termed the discrete interaction approximation was calibrated to match the front lobe of the wave-wave interaction source function but appears to have serious deficiencies in its ability to represent S_{NL} in other regions of the spectrum (Figure 2). Since this is a critical element in third-generation models it is not clear that this type of parameterization is at all adequate for third-generation models.

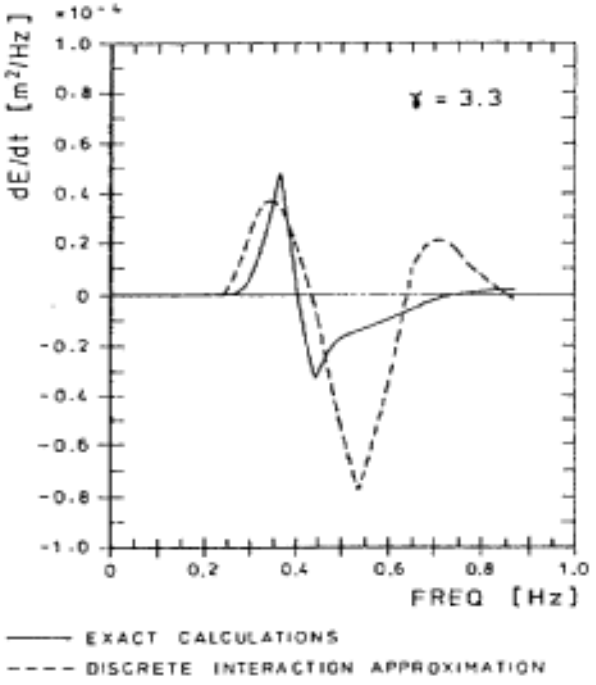

Figure 2. Comparison of the exact one-dimensional distribution S_{NL} with the discrete-interaction approximation for a JONSWAP spectrum. (From: Hasselmann et al., 1985).

Most second-generation models assume that there is a strong tendency toward an equilibrium at frequencies above the spectral peak; consequently, they neglect the wave breaking source term, SDISS, and replace it by the constraint that a balance between S_{IN} and S_{NL} controls the energy levels and spectral shape in this region. Third-generation models do not assume that the tendency toward an equilibrium is strong in this region and attempt to model this balance explicitly. It is important to note that this approach of itself does not constitute "better physics" or the application of "first principles," as has been claimed in several articles dealing with third-generation models.

Recent work in the numerical integration of the full Boltzmann integral has been completed by Resio (1987, 1988) and Resio and Perrie (1989a,b). This work has produced the first integral solution capable of yielding non-erratic estimates of the nonlinear source function and of providing accurate estimates of energy, action, and momentum fluxes through a spectrum. Figure 3 shows a typical result from this numerical tool compared to a result for the same spectrum from Hasselmann and Hasselmann. Figure 4 shows the result from a calculation of energy fluxes through the spectrum. This new tool provides a major improvement over older codes which have attempted to solve the exact Boltzmann integrals since those older methods had to be significantly constrained and smoothed before they could be used in a time-stepping solution of spectral evolution.

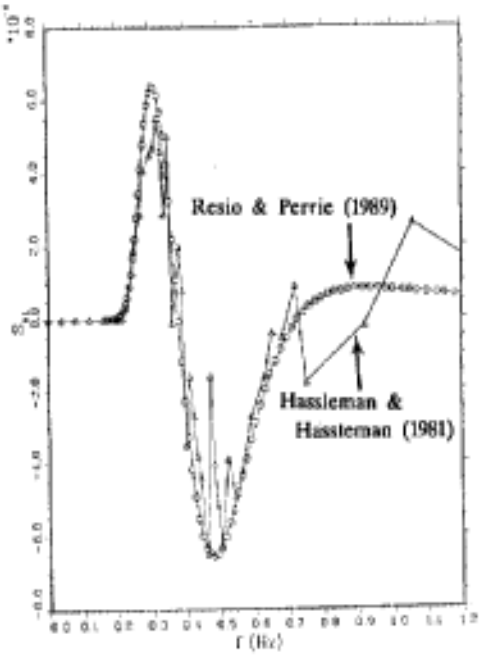

Figure 3. Comparison of Resio-Perrie (1989) Boltzmann integration technique to that of Hasselmann and Hasselmann (1981).

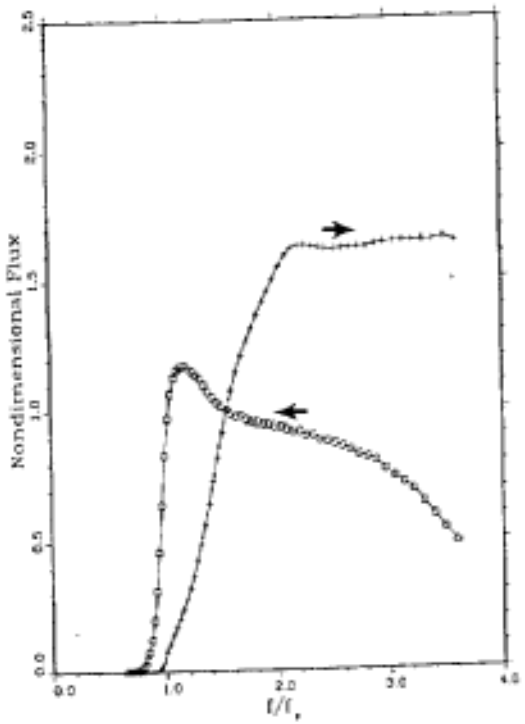

Figure 4. Dimensionless energy fluxes through a wave spectrum. Arrows denote direction of fluxes.

Using this new tool various short- and long-term simulations of different combinations of initial conditions (starting spectrum) and source terms have been completed. Four major conclusions can be drawn from these simulations.

1. There is a very strong tendency toward equilibrium at frequencies above the spectral peak (Figure 5).

2. No matter what other source terms get added to S_{NL}, S_{NL} still forces the spectral evolution to a reasonable equilibrium. All the tests with S_{IN} and S_{DISS} for a particular spectrum really cannot be used to determine which magnitude and form of those other terms are required to attain and/or maintain an equilibrium. The apparent solutions in those papers are actually only dependent on the selected initial spectrum.

3. The concept of a Komolgorov range with energy cascading from low frequencies toward high frequencies through the spectrum is not valid. Actually as seen in Figure 4 , the fluxes are about equal in both directions in the equilibrium range. This provides an important insight into the directional relaxation of a spectrum as pointed out by Toba et al. (1988).

4. The role of S_{IN} and S_{DISS} appears to be that of controlling the net energy gain and shift in peak frequency. It does not appear possible to determine appropriate forms for S_{NL} and S_{DISS} simply from running an experimental wave model. Field evidence is essential.

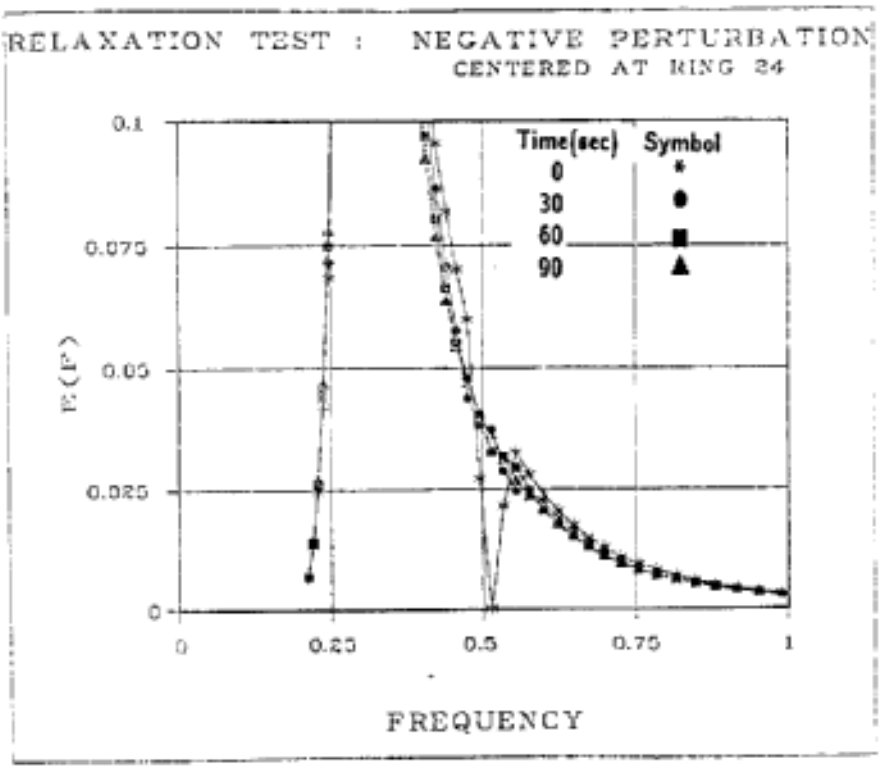

Figure 5. Relaxation of wave spectrum from an initial perturbation.

3. PRACTICAL CONSEQUENCES IN THE USE OF DIFFERENT GENERATION WAVE MODELS

3.1 Overall Consideration

Using the full nonlinear model (FNM) described in Resio and Perrie (1989), four scenarios of wave generation were tested and compared to various generation wave models that have been reported in the literature. These four scenarios are as follows:

1. fetch-limited wave generation;
2. curation-limited wave generation;
3. turning wind conditions; and
4. sea-to-swell transition.

Each of these will now be addressed in turn.

3.2 Fetch-limited Wave Growth

Figure 6 shows the various relationships between dimensionless wave energy, $\hat{E}_o$, defined as

$$\hat{E}_o = \frac{g^2 E_o}{u_*^2}$$

Where g is gravity and E_o is total energy in the wave spectrum, and dimensionless fetch, $\hat{x}$, defined as

$$\hat{x} = \frac{gx}{u_*^2}$$

where x is the available fetch for wave generation. As seen there, the first- and third-generation models yield surprisingly similar results (strongly curved lines) for a certain range of $\hat{x}$; whereas the second-generation model shows a substantially different relationship (straight lines). The FNM can be calibrated to give any of these results as shown in Figure 6 . If we include very strong terms which are independent of f_p, we can produce an FNM which takes on one fetch-growth pattern. If we operate under a different (equally valid theoretically) set of rules, we can produce an FNM which takes on a fetch-growth pattern similar to the second-generation models. In no way is the "better physics" of the third-generation model apparent in this practical test. In fact, if anything, these results show that a model alone cannot be used to determine improved physics. Intuitively, the results which appear to conform best with independent empirical results probably come closer to representing the actual physics.

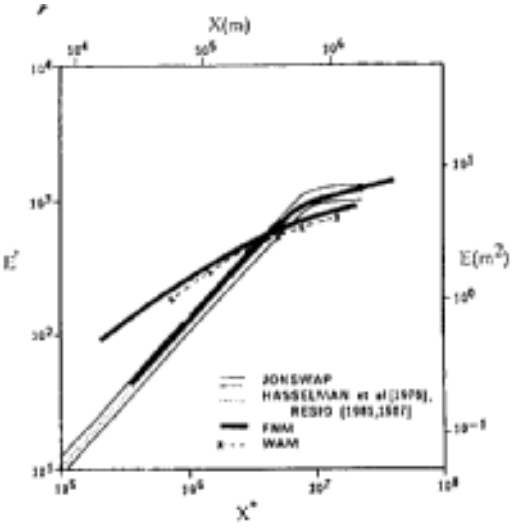

Figure 6. Characteristic Relationships between dimensionless energy and dimensionless fetch in selected models.

It should be pointed out, however, that there is one major difference between first-generation models, which do not include S_{NL} terms, and second- and third-generation models, which do. As shown by Resio and Vincent (1979), the first-generation models have a significantly shorter time required to attain fetch-limited conditions (Table 2). This means the first-generation models, calibrated to produce duration growth rates comparable to second- and third-generation models, will predict significantly lower waves in fetch-limited conditions. This does not of itself infer which is correct, but only that models with and without S_{NL} cannot be calibrated to produce similar results.

Table 2

COMPARISON OF DURATIONS REQUIRED TO ACHIEVE FETCH-LIMITED CONDITIONS IN MODELS DOMINATED BY ATMOSPHERE INPUT AND WAVE/WAVE INTERACTION SOURCE TERMS
(From: Resio and Vincent, 1979)

Wind Speed (knots)	Wind Speed (m/s)	Dominant Source Term	Fetch, nautical miles (km) 10(18.5) (hours)	50(92.5) (hours)	100(185.0) (hours)	500(925.0) (hours)
20	39	G_{AT}	2.3	6.9	11.3	31.4
		G_{NL}	3.2	9.4	14.9	44.0
40	78	G_{AT}	1.6	4.6	7.5	22.3
		G_{NL}	2.2	6.4	10.2	30.2
60	117	G_{AT}	1.6	4.2	7.2	23.1
		G_{NL}	1.9	5.5	8.8	26.0

3.3 Duration-limited Wave Generation

Figure 7 shows various relationships between nondimensional wave energy and nondimensional time, t, defined as

$$t = \frac{gt}{u_*}.$$

As was the case in the previous section, the FNM alone cannot be used to determine the correct growth rate. With one set of assumptions for

S_{IN} and S_{DISS} it yields results similar to the existing first-, second-, or third-generation wave models.

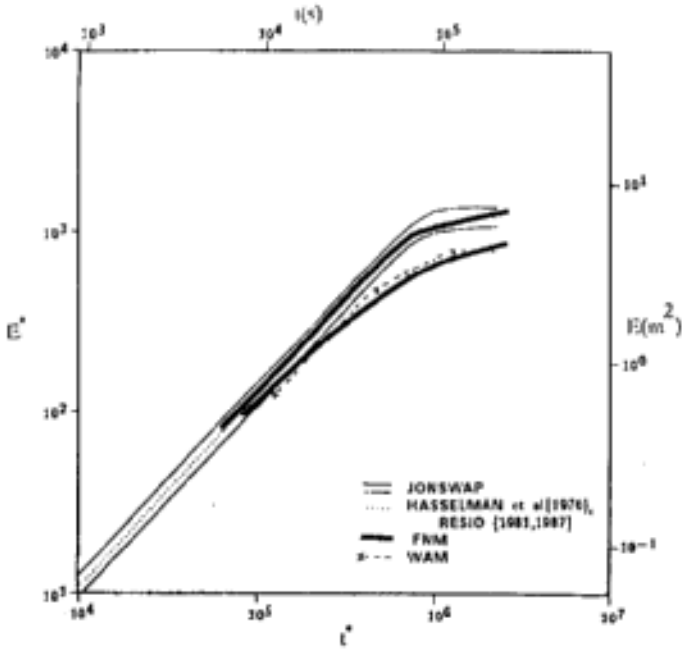

Figure 7. Characteristic relationships between dimensionless energy and dimensionless time in selected models.

3.4 Rapidly Turning Winds

The FNM provides valuable insights into how a wave spectrum responds to rapidly turning winds. Our preliminary results show that there are significant differences in the ways in which different generation models respond. However, the assumptions regarding where the wind input enters the spectrum, in terms of angles and frequencies, can alter the rate of wave angle turning substantially. Thus, the use of even a full Boltzmann integral for SNL cannot, of itself, provide conclusive information concerning the wave response to turning winds.

3.5 Transition from Sea to Swell

Here is the one area where the FNM provides results which differ from all previous wave models, even existing third-generation models. In all of these models, after the wave spectrum reaches a "fully-developed" state, the nonlinear source terms and other source terms are presumed to produce a steady-state net balance. In the FNM, even without SDISS, the rate of wave growth slows dramatically after passing the limit where f_p is actively receiving momentum from the wind. However, in spite of this slowing of wave growth, it does not abruptly stop at the Pierson-Moskowitz limit. It is possible that

present models may be neglecting an important facet of the transition from sea to swell in their present configuration. In large, long-duration storms this effect might produce significantly longer-period waves than are predicted in present models.

4. COMPUTER DEMANDS ASSOCIATED WITH VARIOUS GENERATION WAVE MODELS

First- and second-generation wave models have roughly the same demands on computer storage and run time. Present third-generation models present a much more formidable task to computers; however, it is probable that much of this demand is not really necessary to preserve accuracies consistent with the goal of a third-generation model. Results from the FNM suggest that a large part of the spectrum can be considered to be in equilibrium with the wind and wave energy fluxes, in any situations where the wind information is only available on an hourly (or greater) basis. Calculations of perturbations from the equilibrium condition are important only for the angular relaxation of the spectrum. An improved parameterization of this effect while rewriting S_{NL} into a self-stabilizing form should dramatically reduce the redundancy and instabilities associated with long time steps in third-generation models, while preserving the potential accuracy of these models.

5. CONCLUSIONS

Several conclusions can be based on the results shown here:

1. Wave models must rely on basic field data to formulate the proper set of wave physics. Different assumptions concerning S_{DISS} and S_{IN}, combined with an accurate representation of S_{NL}, can produce significantly different model performance.

2. First-generation wave models cannot produce the same fetch- and duration-growth characteristics as second- and third-generation models. Second generation models and third-generation models can produce comparable (identical) fetch- and duration-growth characteristics.

3. The full nonlinear model (FNM) based on an exact solution to the Boltzmann integral provides an excellent tool to analyze the evolution of wave spectra under different sets of source terms.

6. ACKNOWLEDGMENTS

This work was partially supported by the Federal Panel on Energy Research and Development (PERD).

7. REFERENCES

Bunting, D. C., 1970;Forecasting of ocean wave spectra. J. Geophys. Res., 75, 4131-4143.

Hasselmann, S., K.Hasselmann, J. H. Allender, and T. P. Barnett, 1985: Computations and parameterizations of the nonlinear energy transfer in a gravity-wave spectrum. Part II: Parameterizations of the nonlinear energy transfer for application in wave models. J. Phys. Oceanogr., 15, 1378-1391.

Hasselmann, S., and K. Hasselmann, 1981: A symmetrical method of computing the nonlinear transfer in A gravity-wave spectrum. Hamburger Geophys. Einzelschr., Riehe A., Wiss. Abh., 52, 163 pp.

Inoue, T., 1967: On the growth of the spectrum of a wind generated sea according to a modified Miles-Phillips mechanism and its application to wave forecasting. N.Y. Univ. Geophys. Sci. Lab. Rep. 67-5.

Resio, D. T. 1987: Shallow-water waves. I: Theory. ASCE J. of Waterway, Port, Coastal, and Ocean ., 113(3), 264-281.

Resio, D. T., 1988: Shallow-water wave. II: Data comparisons. ASCE J. of Waterway, Port, Coastal, and Ocean Engrg., 114(1), 50-65.

Resio, D. T., and W. Perrie, 1989: Implications of an f-4 equilibrium range for wind-generated waves. J. Phys. Oceanogr., February, 193-204.

Resio, D. T., and W. Perrie, 1989: A numerical study of nonlinear energy fluxes due to wave-wave interactions in a wave spectrum. Part I: Methodology and basic results. Submitted to J. Fluid Mech. for publication.

Resio, D. T., and C. L. Vincent, 1979: A comparison of various numerical wave prediction techniques. Presented at the 11th Annual Offshore Tech. Conf., Houston, Pap. 3642.

Toba, Y., K. Okada, and 1. S. F. Jones, 1988: The response of wind-wave spectra to changing winds. Part I: Increasing winds. Am. Met. Soc., 18, 1231-1240.

A SURVEY OF PARAMETERIZATIONS OF DYNAMICAL PROCESSES IN THIRD GENERATION WAVE MODELS

by

Will Perrie[1] and Donald T. Resio[2]

[1]Physical and Chemical Sciences Scotia-Fundy Region
Department of Fisheries and Oceans
Bedford Institute of Oceanography
Dartmouth, Nova Scotia
B2Y 4A2 CANADA

[2]OCTI, 911 Clay St.
Vicksburg, Mississippi 39180
USA

ABSTRACT

In deep water, the dominating factors determining the evolution of wind generated surface waves are spectral energy input by the wind, nonlinear transfer due to wave-wave-interactions and dissipation of energy due wave breaking and white capping. We examine formulations of these terms and assess the manner in which they couple with each other by explicitly integrating the spectral balance equation with respect to time. We find that wind input and nonlinear transfer constitute the main balance, achieving a behavior and self-similarity that has features common to observed spectra.

PREAMBLE

There have been many recent efforts to observe and analyse wind-generated surface gravity waves in deep water. A consensus has emerged that the spectral balance is dominated by the input of energy due to forcing by the wind, nonlinear transfer between spectral components due to wave-wave interactions, dissipation of energy due to wave breaking and whitecap processes, and propagation of energy at the wave group velocity $\underline{c}_g$. The issues involved in how these processes combine with one another are discussed in Kitaigorodskii (1983), Komen et al (1984), Phillips (1985), Resio (1987) and Resio and Perrie (1989a) and many others.

Present wave models are applications of these analyses and are limited in the manner they represent these physical processes, especially the nonlinear transfer. As derived by Hasselmann (1961, 1963*a*, 1963*b*), an exact computation of the complete Boltzmann integral is not possible except in the simplest two-dimensional wave situations. First generation wave models simply ignore nonlinear transfer and implement empirical growth algorithms. Second generation

models parameterize nonlinear transfer with a few variables depending on spectral growth with fetch as specified by the JONSWAP study of Hasselmann et al (1973), Donelan et al (1985) and Dobson et al (1989) and others. These models generally perform well for the simple wave fields for which they are calibrated but lack the degrees of freedom to accurately respond to complicated wind forcings, as exemplified in the strongly nonstationary, inhomogeneous situations addressed in the SWAMP study of Allender et al (1985), when the spectrum is not self-similar. To date there are no measurements for the scale in space and time over which self-similarity is recovered because instruments used in observations assume stationarity over a measurement period of approximately half an hour.

In the third generation (WAM) model described by Hasselmann et al (1985), Hasselmann and Hasselmann (1985) and Hasselmann et al (1989). the complete set of interactions possible for nonlinear transfer is replaced by a small subset of interaction configurations. The subset, constituting the discrete interaction approximation (DIA), is assumed independent of the functional form for the spectral energy and capable of representing nonlinear transfers involving other parts of the interaction configuration space. DIA is calibrated against the nonlinear transfer from the complete Boltzmann integral. The third generation WAM model is calibrated so that the fetch-limited growth curves for peak frequency f_p, and total energy E compare with the experimental results of JONSWAP and other efforts. Finally, the high frequency tail is required to have an f^{-5} behavior above $2.5f_p$ and deviation from that shape due to source terms is ignored. Self-similarity is thus calibrated and implemented in the third generation WAM model. Self-similarity is not explained by this model.

Snyder et al (1981), Plant (1982) and Phillips (1985) present various forms for spectral energy input by the wind S_{in}. Resio and Perrie (1989*a*) discuss these from the point of view of consistency with JONSWAP fetch laws and an f^{-4} high frequency spectral tail. The approach of Webb (1978) in transforming the nonlinear transfer source term S_{nl} is developed in Tracy and Resio (1982). This is shown to lead to an efficient stable and economical method to compute S_{nl} by Resio and Perrie (1989*b*).

Dissipation may be represented following Komen et al (1984), and the third generation WAM model of Hasselmann et al (1989). However, integrations of nonlinear transfer of Komen et al (1984) and Hasselmann et al (1989) have inherent numerical instability because they work from the original integral derived from Hasselmann (1961, 1963*a*, 1963*b*) rather from transformed versions as given by Masada (1980) or Webb (1978), and spectral balance was assumed to involve all source terms S_{in}, S_{nl} and S_{ds}. This is in contrast to the picture originated by Kitaigorodskii (1983), of a Kolmogorov-style cascade of

energy to high frequencies involving S_{nl} alone in the equilibrium range. The Komen et al (1984) representation for dissipation is therefore biased by assumptions on the modelling of nonlinear transfer S_{nl}, the dynamics of spectral balance, and the manner in which source terms combine with one another.

We compare combinations of source terms S_{in}, S_{nl} and S_{ds}, by computing the evolution with respect to time of the one-dimensional spectral energy $\hat{E}(f)$ and one-dimensional normalized spectral energy $\mathbb{E}(f)$. Connections are made to the SWAMP intercomparison as well as CASP and JONSWAP observations. The ability, or lack thereof, to model the self-similarity of a growing wind sea is evident in each case, Optimization in terms of model accuracy and computational requirements follows from the results of this survey.

SPECTRAL BALANCE

With respect to time and space, the general governing equation for the evolution of spectral energy density in deep water can be expressed as

$$\frac{\partial \mathbb{E}(f,\theta)}{\partial t} + \underline{c}_g \cdot \nabla \mathbb{E}(f,\theta) = S_{in} + S_{nl} + S_{ds} \qquad (1)$$

where $\mathbb{E}(f,\theta)$ is the two-dimensional energy density at frequency f and direction Θ. Hasselmann et al (1976) concluded that S_{nl} dominated the spectral evolution. Komen et al (1984) did a numerical study of the balance of S_{in}, S_{nl} and S_{ds} and the particular role of S_{nl} in defining the spectral shape with respect to S_{in} and S_{ds}. Kitaigorodskii (1983) and Resio (1987) suggest a balance between S_{in} and S_{ds} determines spectral development. Lastly, Phillips (1985) explains spectral evolution as an interaction of the three source terms S_{in}, S_{nl} and S_{ds}. We try to clarify the roles of all source terms acting alone and in concert with one another. Specifically, we neglect propagation and consider the evolution in time of (i) S_{nl} (ii) S_{in} + S_{nl}, (iii) S_{nl} + S_{ds}, and (iv) S_{in} + S_{nl} + S_{ds}.

(i) S_{nl} ALONE

We computed the evolution of spectral energy with respect to time in the absence of wave breaking dissipation S_{ds} and wind input energy S_{in}. Starting with the Hasselmann (1961, 1963*a*, 1963*b*) formulation for nonlinear transfer S_{nl} as the Boltzmann integral

$$S_{nl}(\underline{k},\infty) = \omega \int d\underline{k}_1 d\underline{k}_2 d\underline{k}_3 \; \mathbb{G}(\underline{k}_1,\underline{k}_2,\underline{k}_3,\underline{k}) \quad \delta(\underline{k}_1+\underline{k}_2-\underline{k}_3-\underline{k}) \cdot \delta(\omega_1+\omega_2-\omega_3-\omega)\left[n_1 n_2 (n_3+n) - n_3 n (n_1+n_2)\right] \qquad (2)$$

where action density $n(\underline{k}) = F(\underline{k})/\omega$ and $\omega=\sqrt{gk}$ and $F(\underline{k})$ is the wavenumber spectral density, we used the transformation developed in Tracy and Resio (1982). Initial spectra assumed a JONSWAP shape function with peak frequency f_p=0.03 Hz, peakedness γ=3.3, σ_a=0.07, σ_b=0.09 and α=0.01. Integrations were done on 30 second time steps for 1 hour.

In this situation the peak frequency f_p moves to lower frequencies without noticeable steepening and only marginal increase in peak height. A high frequency equilibrium range is clearly maintained with the lower boundary at ~1.6 f_p migrating slowly to lower frequencies as time evolves. Normalizing by multiplying $E(f)$ by f^4 results in an evident undershoot region at 1.25-1.6 fp. This is comparable to Figure 12 in Donelan et al (1985), and relative to the energy level of the equilibrium range, is about 20% depressed.

The dominant feature is the relaxation/migration of the peak to lower frequencies with evolving time. The slight steepening of the spectral peak is due to wave-wave interactions. There is a net energy flux to the high frequency equilibrium range of the spectrum and to the tail of the spectrum beyond the equilibrium range.

(ii) S_{in} + S_{nl}

In considering the spectral evolution as a response to wind input energy S_{in} and nonlinear transfer S_{nl}, we parameterize S_{in} following Synder et al (1981), which is typical of third generation models such as the WAM model in terms of friction velocity u_* and phase velocity c

$$S_{in}(f,\theta,) = \max\left\{0,\ 0.25\frac{\rho_a}{\rho_w}\left[\frac{28u_*}{c}\cos\phi - 1\right]\omega E(f,\theta)\right\} \qquad (3)$$

where ρ_a and ρ_w are the densities of air and water respectively, $\omega=2\pi f$ and ϕ is the angle between the wind vector and the wave propagation direction.

Integration over 1 hour at 30 second timesteps shows the peak frequency moving to lower frequencies as time evolves. Steepening of the spectral peak is clear, with the energy at the peak more than doubling in the course of this integration (as compared to ~10% increase in the spectral peak when S_{nl} alone is present as in the previous case). At this writing the ultimate shape of the spectrum was not resolved because of restrictions on computer time. It does tend to a time independent spectral shape, as wind input reaches a balance with energy fluxes to the high frequency regions of the spectrum.

Comparing the normalized results for the energy spectra $E(f)$ obtained here to those of the S_{nl} alone situation is illuminating. Whereas in the latter case the energy peak decreases as time evolves because of energy fluxes to higher frequencies, in the S_{in} + S_{nl} case these energy fluxes are balanced by wind input S_{in}, and the spectral peak maintains itself. The undershoot region, at ~ 50% depression relative to the equilibrium range energy level, is comparable to Figure 15 in Donelan et al (1985). The resultant self-similarity seen in the sharpening of the spectral peak and the maintenance of the level of the spectral peak in the normalized computations is comparable to observations of the JONSWAP study of Hasselmann et al (1973), the CASP results of Dobson et al (1989), or the Lake Ontario results of Donelan et al (1985). Duration limited computations are still in preparation at this writing but are quite relevant to similar studies in the SWAMP intercomparison of Allender et al (1985).

(iii) S_{nl} + S_{ds}

In considering the coupling of nonlinear transfer S_{nl} and wave breaking dissipation S_{ds} we use the parameterization of S_{ds} obtained in Bouws and Komen (1983) and Komen et al (1984), which is commonly used in third generation models such as the WAM model,

$$S_{ds}(f,\theta) = -3.33\times10^{-5} \langle\omega\rangle \left(\frac{\omega}{\langle\omega\rangle}\right)^2 \left(\hat{\alpha}/\hat{\alpha}_{PM}\right)^2 E(f,\theta) \qquad (4)$$

where â is a measure of wave steepness expressed in term of mean frequency

$$\hat{a} = \epsilon\langle\omega\rangle^4/g^2$$

where

$$\langle\omega\rangle = \epsilon^{-1} \int E(f,\theta)\ \omega\ df\ d\theta \qquad (5)$$

$$\epsilon = \int E(f,\theta)\ df\ d\theta \qquad (6)$$

and $\hat{a}_{PM}=4.57\times10^{-3}$ which is â for a Pierson-Moskowitz spectrum. The general form for (4) follows the Hasselmann (1974) derivation for small-scale local weak-in-the-mean processes such as whitecapping.

In integrating for 1 hour at 30 second timesteps, we found that the peak frequency migrates to lower frequencies as before, with only a

minor amount of steepening, and ~ 5% decrease in spectral energy at the peak, which does not represent a dominating effect. Steepening is due to S_{nl} whereas reduction in the spectral peak is due to S_{ds} and the fluxing of energy to the high frequency equilibrium range and beyond. Comparison among the normalized computations of $E(f)$ reveals that in this case, $S_{nl} + S_{ds}$, there is a greater depression in the energy levels than has been obtained in either S alone, or $S_{in} + S_{nl}$. The parameterization of S_{in} due to Snyder et al (1981) allows the system to tend towards an equilibrium state. S_{ds} merely represents a dissipation in the spectrum, and relative to S_{in}, has a rather minor influence. Resulting computations are not a whole lot different from those for S_{nl} alone. The situation involving two-dimensional spectra, as in Komen et al (1984) and total energy E, have not been completed at this writing.

(iv) $S_{in} + S_{nl} + S_{ds}$

Finally, we consider the spectral evolution with time when all three source terms are present. Integrating over 1 hour with 30 second time steps, we find that there is a definite similarity between this $S_{in} + S_{nl} + S_{ds}$ case and the $S_{in} + S_{nl}$ case in that undershoot and equilibrium ranges are almost the same, with only slightly lower values in the $S_{in} + S_{nl} + S_{ds}$ case. S_{ds} is evidently most important at the peak of the spectrum in the parameterization we have used. S_{ds} also appears to slow the migration of the spectral peak to lower frequencies, and to lower the level that the spectral peak is allowed to rise to in the space of a one hour integration. Completion of the two-dimensional cases should allow us to investigate the detailed balance of source terms as in Komen et al (1984). We suggest that the formulation of S_{ds} in Komen et al (1984), with assumptions about the coupling of S_{in}, S_{nl}, and S_{ds} as well as the method of computation of S_{nl} with its associated numerical instability will be seen to be important in these computations. We have yet to complete computations of total energy E as a function of time, and make comparisons with results from the SWAMP study of Allender et al (1985), and the observations of Dobson et al (1989) and Donelan et al (1985).

TENTATIVE RECOMMENDATIONS AND CONCLUSIONS

We have presented integrations of the spectral evolution with respect to time allowing as source terms: (i) S_{nl} , (ii) $S_{in} + S_{nl}$ (iii) $S_{nl} + S_{ds}$, and (iv) $S_{in} + S_{nl} + S_{ds}$. Wave models typically try to include all source terms explicitly, as in case (iv), or implicitly by modifying cases (i)-(iii). Our purpose in doing this was to assess the manner in which these source terms couple with one another.

In terms of a complete numerical evaluation of the Boltzmann integrals for nonlinear transfer S_{nl}, the algorithm originally

motivated by Webb (1978) and developed in Tracy and Resio (1982) allows an economical and numerically stable computation. This is in contrast to methods based on the original Boltzmann integrals derived by Hasslemann (1961, 1963*a*, 1963*b*), which are the basis of the Komen et al (1984) study.

The dominating source terms in the spectral balance equation are S_{in} and S_{nl}. Compared to these, S_{ds} has a lower order of importance. Overall features such as self-similarity, and the equilibrium range are evident when S_{in} and S_{nl} are present, without S_{ds}. The considerations of two-dimensional spectra were not complete at the time of this writing.

Although further investigation is clearly needed into the formulation of S_{ds} and efficient operational computational algorithms for S_{nl}, results of this survey suggest that wave models can be substantially optimized in terms of their accuracy and computational requirements. This optimization should play an important role in developing more accurate, more efficient wave models for hindcasts and operational predictions.

ACKNOWLEDGEMENTS

This work was partially supported by the Federal Panel on Energy Research and Development (PERD).

REFERENCES

Allender, J. H., Barnett, T. P., Bertotti, L., Bruinsina, J., Cardone, V. J., Cavaleri, L., Ephraums, J. J., Golding, B., Greenwood, A., Guddal, J., Gfinther, H., Hasselmann, K., Hasselmann, S., Joseph, P., Kawai, S., Komen, G. J., Lawson, L., Linne, H., Long, R. B., Lybanon, M., Maeland, E., Rosenthal, W., Toba, Y., Uji, T. and de Voogt, W. J. P. (1985) Sea Wave Modelling Project (SWAMP): An intercomparison study of wind-wave prediction models, Part I - Principle results and conclusions. Proc. IUCRM Symp. on Wave Dynamics and Radio Probing of the Ocean Surface, Miami, Plenum Press.

Donelan M. A., Hamilton, J. & Hui, W. H. 1985 Directional spectra of wind-generated waves. *Phil. Trans. R. Soc. Lond.* A 315, 509-562.

Dobson, F., Perrie, W. and Toulany, B. (1989) On the deep-water fetch laws for wind-generated surface gravity waves. In press in Atmosphere-Ocean.

Hasselmann, K. 1961 On the nonlinear energy transfer in a gravity-wave spectrum. Part 1. General theory. *J. Fluid Mech.* 12, 481-500.

Hasselmann, K. 1963a on the nonlinear energy transfer in a gravity-wave spectrum. Part 2. Conservation theorems; wave-particle analogy; irreversibility. *J. Fluid Mech*. 15, 273–281.

Hasselmann, K. 1963b On the nonlinear energy transfer in a gravity-wave spectrum. Part 3.Evaluation of the energy flux and swell-sea interaction for a Neumann spectrum. *J. Fluid Mech*. 15, 385–398.

Hasselmann, K. 1974 On the spectral dissipation of ocean waves due to white capping. *Bound.-Layer Meteor.*, 6, 107–127.

Hasselmann, K.,Barnett, T. P., Bouws, E., Carlson, H., Cartwright, D. E., Enke, K., Ewing, J. A., Gienapp, H., Hasselmann, D. E., Kruseman, P., Meerburg, A., Mialler, P., Olbers, D. J., Richter, K., Sell, W., Walden, H., 1973 Measurements of wind-wave growth and swell decay during the Joint North Sea Wave Project (JONSWAP). *Deutsche Hydrograpli. Zeit.*, Erganzungsheft Reihe A (8^0), Nr. 12.

Hasselmann, K., Ross, D. B., Midller, P. & Sell, W., et al 1976 A parametric wave prediction model. *J. Phys. Oceanogr.* 6, 200–228.

Hasselmann, S. & Hasselmann, K., 1981 A symmetrical method of computing the nonlinear transfer in a gravity-wave spectrum. *Hamburger Geophys. Einzelschr.*, Riehe A., Wiss. Abh., 52, 163 pp.

Hasselmann, S. & Hasselmann, K. 1985 Computation and parameterizations of the nonlinear energy transfer in a gravity wave spectrum. Part I: A new method for efficient computations of the exact nonlinear transfer integral. *J. Phys. Oceanogr.*, 15, 1369–1377.

Hasselmann, S., Hasselmann, K., Allender, J. H. & Barnett, T. P. 1985 Computation and parameterizations of the nonlinear energy transfer in a gravity wave spectrum. Part II: Parameterizations of the nonlinear energy transfer for application in wave models. *J. Phys. Oceanogr.*, 15t 1378–1391.

Hasselmann, S., Hasselmann, K., Komen, G. K., Janssen, P., Ewing, J. A. & Cardone, V. 1989 The WAM model- A third generation ocean wave prediction model. *J. Phys. Oceanogr.*, 18, 1775–1810.

Kitaigorodskii, S. A., 1983 On the theory of the equilibrium range in the spectrum of wind-generated gravity waves. *J. Phys., Oceanogr.*, 13, 816–827.

Komen, G. J., Hasselmann, S. & Hasselmann, K. 1984 On the existence of a fully developed windsea spectrum. *J. Phys., Oceanogr.*, 14, 1271–1285.

Masada, A. 1980 Nonliear energy transfer between wind waves. *J.*

Phys. Oceanogr., 15, 1369–1377.

Phillips, 0. M. 1985 Spectral and statistical properties of the equilibrium range in wind-generated gravity waves. *J. Fluid Mech.*, 156, 505–531.

Plant, W. J. 1982 A relationship between wind stress and wave slope. *J. Geophys. Res.* 87, 1961–1967.

Resio, D. T. 1987 Shallow-water waves. I: theory. *J. Waterway, Port, and Ocean Engineering*, 113 (3), 264–281.

Resio D. T. & Perrie W. A. 1989*a* Implications of an f^{-4} equilibrium range for wind-generated waves. In press in *J. Phys. Oceanogr*.

Resio D. T. & Perrie W. A. 1989*b* A numerical study of nonlinear energy fluxes due to wave-wave interactions in a wave spectrum. Part I: Methodology and basic results. Submitted to *J. Fluid Mech*.

Snyder, R. L., Dobson, F. W., Elliott, J. A. and Long, R. B. (1981) Array measurements of atmospheric pressure fluctuations above surface gravity waves. *J. Fluid Mech.*, 102, 1–59.

Tracy B. A. & Resio D. T. 1982 Theory and calculations of the nonlinear energy transfer between sea waves in deep water. *WES Report* No. 11, U.S. Army Engineer Waterways Experiment Station, Vicksburg, MS.

Webb, D. J. 1978 Nonlinear transfer between sea waves. *Deep-sea Res.* 25, 279–298.

ON THE DEEP-WATER FETCH LAWS FOR WIND-GENERATED SURFACE GRAVITY WAVES

F. Dobson, W. Perrie and B. Toulany

Canada Dept. of Fisheries & Oceans.,
Physical & Chemical Sciences,

Bedford Institute of Oceanography,
Dartmouth NS B2Y 4A2

ABSTRACT

With the object of providing an accurate set of open-sea wave spectra in a variety of conditions, we deployed, in conjunction with CASP, an array of 9 wave buoys (3 directional, 6 non-directional) along a 25-km line offshore from Martinique Beach, N.S. A large set of high-quality wave spectra was collected in conjunction with extensive meteorological information. The data set is unique in the sense that a large onshore swell component was normally present.

Offshore-wind cases for three windows: ±5°, ±15° and ±30° with respect to the shore normal, have been considered. Wind speed was found to be a strong function of fetch, and attempts were made to allow for this in the analysis. Power-law regressions have been produced of dimensionless sea energy, peak frequency and high-frequency spectral level (the Kitaigorodskii "alpha" parameter) vs. dimensionless fetch and wind speed (inverse wave age). The regressions are compared with earlier work: the Joint North Sea Waves Project (JONSWAP) and the Canada Centre for Inland Waters (CCIW) Lake Ontario study.

The comparisons indicate that dimensionless wave energies, peak frequencies and alpha values in this experiment are comparable with those from earlier experiments: in spite of different wind analysis methods, the CASP and CCIW fetch-limited growth laws are consistent within the contexts of the two experiments. Differences among the estimated parameters were as large within the analyses of the three windows as they are among the three experiments we compare.

1. Introduction

We describe our initial findings from the analysis of the offshore-winds subset of the well-calibrated wave spectra and accompanying winds collected during the Canadian Atlantic Storms Program (CASP) (Dobson, Perrie and Toulany, 1989). Since these spectra were collected in the North Atlantic ocean in the winter season, they are representative of truly open-sea conditions, and we report here on comparisons with wave spectra collected in enclosed or semi-enclosed areas. Since we had available to us aircraft estimates of the wind velocity and wind stress as a function of fetch (Smith & MacPherson,

1987), we were able for the first time to investigate in detail the effect of variability of the wind along the fetch.

Recent intercomparison studies (e.g. Allender et al, 1985) indicate that the parametric equations used for describing wave- growth in present-day operational wave models, such as the WAM model of Hasselmann and Hasselmann (1988), contain substantial departures from reality. We present a set of growth curves which are based on well-calibrated wave and wind measurements in the open ocean, which are consistent with past measurements when past analysis deficiencies are allowed for, and which cover most of the parameter range of interest to global ocean modelling.

At the end, we discuss the difficulties associated with relating these growth curves to models which scale with the friction velocity instead of the wind speed. To be sure, the friction velocity is the correct physical variable to use in predicting ocean waves; our question is (see e.g. Geernaert *et al*, 1987), "How can we make suitable estimates of wave growth when the physical variable the problem is most sensitive to is a function of the solution itself?"

2. Measurements

As part of CASP, we deployed 3 Datawell "Wavec" directional wave buoys and 6 "Waverider" wave height buoys along a 25-km line on a bearing of 340/160° offshore from Martinique Beach, NS (Figure 1). The data were telemetered to a shore site, where they were stored along with the spectra computed from them and sent over telephone lines to BIO for the use of real-time forecasters (METOC, MacLaren-PlanSearch) and data quality monitoring. The line consisted of three directional buoys and two nondirectional buoys in line offshore, and two sets of two "outriders":

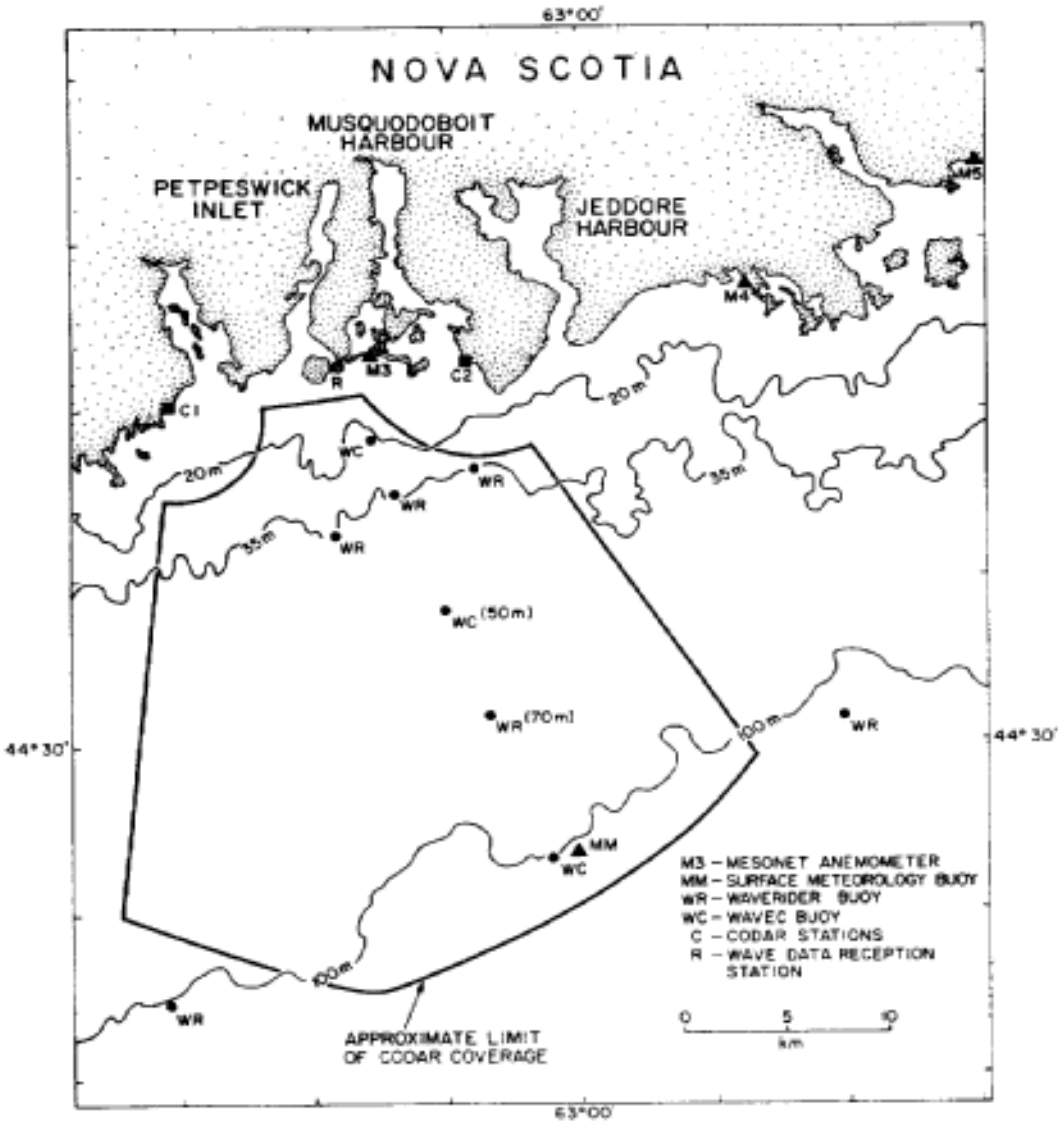

Figure 1 The CASP wave buoy array. After Dobson et al, 1989.

nondirectional buoys at 5 km from the line at the nearshore end and 20 km at the offshore end. The water depths ranged from 15m at the inshore end to 100m at the offshore end, which amounts to deep water for all waves generated by offshore winds. The buoys were calibrated for heave and directional response both before and after CASP.

In addition to the wave buoy array, wind sensors were deployed on the shoreline by the Atmospheric Environment Service (AES) Boundary Layer Research Division as part of a "Mesonet array" (cf Strapp et al., 1989). The three shoreline stations nearest the line were used in this analysis. A Coastal Climate "Minimet" buoy provided marine winds

and sea temperatures at the end of the wave buoy line. All these sensors were extensively calibrated before the experiment and intercalibrated afterwards. Along-the-line profiles of wind velocity and turbulent heat and momentum fluxes at a 50-m height were taken (Smith & MacPherson, 1987) in clear conditions during cold-air outbreaks of offshore winds following frontal passages.

The wave heights were sampled one every 0.78125 sec for 30 min at the beginning of each hour, and spectra formed from the resulting time series. The winds from the Mesonet and Minimet sensors were sampled once/sec and vector-averaged over 10 min, starting at the top of the hour; they were subsequently smoothed and subsampled over the same 30-min period as the wave sampling period.

3. Winds

Knowing that the wind speed is the most important parameter in the parameterization of the fetch-limited growth laws, we took some care in the cross-checking and analysis of the wind fields we have used. Our principal source of wind measurements was the "Minimet" buoy at the outer end of the line of wave buoys. Two Minimet components failed to give accurate or useful data: the direction indicator, and the air temperature. The direction series was "corrected", after extensive investigations, by adding 250 to the indicated value; the resulting time series has the same direction (to $\pm 50^{\circ}$) averaged over the whole of CASP as does the nearest AES shoreline station: Martinique Beach. The data from the air temperature recorder were irrecoverable: ice damaged the connector of the sensor cable; the air temperature was replaced with that from the Martinique Beach AES Mesonet station. The wind speed was extensively intercompared with the winds from the shore stations, and found to agree with them to better than $\pm 2\%$ with standard error of the mean 2.5% when only onshore winds (within $\pm 50^{\circ}$ of the shoreline normal) were included in the intercomparison. Since we have good evidence (Smith & MacPherson, 1987) that the shore station wind is a strong function of the upwind roughness during offshore and alongshore winds, we chose the Minimet winds as the best standard for marine winds.

We also performed an error analysis on the winds measured by a buoy like the Minimet, which moves considerably in any sort of a sea. There should be errors due to its heaving motion in the logarithmic boundary near the sea surface, as well as bias and sampling errors as it performs its vector average in the wave-induced oscillations of the anemometer in the wind field over the waves. Hasse *et al* (1978) looked at some of these effects; our final conclusion, after correction of the winds to a 10 m reference height (the fact we used the shore station's air temperatures instead of the *in situ* values contributed to the error), was that all errors combined should introduce a bias no greater than 2%, which we took to be negligible.

The anemometers from the shore stations showed expected errors of less than ±5% in wind speed and ±5° in direction. The principal source of error with the shore stations has been found to be their wind direction sensitivity during offshore winds. Since the wind speed at a given height (10m for the AES mesonet masts) varies with the upwind roughness, changes of a few tens of degrees in wind direction cause significant changes in the recorded wind speed, and in particular have a strong effect on the shoreline wind- marine wind ratio and the offshore profile of wind speed with fetch.

Smith and MacPherson (1987) measured the fetch profile of wind speed during offshore winds in the CASP experiment, and produced an empirical (least-squares) fit to their measured winds whereby the wind speed U_{50} at 50m height varied with the fetch x in km according to

$$U_{50}(x) = U_{50}(x=0)\left\{\frac{1 - 0.27\, e^{-x/9.3}}{0.73}\right\} \qquad (1)$$

where x=0 is at the shoreline.

Our approach was to replace the empirical fit with a model, which we could apply at any height and which would produce an algorithm for use in producing fetch averages of the wind speed. We chose the model of Taylor and Lee (1984). The premise is that flow over changes in the roughness can be represented by assuming (after Elliott, 1958) the presence of an "internal boundary layer" of thickness δ_I which starts at the roughness change and becomes thicker with fetch as

$$\delta_I = 0.75\, z_o (\varkappa / z_o)^{0.8} \qquad (2)$$

where $\varkappa$ is the upwind distance to the step change in roughness, measured in m, and z_o is the roughness length, also in m. Taylor and Lee (1984) show that, given this form of the boundary layer, the fractional change in wind speed, given by $\Delta R = [U(\varkappa)-U(0)]/U(0)$ where $\varkappa = 0$ is the position of the change in roughness:

$$\Delta R = \qquad z \geq \delta_I$$

$$\Delta R = \frac{\ln (z/z_o)\, \ln (\delta_I/z_{ou})}{\ln (\delta_I/z_o)\, \ln (z/z_{ou})} \qquad z < \delta_I \qquad (3)$$

where z is the measurement height and the "u" subscript means "upwind of the roughness change". The vertical wind profiles assumed to be everywhere steady and logarithmic.

We verified the model by comparing its prediction with the Smith and MacPherson (1987) fit and found (Dobson, Perrie & Toulany, 1989)

that a choice of 10^{-4} m for z_o and 0.07m for z_{ou} produced a wind fetch profile at 50m essentially identical with the aircraft profile. We use this model in all our subsequent determinations of the wind speed as a function of fetch over the CASP site.

4. Waves

Aside from the standard quality control measures taken during data logging and subsequent buoy-buoy intercomparisons, the CASP wave spectra required very few corrections. They were smoothed over 4 raw frequency bands to provide a final bandwidth of 0.1 Hz and a Nyquist frequency (half the sampling frequency) of 0.64 Hz, and the first and last estimates were assumed to be noisy and deleted from the analysis. After correction and deletion of faulty spectra and separating out the offshore wind cases, we were left with over 200 directional spectra with which to form our growth curves; the total set includes over 5,000 directional and 10,000 nondirectional spectra.

The CASP wave spectra exhibit the form most common in the open ocean: a long-period swell peak, typically from the south at periods of about 10s, and a shorter-period peak or peaks related to the locally-generated wind sea. Before analysis could commence on our large set of spectra, it was necessary to develop a reliable and accurate means of separating sea from swell automatically (i.e. by computer). Our technique is based on the idea that waves being actively generated by the wind cannot travel faster than the component of the wind in their direction of travel. We used the finite-depth dispersion relation to define a "critical frequency" f_c, such that

$$U_{10} \cos \Theta(f) = \mathcal{C}(f) \quad (4)$$

where $\Theta(f)$ is the wind-wave angle determined from the Wavec directional spectrum and the Minimet buoy, and $\mathcal{C}(f)$ is the phase velocity of the wave field at frequency f from the dispersion relation. To find the "separation" frequency f_s below which all energy is taken to be swell we allowed the sea spectrum to have a "front face" modelled after the "JONSWAP" spectrum, which meant moving to a frequency 0.03 Hz below f_c (equivalent to finding the half-power point of the JONSWAP nonlinear transfer rate spectrum (see e.g. Hasselmann & Hasselmann, 1981), which controls the rolloff to low frequencies of the spectrum front face). This method (Dobson, Perrie and Toulany, 1989) enables us to separate swell from wind sea in all but the most ambiguous situations. Having done this. It becomes possible to compute the wind sea energy E_o and the frequency f_m of the wind sea spectral maximum for the fetch-limited cases.

5. Scaling the growth laws

The three wave variables we scale with wind velocity and g are E_o, the total energy in the locally-generated wind sea, f_m, the frequency at

the maximum of the wind sea spectrum , and x, the fetch in the wave direction at the maximum in the wind sea spectrum. The scaling rules we use are identical to those used by Hasselmann et al (1973) and Donelan et al (1985). E_o is given by

$$E_o = \int \phi(f)\,df \qquad (5)$$

where ϕ is the wave power spectrum and the integral is over wind sea frequencies (i.e., swell is excluded). It remains to determine the fetch and compute the wind velocity. The fetch we take to be the longest distance from each buoy to the shore in three "windows": ±30, ±15, and ± 5 degrees about the offshore normal.

The wind velocity required considerable care. The technique we finally settled on, after trying several, was to form an average based on the Taylor-Lee model and the Minimet and shore station measurements. We first use the model to extrapolate the Minimet wind shoreward along its direction. We then form the average of the two shoreline stations nearest the point where the Minimet direction intersected the shore, weighted by their distance from the intersection point, and use the model to extrapolate that average wind speed back to the Minimet. The fetch profile of wind speed is then taken as the average of the two model extrapolations. The wind speed used in scaling the growth laws is the simple linear average of this fetch profile along the fetch.

We considered other possibilities for the best average to use: the wind sea "remembers" the winds which create it, but it is not clear how far the "memory" extends. Another possibility is to use an average of $(\text{wind speed})^2$ on the grounds that the wave height at least depends on that quantity. We finally chose the linear average as the simplest available form which goes beyond the idea of using the local wind, which we feel is inadequate for the reasons stated.

We then scale our wave variables with the fetch-averaged wind velocity U_{10} at 10m height, or with the component $U_{10}\cos\Theta$ in the direction of the waves (Θ is the angle between the wind and the wave directions as measured by Wavec and Minimet respectively), and with the acceleration of gravity g.

6. The growth laws

We present the growth laws (Table 1) as slope and intercept of the (least-squares) best-fit straight lines to the data points on log-log plots: that is, as the exponent and the multiplier of power laws. We include for comparison the results of the JONSWAP experiment (field data only; the original JONSWAP growth rate equations contain laboratory data) and the CCIW experiment. The first two columns are

scaled with our fetch-averaged U_{10} for comparison with the JONSWAP laws, and the last two with $U_c = U_{10}\cos\Theta$, for comparison with the CCIW laws. Note the approach to the JONSWAP results as the window is opened from ± 5 to $\pm 30^\circ$ in the first two columns, and the close agreement with the CCIW laws in the last two columns (the $\tilde{\chi}$ vs U_c/C_m fit is not as close because of the limited $\tilde{\chi}$ range in the CASP experiment).

The CASP spectra, collected in the winter months in the North Atlantic ocean, always had large low-frequency swell peaks associated with them. If the presence of the swell affects wave growth (see e.g. Donelan, 1986) it should show up in differences between our growth laws and those reported by Donelan *et al* (1985). The satisfactory growth law comparisons with earlier work in enclosed waters give credence both to our ability to remove the effects of swell and to the relative lack of importance of the presence of swell in wind wave growth, that is, that the earlier results are seen to be representative of open-ocean conditions. We point out that the good agreement with the JONSWAP laws is based on comparisons against their field data only, suggesting that the JONSWAP approach of lumping field with laboratory data prior to the (linear log-log) fit is unrealistic. The agreement with the CCIW U_c scaling indicates it is the proper wind scaling to use. We are at a loss to explain why the CASP growth laws, scaled with a fetch-averaged wind, should agree as well as they do with the CCIW laws, which were scaled with the *in situ* wind at each measurement site. We can only assume that, for the particular circumstances of the CCIW and CASP experiments, the winds determined in the two ways were essentially identical.

7. Wind velocity scales

Wave forecasters have been plagued since the beginning with the problem of wind velocity scaling (see the arguments in Hasselmann *et al*, 1973, for example). The only wind scale available to the experimentalist and to the forecaster is the wind velocity at some standard measurement height, such as 19.5m or 10m. on the other hand, there are good theoretical reasons for scaling with a variable more closely related to the physics of the wave generation process, such as the friction velocity, for example,

$$u_* = \sqrt{\tau/\rho} = \sqrt{C_{10}}\, U_{10} \qquad (6)$$

Table 1: CASP best-fit slopes and intercepts for (log-log) fetch laws, with slope standard deviations σ.

Parameters	$\tilde{E}_o$ vs $\tilde{X}^{(1)}$			$\tilde{f}_m$ vs $\tilde{X}^{(1)}$			$\tilde{E}_o$ vs $U_c \backslash \tilde{c}_m^{(2)}$			$\tilde{X}$ vs $U_c \backslash \tilde{c}_m^{(2)}$		
	slope	σ	int.x10^7	slope	σ	int.	slope	σ	int.x10^3	slope	σ	int.x10^{-4}
± 5°window												
	0.75	0.15	12.7	-0.24	0.03	1.7	-3.4	0.23	2.6	-3.3	0.41	1.2
±15°window												
	0.75	0.09	2.7	-0.24	0.02	1.7	-3.3	0.13	2.7	-3.1	0.29	1.1
±30°window												
	0.80	0.06	7.0	-0.25	0.02	1.9	-3.4	0.08	2.6	-2.6	0.18	1.0
JONSWAP[3]												
	0.90	-	3.0	-0.30	-	3.0	-3.0	-	2.0			
Donelan et al (1985)[2]												
	0.76	-	8.4	-0.23	-	1.9	-3.3	-	2.7	-4.4	-	4.2

NOTES: 1. Scaled with fetch averaged Minimet and shore station wind U_{10}.

2. Scaled with $U_c = U_{10} \cos\theta$ where θ is angle between wind and waves.

3. Slopes and intercepts for the field data only, from Müller (1970) and Hasselmann et al, (1973).

where τ is the flux of horizontal momentum into the ocean surface, ρ is the water density, and C_{10} is a dimensionless "drag coefficient".

The drag coefficient itself has been the subject of extensive experimental studies. The present standard is set by Smith (1980) and Large and Pond (1981). Their fits both produce a drag coefficient of about 1.3×10^{-3} for a wind speed of 10 m/s, which we use below for our constant drag coefficient C_{10}. More recent work, e.g. Geernaert *et al* (1987), presents good evidence that C_{10} varies with sea state. This

raises the specter of having to predict a wave field from a wind field which is related to the wave field being predicted. Geernaert et al indicate a doubling of the drag coefficient as the wave age parameter C_m/U_{10} varies from 1 (old, fully-developed) to 0.3 (young, newly-generated). Based on some recent work by S.D Smith and R.J Anderson during the HEXOS experiment (Smith, S.D., Bedford Institute of Oceanography, pers. comm., 1989), we choose a less strong behaviour for our sea state dependence:

$$C_{10}(C_m/U_{10}) = C_{10}(2-C_m/U_{10}) \quad 0 < C_m/U_{10} < 1 \quad (7)$$

$$= C_{10} \quad \text{Otherwise}$$

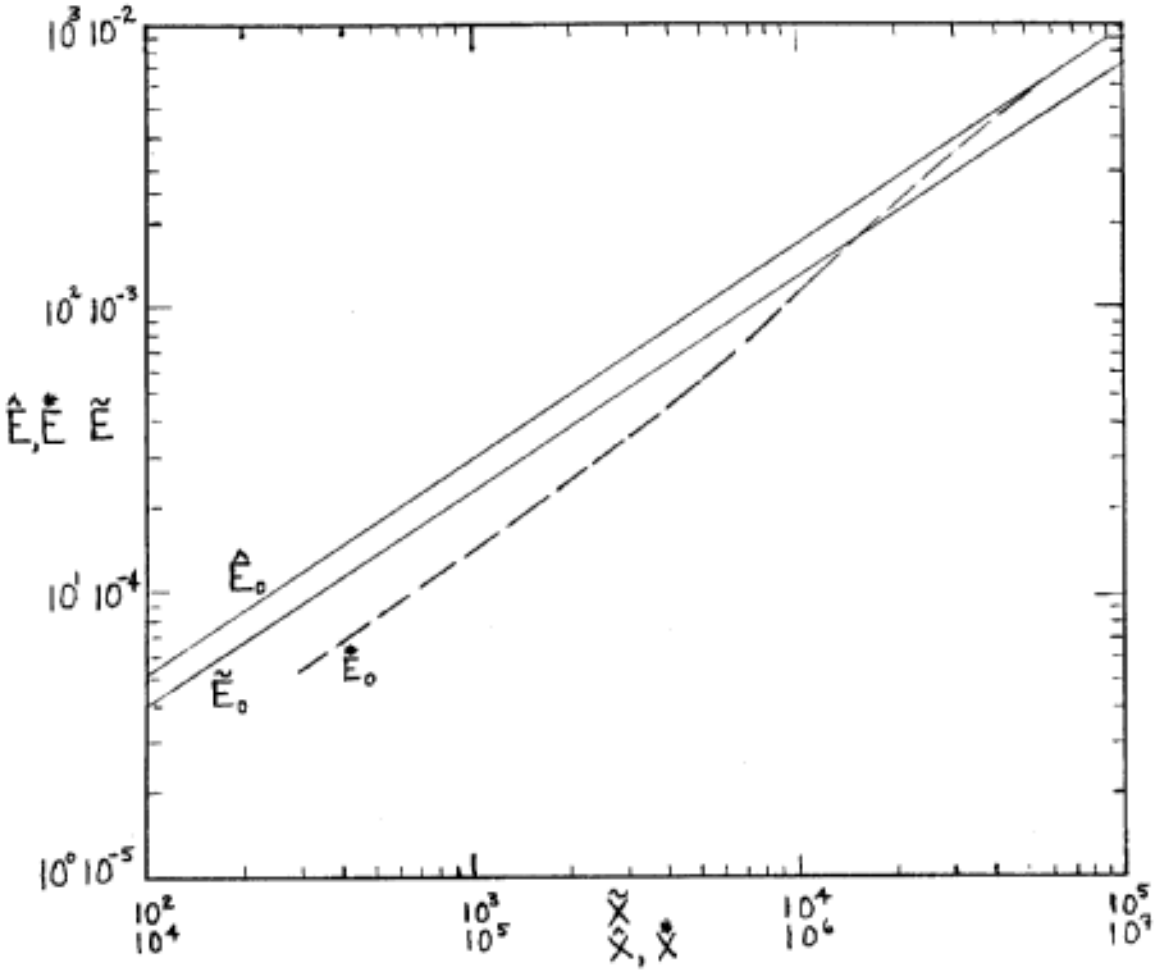

Figure 2 Comparison of three ways of scaling the energy vs fetch growth law: tilde superscript (~) scaled with U_{10}; hat (^) scaled with u_* with constant drag coefficient C_{10}; star (*) scaled with u_* with variable drag coefficient $C_{10}(C_m/U_{10}) = C_{10}(2 - C_m/U_{10})$.

To give an indication of the magnitude of the problem we have plotted (Figure 2) the dimensionless E_0 vs X relation with three wind speed scalings:

$$U_{10}: (\tilde{E}_0, \tilde{X}); u_*: (\hat{E}_0, \hat{X}); \text{ and } u_*(c_m/U_{10}): (\overset{*}{E}_0, \overset{*}{X})$$

$\tilde{E}_o$ and $\hat{E}_o$ have the same slope on the log-log plot because they differ by a constant factor, while the slope of the $\overset{*}{E}_0$ line varies with $\overset{*}{X}$, and at low $\overset{*}{X}$ the "predicted" $\overset{*}{E}_0$ value is almost a factor of 2 lower than $\hat{E}_o$. The problem faced by the forecaster is, given a wave model such as the third-generation WAM (Hasselmann *et al*, 1988) which is couched entirely in terms of u_* scaling, what relation should be chosen to get from the measured U to the model u_*? And, since the growth law contains a feedback from the sea state to the scaling parameter, should the prediction algorithm be an iterative one?

The answers to both these questions lie beyond the scope of the present paper; we only intend here to identify the problem. Without addressing the details of the relationship between the wind and the friction velocity and between the friction velocity and the sea state, we cannot expect to make significant progress in improving the wave growth scaling laws in the models we use; without such improvements we are forced back on empiricism. And if we choose empiricism, why choose to use something as complex as 3-G WAM

9. References

Allender, J. H., Barnett, T. P., Bertotti, L., Bruinsma, J., Cardone, V. J., Cavaleri. L., Ephraums, J. J., Golding., B., Greenwood, A., Guddal, J., Günther, H., Hasselmann, K., Hasselmann., S., Joseph, P., Kawai, S., Komen, G. J., Lawson., L., Linne, H., Long, R., B., Lybanon, M., Maeland, E., Rosenthal, W., Toba, Y., Uji, T. and de Voogt, W. J. P. (1985) Sea Wave Modelling ProJect (SWAMP): An intercomparison study of wind-wave prediction models,. Part 1 - Principal results and conclusions. Proc. IUCRM Symp. on Wave Dynamics and Radio Probing of the Ocean Surface, Miami, Plenum Press.

Dobson, F. W., W. Perrie and B. Toulany (1989) On the deep-water fetch laws for wind-generated surface gravity waves. Atmosphere-Ocean., 27(1): In the press.

Donelan, M. A.(1986) The Effect of Swell on the Growth of Wind Waves. Technical Digest, J. Hopkins Univ., 8, 18-23.

Donelan,.A., J. Hamilton and W.H. Hui (1985) Directional Spectra of Wind-Generated Waves. Proc. R. Soc. Lond. A., :315: 509-562.

Dunphy, P. (1986) CASP Wave buoy logging system. Unpublished BIO Internal Note. P.O. Box 1006, Dartmouth, NS B2Y 4A2, Canada. 150pp., Canada. 150pp.

Elliott, W. P. (1958) The Growth of the Atmospheric Internal Boundary layer. Trans. Amer. Geophys. Union, 39, 1048-1054.

Geernaert, G. L., S. E. Larsen and F. Hansen (1987) Measurements of Wind

Stress, heat Flux, and Turbulence intensity During Storm Conditions over the North Sea. J. Geophys. Res., 92: 13127-13139.Hasse, L., M. Grünewald, and D. E. Hasselmann (1978) Field Observations of Air Flow Over Waves. In Turbulent Fluxes Through the Sea Surface, Wave Dynamics and Prediction, Eds. A. Favre and K. Hasselmann, Plenum, N. Y.: 483-494.

Hasselmann, K., Barnett, T. P., Bouws, E., Carlson, H., Cartwright, D. E., Enke, K., Ewing, J. A., Glenapp, H., Hasselmann, D. E., Kruseman, P., Meerburg, A., Müller, P., Olbers, D.J., Richter, K, Sell., W. and Walden, H. (1973) Measurements of wind-wave growth and swell decay during the Joint North Sea Wave Project. (JONSWAP). Deut. Hydrogr. Z., Reihe A (8°), Nr.12.

Hasselmann., S. and Hasselmann, K. (1981) A symmetrical method of computing the nonlinear transfer in a gravity-wave spectrum. Hamb. Geophys. Einzelschriften, Reihe: Wiss. Abhand., 52, 138 pp.

Hasselmann, S., K. Hasselmann, E. Bauer, P. A. E. M. Janssen, G. J. Komen, L. Bertotti, P. Lionello, A. Guillaume, V. C. Cardone, J. A. Greenwood, M. Reistad, L. Zambresky and J. A. Ewing. (1988) The WAM Model - a Third Generation Ocean Wave Prediction Model. J. Phys. oceanogr., 18: 1775-1810.

Large, W. G. and S. Pond (1981) open ocean momentum flux measurements in moderate to strong winds. J. Phys. Oceanogr., 11 : 324-336.

Müller, P. (1970) Parameterization of One-Dimensional Wind Wave Spectra and Their Dependence on the State of Development. Hamburger Geophysik. Einzelschr., 31, 177 pp.

Smith,P.C. and J.T. MacPherson (1987) Cross-Shore Variations of Near-Surface Wind Velocity and Atmospheric Turbulence at the Land-Sea Boundary during CASP. Atmosphere-Ocean., 25: 279-303.

Smith, S.D. (1980) Wind Stress and Heat Flux over the ocean in Gale Force Winds. J. Phys. Oceanogr., 10: 709-726.

Strapp, J.W., C. Banic and C. Anderson (1987) CASP Data Inventory. Canadian Atlantic Storms Program., Atmos. Environ. Serv., 4905 Dufferin St., Downsview, Ont. M3H 2T5. 214 pp.

Taylor, P.A. and R.J. Lee (1984) Simple Guidelines for Estimating Wind Speed Variations due to Small-Scale Topographic Features. Climatol. Bull., 18: 3-32.

WAVE GROWTH IN SLANTING FETCH CONDITIONS

[1]H. Günther, [1]W. Rosenthal, [2]J.G. Briz and [2]J.E. de Luis

[1]GKSS-Forschungszentrum
Geesthacht, FRG

[2]Programa de Clima Maritimo
Madrid, Spain

1. INTRODUCTION

Numerical wave prediction models are based on the theory of wave dynamics and on empirical data. The data used to tune the models are fetch and/or duration limited growth curves. These laws are observed under highly ideal conditions, e.g. homogeneous, stationary perpendicular off-shore blowing winds.

The commonly occurring off-shore winds are directed in an arbitrary angle to the coast line. Therefore slanting fetch cases are of considerable practical concern for all near shore marine operations.

In the next chapter we summarize case III (slanting fetch) of the SWAMP-study (1985), and outline the basic processes governing the wave development in this situations. Chapter 3 reviews the empirical results of Donelan (1980) of wave growth in Lake Ontario, where slanting fetch conditions are always present. These results are used to update the boundary value supply in the HYPA wave model (Günther et al. 1981), and the new model results are compared to the SWAMP study in Chapter 4 .

In the last chapter of this paper a model application around the Iberian Peninsula is presented and the old and new HYPA versions are compared with measurements taken close to Bilbao.

2. SWAMP CASE III

The setup of the wave model experiment is shown in Fig. 1 . A uniform wind of 20 m/s, directed diagonally is blowing over the entire grid. The upwind boundaries are closed to simulate shorelines, whereas the down wind boundaries are open. The waves developed from the models on the diagonal of the grid, followed slightly reduced model growth curves (in the final stationary case the model fetch law). Outside the diagonal the wave energies gradually decrease towards the coast lines and the mean wave direction is turned by about 201 towards shore. The Figures 2 and 3 show the stationary wave field calculated by the HYPA model. The wave growth parallel to the shore cannot be explained by the model fetch law, even if it is applied to the upwind distance to the coast. As the wind has a shore (x-axis) parallel component, at

the output point F in figure 1 lower frequency energy is developed due to the remarkable increased fetch length. Additional low frequency energy is received at point F from the whole triangle D, B, F, by propagation. Therefore the waves at this side are influenced by the growth in the whole triangle D, B, F by propagation towards F and because of the non-linear wave-wave interaction by the coupling between different directional wave components.

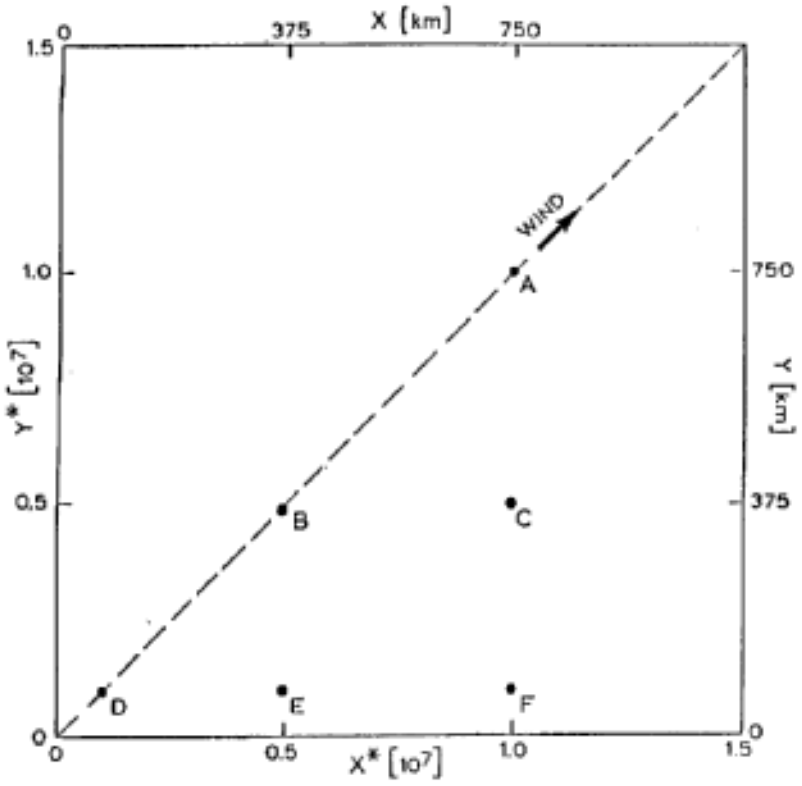

Figure 1. Setup of the SWAMP case III test. Special output points are denoted A-F. (from SWAMP, 1985).

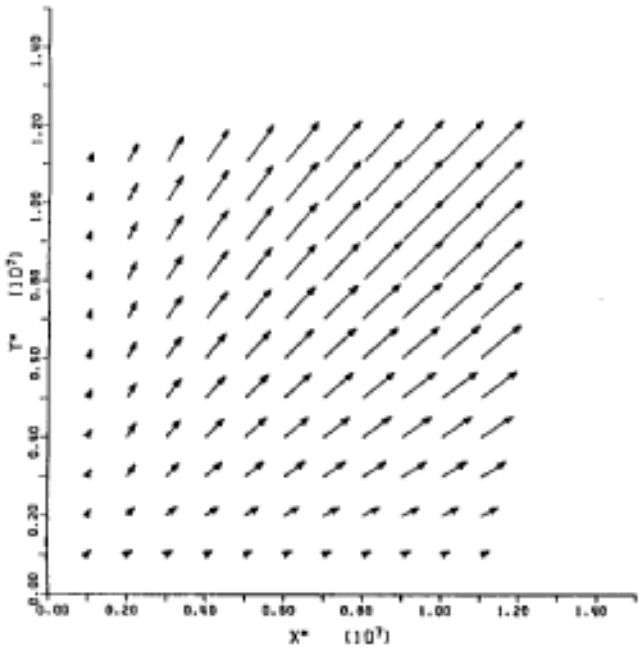

Fig. 2. Case III results of HYPA The length of the vectors proportional to energy and the direction denotes mean sea direction.

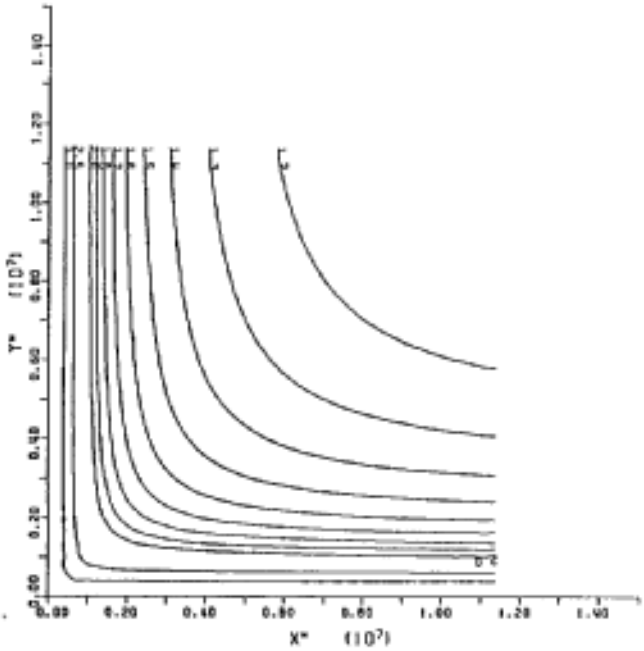

Fig. 3. Case III results HYPA. Isolines of peak frequency, normalized by the Pierson-Moskowitz frequency for 20 m/s windspeed.

In the SWAMP study all coupled second generation wave models and the later third generation wave model of the WAM group (Hasselmann, 1985) show comparable behaviour, supported qualitatively by studies of directional distributions of waves for slanting fetch situations off the Dutch coast (Holthuijens, 1983). Nevertheless a detailed quantitative analysis is still lacking, because two-dimensional wave spectra are rare, but will hopefully be available in the near future, when radar measurements will be in routine operation. The empirical model for wave development in a lake, where slanting fetches are common, by Donelan (1980) will be discussed in the next chapter and may be helpful to get a better quantitative understanding of the situation.

3. WAVE GROWTH IN A LAKE

We first concentrate on the fetch limited wave field. As already mentioned, in simple geometries (e.g. perpendicular off-shore blowing wind) the wave field can be described by growth curves. In the HYPA model for instance the peak frequency of a fetch limited wave field F(x,u) with the fetch length x and windspeed u at 10 metres above sea surface is given as

$$F(x,u) = \text{Maximum } (f_m, f_{PM}\} \quad (1)$$

where

$$f_m = \frac{g}{u} 2.84 \left(\frac{xg}{u^2}\right)^{-0.3} \quad (2)$$

and

$$f_{PM} = \frac{g}{u} 0.13 \quad (3)$$

is the Pierson – Moskowitz limit to avoid overdevelopment.

The more complex geometry in a lake, shown in Figure 4 , has been investigated by Donelan (1980). Assuming a wind of speed u and direction ϕ is blowing to the observation point 0. The peak frequency f_p of the waves at the observation point in stationary, homogeneous situations is determined by the minimum of all frequencies calculated over all possible fetches with a component of the wind pointing towards 0;

$$f_p = \underset{\Psi}{\text{Minimum}} \{F(x(\Psi), u \cos(\phi-\Psi))\} \quad (4)$$

where the angle Θ between wind and fetch direction fullfills

$$|\Theta| = |\Phi - \Psi| < 90° \quad (5)$$

The dominant wave direction at the observation point is given by the fetch direction Ψ, that solves equ.(4).

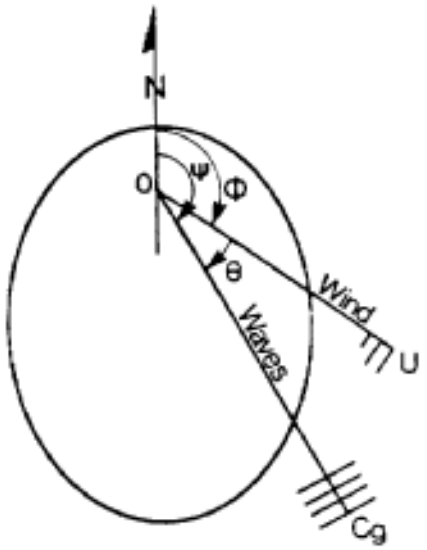

Figure 4. Definition sketch showing the direction of approach of the wind Φ and waves Ψ as seen from a point 0. (from Donelan, 1980)

The Donelan fetch law

$$f_m = \frac{g}{u} 1.84 \left(\frac{xg}{u^2}\right)^{-0.33} \quad (6)$$

differs slightly from equ. (2), but is comparable in the range of normally occurring cases. To be consistent within the HYPA model we will apply equ.(2) in the following.

For long fetches and short durations the above presented diagnostic model will overestimate the seastate, because the waves will be duration limited. To correct for this effect for each wind speed and fetch length the growth is further limited by the time, which the waves need to propagate over the upwind fetch distance

$$\tau(x,u) = \int_0^x \frac{dx}{c_g(f_p)} \quad (7)$$

where $c_g(f_p)$ denotes the group velocity of the peak frequency, defined by the fetch law.

4. THE HYPA BOUNDARY VALUE SUPPLY

The HYPA wave model needs boundary values at the first grid point off-shore, when the wind direction is off-shore. The parameters of the JONSWAP spectrum have to be defined. In the model version applied in the SWAMP exercise fetch laws have been used, equ. (1) was applied to the local windspeed and the gridspacing Dx to fix the peak frequency at boundary points. The remaining JONSWAP parameter were defined by equilibrium laws, like the so-called α - v relation, which depend on windspeed and peak frequency only. The mean wave direction was taken parallel to the wind direction.

Therefore in the above described SWAMP case III the first row of grid points (not shown in the Figures 2 and 3) has constant wave height all along the shore (x-axis). The growth visible in the figures results from internal model balance of the above mentioned processes, but is of course limited by the rather small values at the first off-shore grid points. To avoid these artificial limitations the results presented in the previous chapter are implemented subsequently into the boundary routine of the model.

The HYPA model works on a rectangular grid with grid spacing Dx. Let P_0 be a point, where boundary values are required, and u the windspeed at P_0, then in the up-wind half plane 4 grid points P_i exist with a positive component u_i of the wind pointing to P_0. These points may be land- or seapoints and the distances x_i to P_0 are Dx or $\sqrt{2}$ Dx.

If P_i is a land point equ. (1) is applied to x_i and ui to compute a fetch limited estimate of the peak frequency

$$f_i = F(x_i, u_i) \qquad (8)$$

At sea points P_i a peak frequency $\tilde{f}_i$ is fixed from the previous time step, which defines an effective fetch Xi, calculated from equ. (1) by solving

$$\tilde{f}_i = F(X_i, u_i) \qquad (9)$$

The estimate at point P_0 is determined again by equ. (1) using as fetch $X_i + x_i$ and windspeed u_i.

In a second step the duration limited growth curve

$$D(t,u) = \text{Maximum}\left(\frac{g}{u}\, 16.3\, \left(\frac{tg}{u}\right)^{-0.43};\ f_{PM}\right) \qquad (10)$$

of the model is used to define the maximum change of the peak frequency at P_0 within one model time step Dt. An effective duration T_i is computed from equ. (10), using u_i and the value of the peak frequency at P_0 from the previous time. Application of (10) for $t = T_i + Dt$ and $u = u_i$ results in the duration limited estimates $\hat{f}_i$.

The maximum of f_i and $\hat{f}_i$ gives the estimate at P_0 resulting from the upwind point P_i and according to the results of Donelan the smallest value is used as new boundary value.

$$f_0 = \min_i \left[\ \text{Maximum}\left(f_i, \hat{f}_i\right)\ \right] \qquad (11)$$

The other JONSWAP parameters at boundary point P_0 are fixed as before depending on f_0 and the local windspeed. The mean wave direction is defined by the direction P_i, P_0, where P_i is the point that satisfies (11), turned into the wind direction by about 10°.

The same grid specification as in the SWAMP study is used to rerun case III with the HYPA wave model using the new boundary value supply. The results are shown in Figures 5 and 6 . The enhanced growth parallel to the coast, compared to Figures 2 and 3 , is clearly visible.

It has to be noticed that this is a result of the diagnostic boundary value supply only. It may be argued that similar results may be achieved if the natural boundary condition zero energy at land points is used all over, the internal physics of the model should give the true answer. This is of course correct as long as the physical processes are parametrized adequately. The third generation wave model

as well as some of the SWAMP models are using zero energy as boundary values and have results similar to the old HYPA version. Applications of the shallow water HYPAs model in the North Sea and comparison with measurement show an improvement of the model results when the new method is used. This raises the question whether the non-linear coupling between different direction bands is to strong in all these models.

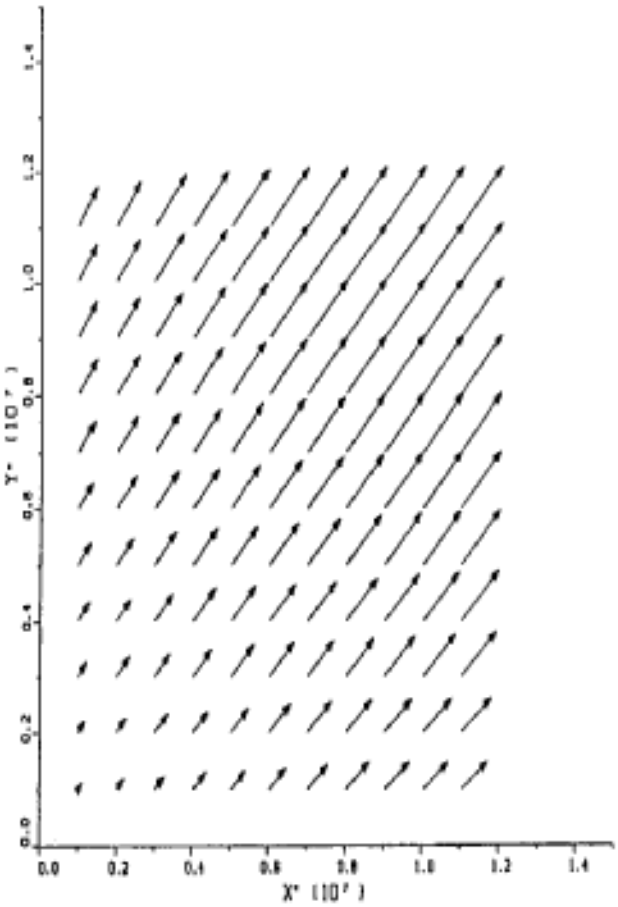

Fig. 5. Same as Fig. 2, but new boundary value supply

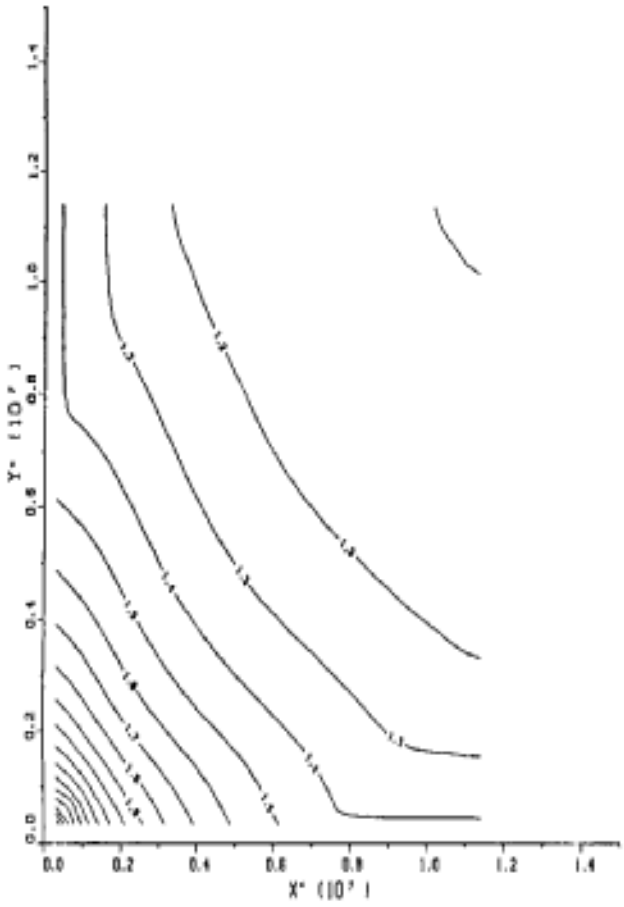

Fig. 6. Same as Fig. 3, but new boundary value supply

5. COMPARISON WITH MEASUREMENTS

An interesting area to study slanting fetch wave development is the north coast of the Iberian Peninsula. The straight shore line is about 700 km. It has a closed corner as in the SWAMP case at the east boundary, whereas the Bay of Biscay is open to the Atlantic Ocean at the West. Figure 7 shows the area which is part of the PCM (Programs de Clima Maritimo) storm hindcast wave model set up (de Luis, 1989). The figure includes at each of the grid points wind vectors on December 20, 1982. The grid spacing is 12.5 km.

Wind fields as shown in the figure occur quite frequently. Here the windspeed is around 17 m/s along the entire shore line and the weather pattern remains constant over about 18 hours from the 19th at 18.00 to the 20th at noon. The direction slightly turns from SW to W during this time.

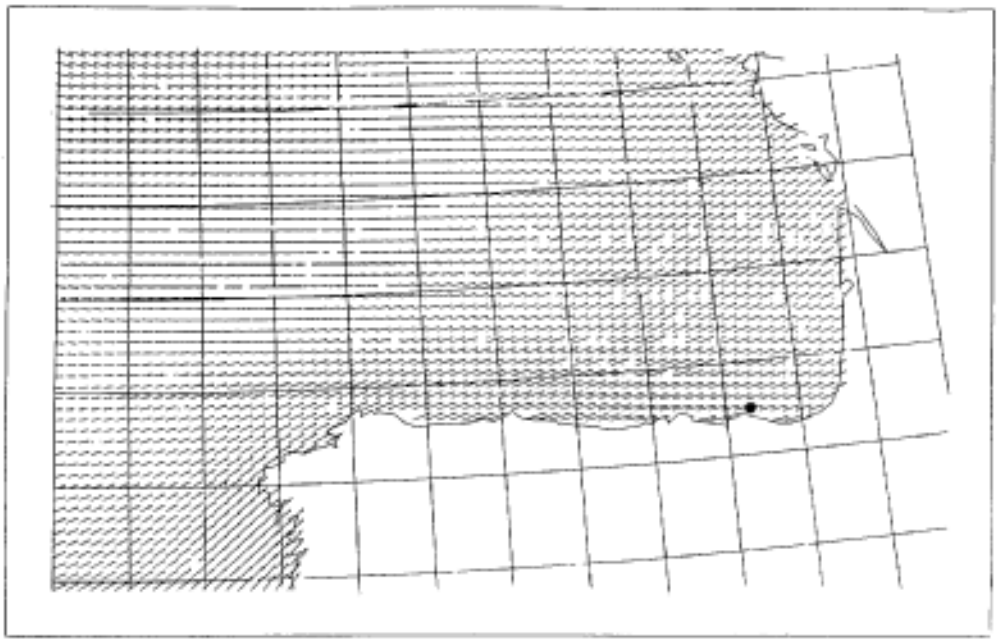

Figure 7. Windfield in the Bay of Biscay on December 20, 1982 at 6.00 hours. The dot denotes the location of the buoy.

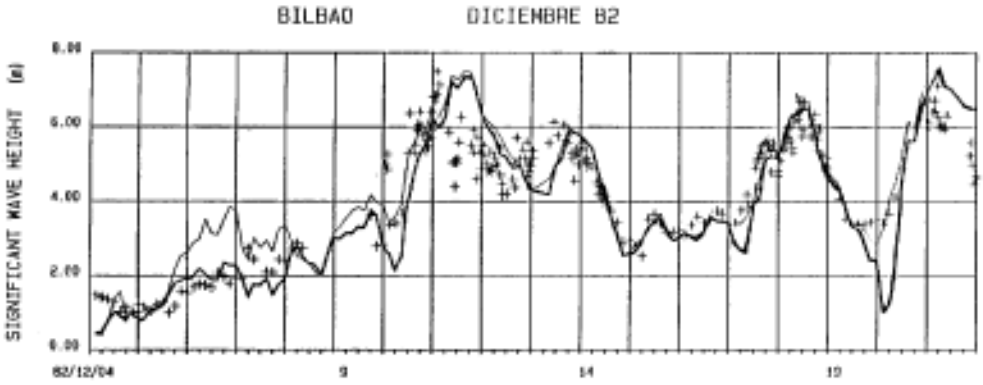

Figure 8. Comparison of HYPA results with measurements of significant wave height. The thick line corresponds to the old, the thin to the new boundary value supply.

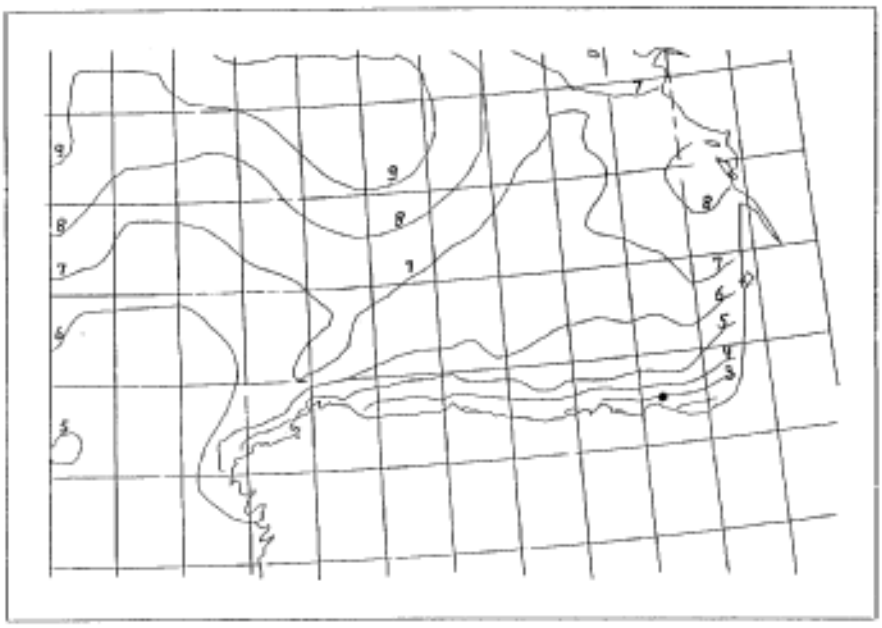

Figure 9. Isolines of significant wave height on December 20, 1982 at 6.00 hours as computed by the HYPA model, using the old boundary value supply.

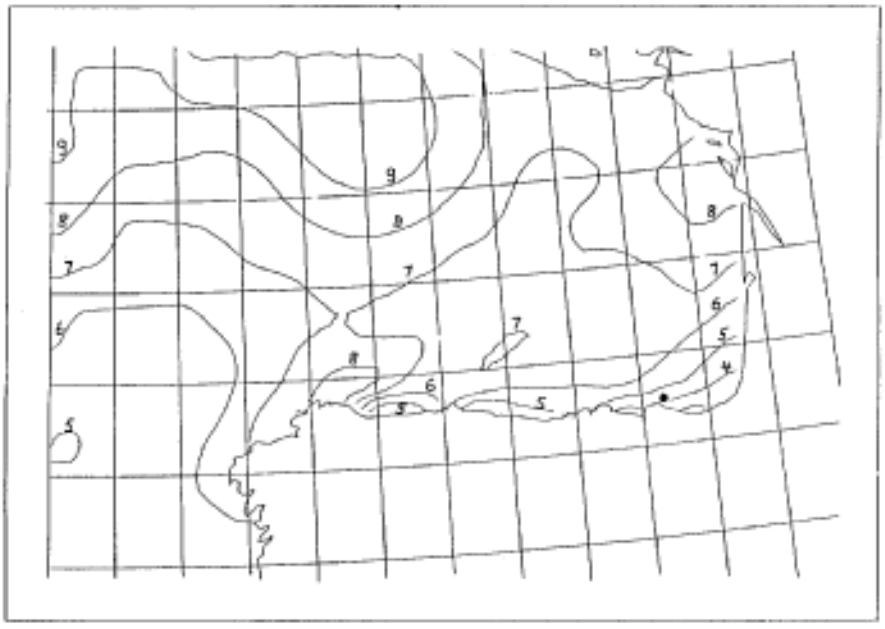

Figure 10. Same as Figure 9, but new boundary value supply.

The thin and thick line in Fig. 8 represents results of the HYPA wave model using the new and old boundary value supply, respectively. In most of the time both models agree with the measurements of the ENIEPSA buoy located close to Bilbao, marked by a dot in Fig. 7 . As expected the model results improved remarkable on the 20th when the new method was applied, but overestimated the wave height on the 6th where the wind direction was parallel to the coast. This is an example of the sensitivity of the method to small charges in wind direction and coastline irregularities.

The space distribution of wave height for both models is given in Figures 9 and 10 . The comparison of the figures shows an increase of the near coast wave heights by 1 to 2 metres. Details of the model performance are shown in Fig. 11 , which compare the two-dimensional model wave spectra at the site Bilbao. On the 20th at 6.00 hours the strong increase of the local wind wave is clearly visible. At 12.00 hours the differences are much smaller because the wind has turned and the energy now is received from North West.

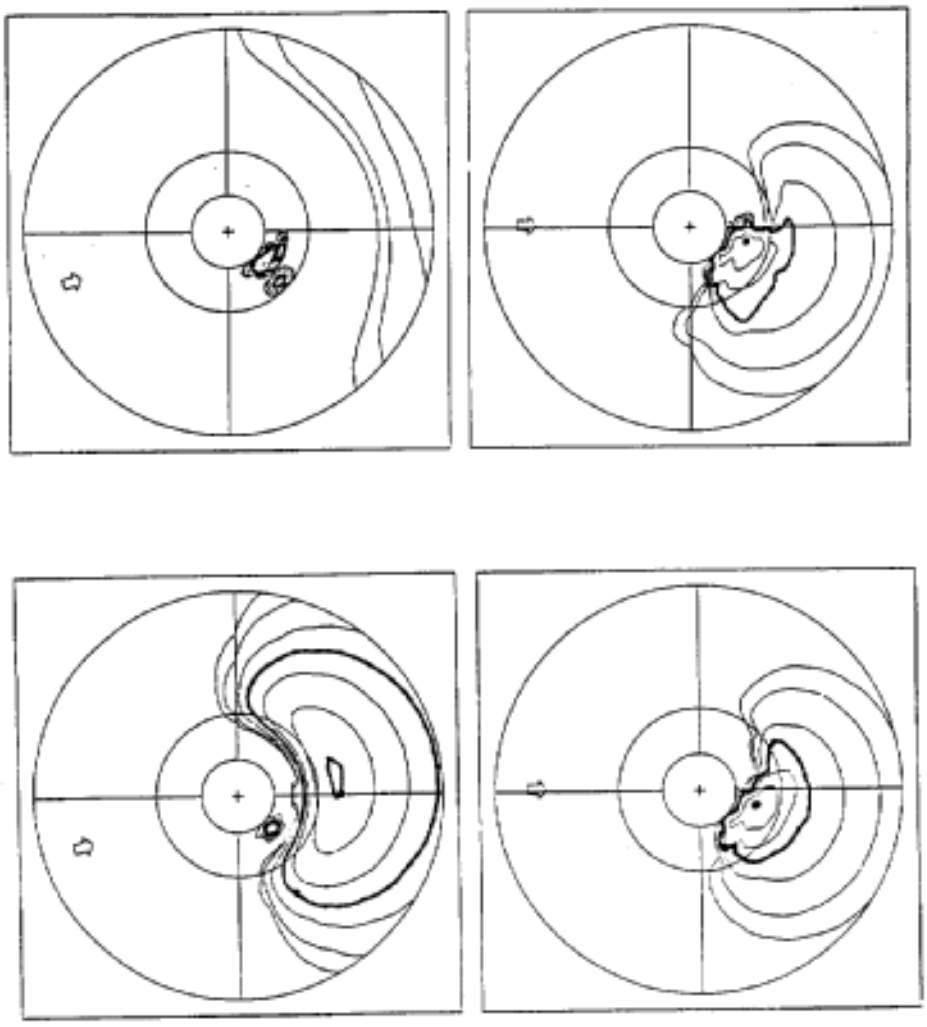

Figure 11. Two dimensional HYPA wave spectra upper panals from the old, lower from the new model version. The left spectra are at 6.00 h, the right ones at 12.00 on December 20, 1982. The vector included denotes wind direction.

6. SUMMARY

Wind wave development in slanting fetch situations have been investigated. Based on the diagnostic method of wave growth in lake Ontario a new boundary value supply for the HYPA wave model was developed and tested in the artificial SWAMP case III and a real situation at the North Spanish coastline.

The new method increased wave development parallel to the shore and shows good agreement with measurements most of the time, but is quite sensitive of small errors in the wind direction and coastline irregularities, which have to be resolved quite well in the specified grid.

The model results with the new boundary value supply may be a hint that the coupling of different direction bands due to non-linear wave-wave interaction have to be reinvestigated.

Unfortunately measurement of two dimensional spectra to resolve this problem are rather rare in slanting fetch conditions, but will hopefully become available in the near future when radar measurement will be in routine operations.

7. REFERENCES

Donelan, M. A. 1980: Similarity theory applied to the forecasting of wave heights, periods and directions. In Proceedings of the Canadian Coastal Conference, 22-24 April, Burlington, Ontario, Canada.

Günther, H., Rosenthal, W., Dunckel, M. 1981: The response of surface gravity waves to changing wind directions. J. Phys. Oceanogr. 11, 718-728.

Hasselmann, S., Hasselmann, K., Allender, J.H., Barnett, T.P. 1985: Computations and parameterizations of the nonlinear energy transfer in a gravity-wave spectrum. Part II: Parameterizations of the nonlinear energy transfer for application in wave models. J. Phys. Oceanogr. 15, 1378-1391.

Holthuijsen, L.H. 1983: Observations of the directional distribution of ocean-wave energy in fetch-limited conditions. J. Phys. Oceanogr. 13, 191-207

De Luis, J.E., Briz, J.G., Günther, H., Rosenthal, W. 1989: Results from PCM Hindcast Projects. In Proceedings of the Second International Workshop on Wave Hindcasting and Forecasting, 25-28 April, Vancouver, British Columbia, Canada.

The SWAMP Group 1985: Sea wave modelling project (SWAMP). An intercomparison study of wind wave prediction models, Part I: Principal results and conclusions. Ocean Wave Modeling, Plenum, 256 pp.

BOTTOM FRICTION FOR RANDOM WAVES DURING STORM CONDITIONS

S.L. Weber

Royal Netherlands Meteorological Institute, The Netherlands

ABSTRACT

The spectral energy dissipation due to friction in the turbulent bottom boundary layer is derived, using two different parameterizations for the turbulent stress: the eddy viscosity model and the quadratic draglaw. The differences between the eddy viscosity expression and the draglaw expression can be explained from the different stochastic characteristics of the parameterizations. Both expressions are used in a hindcast of a severe depth-limited storm with a regional version of the third generation WAM model. The results are compared with measurements from two different stations.

1. INTRODUCTION

Surface gravity waves with wave lengths, which are long compared to the water depth, give rise to a thin wave boundary layer at the sea bottom. In this boundary layer, the wave orbital velocity increases rapidly from zero at the bottom to a finite value, determined by the outer flow, at the top. Under storm conditions, characteristic velocities $U > 0.1$ m/s and characteristic boundary layer thickness $d > 0.1$ m are easily found. This means that the boundary layer Reynolds number $R = Ud/\nu > 10^4$ (where $\nu \sim 10^{-6}$ m^2/s), so that the boundary layer is turbulent. If the wave velocities are large enough to initiate sand movement, ripples may form, which increases the roughness experienced by the waves.

The wave energy loss due to friction in the turbulent bottom boundary layer is to first order in wave steepness completely determined by the free stream velocity and by the value of the stress at the bottom (Kajiura, 1968). The dissipation therefore depends on the parameterization used for the turbulent stress. In case of a random wave field, the statistical characteristics of the parameterization have to be taken into account.

In Weber (1989) a formal parameterization of the stress in terms of the outer flow was applied to investigate the dependence of the energy dissipation on the statistical characteristics of the stress. The energy dissipation was found to be proportional to a characteristic velocity and to a dimensionless function of the scaled bottom roughness

length. The form of the dissipation expression and the strength of the dissipation were found to depend on the statistical characteristics of the stress. Examples of this formal parameterization are the eddy

viscosity model and the quadratic draglaw. An expression for the energy dissipation based on the quadratic draglaw has been given before by Hasselmann and Collins (1968).

In the present study the dissipation expressions, which can be derived from the eddy viscosity model and from the quadratic draglaw, are discussed. Emphasis is laid on the different statistical characteristics of the two models. Only main results are given in this paper, for a more extensive account reference is made to Weber (1989). Both dissipation expressions have been used to hindcast a severe depth-limited storm; the hindcast results illustrate the characteristic features of both parameterizations. The hindcasts were done with a regional version of the third generation WAM model (Riepma and Bouws, this volume). Results are compared with measurements from two different stations.

2. BOTTOM FRICTION FOR RANDOM WAVES

Ocean surface waves are almost always random, in the sense that the surface elevation has to be regarded as a stochastic variable. The surface elevation n is given as the sum of a large number of wave components with independent random phase angles. From the Central Limit Theorem it follows that η and functions linearly depending on are jointly Gaussian (see e.g. Phillips, 1980).

Correct to first order in wave steepness the surface elevation η is given by:

$$\eta = \sum_{\underline{k}} \tilde{\eta}_{\underline{k}} + \text{c.c.} \qquad (2.1)$$

with $$\tilde{\eta}_{\underline{k}} = \tfrac{1}{2} A_{\underline{k}} \, e^{i(\underline{k}.\underline{x} - \omega t)}$$

Here $A_{\underline{k}}$ is the random wave amplitude, $\underline{k} = (k_1, k_2) = (k \cos\theta, k \sin\theta)$ the wave number of a wave component with modulus k and direction θ, ω is the radian frequency, related to k and the water depth h by: $\omega^2 = gk \tanh(kh)$· $\underline{x}$ is the horizontal place coordinate, t is time. The mean of a wave component is taken to be zero and the only non-zero second moment is:

$$\langle \tilde{\eta}_{\underline{k}} \, \tilde{\eta}^{*}_{\underline{k}} \rangle = \tfrac{1}{2} F(\underline{k}) \, \Delta\underline{k} \qquad (2.2)$$

with $F(\underline{k})$ the two dimensional wave number spectrum and $\Delta\underline{k}$ the wave number increment, <.> stands for ensemble averaging.

If the boundary layer thickness is small compared to a horizontal length scale, say a wave length, the boundary layer can be treated as

a correction to the inviscid, non-turbulent outer layer. The boundary layer regime is determined by the (horizontal) free stream velocity $\underline{U}$ at the top of the boundary layer and by the bottom roughness.

$\underline{U} = (U_1, U_2)$ is given by (i = 1,2):

$$U_i = \sum_{\underline{k}} \frac{k_i}{k} \tilde{U}_{\underline{k}} + c.c. \qquad (2.3)$$

with $\tilde{U}_{\underline{k}} = \frac{\omega}{\sinh kh} \tilde{\eta}_{\underline{k}}$

The spectral energy dissipation due to friction in the boundary layer is given by:

$$g \frac{\partial}{\partial t} F(\underline{k}) = - \langle \underline{\tau}(y_0) . \underline{U}_{\underline{k}} \rangle \qquad (2.4)$$

Here the dot denotes the inner product, g is the gravitational acceleration. $\underline{\tau} = (\tau 1, \tau 2)$ denotes the turbulent shear stress and $Y_0 = -h + k_N/30$ is the theoretical bottom level, where the velocity is taken to be zero in case of a hydrodynamically rough bottom, k_N has to be determined experimentally as a function of the roughness elements (sand grains, ripples). The right hand side of (2.4) can be worked out by substitution of a parameterization for the stress in terms of a known quantity, such as the free stream velocity $\underline{U}$. This will be done in section 3 with the eddy viscosity model and in section 4 with the draglaw.

The empirical JONSWAP (1973) expression, which is used up till now in the WAM model, is:

$$\frac{\partial}{\partial t} F(\underline{k}) = - C \frac{k}{\sinh 2kh} F(\underline{k}) \qquad (2.5)$$

where C is a dissipation coefficient, which is taken equal to the mean JONSWAP value 0.008 m/s (C is related to the coefficient Γ, which is used in JONSWAP by: $2\Gamma/g = C$). In case of the Texel storm the dissipation rate (2.5) was found to be much too low.

3. THE EDDY VISCOSITY MODEL

The eddy viscosity model has first been applied to the monochromatic wave boundary layer by Kajiura (1968). Extensions to a combined (monochromatic) wave-current model and a model for the sediment-wave interaction have been developed by Grant and Madsen (1979, 1982). The case of a random wave boundary layer is treated in Weber (1989).

In the eddy viscosity model the turbulent shear stress is parameterized in analogy to the viscous stress, with the coefficient of molecular viscosity replaced by a turbulent eddy viscosity coefficient. Here the eddy viscosity coefficient is taken to be proportional to the distance from the bottom and to the averaged friction velocity u*, which is defined by:

$$u^* = \langle \underline{\tau}_0^{1/2} \rangle = \langle [\tau_1^2(y_0) + \tau_2^2(y_0)]^{1/4} \rangle \qquad (3.1)$$

(For notational convenience the density of water is taken to be 1 kg/m^3 in the remainder of this paper.)

The stress and the velocity in the boundary layer can be found by substitution of the parameterization in the boundary layer equations. This yields for the stress (i=1.2):

$$\tau_i(y_0) = u^* \sum_{\underline{k}} \frac{k_i}{k} T_{\underline{k}}(\xi_0)\, \tilde{U}_{\underline{k}} + \text{c.c.} \qquad (3.2)$$

The proportionality factor $T_{\underline{k}}(\xi_0)$ is a dimensionless complex function of the scaled roughness length $\xi_0=(4y_o\omega/\kappa u^*)^{1/2}$, with κ = 0.4 von Kármán's constant. ξ_0 reflects the ratio between the roughness length and the boundary layer thickness, which scales with u^*/ω. The stress components in (3.2) are in the statistical sense linear functions of the free stream velocity components, as u* is an averaged quantity. Note that (3.2) is not linear in the free stream velocity in the usual meaning of the word. The stress contains only first harmonics in this formulation.

From (3.2) it follows that τ_1, τ_2, are jointly Gaussian. From the known distribution function u* can be rewritten as:

$$u^* = \sigma_{11}^{1/2}\, F_3(A) \qquad (3.3)$$

where $A = 1 - \sigma_{22}/\sigma_{11}$ is a measure of the directional spread of the bottom stress spectrum, F_3 is denoted in fig. 1 . The bottom stress variances, normalized by u*, are given by (i,j = 1,2):

$$\sigma_{ij} = \left\langle \frac{\tau_i \tau_j}{u^{*2}} \right\rangle = \int_{\underline{k}} \frac{k_i k_j}{k^2} T_{\underline{k}}(\xi_0)\, T^*_{\underline{k}}(\xi_0)\, \frac{\omega^2}{\sinh^2 kh}\, F(\underline{k})\, d\underline{k} \qquad (3.4)$$

The friction velocity has to be determined iteratively from (3.3) and (3.4), as the bottom stress variances depend on u* through the argument ξ_0 of $T_{\underline{k}}T_{\underline{k}}^*$. The iteration converges to a unique solution, so that u* is uniquely defined for each Surface elevation spectrum, water depth and bottom roughness k_N. The friction velocity does not depend sensitively on the value of k_N.

The spectral energy dissipation now follows from substitution of (3.2) in (2.4) as:

$$\frac{\partial}{\partial t} F(\underline{k}) = - u^* [T_{\underline{k}}(\xi_0) + T^*_{\underline{k}}(\xi_0)] \frac{k}{\sinh 2kh} F(\underline{k}) \qquad (3.5)$$

The basic form of this expression is the same as that of (2.5), but now C has been replaced by:

$$C_{eddy} = u^* [T_{\underline{k}}(\xi_0) + T^*_{\underline{k}}(\xi_0)] \qquad (3.6)$$

In fig, 2 $T_{\underline{k}}(\xi_0) + T^*_{\underline{k}}(\xi_0)$ is given as a function of the scaled roughness length.

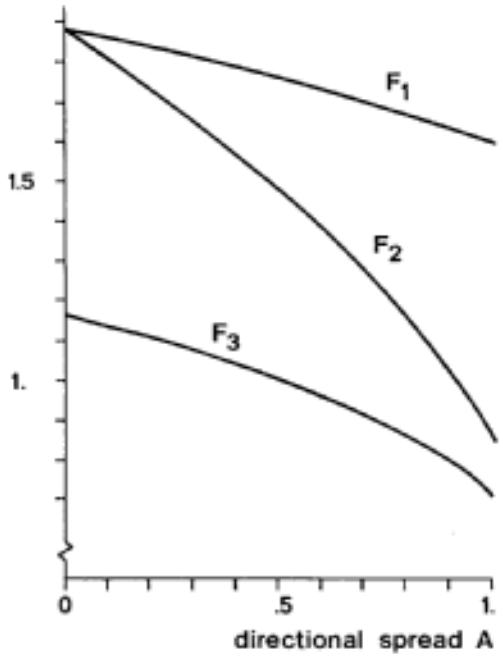

fig. 1 F_1, F_2 and F_3 as functions of A, see (3.3) and (4.4). In the limit of a one dimensional spectrum A = 1, for an isotropic spectrum A = 0.

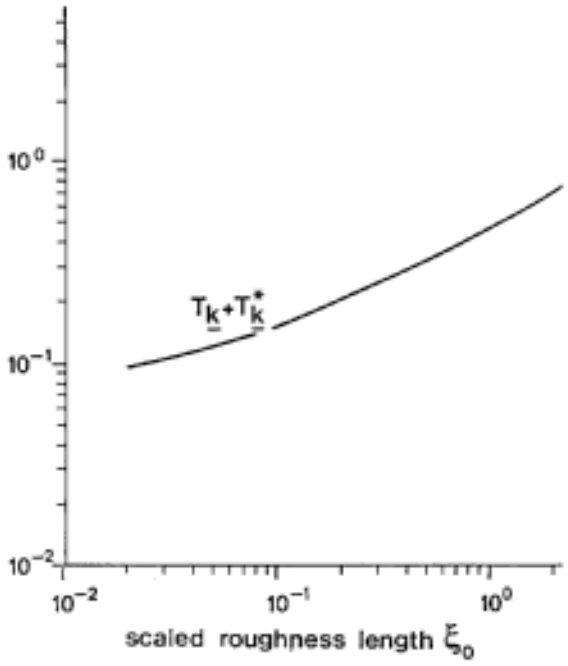

fig. 2 The proportionality factor $T_{\underline{k}} + T^*_{\underline{k}}$, which relates the energy dissipation to the scaled bottom roughness length ξ_0, see (3.5).

In the Texelstorm hindcast the bottom roughness is taken to be of the order of magnitude of the ripple height, as a value of the order of magnitude of a sand grain diameter was found to yield a dissipation rate, which is much too low. As a first guess the roughness length was taken as kN = 0.04 m. Assuming that kN is four times the ripple height, this corresponds to 1 cm ripples.

4. THE DRAGLAW

In the quadratic draglaw the bottom stress is expressed directly in terms of the free stream velocity at the top of the boundary layer as (i=1.2):

$$\tau i(y_o) = c_f \; U \; U_i \qquad (4.1)$$

with U = (U12 + U22)1/2 and c_f a friction coefficient which has to be determined experimentally as a function of the (scaled) bottom roughness, Hasselmann and Collins (1968) estimated that cf could be taken as constant with c_f = 0.015. This value will be used in the following. As $\tau_0^{1/2} = c_f^{1/2} U$, (4.1) can be rewritten as:

$$\tau_i(y_0) = \tau_0^{1/2} \sum_{\underline{k}} \frac{k_1}{k} c_f^{1/2} \bar{U}_{\underline{k}} + c.c. \qquad (4.2)$$

This expression for the bottom stress is similar to the eddy viscosity expression (3.2), but in (4.2) the instantaneous friction velocity $\tau_0^{1/2}$ appears and $T_k(\xi_0)$ has been replaced by $c_f^{1/2}$. According to this parameterization, the stress and the velocity in the bottom boundary layer contain higher harmonics (of linear order in wave steepness!).

Only the first harmonics however can contribute to the energy dissipation. These can be determined as:

$$\tau_i(y_0) = \sum_{\underline{k}} v_t \frac{k_1}{k} c_f^{1/2} \bar{U}_{\underline{k}} + c.c. \qquad (4.3)$$

Here v_t is a characteristic velocity, analogous to the friction velocity u in the eddy viscosity model, defined by:

$$v_t = \sigma_{11}^{1/2} \left[F_1(A) \cos^2(\theta-\phi) + F_2(A) \sin^2(\theta-\phi) \right] \qquad (4.4)$$

with $\sigma 11 = c_f \langle U_1^2 \rangle$; $A = 1 - \sigma_{22}/\sigma_{11}$ is a measure of the directional spread of the bottom velocity spectrum. F_1 and F_2 are given in fig. 2 . $\theta-\phi$ is the angle between a wave component and the average main direction of the bottom velocity spectrum, v_t characterizes the intensity of the bottom stress as it works on the mean flow.

Substitution of (4.3) in (2.4) yields:

$$\frac{\partial}{\partial t} F(\underline{k}) = - 2 c_f^{1/2} v_t \frac{k}{\sinh 2kh} F(\underline{k}) \qquad (4.5)$$

This expression is equivalent to the one given by Hasselmann and Collins. It is again similar to (2.5). with C replaced by:

$$C_{drag} = 2\, c_f \langle U_1^2 \rangle^{1/2} \left[F_1(A) \cos^2(\theta-\phi) + F_2(A) \sin^2(\theta-\phi) \right] \qquad (4.6)$$

The fact that C_{drag} depends on the direction of a wave component, whereas C_{eddy} is isotropic, arises solely because the parameterization (4.1) is non-linear in the statistical sense. A non-linear parameterization usually yields a larger dissipation coefficient than a linear one, because the functions F_1 and F_2, which appear in the nonlinear characteristic velocity v_t, have larger values than F_3, which appears in the linear characteristic velocity u*.

Comparing the draglaw dissipation (4.5) with the eddy viscosity dissipation (3.5) it is seen that v_t replaces u* and $2c_f^{1/2}$ replaces $T_{\underline{k}} + T_{\underline{k}}^*$. The draglaw expression does not explicitly depend on the bottom roughness, as c_f is taken to be a constant.

5. COMPARISON

To give an idea of the order of magnitude of various quantities, which appear in the eddy viscosity model, hindcast results of the Texelstorm with the WAM model, where (2.5) has been replaced by (3.5), are given in fig. 3 . After a sharp increase at the beginning of the storm, the friction velocity u* remains approximately constant at 6 cm/s. The boundary layer thickness d is found to be ~ 50 cm/s. The scaled roughness length ξ_0 ~ 0.4. From fig. 2 the corresponding value for $T_{\underline{k}} + T_{\underline{k}}^*$ can be found as 0.25. The eddy viscosity dissipation coefficient thus follows as C_{eddy} ~ 0.015 m/s For a $\cos^2$ -angular eddy distribution, the directional spread A = 2/3. Here the spectrum is more narrow, with A ~ 0.8, so that $F_3(A)$ ~ 0.86.

For comparison Cdrag is computed from the values of the rms bottom velocity component $\langle U_1^2 \rangle^{1/2}$ which are found in the eddy viscosity hindcast, $\langle U_1^2 \rangle^{1/2}$ varies from 40 cm/s to 55 cm/s. For A = 0.8, $F_1(A)$ ~ 1.67 and $F_2(A)$ ~ 1.16. For the main direction $\theta = \phi$, C_{drag} ~ 0.025 m/s, which is 1.7 times Ceddy (for the transverse direction Cdrag ~ 0.017 m/s, which is 1.1 times C_{eddy}). As $2 c_f^{1/2} - T_{\underline{k}} + T_{\underline{k}}^*$, this difference is mainly due to the differences between the Characteristic velocities v_t and u*. These reflect the differences between the two models in their accounting for the directional spread of the bottom stress spectrum. This is related to the different statistical characteristics of the assumed relationship between the stress and the outer flow in the draglaw formulation (4.2) and in the eddy viscosity formulation (3.2).

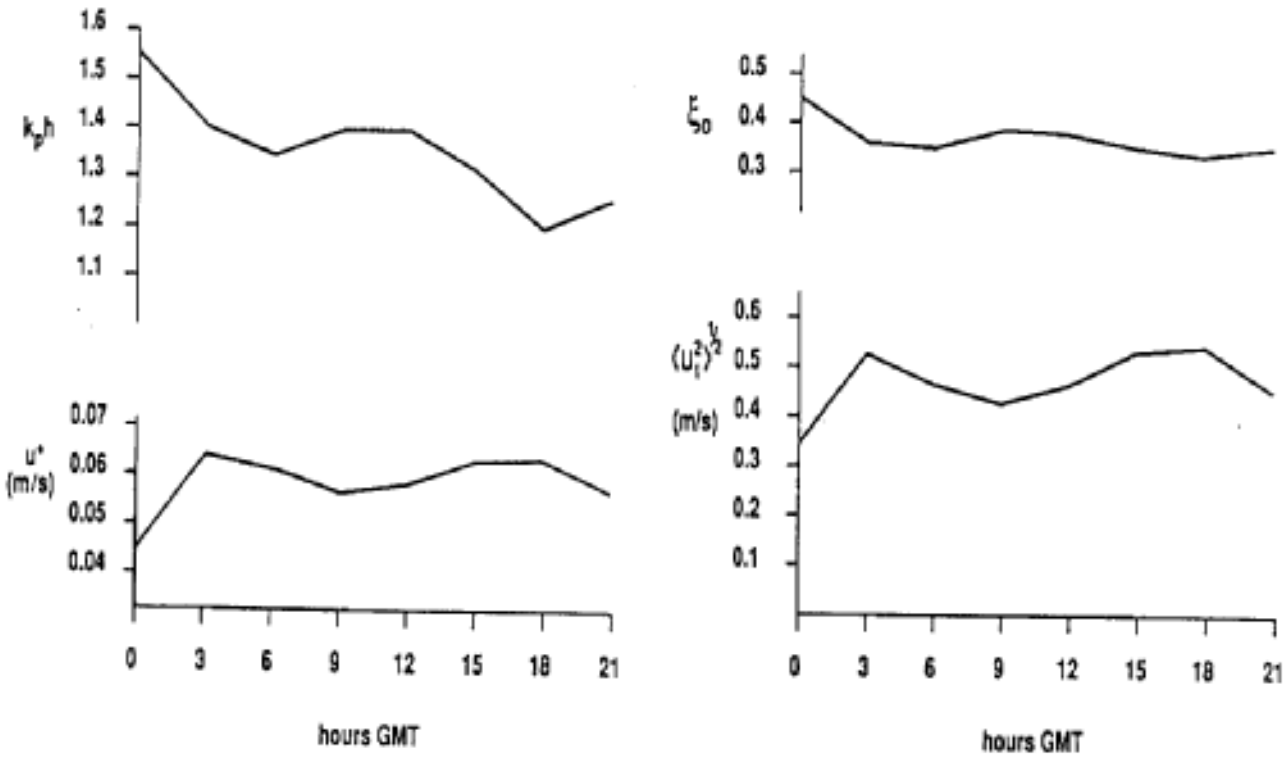

fig 3 Hindcast results of the Texelstorm, January 3, 1976, with the eddy viscosity dissipation (3.5). (a) wave length to depth ratio $k_p h$, with k_p the peak wave number and h the water depth (b) the friction velocity u* (c) the scaled bottom roughness length ξ_0 (d) the root mean square bottom velocity in the main direction $\langle u_1^2 \rangle^{\frac{1}{2}}$.

6. HINDCAST RESULTS

A severe storm occurred on January 3, 1976, in the southern part of the North Sea, where the depth is 15-50 m. This storm was characterized by approximately stationary wind conditions, with windspeed U_{10} ~ 25 m/s and wind direction ~ 300°. Significant wave height at Texel (53°2'N, 4°17'E) local depth h ~ 30 m , remained approximately constant at H_s ~ 6.5 m for 15 hours. The peak frequency of the spectrum decreased from 0.10 Hz to 0.08 Hz during this period. This so called Texelstorm has been used before to test the balance between wind input and dissipation by Bouws and Komen (1983), who could only simulate an equilibrium by increasing the dissipation coefficient C in (2.5) from 0.008 to 0.014 m/s. Measurements are available from Texel and from Eurochannel (52°0'N, 3°41'E).

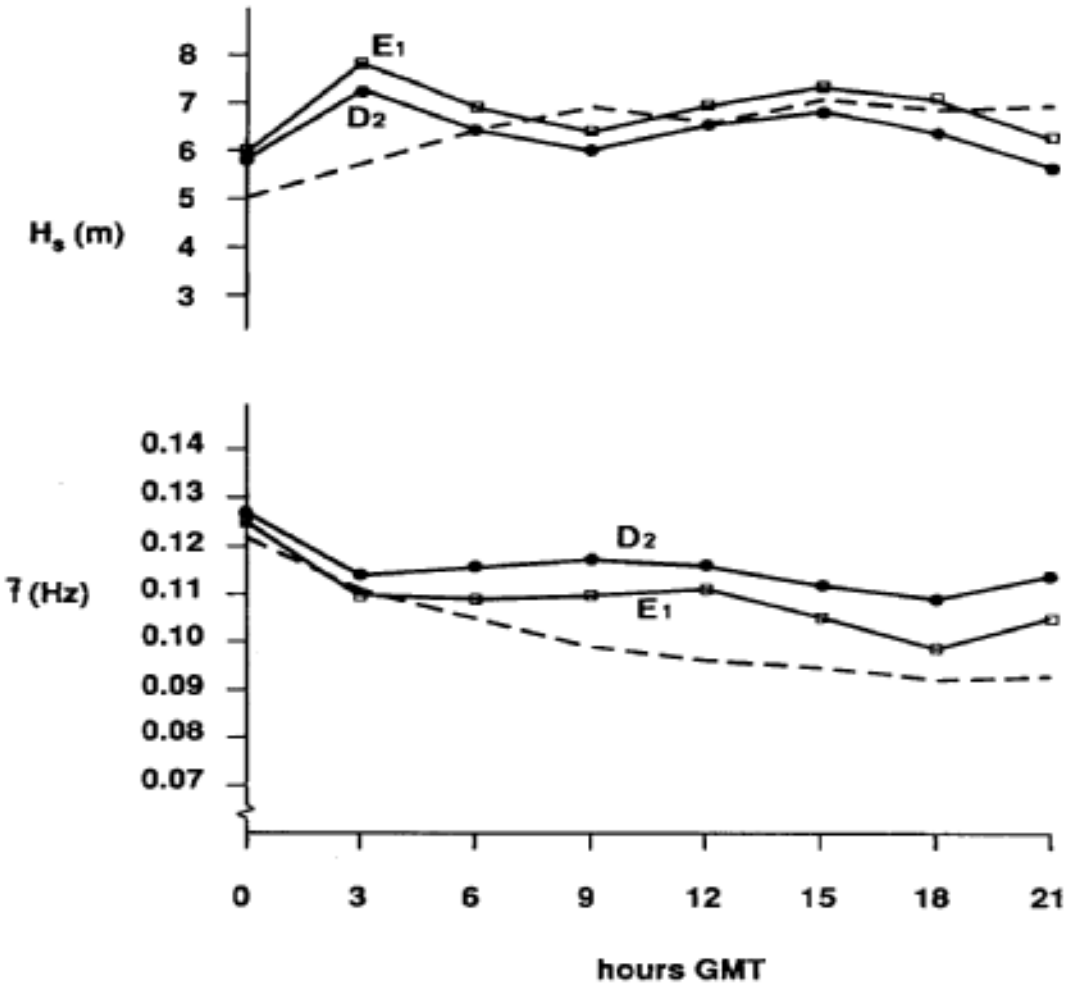

fig. 4 Significant wave height H_s and mean frequency $\bar{f}$ for Texel, January 3, 1976.
- - - measurements —□— hindcast results with the eddy viscosity dissipation (3.5)
—●— hindcast results with the draglaw dissipation (4.5).

Two hindcasts were made with the regional version of WAM:

(E1) one with the bottom dissipation (2.5) replaced by the eddy viscosity dissipation (3.5).Some results of this run have already been discussed in section 5 .
(D2) one with the bottom dissipation (2.5) replaced by the draglaw dissipation (4.5).

Hindcast results for the significant wave height H_s and the mean frequency $\bar{f}$ at Texel are given in fig. 4 . The empirical expression (2.5) overpredicted H_s with 1-2 m, but performed rather well for $\bar{f}$ (see Riepma and Bouws, this volume). The eddy viscosity model E1 as

well as the draglaw D2 yield much more realistic results for H_s, with E1 performing slightly better than D2. Both models however overpredict $\bar{f}$; the eddy viscosity model with 0.01 Hz, the draglaw with 0.015 Hz. The eddy viscosity model yields a dissipation coefficient C_{eddy} – 0.015 m/s at the peak frequency. The draglaw model yields values for $\langle u_1^2 \rangle^{1/2}$ which lie 5–10 cm/s below those obtained from the eddy viscosity model, so that the actual C_{drag} ~ 0.022 m/s for the main direction.

The WAM model significantly overpredicts H_s at the early stages of the storm, both at Eurochannel and at Texel. It is not clear at this point why this is the case (see also Riepma and Bouws, this volume). The E1 and the D2 growth curves for H_s and $\bar{f}$ are similar, which indicates that the main difference between the two models is the value of the dissipation coefficient. The directional dependence of C_{drag} seems to be of little importance.

At Eurochannel both the eddy viscosity model and the draglaw predict H_s within 0.5 m, apart from an overprediction in the early stage of the storm analogous to Texel. Again the eddy viscosity model performs slightly better. Agreement with measurements is very well for $\bar{f}$ for the eddy viscosity model, the draglaw however overpredicts $\bar{f}$ with 0.005 Hz. C_{eddy} ~ 0.015 m/s and C_{drag} ~ 0.019 m/s (for the peak frequency respectively the main direction).

7. CONCLUSIONS

A general expression for the dissipation of wave energy due to friction in the turbulent bottom boundary layer is:

$$\frac{\partial}{\partial t} F(\underline{k}) = - C \frac{k}{\sinh 2kh} F(\underline{k}) \qquad (7.1)$$

In the present paper, two models were discussed, which give expressions for C in terms of the surface elevation spectrum, the water depth and the bottom roughness length. Firstly, the eddy viscosity model E1. which expresses C as:

$$C_{eddy} = u^* \left[T_{\underline{k}}(\xi_0) + T^*_{\underline{k}}(\xi_0) \right] \qquad (7.2)$$

Secondly, the draglaw D2, which yields:

Secondly, the draglaw D2, which yields:

$$C_{drag} = 2 c_f \langle u_1^2 \rangle^{1/2} \left[F_1(A) \cos^2(\theta-\phi) + F_2(A) \sin^2(\theta-\phi) \right] \qquad (7.3)$$

The different forms of these expressions could be traced back to the statistical characteristics of the two models. An expression of the second type (which follows from a stochastically non-linear model) generally yields a larger dissipation coefficient than an expression of the first type (which follows from a stochastically linear model).

Both expressions were tested in a hindcast of the so called Texelstorm. The ratio C_{eddy}/C_{drag} was found to be 0.7 for Texel and 0.8 for Eurochannel. Both the eddy viscosity model and the draglaw show promising improvements over the empirical expression used before. This holds especially for the predicted values for the significant wave height.

Bouws and Komen (1983) analysed the Texel storm before, assuming a stationary situation between 6 and 21 hours on January 3, 1976. From fig, 4 it is seen that this is true for H_s, but $\bar{f}$ still decreases during this period. This effect is not well predicted by either E1 or D2, although E1 performs better than D2. The dissipation coefficient $C_{eddy} \sim 0.015$ m/s both at Eurochannel and at Texel, which is close to the value 0.014 m/s proposed by Bouws and Komen for Texel, Cdrag - 0.022 m/s at Texel and - 0.019 m/s at Eurochannel.

REFERENCES

Bouws, E, and G.J. Komen, 1983: On the balance between growth and dissipation in an extreme depth-limited wind-sea in the southern North Sea, J. Phys, Oceanogr., 13, 1653-1658.

Grant, W,D. and O.S. Madsen, 1979: Combined wave and current interaction with a rough bottom. J, Geophys, Res., 84(C4), 1797-1808.

Grant, W,D. and O.S. Madsen, 1982: Movable bed roughness in an unsteady oscillatory flow. J. Geophys, Res., 87(C1), 496-481.

Hasselmann, K. and J.I. Collins, 1968: Spectral dissipation of finite depth gravity waves due to turbulent bottom friction, J. Mar, Res., 26(l), 1-12.

JONSWAP: Hasselmann, K., et al, 1973: Measurements of wind-wave growth and swell decay during the Joint North Sea Wave Project. Dtsch, Hydrogr. Z., A8(12).

Kajiura, K., 1968: A model of the bottom boundary layer in water waves, Bull, Earthquake Res. Inst., 46, 75-123.

Phillips, O.M., 1980: The dynamics of the upper ocean, Cambridge Univ, Press.

Riepma, H,W, and E. Bouws, 1989: Preliminary results of the NEDWAM

model. This volume.

Weber, S.L., 1989: Eddy viscosity and draglaw models for random wave dissipation. Submitted for publication.

PREDICTING STORM WAVES IN THE NEARSHORE ZONE

Ronald J. Lai

David Taylor Research Center
Bethesda, Maryland

1. INTRODUCTION

Several wave models are currently in operation world wide (The SWAMP, 1985). Their goals are forecasting/hindcasting wind and deep water waves for the open ocean. None of them take into account the effects of bottom topography and other local dynamical factors. The extension of the operational wave model to the nearshore zone is thus limited. With the vast increase of population, and other commercial and recreational activities in the coastal area, the forecasting/hindcasting of wind and wave in this region, especially the storm wave, becomes an urgent task.

The characteristics of storm waves in the nearshore zone are complex and unique. They depend not only on the origin of the storm, but also on the bottom topography and local dynamical parameters in the surrounding area which control the transformation and dissipation processes. As these offshore generated storm waves approach the shore, several interaction and transition phenomena take place. The generalization of these processes are almost impossible. A semi-empirical method has been developed to transfer the hindcast offshore wave data of the Spectral ocean Wave Model (SOWM) to the nearshore zone according to the local topography and dynamical parameters. Shallow water wave statistics were generated by means of this method,(Lai, et.al., 1984). The statistical results have been partially verified by the available field data(Lai and Bales, 1986).

Some of the measured offshore and near shore storm waves in the Southeast coast of the United State have been analyzed. The analyzed results are presented here, and can be used as a guide to modify the operating deep water wave model to predict the storm wave in the nearshore zone.

2. FIELD DATA

Near shore wave data are derived from two measuring sites located in the SE coast of the United State. One station is in Cape Canaveral, Florida (28.34 N, 80.42 W) with water depth of 17.5 m, and the other is in St. Mary's Inlet, Georgia (30.68 N, 81.28 W) with depth of 18.0 m (Figure lb). The near shore data consist of directional wave spectra and mean current (Lai and Foley, 1986). The offshore data are derived from NOAA Buoy #41006 (29.30 N, 77.30 W) and consist of point spectra of wave, wind speed and direction, and air and water temperatures.

The storm waves analyzed here are classified into two categories: namely tropical and subtropical storms. The data were obtained in the period September, 1985, to May, 1986. The distance between offshore and nearshore stations is 140 miles (237 km), and northbound Gulf Stream separates these stations. As the offshore storm waves approach the nearshore zone, they interact with the strong current of the Gulf Stream. Consequently the storm waves in the nearshore zone have gone through a series of interactions with wind, current and bottom topography.

In order to investigate the changes of wave characteristics from offshore to the nearshore zones, the traveling time between two stations has to be determined. The wave group velocity (C_g) has been used to compute the propagation of wave energy. The group velocity equals half of the phase velocity (C) in deep water and approach the phase velocity in shallow water. The value of C_g in deep water is:

$$C_g = 1/2 \times C = 1/2 (g/\omega)$$

where g is gravity acceleration and ω is radian frequency, i.e., $\omega = 2\pi f$, and f is wave frequency. The peak frequencies of the storm waves in the SE Coast range from 0.09 to 0.15 Hz. However, only the long waves, i.e., f< 0.12 Hz. can reach the nearshore zone under the effects of the Gulf Stream. For the present analysis the mean spectrum with peak frequency of 0.1 Hz was used to compute the traveling time of the storm waves. The group velocities based on average f_p and $f_{½}$ were adopted to compute the traveling times. This process yielded traveling time of 8.5 and 6.0 hours. After careful evaluation of changes in spectral shape and frequency shift, a traveling time of 6.0 hours was adopted. Some of the wave spectra at the two stations are presented in the following sections.

A. Subtropical Storm: Northeaster

The mean characteristics of the September 1985 storm, in both offshore and near shore zones are shown in Figure 2a . The values of significant wave height ($H_{1/3}$), peak frequency, primary wave direction, and wind speed and direction for both stations are displayed. Since six hours of traveling time was adopted, the data of the nearshore station are shifted by six hours in the figure. There are no wind data available for the nearshore zone. The wind data at the Jacksonville Airport, Florida, which is located five miles inland were used here as a reference.

The storm started on 13 September, 1985, and continued through 24 September, 1985. At that time, a tropical storm (Hurricane Gloria) approached and dominated the weather pattern. The hurricane waves are discussed in the next section. The pattern of the first Northeaster could be traced from the available offshore wind. The generation,

growth and decay of storm waves were closely related to the wind at the offshore station but not at the nearshore station. Further discussion is given later in the paper.

A series of measured wave spectra displaying storm wave changes at different stages of development are given in Figures 3 and 4 . The spectra in Figure 3 show the generation and growing stages of the storm waves. In the early stage, the waves at the offshore station grew continuously as they approached the nearshore station. The effect of currents was not clearly demonstrated. The wind force seems to dominate the wave mechanism (Figure 3b). This was the only case that the wave energy in the nearshore zone was larger than the offshore zone. Beyond this stage, the wind speed ceased to increase and maintained a constant value. The wave reached a saturation or decay stage at that time. The mechanism of wave energy dissipation by the current through breaking and eddy diffusion then overtook the wind input. Consequently, the offshore storm waves were attenuated as they reached the nearshore zone. The reduction of 30 to 40% in wave energy at the nearshore zone from offshore zone are displayed in Figures 3c , 3d and 3e . Further evidence is reviewed in Figure 4 which displays the storm in a later stage. During this period, the wind speed was sustained at over 9.0 m/s and continuously pumped energy into the wave system. However, the dissipation by turbulence, breaking and regrouping reduced the wave energy as they reached near shore zone.

B. Tropical Storm: Hurricane

On 21 September, 1985, there was a tropical depression formed in the SE Atlantic Ocean which became hurricane Gloria. The track of hurricane Gloria is shown in Figure la . Hurricane Gloria moved in the NW and N directions and made landfall at Cape Hatteras, North Carolina. All the SE Atlantic coast was subjected to hurricane Gloria's waves. The mean values of wave characteristics and wind speed are displayed in Figure 2b . The sudden increase of wind speed indicated the arrival of the hurricane, and the sudden change of wind direction indicated the departure of the hurricane. It is interest to note that the measured wind speed at the nearshore station did not provide any sign of the passing hurricane. This implied that Jacksonville area was not under the direct impact of hurricane wind force. However the measured waves at these stations may be traced to the passing of the hurricane as compared with measured offshore wave data. Some of the measured wave spectra at these two stations are displayed in Figure 5 . Large reductions of the wave energy at the nearshore station were observed which demonstrate the strong effects of the Gulf Stream on the mechanism of energy dissipation. Further analysis and discussion are given in the following section.

3. DISCUSSION OF THE RESULTS

A. Bottom topography

Important energy dissipation processes in the nearshore zone are shoaling, refraction, and friction loss by the bottom topography. A shallow water wave model for Cape Canaveral, Florida has been developed (Lai and Silver, 1986). This model, with the initial offshore grid point located 100 km from shore and with water depth of 74 m. was used to compute the bottom effects. Based on the measured field data, a friction factor of 0.008 was determined which represented sand with a medium grain size of the region (Wang and Yang, 1981). This friction factor was used throughout the computation.

The effects of the bottom topography depend not only on local water depth but also on the surrounding geometry. The large shoaling zone of the Cape Canaveral area strongly modified the waves from the NE direction. The storm waves from the NE direction dissipated energy faster than the waves from the SE direction, especially in the long wave range, i, e. . f <O. 12 Hz. In this low frequency range, the computed results indicated that the waves from NE direction reduced up to 35% of the original energy and waves from the SE direction reduced only up to 15%. The bottom effects model has been applied to evaluate the overall storm waves dissipation process in the nearshore zone.

B. Wind Force

Wind provides an important energy source to the wave system, especially during the passage of the storm. Although the wind was continuously pumping energy to the wave system, the net gain for the wave system depended on the balance of the wind force with other source and sink terms through their interaction processes. As shown in Figure 2a , the wind speed of 11 m/s and from 40 degrees north was blowing for 48 hours in the early stage. The responses of wave systems were different and are displayed in spectral forms in Figure 3 . The waves of the offshore zone revealed the growing, saturation, and decay stages as in Figure 3b , 3d and 3e . The waves in the nearshore zone revealed the rapid growing stage (Figure 3b) and reached the equilibrium stage afterward (Figure 3d and 3e). The extra wave energy gained in the offshore area was dissipated by interaction with the shear current. Furthermore, the intensity of the shear current was enhanced by the wind force. Consequently, the wind force provided the direct energy input to the wave system on one hand and enhanced the shear current and turbulence to speed up the wave dissipation processes on the other hand.

Another effect of wind force on the wave system was the generation of multiple peaks in the nearshore zone spectra. Multiple peak wave

spectra were frequently measured in the nearshore zone during the growing stage of the storm or during a sudden change of wind direction (Lai and Foley, 1986). As the wave reached the saturation stage at the offshore station and propagated to the near shore area, it had to cross the Gulf Stream. The shear current of the Gulf Stream changed the wave energy and interrupted the down shift process of wave energy. After the passage, the local wind started to generate the wind wave in the higher frequency range, i.e., f>0.18 Hz, as shown in Figure 3d . The wave energy in the higher frequency range was larger for the near shore zone than the offshore zone due to the local wind force and is consistent with other measurements (Knowles, 1983; McLeish and Ross, 1985). These phenomena of local wind input are also shown in Figure 3c , 4b and 4c .

C. Currents

The effects of current on the waves are not fully understood, especially in the complex ocean environment. Although numerous theoretical results have been published in the literature, the observation side of the record is almost non-existent (Peregrine, 1976; Peregrine and Jonsson, 1983). A series of laboratory experiments have been conducted, and some of the results on wave kinematics will be published (Lai, et.al, 1988). The preliminary results suggest breaking, regrouping and turbulence play an important role in wave dynamics during the process of current-wave interaction.

Breaking and turbulence in the upper ocean are complex and interrelated. When the surface waves encounter an opposing current, the phenomena of breaking and turbulence enhancement occur simultaneously. The percentage and intensity of breaking are difficult to determine in the field. The energy dissipation by breaking has been computed by a statistical method (Tung and Huang, 1987). Furthermore, the values of eddy viscosity for the ocean surface which may be derived from the shear current and turbulence vary between 10 to 1000 cm/s from the available literature. The formation of eddy current, breaking and direct wind input all contribute to the value of eddy viscosity. This large variation of eddy viscosity made the computation of wave energy dissipation a difficult task. This has been demonstrated from the large difference in the wave energy dissipation resulting from the Northeaster and the Hurricane (see Figures 3 , 4 and 5).

Most of the storm waves generated by the Northeaster were from North and Northeast directions. As these waves passed the Gulf Stream en route to the nearshore zone, they encountered a strong opposing current, and refracted and partially broke. Some of the energy was dissipated by breaking and turbulence. Even though the waves continuously received energy from the wind, the net results were a

reduction of wave energy of up to 40% of the offshore values. On the other hand, the storm waves generated by Hurricane Gloria were from the Southeast and East directions. As these waves passed the Gulf Stream on their way to near shore zone, the waves were riding or crossing the currents. Thus the hurricane waves would not be broken by the Gulf Stream. The large reduction of the hurricane waves from offshore to nearshore as shown in Figures 2b and 5 should be attributed to the strong interaction with the shear current, veering wind, turbulence, and bottom topography.

One possible mechanism of wave energy reduction in the Gulf Stream is the reflection and trapping of the waves (Kenyon, 1971; Hayes, 1980). The existence of current filaments near the center of the Gulf Stream might cause partial reflection or trapping of the passing waves. Without this it is difficult to account for up to an 80% reduction of wave energy of Hurricane Gloria in near shore zone by the Gulf Stream (Figure 5).

4. CONCLUSION AND RECOMMENDATION

The storm waves in the nearshore zone depend on the characteristics of the bottom topography, the transition zone (between deep and shallow water), and the origin of the storm. The example presented here is the measured storm waves in the SE coast of the U.S. The strong effects of the Gulf Stream, and sudden changes of wind direction in fast moving storms (Young, et.al., 1987) seem to dominate a large portion of the energy dissipation process. To apply the operational deep water wave model to near shore zone, one has to consider these current, wind and bottom topography effects. Until these mechanisms are fully understood and implemented in the model, the forecasting of the storm waves in near shore zone is not in satisfactory state and has to rely on a semi-empirical approach.

ACKNOWLEDGEMENTS

This work is supported in part by a contract from the office of Naval Research Fluid Dynamics Program and Naval Laboratory Participation Program (NLPP).

REFERENCES

Hayes, J. G.f 1980: Ocean current wave interaction study. J. Geophys. Res., 85, 5025-5031.

Kenyon, K. E,r 1971: Wave refraction in ocean currents. Deep Sea Res., 18, 1023-1034.

Knowles, C. E., 1982: On the effects of finite depth on wind-wave spectra: I. A comparison with deep-water equilibrium-range slope and other spectral parameters. J. Phy. Oceanogr., 12, 556-568.

Lai, R. J., A. L. Silver and S. L. Bales, 1984: Wave statistics in nearshore zones. Proceeding of Ocean Structure '84, Corvallis, Oregon.

Lai, R, J., and S. L. Bales, 1986: Effects of the Gulf Stream on nearshore wave climate. ASCE, 20th international Conf. of Coastal Eng., Taipei, Taiwan, ROC.

Lai, R. J., and E. W. Foley, 1986: Field measurements of nearshore wave environment at Cape Canaveral, Florida and Kings Bay, Georgia. Report DTNSRDC/SPD-11909-02, Bethesda, Maryland.

Lai, R. J. , and A. L. Silver, 1986: Shallow water wave model at Cape Canaveral, Florida and Kings Bay, Georgia, Report DTNSRDC/SPD-1190-01. Bethesda, Maryland.

Lai, R. J. , S. R. Long and N. E. Huang, 1989: Laboratory studies of wave-current interaction: kinematics of the strong interaction. To be appeared in J. Geophys. Res..

McLeish, W., and D. B. Ross, 1985: Wave refraction in an ocean front. J. Geophys. Res,. 90, 11929-11938.

Peregrine, D. H.r 1976: Interaction of water wave and currents. Adv. Appl. Mech., 16, 9-117.

Peregrine, D. H, . and I. G. Jonsson, 1983: Interaction of waves and currents. U. S. Army Corps of Eng., CERC MR 83-6, Vicksburg, MS.

The SWAMP GROUP, 1985: Ocean wave modeling. Plenum press, 256pp.

Tung, C. C., and N. E. Huang, 1987: The effects of wave breaking on the wave energy spectrum, J. Phy. Oceanogr., 17, 1317-1338.

Wang, S. and W. C. Yang, 1981: Measurements and computation of wave spectral transformation at Island of Sylt, North Sea. Coastal Engineering, 5, 1-34.

Young, I. R., S. Hasselemann, and K. Hasselemann, 1987: Computations of the response of a wave spectrum to a sudden change in wind direction. J. Phy. Oceanogr., 17, 1317-1338.

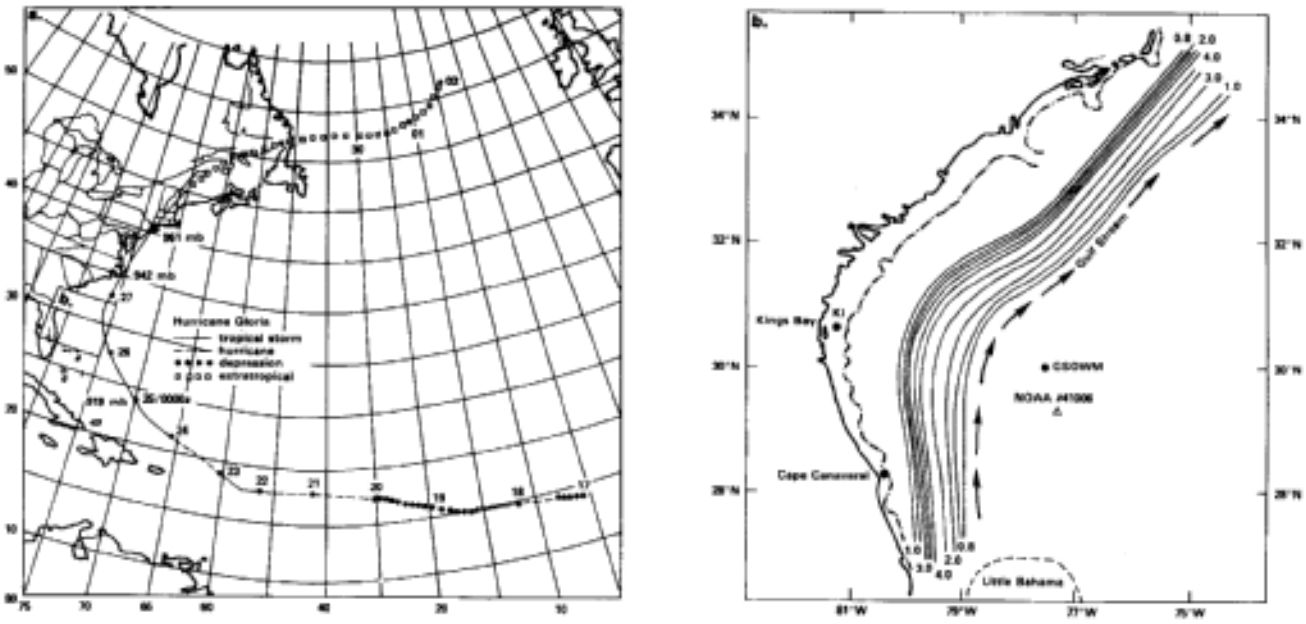

Figure. 1. Map of NW Atlantic Ocean with (a) Track of the Hurricane Gloria of 1985; (b) location of NOAA offshore buoy #41006, GSOWM grid point (30N, 77.5W), and near shore measuring stations at Cape Canaveral (c-1) and Kings Bay (k-1), where the Gulf Stream speeds are indicated in knots.

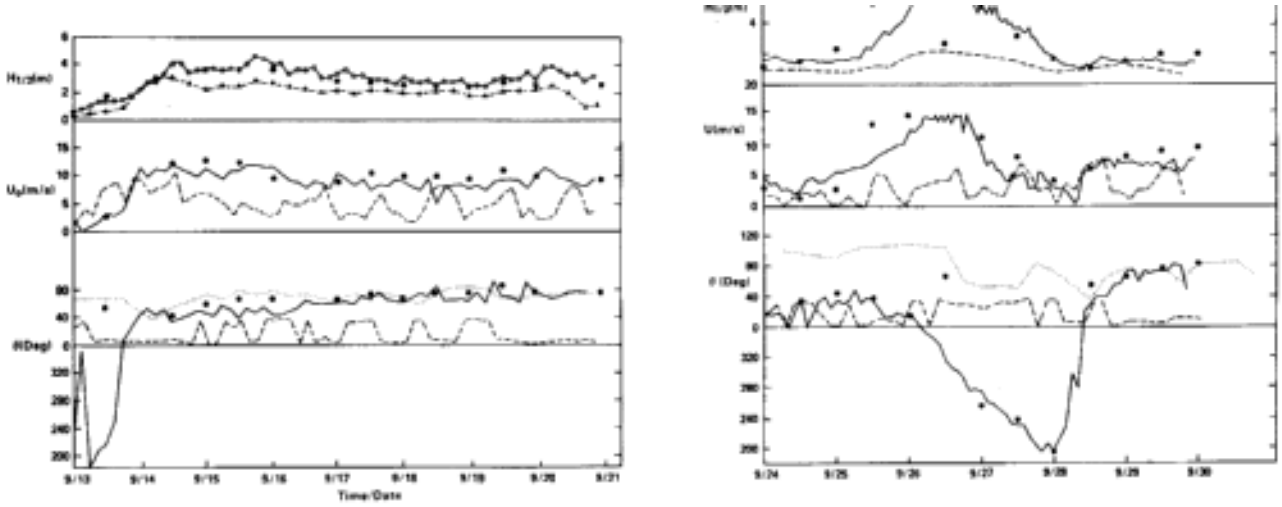

Figure 2. Mean wind and wave values during: (a) the Northeaster, and (b) the Hurricane Gloria in September of 1985; where u = wind speed, θ = wind and wave directions, $H_{1/3}$ = significant wave height, f_p = peak frequency; and where solid lines represent offshore data, dashed lines represent near shore data at Cape Canaveral, and dotted line represent corresponding near shore wave direction, and where the data points in the figure are from GSOWM hindcast data near NOAA Buoy #41006.

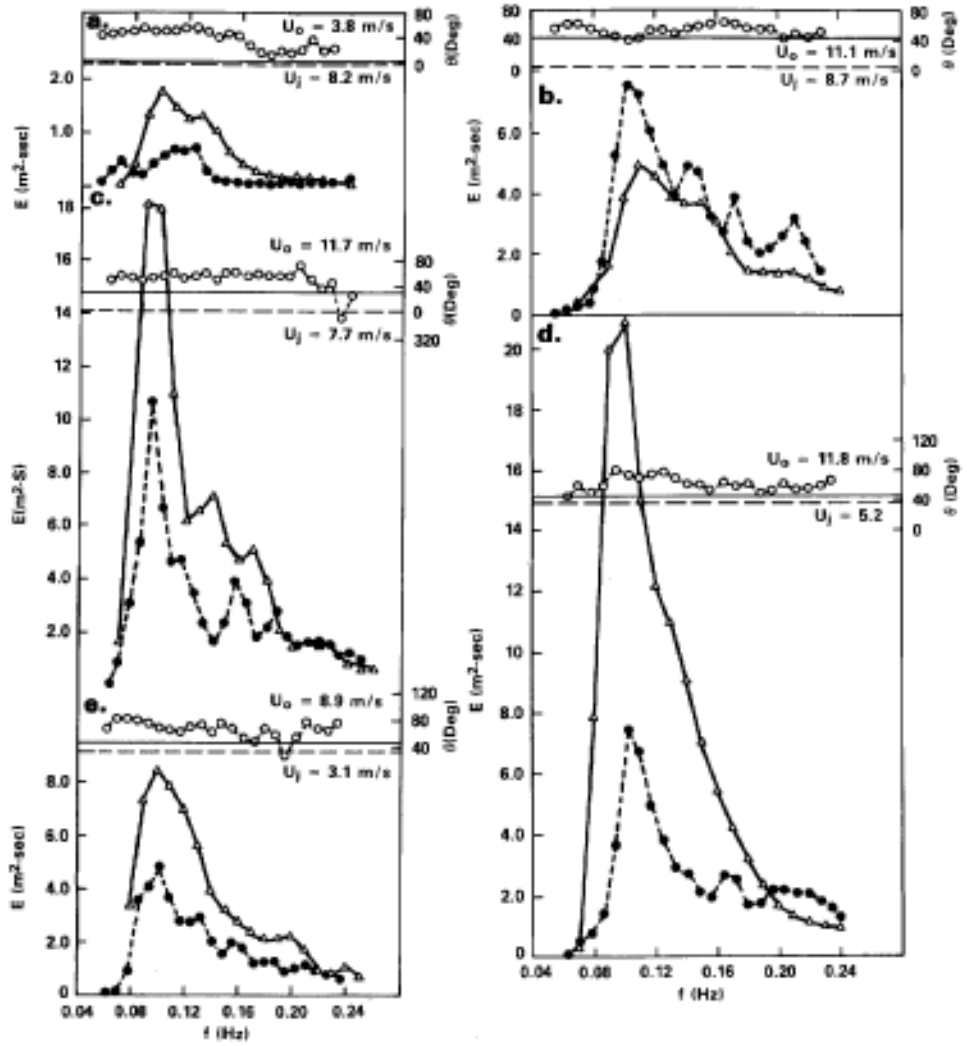

Figure 3. Spectra of the Northeaster, where solid lines represent offshore data and dashed lines represent near shore data, and the data of wave direction at near shore station, and both offshore and near shore wind directions and amplitudes are also given in the upper section of the figure, and where (a) 18z, September 13, (b) 6z, September 14, (c) 12z, September 14, (d) 18z, September 15, and (e) 6z, September 16, all of 1985.

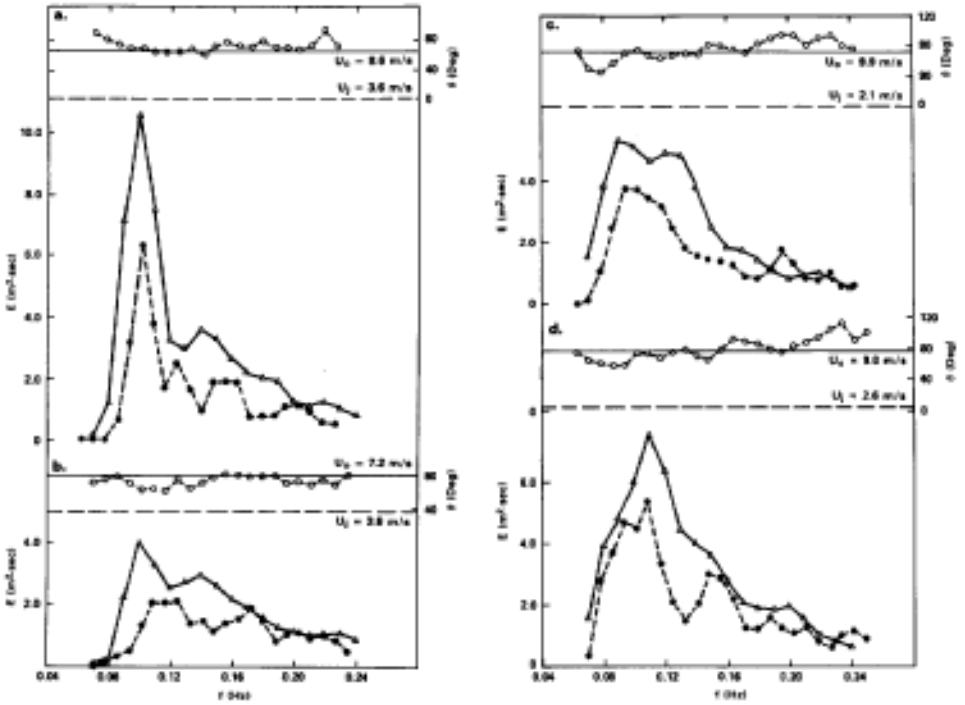

Figure 4. Spectra of the Northeaster storm in later stage, same caption in Fig. 3, and where (a) 0z, September 18, (b) 6z, September 19, (c) 0z, September 20, and (d) 12z, September 20, all of 1985.

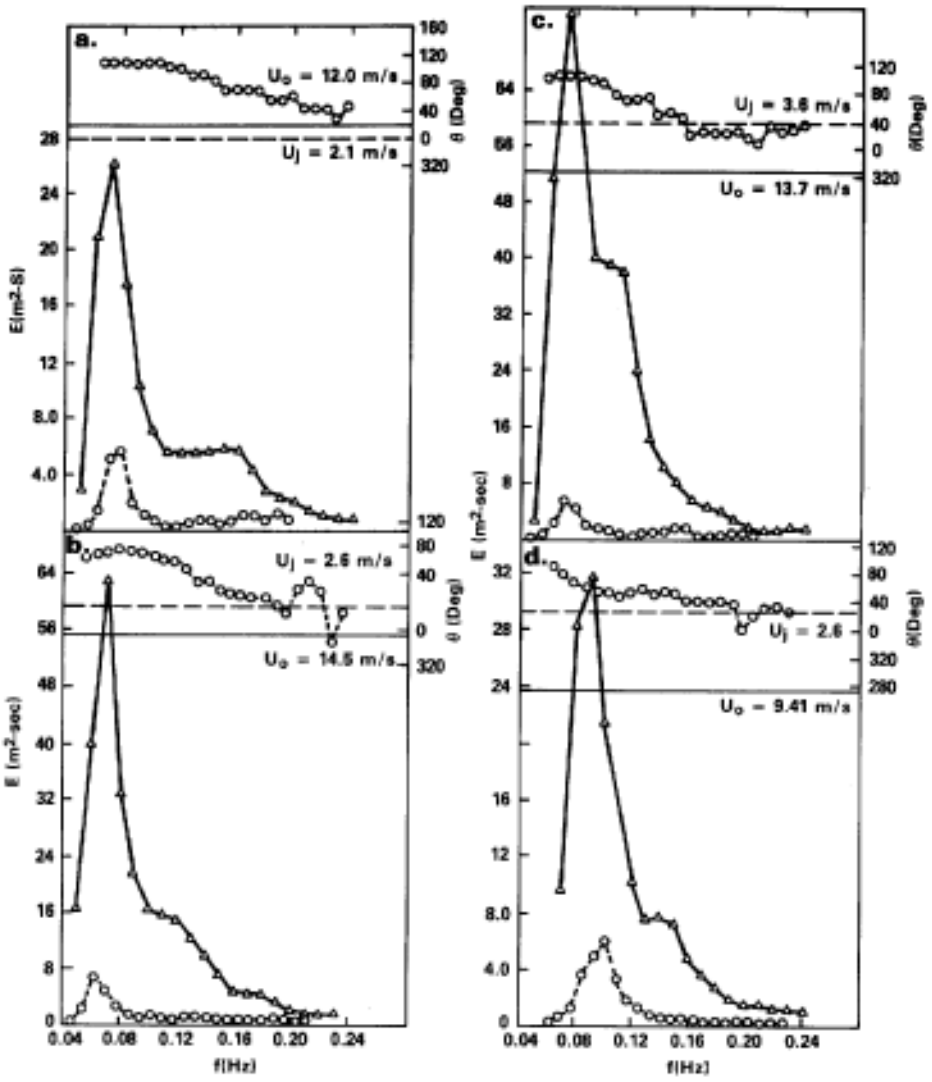

Figure 5. Spectra of the Hurricane waves measured in both offshore and near shore stations, same caption in Fig. 3, and where (a) 0z, September 26, (b) 6z, September 26, (c) 12z, September 26, and (d) 0z, September 27, all od 1985.

DEVELOPMENT OF EXTREME WIND AND WAVE CRITERIA FOR HIBERNIA

V. J. Cardone[1], D. Szabo[2].
and F. J. Dello Stritto[2]

[1] Oceanweather, Inc., Cos Cob, Connecticut
[2] Mobil Research & Development Corp., Dallas Texas

ABSTRACT

Extreme wind and wave criteria for the Hibernia field off the East Coast of Canada are estimated through hindcasting and extremal analysis. Specific elements in the determination are: (1) severe storm identification; (2) hindcast modeling; (3) verification with data; (4) fits of hindcast wind speeds and significant wave height to extremal distributions and (5) statistical and empirical analyses to obtain engineering parameters. Twenty nine severe storms are selected from January 1951 through December 1984. Wind fields for each of the 29 storms are developed from available historical meteorological archives. Seastates are hindcast using a version of the ODGP numerical wave model. Accuracy of the model estimates is verified with measured data near Hibernia. Extremal analyses of 26 of the hindcast peaks estimate long return period significant wave heights. Further statistical analyses produce parameters necessary for engineering and design applications, such as height and period of maximum waves, and parametric spectra.

INTRODUCTION

This is the first of five related papers [1-4] describing development of extreme wind and wave criteria for the Hibernia site on the Grand Banks. While some novel items are included, completeness rather than innovation is the theme. The set is believed to be the first which details all steps in estimating criteria necessary for offshore development. These steps range from use of numerical wave models to the empirical tools and "rules of thumb" for obtaining engineering parameters. The intent is that, by documenting the Hibernia application fully, further development may be directed to areas of greatest need.

Extreme wind speed and seastate estimates are essential requirements for offshore design. Ideally, extremal estimates should be based on data recorded continuously for time spans much longer than the return periods of interest. Since return periods for offshore applications are typically 100 years, sufficient measured data records do not exist. Hindcasting and extremal analysis methods must be used. Hindcasting estimates past environmental conditions from archived information. For wind and wave conditions, archived data consist largely of surface weather maps and ships' observations. Windfields during past storms are reconstructed from the available meteorological

data. These are then input to a numerical wave model to estimate directional wave spectra throughout each storm. A synthetic data base thus may be constructed, from which long return period extremes are derived.

Extreme environmental criteria calculated from such synthetic, finite data bases have inherent uncertainty and subjectivity. Diverse technologies underlying the procedure have been extensively developed over the past twenty years. Hindcasting and extremal techniques have been successfully applied to most areas of offshore industry activity. Most past applications have been, like the present one, site-specific studies--that is, storm selection and hindcast verification focus on a single site and not an entire basin or coastal area. Recent trends are towards regional criteria studies [14], which due to their much greater cost and complexity require joint industry or industry-government funding. Regional studies can achieve accuracies comparable to site-specific studies only through much larger expenditures. Otherwise, such hindcasts are properly recognized as appropriate only for general qualitative assessments and first approximations of environmental conditions.

Hibernia, and the Grand Banks in general (Figure 1) are well suited to hindcasting/extremal analysis techniques. High quality archived meteorological data for the area are available for approximately the past 40 years. Such data are critical inputs to identification of severe historical storms and construction of the windfields. Throughout the early 1980's, nearly continuous measurements of wind and wave data, often at multiple sites, were recorded at drilling sites [7]. The measurement period includes occurrences of several severe storms. Verification of the numerical wave model, another key step in criteria determination, can thus be performed with meaningful data. Lastly, earlier hindcasting experience [8] for similar areas subject to extratropical storms, such as the Gulf of Alaska and South Atlantic, is readily applicable to the Grand Banks.

Specific steps in the Hibernia criteria development are as follows. Twenty nine severe storms (Table 1) occurring between January 1951 to December 1984 are selected from archived meteorological charts, early regional hindcasts and recorded data. Windfields for the 29 storms are developed from archived charts modified with available ship and weather station observations. Directional wave spectra are hindcast using a numerical wave model. Extensive comparison of model estimates to recorded wave data show that possible model inaccuracies are minor. Three of the 29 storms failed to generate severe waves, and the remaining 26 maxima are input into the extremal analysis. Peak wind speeds, V, are fit to a Gumbel distribution; peak significant wave heights, Hs, are fit to a Borgman distribution, (i.e., Gumbel distribution in Hs^2), and extreme values at various return periods are

estimated (Table 2). Spectral peak period, Tp, is associated with the return period significant wave height estimates based on correlations of hindcast peak Hs and Tp. Maximum wave heights are estimated with empirical distributions of wave heights within a wave field, fit to wave staff data.

SEVERE STORM IDENTIFICATION

Storms causing extreme seastates at Hibernia are intense extratropical cyclones. These typically enter the Grand Banks either from the southwest, west or northwest. They move through the region defined by 45-55°N, 45-55°W, with central pressures of approximately 975mb or less. Southwesters typically form off the U.S. East Coast and rapidly intensify as they move northeastward. Northwesters are associated with intense, slow moving cyclones centered east of the the Grand Banks.

Severe storms are selected for the period from January 1951 to December 1984. For 1951 through 1979, very few wave measurements are available, and storm selection is based largely on archived weather and meteorological information, and regional hindcasts. Storms for 1980-1984 are identified from wave buoy data recorded at Hibernia drill sites, as well as archived data. Table 1 lists the 29 storms selected for hindcasting.

Data sources used to identify the historical severe storm population include surface synoptic weather charts, vessel observations and METOC (Canadian Meteorological and Oceanographic Weather Center) wave charts produced through manual analysis of meteorological data. Also reviewed are two 20-year hindcast studies [6]--SOWM (Spectral Ocean Wave Model) produced by the U.S. Navy Fleet Numerical Oceanographic Center (FNOC) and WES produced by Waterways Experiment Station of the U.S. Army Corps of Engineers. These are hindcasts of directional wave spectra for 1956-1975 at six-hour intervals. Since sea ice affects waves generated by northwest storms, archived sea ice concentration data are also reviewed.

In reviewing weather charts, factors considered include: (1) track, speed, and intensity of centers of extratropical cyclones; (2) influence of previous storm systems on the initial state of the sea for a candidate storm; (3) the configuration of the surface isobar pattern and associated wind field about cyclone centers; and (4) fetch. limitations imposed by land and ice.

Accuracy of WES and SOWM hindcasts is not adequate for criteria determination, but the two series are used for initial screening for storms between 1956 to 1975. Storms with peak Hs estimated by WES or SOWM to exceed 9 meters near Hibernia are identified. A reduced list is made by examination of the orientation, linearity, and intensity of

the pressure gradient in the major fetch zones of wave generation directed towards Hibernia.

Of the 29 storms selected, five generated the top ranked seastates in the WES climatology. Two were initially identified from pre-1980 drill rig wave data, thirteen from archived meteorological data, and nine from 1980-1984 wave buoy data. Four of the latter group are two pairs of double-peaked storms--that is two separate storm systems which passed Hibernia approximately a day apart.

WINDFIELD REPRESENTATION

Inaccuracies in windfields are the principal source of error in hindcast results [10]. operational surface weather maps can misrepresent windfields; and considerable reanalysis is generally required. For all the selected storms, winds are first calculated from hand-drawn pressure maps based on synoptic measurements available in real-time. The raw windfields are then modified through kinematic analysis and the inclusion of pressure and wind data not reported in real-time.

Kinematic analysis accounts for such influences as deformation in winds near and downstream of coasts, and inertial accelerations associated with large spatial and temporal variations in surface pressure gradients. Kinematic analysis involves: (1) plotting all available synoptic observations of wind speed and direction and sea level pressure; (2) rejection of obviously erroneous reports; (3) construction of a continuity chart to track storm movement; (4) construction of streamlines and isotachs; and (5) gridding of wind speed and direction.

Storm winds are modelled in two phases. A "spinup" period determines the background sea state prior to storm arrival; and a "storm" period occurs when the storm center crosses the Grand Banks. Generally each phase lasts approximately two days. Kinematic analysis is necessary during the storm period only in an area centered about Hibernia (generally within 40-60°N and 30-60°W) . During spinup, when extreme accuracy in the windfield is not essential, winds are specified by the sea-level pressure analyses on the Northern Hemisphere surface analysis series. Accuracies of surface winds from kinematic analysis are verified to approach the basic accuracy of ships' wind observations (about 2.5 m/sec in speed, 20° in direction). Procedures for deriving windfields varies slightly for each storm, depending on available data.

Figure 2 compares modelled winds at the grid point nearest Hibernia to measured winds in storm 21. The measured data are one-minute means of wind speed and direction (instrumentally measured at approximately 80m elevation, and visually averaged, and reduced to 20m elevation) at

three rigs over 3-hour intervals. Agreement is generally quite good except late in the period modelled, when a secondary disturbance caused an increase in surface wind speed not well resolved in winds derived from the operational surface pressure analysis.

NUMERICAL WAVE HINDCAST MODEL

Waves are hindcast using a modified version of the ODGP (ocean Data Gathering Program) model [9]. The model is constructed of two basic parts. One affects propagation of waves through a grid. The second part simulates, at each time step and grid point, the change to each spectral component of the directional spectrum, caused by growth and dissipation. The growth/dissipation algorithms are routinely applied to a spectrum partitioned in 15 frequency bands and 24 directional bands. "Growth" addresses only those components propagating within +/-90° of the local wind direction. The growth model is:

$$dS(f,\emptyset)/dt=[A(f,\emptyset,V)+B(f,\emptyset,V)S(f,\emptyset)]x(1-[S(f,\emptyset)/S_{PM}(f,\emptyset,V)]^2)$$

where $S(f,\emptyset)$ is the directional wave spectrum
- f is wave frequency;
- $\emptyset$ is wave direction;
- V is the wind speed;
- $A(f,\emptyset,V)$ is the linear growth rate;
- $B(f,\emptyset,V)$ is the exponential growth rate; and
- $S_{PM}(f,\emptyset,V)$ is the Pierson-Moskowitz (PM) spectrum of a fully developed sea.

Over the four year period that the the various hindcasts were actually performed, changes to the grid system were introduced. These changes address grid coarseness/fineness, and hindcast results at Hibernia are only negligibly affected. For hindcasts of Storms 1 through 20, a 2° grid spacing is used. Boundaries are placed at 81W, 6E, 26.45N, and 64.63N. Grid spacing varies from 51nmi to 107nmi; the total number of grid points is 932 with 81nmi spacing at Grand Banks. The propagation scheme conserves energy rigorously, accounts for great circle propagation, and simulates lateral and longitudinal spreading with finite bandwidth spectral components. Propagation tables are developed which contain the interpolation coefficients. The energy balance equation is approximated by iterating each 3-hour propagation steps between two growth steps of 1.5 hours duration. Each 6-hour wind field is used for successive steps centered on the analysis time. At the start of the hindcast the sea is assumed calm everywhere. Regions with 50% or greater ice coverage are specified as "land".

For Storms 21 and 23, a nested grid system (Figure 1) is used. A fine grid of spacing half the nominal grid length is nested within the "coarse" grid to better resolve sharp gradients in the wind field and possibly the wave field in the vicinity of the measurement sites. The time step on the fine grid is 1.5 hours.

Slight differences in the grid system and in the binning of the 15 frequency bands are introduced for Storms 22 and 24-29. The grid system consists of a coarse grid of spacing 1.25° latitude and 2.50° longitude, covering most of the North Atlantic Ocean west of 20°W, and a nested fine grid with spacing half that of the coarse. The time step for the model is 3 hours, and consists of a full time step of propagation between two half time steps of growth.

VERIFICATION WITH DATA

Verification of hindcast performance is required at each site of application to assess accuracies of both the numerical model and the windfield input. For 9 of the 29 hindcast storms (Storms 21-29), wave and wind data were recorded simultaneously at several wellsites. Wave buoys were routinely deployed at wellsites on the Grand Banks [7]. During non-severe seastates, data were recorded for approximately 18.2 minutes every 3 hours. During storm conditions data are recorded quasi-continuously (18.2 minutes every 20 minutes).

A time history of hindcast and measured significant wave height for each storm is developed. Figure 3 shows the buildup and decay of Hs for Storm 21, one of the less accurate hindcasts. In a given storm, discrepancies between hindcasts and measurements tend to be spatially correlated across the measurement stations. Shallow water effects [16] and errors in the input wind fields are considered the dominant cause of possible wave hindcast errors in these series.

Standard statistical measures are used to assess the fit of the hindcasts to the measurements throughout the period of storm build-up and decay. Except for Storm 25, the scatter index (i.e., rms difference divided by mean of measurement sample) is 20% or less, which is at the lower end of the range reported for detailed storms hindcast with calibrated models [12]. Peak conditions are well modelled in Storm 25, and the high scatter index is due to cumulative errors throughout storm buildup and decay. Table 3 summarizes 17 comparisons of measured and modeled peak Hs and associated spectral peak periods for Storms 21-29. The mean difference in Hs is +0.26m (hindcasts greater than measurements), and is a result mainly of the bias of Storms 21 and 23. Overestimation of peak Hs for these two storms may be a result of the small time step used only in these hindcasts. Also, in such severe seastates, in which considerable low-frequency energy is usually present, wave development may be limited by water depth. Shallow water effects are not included in the hindcast model. The higher Hs values for these two storms are retained in the extremal analysis to ensure a degree of conservatism. The rms difference for Storms 21-29 is 1.19m. For this severe storm sample (mean measured Hs of 9.3m), the scatter index is therefore 12.8%, which is close to the scatter index of 11.9% in the ODGP storm

hindcast comparisons in various meteorological systems [15]. Mean and rms differences in spectral peak period of 0.60 sec and 1.17 sec, respectively, are also comparable to the ODGP errors. These comparisons are convincing evidence that the maximum accuracy achievable in mid-latitude basins has been attained, and that the mean difference in hindcasts of severe seastates in historical storms at Hibernia is small enough to be ignored in the assessment of the extreme wave climate.

ANALYSES OF HINDCAST RESULTS

Among the chief wind and wave parameters needed for engineering applications are [3]:

-Sustained wind speed, V. as a function of return period.
-Gust wind speeds associated with V,
-Significant wave height, Hs. as a function of return period,
-Correlation of spectral peak period, Tp, with Hs,
-Maximum wave height, Hmax, and associated period, Thmax, and
-Spectral shape associated with Hs and Tp.

Monthly extremes are also needed principally for duration-limited operations (e.g., towouts, installations). The procedures described in this paper may be used in principle, but require that a severe event population be selected and hindcast for each month. As an alternative to such a large number of hindcasts (approximately 360) different methods and data bases are used as described in [4].

Extremal Analyses of Wind Speed and Wave Height:

Gumbel and Borgman distributions are tested to estimate extreme winds and waves. Fits of the 26 storm peaks (3 of the 29 storms failed to generate high seastates for various reasons) are achieved by a Gumbel distribution for V and a Borgman distribution for Hs. Fitted parameters are:

$$Pr(v.le.V) = \exp\{-\exp[-(V-a_1)/b_1]\},$$

$$Pr(h.le.Hs) = \exp\{-\exp[-(Hs^2-a_2)/b_2]\},$$

with $a_1 = 96.4$ $a_2 = 23.8$
$b_1 = 25.8$ $b_2 = 3.4$

The 100 year return period Hs is 14.4m; the 90% control value is 15.9m. The 100-year extreme V (nominally a 1-hour mean at 20m elevation) is 38.5m/sec. Wind gust speeds may be estimated from a variety of sources, which generally agree quite well [11]. Estimates are generally more sensitive to the adopted distribution than to the accuracy in the hindcast values. For example, the extremes are not markedly affected by using 29 peak wind speeds instead of 26, or by using the greater of either the measured or hindcast peak Hs.

Spectral Peak Period:

Tp associated with maximum Hs during a storm is estimated from a correlation of the form:

$$T_p = A\ (Hs)^B,$$

fitted to the 26 storm hindcast series. The fitted constants are A=5.1686 and B=0.4490. For most engineering applications, peak periods ranging +/- 2 seconds about the estimated value are used.

Maximum Wave Height and Period:

Expected maximum individual wave height, Hmax, occurring in a storm is expressed as a factor times the peak Hs. The factor is based on a distribution of wave heights within a seastate (described by Hs) and on the integration of that distribution over a storm history (described by a growth and decay in Hs). A Rayleigh distribution, empirically modified with fits to measured data, is used [13]:

$$P(h.ge.H) = \exp\{-B(t)\},\ B(t) = [H^2/m_o(t)]^{1.063}/8.42$$

where $m_o(t)$ is the zeroth moment of the seastate spectrum. Hmax is then calculated through a Borgman integral:

$$P(h.le.Hmax) = \exp\int_{t_a}^{t_b}[\ln(1 - \exp(B(t))/T_s(t)]dt\ ;$$

where t_a and t_b are the beginning and end of the storm period, and $T_s(t)$ is the significant wave period throughout the storm. For Storms 22 and 24-29, the integral yields an Hmax/Hs value of 1.84, at a standard deviation of 0.06.

Analysis of periods of high waves recorded at Hibernia agrees quite well with previous analyses for other locales [5], and suggests a value of T_{Hmax}, the period of the maximum wave as approximately 0.90Tp.

Spectral Shape

A commonly used parametric, unidirectional spectral form is a Jonswap-like shape:

$$S(f) = C(0.3125H_s^2 fp^4/f^5)\exp(-1.25fp^4/f^4)G^b,$$

where fp is the spectral peak frequency (=1/Tp),
b is $\exp[-(f-fp)^2/(2\sigma^2 fp^2)]$,
σ is 0.07 for f.le.fp, and 0.09 for f.ge.fp
G is the peak enhancement factor,

C is factor ensuring that the integral of S(f) equals approximately $16.0Hs^2$ (as is true for Rayleigh distributed wave heights), and is approximated by {1 - 0.29071nG) for the above parameter values.

The diversity of spectral shapes both within a single storm and over the storm population precludes a single definitive shape. However, at storm peaks, the relationship TP*C*G = 20 rather consistently fits the Hibernia data.

Directional characteristics of severe storms are estimated from hindcast directional spectra of the most severe SW storms, Table 4 summarizes directional properties of three of the top ranked SW storms. Spectra in Storms 18 and 23 are similar in that the direction of maximum energy, dominant direction, and inline/total energy ratio match closely. The inline to total energy ratios of about 0.75 for these storms correspond to a cosine-squared energy spreading. Also, the direction of maximum energy in these peak spectra varies slightly with frequency, suggesting that for extreme SW storms, the directions probably characterize the direction of propagation of the largest individual waves fairly well. However, Storm 13 implies that this simple model is not always correct, In Storm 13, the spectrum of peak seastate contained two directional maxima, Use of a variety of spectral shapes, depending on the application, may be warranted.

CONCLUSION

Wind and wave hindcasting, and extremal analyses for hindcast results are principal tools in estimating extreme environmental conditions. Available archived data are sufficient for identifying severe storms at Hibernia since at least as early as 1951, and for constructing detailed windfields. Likewise, as verified by comparisons to measured data, numerical wave models accurately estimate seastate conditions during these storms. Extremal analyses of hindcast results yield long return period extremes of wind speed and significant wave height as functions of return period, other wind and wave parameters necessary for the design and analysis of offshore structures are associated with the extremes through a variety of statistical analyses.

ACKNOWLEDGEMENTS

Gratitude is expressed to the organizations which funded much of this work: the four members of the Hibernia Partnership--Mobil oil Canada Properties, Chevron Canada Resources Ltd., Gulf Canada Corporation And Petro-Canada Resources; and Mobil Research & Development Corporation. Likewise, thanks are extended to the Canadian Marine Environmental Data Service of Ottawa for their cooperation and far-sighted data collection program, and to H.V. Leder of Texas A&M University for his assistance in preparing the text.

REFERENCES

1. Szabo D., Cardone V.J., Eid B. & Dello Stritto F.J., 1989, "Verification of Numerical Wave Hindcasts for Severe Storms at Hibernia", 2nd International Workshop on Wave Hindcasting and Forecasting (SIWWHF), Vancouver, British Columbia, 25-28 April 1989.

2. Szabo D., Cardone, V.J. & Callahan B.T., 1989, "Severe Storm Identification for Extreme Criteria Determination by Hindcasting". SIWWHF.

3. Cardone V.J., Greenwood J.A., Szabo, D. & Dello Stritto F.J., 1989. "Engineering Parameters from Hindcast Results". SIWWHF.

4. Bolen Z.K. & Dello Stritto F.J., 1989. "Estimation of Extreme Wave Heights through Weibull Distributions", SIWWHF.

5. Arhan, M.F., Cavanie, A.G. and Ezraty, R.S., 1979, "Determination of the Period Range Associated to the Design Wave". Proceedings of the 11th offshore Technology Conference, 8-11 May 1979, Houston, Texas.

6. Brown, R.D., Roebber, P. & Walsh, K. 1984, Climatology of Severe Storms Affecting Canadian East Coast Areas, Canadian Environmental Studies Revolving Fund Report No. 040-25-08, Canada Oil & Gas Lands Administration, Ottawa, Ontario.

7. Canadian Marine Environmental Data Service, 1989. Historical Wave Measuring Stations, 26 January 1989, Ottawa, Ontario.

8. Cardone, V.J,. 1974, "Ocean Wave Predictions: Two Decades of Progress and Future Prospects". Seakeeping 1953-1973. October 28-29, 1973, Society of Naval Architects and Marine Engineers, New York, New York, pp 5-18.

9. Cardone, V.J., Pierson, W.J. and Ward, E.G., 1976, "Hindcasting the Directional Spectrum of Hurricane Generated Waves". J. of Petroleum Technology, 28 April 1976.

10. Cardone, V.J. & Szabo, D., 1985, "Impact of Uncertainty in Measurements of offshore Wind on Accuracy of Wave Hindcasts and Forecasts". Proceedings of the International Workshop on Offshore Winds and Icing (IWOWI), 7-11 October 1985, Halifax, Nova Scotia.

11. Dello Stritto, F.J., Benoit, J.R. & Ransom, J.A.N., 1985, "Wind Related Needs of Offshore Industry: A Select Review", IWOWI.

12. Ewing., J.A., 1971, "A Numerical Wave Prediction Method for the North Atlantic Ocean". Deutsche Hydrographische Zeitschrift, 24.

13. Forristall, G.Z., 1978, "On the Statistical Distribution of Wave Heights in a Storm", J. of Geophysical Research, 83.

14. Francis, P.E., 1986, "The North Europe Storm Study (NESS)", Proceedings of the International Workshop on Wave Hindcasting and Forecasting, 23-26 September 1986, Halifax, Nova Scotia.

15. Reece, A. & Cardone, V.J., 1982, "Test of Wave Hindcast Model Results Against Measurements During Four Different Meteorological Systems". Proceedings of the 14th offshore Technology Conference, 3-6 May 1982, Houston, Texas.

16. Swail, V.R., Cardone, V.J. & Eid, B., "An Extremes Wind and Wave Hindcast off the East Coast of Canada". SIWWHF.

Storm	Hindcast Period	Type	Minimum Central Pressure (mb)	Maximum Deepening Rate (mb/24hr)	Maximum Hindcast Hs (m)	Conditions occurring at time of Max. Hs: Tp(sec)	Direction of Maximum Energy(°T)	Sustained Wind Speed(m/s)	Sustained Wind Dir(°T)
1*	10-14Nov52	SW	950	34	7.1*	12.9	60	20.3	238
2	08-11Feb54	SW	952	41	11.6	16.0	46	27.7	223
3	20-23Sep55	SW	970	18	9.5	15.4	68	24.5	251
4	09-13Dec55	SW	954	36	10.7	15.8	61	26.2	242
5	20-23Jan61	SW	958	14	11.7	16.8	64	25.8	264
6	15-18Dec61	NW	958	38	9.7	13.4	151	26.3	270
7*	10-14Jan64	NW	962	14	6.3*	11.0	102	20.8	309
8	14-18Mar64	NW	954	22	8.4	13.3	181	12.2	293
9	17-20Feb65	NW	962	28	9.9	13.9	148	31.8	308
10	13-17Feb66	NW	958	25	10.4	14.5	145	27.5	307
11	21-24Feb66	NW	962	22	8.9	15.7	194	20.6	332
12	20-24Feb67	SW	954	40	11.9	16.0	57	27.2	270
13	20-24Jan70	SW	948	48	12.1	14.6	50	28.5	286
14	16-19Jan71	SW	940	34	11.8	15.3	77	31.8	258
15	26-29Oct73	SW	962	16	11.1	14.4	27	29.2	269
16	08-13Mar74	SW	946	56	10.4	14.2	50	29.8	227
17	16-20Mar76	SW	953	29	10.3	15.2	68	27.7	244
18	19-22Jan77	SW	942	30	12.1	16.1	55	30.6	238
19	01-05Mar78	NW	944	48	10.2	13.9	157	28.2	319
20	02-06Jan80	SW	962	24	8.9	13.1	63	25.9	256
21	13-18Jan82	SW	952	45	11.7	16.9	58	26.0	237
22	01-04Feb82	NW	972	20	9.2	13.4	129	24.0	328
23	11-16Feb82	SW	950	38	13.4	16.6	50	31.4	250
24	07-12Dec82	NW	960	37	8.6	13.2	103	26.0	291
25	05-11Mar83	NW	970	20	9.2	14.1	180	26.4	001
26	25Nov-	NW	969	12	8.8	13.5	146	25.9	319
27*	-02Dec83	NW	973	16	6.7*	12.6	71	8.7	277
28	18Dec-	SW	950	40	11.2	15.9	163	26.4	342
29	27Dec83	SW	948	36	8.8	14.2	57	20.4	269

Notes - SW--Storms from the southwest; NW--Storms from the northwest.
- Wind direction and direction of maximum energy are directions towards.
- Sustained wind speeds nominally represent 1-hour mean speeds at 10m elevation.

* Excluded from extremal analysis

Table 1: Parameters & Hindcast Results for 29 Hibernia Storms Occurring from 1951-1984

Return Period (years)	Extreme Sig. Wave Ht. Best Fit (m)	90% Control Level (m)	Associated with Extreme Hs: Tp (sec)	Hmax (m)	Thmax (sec)	Wind Speed (m/sec)	Extreme Wind Speed Irrespective of Hs (m/sec)
10	12.1	13.0	14.5-18.5	23.9	13.5-16.5	28.5	30.5
25	13.1	14.2	15.0-19.0	26.1	14.0-17.0	30.9	33.7
50	13.8	15.1	15.5-19.5	27.8	14.5-17.5	32.7	36.1
100	14.4	15.9	16.0-20.0	29.3	15.0-18.0	34.5	38.5

Notes: 1) Best fit and 90% control level extreme Hs-values are based on least-squares fits of peak Hs from 26 storms over 34 years to a Borgman distribution (i.e., Gumbel distribution of Hs^2).
2) Wind speed and spectral peak period, Tp, "associated with maximum Hs" are those expected simultaneously with the maximum Hs, and are not necessarily extreme values of those parameters.
3) Height and period of the highest wave (Hmax and Thmax) "associated with maximum Hs" are those expected during a storm with the corresponding peak Hs, and not necessarily occurring simultaneously with the peak Hs.
4) Ranges are specified for the wave periods due to the natural distribution of periods associated with a specified height, and the varying dependence of engineering applications to wave period.
5) Extreme wind speeds "irrespective of Hs" are based on least squares fit of peak wind speeds from 26 storms over 34 years to a Gumbel distribution.
6) Sustained wind speeds nominally represent 1-hour mean speeds at 10 meters elevation.

Table 2: Extreme Values of Significant Wave Height and Sustained Wind Speeds, and Associated Seastate Parameters Based on Extremal Analyses of Hindcasts of Severe Storms at Hibernia Occurring between 1951 and 1984.

Storm	Date	MEDS Site	Hs (m) Measured	Hs (m) Hindcast	Tp (sec) Measured	Tp (sec) Hindcast
21	16Jan82	134	9.5	11.9	14.4	16.8
		156	10.0	11.9	14.4	16.8
22	02Feb82	134	8.0	9.2	11.4	13.4
		140	7.5	9.0	11.4	13.4
		156	7.7	9.2	11.4	13.4
23	14Feb82	140	11.5	13.4	15.2	16.6
24	10Dec82	134	9.5	8.6	13.7	12.8
25	08Mar83	134	8.8	8.4	13.0	13.3
26	29Nov83	134	7.8	8.2	13.7	13.4
		168	9.5	8.5	13.7	13.4
		185	9.2	8.8	13.7	13.5
27	01Dec83	134	6.8	6.5	12.4	12.1
		168	7.5	6.5	12.4	12.3
		185	7.0	6.7	11.9	12.5
28	23Dec83	134	12.3	11.5	17.1	15.8
		168	12.5	11.4	16.1	15.7
29	26Dec83	134	8.6	8.5	13.0	13.5
Mean Difference (hindcast - measured)				0.26m		0.6s
RMS Difference				1.19m		1.2s

Table 3: Comparison of Hindcast and Measured Peak Significant Wave Heights and Spectral Peak Periods for Nine Storms at Hibernia

Storm	Max Hs	Tp	Wind Direction	Dir. of Max. Energy	Dominant Direction	Inline/Total Energy Ratio
13	12.2m	14.6s	286°	50°	49°	0.60
18	12.1m	16.1s	238°	55°	52°	0.75
23	13.4m	16.6s	250°	51°	46°	0.74

Note: Wind Direction is direction from, all other directions are direction toward.
Storm 13 is double peaked, with secondary peak at 152°

Table 4: Direction Properties of Maximum Hindcast Seastates in 3 Severe Hibernia Southwest Storms

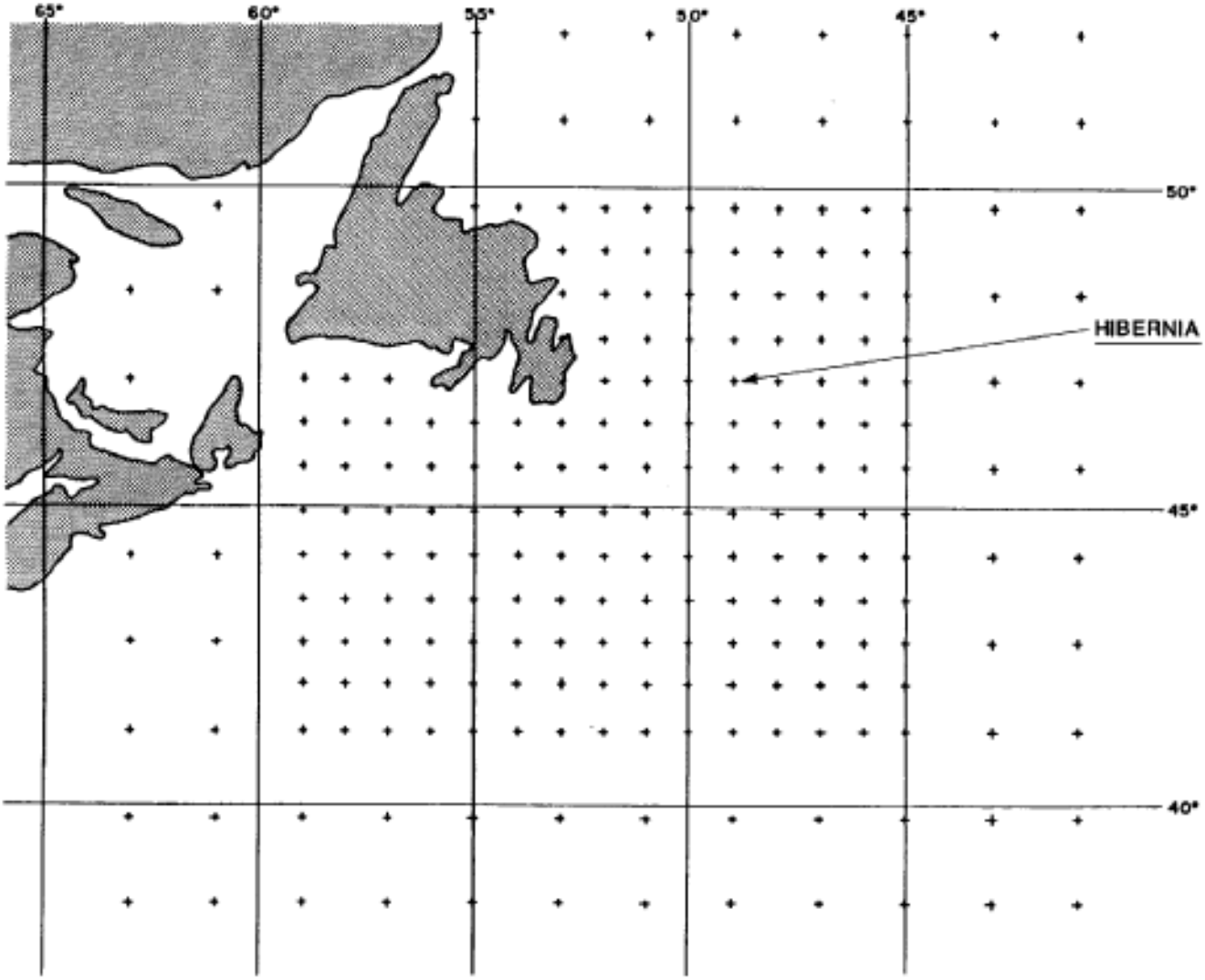

FIGURE 1. MAP OF THE GRAND BANKS WITH GRID SYSTEM FOR NUMERICAL WAVE HINDCAST MODEL, USED FOR STORMS 21-29.

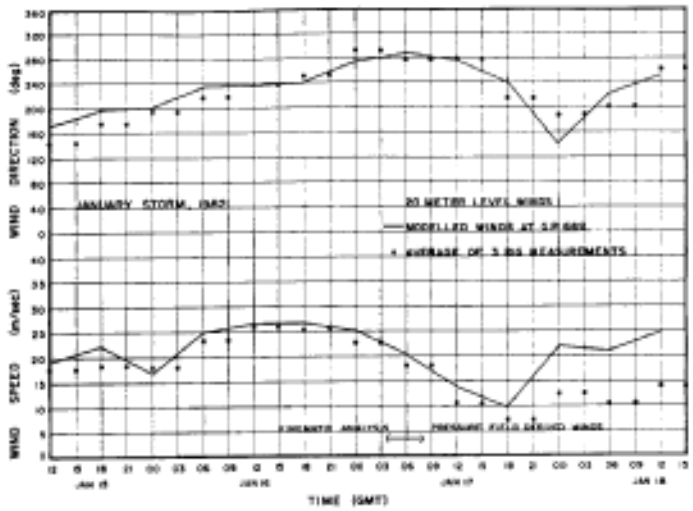

FIGURE 2. COMPARISON OF MEASURED AND MODELED WIND SPEED AND DIRECTON FOR STORM 21, JANUARY 1982.

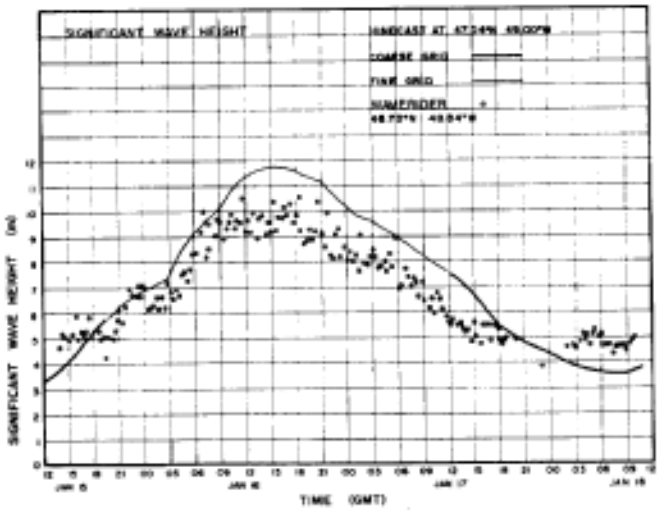

FIGURE 3. COMPARISON OF MEASURED AND MODELED SIGNIFICANT WAVE HEIGHT FOR STORM 21, JANUARY 1982.

SEVERE STORM IDENTIFICATION FOR EXTREME CRITERIA DETERMINATION BY HINDCASTING

by D. Szabo[1], V.J. Cardone[2], and B.T. Callahan[2]

[1] Mobil Research and Development Corporation, Dallas, Texas
[2] Oceanweather, Inc., Cos Cob, Connecticut

ABSTRACT

Severe storm selection for hindcasting is an important, though inherently subjective, step in determining extreme wave criteria. An efficient, objective procedure is proposed to improve and simplify storm selection methods. The procedure is based on estimating peak significant wave height from gross storm parameters by linear regression analysis. Using Hibernia as a test case, archived meteorological charts between 1951 and 1986 are reviewed. Ninety three potentially severe storms are identified, in 43 of which reliable estimates of peak significant wave height are available. For each storm, parameters such as deepening rate, maximum pressure gradient, and duration and fetch characteristics are estimated. For the 43 measured or hindcast storms, correlations of peak significant wave height with storm parameters are quantified. These include simple threshold analysis and single and multiple parameter linear regression. Based on correlation analyses, estimates of significant wave height for the remaining 50 storms are made. Three of the most severe of these storms are hindcast to assess procedure accuracy.

INTRODUCTION

This is the third of five related papers (1-4) describing development of extreme wind and wave criteria for the Hibernia site on the Grand Banks. While some novel items are included, completeness rather than innovation is the theme. The set is believed to be the first which details all steps in estimating criteria necessary for offshore development. These steps range from use of numerical wave models to the empirical tools and "rules of thumb" for obtaining engineering parameters. The intent is that, by documenting the Hibernia application fully, further development may be directed to areas of greatest need.

Ideally, extreme wave criteria should be based on data sets much longer than the return periods of interest. For offshore structure design, return periods are typically 100 years; and such data sets do not exist. Therefore, wave criteria are most accurately determined through extremal analysis of severe seastates occurring over a shorter period (often 20-30 years for offshore structures, comparable to the design life of the structure). If continuous significant wave height estimates are available over these years, merely selecting the largest peak values is sufficient for input to the extremal analysis. Measured

or observed data of acceptable accuracy or duration exist for very few locations. Synthetic data bases can be constructed by numerical wave hindcasting over the entire period, and several of these long-term (20 years or more) hindcasts are available for some regions [5]. Generally, accuracies of existing long-term hindcasts can be adequate for first approximations to extremes, but not for final criteria used in design.

Within the limitations posed above, the best alternative is to select severe wave events from historical records for short-term (typically several days) hindcasting. Peak significant wave heights from these hindcasts are then input to the extremal analysis. Identifying the most severe storms occurring over a period of decades is inherently uncertain. Often, selection is based largely on a review of archived meteorological records. It involves weighing the influence on wave generation of storm size, track, intensity and other factors. Such subjectivity reduces confidence in the extreme criteria estimates. With accuracies of state-of-the-art windfield analysis and numerical wave models approaching those of measured data, storm selection may be the largest single source of uncertainty and potential error in the criteria [6]. It is also costly and manpower intensive, as review of daily pressure charts spanning many years is involved.

An efficient, objective method is described below for estimating Hs from easily derived gross storm parameters. Sensitivity of criteria estimates to storm selection subjectivity is also assessed. The procedure is not intended to replace numerical hindcasting, but rather to provide a quantitative measure of seastate severity which minimizes human subjectivity. The method has been developed for and applied to Hibernia, and in principle may be extended to other areas.

SUMMARY OF APPLICATION TO HIBERNIA

Specific steps in development of the Hibernia application are:

1) Archived pressure charts for the Grand Banks for a 36 year period between 1951 through 1986 are reviewed, and 93 severe storms with potential for generating severe seastates near Hibernia are identified (Table 1). For 43 of the storms, reliable estimates of peak Hs exist.

2) Twelve gross storm parameters readily identified for each storm from the pressure charts are:

MCP = Minimum central pressure (mb)
MPG = Maximum pressure gradient in fetch (mb/°lat)
MDR = Maximum deepening rate (mb/24hr)
TPG = Total storm pressure gradient (mb/°lat)
DMG = Duration of 75% or more of MPG (hr)

STD = Storm track direction (°T)
FOR = Fetch orientation (°T)
LOF = Length of fetch (km)
WOF = Width of fetch (km)
RFT = Rate of fetch turning during DMG (°/6hr)
SIT = Storm Intensity ([mb/°lat]^{2}hours)
SCD = Storm center distance from the site (km)

FOR is the direction of the fetch with respect to the site; RFT is the time rate of change of fetch orientation. Storm intensity is defined as $0.5(MPG^2)(DMG)$. Other parameters are self explanatory.

3) These storm parameters are correlated to Hs, using simple threshold analyses and linear regressions, for each of the 43 storms with known maximum seastates. Of the 12 parameters, SIT is used only in simple linear regression analyses; and the two directional parameters (STD and FOR) are not used in regressions since they are not linear. The multi-variate linear regression fit of maximum Hs is therefore based on a maximum of 9 gross storm parameters. For the purposes of the correlation, possible errors in the "known" Hs values are not considered; reference (2) describes these for both hindcast and measured values. Based on the correlation analyses, estimates of the maximum Hs for each of the remaining 50 storms with no available wave data are made.

4) From the set of 50 Hs estimates, three storms which may have generated seastates comparable to those of the hindcast series are hindcast. Hindcast estimates of maximum Hs values for each storm are considered accurate to within 1 meter, and are used to assess accuracy of the correlation method predictions.

ANALYSIS OF THE HISTORICAL METEOROLOGICAL ARCHIVE

Ninety three storms are identified in Table 1 which occurred during the period from 1951 through the winter season of 1985-86. Selection of these storms is based on an initial screening of hundreds of candidate storms. The screening eliminates, for example, storms with MCP greater than 980 mb. The 93 events include 29 storms previously hindcast [1], and another 14 storms with available wave buoy data. The 12 parameters listed above are estimated for the 43 storms from available archived weather maps. Each of the parameters has in principle some influence on wave generation. The goal of the analysis of storm parameters is to determine how accurately maximum seastates may be estimated from them.

THRESHOLD ANALYSIS (TAR)

To estimate storm severity, a grading system based on meteorological parameters with the assumed greatest affect on wave generation is used. Five thresholds are established:

(1) MCP less than or equal to 967 mb;
(2) MDR greater than or equal to 18 mb/24hr;
(3) MPG greater than or equal to 6 mb/(° of latitude);
(4) SIT greater than or equal to 324 mb^2hours/(° of latitude)^2;
(5) TPG greater than or equal to 67 mb.

These thresholds are met or exceeded by the top ten hindcast storms, all of whose peak Hs exceeded 11 meters. The original 93 storms are ranked by assigning one point for each threshold met. Besides the 10 highest ranked hindcast storms, thirteen other storms achieve a rating of 5. These include: six hindcast storms whose maximum hindcast Hs ranges from 9.5 to 10.7 meters; four storms with available wave measurements; and three storms for which no estimate of Hs is available. Table 1 lists the TAR rating for each storm.

The grading system is a crude first attempt at stratification. Despite a few apparent inconsistencies (i.e., two storms with ratings less than 5 have Hs estimates exceeding 10m, and one storm rated 5 has an estimated Hs of only 8.2m), the procedure is a simple method for estimating the most severe storms from 5 easily assessed parameters.

SIMPLE LINEAR REGRESSION ANALYSIS (SLR)

Regression analyses provide a more objective and standard severity assessment than the threshold procedure. Due to largely unknown functional relationships between storm parameters and maximum storm sea states, only linear regression analysis is employed. Table 2 lists results of simple linear regression applied to the subset of storms with hindcast or measured Hs greater than 8m. The absolute mean squared error (difference between regression and known wave height) for each regression parameter is shown. Better correlation is found for parameters related to pressure estimates (MCP, MDR, MPG, and TPG), all of which had mean absolute differences less than 3 meters. Although DMG is important in wave generation, the parameter does not by itself correlate well to maximum storm wave heights. SIT, a function of DMG and MPG, correlates much better. Table 2 also provides SIR results for only hindcast storms. This selection reduces the total number of storms with maximum Hs greater than 8.0m from 34 to 26. Results indicate relatively little difference in mean error statistics except for RFT, Maximum hindcast wind speed correlates quite well to maximum hindcast Hs with an RMS error of approximately 1.3m, lower than any of the pressure chart parameters.

Although mean error is relatively low for five parameters, significant variation exists in SLR estimates among the different parameters for the same storm, Table 2 includes the SIR estimate for each of the five best-fitting lowest parameters (MCP, MDR, MPG, TPG and SIT) for each storm. The mean of the Hs-estimates for these five parameters

(also shown in Table 2) is a significantly better predictor than any of them individually. Such a result suggests that multiple regression analysis may be more appropriate.

MULTIPLE LINEAR REGRESSION ANALYSIS (MLR)

Averaging individual SIR estimates yields a low RMS error, comparable to that based on hindcast wind speed alone. Averaging implicitly assigns equal weight to each parameter. A more rigorous approach is a 9-parameter multi-variate regression. Table 2 shows greatly improved error statistics. The rms errors are about half those of the mean SLR and hindcast wind correlations. Table 2 also lists the regression coefficients, and lists the MLR estimate for each storm. Figure 1 illustrates a limitation of the MLR approach--higher maximum Hs are generally underestimated and lower values overestimated.

PREDICTION TESTING THROUGH HINDCASTING

Using the TAR, SLR and MLR results, estimates for peak Hs of the remaining 50 storms are obtained. Table 3 lists 15 of these storms for which either SLR or MLR fits predict Hs greater than 8m. For each of the 15, a partial reanalysis of the archived meteorological data is performed to identify the three most likely to generate extreme wave heights at Hibernia. NMC 6-hourly surface weather charts for each event are reexamined with additional synoptic ship report data. Ship reports are computer-plotted after reported winds are adjusted to effective neutral 20m level average winds. These results are used to estimate peak wind speed, which, as shown above, correlates well with maximum hindcast Hs. The reanalysis indicates that peak seastates at Hibernia were probably not very severe for nine of the 15 storms; and were at most comparable to those already hindcast. The three remaining storms (29Mar74, 07Feb77 and 17Feb83) had high wave-generating potential at Hibernia.

The three storms selected are hindcast by the methods and models described in [1]. Peak hindcast Hs values are listed in Table 3 . For two storms, hindcast maxima are within 0.4m of the MLR predictions; for one the hindcast is more than 3m lower. The limited comparison illustrates the limitations of MLR or any such analysis for accurate seastate prediction; but does support its use for storm selection.

SENSITIVITY OF EXTREME ESTIMATES TO STORM POPULATION

Methods summarized above are attempts to improve storm selection for input to hindcasting/extremal analysis techniques. The goal is to identify the most severe storms over a span of decades without hindcasting seastates for the entire period. Based on the three storms identified above, the original storm selection for Hibernia [1] is not

completely correct. The three "new" storms rank 16th, 19th and 23rd among the 29 most severe occurring between 1951 and 1984 (26 from the original hindcast set plus the three additional storms).

Sensitivity of extremal estimates to storm selection may be assessed with available hindcast and measured seastate data. Table 4 lists 100-year extreme Hs values using 6 subsets of the data; one being that used in [1] for criteria determination, Table 4 also shows extremes for three different Hs thresholds--that is a storm is only included in the subset if its peak Hs exceeds the threshold. Such thresholds are an implicit source of subjectivity in hindcasting/extremal techniques, since a decision must be introduced on the number of severe events included (or, equivalently, what constitutes a severe event). The common practice of selecting, on average, one event per year is arbitrary and in effect introduces a threshold. At Hibernia, for example, seastates exceeding 10m occur on average about 0.5 times per year, and seastates exceeding 8m at approximately twice that rate.

Table 4 shows that the 100-year estimate is not sensitive to the subset used when the whole hindcast period is considered (1951 to 1984 or 1986). For the Hibernia data set, dividing the 36 year period into two 18 year periods gives about a 10% difference in the 100-year Hs. The difference is mainly due to the cluster of very severe storms during 1982-1983. Generally, extremal estimates are much more sensitive to the assumed extremal distribution [4], than to the modest changes in the storm population.

In practice, errors in storm selection usually result in conservative extremal estimates, because very severe storms are the most easily identified. Selection errors tend to occur for storms close to the lower threshold. For example, the three storms added to the Hibernia hindcast set all have peak Hs less than 10m, and are ranked in the lower half of the hindcast set. Therefore, the high end of the extremal distribution is more accurate than the low end, which, if incorrect, is too low. The result is overestimation of the slope of the distribution and, upon extrapolation, overestimation of estimates of long return period extremes.

CONCLUSION

Severe storm selection is an inherently subjective step in the development of extreme environmental criteria by hindcasting and extremal analysis techniques. Several methods are proposed which allow objective storm selection from readily quantifiable storm parameters. All (threshold analysis, simple linear regression, multiple linear regression) are based on correlating peak Hs in a storm to meteorological parameters. Their application to Hibernia demonstrates both their strengths and weaknesses. Multiple linear regression, the

most sophisticated of the methods, achieves rather low error statistics over a large storm population. However, it can grossly miscalculate peak Hs for individual storms, and has an overall tendency to underestimate high Hs values and overestimate low ones. Therefore, it is not a flawless storm selector, and hardly a substitute for hindcast modeling. The single storm parameter which best predicts peak Hs is the peak sustained surface wind speed. However, accurate estimates of such wind speeds are only slightly more available than peak Hs itself.

TAR, SLR and MLR procedures assist in storm selection by providing objective and quantifiable measures of storm severity. For the Hibernia application, they also provide a check on conventional, subjective storm selection. The procedures objectively reduce a list of 50 possibly severe storms to 15. Further reduction to 3 storms requires partial kinematic analysis. Results of the kinematic analysis of this small number of storms are easily documented. The final result is that subjectivity and the degree of kinematic analysis has been substantially reduced. In areas where hindcast or measured data do not exist, an adaption of TAR may be used for an initial selection, regression to shortlist the potentially severe storms; and kinematic analyses to obtain the final set of severe storms.

Within reasonable bounds, extreme Hs estimates are not highly sensitive to storm selection subjectivity. The few most severe storms occurring over a span of decades are rather easily identified. Subjectivity mainly influences selection of the lower half of the severe storm set. Such errors tend to produce overestimates of the extreme values. Estimates of extremes based on six overlapping sets of severe Hibernia storms illustrate the low sensitivity. Extreme estimates are more sensitive to the lower threshold of what constitutes a severe event, and to the assumed extremal distribution than to modest variations in storm selection.

ACKNOWLEDGEMENTS

Gratitude is expressed to the organizations which funded much of this work: the four members of the Hibernia Partnership--Mobil Oil Canada Properties, Chevron Canada Resources Ltd., Gulf Canada Corporation and Petro-Canada Resources; and Mobil Research & Development Corporation (MRDC). Likewise, thanks are extended to the Canadian Marine Environmental Data Service of Ottawa for their cooperation and far-sighted data collection program, and to F. J. Dello Stritto of MRDC for his assistance in preparing the text.

REFERENCES

1. Cardone V.J., Szabo D. & Dello Stritto F.J., 1989, "Development of Extreme Wind and Wave Criteria for Hibernia", 2nd International

Workshop on Wave Hindcasting and Forecasting (SIWWHF), 25-28 April 1989, Vancouver, British Columbia.

2. Szabo D., Cardone V.J., Eid B. & Dello Stritto F.J., 1989, "Verification of Numerical Wave Hindcasts for Severe Storms at Hibernia", SIWWHF.

3. Cardone V.J., Greenwood J.A., Szabo, D. & Dello Stritto F.J., 1989, "Engineering Parameters from Hindcast Results", SIWWHF.

4. Bolen Z.K. & Dello Stritto F.J., 1989, "Estimation of Extreme wave Heights through Weibull Distributions", SIWWHF.

5. Brown, R.D., Roebber, P. & Walsh, K., 1984, Climatology of Severe Storms Affecting Canadian East Coast Areas, Canadian Environmental Studies Revolving Fund Report 040-25-08. Canada Oil & Gas Lands Administration, Ottawa, Canada.

6. Cardone, V.J. & Szabo, D., 185, "Impact of Uncertainty in Measurements of Offshore Wind on Accuracy of Wave Hindcasts and Forecasts". Proceedings of the International Workshop on Offshore Winds and Icing, Halifax, Nova Scotia, 7-11 October 1985.

Storm	Date	Max.V	Max.Hs	TAR	Storm	Date	Max.V	Max.Hs	TAR
1	15Jan51			2	47	24Nov73		5.8	4
2	15Dec51			3	48	04Jan74			4
3	19Dec51			3	49(16)	12Mar74	29.8	10.4	5
4	06Nov52			1	50	29Mar74			4
5(1)	13Nov52	20.3	7.1	4	51	18Mar75			2
6	17Jan53			2	52(17)	18Mar76	27.7	10.3	3
7	23Jan53			1	53	14Jun76			1
8	22Feb53			3	54	07Nov76			2
9	29Jan54			0	55	10Nov76			3
10(2)	10Feb54	27.7	11.6	5	56	14Jan77			2
11	06Oct54			3	57(18)	21Jan77	30.5	12.1	5
12	25Oct54			3	58	07Feb77			5
13(3)	22Sep55	24.5	9.5	5	59	04Jan78			2
14	27Nov55			4	60	01Mar78			1
15(4)	12Dec55	26.2	10.7	5	61(19)	03Mar78	28.2	10.2	5
16	31Dec56			3	62	22Dec78			2
17	29Mar57			2	63(20)	04Jan80	25.9	8.9	4
18	08Feb59			5	64	18Nov80		8.2	4
19	06Mar60			2	65	21Nov80		8.2	5
20(5)	22Jan61	25.8	11.7	5	66	01Nov81		7.5	0
21(6)	17Dec61	26.3	9.7	5	67	31Dec81		8.2	3
22	05Jan62			3	68(21)	16Jan82	26.0	11.4	5
23	03Mar62			2	69	19Jan82		8.7	3
24	16Nov63			4	70	23Jan82		7.2	3
25	31Dec63			4	71(22)	02Feb82	24.0	9.2	3
26	09Jan64			3	72	07Feb82		7.2	3
27(7)	14Jan64	20.8	6.3	4	73(23)	15Feb82	31.4	13.4	5
28(8)	18Mar64	21.2	8.4	4	74	10Apr82			4
29	06Nov64			2	75	13Apr82			2
30(9)	19Feb65	31.8	9.8	3	76	17Nov82			3
31	03Jan66			1	77(24)	10Dec82	26.0	8.6	3
32	11Jan66			5	78	07Jan83			4
33(10)	17Feb66	27.5	10.4	5	79	14Feb83			2
34(11)	24Feb66	20.6	8.9	4	80	17Feb83			5
35	14Feb67			1	81(25)	09Mar83	26.4	9.2	3
36(12)	23Feb67	27.2	11.9	5	82(26)	29Nov83	25.9	8.8	2
37	06Jan68			3	83(27)	01Dec83	8.7	6.7	0
38(13)	23Jan70	28.5	12.2	5	84	05Dec83		7.2	3
39	08Jan71			3	85(28)	22Dec83	26.4	11.2	5
40(14)	18Jan71	31.8	11.8	5	86(29)	26Dec83	20.4	8.8	4
41	24Feb71			0	87	27Jan84		9.5	3
42	02Jan72			3	88	11Mar84			1
43	04Jan72			4	89	28Mar84		6.5	3
44	20Apr72			4	90	29Jan85		10.1	5
45	15Mar73			4	91	16Dec85		10.8	5
46(15)	29Oct73	29.2	11.1	5	92	19Dec85		11.5	4
					93	05Jan86			2

Note: Max.V--Peak wind speed (m/s; nominally 1-hour mean at 10m)
Max.Hs--Peak significant wave height (m)
TAR--Threshold Analysis Rating
(xx)--Numbers in the hindcast storm set [1]. Hs for these storms are from hindcasts, others are from MEDS data

Table 1: Parameters of 93 Hibernia Storms Occurring 1951-1986

Storm	Peak Sig. Wave Height (m, Max.Hs) Estimated by Simple Linear Regression (Max.Hs = a + bXXX, where XXX a one of the following parameters)											Hindc. or Measd. Max.Hs	MLR
	SCD	MCP	MDR	LOF	WOF	MPG	DMG	RFT	TPG	SIT	AVE	Max.V	
10		11.6	17.4			8.7	9.1		9.9		11.3	10.7	11.6	10.8
13		10.8	8.6			8.7	7.1		12.5		9.5	10.0	9.5	9.9
15		10.8	13.1			15.0	15.3		13.1		13.1	10.3	10.7	11.2
20		9.2	7.2			8.7	9.1		9.1		8.6	10.3	11.7	10.1
21		12.3	12.1			8.7	9.1		15.5		11.5	10.4	9.7	10.1
28		10.8	7.9			8.7	9.1		4.5		8.2	7.4	8.4	8.6
30		8.4	2.6			11.8	14.7		2.3		8.0	11.5	9.8	9.6
33		12.3	6.5			8.7	11.1		13.9		10.3	10.6	10.4	10.0
34		6.1	8.9			5.5	12.2		9.1		8.4	9.2	8.9	9.2
36		11.6	15.3			8.7	9.1		10.6		11.0	10.6	11.9	10.6
38		12.3	15.6			15.0	11.8		10.6		13.1	10.8	12.2	12.2
40		15.0	12.8			11.8	14.7		12.5		13.4	11.5	11.8	11.3
46		5.7	5.1			8.7	7.1		8.7		7.1	11.0	11.1	8.9
49		13.9	16.3			15.0	11.8		14.4		14.3	11.1	10.4	10.6
52		10.8	11.4			5.5	6.6		10.6		9.0	10.7	10.3	10.6
57		16.2	13.9			8.7	11.1		11.7		12.3	11.3	12.1	10.7
61		13.9	9.3			15.0	15.3		12.5		13.2	10.8	10.2	10.3
63		6.1	7.2			8.7	7.1		4.5		6.7	10.3	8.9	8.6
64		7.7	9.3			11.8	12.0		6.8		9.5		8.2	9.5
65		9.2	9.6			15.0	15.3		10.6		12.0		8.2	10.3
67		6.1	9.6			8.7	5.1		3.0		6.5		8.2	7.9
68		11.6	11.1			15.0	15.3		9.9		12.6	10.3	11.4	11.5
69		11.6	9.3			2.3	6.4		12.1		8.3		8.7	9.6
71		1.5	5.8			8.7	5.1		8.7		5.9	9.9	9.2	8.8
73		10.8	14.2			18.1	16.1		13.3		13.3	11.4	13.4	11.8
77		7.7	9.6			5.5	3.8		10.6		7.5	10.3	8.6	10.0
81		3.8	6.5			15.0	15.3		6.4		9.4	10.4	9.2	10.0
82		4.6	10.7			8.7	3.1		6.4		6.7	10.3	8.8	9.4
85		5.3	5.4			11.8	12.0		9.9		8.9	10.4	11.2	11.0
86		17.0	11.4			8.7	5.1		9.9		10.4	9.1	8.8	10.6
87		10.8	13.5			5.6	3.8		15.2		9.8		9.5	10.2
90		16.2	9.6			8.7	13.1		12.9		12.1		10.1	9.6
91		12.3	10.0			8.7	9.1		11.4		10.3		10.8	11.1
92		10.8	9.3			8.7	5.1		12.9		9.3		11.5	10.4
Absolute Error (All Storms Hs ≥ 8m):		7.8	2.6	2.4	7.6	4.8	2.7	11.4	27.7	2.3	3.6	1.6			0.7
Mean Squared Error (All Storms Hs ≥ 8m):		102	11	9	107	36	11	240	1482	9	20	4			0.9
Absolute Error (All Hindcast Storms Hs ≥ 8m):		8.8	2.6	3.0	8.1	6.3	3.1	16.3	5.4	2.2		1.4	1.3		
Mean Squared Error (All Hindcast Storms Hs ≥ 8m):		130	11	6	130	63	6	265	53	8		3	2.3		
MLR Coefficients:															
Mean:	0.19	-0.01	0.03	0.04	0.41	0.66	0.04	0.03	0.03						
LCL:	-0.06	-0.07	-0.02	-0.41	-0.46	0.23	-0.02	-0.02	-0.03						
UCL:	0.43	0.05	0.08	0.50	1.28	10.9	0.10	0.09	0.09						

Notes:

- SCD = Storm center distance from Hibernia
- MCP = Minimum central pressure
- MDR = Maximum deepening rate
- LOF = Length of fetch
- WOF = Width of fetch
- MPG = Max. pressure gradient in fetch
- DMG = Duration of 75% or more of MPG
- RFT = Rate of fetch turning during DMG
- TPG = Total storm pressure gradient
- SIT = Storm Intensity
- AVE = Mean of Hs-estimates from MCP, MDR, MPG, DMG and TPG simple linear regressions.
- Max.V = Peak wind speed (nominally 1-hr mean at 10m)
- Max.Hs = Peak measured or hindcast significant wave height
- MLR = Multiple Linear Regression fit of Hs to SCD, MCP, MDR, LOF, WOF, MPG, DMG, DMG, RFT, TPG and TPG
- LCL = 90% lower control limit of MLR coefficient
- UCL = 90% upper control limit of MLR coefficient

Table 2: Results of Simple and Multiple Linear Regression Fits of Peak Significant Wave Height to Various Storm Parameters, for Measured or Hindcast Hibernia Storms with Peak Significant Wave Heights Greater than or Equal to 8m.

Significant Storm	Date	TAR	Estimate of Peak Hs SLR	MLR	Estimated Peak Wind Speed(knt)	Hindcast Peak Wave Height(m)
3	19Dec51	3	9.6	10.9	40	
14	27Nov55	4	8.4	9.5	40	
18	08Feb59	5	12.1	10.5	50	
24	16Nov63	4	9.4	9.1	45	
25	31Dec63	4	10.6	8.9	45	
32	11Jan66	5	9.0	8.9	40	
43	04Jan72	4	7.6	9.2	45	
44	20Apr72	4	8.5	9.6	35-40	
45	15Mar73	4	6.8	8.5	35	
48	04Jan74	4	11.3	10.0	45-50	
50	29Mar74	4	8.4	9.2	50	9.6
58	07Feb77	5	9.8	9.6	55	9.9
74	10Apr82	4	7.2	8.6	45	
78	07Jan83	4	11.7	10.4	45-50	
80	17Feb83	5	15.6	12.1	60	9.0

Note:
TAR--Threshold Analysis Rating MLR--Multiple Linear Regression
SLR--Mean of Simple Linear Regressions with MCP, MPG, MDR, SIT, TPG
Peak Wind Speed approximated from partial reanalysis of archived meteorological data.

Table 3: Hibernia Storms Predicted by Simple Linear Regression or Multiple Linear Regression with Peak Significant Wave Height Greater than 8m.

Severe Storm Set	100-Year Extreme Hs, estimated using the Borgman Distribution one of the following thresholds Hs.ge.8m	Hs.ge.9m	Hs.ge.10m
1) Original Hindcast Set (see [1])	14.4(26)	14.2(20)	13.9(15)
2) Hindcast + Measured Storms	14.4(34)	14.0(24)	13.8(18)
3) Hindcast + Measured + MLR Storms	14.0(60)	13.9(42)	13.7(23)
4) Hindcast + Measured + SLR Storms	14.4(52)	14.0(34)	13.8(23)
5) Set (4) for 1951-1968	13.9(22)	13.8(15)	13.4(7)
6) Set (4) for 1969-1986	15.2(30)	14.6(19)	14.2(16)

Notes: Number of Storms used in each estimate is in parentheses.
SLR--Simple Linear Regression; MLR--Multiple Linear Regression
Set (1) is for 1951-1984, all others are 1951-1986.

Table 4: Estimates of 100-year Extreme Significant Wave Height from the Borgman Distribution, Based on Six Storm Sets and Three Thresholds for Measured and Hindcast Hibernia Storms Occurring Between 1951 and 1986.

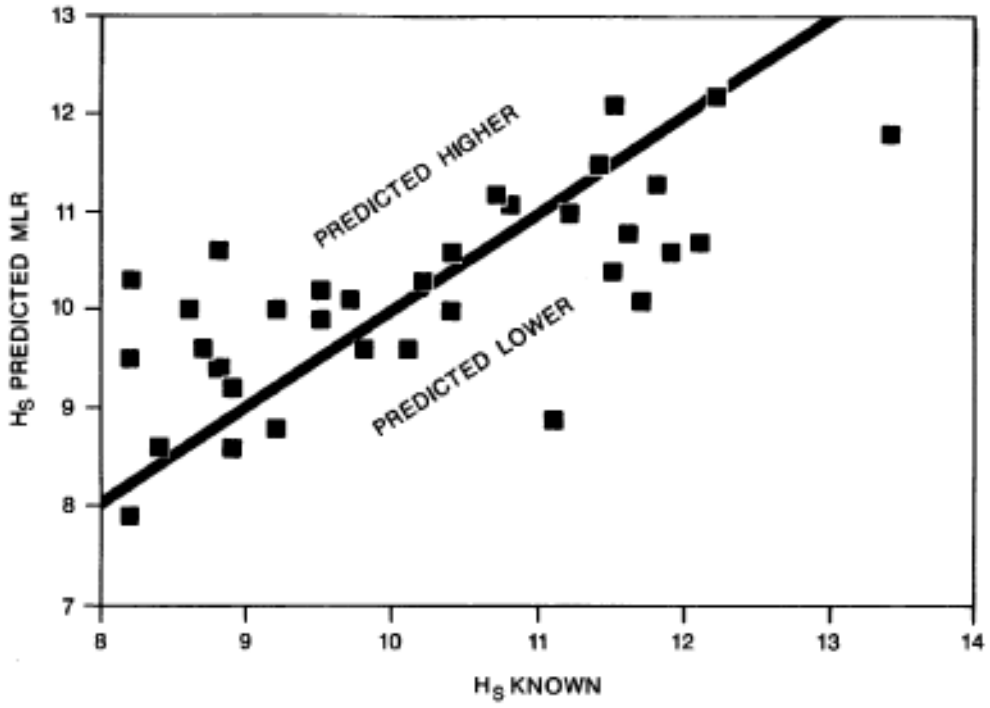

FIGURE 1. RESULT OF MULTIPLE LINEAR REGRESSION FIT OF 9 STORM PARAMETERS TO PEAK SIGNIFICANT WAVE HEIGHT FOR HINDCAST AND MEASURED HIBERNIA STORMS OCCURRING BETWEEN 1951 AND 1986.

VERIFICATION OF NUMERICAL WAVE HINDCASTS FOR SEVERE STORMS AT HIBERNIA

by D. Szabo[1], V. J. Cardone[2], B. Eid[3], and F. J. Dello Stritto[1]

[1] Mobil Research & Development Corporation, Dallas, Texas
[2] Oceanweather, Inc., Cos Cob, Connecticut
[3] MacLaren Plansearch Ltd., Halifax, Nova Scotia

ABSTRACT

Accuracy of wave hindcasts at Hibernia is verified through comparison of modeled and measured data. Assessed parameters include significant wave height and peak period, throughout storm histories and at storm peaks, and spectral shape at storm peaks. scatter indices within 20% are generally achieved throughout nine major storms occurring in 1982 and 1983. Near storm peaks, scatter indices are typically 12%. The verification considers accuracy of measured data; overall, Hibernia data are of adequate quality. Multiple wave buoys were deployed, with near-continuous recordings for most of the storms. Such continuous recordings allow estimation of an optimum record length that balances the opposing influences of stationarity and sampling variability. In severe, confused seas sources of error inherent to wave buoy data, namely instrument and transmission limitations, must be assessed. The chief instrument limitation is the inability of wave buoys to accurately capture profiles of steep short-crested waves. Large waves may block transmission signals sent from wave buoys to receiving stations. Both influences degrade data quality, but such gross seastate parameters as significant wave height are sufficiently accurate for valid comparisons.

INTRODUCTION

This is the second of five related papers [1-4] describing development of extreme wind and wave criteria for the Hibernia site on the Grand Banks. While some novel items are included, completeness rather than innovation is the theme. The set is believed to be the first which details all steps in estimating criteria necessary for offshore development. These steps range from use of numerical wave models to the empirical tools and "rules of thumb" for obtaining engineering parameters. The intent is that, by documenting the Hibernia application fully, further development may be directed to areas of greatest need.

Extreme wave criteria are essential requirements for the design of offshore structures. The most accurate practical means of calculating such values is extremal analysis of peak seastates of severe historical storms. As reliable wave measurements for these storms are largely lacking, a numerical wave hindcast model is used to estimate

directional wave spectra at each grid point throughout each storm. Due to extensive development over the past twenty years, wave models can approach the accuracy of conventional wave buoy measurements. Despite such advances wave model verification through comparisons with instrumentally measured data remains a key element in the overall criteria determination sensitivity of wave model output to a number of factors, particularly windfield specification and grid structure, require such objective checks.

As with virtually every region of offshore industry activity, extreme wave criteria for Hibernia are based on extremal analyses of hindcast estimations [1]. Twenty nine severe storms occurring between 1951 and 1984 have been hindcast by a version of the ODGP wave model. Wave data from drilling sites are available for nine of these Hibernia storms, and are used for verifying model accuracy. Significant wave height, spectral peak period and spectral shape (Hs. Tp and S(f)) are compared. Storm data are generally available simultaneously at two or three stations. During storm periods (Hs exceeding 4m) , recordings are near-continuous. Due to wellsite changes, measurement stations and grid points nearest them are not constant over the verification period. Typical recording stations and wave model grid points are shown in Figures 1A and 1B .

Discrepancies between measured and hindcast values are not necessarily indicative of the accuracy of either. All comparison parameters are estimated from the hindcast spectra and from the measured time series or the "measured" spectra calculated from them. Intrinsic properties of the two, not attributable to errors, can lead to comparison differences. Hindcast spectra nominally represent averages over time spans comparable to the model time step (1.5 to 6 hours) and include spatial averaging. Spectra based on recorded data of much shorter lengths (typically 20 minutes or less) are affected by sampling variability, conversely, record lengths comparable to the model time step may violate stationarity. Both influences can corrupt comparisons. Near-continuous, multi-station recordings typical of Hibernia wave buoy data allow determination of an optimum record length for use in model comparisons. Data from storm periods occurring in 1981 and 1982 are used to assess the record length which balances the opposing factors of sampling variability and stationarity.

As wave model accuracy nears that of measurements, the measurements themselves can no longer be accepted a priori as absolute ground truth. Estimation of measurement error is necessary to avoid tuning numerical models beyond practical limits and to assess correctly model performance. As seastates increase, instrument and transmission limitations cause potential inaccuracies. Wave buoys may not accurately capture profiles of steep short-crested waves, and large wave heights can be underestimated. Hibernia wave buoys transmit data

to the nearby drilling rigs. In severe seas, transmission can be blocked as buoys ride into troughs, and large crests block signals. Incomplete data sets result causing errors in spectral analyses. Quantitative assessment of the errors is limited by the lack of an absolute reference value.

STORM SELECTION

Nine major storms occurring between January 1982 and December 1983 are used to compare numerical wave hindcast model results with wave buoy measurements. The period is a particularly stormy one on the Grand Banks. These storms (Table 1 of Reference [1]) are ranked among the 29 most severe occurring between 1951 and 1984 [1].

Storms 26 and 27, and Storms 28 and 29 occur within days of each other. The pairs are not double peaked single storms, but separate storm systems occurring in close proximity.

As described above, a key difference between parameters derived from hindcasts and measured data is the implicit averaging time. Hindcasts represent a 3 to 6 hour time average, whereas raw measurements are in approximately 20 minutes blocks. By combining consecutive blocks, the effective averaging time of the data can be lengthened until stationarity assumptions are violated. A separate set of wave measurements from storm periods (Table 1) is used to determine an optimum time scale for parameter estimates. From available data, 24 storm periods are selected in which there are: maximum significant wave height greater than 5.0 meters; data recorded at 20 minute intervals through most of the storm; and measurements generally at more than one recording station.

STORM DATA

Wave measurements are routinely made at Canadian east coast drill sites. Details of the overall measurement program and instruments are available in [5]. Wave buoys are deployed in general proximity to the drilling rigs and transmit data to the rigs for storage. For the hindcast comparison storms, as many as three wellsites, and thus three buoys, were active simultaneously. During non-storm conditions, data were recorded for approximately 18.2 minutes every 3 hours. During storm conditions, defined as Hs exceeding 4.0 meters or wind speed exceeding 34 knots, data were recorded near-continuously (for 18.2 minutes every 20 minutes). The multi-station, near-continuous recordings permit sufficient resolution for detailed analysis of storm evolution and decay.

Spectral wave parameters including significant wave height, peak period, and spectral density values are calculated from raw data by the Canadian Marine Environmental Data Service (MEDS). Spectral

estimates are based on 18.2 minute analog recordings, sampled at a rate of 7.5 Hertz. The digitized record is divided into eight segments of 1024 points each. Spectra are calculated for each segment, and then averaged to yield a single smoothed 512-point spectrum with bandwidth of .007324 hz. Sixty two of the estimates, which span from 0.0513 to 0.4980 hz are archived (referred to below as the "smoothed spectral estimates") Very little energy is contained in frequencies outside this range. Time histories of Hs and Tp are developed from spectral estimates. Hs is approximated as four times the square root of the total variance of the spectrum (i.e., area under the spectrum).

STATIONARITY AND SAMPLING VARIABILITY

Several scales of spectral variation are apparent through typical Hibernia storms in plots of Hs versus time. The major one is on the order of days and is due to the passage of the entire storm. Variations at a scale of approximately 6 hours may be attributed to the development of a particular storm and seastate. As Figure 2 shows, a higher frequency variation of Hs is also imbedded in the sea response. Figure 2 is an expanded time trace of Hs and Tp, from consecutive 18.2 minute records, for Storm 21 (15-18 January 1982, #13 in Table 1). Fluctuations in Hs from one measurement interval to the next are on the order of 10%. Such variations are probably not due to true variations in the seastate.

Hs-variations at a 20 minute time scale cannot be predicted by deterministic wave analysis. If assumed real, the fluctuations imply a seastate much more responsive to transient windfield changes than is generally accepted. Instead, variations are assumed due to the short term sampling of a quasi-stationary Gaussian process. Accordingly, the ratio of sample spectral estimates to the true spectral estimate, multiplied by n, the number of degrees of freedom, (n=16 for MEDS data) is chi-square distributed with n degrees of freedom. To test this assumption, the true spectral estimate is approximated by averages of 2 to 12 consecutive spectral estimates (corresponding to 40 minutes to 4 hours of near-continuous recordings) during all periods when such estimates are available, for the storms listed in Table 1 . The estimate is calculated for the first 30 smoothed spectral estimates, corresponding to wave periods greater than 4 seconds, and results are combined for all frequencies and storm periods. Probability density functions are calculated and compared to the chi-square distribution for each wave buoy. Figure 3 shows the RMS difference between the sample and the chi-square distributions versus the number of estimates used in estimating the true spectrum. Error is large for averages of 2 to 5 spectra since the estimate of the true spectrum is poor due to the small number of degrees of freedom. Error is minimum at 9 to 10 spectra and increases at longer

periods (11 to 12 spectra), presumably due to non-stationarity. Based on these results, the Gaussian process is accepted, in general, as a valid assumption for storm seastates at Hibernia for time intervals up to about 3 hours. The assumption also allows an approximate separation between spectral variations due to stochastic and deterministic causes.

Best chi-squared results are obtained from averaging 9 to 10 smoothed spectra. Spectra used for model comparisons (and for fitting a parametricspectral function, see (3)) are based, however, on 7 consecutive spectra (corresponding to 2 hours and 20 minutes). In determining extreme criteria, seastates near the storm peak are the chief interest. Stationarity is likely to be less at the peak than for the overall storm period, and hence a shorter averaging interval for the spectra is used.

Variation of smoothed spectral estimates over consecutive measurement intervals is even greater than the 10% typical of Hs-estimates. The Gaussian process assumption indicates that, at the 90% confidence limit, a true spectral estimate lies within a range of .55 to 1.80 times the smoothed estimate. Averaging 7 consecutive spectra increases the number of degrees of freedom from 16 to 112 and thus increases accuracy of the estimates. Corresponding factors are 0.83 and 1.20.

In the sections below, "measured spectral" are spectra based on the averaging scheme described above, using 7 consecutive individual smoothed spectra. Likewise, "measured Hs and Tp" are derived from the measured spectra.

VERIFICATION

Time histories of hindcast and measured Hs and Tp are shown in Figures 4A and 4B for Storms 22 and 24, which are typical of the comparisons. Due to the small separations between measurement locations and fine-mesh model grid points, spatial gradients in input wind fields probably do not contribute significantly to differences seen. Also, hindcast errors in a given storm tend to be spatially correlated across the domain of measurement stations. For example, in Storm 22, the hindcast of Hs appears biased high by 1-2m at all sites, while in Storm 24, hindcast Hs series is in closer agreement with measurements. These comparisons support the contention that errors in input windfields, which tend to be strongly correlated spatially over oceans, are the dominant cause of wave hindcast errors in these series. Scatter index (i.e., rms error/mean of measurement sample) between measured and modeled Hs and Tp, throughout storm evolution, is 20% or less for all storms except Storm 25.

Figures 5A and 5B compare hindcast and measured spectra at measurement sites at the peaks of Storms 22 and 24. In Storm 22,

hindcast spectra show, in comparison to measured data, an excess of low frequency energy and a peak frequency shifted about one band to the left, Both of these differences, however, are consistent with the positive bias seen in peak Hs at all sites seen in this particular storm. The hindcast and measured peak spectra are in much better agreement in Storm 224. In this storm, the small negative bias in Hs is associated with a small deficiency of energy in the forward face of the hindcast spectrum.

Table 2 in [1] summarizes comparisons of measured and hindcast peak significant wave heights and associated spectral peak periods in 17 comparisons. Hindcast values from surrounding grid points were interpolated to the measurement sites. The mean difference in Hs is +0.26m (hindcast higher than measured), and is a result mainly of positive bias seen in Storms 21 and 22. The rms difference in Hs is 1.19m. For this severe storm sample, the scatter index is therefore 12.8%, which is close to scatter of 11.9% found in other storm hindcast comparisons using similar numerical wave models [7]. Mean and rms differences in spectral peak period of 0.60 sec and 1.17 sec are also comparable to errors associated with similar models. These comparisons indicate that accuracies comparable to the best yet achieved by such wave model applications have been approached [6].

Also, as described below, the differences in measured and hindcast values are approaching the magnitude of the likely error in the measurements. Therefore, the potential main error in hindcasts of severe seastates in historical storms at Hibernia is small enough to be ignored in assessment of the extreme wave climate.

WAVE DATA QUALITY

While measured Hs, Tp and S(f) are accepted as ground truth for model verification, they are neither "truth" nor directly measured. They include potential errors from both the raw measurements and the calculation procedure. Calculation error is reduced by averaging over record lengths compatible with seastate stationarity. Limitations in the raw data are independent sources of error. In general the MEDS wave buoy data are of good quality, but are potentially influenced by both measurement and transmission problems. Under very close scrutiny most wave data recordings reveal similar limitations. The overall fine agreement of the hindcast model and measurements warrants such scrutiny to assess true model performance and opportunities for further improvement.

Wave buoys used at Hibernia move with the sea surface and measure their accelerations, from which surface elevation records and spectra are calculated. In severe, confused seas, the ability of wave buoys to accurately capture wave profiles deteriorates, as the buoys tend to

move "around" rather than "over" wave crests, Accordingly, wave buoy data are generally not acceptable for time traces of waves. The limitation is Qualitatively shown in Table 2 which lists the 10 waves of Storm 28 with heights exceeding 20m. Such high waves tend to be rather crested, with crest-to-wave height (C/H) values often greater than 0.60. As Table 2 shows, 4 of the 10 profiles have C/H less than 0.50 (i.e, more trough than crest), and the highest C/H is 0.58. Evidence in Table 2 is purely suggestive, since the true heights and crests of these waves is unknown, and the measured values are quite possible physically, Also, for the severe storm in which the 10 waves occurred, further errors may be introduced through data transmission.

Errors arise from buoy-to-rig data transmission due to physical blockage from passing vessels or large waves, and radio interference. In severe seas, the dominant blockage is due to high wave crests, especially as the buoy moves into troughs. The rig-based receiver flags weak signals, which are not used by MEDS in calculating smoothed spectra. All recorded data, however, are included in MEDS' digitized surface elevation records. Comparisons of Hs calculated from the spectra variances (Hs_{Sp}) and the surface elevation records (Hs_{SER}) again provide qualitative evidence of possible errors. Figure 6 shows two curves--the theoretical distribution of [HSSER/HsSp] due to differences in the record lengths used by MEDS in each calculation; and the actual distribution based on 3000 Hibernia wave measurements from storm periods listed in Table 1 . Deviations between the two curves are presumed to result mainly from shortened records used in the spectral calculation due to transmission errors. The means of the theoretical and actual distributions are 1.00 and 1.02. Since the full accuracy of neither Hs estimate is known, an absolute measure of transmission error cannot be obtained.

CONCLUSION

Accuracy of numerical wave hindcasts of Hibernia storms is demonstrated through comparisons with measured data from nine severe storms. Accuracy is comparable to that achieved in hindcasts of other geographical regions. Mean differences between measured and hindcast significant wave height (positive hindcast bias of 0.26m, rms of 1.19m) mainly result from positive biases in storms 21 and 23. Such differences are not major sources of error in the subsequent use of the hindcasts in extremal analysis.

Measured data are the only objective means of quantifying hindcast performance. Assessment of data quality is required, however, to determine the value of the comparisons. Hibernia wave buoy data are generally of good quality, though limitations arise from finite record

lengths, measurement errors and transmission errors. Potential errors due to record lengths are minimized by averaging consecutive records. An optimum length is achieved which balances sampling variability and stationarity considerations. Measurement and transmission errors can be only qualitatively assessed. Wave buoys do not capture accurately profiles of steep short-crested waves. Transmission errors arise since Hibernia wave buoys are not internally recording, but rather radio data to rig-based receivers, Transmission blockage can occur in high seas, The result of these errors is a possible underestimation of severe seas, which supports the positive bias of the hindcasts. Due to these potential errors, further tuning of the hindcast model to improve agreement with data is not warranted.

ACKNOWLEDGEMENTS

Gratitude is expressed to the organizations which funded much of this work: the four members of the Hibernia Partnership--Mobil Oil Canada Properties, Chevron Canada Resources Ltd., Gulf Canada Corporation and Petro-Canada Resources; and Mobil Research & Development Corporation. Likewise, thanks are extended to the Canadian Marine Environmental Data Service of Ottawa for their cooperation and far-sighted data collection program, and to H. V. Leder of Texas A&M University for his assistance in preparing the text.

REFERENCES

1. Cardone V.J., Szabo D. & Dello Stritto F.J., 1989, "Development of Extreme Wind and Wave criteria for Hibernia", 2nd International Workshop on Wave Hindcasting and Forecasting (SIWWHF), 25-28 April 1989, Vancouver, British Columbia.

2. Szabo D., Cardone, V.J. & Callahan B.T., 1989, "Severe Storm Identification for Extreme Criteria Determination by Hindcasting", SIWWHF.

3. Cardone V.J., Greenwood J.A., Szabo, D. & Dello Stritto F.J., 1989, "Engineering Parameters from Hindcast Results", SIWWHF.

4. Bolen Z.K. & Dello Stritto F.J., 1989, "Estimation of Extreme Wave Heights through Weibull Distributions", SIWWHF.

5 Canadian Marine Environmental Data Services, 1989, Historical Wave Measuring Stations, 26 January 1989, Ottawa, Canada.

6. Ewing, J.A., 1971, "A Numerical Wave Prediction Method for the North Atlantic Ocean", Deutsche Hydrographische Zeitschrift, 24F pp. 241-261.

7. Reece, A. & Cardone, V.J., 1982. "Test of Wave Hindcast Model Results Against Measurements During Four Different Meteorological

Systems". Proceedings of the 14th offshore Technology Conference, 3-6 May 1982.

Storm Period	Date	MEDS Site 134 Max Hs	Tp	MEDS Site 140 Max Hs	Tp	MEDS Site 156 Max Hs	Tp
1	01-03Apr81	6.9	11.4	7.7	12.4	7.3	11.4
2	13-15Apr81	4.8	12.2			6.1	14.0
3	19-22Sep81			4.4	9.6	5.5	10.4
4	26-30Sep81*			7.2	11.9	7.8	13.0
				7.2	12.4	7.7	12.4
5	17-21Oct81			5.3	10.5	5.7	12.0
6	28Oct-04Nov81	7.6	13.0	7.7	13.0		
7	18-22Nov81	5.6	12.5	5.1	12.4		
8	26-30Nov81	5.3	13.0	5.9	13.0		
9	16-20Dec81	6.8	12.4	6.9	12.1	7.0	11.9
10	24-29Dec81			7.0	11.6	7.2	10.9
11	30Dec81-03Jan82*	7.1	9.5	8.2	13.2		
		7.3	16.0	8.4	13.2	8.0	17.2
12	08-12Jan82	6.7	12.5	7.3	13.0	7.2	12.4
13**	15-18Jan82*			10.0	13.2	9.7	13.7
		9.5	14.4	10.3	15.4	10.0	14.4
14	18-21Jan82	8.2	13.0	9.0	13.8	8.7	13.0
15	21-25Jan82	6.6	13.0	7.1	13.0	7.0	13.7
16	25-27Jan82	6.0	10.1	6.3	10.9	6.3	10.9
17	27-30Jan82	6.5	11.7	6.6	11.9	6.9	11.9
18	30-31Jan82	6.0	10.8	5.9	10.4	6.1	10.5
19	31Jan-02Feb82	6.7	10.5	6.7	10.9	6.9	10.9
20**	02-05Feb82	8.0	11.4	7.5	11.4	7.6	11.9
21	07-09Feb82	6.7	10.9	6.5	11.6	6.8	10.5
22	09-11Feb82	6.6	9.9	6.0	10.9	5.7	10.5
23	11-13Feb82	5.9	9.9	6.0	10.8		
24**	13-18Feb82			11.5	15.2		
25	20-24Feb82			5.7	10.3		

Notes:

* Storm period is double peaked, both Hs maxima are shown.
Peaks in some records are not well defined; values listed above may vary depending on calculation method.

** Storm period selected for hindcasting in Hibernia extreme criteria determination [1]. Storm periods 13, 20 and 24 correspond to hindcast Storms 21, 22, and 23.

-- Tp is the spectral peak period occurring simultaneously with the maximum significant wave height, Hs.

__ MEDS measurement sites correspond to particular drilling rigs, which periodically change location. All are on the Grand Banks near Hibernia. For precise locations see [5].

Table 1: Periods of Measured Storm Seastates Used for Determining Optimum Wave Data Record Length for Verifying Hindcasts

Wave Height (m)	Wave Period (sec)	Crest Height (m)	Crest/Wave Height	Steepness Parameter (m/s**2)	Seastate Parameters Hs (m)	H1/3 (m)	Tp (sec)
24.8	15.6	12.9	0.52	0.10	11.7	13.5	19.5
21.8	13.7	11.6	0.53	0.12	11.8	12.2	19.5
20.8	15.7	12.1	0.58	0.11	11.4	12.2	17.1
20.6	14.6	10.5	0.51	0.10	12.6	13.1	15.2
20.5	12.2	10.3	0.50	0.14	12.1	12.6	17.1
20.3	12.9	9.5	0.47	0.12	10.9	11.3	15.2
20.2	13.4	9.7	0.48	0.11	11.7	11.9	15.2
20.2	15.1	9.7	0.48	0.09	11.5	11.6	17.1
20.0	12.5	9.6	0.48	0.13	11.7	11.9	17.1
20.0	12.0	10.0	0.50	0.14	11.7	10.7	17.1
100-Year Extreme for Hibernia [1]							
29.3	15.0-18.0	17.9-18.1	0.61-0.62	0.13-0.09	15.9	15.9	16.0-20.0

Notes:
1) C/H - (Crest Height/Wave Height)
2) Steepness Parameter = (Wave Height/Period^2)
3) Hs is calculated as four times the variance of the surface wave spectrum.
4) H1/3 is the characteristic wave height, defined as the mean of the one-third highest waves.
5) Parameters for 100-Year Extreme for Hibernia are based on hindcasts/extremal analysis summarized in [1], a 10th order stream function wave theory (regular, 2-D wave profile), using an approximated water depth of 80m.
6) In principle, Hs and H1/3 should be approximately equal. Differences between them are indicative of measurement and data transmission limitations.
7) 100-year extreme wave parameters are provided for comparison only. Steepness ranges of the extreme bracket the measured values, but measured C/H are consistently lower than that of the 2-dimensional, symmetrical profile of the 100-year extreme.

Table 2: Parameters of 10 Highest Wave Profiles Recorded During 22-23 December 1983 (Storm 28) at Hibernia

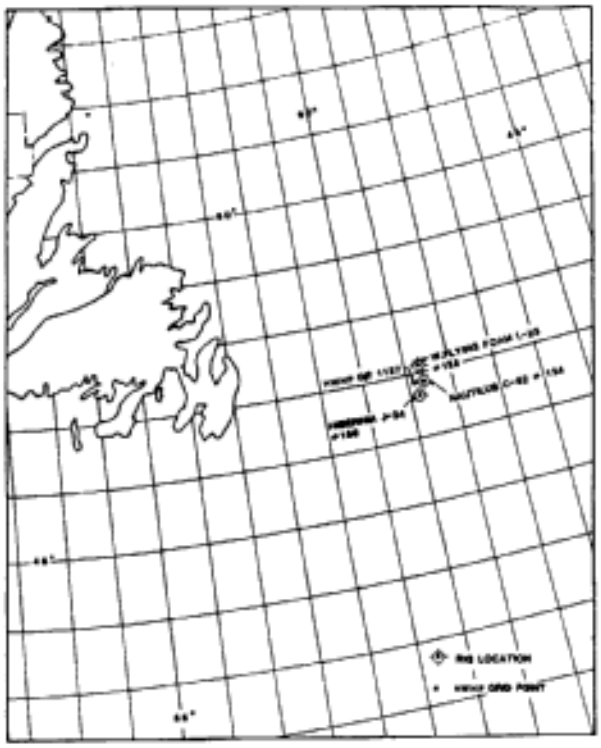

FIGURE 1A. DRILLING RIG LOCATIONS AND HINDCAST MODEL GRID POINTS FOR STORM 22, FEBRUARY 1982.

FIGURE 1B. DRILLING RIG LOCATIONS AND HINDCAST MODEL GRID POINTS FOR STORM 24, DECEMBER 1982.

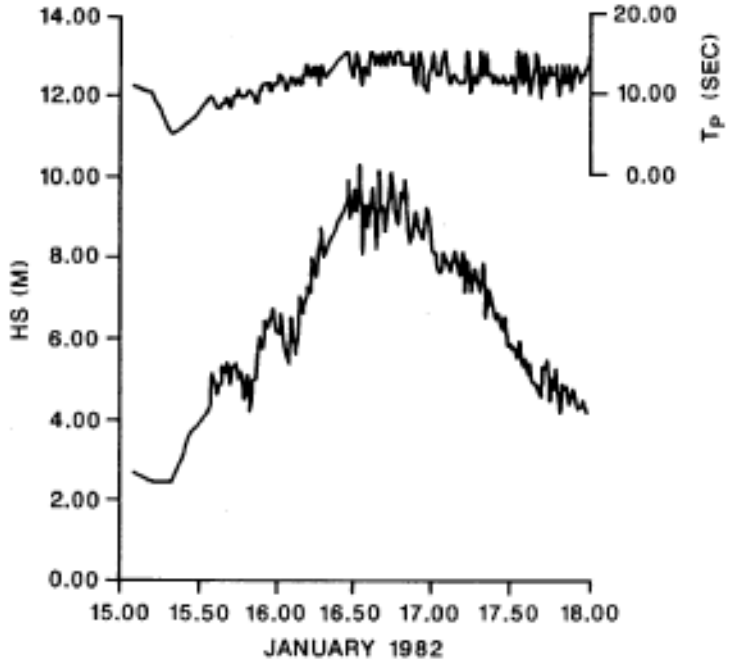

FIGURE 2. EXPANDED TIME TRACE OF SIGNIFICANT WAVE HEIGHT, H_S, AND SPECTRAL PEAK PERIOD, T_p, FOR STORM 21.

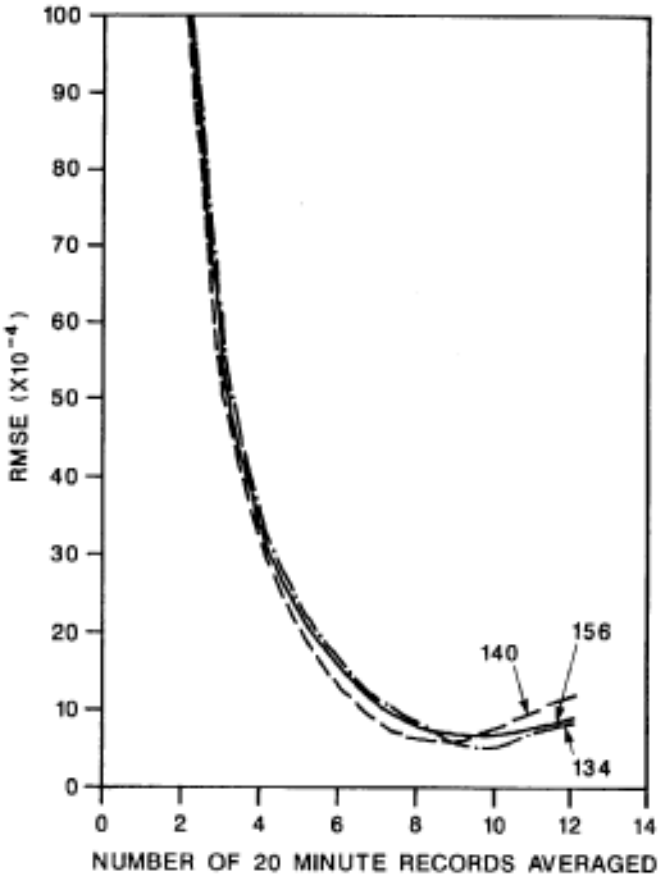

FIGURE 3. RMS DIFFERENCE OF CHI-SQUARE ESTIMATE AND ESTIMATE BASED ON AVERAGE 18.2 MINUTE RECORDS, AS FUNCTION OF NUMBER OF RECORDS AT 3 HIBERNIA WAVE BUOYS.

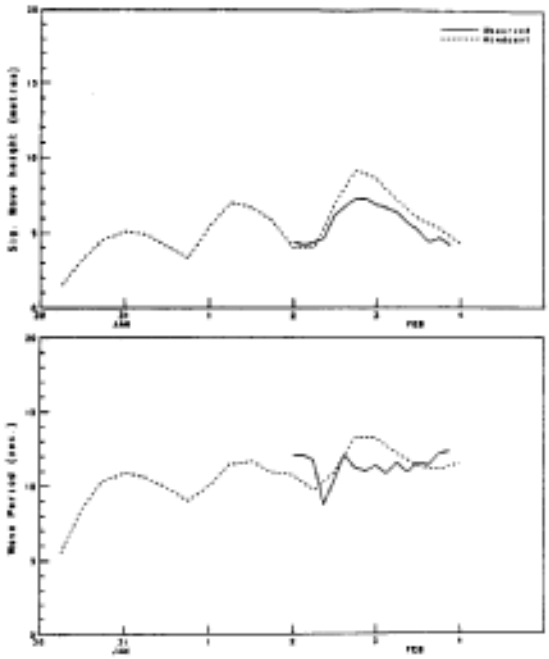

FIGURE 4A. COMPARISON OF MEASURED AND HINDCAST SIGNIFICANT WAVE HEIGHT AND SPECTRAL PEAK PERIOD FOR STORM 22.

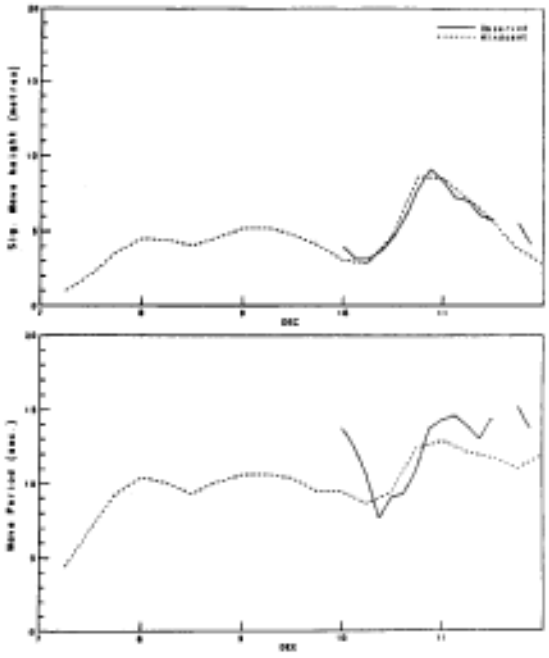

FIGURE 4B. COMPARISON OF MEASURED AND HINDCAST SIGNIFICANT WAVE HEIGHT AND SPECTRAL PEAK PERIOD FOR STORM 24.

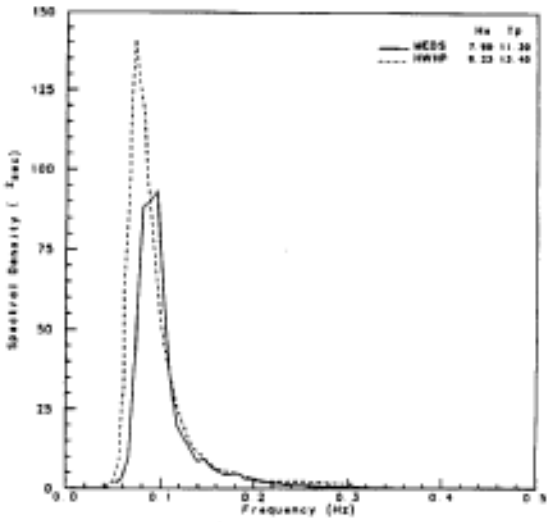

FIGURE 5A. COMPARISON OF MEASURED AND HINDCAST SEA SURFACE SPECTRA AT PEAK OF STORM 22.

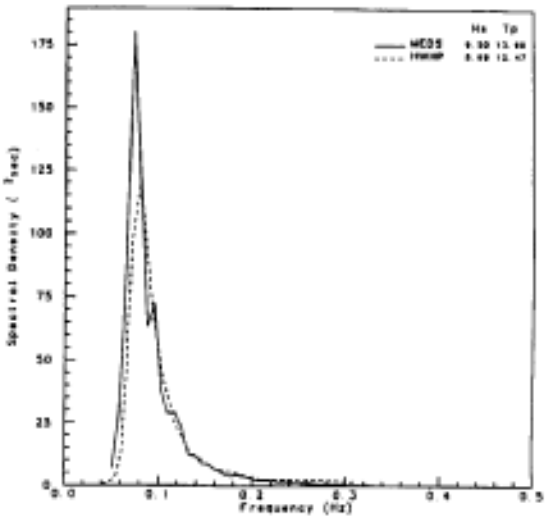

FIGURE 5B. COMPARISON OF MEASURED AND HINDCAST SEA SURFACE SPECTRA AT PEAK OF STORM 24.

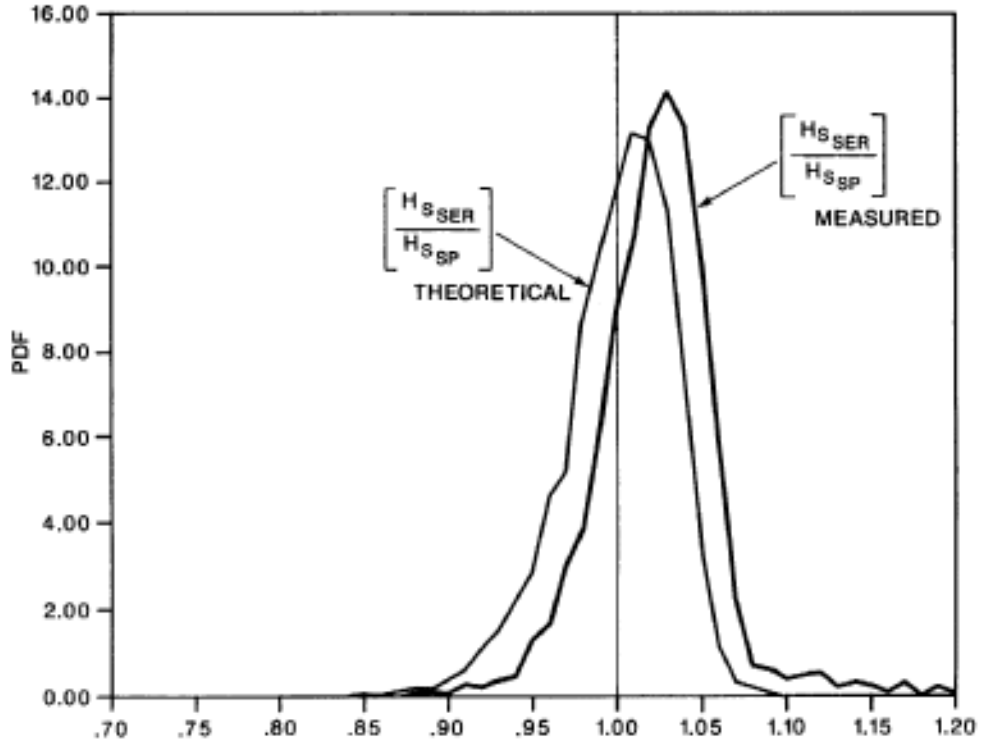

FIGURE 6. COMPARISON OF THEORETICAL AND MEASURED DISTRIBUTIONS OF $H_{S_{SER}}$ (SIGNIFICANT WAVE HEIGHT CALCULATED FROM MEDS SURFACE ELEVATION RECORDS)/$H_{S_{SP}}$ (SIGNIFICANT WAVE HEIGHT CALCULATED FROM MEDS SPECTRA).

ENGINEERING PARAMETERS FROM HINDCAST RESULTS

by V. J. Cardone[1], J. A. Greenwood[1]
D.Szabo[2], and F. J. Dello Stritto[2]

[1] Oceanweather, Inc.
[2] Mobil Research and Development Corporation, Dallas, Texas

ABSTRACT

Measured data and hindcasts of severe storms provide basic input to statistical analyses from which environmental criteria and engineering parameters are derived. These include extreme wind speed, and significant and maximum wave heights as functions of return period; wave periods associated with the extreme waves; and wave spectral and directional information. Data and hindcasts from Hibernia are used to estimate such parameters through a variety of analytical and empirical methods. Extremal analyses produce return period values. Correlation relationships of hindcast significant wave height and spectral peak period are used to derive wave periods associated with extreme waves. Empirically modified Rayleigh distributions estimate maximum wave heights, and wave buoy data are used to define the range of likely periods of maximum waves. Parametric spectral shapes are fit to measured data, and directional characteristics of severe seastates are estimated from hindcast spectra. A plausible 100 year directional spectrum is obtained by hindcasting a synthetically enhanced windfield, which produces the 100 year significant wave height.

INTRODUCTION

This is the fourth of five related papers [1-4) describing development of extreme wind and wave criteria for the Hibernia site on the Grand Banks. While some novel items are included, completeness rather than innovation is the theme. The set is believed to be the first which details all steps in estimating criteria necessary for offshore development. These steps range from use of numerical wave models to the empirical tools and "rules of thumb" for obtaining engineering parameters. The intent is that, by documenting the Hibernia application fully, further development may be directed to areas of greatest need.

Estimating extreme wind and seastate conditions through hindcast modeling and extremal analyses is a common procedure in offshore industry. Steps in the procedure are (1) identification of severe historical storms for hindcasting, (2) hindcast modeling of selected storms to estimate windfields and seastates, (3) verification of the hindcasts with measured data, (4) extremal analysis of the peak storm conditions to obtain extremes as functions of return period, and (5) statistical and empirical analyses to obtain engineering parameters. Application of the procedure to Hibernia is summarized in (1). Steps 4

and 5 of the Hibernia application is described in detail in the following sections.

Early development of the procedure focussed primarily on steps 2 and 3, since reconstructing wind and wave conditions from archived data was initially an obvious weakness. Model development has been quite successful [2], and accuracies of well tuned and tested models are approaching those of conventional measurements. Severe storm identification remains a somewhat subjective effort whose accuracy is dependent on the quality of archived data. Reference (3] proposes an objective method to assist in storm selection. It also concludes that, provided the few most severe storms, which are relatively easy to identify, are included, extreme estimates are not highly sensitive to the storm selection. Step 4 is basically fitting hindcast data to well established distributions, and goodness-of-fit measures indicate the distribution best representing the data,

Step 5, calculation of engineering parameters, is by far the least precisely defined step of the procedure, and industry practice is not uniform. The parameters may vary according to application, but usually include spectral shape (S(f)) and peak period (Tp) during maximum seastate, and maximum individual wave height (Hmax), associated period (Thmax) and crest height. A number of methods exist for estimating these. For example, crest height calculations usually require a wave kinematics theory [14], of which many are available. Also, the crest height definition varies throughout industry--crest of the maximum wave in seastate, or maximum crest height in a seastate. The approaches described below are, with one exception, roughly typical of any in use. Most aim toward "reasonably conservative" values--i.e., more conservative than statistical best estimates, but not punitive to the application.

The exception noted above is the modeling of a synthetic 100-year storm. Based on historical Hibernia storms, a storm system is constructed whose peak seastate equals the 100-year extreme. "Hindcasts" of this storm provide directional spectra throughout its buildup and decay. The synthetic storm is not unique, in that many such systems could be postulated which would generate comparable seastates,

Lack of uniformity in industry practice for calculating engineering parameters arises from several sources. Steps 1-4 in criteria determination have been approached as elements of environmental specification, subject to varying degrees of joint industry/academia/ government development. Step 5 has been treated more as a design and engineering concern. Consequently, the latitude and diversity, as well as a somewhat empirical approach, typical of design practice are reflected in Step 5. Another factor is an implicit difference in the

target accuracies, from scientific quality for Steps 1-4 to engineering quality for Step 5. For example, differences in severe storm selection described in [3] imply the need for further development of the technique. Such differences, at least for the Hibernia application, have virtually no impact on the design of most offshore structures. Lastly, any movement towards a more uniform approach has probably been slowed by the recent surge of innovative designs for deepwater and hostile environments. Most of these unique designs require unique types of criteria--many involving joint distributions of parameters, and separate paths of development are thus followed.

Development efforts on all steps of the criteria determination procedure continue. The greatest practical influence on criteria determination will probably be in translating hindcast results to engineering parameters, particularly for distributions of wave heights and periods in a seastate. Meaningful advances in specifying these require a large body of high-quality time trace measurements (wave buoy data are not adequate) in severe seastates.

The following sections, except where noted, do not consider possible inaccuracies in the basic data. Such potential errors are summarized in [1], and described in some detail in [2] and [3], These data are hindcast peak wind and seastate conditions of 26 severe Hibernia storms occurring between 1951 and 1984, and wave buoy measurements made near Hibernia drill sites, particularly for 1981-1983.

WIND SPEED AND SIGNIFICANT WAVE HEIGHT AS FUNCTIONS OF RETURN PERIOD

Table 1 lists extreme significant wave height, Hs (nominally for a 3-hr stationary seastate), and sustained wind speed, V (nominally the 1-hr mean speed at 20m elevation) as functions of return period. Values are based on the 26 most severe peak seastates occurring between 1951 and 1984, fit to two extremal distributions:

Gumbel: $Pr[x.le.X] = \exp(-\exp[-(X-a)/b])$;

Borgman: $Pr[x.le.X) = \exp(-\exp(-(X^2-c)/d])$;

where X is Hs or V, and a, b, c and d are constants determined from the fit of hindcast data. The cumulative distribution function P_{Tr}, corresponding to return period, Tr, is:

$\overline{P_{Tr}} = 1 - Y/nTr$;

where n is the number of storms in the extremal population (26), and Y time span of the extremal population (34 years). Correlating the candidate distributions, Pr[x.le.X], to the distribution, P_{Tr}, of return period Tr yields:

$X_{Tr} = [a - b\ 1n(-ln\ (P))]C.$

where c = 1 for the Gumbel distribution, and 0.5 for the Borgman.

The Borgman distribution, which is the Gumbel distribution in X^2, has several attractive features for extreme seastate estimation. Since HS^2 is proportional to the seastate variance (zeroth moment of the seastate spectrum), it is arguably a more fundamental physical parameter than Hs. Also, the distribution gives more weight to the higher Hs values. Lastly, distributions in X^2 capture a property often seen in environmental data in general and seastate in particular. Their extreme distributions tend to "flatten" in high values--i.e., the slope of X vs Pr(x.le.X) decreases with increasing X. Asymptotically, the Borgman and Gumbel distributions are equivalent. With the sample sizes encountered in extreme wave studies, the Borgman distribution often achieves improvement in the extrapolated Hs.

Table 1 includes the best fit and the 90% upper and lower control limit Hs and V values at key return periods. The 34-year return period values are included for comparison with the highest value hindcast for the 34-year period (1951-1984). The span of upper to lower 90% control limit values, normalized by the best fit value ([UCL-LCL]/Mean), is a relative measure of the goodness-of-fit. Both significant wave height and wind speed fit the Borgman distribution somewhat better than the Gumbel. Control limits are computed by the method described in [9].

Upper and lower control limits are influenced only by statistical traits of the input data set, and do not consider possible errors in storm selection [2] and hindcast accuracy [3]. These primarily affect Hs estimates. To ensure reasonably conservative criteria, the 90% upper control limit Hs values from the Borgman distribution are used. Extreme winds are selected from the Gumbel fit, even though the Borgman distribution apparently fits the data better. Use of the Gumbel is more consistent with past practice and again ensures some conservatism. Another source of conservatism in the wind criteria is that time lags between peak seastates and peak winds are ignored. Table 2 of [1] lists two sets of extreme winds--simultaneous with, and irrespective of, peak Hs. The second set, which is necessarily the more severe, is used in all applications, Gust speeds associated with the extreme sustained wind speed may be estimated from a variety of sets of conversion factors [7]. While these formulations and development of these sets are often quite diverse, the results agree quite well for engineering applications.

Most other criteria are indexed to or derived from the maximum Hs and V. With conscious and intentional conservatism in these parameters, the remaining criteria are based on mean or best-fit results from the methods employed. Degrees of conservatism in all criteria are, therefore, more easily identified since they derive from a single common source.

MAXIMUM WAVE HEIGHT IN A STORM

Significant wave height, Hs, is the basic parameter to which most other seastate parameters are related. For many offshore applications the most prominent is Hmax, the maximum individual wave height. Hmax, termed the n-year wave (e.g., the 100-year wave), is more precisely defined as the maximum expected wave height in a seastate whose peak Hs has a return period of n years. Hmax need not occur simultaneously with the peak Hs, and, for typical Hibernia storms, is not likely to. The procedure for estimating Hmax is

1) A conditional distribution, Pr[h.le.H|Hs], of wave heights within a stationary seastate of significant wave height Hs is adopted.
2) Hibernia storms records, each with a unique buildup and decay about its peak, are divided into a series of 3-hour stationary seas,
3) The statistical distribution for each segment can be calculated and these can be combined to obtain an overall distribution for each storm. The mean of Hmax/Hs for all the storms is then obtained.

Wave heights within a seastate are often assumed Rayleigh distributed. Available wave data and analytical development show it to overestimate Hmax [15]. Limitations in the data base preclude specifying a definitive Pr[h.le.H|Hs]. A number of alternatives have been proposed, some of which are empirical modifications of the Rayleigh form:

$$P[h.le.H] = 1-\exp\{-B\},$$

where $B = (h^2/8m_o)$ for the Rayleigh distribution;
$= (h^2/8m_o)^{1.08}/8.42$ for the Ward distribution [16];
$= (h^2/8m_o)^{1.063}/8.42$ for the Forristall distribution [10];
and
m_o = the zeroth moment of the seastate spectrum, which can be approximated as $(4Hs)^2$.

The Ward distribution is based in part on hindcast Hs data, whereas the Forristall is based entirely on measurements. For both, the data are from tropical storms, not extratropical storms typical of Hibernia.

Steps 2 and 3 above are most efficiently handled through Borgman's integral [6]:

$$P[h.le.Hmax] = \exp \int_{t_a}^{t_b} [\ln (1 - e^{B(t)}) / T(t)]dt$$

where t_a and t_b are the beginning and end of each storm, and T(t) is the significant wave period.

B(t) is defined above, and is expressed as a function of time as $m_o(t)$ varies throughout the storm. The integration limits are chosen such that $HS^2(t_a)$ and $HS^2(t_b)$ are less than half the maximum value of Hs^2.

The integral is applied throughout the first 20 hindcast storms to obtain the expected Hmax of each storm for the three wave height distributions. Table 2 shows calculated maximum wave heights at the Hibernia grid point. The Forristall distribution result (Hmax/Hs = 1.84) is chosen as it is based on measured data.

PEAK SPECTRAL PERIOD AND PERIOD OF MAXIMUM WAVE HEIGHT

Peak spectral periods associated with the peak Hs of the 26 hindcast storms are used to relate Tp to Hs. A least squares fit to:

$$Tp = A\ (Hs)^B.$$

yields coefficients of A = 5.1686 and B = 0.4490. As a span of plausible periods may be associated with a particular wave height, estimates of Tp as a function of return period are expressed as a range--generally two seconds about the mean period.

To associate a period with Hmax, (Thmax/Tp) is determined from Hibernia wave buoy data, where Thmax is the period of the highest wave in each 18.2 minute segment. The implicit assumption is that, while wave buoys may not accurately capture the profiles of very high waves (2]. the data do adequately record wave period. Because Tp results from spectral analysis of digitized time series, it can only assume one of a set of discrete values. Due to discretization, uncertainty in Tp's correct or true value is approximately 1.5s in the period range of interest. Since Thmax is continuous, the distribution of Thmax/Tp averages the Tp-error if the sample size is large enough. Figure 1 shows distributions of Thmax/Tp and Thmax2/Tp (where Thmax2 is the period of the second highest wave in the record) for seastates of Hs greater than 9.0m. Virtually no difference exists in the two distributions. The mean value of Thmax/Tp is approximately 0.85-0.90, which is approximately equal to the significant wave period ([14), i.e., the mean period of the one-third highest waves), and agrees with other analyses of wave period distributions [9, 11]. As with the final Tp specification, a range is associated with Thmax.

CREST HEIGHT OF THE MAXIMUM WAVE

With Hmax, the range of Thmax and the water depth (nominally 80m at Hibernia) specified, a first approximation of the crest of the maximum wave may be obtained from an appropriate wave kinematics theory. Use of a 10th Order Stream Function Theory (14] yields crests of a 29.3m wave of approximately 18m. Since the theory assumes regular symmetric waves, real wave crests can easily be greater, and the crest of the regular wave estimate is usually empirically increased by 10%. Model tests (13) of a family of 100-year Hibernia waves (i.e., waves of height Hmax, with varying periods and profiles) produced crests ranging from approximately 15 to 20m. The crest height of the maximum

wave in a seastate, like the maximum crest in a seastate (not necessarily associated with the maximum wave), is a random variable. An empirical distribution of the maximum crest height has been developed [12]. which like the Forristall distribution for wave heights, is a modified Rayleigh distribution fit to Gulf of Mexico wave data.

PARAMETRIC SPECTRAL SHAPE

Directional digitized seastate spectra are produced from the hindcasts. These may be empirically magnified to produce a family of spectra with the 100-year Hs. For many practical applications, a simple unidirectional form is needed. Spectra estimated from Hibernia wave buoy data are fit to a variation of the Jonswap [14] form:

$$S(f) = C[0.3125Hs^2Tp^{-4}]f^{-4}(\exp\{-1.25Tp^{-4}f^{-4}\}]G^b$$

where S(f) is the spectrum and f is the circular frequency;
G is the peak enhancement factor;
$b = \exp[-(f-1/Tp)^2Tp^2/2s^2]$;
$s = 0.07$ for f.le.1/Tp and 0.09 for f.gt.1/Tp; and
C is a factor which ensures that m_o is approximately $(4Hs)^2$ and is approximated by $\{1 - 0.2907\ln G\}$.

The value of the peak enhancement factor, G, determined from least-squares fits to spectra estimated from 25 storm periods summarized in Table 3 . Reference [2] details determination of data record lengths to balance the opposing influences of stationarity and sampling variability. Considerable variation in shape and G-fit occur both throughout any single storm, and from storm to storm. At storm peak, however, G is rather consistently approximated by 20/(TpC).

The parametric form can be given symmetric directionality through a spreading function: $S(f,\phi) = S(f)D(\phi)$. Directional characteristics of Hibernia storms vary greatly. Table 4 of [1] summarizes the directional properties during the peaks of three top-ranked hindcast, southwest storms. The dominant direction, direction of maximum energy and ratio of inline to total energy match closely in Storms 18 and 23 in the Table. The inline/total energy ratio of about 0.75 for these storms corresponds to a cosine-squared energy spreading function:

$$D(\phi) = (2/\Uparrow)\cos2(\phi - \phi o), \text{ for } \phi \text{ .le. } (\Uparrow/2)$$
$$= 0 \qquad \text{otherwise}$$

As Storm 13 of Table 4 of [1] attests, simple parametric models may represent a wide range of possible storms, but by no means all. At Storm 13's peak, the spectrum contains two directional maxima, and inline/total energy is 0.60. Many engineering applications are not highly sensitive to spectral shape; and for most applications

unidirectionality is the most conservative assumption. Due to the diversity of possible shapes and to the recent proliferation of innovative offshore designs, potential sensitivity in a variety of shapes must be considered.

For many recent applications, especially in deepwater (nominally, greater than 350m), wind spectra are required to assess the dynamic response of compliant structures to wind [8]. For the relatively shallow Hibernia site, no practical need exists for wind spectra, and none has been specified.

HINDCAST OF SYNTHETIC 100-YEAR STORM

Maximum seastates of a number of the hindcast storms are within a few meters of the 100-year Hs. Therefore, modest intensification of the modeled windfields could produce a synthetic 100-year storm (i.e., a storm generating a peak seastate with the 100-year Hs) . While no imminent application exists for such a construct, it offers a potentially very useful tool--directional spectra at each grid point throughout buildup and passage of a 100 year storm.

The maximum hindcast Hs of 13.4m in the hindcast study (Storm 23 in [1]) is approximately 1.0m lower than the expected 100 year return period Hs for Hibernia. Three separate hindcasts are performed with a slightly different version of the original hindcast model (similar to that used for Storms 22 and 24-29, [1]). For the first run, the original hand-drawn kinematic analyses wind fields produced for the storm are regridded at 6-hourly intervals. A 1° latitude/longitude grid is used in the validation model interpolated to the hindcast model grid. The maximum Hs in the rehindcasting of the storm is 11.9m at Hibernia, which is very close to the value of 11.5m estimated from measurements.

For the second run the wind speeds are inflated at all grid points and all time steps. The increase is such that the uninflated maximum speed of 33.5m/s (at anemometer height, 19.5m) is increased to 37.3m/s, which is the Hibernia 100-year wind speed (note: for Storm 23, this maximum does not occur at the Hibernia grid point). The increase is imposed with a linear ramp function, which leaves all wind speeds less than 18m/s unchanged. The intensification is equivalent to about a 10% increase in the strength of the pressure gradient in the cyclone flow about the center of the storm. The inflated wind field provided a maximum wind of 33.8m/s at the Hibernia grid point.

For the third run wind speeds are again inflated at all grid points and time steps, such that the maximum wind speed at the Hibernia grid point on the wave model grid is 37.3m/s. The same linear ramp function. This third wind field implies about a 20% increase in the strength of the pressure gradient about the center over the nominal pressure field.

Table 4 compares the peak hindcast sea state at Hibernia produced by these three sensitivity runs. The two inflated wind fields provide hindcasts of Hs at Hibernia which bracket the 100-year return period extreme based on Borgman distribution. The intense wind fields produced by the inflation procedures are entirely plausible. No doubt, modification of other features of the windfield could produce similar increased seastates.

CONCLUSION

Final steps in developing wind and wave criteria for offshore applications involve (1) expressing extreme peak significant wave height and sustained wind speeds as functions of return periods, and (2) estimating a variety of parameters which are indexed to or derived from these two key parameters. Calculating return period values is basically curve-fitting from a number of established extremal distributions; and goodness-of-fit measures identify the curve most appropriate for the data set. To account for uncertainty in deriving other parameters, a degree of intentional conservatism is included in the final specified values. Procedures for calculating other parameters (gust speeds, peak spectral period, maximum wave height with associated period and crest, wave and wind spectra) are quite diverse, and not uniformly applied in practice. Also, they rely in varying degrees on precedent and limited data bases. Those described here are typical of the range of methods in common practice.

ACKNOWLEDGEMENTS

Gratitude is expressed to the organizations which funded much of this work: the four members of the Hibernia Partnership--Mobil Oil Canada Properties, Chevron Canada Resources Ltd., Gulf Canada Corporation and Petro-Canada Resources; and Mobil Research & Development Corporation. Likewise, thanks are extended to the Canadian Marine Environmental Data Service of Ottawa for their cooperation and far-sighted data collection program, and to H. V. Leder of Texas A&M University for his assistance in preparing the text.

REFERENCES

1. Cardone V.J., Szabo D. & Dello Stritto F.J., 1989, "Development of Extreme Wind and Wave Criteria for Hibernia", 2nd International Workshop on Wave Hindcasting and Forecasting (SIWWHF), 25-28 April 1989, Vancouver, British Columbia.

2. Szabo D., Cardone V.J., Eid B. & Dello Stritto F.J., 1989, "Verification of Numerical Wave Hindcasts for Severe Storms at Hibernia", SIWWHF.

3. Szabo D., Cardone, V.J. & Callahan B.T.,1989, "Severe Storm Identification for Extreme Criteria Determination by Hindcasting", SIWWHF.

4. Bolen Z.K. & Dello Stritto F.J., 1989, "Estimation of Extreme Wave Heights through Weibull Distributions", SIWWHF.

5. Arhan, M.F., Cavanie, A.G. & Ezraty, R.S., 1979, "Determination of the Period Range Associated to the Design Wave", Proceedings of the 11th offshore Technology Conference, 8-11 May 1979, Houston, Texas.

6. Borgman, L.E., 1973, "Probabilities for the Highest Wave in a Hurricane", J of Waterways, Harbors and Coastal Engineering Div., ASCE, pp. 185-207.

7. Canadian Marine Environmental Data Services, 1989, Historical Wave Measuring Stations, 26 January 1989, Ottawa.

8. Dello Stritto, F.J., Benoit, J.R. & Ransom, J.A.N., 1985, "Wind-Related Needs of Offshore Industry: A Select Review", Proceedings of the International Workshop on Offshore Winds and Icing, Halifax, Nova Scotia, 7-11 October 1985.

9. Dick, I.D. & Darwin, J.H. 1954. "The Prediction of Floods", New Zealand Engineer, 8:99.

10. Forristall, G.Z., 1978, "On the Statistical Distribution of Wave Heights in a Storm", J. of Geophys. Res., 83, pp. 2353-2358.

11. Goda, Y., 1976, "The Observed Joint Distribution of Periods and Heights of Sea Waves," Proceedings of the 15th Coastal Engineering Conference, 11-17 July 1976, Honolulu, Hawaii.

12. Haring, R.E., Osborne, A.R. & Spencer, L.R., 1976, "Extreme Wave Parameters Based on Continental Shelf Storm Wave Records". Proceedings of the 15th Coastal Engineering Conference, 11-17 July 1976, Honolulu.

13. Mogridge, G.R., Funke, E.R. & Bryce, P.W., 1989, "Wave Simulation for Run-Up and Deck Clearance Tests on a Gravity-Based Structure", Proceedings of the 8th Joint International Conference on Offshore Mechanics and Polar Engineering, 19-23 March 1989, The Hague, The Netherlands.

14. Sarpkaya, T. & Isaacson, M., 1981, Mechanics of Wave Forces on Offshore Structures, Van Nostrand Reinhold Company, New York

15. Tayfun, M.A., 1983, "Frequency Analysis of Wave Heights Based on Wave Envelope", J. of Geophysical Research, 88, pp. 7573-7587.

16. Ward, E.G., Borgman, L.E. & Cardone, V.J., 1979. "Statistics of Hurricane Waves in the Gulf of Mexico", J. of Petroleum Technology, 31, pp. 632-642.

Return Period (years)	Gumbel Distribution 90%LCL (m)	Mean (m)	90%UCL (m)	(UCL-LCL) Mean	Borgman Distribution 90%LCL (m)	Mean (m)	90%UCL (m)	(UCL-LCL) Mean
Significant Wave Height:								
10	11.1	12.2	13.2	0.17	11.2	12.1	13.0	0.15
25	11.9	13.3	14.8	0.22	11.9	13.1	14.2	0.18
34	12.1	13.7	15.3	0.23	12.1	13.4	14.6	0.19
50	12.4	14.2	15.9	0.25	12.4	13.8	15.1	0.20
100	13.0	15.0	17.1	0.27	12.9	14.4	15.9	0.21
Sustained Wind Speed:								
10	28.3	30.7	33.2	0.16	28.4	30.6	32.6	0.14
25	30.1	33.4	36.7	0.20	30.0	32.8	35.3	0.16
34	30.7	34.2	37.8	0.21	30.5	33.4	36.1	0.17
50	31.4	35.3	39.2	0.22	31.1	34.3	37.2	0.18
100	32.7	37.3	41.8	0.24	32.2	35.7	38.9	0.19

Note: 34-year return period value is listed, as the span for storm selection is 34 years.
90%UCL--90% upper control limit
90%LCL--90% lower control limit

Table 1: Extreme Significant Wave Height and Sustained Wind Speed at Various Return Periods, Estimated by Gumbel Distribution and Borgman Distribution Fits to 26 Severe Events Occurring from 1951 to 1984

Storm	Date	Peak Hs(m)	Hmax(m) Estimated from Rayleigh Distribution Hmax	Rayleigh Distribution Hmax/Hs	Forristall Distribution Hmax	Forristall Distribution Hmax/Hs	Ward et al. Distribution Hmax	Ward et al. Distribution Hmax/Hs
1	10-14Nov52	7.1	14.7	2.07	13.2	1.86	12.8	1.80
2	08-11Feb54	11.6	22.8	1.97	20.6	1.78	20.0	1.73
3	20-23Sep55	9.5	19.5	2.05	17.6	1.85	17.1	1.79
4	09-13Dec55	10.7	22.0	2.05	19.8	1.85	19.2	1.79
5	20-23Jan61	11.7	24.0	2.04	21.6	1.85	21.0	1.79
6	15-18Dec61	9.7	20.4	2.11	18.4	1.90	17.8	1.84
7	10-14Jan64	6.3	13.8	2.20	12.4	1.97	12.0	1.91
8	14-18Mar64	8.4	17.2	2.05	15.8	1.88	15.0	1.79
9	17-20Feb65	9.9	20.0	2.02	18.0	1.82	17.5	1.76
10	13-17Feb66	10.4	22.0	2.11	19.8	1.90	19.1	1.84
11	21-24Feb66	8.9	18.5	2.08	16.6	1.88	16.1	1.82
12	20-24Feb67	11.9	23.7	1.99	21.4	1.80	20.7	1.75
13	20-24Jan70	12.2	24.7	2.03	22.3	1.83	21.6	1.77
14	16-19Jan71	11.8	23.9	2.02	21.6	1.82	20.9	1.77
15	26-29Oct73	11.1	22.1	1.98	20.2	1.82	19.3	1.73
16	08-13Mar74	10.4	21.0	2.02	18.7	1.80	18.1	1.74
17	16-20Mar76	10.3	20.1	1.95	18.2	1.77	17.6	1.71
18	19-22Jan77	12.1	25.2	2.09	22.5	1.87	21.8	1.80
19	01-05Mar78	10.2	22.7	2.23	18.7	1.83	18.1	1.77
20	02-06Jan80	8.9	18.0	2.02	16.3	1.82	15.8	1.76
Mean Hmax/Hs				2.04		1.84		1.78
Standard Deviation of Hmax/Hs				0.06		0.05		0.05

Table 2: Maximum Individual Wave Height in a Storm, Estimated from Borgman's Integral and Three Wave Height Distributions Applied to 20 Hibernia Storms

Date (Storm Period)	MEDS Station 134 Hs(m)	Tp(s)	G	MEDS Station 140 Hs(m)	Tp(s)	G	MEDS Station 156 Hs(m)	Tp(s)	G
01-03Apr81(1)	6.9	11.4	1.75				7.3	11.4	1.75
26-30Apr81(4)*				7.2	11.9	1.50			
				7.2	12.4	1.10	7.7	12.4	1.30
17-21Oct81(5)				5.3	10.5	1.40			
28Oct-04Nov81(6)	7.6	13.0	1.00	7.7	13.0	1.00			
26-30Nov81(8)	5.3	13.0	1.30	5.9	13.0	1.25			
16-20Dec81(9)	6.8	12.4	1.00				7.0	11.9	1.00
24-29Dec81(10)							7.2	10.9	1.65
08-12Jan82(12)							7.2	12.4	1.35
15-18Jan82(13)*							9.7	13.7	1.10
	9.5	14.4	1.35				10.0	14.4	1.20
18-21Jan82(14)	8.2	13.0	1.55				8.7	13.0	1.50
21-25Jan82(15)	6.6	13.0	1.00	7.1	13.0	1.00	7.0	13.7	1.00
25-27Jan82(16)	6.0	10.1	1.65	6.3	10.9	1.60	6.3	10.9	1.65
27-30Jan82(17)				6.6	11.9	1.70	6.9	11.9	1.75
31Jan-02Feb82(19)	6.7	10.5	1.75	6.7	10.9	1.75	6.9	10.9	1.75
02-05Feb82(20)	8.0	11.4	1.55	7.5	11.4	1.50	7.6	11.9	1.60
07-09Feb82(21)	6.7	10.9	1.75				6.8	10.5	1.75
13-18Feb82(24)				11.5	15.2	1.15			

Note: Storm Period in parentheses corresponds to numbering in Table 1 of [2].
MEDS measurement sites correspond to particular drilling rigs, which periodically change location. All are on the Grand Banks near Hibernia. For precise locations see [7].
Hs is the peak significant wave height of the storm; Tp and G are the spectral peak period and spectral peak enhancement factor simultaneous with Hs.
* Storm period is double peaked.

Table 3: Peak Enhancement Factor of the Jonswap Parametric Spectral Shape Estimated for 17 Hibernia Storm Periods

	Unintensified	Intensifications 1	Intensifications 2	100-Year Extremes Mean	100-Year Extremes 90UCL
Hs_{max}(m)	11.9	13.7	15.8	14.4	15.9
Tp(sec)	15.2	16.4	17.8	17.1	17.9
DME(^{o}T)	228	231	233		
Vmax(m/sec)	30.9	33.6	37.3	37.3	
WD(^{o}T)	250	250	250		

Notes: Hs--Peak significant wave height of the storm
Tp--Spectral peak wave period occurring simultaneously with Hs
DME--Direction (toward) of maximum wave energy
Vmax--Peak sustained wind speed (nominally 1-hour mean at 10m elevation)
WD--Direction (toward) at peak sustained winds
90UCL--90% Upper Control Limit

Table 4: Comparison of 100-Year Criteria for Hibernia and Hindcast of Unintensified and Intensified Storm 23

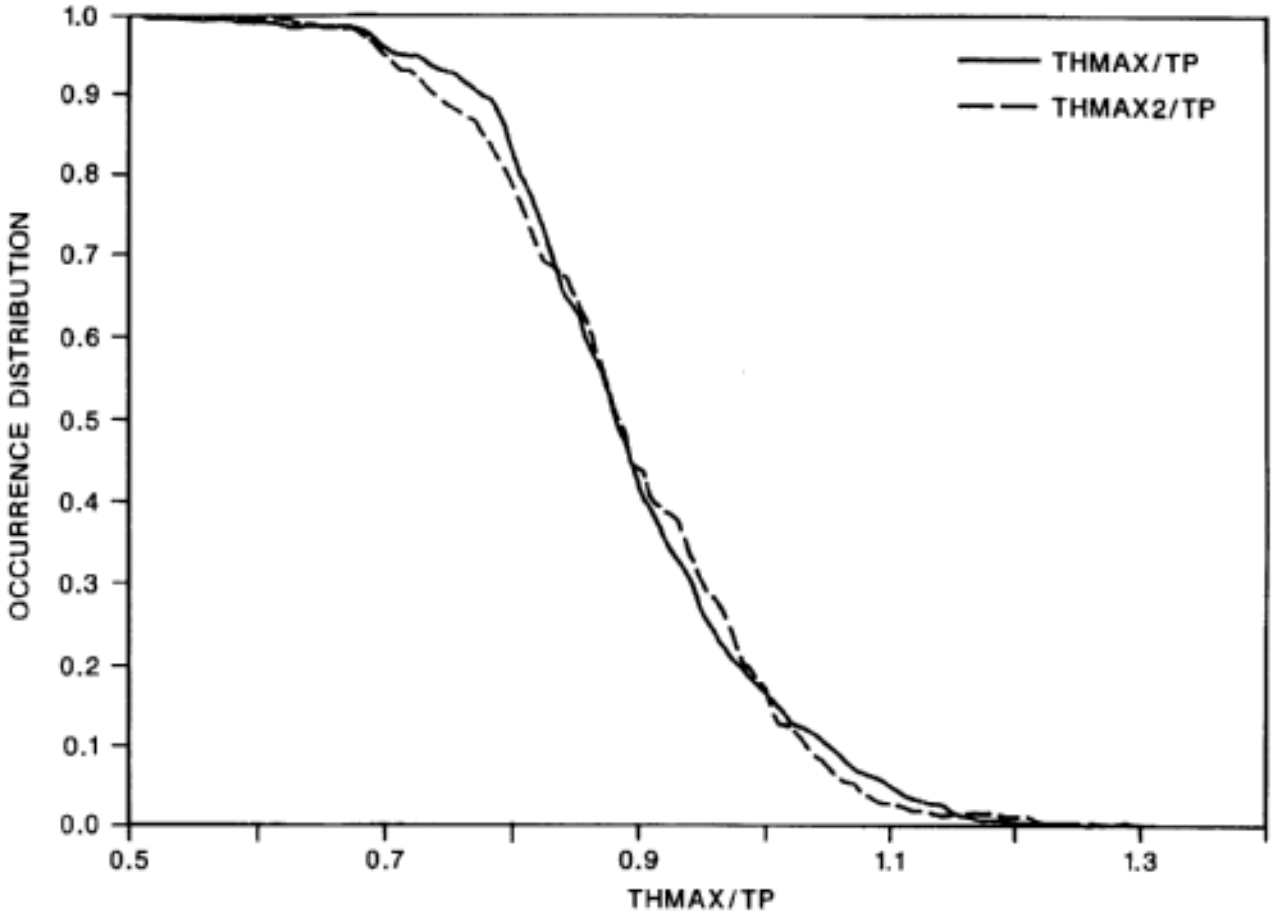

FIGURE 1. DISTRIBUTION OF PERIODS OF HIGHEST (THMAX) AND SECOND HIGHEST (THMAX2) WAVES IN A SEASTATE AS FRACTION OF PEAK SPECTRAL PERIOD (TP) FOR HIBERNIA SEASTATES WITH $H_S \geq 9.0M$.

ESTIMATION OF EXTREME WAVE HEIGHTS THROUGH WEIBULL DISTRIBUTIONS

by Z. K. Bolen[1], S. L. M, Hodgins[2] and F. J. Dello Stritto[1]

[1] Mobil Research and Development Corporation, Dallas, Texas
[2] Seaconsult Limited, Vancouver, British Columbia

ABSTRACT

Weibull distributions are often used to estimate extreme environmental parameters for engineering use. Where available data span periods much too short for proper extremal analysis, fits to distributions such as the Weibull are the only viable means for estimating extremes. Weibull fits of five years of continuous wave buoy data recorded at Hibernia produce long return period extreme estimates. A three parameter Weibull distribution is used. Results are somewhat sensitive to parameters determined in the fit, and a correlation coefficient of 0.99 is obtained. Estimates compare well with values obtained by extremal analysis of hindcast severe seastates over 34 years. Estimates of monthly extremes, for which hindcasting and extremal analysis are not appropriate, are also obtained.

INTRODUCTION

This is fifth of five related papers [1-4] describing development of extreme wind and wave criteria for the Hibernia site on the Grand Banks. While some novel items are included, completeness rather than innovation is the theme. The set is believed to be the first which details all steps in estimating criteria necessary for offshore development. These steps range from use of numerical wave models to the empirical tools and "rules of thumb" for obtaining engineering parameters. The intent is that, by documenting the Hibernia application fully, further development may be directed to areas of greatest need.

References [1-4] detail development of extreme wind and wave criteria for Hibernia, through hindcast modeling/extremal analysis techniques. Such techniques are regularly used in offshore applications to obtain annual extremes. Among the procedure's practical shortcomings are:

1) Even for site specification criteria, significant lead time is required. Work reported in [1-4] was performed intermittently from 1980-1986. A continuous effort would require at least a calendar year's time.

2) In principle, the procedure may be used to estimate monthly extremes, but the 12-fold increase in work is not practical. Storm selection and hindcasting would involve approximately 360 storms, instead of approximately 30.

Initial planning and feasibility studies for offshore development rarely afford sufficient time or budget for accurate hindcast studies. Therefore, a simple means of estimating first approximations of annual extremes is needed. Though annual extremes are the principle environmental criteria, monthly extremes can be very important. These are required for short duration activities such as tow-outs and installations, during which some structural members may experience their greatest loads. The time and volume of work required to obtain such criteria through hindcasting/extremal analysis is not practical for site specific studies. Again, a simpler alternative is needed.

That alternative depends on the type and quantity of data available. For Hibernia, approximately five years (1980-1984) of almost continuous wave buoy measurements are available from drill sites in fairly close proximity [5]. The pertinent data are significant wave heights, Hs, from 18.2 minute records at 3 hour intervals. Fitting a probability distribution, whose tail is assumed the distribution of extremes, to the data is readily performed. The obvious ease of the method is offset by several potential limitations, which are described below. Among these is the simple fact that the extreme statistic obtained from such a fit does not have the same definition as that obtained from proper extremal analysis. As extreme annual criteria for Hibernia are available from a hindcast/extremal analysis study, compatibility of the two extreme estimates can be assessed.

Only monthly criteria are addressed here, though seasonal criteria are often used in offshore applications [7]. For many locations, the calendar seasons do not have significant relevance to seastate variations (i.e., annual cycles in the wave climate are not synchronous with the seasons). A consequence is that three-month seasons can span considerable changes in the mean Hs. Seasonal criteria can be overconservative at the end of the season, and underconservative at its beginning or vice versa. In monthly criteria, the problem is greatly diminished, and in practice often quite negligible.

WAVE DATA

Wave buoys are routinely deployed in conjunction with Canadian east coast offshore drilling activities. The overall measurement program is detailed in [5]; data quality and time series characteristics are summarized in [2]. Raw data are processed by the Canadian Marine Environmental Data Service (MEDS), and various data products, including significant wave height, Hs, are produced from the wave spectra. Sporadic records are available for the Grand Banks back to 1973. Measurements during the years of peak drilling activity, 1979-1986, are almost continuous, often with several wave buoys deployed simultaneously. Figure 1 illustrates the spatial and temporal distribution of measurements near Hibernia for 1980-1984.

As input to the probability distribution fit, a continuous seastate time history is constructed for 1980-1984. The time record consists of Hs estimates at 3-hour intervals from 1 January 1980 to 31 December 1984. For approximately 90-95% of the span, wave buoy measurements near Hibernia are available. Hs-values are based on 18.2 minute data records. Overall data accuracy and sampling variability due to the record length are described in [2], but their possible influence is not considered here. Wave buoy locations vary over the time span due to drilling rig relocations. All the measurements are in close proximity to Hibernia (nominally 46°46'N, 48°48'W); and possible small Hs differences due to spatial separations are not considered. Precise instrument locations are documented in (5). The continuous time record is constructed as follows:

1) Data are taken from a single measurement site, for as long as the site is active. When more than one site is available, the site with the longest run is used.

2) When the chosen site becomes inactive, another is selected using the same criteria.

3) All measured Hs are quality checked for internal consistency (identifying data spikes) and consistency with other data. Suspect data are replaced (when other measurements are available) or removed.

4) Gaps for which no measurements are available are infilled by a variety of methods, depending on month of occurrence and duration. Small gaps during non-severe weather are infilled by interpolation. For gaps during storms, Hs-estimates are often available from other sources. A simple wind speed/wave height relationship is used when no better information is available.

Monthly and annual distributions from the constructed time record are listed in Table 1 . In addition to the estimation of extremes, such a continuous time history has many practical uses. These include calculation of persistence statistics, and time domain simulations for operating efficiencies and various operational scenarios.

WEIBULL DISTRIBUTION

The Weibull distribution is named for the Swiss physicist, Waloddi Weibull, who applied the distribution to the breaking strength of materials. The distribution has been used extensively in reliability and quality control work [6]. The cumulative Weibull distribution is:

$$\begin{aligned} Pr(hs.le.Hs) &= 1 - \exp[-\{(Hs-a)/b\}^c] \quad \text{for } Hs.gt.0 \\ &= \qquad\qquad\qquad\qquad\quad \text{for } Hs.le.0 \end{aligned}$$

where Pr(hs.le.Hs) is the probability that the significant wave height is less than or equal to Hs,

a, b and c are coefficients determined in the fit.

The Weibull distribution is not an extremal distribution (i.e., not a distribution of independent maxima). It has been used as such, however, and is quite similar to the Fisher-Tippett Type III (FT-3) distribution [8]. The chief difference is that FT-3 is an upper bound distribution (i.e., the exponential contains [a-Hs]) whereas the Weibull is a lower bound distribution (i.e., [Hs-a]). The Weibull distribution has often been used to obtain extremal estimates, and was apparently first applied to extreme wave heights in [9], which fit the distribution to 22 hindcast U.S. west coast storms.

Unlike true extremal distributions, the Weibull distribution is usually fit to an entire data set (e.g. for this application, the continuous set of Hs for 1980-1984), rather than the independent maxima. For estimating extremes, the underlying assumption is that long term return period values can be estimated from an extrapolation of all of the data. Potential weaknesses of such an approach are as follows:

1) The implicit assumption is that extreme values can be predicted from usually non-extreme conditions. At Hibernia, extreme waves are generated by intense extratropical storms, whereas a number of other physical mechanisms influence the overall wave climate.

2) The approach does not distinguish between a climate with many maxima of short duration and one with few maxima of long duration. Both produce comparable probability distributions, though their distributions of maxima are quite different.

A consequence of (2) is that the "100-year extreme Hs" computed by the method described below and by a proper extremal analysis are not the same statistic. The latter is the 100-year return period value of peak significant wave height of a storm. A fit of continuous Hs data to a probability distribution yields a 100-year exceedance Hs. That is the value equalled or exceeded on average once in N100 data points, where N100 is the number of data points occurring in 100 years (N100=292200 for the Hibernia Hs data). This so-called 100-year exceedance value cannot, in principle, be less than the 100-year return period peak Hs.

For most practical applications, the main limitation is not related to any distribution but to the short data span--5 years for the Hibernia application, or 5% of the return period of chief interest. In addition to the intrinsic uncertainties of such extrapolation is possible interannual variability on the wave climate. Five years of data could capture predominately mild or severe periods, and yield biased extreme estimates. The years 1980-1984 are believed to be relatively stormy ones on the Grand Banks. A Hibernia storm selection study [3] determined that 27 of the 93 potentially most severe storms between

1951-1986 occurred during these years (also, 10 of 29 of the storms actually hindcast).

In practice, fits to the Weibull distribution can be performed as follows:

1) The distribution is reduced to fit a linear equation of the form,

$$Y = cX - c\ln(b)$$

where $Y = \ln[-\ln\{1 - Pr(hs.le.Hs)\}]$ and $X = \ln(Hs - a)$.

2) The value of "a" is varied between 0 and the minimum Hs. Higher values may be used, but data values less than "a" are then not used in the fit. A simple linear regression yields b and c coefficients associated with each a. The a-value is chosen to maximize, R2, the coefficient of determination [10]:

$$R2 = [\Sigma XY - (\Sigma X \Sigma Y/N)]^2 / \{[\Sigma X^2 - (\Sigma X)^2/N][\Sigma Y^2 - (\Sigma Y)^2/N]\}$$

where N is the number Hs bands for the selected time period. R^2 equals 1.0 for perfect fits. Experience with various data sets shows that Weibull fits often achieve values greater than 0.98, and values greater than 0.99 are common. A rule of thumb, hardly universally practiced, is that fits with R^2 less than 0.95 are rejected.

3) With Hs as a function of probability, probabilities are equated to returns periods (in years) by the following relationship:

$$Pr(hs.le.Hs) = 1 - 1/\{Return\ Period*(Number\ of\ points/year)\}$$

For the Hibernia data (8 data points daily, 2922 yearly), the 100-year return period annual extreme Hs has an exceedance probability [1-Pr(hs.le.Hs)] of 3.42×10^{-7}. Monthly extremes are be computed using the same technique with subsets of the Hs time record for each month, and the proper number of data points per month (240 for a 30 day month).

RESULTS

Application of the fitting procedure to the Hibernia 1980-1984 Hs time series yields results summarized in Tables 2 and 3 . In general, the fits for both annual and monthly extremes are quite good. The mean R^2 is 0.995; the lowest attained, for February, is 0.986. Table 2 lists the estimated annual and February (the most severe month, as well as the most difficult to fit) extremes, and the annual extremes from the hindcast/extremal analysis study [1]. The two "100-year extremes", which as described above are actually different statistics, are 14.3m from the Weibull fit and 14.4m from extremal analysis (fit

of a Borgman distribution to 26 peak Hs occurring in 34 years; a Borgman distribution is a Gumbel distribution in Hs^2). The difference is less than those from alternative extremal distributions applied to the hindcast data [4]. Both estimates are believed somewhat conservative: the exceedance (Weibull) estimate due to wave climate severity during the 5-year data span; the of extremal estimate due to positive bias in the hindcast results [1].

As Table 2 shows, extreme estimates for February are approximately a meter less than the annual extremes. This result is as expected, since monthly extremes in principle are at most equal to the annual (though for some data sets, the opposite occurs--a spurious result due to curve-fitting a small number of data points). Uncertainty in the rare event magnitudes increases as the time unit (month versus year) decreases. A measure of conservatism, consistent with the final annual criteria [4], is added by a strictly empirical adjustment to the raw results. In Table 3 , all monthly extremes are proportionately increased such that the highest of the monthly extremes (February) equals the annual extreme. In [4] extremes at the 90% control limit are adopted as the specified criteria. These values, shown for the hindcast/extremal analysis in Tables 2 and 3 (100-year Hs = 15.9m), are the target to which the monthly extremes are adjusted.

The annual criterion for the 1-year extreme Hs (10.6m) is taken from the Weibull fit, and is an indicator of the conservatism of the results. In the 34-year hindcast storm set peak Hs has been exceeded 11 times, implying that 10.6m is closer to a 3-year value.

CONCLUSION

Extremal analysis of peak seastates is an accepted, well developed practical means of determining extreme environmental criteria for offshore development. A need exists, however, for a simpler alternative to this detailed procedure, to estimate preliminary annual criteria and for monthly or seasonal criteria. A method well-suited to Hibernia, due to the almost continuous seastate measurements from 1980-1984, is fitting a Weibull distribution to that data. Limitations of the method in calculating magnitudes of rare occurrences include:

1) Use of a 5-year data base to calculate 100-year extremes has potential for error, due largely to interannual variability in the wave climate. The years 1980-1984 were an unusually stormy period at Hibernia.

2) 100-year extremes obtained by proper extremal analysis and by fitting probability distributions are not the same statistic. The latter is an overall exceedance value; extremal analysis yields occurrence probabilities of maxima (e.g. peak Hs in a storm).

Despite these restrictions, the Weibull fits and extremal analysis of hindcast storm peaks agree quite well. The 100-year annual extremes of the two methods are virtually equal. Likewise, monthly extremes from the Weibull fit are reasonable, though intrinsically more uncertain. Due to this greater uncertainty, monthly criteria are empirically adjusted such that extremes of the most severe month equal the annual extremes. The adjustment introduces a degree of conservatism consistent with that in the annual criteria into the final values.

ACKNOWLEDGEMENTS

Gratitude is expressed to the organizations which funded much of this work: the four members of the Hibernia Partnership--Mobil Oil Canada Properties, Chevron Canada Resources Ltd., Gulf Canada Corporation and Petro-Canada Resources; and Mobil Research & Development Corporation. Likewise, thanks are extended to the Canadian Marine Environmental Data Service of Ottawa for their cooperation and far-sighted data collection program.

REFERENCES

1. Cardone V.J., Szabo D, & Dello Stritto F.J., 1989, "Development of Extreme Wind and Wave Criteria for Hibernia", 2nd International Workshop on Wave Hindcasting and Forecasting (SIWWHF), 25-28 April 1989, British Columbia.

2. Szabo D., Cardone V.J., Eid B. & Dello Stritto F.J., 1989, "Verification of Numerical Wave Hindcasts for Severe Storms at Hibernia", SIWWHF.

3. Szabo D., Cardone, V.J. & Callahan B.T,,1989, "Severe Storm Identification for Extreme Criteria Determination by Hindcasting", SIWWHF.

4. Cardone V,J., Greenwood J.A,, Szabo, D. & Dello Stritto F.J., 1989, "Engineering Parameters from Hindcast Results", SIWWHF.

5. Canadian Marine Environmental Data Services, 1989, Historical Wave Measuring Stations, 26 January 1989, Ottawa, Ontario.

6. Johnson, N.L. & Kotz, S., 1970, Continuous Univariate Distributions Volume 1, Houghton Mifflin Company,

7. Morgan, S.K, & Babbedge, H.N., 1985, "Transportation Criteria for Offshore and Industrial Equipment", Proceedings of the International Symposium on Offshore Transport and Installation, 26-27 March 1985, London, U.K.

8. Muir, L.R. & El-Shaarawi, A.H., 1986, "On the Calculation of Extreme Wave Heights: A Review", Ocean Engineering, Volume 13, No. 1, pp. 93-118, 1986.

9. Petrauskas, C. & Aagaard, P.M., 1970, "Extrapolation of Historical Storm Data for Estimating Design-Wave Heights", Proceedings of the 2nd Offshore Technology Conference, 4-7 May 1970, Houston, Texas.

10. Johnson, Robert, 1976, Elementary Statistics, 2nd Edition, Duxbury Press.

Hs Range (m)	Percent Frequency of Occurrence of Significant Wave Height in Hs Range												
	Jan	Feb	Mar	Apr	May	Jun	Jul	Aug	Sep	Oct	Nov	Dec	Annual
< 1	0.2	3.4	1.5	0.5	5.9	10.5	17.5	12.3	1.6	0.3	0.4		4.5
1 - 2	10.0	9.9	14.2	32.9	59.9	66.3	64.7	63.3	44.1	17.1	10.8	8.1	33.4
2 - 3	27.7	30.0	36.1	40.1	24.6	20.1	14.4	19.8	37.0	38.9	33.3	28.7	29.2
3 - 4	32.5	25.9	28.5	20.6	9.1	1.9	2.7	3.1	12.1	26.2	29.0	34.4	18.8
4 - 5	16.4	15.4	9.1	4.1	0.5	1.1	0.7	1.3	3.3	11.0	16.2	17.5	8.1
5 - 6	6.3	8.2	8.2	1.0		0.1		0.1	1.3	3.8	7.4	7.4	3.7
6 - 7	3.8	3.3	1.7	0.4				0.1	0.4	1.7	1.9	2.8	1.3
7 - 8	1.7	1.5	0.4	0.2					0.2	0.7	0.7	0.4	0.5
8 - 9	0.9	1.0	0.3	0.2						0.1	0.3	0.4	0.3
9 - 10	0.5	0.4								0.1			0.1
10 - 11		0.9								0.1		0.2	0.1
11 <		0.1										0.1	+

Note: + means percentage less than 0.05 and greater than 0.0

Table 1: Percent Frequency of Occurrence of Significant Wave Height at Hibernia, Estimated from a Continuous Five-Year Time Record, Constructed from Waverider Data

---

Return Period (years)	Extreme Significant Wave Height (m) from Fits to Weibull Distribution		from Hindcasting/Extremal Analysis	
	February	Annual	Annual (Mean)	Annual (90%UCL)
1	9.7	10.4	--	--
10	11.7	12.4	12.1	13.0
25	12.4	13.2	12.9	14.2
50	12.9	13.8	13.8	15.1
100	13.4	14.3	14.4	15.9

Table 2: Extreme Significant Wave Heights for Hibernia, Estimated by Fits of the Weibull Distribution and by Hindcasting/Extremal Analysis Techniques

---

Return Period (years)	Extreme Significant Wave Height (m)												
	Jan	Feb	Mar	Apr	May	Jun	Jul	Aug	Sep	Oct	Nov	Dec	Annual
1	10.2	10.6	8.7	7.9	5.1	5.1	5.1	5.7	7.4	9.4	8.7	10.5	10.6
10	12.0	13.0	10.2	9.8	6.1	6.7	6.8	7.5	9.3	11.4	10.2	13.0	13.0
20	12.4	13.9	10.6	10.4	6.3	7.2	7.3	8.1	9.9	12.0	10.5	13.7	13.9
50	13.0	15.1	11.1	11.0	6.7	7.7	7.9	8.8	10.6	12.7	11.0	14.6	15.1
100	13.5	15.9	11.5	11.6	6.9	8.1	8.1	9.4	11.1	13.2	11.4	15.3	15.9

Table 3: Extreme Monthly Significant Wave Height for Hibernia, Estimated by Fits of the Weibull Distribution to Continuous Data for 1980-1984 and Empirically Adjusted for Consistency with Annual Extremes Estimated by Hindcasting/Extremal Analysis Techniques.

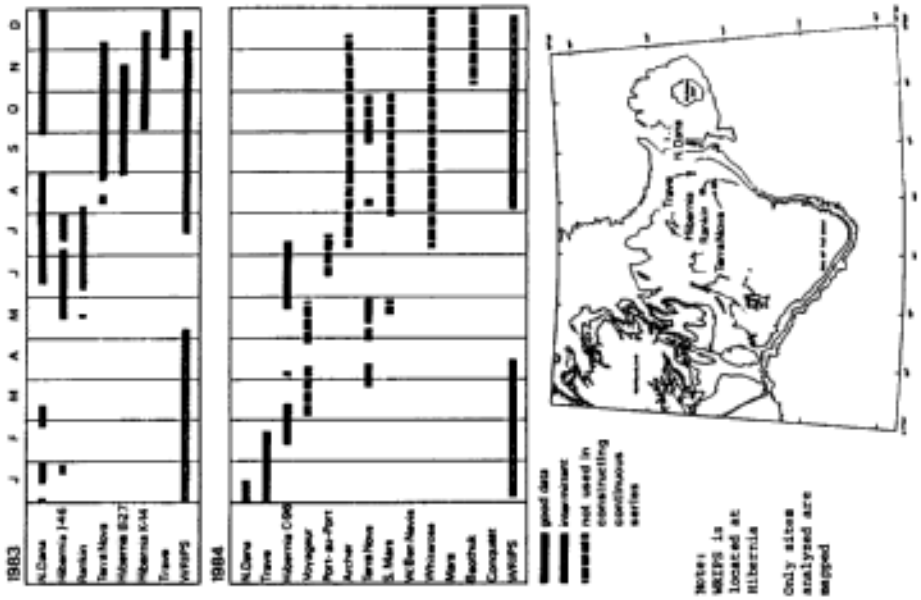

FIGURE 1B. LOCATION AND DATA RECOVERY FOR WAVE BUOYS DEPLOYED NEAR HIBERNIA WELLSITES (1983–1984).

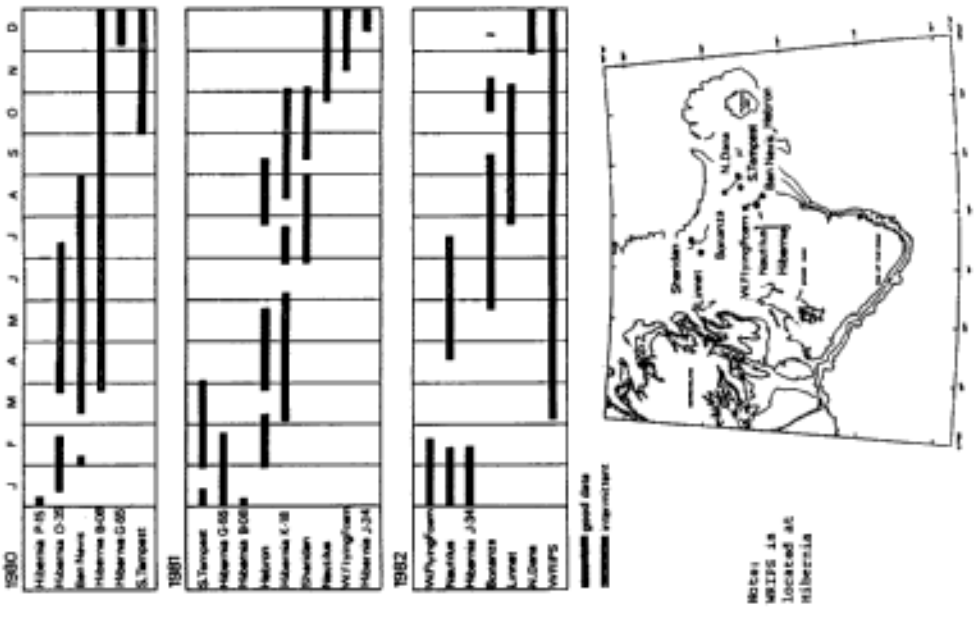

FIGURE 1A. LOCATION AND DATA RECOVERY FOR WAVE BUOYS DEPLOYED NEAR HIBERNIA WELLSITES (1983–1984).

DEVELOPMENT AND EVALUATION OF A WAVE CLIMATE DATA BASE FOR THE EAST COAST OF CANADA

[1]B.M. Eid, [1]C.M. Morton, and [2]V.J. Cardone, [2]J.A. Greenwood

[1]MacLaren Plansearch Limited
Halifax, Nova Scotia, Canada

[2]OCeanweather Inc.
Cos Cob, Connecticut, USA

1. INTRODUCTION

The present Canadian wave climate study program consists mainly of three components: (1) a measurement program; (2) development of hindcast techniques and evaluation of existing wave hindcast products, and (3) an archival service which makes available products developed under (1) and (2).

The data base of instrumental wave measurement series acquired mainly by the Marine Environmental Data Service (MEDS) is substantial. This data base in itself, however, does not satisfy the broad scope of planning and engineering requirements. Existing series are specific to sites of past interest, and measurements are not usually available for very long periods in new areas of industry interest. Also, at any given date, the measurement series are not continuous since measurements were keyed, in general, to periods of active exploratory drilling. These data gaps are particularly troublesome for applications which require duration and persistence type wave statistics. Finally, the present waverider-based measurements provide no directional information.

For certain applications, long-term directional wave information is required. Present studies often resort to crude estimates of wave direction and directional spreading based upon local winds. Even in well-monitored specific situations, wave height and frequency spectra may be inadequate. For example, in the Ocean Ranger storm, three operational waveriders were moored literally within sight of the position of the lost rig. Nevertheless, the data returned from the waveriders were not sufficient to allow a full simulation and understanding of the response of the rig in the complicated storm wave pattern of the Grand Banks during this storm. This required a detailed hindcast study with a directional wave model to support investigations of the Royal Commission on the Ocean Ranger Marine Disaster.

Two separate 20-year wave hindcast series based upon spectral models (the U.S. Navy SOWM and U.S. Army WES) have been evaluated for their application in Canadian waters in recent years (e.g. Baird and Readshaw, 1981; MacLaren Plansearch Limited, 1985). At the few grid

points available in Canadian east coast waters, these products have been found to be seriously deficient both for estimation of the extreme wave climate and for operational wave statistics. While there have been some recommendations for a repetition of the 20-year hindcast with improved models and more accurate wind fields, the need for site-specific extreme wave climate estimates is perhaps being better met by detailed hindcast studies which treat only severe storms selected from a historical period much longer than 20 years (see Swail et al., 1989). On the other hand, most operational questions can be answered with a continuous and accessible series spanning several years, provided the period simulated also includes several typically severe "operational" storms. This study was designed to provide such a product, initially for a three-year period which appears to represent well the operational wave climate of the Canadian east coast.

2. PREPARATION OF THE DATA BASE

2.1 ODGP Operational Wave Hindcast Model

The ODGP deep water spectral wave model has been adopted for use in an operational wave analysis and forecast system, on a grid system shown in Figure 1 . The grid consists of a coarse grid of spacing 1.25° latitude and 2.50° longitude covering most of the North Atlantic Ocean west of 20° W and north of 25°N. and a nested fine grid in which the grid spacing is half that of the coarse. The fine grid covers the Scotian shelf and the Grand Banks of Newfoundland. The time step of the wave model is 2 hours. Each time step consists of a full-time step of wave propagation between two half-time steps of wave growth. The model is fully directional which resolves the wave spectra in 24 directions and 15 frequency bands.

The ODGP model evolved from the Spectral Ocean Wave Model (SOWM) of the U.S. Navy about a decade ago. Details of the model algorithm can be found in MacLaren Plansearch Limited (1985), Eid and Cardone (1987). The ODGP model has since been tested against a broader range of wave regimes than any other existing model. The model incorporates a relatively simple representation of the source terms in the spectral energy balance equation compared to more recent formulations. The calibration of these parameterizations has remained stable over many years, unlike most contemporary models, which appear to undergo continuous tuning.

Winds were provided to the wave model from sea-level pressure analysis fields, which were derived in a man-machine procedure from synoptic weather charts, surface ship, buoy, and rig reports. The basis of the sea-level pressure analysis was the 6-hourly NMC North Atlantic surface pressure maps on which all land and surface-ship observations were computer-plotted and hand-analyzed isobars were drawn. Positions of lows, highs and fronts were also indicated.

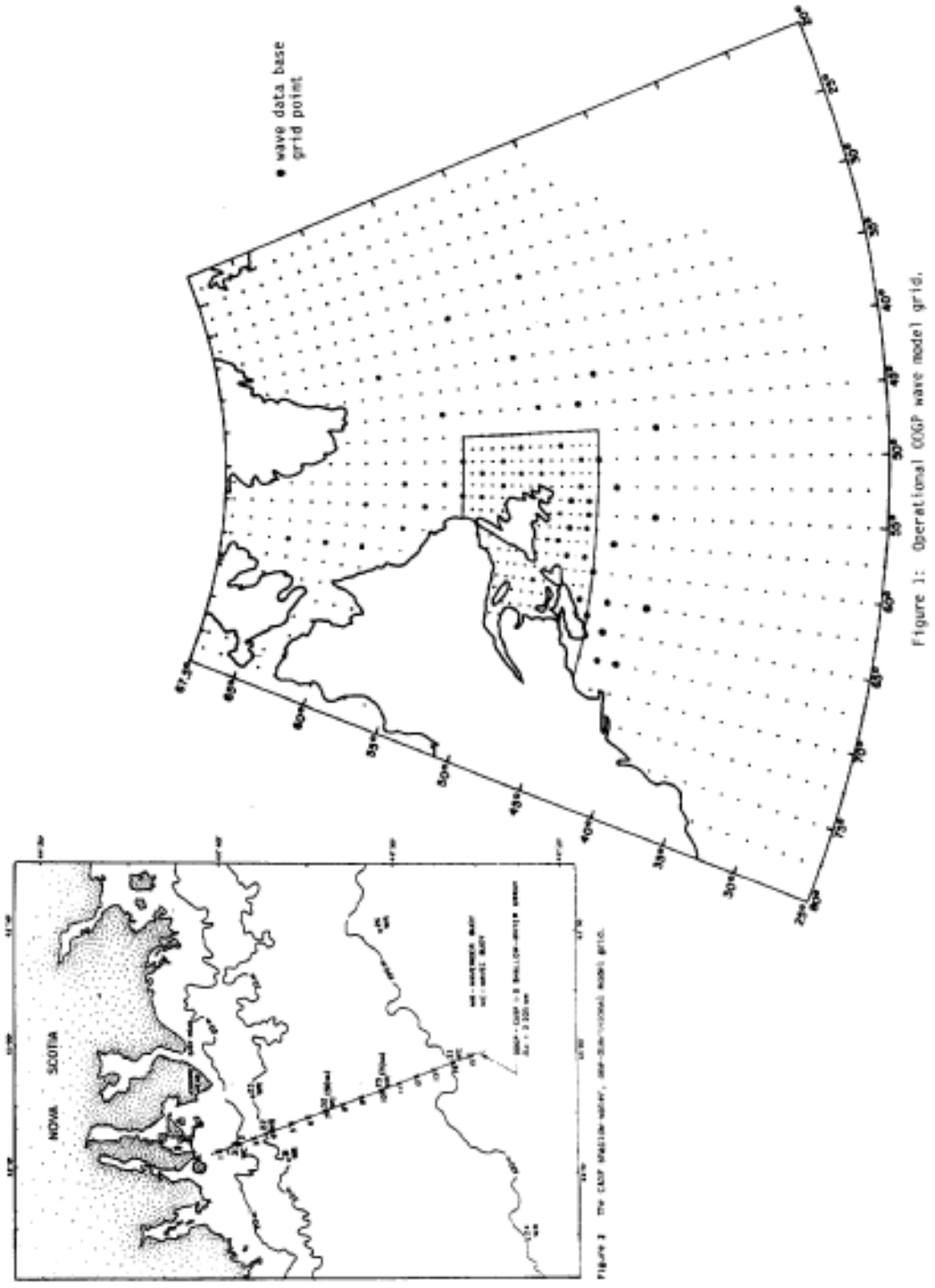

Figure 1: Operational OOGP wave model grid.

An important difference between this analysis product and the corresponding product available as a by-product of fully automated systems, is the extra level of accuracy in the specification of wind fields and quality control afforded by the man-machine mix system. The marine planetary boundary layer (MPBL) model used to calculate grid winds from the digitized pressures was based on Cardone (1969) and Cardone et al. (1978). The model takes into account atmospheric stability in the boundary layer and provides effective neutral winds at 19.5 m above sea level.

2.2 Shallow Water Extension of ODGP Model

We regard the general problem of wave climate specification in the Canadian East Coast waters as basically a three-scale problem. The largest scale requires a grid of about 100 km spacing covering most of the North Atlantic Ocean (e.g. the ODGP coarse grid). The second scale requires a grid no more than about 50 km spacing (e.g. the ODGP fine grid) to resolve large islands and capes and irregular shoreline geometry, large scale ice cover effects, and smaller scale features in the wind field. Given that the typical shelf width (to depths of 50 m) in Canadian East Coast waters of interest is of order 50 km, it is appropriate that the coarse and find grid scales be treated as deep water. The third scale should resolve the shallow shelf width explicitly on a grid of the order 1 - 2 km spacing. While the time step in a wave model on the larger two scales is 2 hours, the time step required in current shallow water wave models of a 1 km grid is typically less than 60 seconds, Clearly the specification of a wave climate in shallow water, using a wave model with shallow water physics is a computing intensive activity to be pursued only on a regional basis as required. The present data base is invaluable in that it can provide the required deep water spectra which the shallow water models require as input.

As a part of the Canadian Atlantic Storms Program (CASP) an experimental shallow water version of the ODGP model was nested within the fine ODGP grid over the CASP-Oceanographic array. The model is basically an extension of the ODGP deep-water propagation and spectral growth algorithms to include shallow water processes of refraction, shoaling, bottom friction and wave-number scalling. Refraction and shoaling are treated within the propagation step, whereas bottom friction and wave-number scalling are modelled with the growth step. The calculation of a table of propagation coefficients is greatly simplified by the assumption of strait, equally spaced bottom contours parallel to the coast line. The principal modifications of the growth subroutines are: (1) transformation of the fully developed Pierson-Moskowitz spectrum form to shallow water; (2) calculation of an explicit attenuation associated with bottom friction; (3) calculation of exponential growth rate using the shallow water

celerity; and (4) use of wave-number scalling of high-frequency saturation range of the spectrum with the equilibrium range coefficient taken as a function of the stage of wave development.

The shallow-water model was adapted on a one-dimensional (1-D) array of grid points laid out along the CASP measurement array, at 2.2 km spacing (Figure 2). The 1-D model was initialized from the deep-water two-dimensional wave spectrum, and wind specified at the ODGP fine-grid point at the end of the array. At the deep-water end of the 1-D array, the full 2-D spectrum contains 12 direction bands that propagate onshore and 12 direction bands that propagate offshore. The wave energy in offshore-propagating spectral components is determined by the local wind field and by a fetch that is limited by the nearby coastline. The fetch-limited spectrum pertaining to all frequency bands in the 12 offshore propagating components, consistent with the local wind speed and direction, was calculated using a parametric model known as the fetch-limited spectral contribution (FLSC) method. The wind duration was assumed to be sufficient to allow development of strictly fetch-limited seas at the site for these directions. The hindcast directional spectrum at the location of interest was then the sum of spectral contributions computed separately for each discrete direction band and frequency according to a directional spectrum appropriate to the direction-dependent fetch. The onshore-propagating spectral components were determined by modifying the propagation scheme to take into account bottom friction, wave number scalling and refraction as described above (see Eid and Cardone, 1987 for details).

2.3 Hindcast Production - Study Output

This study provided three main outputs: (a) Wind/Wave data base; (b) evaluation and documentation of the data base accuracy; and (c) evaluation of a local shallow water wave prediction model for coastal areas.

The prime study output was a fully directional spectral wave database at a selected 54 grid pints (Figure 1). In addition, significant wave height, peak period, average period, vector mean direction, wind speed and direction, and wind shear velocity U* were also provided. In addition, the gridded wind fields were archived at all model grid points (coarse and fine). The data base extended from October 1. 1983 to September 30, 1986. The database is currently maintained by Marine Environmental Data Service, Ottawa.

3. EVALUATION OF THE DATABASE ACCURACY

An extensive evaluation of the database was carried out for the entire 3 year duration and for a selected number of storms during this period. The model results were evaluated against buoy measurements at

a number of locations in three regions in the study domain (Figure 3): (1) Georges Bank (GE) at NOAA buoys #44011 and 44005 near ODGP grid points #277 and 298; (2) Scotian Shelf (SS) near Sable Island at grid point #1012; and (3) Grand Banks near Hibernia field near grid point #1106.

During the study period over a dozen offshore drilling rigs collected considerable amount of wave data on SS and GB with sufficient overlaps to provide almost continuous wave measurement series covering most of the 3 year period. On Georges Bank, NOAA buoys provided a continuous series for the entire period. Figure 4 shows data coverage used the evaluation of model predictions.

Time series plots of hindcast vs. measured data were produced for the 3 years at the above 3 evaluation areas. The hindcast wave spectra were compared with estimated spectra from buoy measurements in a selected number of storms. A very limited (2-D) directional wave measurements (from WAVEC buoys) were available during the study period, most of which was obtained during CASP. These were used in validation of model hindcasts.

A quantitative statistical analysis was carried out to provide average error structure in the hindcast significant wave height (Hs) and peak period (Tp)). The statistical parameters considered are:mean error (bias), mean absolute error (MAE), root mean square error (RMSE), scatter index (RMSE/average), and linear correlation coefficient. Scatter diagrams of predicted versus measured Hs and Tp were also produced.

4. EVALUATION RESULTS

The 3-year hindcast Hs and Tp were compared against the corresponding measured data in the three deep water regions. Figure 5 shows time series plots of a typical fall/winter period in the study duration for SS and GB areas. The shallow-water model results were compared against 3 WAVEC buoy measurements collected by BIO at 100m (site 419 WAVEC #33)9 50m (site 42, WAVEC #32) and 25m (site 43, WAVEC #31) during CASP duration, January 15 to March 31, 1986, Figure 6 shows results at 50m and 25m depths.

Table 1 represents a summary of error statistics for GE, SS, and CB for 3 year series, storm cases, and for the three shallow water sites. Scatter plots of hindcast versus measured Hs and Tp are shown in Figure 7 (3 year series) and Figure 8 (storms).

Storm Cases. The following thirteen storm events were selected during the study period:

Storm #	Date Covered	Storm #	Date Covered
1	Oct. 22 - Oct. 28, 1983	7	Jan. 15 - Jan. 19, 1985
2	Nov. 25 - Dec. 01, 1983	8	Jan. 20 - Jan. 25, 1985
3	Dec. 20 - Dec. 26, 1983	9	Jan. 27 - Jan. 31, 1985
4	Mar. 09 - Mar. 13, 1984 (2-D)	10	Jan. 19 - Jan. 13, 1986
5	Mar. 27 - Mar. 31, 1984 (2-D)	11	Jan. 26 - Jan. 30, 1986 (CASP)
6	Mar. 31 - Apr. 03, 1984 (2-D)	12	Feb. 15 - Feb. 20, 1986 (CASP)
		13	Mar. 10 - Mar. 14, 1986 (CASP)

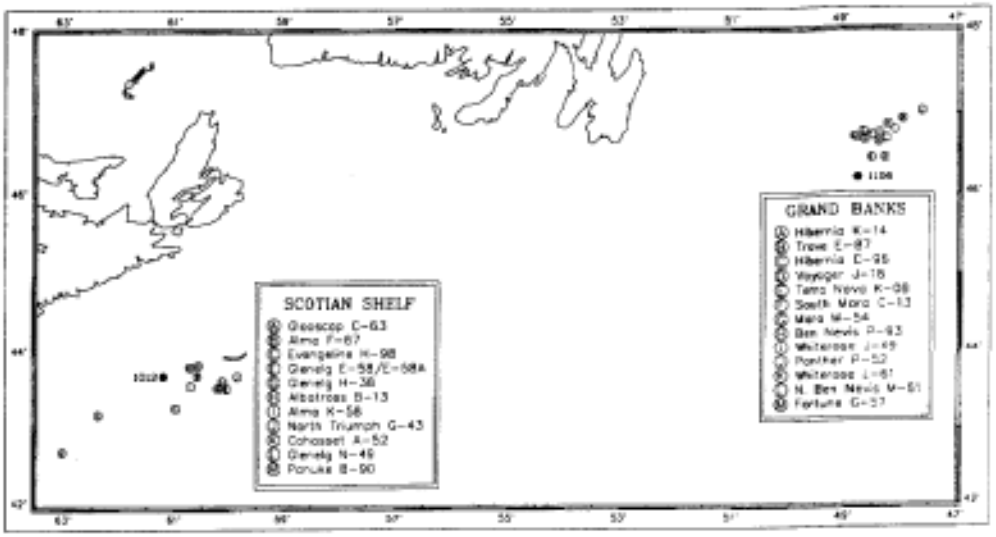

Figure 3: Wave measurement sites (SS & GB).

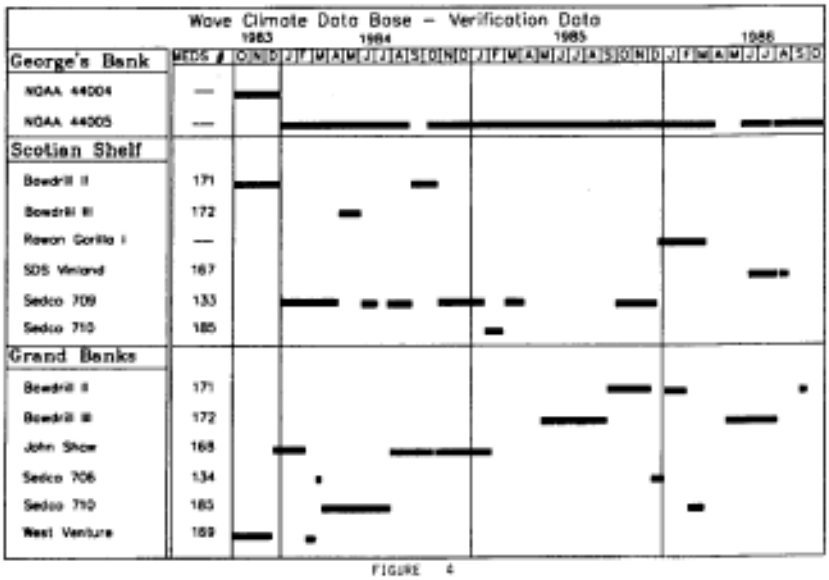

FIGURE 4

Table 1

Summary of Error Statistics for 3 Years, storm cases and shallow water hindcast results

Yar	Site	Num of Points	Average Obs	Standard Dev.	Average Model	Standard Dev	Mean Err	Absolute Mean Err	RMSE	Scatter Index	Corr Coef
3 Year Overall Statistics											
HS	Georges Bank	3563	1.72	1.03	1.81	1.07	0.08	0.49	0.64	37.24	0.816
	Scotian Shelf	2402	2.33	1.31	2.49	1.32	0.16	0.53	0.70	30.13	0.905
	Grand Banks	3025	2.75	1.39	3.08	1.52	0.33	0.66	0.86	31.21	0.856
TP	Georges Bank	3499	6.42	1.91	7.08	2.03	0.66	1.88	2.43	37.80	0.300
	Scotian Shelf	2402	8.47	2.16	8.16	1.97	-0.31	1.48	2.07	24.46	0.494
	Grand Banks	2913	9.83	2.33	9.24	1.86	-0.59	1.74	2.37	24.14	0.418
Storm Statistics											
HS	Georges Bank	231	2.80	1.58	2.78	1.54	-0.02	0.66	0.84	29.98	0.856
	Scotian Shelf	186	3.43	1.57	3.68	1.67	0.25	0.63	0.82	23.87	0.886
	Grand Banks	229	4.12	1.65	4.55	1.86	0.43	0.82	1.08	26.21	0.848
TP	Georges Bank	227	7.44	2.72	8.48	2.27	1.04	2.32	3.10	41.64	0.327
	Scotian Shelf	186	9.52	2.27	9.45	1.73	-0.07	1.45	1.96	20.55	0.550
	Grand Banks	194	11.16	1.94	10.84	1.82	-0.32	1.54	2.02	18.07	0.440
Shallow Water Statistics											
HS	Site 41 (100m)	129	1.75	1.03	1.48	0.92	-0.28	0.51	0.65	37.31	0.820
	Site 42 (50m)	186	1.78	1.13	1.55	0.98	-0.23	0.49	0.62	34.70	0.863
	Site 43 (25m)	184	1.40	0.96	1.32	0.89	-0.08	0.38	0.48	34.57	0.868
	Overall	499	1.63	1.06	1.44	0.96	-0.19	0.45	0.58	35.67	0.854
TP	Site 41 (100m)	129	9.02	2.41	8.22	2.45	-0.80	1.79	2.66	29.48	0.457
	Site 42 (50m)	186	9.13	2.51	8.09	2.22	-1.04	1.72	2.40	26.27	0.587
	Site 43 (25m)	184	9.43	2.38	8.11	2.43	-1.31	2.10	2.91	30.91	0.416
	Overall	499	9.21	2.44	8.13	2.36	-1.08	1.88	2.67	28.93	0.486

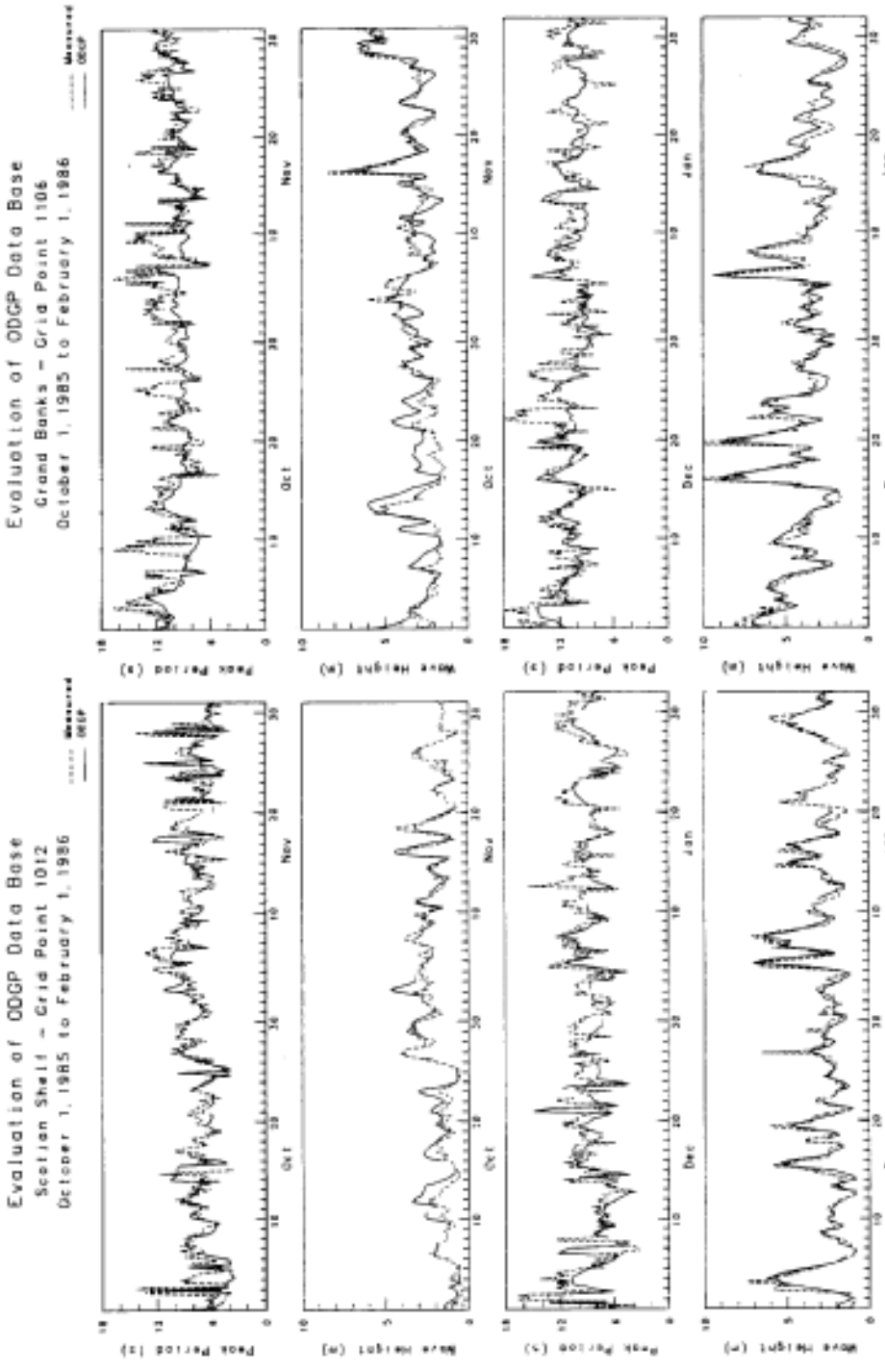

Figure 5: Time series hindcast vs. measured wave height and peak period.

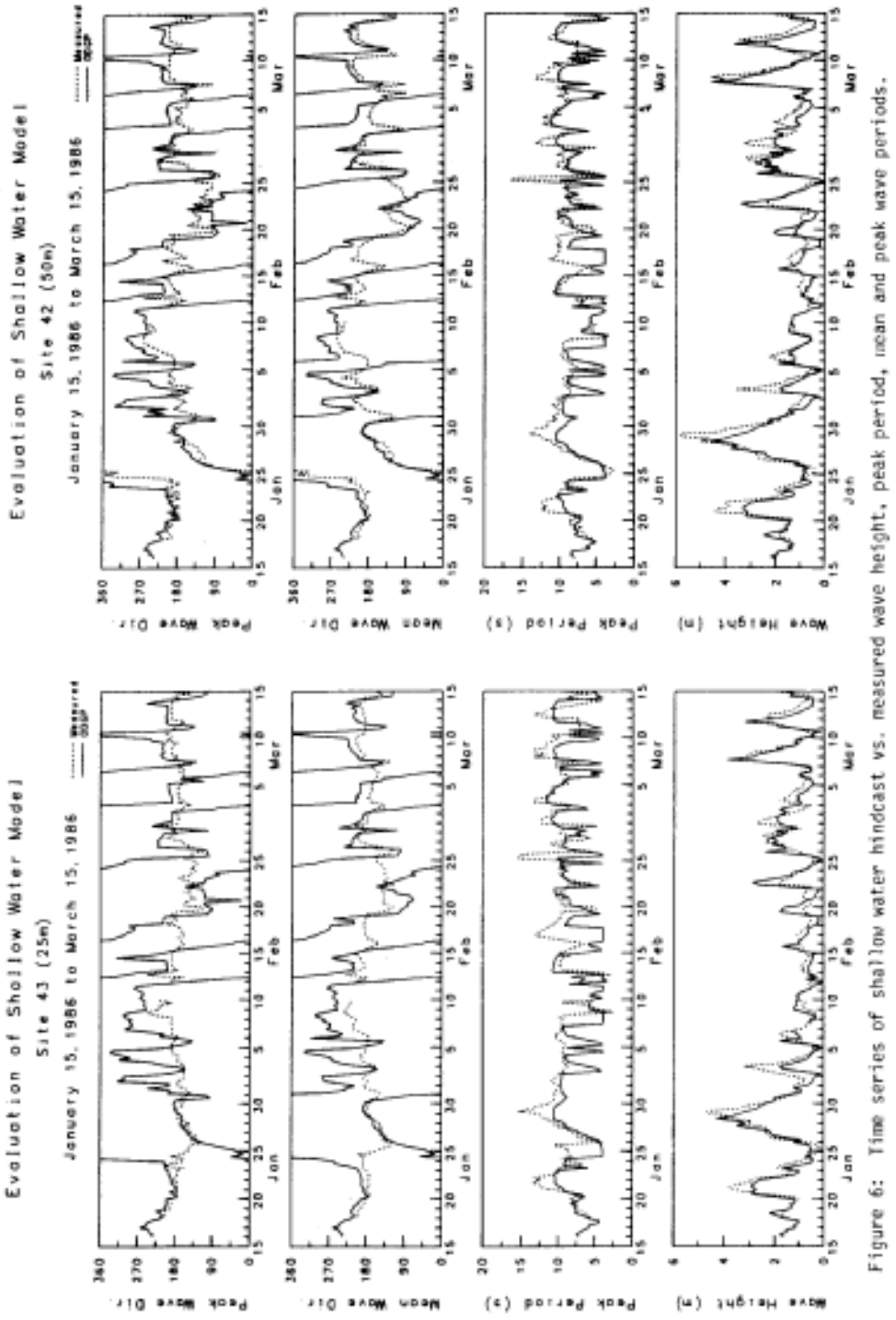

Figure 6: Time series of shallow water hindcast vs. measured wave height, peak period, mean and peak wave periods.

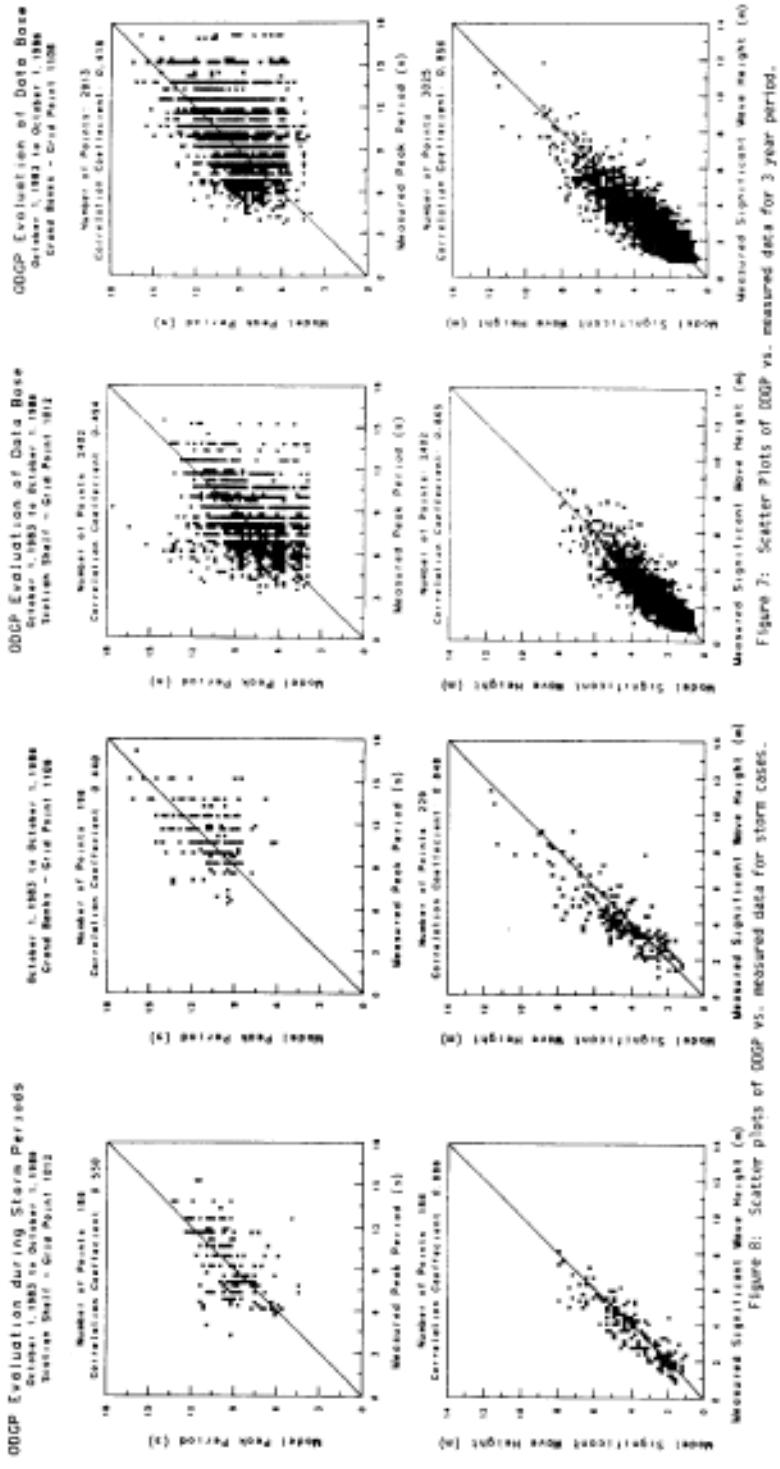

Figure 7: Scatter Plots of ODGP vs. measured data for 3 year period.

Figure 8: Scatter plots of ODGP vs. measured data for storm cases.

As shown, in general, the model results compare well with measured data. The model tends to slightly overpredict (+ve bias) wave height at evaluation sites most of which were in less than 100m depth, where shallow water effect may have contributed to above bias. However, the mean error in model prediction of Hs is less than 0.4m and RMSE of 0.64 to 0.86m with correlation coefficient in the range 0.82 to 0.86 were found over the 3 year period in the 3 regions. The peak period was predicted with mean error (bias) varied from -0.31 to +0.66s, and RMSE of less than 2.5s over the 3 year period. However, larger scatter can be seen in wave period series when compared with the scatter in Hs.

The evaluation of the 1-D and 2-D energy spectra has indicated that the ODGP spectra are in good agreement with the measured values when there is a good agreement between measured and hindcast Hs and To, In addition, the shallow water model produced promising results which compared well with measured data (both time series and spectra). This suggests that this simple model may be sufficient for operational purposes.

5. DISCUSSION AND CONCLUSIONS

The assembly of a comprehensive base of measured wave data at specific sites in each of three areas (GE, SS, GB) covering the same years simulated, allowed an extensive evaluation of a few properties of the two-dimensional spectra generated, such as significant wave height, peak spectral period, and a more limited evaluation of the wave frequency spectrum.

The overall statistical measures of difference between the modelled and measured significant wave height series at the sites examined suggest that the database provides a nearly unbiased description of the wave climate in this regard. The bias was found to be negligible at Georges Bank and Scotian Shelf, and less than 0.4 meters at Grand Banks. The RMS difference in Hs varied between 0.6 and 0.9m and correlation coefficient between 0.8 to 0.9. The scatter index in Hs ranged between 30 and 35 percent, which is higher than found in storm hindcast, because the mean wave heights over the series of measured data are quite low (1.7m at GE, 2.3m at SS, and 2.7m at GB).

The specification of peak spectral period in the database does not at first appear to be as skillful as the specification of wave height, with correlation coefficients generally less than 0.5. This property of the spectrum, however, is subject to many sources of scatter, including effects of sampling variability, and the unreliability of estimates of peak period if the spectrum is relatively flat or multi peaked. Further , the comparisons involving data from the NOAA buoys are believed to be contaminated by changes in the definition of wave period during the time period studied. However for the most reliable

data, there does appear to be a negative bias of about 0.4 seconds in the database (model periods lower than observed), which is probably attributable to difficulty in representing background swell in non-storm conditions, especially in summer and transition seasons, when the sources of the swell may be outside the model domain. On the other hand, differences between modelled and estimated peak wave period are lower both in an absolute and percentage sense in the storm periods evaluated.
The storm comparisons also show that when the model has correctly specified the total variance in the spectrum, it has typically also well represented a the shape of the frequency spectrum, including the spectral width the location and amplitude of the spectral peak, and energy level of the high-frequency equilibrium range.

The shallow water wave analyses were found to be at least as skillful as the deep water analysis spectra used as boundary conditions for the shallow water model, suggesting that this type of application of the data is viable. The modelled spectra agreed reasonably well with these obtained from the WAVEC buoys especially when the predicted and measured wave heights are in good agreement.

ACKNOWLEDGMENTS: This study was funded by Supply and Services Canada (Unsolicited Proposal Funds) and contributions from marine Environmental Data Service and Bedford Institute of Oceanography (DFO), Defence Research Establishment Atlantic (DND), and the Federal Panel on Energy R&D (PERD). The Scientific Authority for this study was Dr. R.J. Wilson of MEDS. We wish acknowledge with gratitude the initiation and support from the Canadian waves committee and the east coast offshore operators for providing their data and supporting the ODGP real-time operation.

REFERENCES

Baird, W.F. and Readshaw, J.S., 1981. A comparison of hindcast and recorded wave data. Marine Environmental Data Services, DFO, Contractor Report No. 1.

Cardone, V.J., 1969. Specification of the wind distribution in the marine boundary layer for wave forecasting. Geophysical Science laboratory, New York University. Report TR-69-1. Available from NTIS AD#702-490, New York, N.Y..

Cardone, V.J., 1978. Specification and prediction of the vector wind on the U.S. continental shelf for application to an oil slick tragectory forecast program. Final Report for NOAA, U.S. Department of Commerce, Silver Spring, Maryland.

Eid, B.M. and V.J. Cardone, 1987. Operational test of wave forecasting models during the Canadian Atlantic Storms Program (CASP). Environmental Studies Research Funds (ESRF), Report Series No. 076.

MacLaren Plansearch Limited, 1985. Evaluation of the spectral ocean wave model (SOWM) for supporting real-time wave forecasting in the Canadian east coast offshore. Report submitted to the Atmospheric Environment Service, Environment Canada.

AN EXTREMES WIND AND WAVE HINDCAST OFF THE EAST COAST OF CANADA

[1]V.R. Swail, [2]V.J. Cardone and [3]B. Eid

[1]Atmospheric Environment Service,
Downsview, Ont.

[2]Oceanweather, Inc.,
Cos Cob, CT

[3]MacLaren Plansearch Ltd.,
Halifax, N.S.

1. INTRODUCTION

Accurate specification of historical wind and wave fields is a critical requirement for many engineering design applications since, in the absence of ice, waves are the dominant load for offshore structures. It is an important regulatory requirement, in respect of the safety of life and property and enhancement and protection of the environment, to verify calculations that will be used in engineering design, thus contributing to improved economic solutions for existing and proposed offshore energy developments, in an environmentally sound manner.

The objective of this study was to specify, following a hindcast approach, the extreme wave climate on the east coast of Canada, by providing accurate surface wind and wave fields in the top-ranked wave-producing storms. The three target areas for the study were the Grand Banks of Newfoundland, the Scotian Shelf and Georges Bank. These areas, which cover most Canadian East Coast offshore exploration areas, are outlined in Figure 1 .

Previous experience with the historical meteorological data base for the N.W. Atlantic ocean basin supports selection of storms from the past 30 years. The data base for earlier periods is much less extensive and wind fields may not be specified as accurately. In addition, the Canadian Meteorological Centre charts on microfilm go back only to 1957. Therefore, the historical period considered in this study extends from 1957 to 1988.

The following paragraphs describe briefly the data bases used, the storm selection methodology, the wind and wave hindcast procedures and verification, and the extremal analysis used to produce the final output product for the study, namely the design wave estimates at specified probability levels for the areas in question.

2. DATA BASE ASSEMBLY

A comprehensive set of historical meteorological data was assembled for storm identification and selection, and the specification of

surface wind fields in selected storms. The data fall into two general categories:

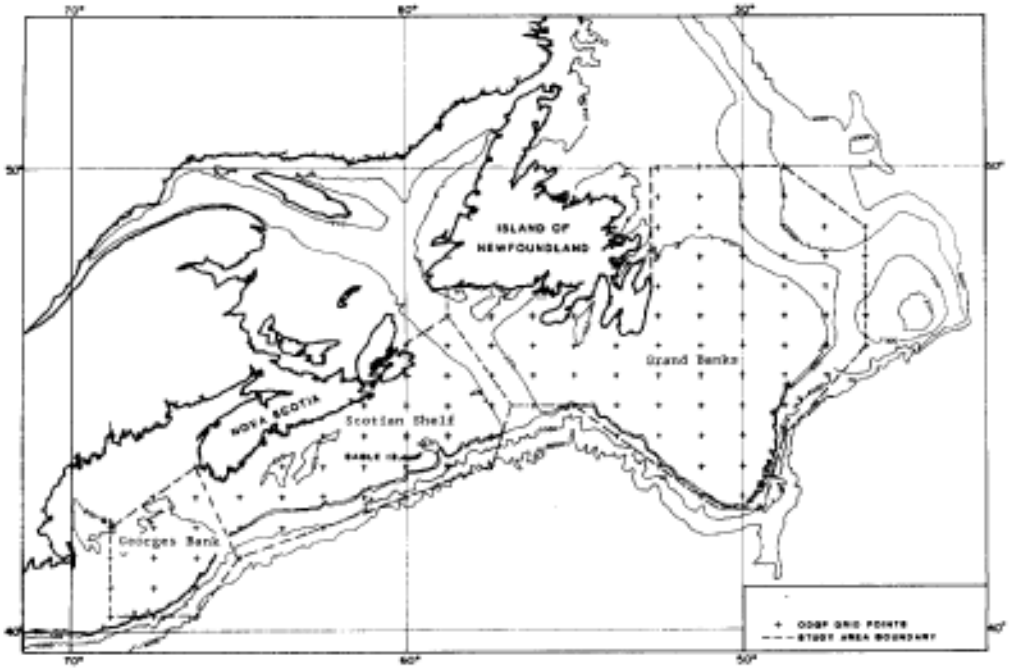

Figure 1. Target area boundaries and model grid points.

2.1 Historical surface weather maps

The following map series of weather and sea ice conditions were utilized for storm selection and hindcasting:

- Canadian Meteorological Centre (CMC) surface analysis charts 1957 - 1988
- Maritimes Weather Centre (MWC) surface analysis charts 1970 - 1988
- National Meteorological Center (NMC) 3-hourly North American surface analyses 1954 1988
- National Meteorological Center (NMC) 6-hourly N. Hemisphere surface analyses 1954 1988
- MacLaren Plansearch 6-hourly surface analysis charts 1981 - 1988
- Oceanweather 6-hourly surface analysis charts
- weekly ice cover charts from AES Ice Central, Ottawa
- Meteorological and Oceanographic Centre (METOC) wave height analyses 1970 - 1988

2.2 Digital Data Bases

The following digital data sets, comprising observations from ships, drill rigs and buoys, and from previous hindcasts for the east coast of Canada, were utilized in this study for

storm identification, hindcasting and verification;

- Comprehensive Ocean Atmosphere Data Set (COADS) ship observations 1854-1979
- Canadian co-operating ships 1980-88
- drill rigs operating in Canadian waters 1972-1988
- NOAA buoy data 1972-87
- AES land-based observations 1953-1988
- Ocean Weather Stations (OWS) Bravo, Delta (1946-72) and Charlie (1946-81) data
- Sambro (1949-66), Lurcher (1949-69) lightship data
- Marine Environmental Data Service wave buoy data
- U.S. National Climatic Data Center (NCDC)
  - "Marine Deck" 1954-1969
  - "Decade of the 1970's" 1970-1979.
  - "Tape Deck 1129" 1980-present
- Geostrophic Wind Climatology data base (Swail, 1985)
- ODGP 3-year hindcast data for the east coast 1983 - 1986 (Eid et al., 1989).
- Spectral Ocean Wave Model North Atlantic hindcast (U.S. Navy, 1983);
- U.S. Army Waterways Experiment Station North Atlantic hindcast (Corson et al., 1982)

There is considerable overlap in the data sets listed above, since COADS contains a large portion of the NCDC data, the Canadian ship observations are sent to NCDC as part of the international data exchange, and the buoy and weathership data also form a part of the NCDC data set. However, to avoid missing important data, all sources were investigated.

3. STORM SELECTION

The storm selection was accomplished in three main steps: (1) selection of potentially severe wave-producing storms in the past 30 years; (2) storm verification, which involved cross-checking between different data sources; (3) storm ranking and final selection.

3.1 Identification of potential severe storms

Potentially severe wave-producing storms in the period 1957-1988 were identified by scanning all of the digital data bases listed in Section 2 . All wind and wave data greater than or equal to specified thresholds (34-40 knots for wind speed and 6 metres for significant wave height) were listed in chronological order for each target area. For each storm identified, the starting and ending dates were abstracted, along with selected wind and wave values. These included maximum wind speed, duration of wind speed above the threshold, and maximum significant wave height measured, observed or predicted from previous hindcast studies.

Previous storm selection and hindcast studies for the east coast areas, including Brown et al. (1986), Lewis and Moran (1984) and Cardone et al. (1989), produced lists of severe storms for a specific site or area. For Georges Bank, literature searches were also conducted for accounts of major individual New England storms capable of generating extreme waves in the Georges Bank area (Monthly Weather Review, Weatherwise, Mariner's Weather Log, the NOAA publication "Storm Data").

The preliminary lists derived from the above screenings were synthesized into a single master candidate coarse storm list (MCL) containing 532 separate events. Storms were classified as either Grand Banks, Scotian Shelf, Georges Bank or combined events.

3.2 Threshold Analysis Ranking (TAR)

Previous studies have established a high correlation between measured wave height in a storm and readily available properties of the surface pressure pattern of extratropical storms, including (1) minimum central pressure; (2) deepening rate; (3) maximum pressure gradient in the critical fetch zone of wave generation; (4) duration of maximum pressure gradient; (5) total pressure drop across the storm, If the properties of a candidate storm exceeded the threshold for each screening parameter, it was assigned a threshold analysis ranking (TAR) score of 5 (i.e. a score of 1 for each parameter described above). The following thresholds were used to establish TAR scores separately for Scotian Shelf (including Georges Bank) and Grand Banks storms. For storms which affected both Scotian Shelf and Grand Banks regions, separate TAR scores were assigned for each region.

Parameter	Scotian Shelf	Grand Banks
1 – min. central pressure (mb)	≤ 980	≤ × 967
2 – max. deepening rate (mb/24 h)	≥ 18	≥ × × × 18
3 – max. pressure gradient (mb/° lat.)	≥ 6	≥ 6
4 – storm intensity (mb^2 h/° lat^2)	≥ 324	≥ 324
5 – total storm gradient (mb)	≥ 50	≥ 67

3.3 Storm ranking and final list

Reduction of the MCL to the target level of 30 storms for hindcasting in each area proceeded in three stages:

(1) assignment of a quasi-objective storm ranking parameter (TAR) to each member of the MCL;

(2) subjective reduction of the MCL through further reference to the individual storm data (i.e. peak wind speed, duration, severity index, peak wave heights, METOC charts and previous storm studies);

(3) intensive subjective study of the 6-hourly map sequences, to develop an estimate of the maximum wind speed and duration in each

fetch zone susceptible of extreme wave generation within the regions of interest, to serve as a critical discriminant between otherwise comparable storms.

3.4 Georges Bank Tropical Storm Selection

A separate list of tropical storms was developed for Georges Bank, since these storms require modelling techniques (Cardone et al., 1976) quite different from those used for extra-tropical storms. In addition to the data sources referred to for extra-tropical storms, the following sources peculiar to tropical storms were also investigated: Neumann et al. (1987), Barks and Richards (1986), Monthly Weather Review and the NOAA National Hurricane Center tape file HURDAT. Tropical cyclones with central pressures less than 990 mb were retained.

4. WIND FIELD ANALYSIS

The model domain and grid specification used for these wind and wave hindcasts are shown below. The model is comprised of two nested grids, a coarse grid and fine grid.

	Coarse	Fine
domain:	25°N – 67.5°N 20°W – 80°W	38.75°N to 53.75°N 42.5°W to the coast
spacing:	1.25°lat x 2.5°long	0.625°lat x 1.25°long
active grid points:	662	333
time step:	2 hours	2 hours

Table 1. Parameters of nested wind and wave grid.

The method used for hindcasting wind fields for the selected storms is based on man-machine mix techniques using a blend of surface pressure analysis and kinematic analysis wind fields.

The hindcast period of each storm consists of the following sub-periods: (a) period of spinup of background seas in the model domain in which principal wave generation occurs prior to the peak of the selected storm; (b) period during which selected storm generates seas in the study areas and including always the period within ±12 hours of expected occurrence of peak states in each area; (c) 24-hour period following (b) in which peak seas continue to decay.

For the spinup and decay periods, the approach was to specify winds from the sea level pressure analyses. Gridded pressures were converted to "effective neutral" 20-m winds through the marine planetary boundary layer (MPBL) model developed by Cardone (1969, 1978). The

"effective neutral" wind speed, introduced by Cardone (1969) to describe the effects of thermal stratification in the marine boundary layer on wave generation, is simply the wind which would produce the same surface stress at the sea surface in a neutrally stratified boundary layer as the wind speed in a boundary layer of a given stratification. This is consistent with the similarity approach and produces analogous functions. The baroclinic forcing term is supplied at each grid point from climatological horizontal air temperature gradients appropriate to the North Atlantic Ocean in the cold season. The atmospheric stability term is specified as a function of local geostrophic wind direction.

Kinematic winds are extracted from the streamline/isotach analyses at the fine mesh grid point locations for the period (b), the peak of the storm, and represent the effective 1-hour average 20-m level neutral wind. Reports of wind speed from ships and rigs equipped with anemometers are transformed into the effective neutral 20 m values. For ships which use estimated wind speeds, values are adjusted according to the Scientific Beaufort scale. The kinematic winds replace the winds derived from the pressure field in the interior of the kinematic domain, and are blended with the pressure-derived winds along the boundaries of the domain.

Kinematic winds are by far the most accurate and least biased winds, primarily because the method allows a thorough re-analysis of the evolution of the wind fields. Kinematic analysis also allows the wind fields to represent effects not well modelled by pressure-wind transformation techniques such as inertial accelerations associated with large spatial and temporal variations in surface pressure gradients and deformation in surface winds near and downstream of coasts.

The final step in the wind field analysis is interpolation from 6 hours to 2 hours (as required to drive the wave model). Linear interpolation in time of zonal and meridional wind components is used for wind direction, while the fourth power of wind speed is used for interpolation of wind speed. Further interpolation is done near centers of rapidly propagating cyclones to avoid errors due to excessive smoothing of winds. Gridded wind fields are produced on the ODGP wave model grid.

5. WAVE HINDCASTS

The ODGP wave model is a deep-water fully spectral model (24 directions by 15 frequencies), which evolved from the Spectral Ocean Wave Model of the U.S. Navy (SOWM) about a decade ago. This model incorporates a relatively simple representation of the source terms in the equation compared to more recent formulations. The calibration of has remained stable over this period, unlike most contemporary undergo

continuous tuning. The ODGP model has been used in hindcast regimes of many different types (e.g. winter cyclones, typhoons, surges). Reece and Cardone (1982) summarized this extensive model a record of hindcast skill which has yet to be surpassed by alternate models. The model, when driven by wind fields of accuracy about ± 2 m/s in speed, ± 20° in direction, provided unbiased specifications of significant wave height and peak frequency with a scatter index of about 10%, which, incidentally, is comparable to the scatter in estimates of these quantities from measured 20-minute wave records. The model exhibits conspicuous skill in the specification of the complicated directional mix of local sea, and propagation swell excited by the moving quasi-circular wind fields of migratory extratropical and tropical storms. A detailed description of the model physics and numerical algorithms is given in Cardone et al. (1976) and MacLaren Plansearch (1985).

6. VERIFICATION

In order to assess the quality of wave model predictions, it is necessary to isolate the errors (i.e. bias or any systematic errors) in the input winds which are used to drive the wave model, and in the output from the wave model.

Ten storms were selected for model validation. All available wave measurements were obtained from automatic wave recording systems (e.g. waverider buoys, non-directional and directional, NOAA buoys). Wind speed and direction (and air and surface water temperature) records were obtained from all the rigs, NOAA buoys, Sable Island, etc. which were in the study area during each of the ten validation storms. All measured winds were converted to "effective neutral" winds at 20 m above the mean sea level similar to those used in running the wave model. Comparisons were carried out between wind and wave parameters at the measurement sites and the closest ODGP grid point. Some results of the verification analysis are shown in Tables 2 - 5 , and Figures 2 - 4 .

	Avg Obs	SD Obs	Avg Mod	SD Mod	Mean Err	Abs M.E.	RMSE	SI	Corr Coeff
W_s (M/S)	25.79	3.27	24.55	1.98	-1.24	2.44	2.88	11.17	0.606
H_s DEEP	9.36	1.73	9.89	1.94	0.53	1.06	1.24	13.21	0.820
TMA	9.36	1.73	8.78	1.44	-0.59	0.73	1.05	11.23	0.864
T_p DEEP	13.05	1.48	14.49	1.77	1.44	1.83	2.15	16.47	0.531
TMA	13.05	1.48	13.73	1.52	0.69	1.16	1.40	10.70	0.672

Table 2. Summary of peak model to peak measured values.

	Avg Obs	SD Obs	Avg Mod	SD Mod	Mean Err	Abs M.E.	RMSE	SI	Corr Coeff
H_s DEEP	4.33	1.92	5.00	2.41	0.66	0.93	1.15	26.57	0.931
TMA	4.33	1.92	4.72	2.14	0.39	0.67	0.81	18.35	0.944
T_p DEEP	9.98	2.25	10.48	2.50	0.50	1.44	1.83	18.35	0.730
TMA	9.98	2.25	10.16	2.22	0.18	1.24	1.62	16.21	0.741

Table 3. Summary of all model/measured comparisons Scotian Shelf.

	Avg Obs	SD Obs	Avg Mod	SD Mod	Mean Err	Abs M.E.	RMSE	SI	Corr Coeff
H_s DEEP	6.02	2.05	7.31	2.70	1.29	1.44	1.75	29.07	0.912
TMA	6.02	2.05	6.66	2.21	0.64	0.89	1.11	18.40	0.913
T_p DEEP	12.10	2.02	13.06	2.30	0.96	1.70	2.16	17.85	0.607
TMA	12.10	2.02	12.42	2.04	0.33	1.39	1.82	15.07	0.609

Table 4. Summary of all model/measured comparisons - Grand Banks.

	Avg Obs	SD Obs	Avg Mod	SD Mod	Mean Err	Abs M.E.	RMSE	SI	Corr Coeff
W_s(M/S)	14.56	7.16	14.33	6.61	-0.24	2.79	3.76	25.83	0.854
W_d	-	-	-	-	3.02	25.41	44.64	-	-

Table 5. Summary of all model/measured wind comparisons.

The mean difference between hindcast and measured peak H_s was +0.53 m (1.24 rms), but there was a systematic tendency to over-hindcast peak H_s in severe storms. To account for the neglect of shallow water processes in the hindcast model, deep water spectra were transformed to shallow water by application of the Kitaigorodskii factor to the whole of the hindcast spectrum, assuming that wind-wave spectra in shallow water followed a self-similar form described by the TMA spectrum (Bouws et al. (1985)). The effect of scaling the hindcast peaks for shallow water effects changed the sign of the mean difference (-0.59 m) and led to lower rms errors overall (1.05 m). The comparison of time histories of wave height and period from unscaled and scaled spectra suggests that most hindcasts of severe storms on the Grand Banks will require a shallow water wave model, even though on a day-today basis, the wave regimes on the Grand Banks may be adequately treated as deep water.

Mean differences between hindcast and measured peak H_s were higher for this study than for the Mobil Hibernia hindcast (+0.26 m, 1.19 m rms). This may actually be a consequence of more accurate hindcasting in this study compared to previous studies. There have been a number of

small refinements in the hindcast procedures used in this study, each of which could have a slight effect on the mean properties of the hindcasts, but which taken together could lead to a small increase in peak wave height. In particular, the wind fields have been calculated on a finer grid and have taken full advantage, in the validation storms, of the rig winds in the kinematic analysis step. The pressure gradients are better resolved on the finer grid, allowing perhaps somewhat higher winds. The interpolation of wind fields to 2-hour time steps using the moving centers algorithm also better conserves wind maxima on time steps intermediate to map times. In the wave model, the fine mesh grid covers a larger domain than used in previous applications on the East Coast. The time step is reduced from 3 hours to 2 hours, and the revised source term can produce slightly higher sea states, other things equal, if the wind field is changing rapidly.

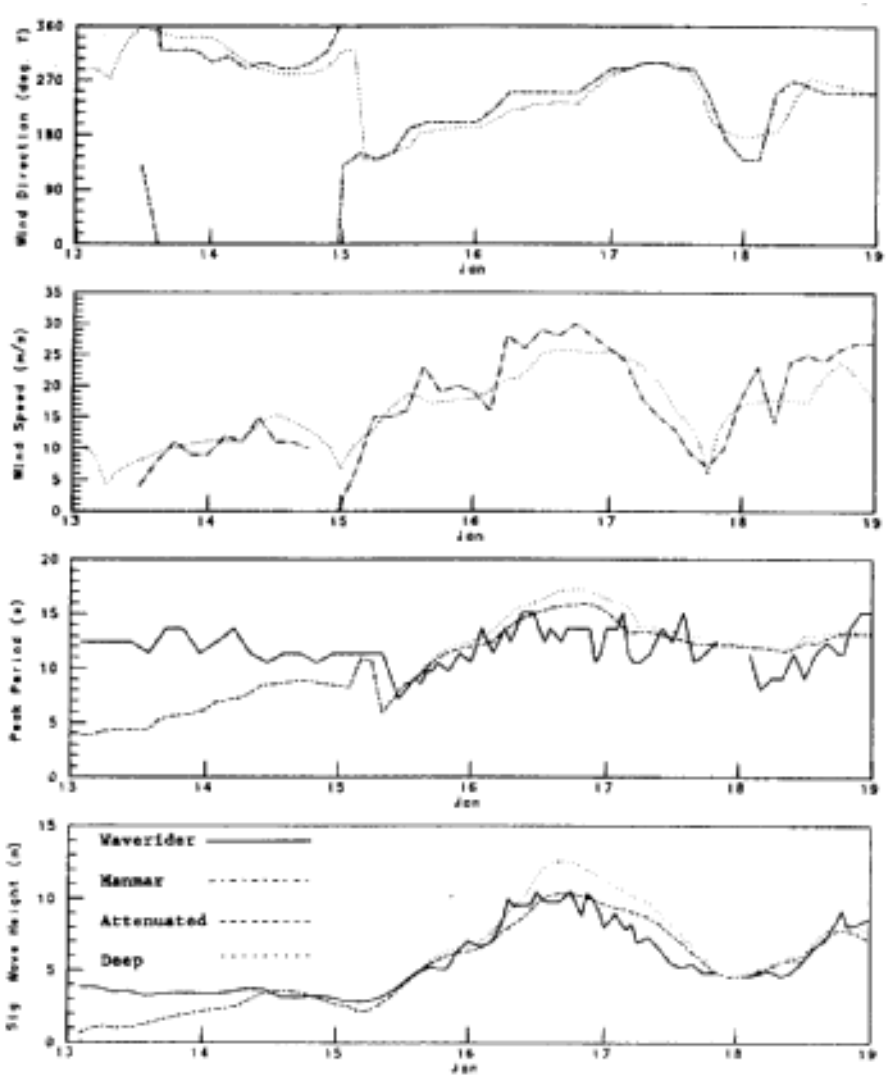

Figure 2. Wind/wave time series comparison for January 1982 - Grand Banks. GP 3744 versus Ocean Ranger at Hibernia J-34.

On the Scotian Shelf, the comparisons between hindcast and measured sea states were significantly affected by the sheltering effects of Sable Island, which was not resolved in the hindcast model. It was obvious from the time history comparisons, that whenever the direction placed the measurement site in the lee of the island, the hindcast sea states were overspecified. Otherwise, the comparisons were generally excellent. Shallow water effects appeared to be secondary to sheltering effects in determining the skill in deep water hindcasts. Probably at most measurement sites the water was deep enough for the spectral content of the sea states excited such that the waves could be considered deep water. Scaling improved the results somewhat at the shallower measurement sites even on the Scotian Shelf.

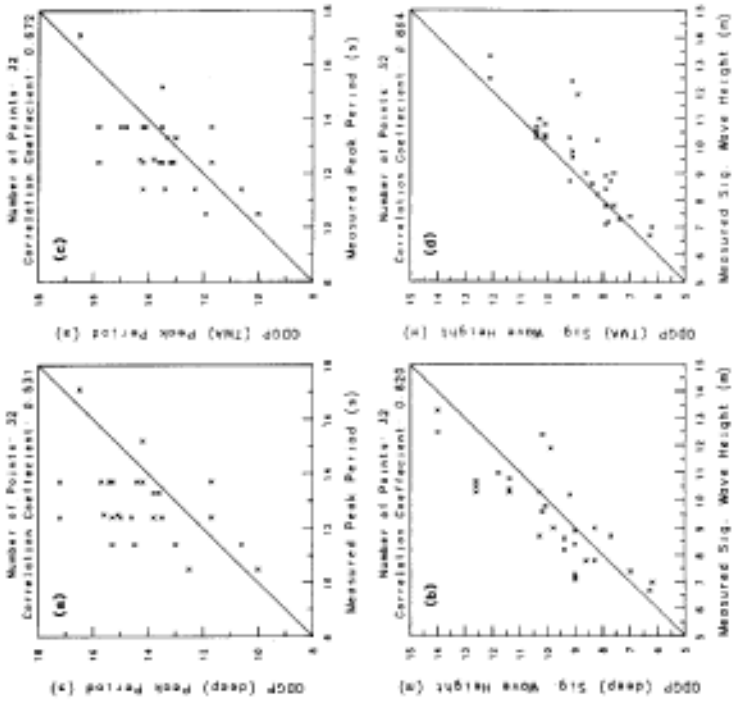

Figure 4. Peak model versus peak measured wave values:
(a), (b) deep water; (c), (d) TMA scaled.

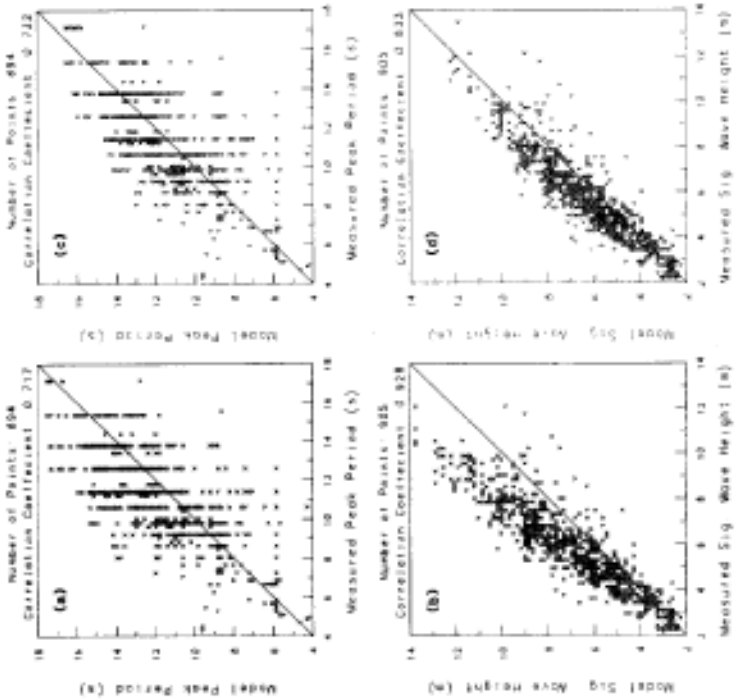

Figure 3. Model versus measured wave values:
(a), (b) deep water; (c), (d) TMA scaled.

Overall, the peak-peak comparisons in H_s and T_p indicated skill comparable to the highest reported in previous studies of this kind. The scatter index of 13.2% (11.2% for scaled data) in H_s is close to the scatter index of 11.9% in the ODGP hindcast comparisons reported by Reece and Cardone (1982), and to the skill reported for even 3rd generation model hindcasts in mid-latitude Northern Hemisphere basins. It should be noted that the peak-peak comparisons in this study have been made from measured peaks taken as the absolute highest sea state estimated within the measured time series. This procedure will tend to degrade the comparisons. Smoothing of the measurements to the time scale of the model might improve the peak-peak wave height comparisons, as would allowing for spatial variations in the selection of hindcast peaks rather than using only the nearest grid point for comparison. However, as in most applications of this kind, the dominant contribution to hindcast errors is probably the effect of spatially coherent wind field errors which, unfortunately, are probably not further reducible, given the present density of surface marine observations and the inherent inaccuracies of ship wind observations.

7. PRODUCTION OF HINDCASTS

Wind and deep-water wave hindcasts were produced for all selected storms following the wind and wave model validation. Wind speed (effective neutral 20-m winds), wind direction, significant wave height, peak period, and vector mean wave direction were archived at all ODGP grid points, both coarse and fine grids, every 2 hours, for each storm. Directional (2-D) spectral variance (15 frequencies x 24 directions) were archived every 6 hours only at 118 selected points. Since only the deep water case was run in the production phase, the hindcast results will tend to be somewhat conservative.

8. EXTREMAL ANALYSIS

From the wind/wave hindcast model the following quantities were available at all points and at each time step:

H_s	significant wave height
T_p	spectral peak period
Θ_d	vector mean wave direction
W_s	1-hour average wind speed
W_d	wind direction

Extremes of H_s, W_s, H_m (maximum individual wave height), were specified at all grid points within the contiguous domain of the fine grid extending from Georges Bank through the Scotian Shelf to the Grand Banks, using the Gumbel extreme value distribution fitted by the method-of-moments. Confidence limits (90%) were also calculated .

At a selected subset of 25 grid points on the fine grid which matched archive grid points in the 3-year wave climate study (Eid et al.,

1989) and grid locations nearest specific exploration areas of high interest (e.g., Venture, Hibernia), a more detailed analysis of extremes was carried out. The maximum individual wave height was estimated in each storm from the hindcast zeroth and first spectral moments following Borgman's (1973) integral expression, which accounts for storm buildup and decay. The integral was evaluated for two assumed maximum individual wave height distributions: (1) Rayleigh; (2) Forristall (1978).

The same approach was used to estimate the maximum crest height (H_c) at a site in a storm using the empirical crest-height distribution of Haring and Heideman (1978). The median of the resulting distributions of H_m and H_c was taken as the characteristic maximum single value in a storm. The mean ratios of H_m/H_s and H_c/H_s were calculated and used to develop a mean ratio to provide extremes of H_m and H_c from fields of extreme H_s.

9. REFERENCES

Barks, E.A. and W.G. Richards, 1986. The climatology of tropical cyclones in Atlantic Canada. Bedford, N.S.: Atmospheric Environment Service Report MAES 4-86, 15 p.

Borgman, L.E., 1973. Probabilities for highest wave in a hurricane. American Society of Civil Engineers, J. of Waterways, Harbours and Coastal Eng. Div., 99(WW2): 185 – 207.

Bouws, E., H. Gunther, W. Rosenthal and C.L. Vincent, 1985. Similarity of the wind wave spectrum in finite depth water, Part I – spectral form. Journal of Geophys. Res., 90(C1): 975 – 986.

Brown, R.D., P. Roebber and K. Walsh, 1986. Climatology of severe storms affecting the Canadian east coast areas. Environmental Studies Research Funds, Report Series No. 020. Ottawa, Ont., 233p.

Cardone, V.J., 1969. Specification of the wind field distribution in the marine boundary layer for wave forecasting. Report TR-69-1, Geophys. Sci. Lab., New York University.

Cardone, V.J., 1978. Specification and prediction of the vector wind on the United States continental shelf for application to an oil slick trajectory forecast program. Final Report, Contract T-35430, NOAA, U.S. Dept. of Commerce, Silver Spring, Maryland.

Cardone, V.J., W.J. Pierson and E.G. Ward, 1976. Hindcasting the directional spectrum of hurricane generated waves. J. Petroleum Technology, 28, 385 – 394.

Cardone, V.J., D. Szabo and F.J. Dello Stritto, 1989. Development

of extreme wind and wave criteria for Hibernia. Proceedings of the 2nd International Workshop on Wave Hindcasting and Forecasting, Vancouver, B.C., April 25-28, 1989.

Corson, W. D., D. T. Resio and C. L. Vincent, 1982. Wave information study for U.S. coastlines, report I: surface pressure field reconstruction for wave hindcasting purposes. Vicksburg, MS: U.S. Army Engineer Waterways Experimental Station, Technical Report HL-80-11, 24 p.

Eid, B.M., C.M. Morton, V.J. Cardone and J.A. Greenwood, 1989. Development and evaluation of a wave climate data base. Proceedings of the 2nd International Workshop on Wave Hindcasting and Forecasting, Vancouver, B.C., April 25-28, 1989.

Forristall, G.Z., 1978. On the statistical distribution of wave heights in a storm. J. of Geophysical Research: 88 (2353 - 2358).

Haring, R.E., and J.C. Heideman, 1978. Gulf of Mexico rare wave return periods. Offshore Technology Conference Paper 3230.

Lewis and Moran, 1984. Severe storms off Canada's east coast: a catalogue summary for the period 1957 to 1983. Canadian Climate Centre Report No. 84-13, AES, Downsview, Ont.

MacLaren Plansearch Limited, 1985. Evaluation of the Spectral Ocean Wave Model (SOWM) for supporting real-time wave forecasting in the Canadian east coast offshore. Prepared under contract for Atmospheric Environment Service, Downsview, Ontario.

Neumann, C.J., G.W. Cry, E.L. Caso and B.R. Jarvinen, 1978. Tropical cyclones of the North Atlantic Ocean, 1971-77. National Oceanic and Atmospheric Administration, Asheville, N.C., 170 p.

Reece, A.M. and V.J. Cardone, 1982. Test of wave hindcast model results against measurements during four different meteorological systems. Offshore Technology Conference Paper 4323.

Swail, V. R., 1985. Geostrophic wind climatology of Canadian marine areas. Downsview, Ontario: Atmospheric Environment Service. Canadian Climate Centre Report 85-9, 52 p.

United States. Naval Oceanography Command Detachment, 1983. U.S. Navy hindcast spectral ocean wave model climatic atlas: North Atlantic Ocean. Washington, DC: U.S. Government Printing Office, Report No. NAVAIR 50-1C-538, 375 pp.

A MULTI-FACETED WIND-WAVE HINDCAST METHOD TO DESCRIBE A SOUTHERN CALIFORNIA WAVE CLIMATE

R.E. Jensen, C.L. Vincent, and R.H. Reinhard

Coastal Engineering Research Center
U.S. Army Engineer Waterways Experiment Station
Vicksburg, Mississippi 39181-0631

1. INTRODUCTION

A 20-year wind-wave hindcast was performed for the Southern California Bight of the Pacific Coast from Point Conception, California to the U.S-Mexican border. This study must resolve a highly complex system of forcing functions and local effects that control the wave climate. Such mechanisms include: large scale forcing by northern Pacific swell; synoptic East Pacific wind fields southern hemisphere swell; and localized effects such as island sheltering and diffraction, as well as meso-scale meteorological systems such as land-sea breezes.

The purpose of this paper is to describe the methodology developed to hindcast wind-waves in Southern California. The hindcast is broken into three parts, wind field generation (synoptic scale and meso-scale), Northern Pacific wave generation, and localized Southern California Bight wave generation.

2. WIND FIELD GENERATION

One of the most important factors governing the estimation of a wave climate is the critical assessment of the winds in the study area. Both the synoptic-scale, and meso-scale effects contribute to the generation of the wave field. This leads to a twofold solution method. Synoptic scale winds were generated from gridded surface pressure fields, Holl and Mendenhall (1971). Calculations of surface wind fields were made in a coordinate system that consisted of great circle paths that included much of the Northern Pacific Ocean Basin, (Figure 1). Geostrophic to gradient to near surface wind conditions were computed from techniques described in Resio, et al. (1982).

The coastal wind pattern along the Southern California Bight is affected by a land-sea breeze pattern. A variation in flow is caused by the heating of the land surface during the day, and cooling during the evening. Historical evidence has suggested that the land breeze (blowing from land to sea) is strongest in the winter months and the sea breeze is strongest in the summer. Eight land based meteorological stations along the Southern California Bight were used to evaluate the land-sea breeze effect, (Figure 2). The data sets spanned the period from 1956-1975, (hourly observations from 1956-1965, and 3-hour

observations from 1965-1975). Although gaps in the records appeared with a certain amount of regularity, they were not detrimental to the analysis outlined later. The land-based meteorological data showed that the synoptic-scale winds were not the only factor governing local wind fields. Synoptic-scale wind variations normally occur over days, whereas the land based station data indicated significant variation over several hours. These variations were assumed to be a result of the land-sea breeze effect.

A procedure was sought to incorporate the land-based winds into the synoptic-scale winds to account for the land-sea breeze. The requirements were that the solution be time dependent and statistically representative of the physical phenomena.

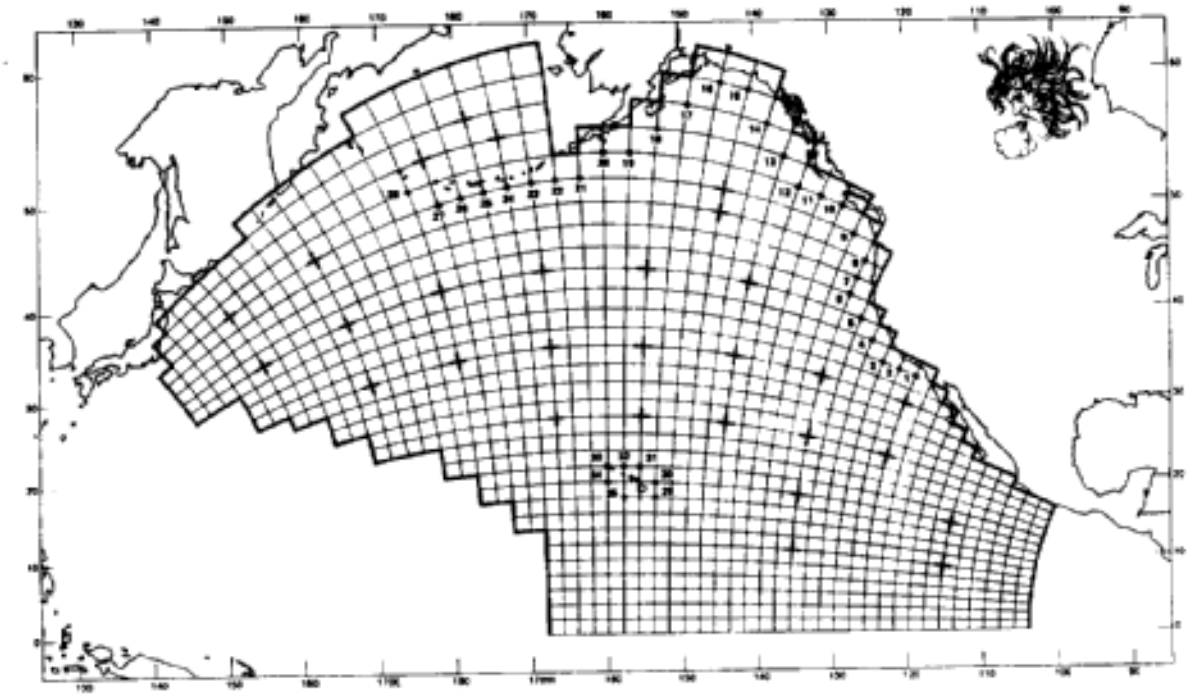

Figure 1. Wave Information Study (WIS) Phase I grid for the North Pacific (2 deg, Mercator projection)

The spatial and temporal variation (on a daily, monthly and yearly basis), the intensity, the lateral extent, the triggering mechanisms, and the overall contribution of the land-sea breeze effect to the synoptic-scale winds had to be considered.

A simple approach decoupling the winds into X and Y components (independent of all other physical properties), was used as a first attempt to describe the land-sea breeze pattern. The months of February, May, August and November were selected as the baseline for the analysis, two months in an intense land-sea breeze regime(February

and August) and two months during a non-land-sea breeze time period. Time histories for each station were resolved into X and Y components. The components were scaled according to the maximum displacement (ranging from 10 to 40 m/s) occurring in any given 24-hour period (Figure 3).

$$X'(t) = [WS(t) \cdot \cos (WD(t) - \bar{X})]/M_x \quad (1)$$

$$Y'(t) = [WS(t) \cdot \sin (WD(t) - \bar{Y})]/M_y \quad (2)$$

Y'(t) =(2)

Where:

WS(t) = hourly or 3-hour wind speed at the 10-m elevation
WD(t) = wind direction (mathematical coordinate system)
$\bar{X}$ = mean X component signal for all 24-hour periods in a month
$\bar{Y}$ = mean Y component signal for all 24-hour periods in a month
M_x = maximum X displacement in the 24-hour period
M_y = maximum Y displacement in the 24-hour period
X'(t) = response function for the X component of the wind
Y'(t) = response function for the Y component of the wind.

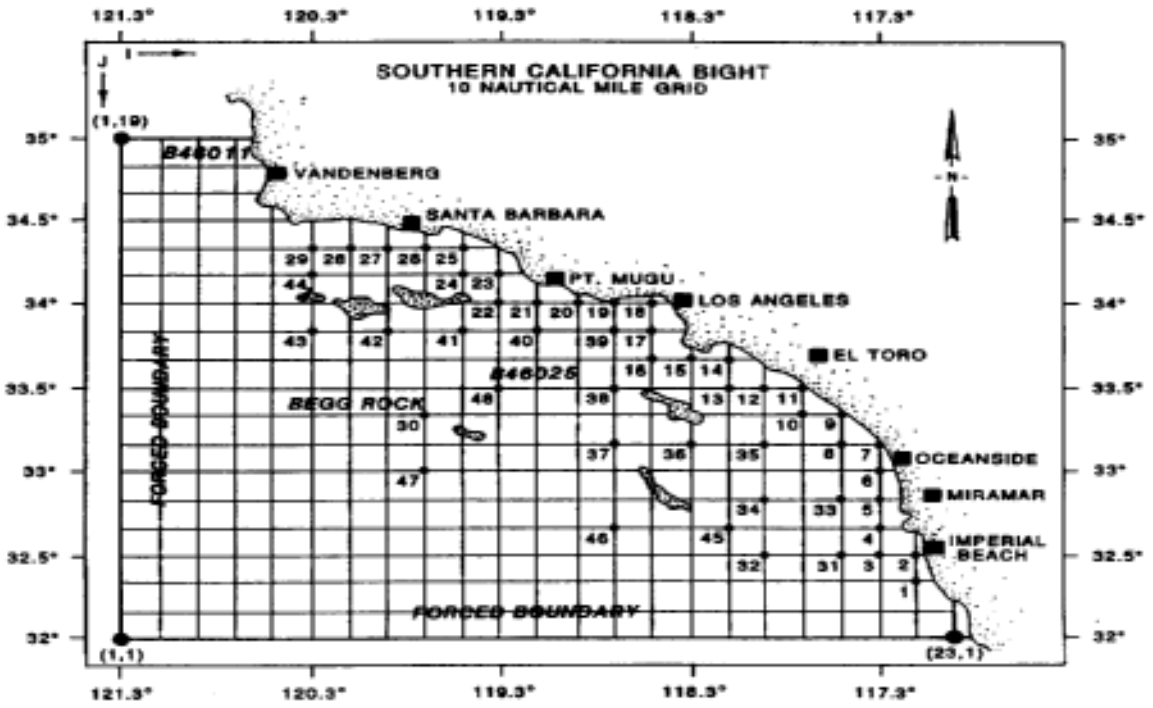

Figure 2. Southern California Bight study area, (10-nm grid)
■ Meteorological stations

Although the variance about the hourly mean signal was large in magnitude, magnified by the formulations used, the trends in the mean response function for all stations were well established. This was further verified through an analysis of the actual deviations from the mean response. The deviations closely approximated a normal distribution. It was concluded that the variations from the mean response could be accounted by simple random noise that was amplified by the nondimensional scaling. This procedure was followed for all 8 stations, and similar trends were displayed indicating that land-sea breeze effects are evident over the entire Southern California Bight. Changes in angles from one site to the next are primarily caused by changes in the shoreline orientation. For example, Imperial Beach displayed a periodic displacement in the East-West direction, winds from Los Angeles varied more Northeast-Southwest, and at Point Mugu, a well defined Southwesterly component was observed. The additional physical parameters governing the land-sea breeze effect such as, wind speed, wind direction, cloudiness, and air-sea temperature differences were assumed to be of lower order and thus neglected. The remaining 8 months were similarly analyzed and response functions (dimensionless hourly average X'(t) and Y'(t) components) defining the land-sea breeze at the 8 station locations were developed.

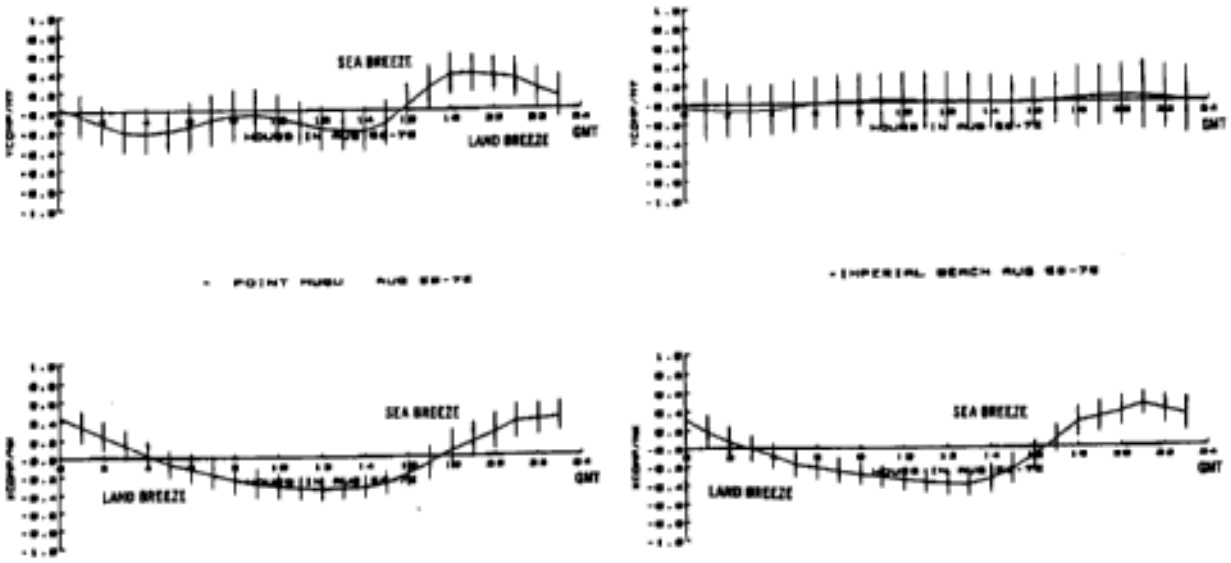

Figure 3. X'(t) and Y'(t) average response function for land station wind information mean conditions for all Januarys 1956-1975. Vertical lines represent one standard deviation

From the above analysis, the land-sea breeze effect was directly related to the shoreline orientation, so rather than work on the Cartesian coordinate system (Figure 2) a new orthogonal coordinate system was created, based on a logarithmic fit to the shoreline. This made the alongshore interpolation between the 8 locations less

cumbersome, and also simplified the calculations of the land-sea breeze extent in the offshore direction. It was assumed that the maximum offshore extent of the land-sea breeze was 20-nm. Weighting functions were generated for spatial interpolation and also for temporal interpolation relating phase differences between the stations. A mapping routine was generated to relate the Shoreline-Normal grid to the original (X,Y) grid (or I,J grid) shown in Figure 2 .

The procedures thus far have dealt with the generation of a statistically sound model that reproduces the land-sea breeze along the entire Southern California Bight. We have established average response functions (X'(t) and Y'(t)) for each station for each month. A 20-year time history (1956-1975) at the 8 locations were used to evaluate the daily X and Y maximum displacements (M_x and M_y) and the values were tabulated. Also, a correlation coefficient was computed relating the daily response functions (in X and Y) to the mean functions. This correlation coefficient was used to determine if that particular day represented a land-sea breeze day.

The procedure to combine the synoptic-scale winds with the land-based meteorological data worked quite simply. It followed:

$$W(I,J) = \lambda \bullet W_{syn}(I,J) + (1 - \lambda) \bullet W_{ind}(I,J) + \varepsilon \bullet W_{ind}(I,J) \quad (3)$$

where:

$W(I,J)$ = blended wind condition at point (I,J),
$W_{syn}(I,J)$ = synoptic scale wind at (I,J),
$W_{ind}(I,J)$ = land based wind condition at (I,J),
λ = Weighting function relating the spatial variation between the land and synoptic scale wind for non-land-sea breeze days,
ε = Weighting function for the land-sea breeze effect, related to the correlation coefficient for the day, and to the temporal variation in offshore extent.

Two important factors are evident in Equation (3), the land-sea breeze effect is an additive effect superimposed on the synoptic-scale wind conditions, and 2) this equation retains the characteristics of the land station information. The triggering of the land-sea breeze effect was based on the precomputed daily correlation coefficient at each station location. From the analysis, a correlation coefficient of 0.6 (or greater) was selected to identify a land-sea breeze day.

Synoptic scale wind fields derived from the WIS Phase I deepwater wind hindcast are input every 3 hours on a 2-deg spherical orthogonal grid. That information is spatially interpolated to a 10-nm grid (Figure 2), and linearly interpolated to a one hour time step. Measured wind conditions from the 8 land based stations are accessed as well as all

pre-computed statistical quantities. For each day the correlation coefficient was checked to determine, if at that particular location a land-sea breeze day was in effect. If so, λ was set to 1.0, and the land-sea breeze was generated based on the synthesis of the daily observations and the mean response function. The temporal interpolation weights were systematically used, covering the 24-hour period. If the meteorological station data indicated that the land-sea breeze effect was not in effect, then the wind speeds were simply blended, (ε = 0.) and based only on spatial parameters.

Unfortunately, few data exist to verify the methods employed in this study. Ship observation information was available, but was limited by the accuracy of the location. Hence, synthetic tests were used to validate the procedures. It was found in all cases that the procedure performed adequately. One source of error was uncovered during this process, the Vandenberg site consistently represented the land-sea breeze effect for a shoreline orientation in a North-South direction, rather than an East-West direction. That meant the site was located closer to the Northern Pacific Basin, and was not indicative of conditions present in the Southern California Bight. Because of this, the Vandenberg information was deleted from the procedure.

3. FORCED TWO-DIMENSIONAL SPECTRAL BOUNDARY CONDITION

The contribution of Northern Pacific storm systems to the wave climate in the Southern California Bight can be included by two methods. The first method is to hindcast the entire Pacific Ocean Basin using the same grid spacing employed in the study area (10-run) . This method becomes computationally and cost prohibitive realizing the geographic extent and the duration of the hindcast. The second method employs successively nesting smaller scale grids until the study area is quantified. This method optimizes computational time in-lieu of resolving details not required in each gridded area. The nested-grid method was adopted in this study.

The Pacific Coast Wave Information Study (PCWIS) generated a 20-year wind-wave hindcast derived from historical surface pressure and measured wind data for the North Pacific Ocean basin (Figure 1). A discrete spectral wave model was used to generate the wave condition, Resio (1981). output information consisted of two-dimensional (frequency/direction) spectral estimates every three hours for the period 1956-1975, Corson, et al. (1986). Twenty frequencies (from 0.03 to 0. 22 Hz), and 16 direction bands (at 22.5 deg intervals) were used to approximate the frequency/direction spectra. Energy derived from wind-seas under active growth were estimated via parametric relationships. Two-dimensional spectra from PCWIS Stations 1-4 (Figure 1) were used to drive the open boundary in the Southern California Bight hindcast study, (Figure 2). Additional spectral estimates from

the Phase II PCWIS study (based on a 0.5-deg grid) supplemented areas between the original 2-deg information, Corson, et al. (1987).

4. SOUTHERN CALIFORNIA BIGHT HINDCAST

An arbitrary water depth, pseudo-discrete, spectral wave model, SHALWV Hughes and Jensen (1986) was employed in the 20-year hindcast study, using the aforementioned wind fields and spectral boundary conditions as input. The theoretical framework relies on four fundamental assumptions. One, the total momentum flux from the atmosphere to the water surface is approximately constant and independent of the water depth. Two, the partitioning of this momentum into the current field and wave field is approximately constant and independent of the water depth. Three, the spectral shape of the waves being generated is approximately constant in wave number space and is independent of the water depth. And four, wave-wave interactions are the primary mechanism by which wave energy transformed to the forward face of the spectrum. Spectral energy is stored in a discrete matrix of frequency and direction bands for each computation point, but the sources and sinks in the energy balance equation associated with energy input, transfer and dissipation are parameterized.

The homogeneous portion of the energy balance equation is solved first. All steady-state mechanisms and associated parameters (such as the ray trajectory equation for refraction and shoaling mechanisms) are precomputed and stored for later use, hence reducing the numerical calculation to a single propagation step in time. Wave energy in each discrete frequency-direction band is propagated independently using a first-order upstream differencing scheme. This is a step-wise solution that estimates the change in energy level and direction along the wave ray that is capable of propagating into the grid point in one time step.

During this process, the effects of island sheltering and diffraction were estimated.

In the 10-nm grid portions of the offshore islands were resolved and defined as land points. No energy is allowed to propagate through these land points. Since many islands are irregular in shape or relatively small compared to the 10-run grid spacing, a method was developed to include spectral energy sheltering. The method of solution is sub-scale modeling of these features, embedded in the 10-run grid. A series of coefficients were generated that represent the percentage of energy in an angle band allowed to reach a grid point. The coefficients were determined via graphical means. Only points surrounding island locations were considered.

Energy propagating toward a point directly behind an island may be geometrically sheltered by an island, but some of the energy will

reach the shadow region by diffraction. Island diffraction is also included in SHALWV, based on original work by Penny and Price (1952). This method applies Sommerfield's solution for diffraction of light waves at the edge of a semi-infinite screen to water wave diffraction at the edge of a semi-infinite breakwater or in this case, an island. The method is based on: a) linear wave theory (and the principle of linear superposition in the spectral version), b) uniform water depth, c) semi-infinite breakwater, and d) complete reflection off the breakwater. Only the effects of diffraction in the lee of the island are considered in this application. Diffractive effects are applied only to energy that has been sheltered. Thus, it adds back a percentage of the energy that was initially lost due to sheltering.

After the propagation sequence, energy is added to or removed from each discrete energy band by the source terms. These source/sink mechanisms consist of wind-wave growth, nonlinear wave-wave interactions, high frequency dissipation, and surf zone breaking Jensen (1987). At the end of each time step (600 seconds for this study), the directional spectrum at each grid point is calculated as the sum of the independently propagated spectral elements and the changes in energy caused by the source/sink mechanisms. This sequence was followed for the Southern California Bight hindcast study for the 20-year period of record, (1956-1975) at two-month intervals, with provisions for a restart mechanism. This insured continuous simulation of the wave environment without loss in energy levels from one run to the next. Actual run time for a two-month simulation was approximately 50 minutes on a CRAY 2 computer.

5. 12-19 JANUARY 1988 STORM SIMULATION

An intense storm, accompanied by high winds and damaging surf, struck the southern California coast on 17-18 January 1988. The storm was associated with an intense extratropical cyclone which formed about 500-nm west of the California coast on 16 January. Three reasons for its damaging effect were the minimum pressure of 990.5 mb (the lowest level measured in over 100 years), the initial generation area location, and eventual storm track relative to the southern California coastline. Measurements of significant wave heights in the area ranged from 6.0 to 10.0 m.

Dr. V.J. Cardone, Oceanweather, Inc., was contracted to develop a description of the surface wind fields (on a 2-deg spherical orthogonal grid, Figure 1) for this storm. The wind fields were produced with the best effort consistent with the meteorological data available at the time Cardone (1988). These data consisted of basic weather maps and surface weather observations available in real time. The wind field estimates are being improved at this time, (based on additional data) and the wave conditions will be re-hindcast based on

those improvements. Hence, the results shown in Figure 4 are preliminary.

The wave hindcast was performed on three spatial scales, a 2-deg grid covering the Northern Pacific Ocean basin, a 0.5-deg grid covering a subscale region from 29 to 41 deg N latitude and 118 to 134 deg W longitude. The final region was the 10-nm grid system shown in Figure 2 . All subscale wind fields (the 0.5-deg and 10-run gridded systems) were generated directly by vectorally averaging the original 2-deg winds. Hence, they are a gross approximation of what occurred during the storm, and are not a direct outcome of Dr. Cardone's original analysis. Comparisons were made to offshore buoy data. Cardone's 2-deg grid wind speeds and directions compared favorably to the buoy data. Comparisons between measured conditions and interpolated winds clearly showed a disparity, principally caused by the interpolation. This will be resolved during the re-analysis process.

Energy-based wave heights and peak spectral wave periods are compared in Figure 4 for various locations in the 0.5-deg grid and the 10-nm grid. Agreement between wave estimates and measured buoy data is good with the exception of Buoy 46011. This buoy is located slightly west of Point Conception. The primary discrepancy between the estimated and measured conditions is caused by the lack of energy in the initial portion of the estimated storm sequence. At the beginning of the storm simulation the buoy measured 3.0 m waves generated by a cyclonic disturbance located in the northern region of the Pacific Ocean basin which was not part of the kinematic analysis procedures used in the estimation of the southern storm system. This energy propagated along the Oregon-California coastline in a south-easterly direction. Wave measurements at Begg Rock (near location I=9, J=9 in Figure 2) exceeded 10 m whereas the model simulation maximum was at 8.5 m. Approximately 20-nm east of this location (Buoy 46025), the wave conditions peaked at 8.0 m, indicating that additional energy producing storm near the Oregon coast influenced selected regions in the Southern California Bight.

6. SUMMARY

A 20-year, wind-wave hindcast for the Southern California Bight was performed. Numerous site-specific techniques were used to resolve the land- sea breeze effect, include wave attenuation from island sheltering and diffraction, and represent multiple wave populations in a complex coastal regime. Results of the study will be presented in a Wave Information Study (WIS) report, documenting the methods and procedures in greater detail.

7. ACKNOWLEDGMENTS

I would like to acknowledge Dr. D. T. Resio, OCTI, Inc. for his efforts in the generation of the land-sea breeze methodology, Ms. Jane M. Smith, CERC, for her assistance in the island sheltering and diffraction portion of this work, Dr. V. J. Cardone, Oceanweather, Inc., for providing the wind fields for the 12-19 January 1988 storm sequence, and Mr. Jack E. Davis, CERC, for generating the final graphics. This research was conducted at the Coastal Engineering Research Center, Waterways Experiment Station, as part of the work unit Wave Estimation for Design" of the Coastal Flooding and Storm Protection Program of the United States Army Corps of Engineers. Permission was granted by the Chief of Engineers to publish these results.

8. REFERENCES

Cardone, V.J., 1988: Surface wind fields in north Pacific storm of January 12 - 19, 1988. Oceanweather, Inc. , Informal Report submitted to Coastal Engineering Research Center, USAE Waterways Expt. Station, Vicksburg, Miss.

Corson, W.D. and Co-Authors, 1986: Pacific coast hindcast deepwater wave information. WIS Report 14, USAE Waterways Expt. Station, Vicksburg, Miss. and Co-Authors, 1987: Pacific coast hindcast Phase II wave information. WIS Report 16, USAE Waterways Experiment Station, Vicksburg, Miss.

Holl, M.M. and B.R. Mendenhall, 1971: The FIB methodology and application. Meteorology International, Inc., Monterey, Calif.

Hughes, S.A. and R.E. Jensen, 1986: A USERS Guide to SHALWV, Numerical model for simulation of shallow-water wave growth, propagation and decay. Instruction Report, CERC-86-2, USAE Waterways Expt. Station, Vicksburg, Miss.

Jensen, R.E., 1987: Modeling spectral wave conditions. Proc. Coastal Hydrodynamics, ASCE, Newark, Del., 28 June-1 July, 603-617.

Penny, W.G. and A.T. Price, 1944: Diffraction of sea waves by a breakwater. Artificial Harbors, Technical History No. 26, Sec. 3-D, Directorate of Miscellaneous Weapons Development.

Resio, D.T., 1981: The estimation of a wind wave spectrum in a discrete spectral model. J. Phys. Oceanogr, 11, 510-525.

Vincent, C.L. and W.D. Corson, 1982: Objective specification of Atlantic ocean wind fields from historical data. WIS Report 4, USAE Waterways Expt. Station, Vicksburg, Miss.

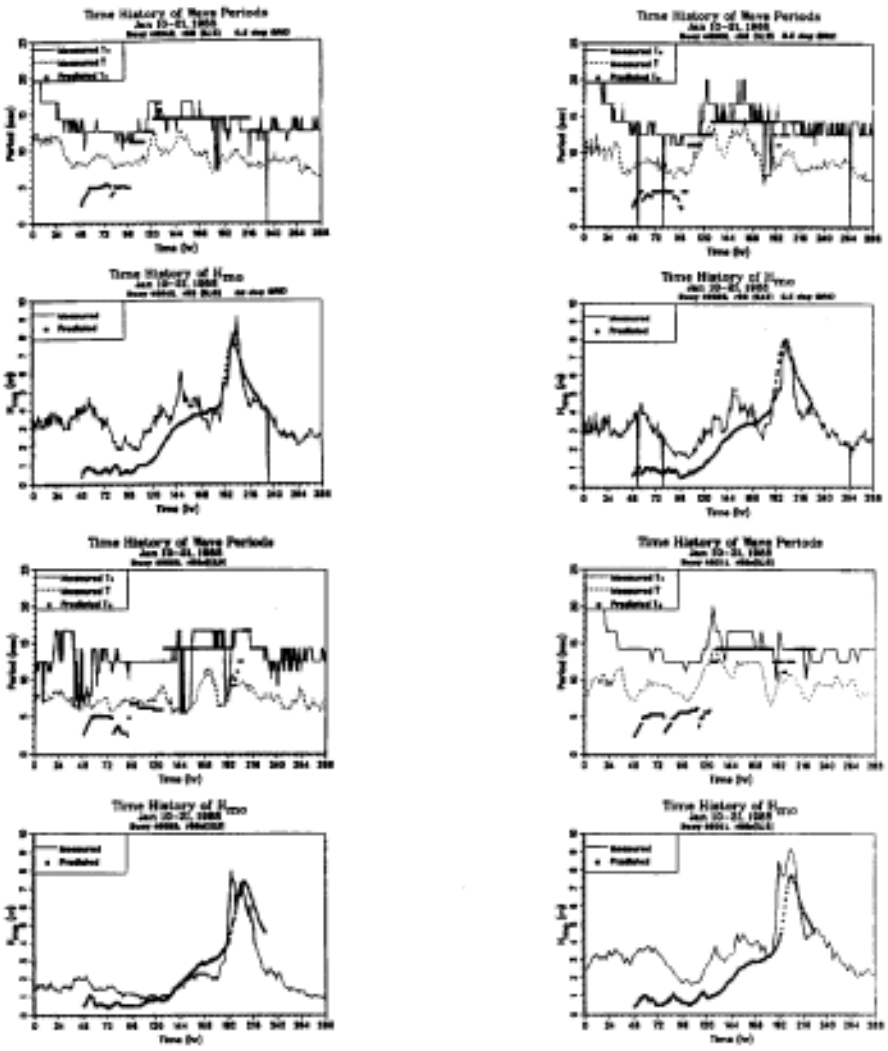

Figure 4. Comparison between hindcast and measured energy based wave heights and peak spectral wave periods. Locations of buoys are: NDBC 46042 (36.8N, 122.4W), NDBC 46028 (35.8N, 121.9W), NDBC 46011 (34.9N, 120.9W), NDBC 46025 (33.7N, 119.1W).

A WINDWAVE HINDCAST FOR THE GREAT LAKES 1956-1987

J.M.Hubertz

CEWESCRO
U,S.Army Engineer Waterways Experiment Station
Vicksburg.Mississippi 39180-0631
601-634-2028

1. INTRODUCTION

The Wave Information Study (WIS) is a project within the U.S. Army Corps of Engineers (USACE) Coastal Field Data Collection Program. The objective of the study is to provide information on the climatology of waves and water levels along U.S. coastlines. The project began in 1976 with a study of storm generated waves on the Great Lakes. Since that time 20 year hindcasts have been completed for the Atlantic, Pacific, and Gulf of Mexico U. S. coastlines. Presently a 32 year hindcast for the 5 Great Lakes is under way.

Previous hindcasts for the Great Lakes include those done by Resio and Vincent (1977,1978) and recent work done by the Canadians, Ontario Ministry of Natural Resources, 1988. The former study considered only storm events up to the early 1970's and reported the results statistically for stations along the U.S. coasts. The time series of wind and wave information was not saved. Since that time, the quantity and quality of meteorological data has improved. The Canadian hindcasts are continuous in time, but the time interval of the hindcasts vary from 1971-1985 for Lake Erie, 1964-1983 for Lake Ontario, 1962-1970 for Lake Superior, and 1953-1987 for Lake Huron, Lake Michigan was not part of the study. Time series of wind and wave information is available, but at a limited number of stations, from 6 to 13, on the Canadian shoreline only.

The present study will add to the wind and wave information database for the Great Lakes by supplying time series of winds and directional wave spectra at stations closest to shore on a 10 mile grid for each of the 5 lakes for the period 1956-1987.

2. WINDFIELDS

The methodology employed in the present study to derive windfields over the lakes is basically the same as in the previous hindcasts mentioned above. It is accepted that the best method to obtain the climatology of winds over a bounded water body such as the lakes is to use available wind records at shore stations. The quality of the derived winds of course depends on the number of shore stations, their location, and the quality of the recorded wind data. The ease of obtaining the winds depends on whether the data are in digital or analog form.

There is a satisfactory number and distribution of land stations on the boundary of the lakes for which digitized wind data are available over a long enough time period to employ this method for each lake. Winds will be better defined on some lakes than on others because of the amount of data available and the size of the lake. The land stations employed in this study are shown in Figure 1 . In addition to the land stations, note that there are National Atmospheric and Oceanographic Administration (NOAA) buoys in four of the five lakes. These buoys provide an added source of wind data for a portion of the hindcast time period. They are removed from the lakes during the winter, typically beginning in Nov.-Dec. and ending in April-May. In addition to wind data, the buoys record wave motion which is analyzed to one dimensional wave spectra (directional spectra are not available), and parameters such as significant wave height and peak period as a function of time.

The first step in the hindcast procedure is to extract wind speed and direction for three hour intervals from archived data supplied by the National Climatic Data Center (NCDC). The windspeed reported to the closest knot is the one minute average windspeed. The wind direction is reported to the closest 10 degrees. The data are edited since there are times when measurements are missing. Most of these gaps are of short duration and values are interpolated to make the time series continuous. Times are adjusted to GMT. A number of corrections are then applied to the edited time series at each station. The wind speeds are adjusted to the 10 meter level from the normal level of 6.1 meters using a power law relationship with an exponent of 1/7, Richards et. al.(1966), Davenport (1960). A correction to the wind speed for the effects of air-sea temperature difference on the stability of the air column and for the difference of surface roughness between land and water is applied according to Schwab (1978). Air-sea temperature differences for each lake as a function of month of year and direction in 10 degree intervals were obtained from Resio and Vincent (1977).

The 32 year time series of windspeeds were processed as above at each of the land stations. The only correction applied to the buoy windspeeds was for elevation. Next windfields were interpolated over the lakes using the land time series of winds and buoy winds when available. The interpolation scheme consists of determining weighting factors, for each model grid point, which depend on the location of the land and buoy stations. An inverse power law is used in determining the weights so that the influence of a station on grid points away from the station could be varied. The higher the power, the less influence the station has on surrounding grid points. The windspeed at a grid point is then the sum of the products of the windspeed at each land and buoy station times the weighting factor

associated with that grid point and land or buoy station. Since the land and buoy locations are fixed, these weighting coefficients need only be calculated once. Windfields are calculated over each lake grid by years and stored on magnetic tape for input to the wave model.

Interpolated winds were verified against buoy measurements by using only land stations to derive the winds and then comparing the calculated winds at a buoy site to those measured by the buoy. Table 1 below summarizes the differences between the interpolated and calculated winds at NOAA buoy 45005 in Lake Erie for 1983. The numbers in the matrix are the differences to the closest percent of the percent occurrence of wind speed at the buoy minus the percent occurrence of interpolated wind speed for various speed and angle bands.

TABLE 1

PERCENT OCCURRENCE DIFFERENCE BETWEEN BUOY AND INTERPOLATED WINDS

Knots	Central angle of 22.5 degree angle bands															
	0	22	45	67	90	112	135	157	180	202	225	247	270	292	315	33
0-1.9	0	0	0	0	0	0	0	0	0	0	0	0	0	0	0	0
2-3.9	0	0	1	0	1	1	0	0	0	0	0	1	0	0	0	0
4-5.9	0	0	1	1	0	1	0	0	0	0	0	0	-2	0	-1	0
6-7.9	0	-1	-2	1	0	0	0	1	0	0	0	1	-2	0	-2	0
8-9.9	0	0	-3	1	0	-1	-2	0	0	0	0	1	-1	0	-2	0
10-11.9	0	0	-3	1	0	-1	-1	0	1	1	-1	1	-1	0	-2	0
12-13.9	0	0	-1	1	0	0	-1	0	0	0	-1	1	0	-1	-1	1
14-15.9	0	1	-1	1	0	0	-1	0	0	0	-1	1	0	0	-1	0
16-17.9	0	0	-1	0	0	0	0	0	0	0	0	1	0	0	0	1
18-19.9	0	0	0	0	0	0	0	0	0	0	0	0	0	0	0	0
20-21.9	0	0	0	0	0	0	0	0	0	0	0	0	0	0	0	0
22-23.9	0	0	0	0	0	0	0	0	0	0	0	0	0	0	0	0
24-25.9	0	0	0	0	0	0	0	0	0	0	0	0	0	0	0	0
26-27.9	0	0	0	0	0	0	0	0	0	0	0	0	0	0	0	0
28-29.9	0	0	0	0	0	0	0	0	0	0	0	0	0	0	0	0
30 & >	0	0	0	0	0	0	0	0	0	0	0	0	0	0	0	0

Table 1 indicates that for this year and location, the interpolated windspeed is distributed across speed and angle bands in the same way as the measured windspeed. Only the period April through December is represented here since all the NOAA buoys are removed from the lakes during the winter season. The differences between the wind speeds and directions (buoy interpolated) for a portion of the 1983 time series at this location are shown in Figures 2 and 3 respectively, illustrating that the calculated winds track the measured winds in time. This is for a time when the windspeed and direction fluctuations are large compared to the summer months when they are smaller. This degree of similarity is typical for other locations where the spacing of land stations is comparable. The standard deviations for windspeed and direction differences are respectively 2.5 knots and 52 degrees.

The large value for direction is due to a number of cases where the difference was large due to one value being greater than 0 and the other less than 360 degrees. Adjusting these cases to fall within the same quadrant while retaining the magnitude of the differences results in a standard deviation of 35 degrees.

FIGURE 1 LOCATIONS OF LAND STATIONS AND BUOYS

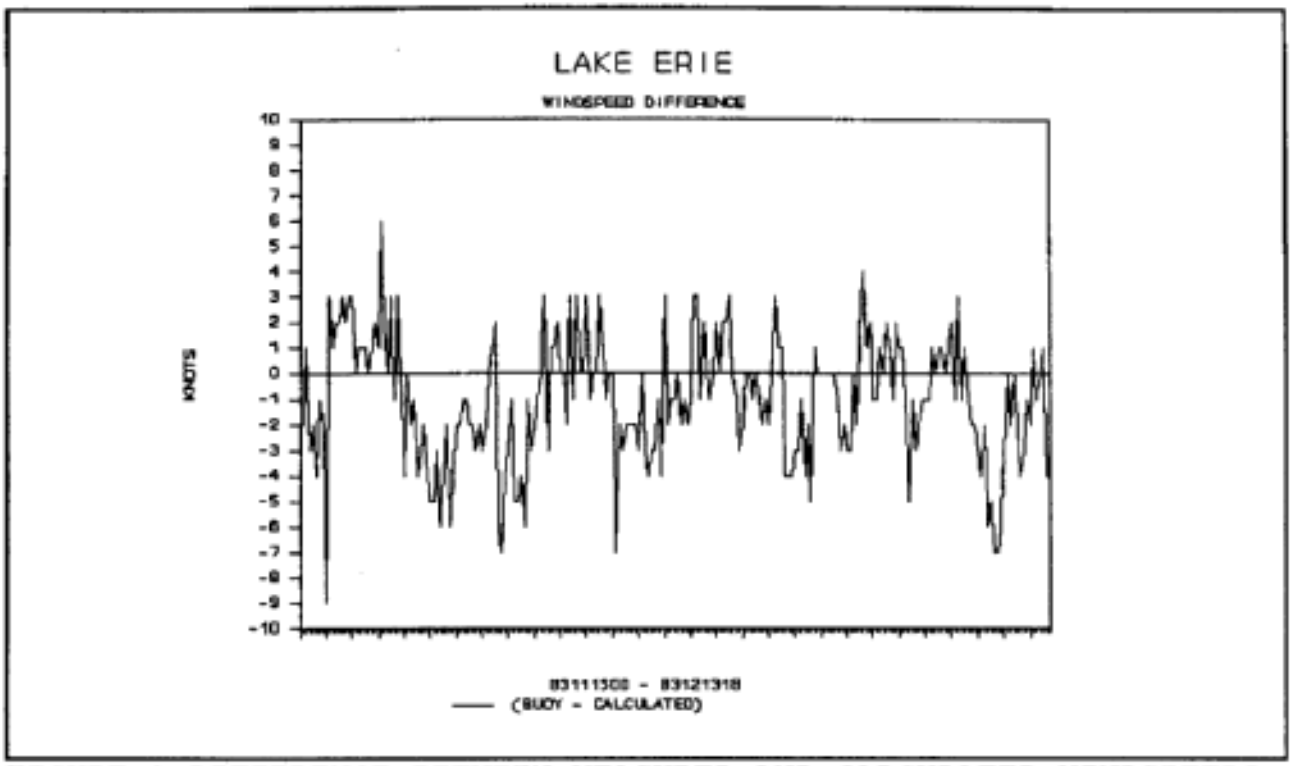

FIGURE 2 DIFFERENCE BETWEEN MEASURED AND CALCULATED WINDSPEEDS

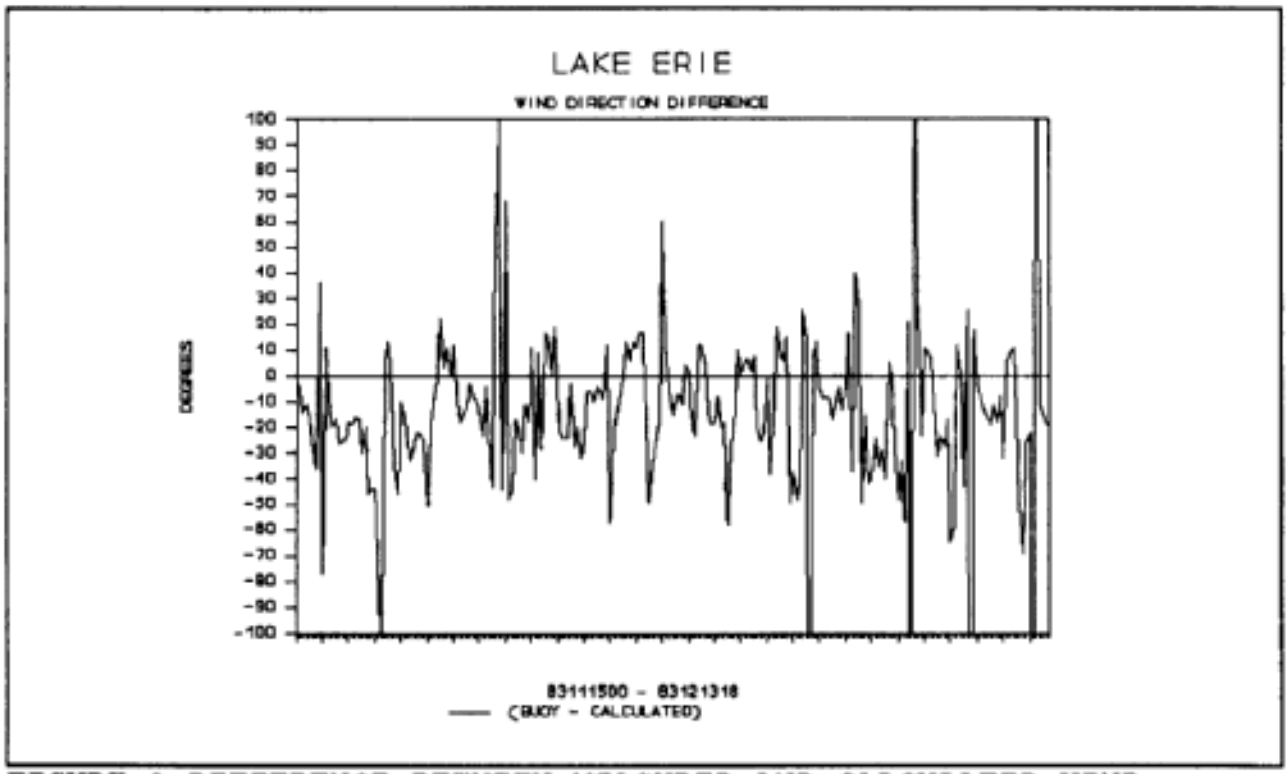

FIGURE 3 DIFFERENCE BETWEEN MEASURED AND CALCULATED WIND DIRECTIONS

3. WAVE MODEL

The WIS deep water wave model used in this study was developed by Resio (1989). It is a discrete directional spectral model which simulates wave growth, dissipation, and propagation in deep water. Spectra are represented by energy in discrete bands of frequency and direction. Typically 20 frequency bands and 16 direction bands. Energy above the highest frequency band is represented in a parametric region extending to a cut off frequency determined by a one knot wind. The model is driven by a wind source term which is a function of wind speed, peak frequency, frequency and direction of the wind and waves. A wave-wave interaction source term controls the transfer of energy across frequency bands while maintaining a frequency to the minus 4 equilibrium range. This source term is dependent on the peak frequency, among other factors, which is allowed to evolve implicitly over a time step rather than remaining fixed as in other models. Four parameters control the rate of change of peak frequency and can be defined independently either on an empirical basis or from numerical constraints. The model satisfactorily reproduces measured wave conditions with these parameters fixed over a range of meteorological conditions from large intense Pacific storms and Gulf and Atlantic hurricanes to relatively low wave conditions in the Great Lakes. The model reproduces wave growth with fetch and duration comparable to that observed in the JONSWAP experiment. The model employs a simple linear upstream differencing propagation scheme which allows faster execution than higher order schemes without detriment to applications.

4. PRELIMINARY RESULTS

Some preliminary wave hindcast results are available at the time of this writing for Lake Michigan. The model was run for a number of wind conditions in 1986 and the results compared to available data from the two buoys in Lake Michigan, Figure 1 . The first comparison, which represents one of the larger occurrences of wave height and period on northern Lake Michigan, is for the case of a low northwest of the lake resulting in southerly winds of 30 knots over a period of about 12 hours. Measured and hindcast wave heights and periods are shown respectively in Figures 4 and 5 . The model represents the change in wave conditions as the front passes over the lake from 25-30 September, but under estimates the peak of wave heights and periods by approximately 1 meter and 2 seconds respectively. The accuracy of the buoy measurements for height and period is respectively plus or minus 0.5 meters and plus or minus I second. Further analysis of this case indicated that the interpolated wind speeds dropped off too quickly to the south of the buoy site. This is a result of the spacing of the land stations used in the interpolation. Special analysis of the windfields with blending of any available ship observations is needed for cases like this.

The second comparison is at the southern buoy for a nine day period from September 9-18 when winds were initially from the south from 9/9 to 9/12, then shifted to from the north from 9/12 to 9/17 and then returned to from the south on 9/18. Wind speeds varied with the maximums being approximately 16 to 25 knots.

FIGURE 4 COMPARISON OF MEASURED AND HINDCAST WAVE HEIGHT RESULTS

FIGURE 5 COMPARISON OF MEASURED AND HINDCAST WAVE PERIODS

Comparisons of measured and hindcast significant wave heights and peak periods are shown in Figures 6 and 7 respectively.

The model satisfactorily represents the fluctuations of wave height and period for this period of varying wind speeds and directions. The model peak period appears low in situations when wind speeds drop, but this is due to the selection criteria of peak period in the model. Examination of the spectrum shows almost equal amounts of energy at lower frequencies. If one of these lower frequencies were chosen as the peak period comparisons would be improved for these cases.

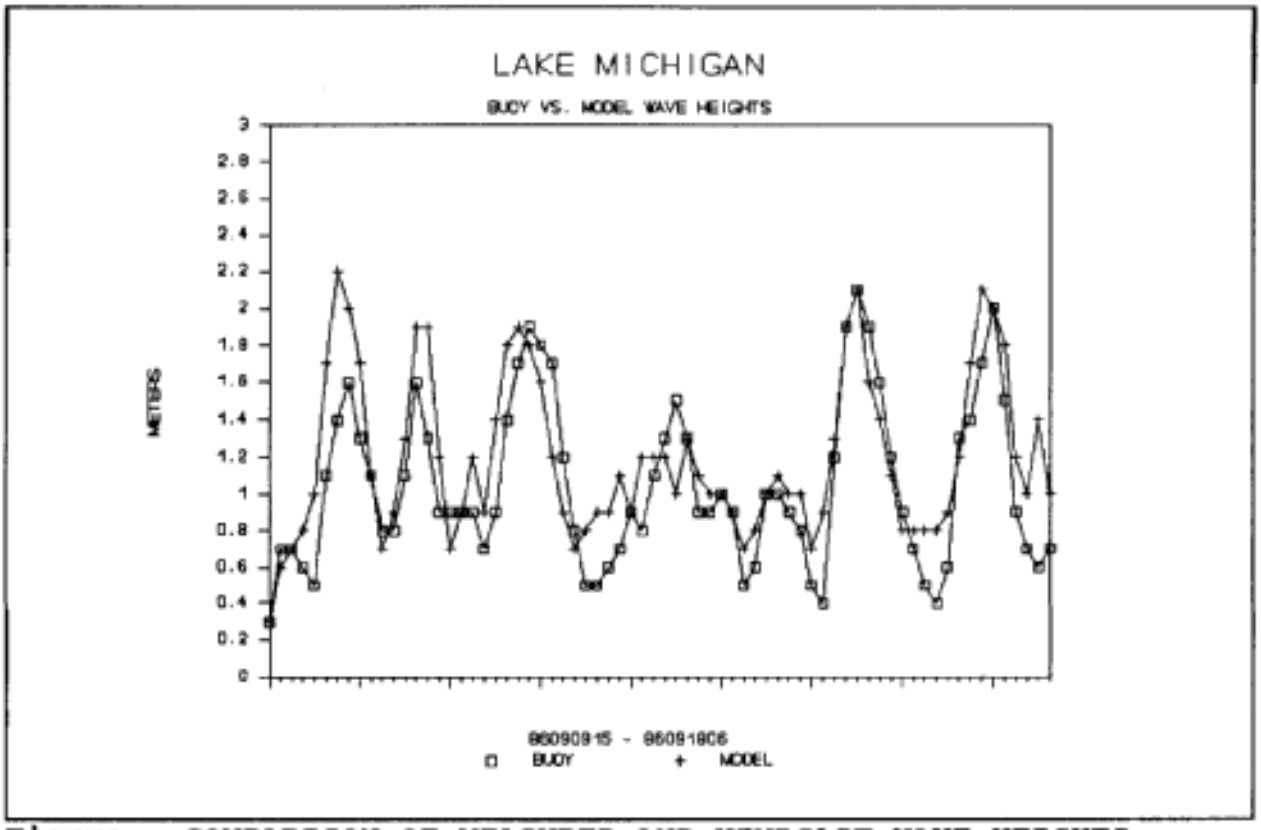

Figure 6 COMPARISON OF MEASURED AND HINDCAST WAVE HEIGHTS

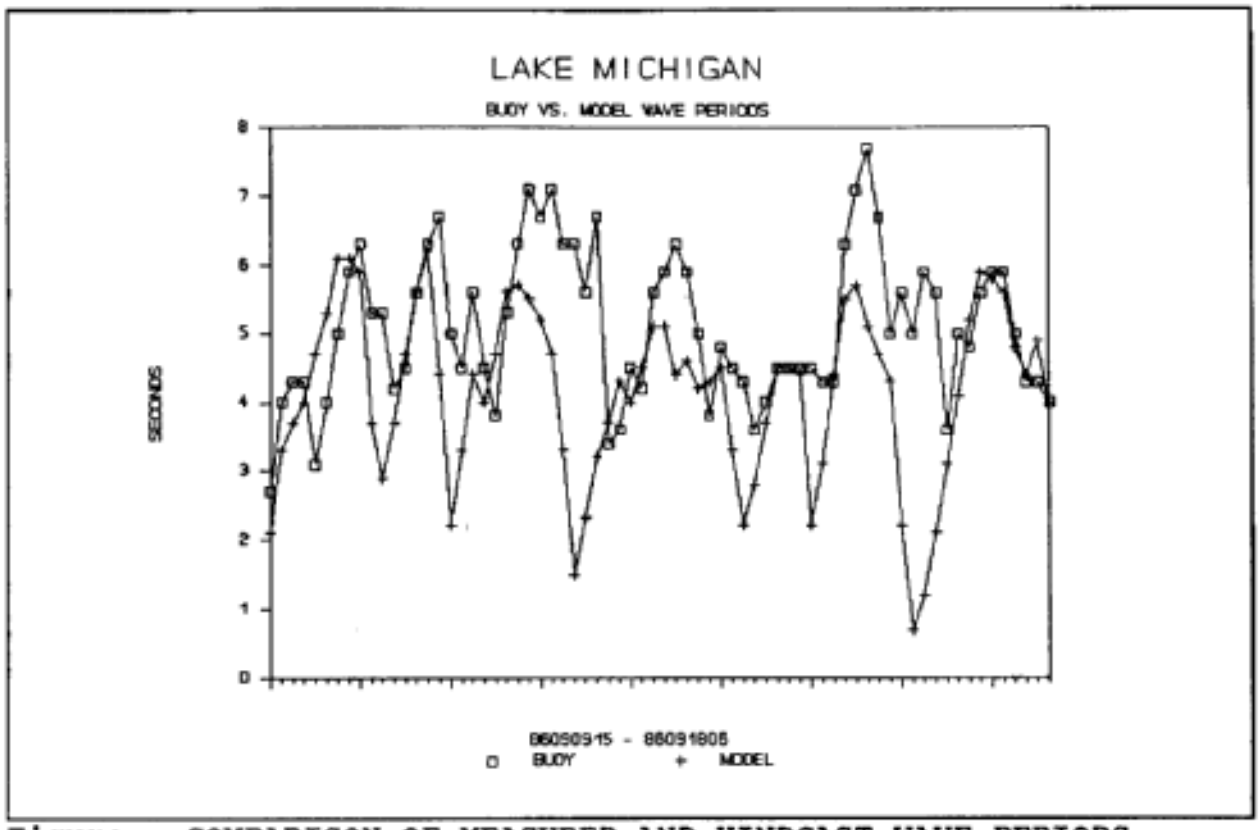

Figure 7 COMPARISON OF MEASURED AND HINDCAST WAVE PERIODS

5. DATABASE

The wave information resulting from these hindcasts will be archived on optical disks by station number as a time series of wind and wave parameters and the two dimensional spectra, in a format similar to the NOAA buoy data. Statistics will be calculated for each station which will summarize; percent occurrence of wave height and period by direction bands and for all directions, mean and maximum wave heights by month for each year, and return periods based on the 32 year hindcast.

6. SCHEDULE

To date windfields have been calculated for lakes Erie, Ontario, and Michigan for the 32 year period. Verification of the wave model based on existing wave measurements is under way on each of the above lakes. Production of wave hindcast information will commence upon completion of the verification studies. Work is beginning on the hindcasts of lakes Huron and Superior and will proceed into 1990 with completion of hindcasts for all the lakes by the end of 1990.

At present, we are hindcasting wave conditions through the winter season assuming no ice coverage and in addition hindcasting the period mid-December through mid-April based on the median ice coverage

reported by Assel et.al.(1983). This median statistic for a 5 km. grid over each lake is based on observations over a 20 year period which are not continuous either in space or time. This lack of data required our use of the median statistic rather than the actual observed percent coverage in the nine two week periods of each year. The observations were made from 1960-1979. We average conditions on the 5 km. grid to determine percent coverage of ice on our 10 mile grid. If the percent coverage is 50 percent or greater, it is assumed that wave generation is zero for the calculation of wave generation with fetch. If the stations closest to shore are ice covered as determined by the 50 percent criteria, wave conditions are assumed zero. Wave information will be reported for both situations, ie assuming no ice coverage and assuming a median coverage.

7. SUMMARY

A wave hindcast of the five Great Lakes for the period 1956-1987 is being conducted by the Wave Information Study of the U.S. Army Corps of Engineers. Results of the study will be presented in reports summarizing statistical wave information. Time series of wave parameters and directional wave spectra at stations on a 10 mile grid over each lake for those stations closest to shore will be available from the WIS database. Completion of the study is scheduled for 1990.

8. ACKNOWLEDGEMENTS

I would like to acknowledge the efforts of Mr. David Driver and Ms. Robin Reinhard in conducting the studies on Lakes Erie and Ontario respectively. They were ably assisted by Mr. Alan Cialone and Mr. “Ike” Eicher throughout the studies.

This work was carried out under CERC’s Wave Information Study, Coastal Field Data Collection Program, Coastal Engineering functional area of Civil Works Research & Development. The author wishes to acknowledge the office of the Chief of Engineers, U. S. Army Corps of Engineers, for authorizing publication of this paper,

9. REFERENCES

Ansel R.A., F.H. Quinn, G.A. Leshkevich, and S.J. Bolsenga, 1983: Great Lakes Ice Atlas, Great Lakes Environmental Research Laboratory, Ann Arbor Michigan 48104.

Davenport, A.G. 1960: Rationale for determining design wind velocities. Amer.Soc.Civil Eng.Struct.Div.J. 86,39-68

Ontario Ministry of Natural Resources, 1988: Great Lakes Wave Climate Database, Policy and Program Development Conservation Authorities and Water Management Branch Room 5620,Whitney Block Queen’s Park,Toronto,Ontario M7A 1W3

Resio, D,T. and C. L, Vincent, 1977: Estimation of winds over the Great Lakes. Amer. Soc. Civil Eng. Waterway, Port, and Coast. Ocean Div. J, 102, 265-283.

Resio, D. T. and C. L, Vincent, 1978: Design wave information for the Great Lakes, Reports 1-5, U.S. Army Waterways Experiment Station Technical Report H-76-1, Vicksburg, MS 39180-0631,

Resio, D.T., 1989: A revised deep water wave model, In Publication by: Coastal Engineering Research Center, U. S. Army Engineers Waterways Experiment Station, P.O. Box 631 Vicksburg,MS 38180-0631.

Richards, T. L., H. Dragert, and D. R. McIntyre, 1966: Influence of atmospheric stability and overwater fetch on winds over the Great Lakes. Mon. Wea. Rev. 94, 448-453.

Schwab, D. J. and J. A. Morton, 1984: Estimation of overtake wind speed from overland wind speed: A comparison of three methods. J. Great Lakes Res. 10 (1), 68-72

RESULTS FROM PCM-SPAIN HINDCAST PROJECTS.

[1]José E. de Luis, [1]José G. Briz, [2]Heinz Günther and [2]Wolfgang Rosenthal.

[1]Programa de Clima Marítimo,
Madrid, Spain.

[2]GKSS, Forachungazentrum
Geesthachtt Federal Republic of Germany.

1.- INTRODUCTION, PROGRAMA DE CLIMA MARITIMO, PCM.

Programa de Clima Marítimo, herein referred as PCM, belongs to the Dirección General de Puertos y Costas, Ministerio de Obras Públicas, SPAIN. Its main goal is the definition of the maritime climate along the Spanish coasts.

PCM is divided into four scientific areas:
- Data base,
- Measured data analysis,
- Wave propagation and oceanographic models,
- Wave generation models.
- and a computer resources area.

PCM gathers, analyzes and archives the wave data collected by the buoys of the REMRO, Spanish buoy net, mostly waveriders, and also wave data from special campaigns, from buoys at the harbours and from some foreign country, -Portugal & Italy, see fig. 1 . A directional Wavescan buoy was deployed in the Bay of Biscay, and another will be deployed in the Mediterranean sea close to Menorca.

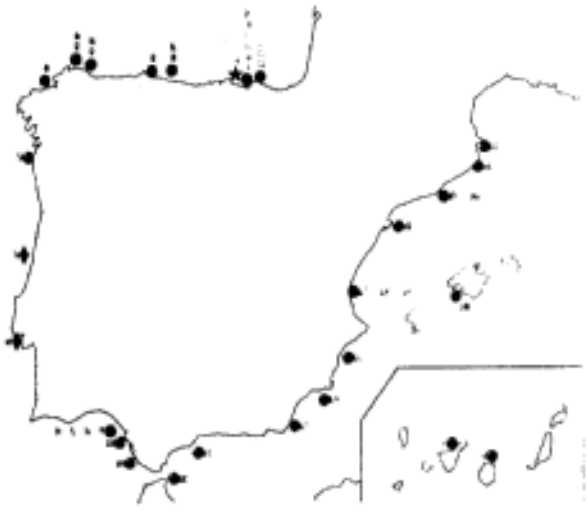

fig. 1.-

PCM Data Base.

Position & identification of the buoys. (Including the Protuguese ones at Figueiras & Cascais).

For hindcast purposes, PCM uses the following models:

- HYPA, its shallow water version, HYPAS, and 3GWAM. HYPA, (the SWAMP Group, 1985), and HYPAS, (the SWIM Group, 1985), were implemented on 1985, are used for most applications. PCM has since then kept a close scientific collaboration with GKSS on the grounds of the application of these models, amongst other subjects.
- As member of the WAM Group, PCM has the 3GWAM model, (WAMDIG, 1988), which is used mainly for research.

2.- HIGHLIGHTS FROM THE NORTH ATLANTIC PILOT WAVE ATLAS.

A two year hindcast was carried out for the development of a North Atlantic Pilot Wave Atlas.

2.1.- Wind calculation from the Spanish Meteorological Office pressure charts.

5000 surface analysis pressure charts, from the Spanish National Meteorological Institute, herein INM, were digitized. From these, a subset covering more than two years was selected, and interpolated to grid fields.

10 m. winds were calculated as geostrophical winds with a correction for friction, based on sea-air temperature differences, Bijvoet (1957), Timmerman (1977). Initially, that difference was made constant, with a seasonal change. Later, actual values from ECMWF archives were used.

2.2.- Pilot hindcast with HYPA.

A pilot hindcast has been run with the above winds. It covered from February 1st. 1981, to March 31st., 1983. HYPA model was used on the grid shown on fig.2 , based on a Lambert conformal projection, and 100 km. grid spacing.

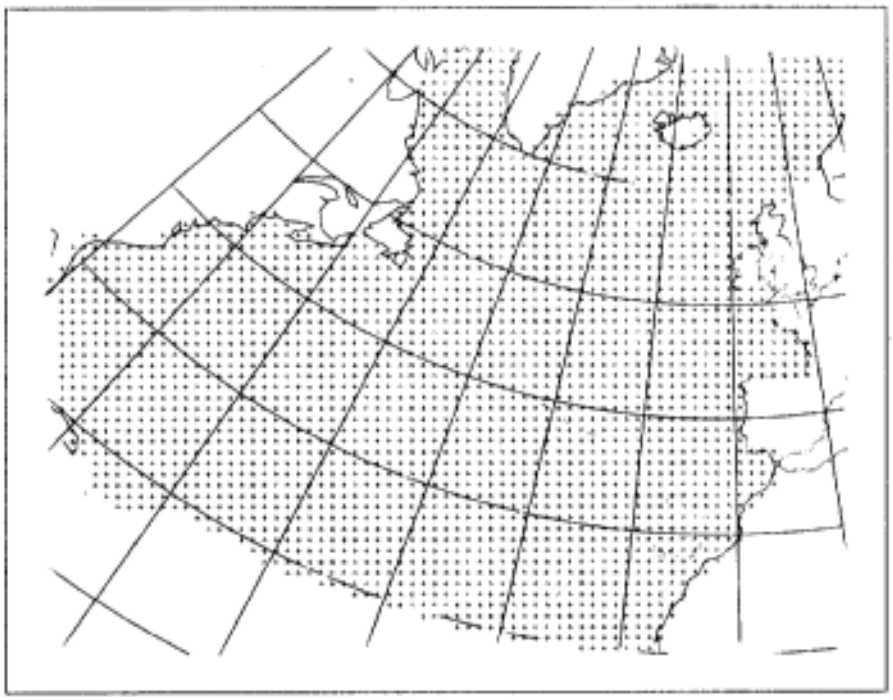

fig. 2.

North Atlantic grid setup for HYPA wave model applications.

Lambert conformal projection.

ENIEPSA buoys location.

HYPA models the windsea with a JONSWAP spectrum and its direction. The swell part is decomposed on 20 frequency bins * 24 directional bins. Open sea boundaries were treated as closed boundaries, and fetch laws were used here.

The following parameters have been archived at each grid point every three hours, (2 bytes per variable, 75 Mbytes per month):

- the windsea JONSWAP parameters and its mean direction,
- directionally integrated swell components, (energy and mean direction per frequency bin),
- integrated parameters (significant wave height, direction, period T_{02}, total windsea energy, total swell energy, mean overall swell direction and peak period, and 1st. and 2nd. order spectral moments), and - wind data, (speed and direction).

2.3.- Statistics/Atlas.

The results from the previous hindcast were used to generate a Pilot Wave Atlas, de Luis, (1988). The atlas was based on a subset of 1.1 variables:

- Total significant wave height, direction and period T_{02},
- wind speed and direction,
- windsea wave height, direction and peak period, and
- swell height, direction and period.

All these variables were archived on a compact format, for all the grid points and every three hours. Thus, all the information for the

whole 24 month hindcast was stored on a single computer tape and the statistics calculation process was simplified.

Mean values were calculated and represented spatially, both for the winter months, (December, January and February), and also for the continuous period, -see fig 3 .

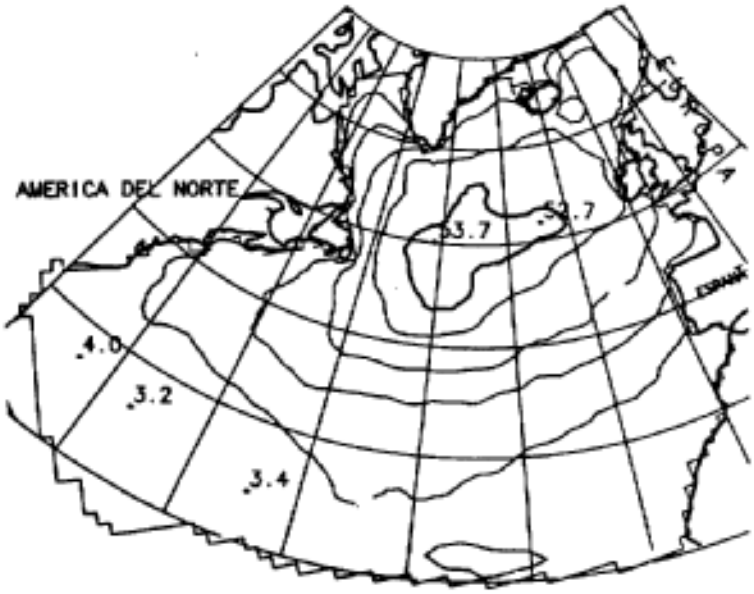

fig. 3.

Pilot Atlas.
Spatial probability distribution for significant wave:

4m. < H_s < 6m.
(Isolines every 10% probability)

Winter months.

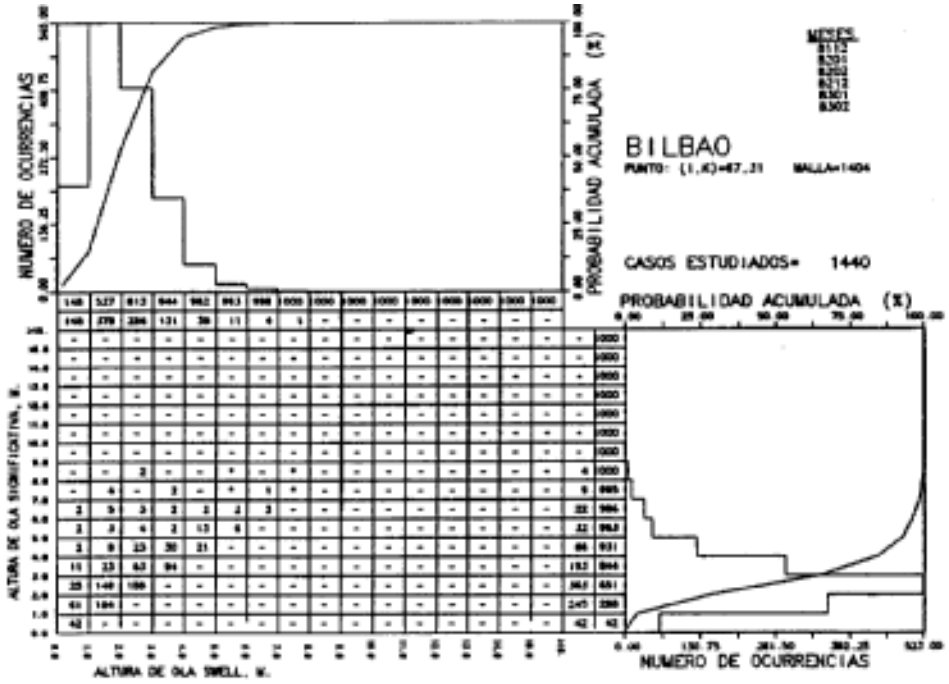

fig. 4.

Pilot Atlas.
Occurrence table, (per thousand cases) at Bilbao

Significant wave height vs. Swell wave height component.

Winter months.

At some selected points, bivariate statistics were processed, -see fig. 4 , as well as persistence studies. Monthly time series were represented for the 11 variables, -see fig. 5 .

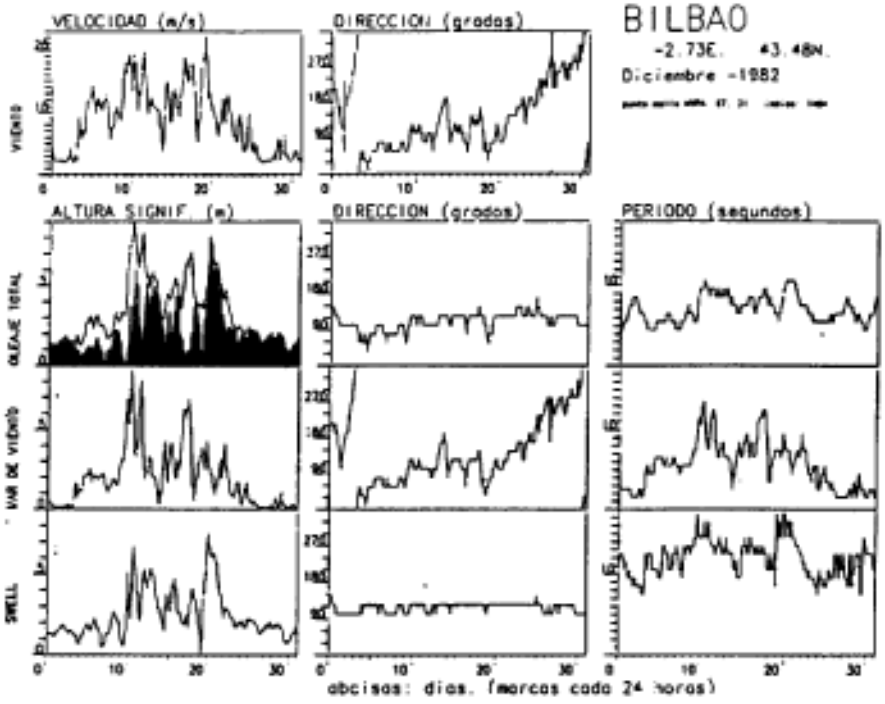

fig. 5.

Pilot Atlas.
Monthly time series at Bilbao, Dec'82.

The darker portion of the significant wave height is its swell component fraction.

2.4.- Validation of the global scheme

Validation studies have been carried out for the global hindcast scheme, based on geostrophic winds calculated from INM surface analysis pressure fields, de Luis, (1988b).

Comparisons have been made with buoy data from different sources: NODC, (U.S), MEDS, (Canada), HALTENBANKEN, (Norway), and buoy data from PCM archives, (SPAIN & Portugal). A subset of the COADS data set for the North Atlantic has also been used, [see 4.1.-]; from here, some other NODC buoys observations have been specifically retrieved, as well as observations from the ocean weather ships CHARLY, MIKE, LIMA and ROMEO. Unfortunately, this subset covers only a few selected periods.

Wind data from both the NODC buoys and meteorological ships have been very helpful for drawing conclusions. Besides local comparisons, spatial ones have also been used, plotting pressure / wind fields *versus* observations. The main conclusions of the validation studies are the following:

* Pressure fields from Spanish INM analysis charts, -and geostrophic wind fields calculated from them, are not reliable

far away from the Spanish shores. This is worse at the West, in the vicinity of the American coasts.

* At the center of the ocean, winds seem to behave better although far away from perfect. This conclusion is only supported by a limited data set from the ocean weather ships extracted from the COADS.

* Haltenbanken data is the only directional data available for the period. At Haltenbanken, the analyst,seems to know the main features of the storm, although he may be missing some local details. Besides, it is close to the extreme of both the weather chart and the HYPA grid. Directional comparisons seems to yield acceptable results,

* Close to the Spanish shores, there are no reliable wind measurements. Wave model results have been checked against buoy measurements at different locations. Unluckily, most of the buoys were deployed near the coast, and were locally protected in some directions; the actual application has not enough resolution. Wave results have been successfully checked against data from the ENIEPSA buoys, at the Bay of Biscay, close to BILBAO, 20 km. away from the coast, see fig. 2 .

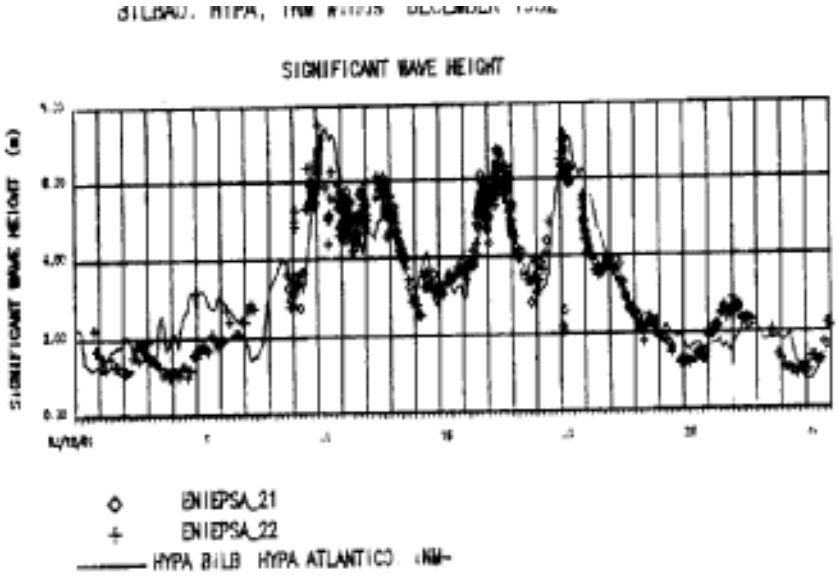

fig. 6.

100 km. North Atlantic grid. (December 1982)

Significant wave height time series:
HYPA results vs. ENIEPSA 21 & 22 buoys measurements. (Bilbao, Bay of Biscay).

Fig 6 . and 7 ., include the comparisons ENIEPSA buoy data versus model results. Although the peaks fit quite well, some model -overshoot happens past them, which explains the scatter.

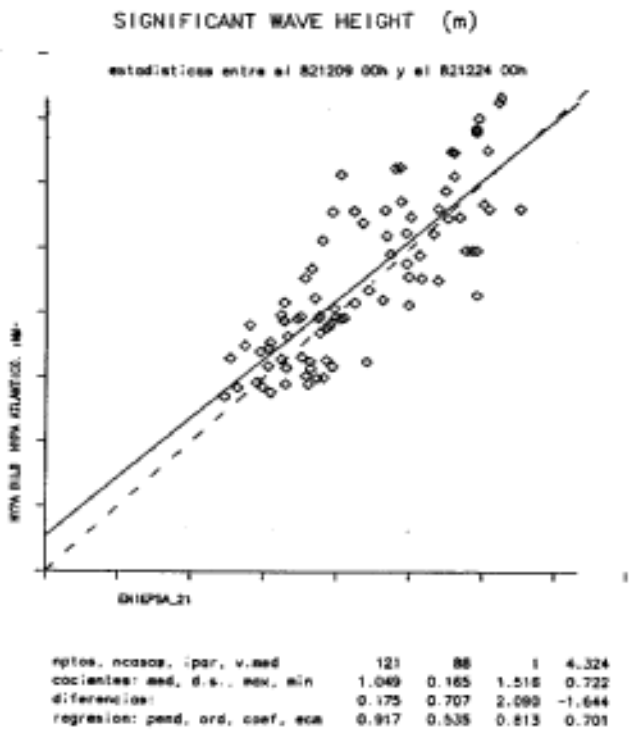

fig. 7.

100 km. North Atlantic grid. December 9-24, 1982, Significant wave height scatter plot: HYPA result vs. ENIEPSA 21 buoy measurement.

2.5.- Wind calculations improvements:

In view of the validation results some actions have been taken in order to improve the windfields.

* Sea-air temperature differences.

Actual values from ECMWF archives have been used instead of seasonal constant values. It showed some model improvements, mostly at Haltenbanken, where the thermal effects might be larger.

* Proper gradient formulation.

The winds were calculated on a regular Cartesian grid defined on the Lambert projection, -true at about 25°N and 62°N. This projection has a -6% error at 45°N, while at the extremes, 20°N and 70°N, the error is +6%. The pressure gradient is calculated with a centered difference scheme. Originally, a constant grid spacing was used, which resulted in overestimations of the winds in the central part of the grid.

Using finite differences formulae with a grid spacing corrected for the local deformation of the projection improved the results.

* Ship-buoy data assimilation through objective reanalysis.

The Objective Analysis Package from the British Met. Office, -herein BMO, has been used in order to improve the wind fields

with actual observations from the reduced data set already extracted from the COADS. Although no final conclusions can be deduced, due to the limited extent of the data set, there are some hints of improvements. Anyhow, if the first guess field is completely wrong, the package might not work properly.

2.6.- Some features of the results.

Swell waves. Storms arriving at the Spanish coasts may sometimes consist mainly of swell. They have been generated by storms reaching the Irish Coasts, drifting later towards Northern Europe. An example of this is the storm that arrives at Bilbao on the 21st. of December 1989, -see fig. 5 and fig. 6 . It has a significant wave height of 7.5 m., as high as the previous wind storm peak. There are some hints from the storm preselection, [see 4.1.-], that this storm may rank around a 10 year return period.

Slanting fetch. During the validation studies, several cases with slanting fetch conditions have been detected, along the Bay of Biscay. It has a very straight shoreline, and there are often winds blowing diagonally from land. These cases are topics of another presentation, Günther, 1989.

Parallel to coast propagation. One of the problems arising when modelling very straights shorelines, and comparing with coastal buoy data, is the propagation component parallel to the coast. It may be affected by the local bathymetry all along its path. Besides the results are very critical with respect to minor deviations in wind directions. Grid and model resolutions are also a very critical factor.

3.- RESULTS FROM MEDITERRANEAN STUDIES.

The Mediterranean Sea is a more complicated case. Both the surrounding orography and its irregular coasts require a high resolution application. The main problem here is to obtain high resolution windfields. Besides there are less reliable wave measurements than in the Atlantic, for model results validation.

BMO wind fields have been used for a study hindcast, using both HYPAS, (25 km. grid) and 3GWAM-cycle 2, (0.5 degrees grid). These winds have a resolution of .9375 degrees longitude *.75 degrees latitude.

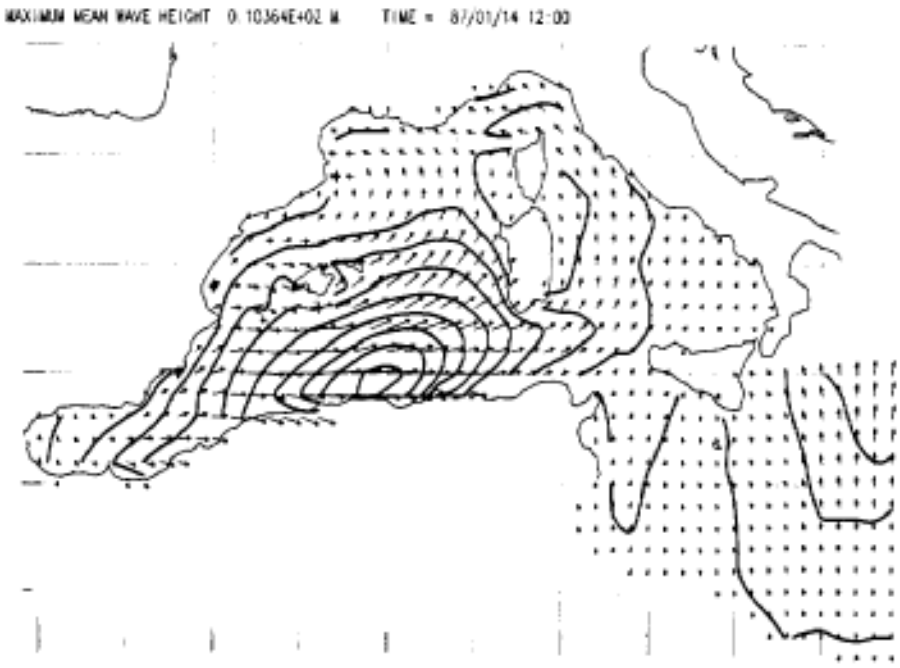

fig. 8.
Western Mediterranean 3GWAM hindcast results with BMO winds. (January 1987)

Significant wave height. 87/01/04 12h.

The main goal behind the current research is to try to define the possible setups that allows a proper execution of the models. (Grid size and orientation, boundary positions, islands, etc.). Actual disagreements between both models could be due to different resolutions, grid setups, different shadowings, etc.

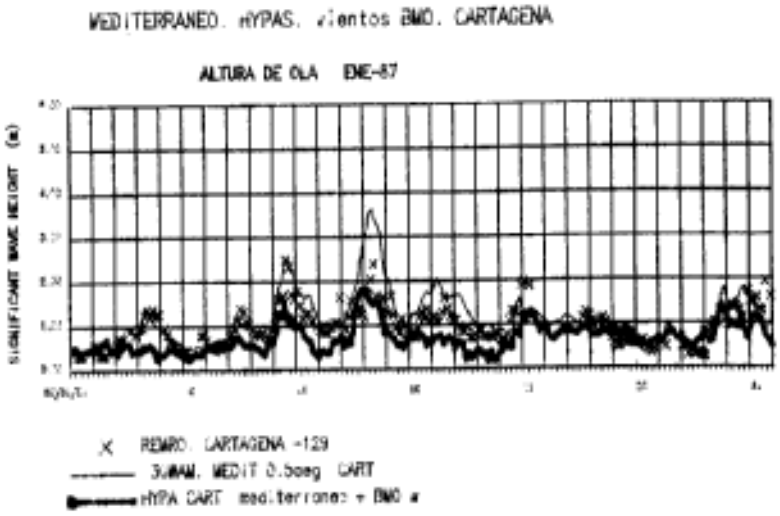

fig. 9.
Western Mediterranean hindcast results with BMO winds. (January 1987)

CARTAGENA REMRO buoy vs. model results:
HYPAS (thick line)
3GWAM (thin line).

Further work should be done also, if higher quality windfields become available, as well as directional wave spectra for validation purposes.

4.- GUIDELINES FOR THE SPANISH STORM AT LAST UNDER DEVELOPMENT,

A Storm hindcast, for the most severe wave height conditions, has been projected under the following assumptions:

4.1.- Guidelines:

* Division into seven regions.

Taking into account the geographical location of the Spanish shores, the area has been divided into 7 regions, as seen in fig 10 .

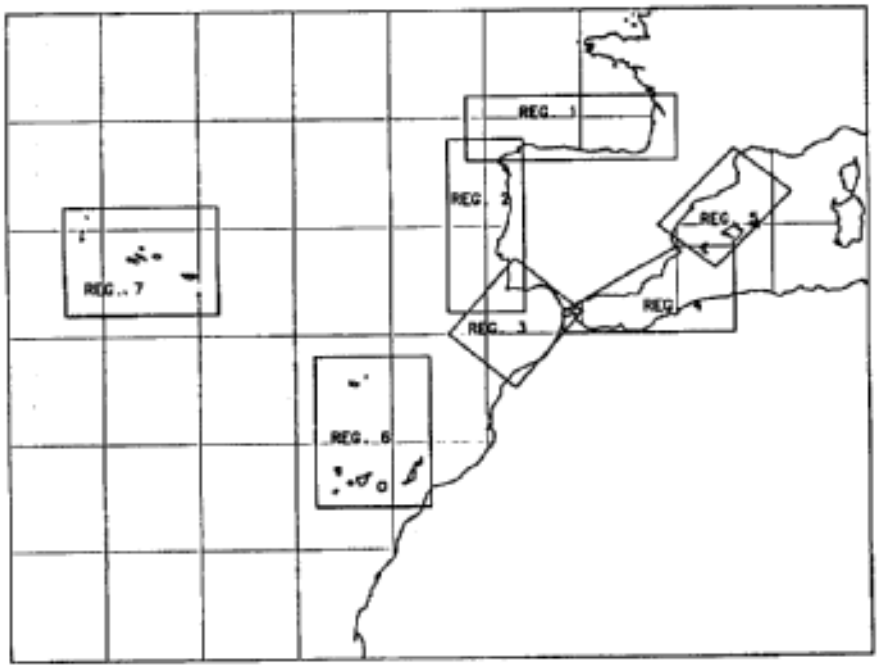

fig. 10.
Storm Atlas.
Study regions.

* Storm preselection carried out by Oceanweather, Inc.

A storm preselection has been done by Oceanweather, for each of the se\-en regions, Oceanweather, (1988). The study objective was to identify occurrences of the top 40 - 50 storms in each of the regions, for the last 25 -35 years. The methodology involved a thorough scan of the following sets of data:

*Synoptic Observations.
*Offshore Buoy Wave Observations.
*Synoptic Ship Observations.
*Surface Weather Charts.
*SOWM Hindcast Results.

Objective criteria were developed correlating the different sets of data. From there, a initial population of storms was selected. Later on, this population was further reduced to the desired size, Trade winds storms were also selected for region 6, the Canary Islands.

* Digitization of surface pressure analysis from NOAA Final Analysis Charts.

NOAA microfilms are copied into paper. A clean cops with the isobars is produced, and then it is captured by a video camera and digitized

in a PC computer workstation. Once they are manually edited, they are transferred to a mainframe, and interpolated to a field on a regular grid.

* Wind calculations. Sea-Air temperature Atlas.

Winds are calculated from Bijvoet model, referred above. Geostrophic winds are corrected for friction with sea-air temperature difference data. This data is obtained from a two year statistical Atlas based on temperature data from ECMWF archives, processed by PCM.

* Wind data improvement by objective re-analysis.

Visual ship observations records for the selected storms have been extracted from the COADS data set. This subset has been reorganized, for an easy retrieval of all the data at a given moment of time.

Pressure and/or wind observations will be blended into the pressure / wind fields using the Objective Package from the BMO. The parameters for the data assimilation are yet to be fixed.

* Nested grid application.

A nested grid scheme will be used. The storm will be run initially on a 100 km grid, covering the whole Atlantic. Windsea and swell data along a specified path are extracted from the coarse grid, and interpolated to the nodes of the fine grid.

A 25 km. grid was originally selected as a reasonable size, although later applications suggest that it may not be fine enough for straight coastlines, such as those at the Bay of Biscay (all the boundary points lie on a single characteristic).
* Full spectrum compact archival.

Code has been developed for creating full spectrum output in compact reduced form, (1-2 bytes for each non-null spectral component). It can be applied to the full grid or to a subset of points. Thus, a finer grid scheme could be applied in the future.

5.- CONCLUSIONS.

The application of a geostrophic wind corrected with sea-air temperature differences has been proven of good quality for its use with the HYPA wave models, provided that the original pressure fields to be reasonably good in the surroundings.

Storms arriving at the Spanish coasts may sometimes consist mainly of swell. They have been generated by storms reaching the Irish Coasts, drifting later towards Northern Europe. A deeper analysis of swell generation and propagation of the models applied is suggested.

It is very costly to process a wave hindcast project. Wind data acquisition is the most expensive part, and sometimes it might not

even be available, -far away wind data needed for long distance swell propagation.

* Archives in meteorological institutions with an already long history in atmospheric modelling should have an easy retrieval of surface data: wind, pressure and sea arid air temperatures.

* Similarly, total spectra at some strategic locations on operational and hindcast wave applications could as well be archived, for further use as boundary data for local hindcast/forecast schemes.

NODC buoys data is very useful for wave model validation along the US coast. Wave measurements data in Europe, is disperse amongst the different countries, and so it is much more difficult to access. An effort should be made in order to classify the available wave spectral data, -directional when possible, to determine standard archival formats, and to facilitate its access.

6.- REFERENCES.

H. C. Bijvoet, 1957. ***A new overlay for the determination of the surface wind over sea from surface weather charts.*** KNMI, Mededelingen en Verhandenlingen. no 71, 1957.

H. Günther, W. Rosenthal, J. de Luis, J. G. Briz, 1989. ***Wave growth in slanting fetch conditions.*** 2nd. International Workshop on Wave hindcasting & Forecasting, (Preprint Volume), Vancouver, April, 1989.

J. de Luis, 1988. ***Atlas Piloto de Oleaje -ATLANTICO.*** Programa de Clima Maritimo, Publication n°25, January 1988.

J. de Luis, 1988b. ***Modelos de GeneraciÓn de Oleaje: Atlántico-1. Verificación HYPA.*** Programa de Clima Maritimo. Publicacion n°29, December 1988.

OCEANWEATHER INC, 1988. ***Selection of Historical Storms in Spanish Waters.*** Final Report, March 1988.

The SWAMP Group, 1985. ***Sea Wave Modelling Project (SWAMP). An intercomparison study of wind wave prediction models.*** Ocean Wave Modelling, Plenum), 1985.

The SWIM Group, 1985. ***Shallow Water Intercomparison of Wave Prediction Models (SWIM).*** Quarterly Journal of Royal Meteorological society, Vol. 111, pp 1087-1113.

H. Timmerman, 1977. ***Meteorological effects on tidal heights in the north sea.*** KNMI, Mededelingen en Verhandenlingen no. 99, 1977.

The WAMDIG, 1988. ***The WAM Model - a third generation ocean wave prediction model.*** (Submitted:Journal of Physical Oceanography, 1988)

BEAUFORT SEA WIND/WAVE-STORM HINDCASTING

[1]T. Agnew, [2]B. Eid, [1]W. Skinner, and [3]V. Cardone

[1]atmospheric Environment Service
Downsview, Ontario, Canada

[2]MacLaren Plansearcb Limited
Halifax, Nova Scotia, Canada

[3]Oceanweather Inc.
Cos. Cob, Connecticut, USA

1. INTRODUCTION

Extreme winds and waves found in the Beaufort Sea are not as severe as on the east or west coasts of Canada. However, when they are combined with cold temperatures and the continuous threat of pack ice even during the open water season, the Beaufort Sea is as arduous a place to work as any offshore area of Canada.

The methodology for selecting extreme storm events is important to any extreme value analysis. In the Beaufort Sea, the situation is complicated by the presence of ice, and ice movement, and its effect on winds and wave-generation. These three environmental parameters are highly interrelated. For example, winds generate waves, winds have a major influence on ice motion, and the ice edge position limits fetch in wind-wave generation. As a result, strong wind producing storms of long duration may not necessarily produce large waves because of the nearby ice edge. Also, the maximum wave producing wind direction with respect to the ice edge position and the coast may not be realized during an extreme event.

A further complicating factor in the selection of extreme storm events is the limited amount of observational marine data for the remote Beaufort Sea area as compared to the east or west coasts of North America. This problem has been less serious in more recent years because of increased oil exploration activity in the region. Atmospheric Environment Service (AES) maintained an advanced Beaufort Weather Office (BWO) in support of drilling activities during the summer season from 1976 to 1985. The BWO analysis charts are the best available for the area during this period.

With these considerations in mind, the following selection methodology was used;

(a) Only the open water season June through October for the 1976 to 1985 period was considered because the largest amount of marine data were available during this period. Most oil production activity takes place during the open water season so that this season is most important from an operational and design point of view as well.

(b) The 10 worst wind producing storms for this period were selected. Independently, the 10 worst wave producing storms for this period were selected.

(c) The data used for the selection were based on the data holdings at the Marine Environmental Data Service (MEDS) of the Department of Fisheries and Oceans (DFO) for the waves and the Canadian Climate Centre (CCC) of AES, Environment Canada for the winds. The available data included oil industry data from Dome Petroleum, and in later years from Gulf, and ESSO.

(d) Once the storms were selected, all pertinent data were collected including BWO and Arctic Weather Centre (AWC) charts and all marine and land station observations. A thorough reanalysis, or hindcast, based on these data, was carried out at 6-hour intervals using the planetary boundary layer technique developed by Cardone. (1969).

2. DATA

Four different data sources were used as input into the hindcast procedure;

- drill rigs/artificial islands (originally from Dome Petroleum Ltd.)
- ships-of-opportunity
- land stations
- BWO and AWC charts

The drill rig and ships-of-opportunity data were used to provide surface pressure and wind data over marine areas. Land station data were used to supplement the marine data by using a transfer function technique.

3. WIND STORM SELECTION

Selection of the 10 worst wind producing storms was done by scanning the Canadian Climate Centre marine wind archives and selecting durations of marine winds above 30 knots. Important factors to be considered were the durations of strong winds and the maximum wind strength. A wind severity index was developed as follows;

$$S_i = T * U_{max},$$

where S_i is the severity index. Storm duration, T, was defined as the number of hours that the marine winds were greater than or equal to 30 knots. All Beaufort Sea marine observations in the archive were used. Wind durations that fell below the 30 knot threshold for only one or two hours were allowed to continue in the analysis. Maximum wind, U_{max}, was defined as the maximum observed hourly sustained wind speed during the storm period in knots.

Table 1 shows the top 32 storms as ranked according to this index. The largest wind severity index occurred for a storm in 1979. Winds were greater than or equal to 30 knots between the period September 30 17z to October 6 4z. The resultant duration was 132 hours and the maximum observed wind was 40 knots. This produced a severity index of 132 hours x 40 knots = 5280. Except for a few wind storms which had data problems, the 10 wind storms with the highest severity index were selected and are marked with a plus sign (+) in the last column of Table 1 .

4. WAVE STORM SELECTION

The Waverider dataset was employed by MEDS to select the 10 worst wave producing storms. The following set of general guidelines (Glenn, 1986) were employed as selection criteria for the extreme wave event study; (1) available synoptic charts (BWO and AWC) in addition to measured winds from land weather stations and marine weather buoys and drill rigs; (2) waves, either recorded or estimated of 3 meters or more in deep water in the Mackenzie shelf/delta area; (3) good Waverider, or equivalent, data coverage in deep and shallow waters; (4) minimum ice conditions which allow a long fetch of 200 kilometers or more for the particular wind direction of the storm; (5) judgement of the storm's representation for typical extreme conditions. The storms which were selected using the wave criterion are marked with an asterisk (*) in the last column of Table 1 . The selected severe wave storms are more or less evenly distributed among the selected severe wind producing storms.

Table 1. Storm selection ranking based on wind severity index. Storms with an asterisk (*) are storms selected based on an independent wave selection criterion. Storms with a plus sign (+) are storms selected based on an independent wind selection criterion.

Year	Start Date	End Date	Duration (hours)	Max.Wind (knots)	Severity Index (Si)	Selection Wind (+) Wave (*)
1979	Sep 30 17z	Oct 06 04z	132	40	5280	+
1977	Oct 06 18z	Oct 11 13z	116	45	5220	+
1977	Sep 23 20z	Sep 28 07z	108	40	4320	*
1978	Oct 06 14z	Oct 10 04z	87	45	3915	+
1978	Sep 29 06z	Oct 02 18z	85	45	3825	+
1978	Aug 31 02z	Sep 03 19z	90	40	3600	+
1985	Sep 16 10z	Sep 18 18z	57	50	2850	*
1977	Sep 06 08z	Sep 09 11z	78	36	2808	
1981	Aug 30 12z	Sep 01 18z	55	45	2475	*
1982	Sep 19 14z	Sep 21 15z	60	41	2460	*
1979	Oct 23 13z	Oct 25 18z	54	45	2430	+
1982	Oct 19 20z	Oct 21 15z	44	54	2376	+
1978	Sep 05 05z	Sep 07 09z	53	40	2120	
1981	Aug 02 06z	Aug 04 09z	52	40	2080	+
1982	Jul 27 17z	Jul 29 09z	41	48	1968	*
1983	Nov 07 12z	Nov 09 06z	43	45	1935	+
1978	Jul 05 15z	Jul 07 07z	41	44	1804	
1984	Sep 16 03z	Sep 18 03z	48	36	1728	
1978	Sep 19 11z	Sep 21 04z	42	40	1680	
1981	Aug 16 18z	Aug 18 06z	37	45	1665	*
1980	Sep 27 04z	Sep 29 02z	47	35	1645	
1977	Aug 06 16z	Aug 08 15z	48	33	1584	
1978	Oct 12 10z	Oct 13 21z	36	42	1512	
1977	Aug 13 23z	Aug 15 14z	40	37	1480	
1981	Sep 27 15z	Sep 29 06z	40	36	1440	*
1982	Sep 10 05z	Sep 12 06z	40	34	1360	
1982	Sep 06 08z	Sep 07 21z	38	34	1292	
1980	Aug 30 04z	Aug 31 08z	29	40	1160	*
1977	Aug 27 22z	Aug 28 13z	16	37	592	*
1977	Sep 21 09z	Sep 21 19z	11	42	462	
1980	Sep 04 04z	Sep 04 09z	6	35	210	+
1979	Aug 22 23z	Aug 23 00z	2	30	60	*

The September 1985 storm which washed away ESSO's artificial island Minuk I-53 is an excellent example of the importance of duration of strong winds in the production of potentially hazardous wave action.

It ranks seventh in wind severity index (S_i) and second in the extreme wave production category. The continuous erosion of the artificial island due to wave action over the two to three day period of this storm caused considerable damage.

5. WIND FIELD SPECIFICATION

Wind fields are specified by the methodology described by Cardone et al. (1980) for marine winds, which combines winds calculated from pressure fields through a marine planetary boundary layer model (MPBL) with winds specified by kinematic analysis of direct wind observations. The kinematic analysis is applied on a small part of the whole analysis area, since, unlike mid-latitude oceanic regions in which ship reports are relatively numerous, in-situ reports in the Canadian Beaufort are available only near the coast and, in recent years, only in areas of offshore drilling. The model domain extends

FIGURE 1. WIND HINDCAST MODEL GRID

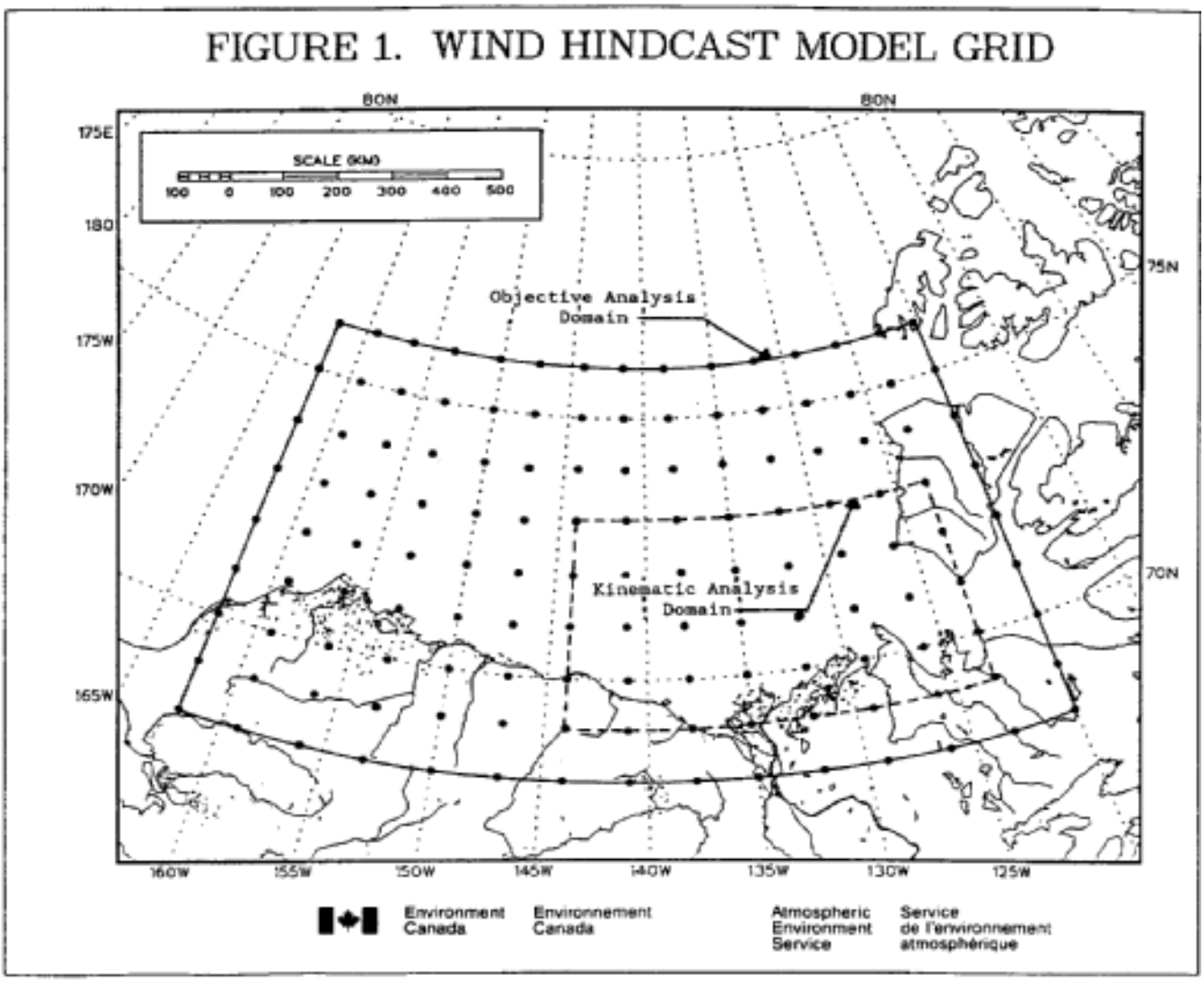

from 68° N to 76° N and 120° W to 162° W as shown in Figure 1 . The grid size was chosen to be 1° latitude by 3° longitude.

5.1 Objective Analysis

In parts of the grid covered at least partially by sea ice, the MPBL used in Cardone's scheme is replaced by an alternate pressure-wind transformation described below. In general, the ice specification is fixed for the duration of a given storm.

Gridded fields of sea level pressure at 6-hourly intervals, were derived from BWO and AES hand-analyzed pressure fields, after some re-analysis was carried out to impose greater time continuity than is possible in real time. Isobars were digitized on a digitizing tablet, pressures were recovered at grid points through polynomial fits, and pressure gradients were calculated by centred differencing.

Over open water, or water with less than four-tenths ice cover, winds were calculated from the MPBL, which in general requires the following parameters at each grid point: sea level pressure gradient; horizontal air transport gradient (baroclinicity effect); air-sea temperature difference (stratification effect). Air and sea temperature fields are not digitized in general, though if available the air-sea temperature difference may be specified at grid points. The horizontal air temperature gradient is specified from climatological data.

The MPBL provides unbiased and reasonably accurate surface winds over open water, when accurate inputs are specified, and acceleration terms are small. The atmospheric boundary layer over sea-ice is rather complicated, even for relatively small fractional covers (about four-tenths or more). The surface wind stress, and the near surface wind field, averaged over a region depends not only on the external conditions of the PBL, but also sensitivity on the details of the distribution and structure of the sea ice, the buoyancy flux associated with leads and polynas, and height of the shallow inversions often characterizing arctic boundary layers.

Overland (1985) has reviewed a large body of published data on the atmospheric boundary layer structure over a wide range of ice conditions, and summarized the surface drag regimes in terms of rather broad surface roughness and stability categories, In terms of the effective 10-m drag coefficient,

$$C_d = U_*/U_{10}$$

where U_* is friction velocity, and U10 is the 10-metre wind speed, Overland estimates 10^3 C_d in the range 1.3 to 1.5 for smooth ice, rising to about 2.2 for small ice concentrations in the marginal ice

zone (MIZ), 2.5 to 3.0 in nearly continuous pack ice, and as high as 3.0 to 3.7 in the unstable boundary layer over the MIZ. Much lower drag coefficients however characterize the winter arctic boundary layer in low inversion conditions.

To specify surface winds from the pressure field over sea ice, we require knowledge of the geostrophic wind ratio U_{10}/G and the turning angle α between U_{10} and G. Overland (1985) has used a second-order closure model of the inversion capped boundary layer to calculate these quantities as functions of $Z_* = U_*/fZ_1$, where f is the coriolis parameter and Z_1 is the inversion height. Only rough estimates of Z_* and C_d are possible on a synoptic basis, and using Overland's model we have adopted the following categories to specify U_{10}/G and α :

MIZ, smooth ice, $Z_* \sim 10$, $10^3 C_d \sim 1.5$, $U_{10}/G \sim 0.7$, α ct $\sim 20°$

MIZ, rough ice, $Z_* \sim 15$, $10^3 C_d \sim 2.5$, $U_{10}/G \sim 0.65$, $\alpha \sim 25°$

Arctic winter, $Z_* \sim 30$, $10^3 C_d \sim 2.5\text{-}3.0$, $U_{10}/G \sim 0.55$, $\alpha \sim 45°$

The wind program utilizes these categories at grid points so specified, with the default winds calculated according to the MPBL. Of course, for the purposes of wave modeling, the impact of errors on surface winds is small in areas of sea-ice concentration greater than four-tenths.

5.2 Kinematic Analysis

The kinematic wind fields are by far the most accurate and least biased winds, primarily because the method allowed a thorough re-analysis of the evolution of the wind field. Kinematic analysis also allows the wind fields to represent effects not well modelled by pressure-wind transformation techniques, such as temporal variations in surface pressure gradients, and deformation in surface winds near the downstream of coasts. However, the degree of accuracy of such analysis is primarily a function of available observations.

Kinematic analysis is a manual process that involves the following basic steps: (1) assembling and plotting all synoptic observations of wind speed and direction, and sea level pressure, from rigs, ships and land stations at 6-hourly intervals on a suitable base map projection for the storm event of usually 2-4 days duration; (2) identification and rejection of erroneous and unrepresentative observations to the extent possible; (3) construction of a continuity chart which defines the movements of storm centres, fronts and other significant features of the surface wind field; (4) construction of streamlines and isotachs; and (5) gridding of wind speed and direction by hand from the streamline/isotach fields.

For the purpose of wave modelling, the period over which wind fields must be specified in selected storm ranges between 2 and 4

days. The storm period may be considered to be composed of three phases: (1) a spinup period (24-48 hrs); (2) the period in which the major storm crosses the region and generates maximum sea states; and (3) the period from 12-24 hours after the occurrence of peak states, during which the wind field no longer plays a critical role in the hindcast but which should be modelled nevertheless so the hindcast wave series will include an adequate period of wave decay at the sites of interest.

Due to limited coverage of marine observations in the Beaufort Sea, the application of the above kinematic analysis for the complete study area is not logical (in terms of costs and accuracy required). Nevertheless, a small area which covers the most critical parts of the wind field required for adequately running a wave model was chosen. The area extended from 69° N to 73° N and from 123° W to 144° W (Figure 1) which includes most shipping locations and represents the average to maximum open-water area in the Canadian Beaufort Sea.

The transformation of wind speed measured at coastal stations to equivalent over-water speed has been studied by Resio and Vincent (1977), Phillips and Irbe (1977) who used data from the Great Lakes, and Lalonde and McCulloch (1975) who analyzed data from the Canadian Beaufort Sea. These empirical studies are quite consistent with each other in demonstrating that the ratio of over-water to over-land wind speed decreases with increases increasing wind speed and depends also on atmospheric stability (in a form of air-sea temperature difference) and fetch. For light winds over-land, the ratio is in the range of two, but for strong winds and unstable stratification it approaches unity (Figure 2). Resio and Vincent (1977) also demonstrated that the Planetary Boundary Layer model of Cardone (1969) may be used to predict the dependence of the ratio of wind speed and stability, given a specification of the anemometer height and terrain roughness of the measurement site. In general, the model predicts the ratio to depend weakly also on latitude. The above technique was used in this study.

A recent study by Kozo and Robe (1986) highlights the influence of the Brooks Mountain Range over the Arctic coastal waters. The orographic effect of these mountains was also used in the kinematic analysis,

5.3 Spatial Blend of Objective and Kinematic Analyses

This method is a blend of the objective and kinematic analyses, with the kinematic analysis reserved for the most critical parts of the wind field as mentioned previously. In this manner, the method is rather a spatial blending of objective and kinematic analysis winds in lieu of local blending at a certain weighting factor. In this case, the kinematic winds replaced the winds derived from the pressure field

in the interior of the kinematic domain and were blended with the pressure-derived winds along the boundaries of that domain (i.e. some smoothing was applied). This was used in the hindcast of the twenty storms.

6. ANALYSIS AND RESULTS

6.1 Hindcast Production

For the selected storm, the pressure fields generated over the study area of the Beaufort Weather Office's (BWO) surface analysis charts were used. Some modifications were made to the analysis charts to add definition in areas of slack pressure gradients or to improve continuity from one chart to the next in some cases. The charts were extended to cover areas north of 74° latitude that were not covered in some BWO charts. For these cases, it was necessary to re-analyze the charts to allow for digitization of the objective domain. The pressure fields from these charts were digitized for each storm periods and the model was run to generate gridded wind field within the model domain.

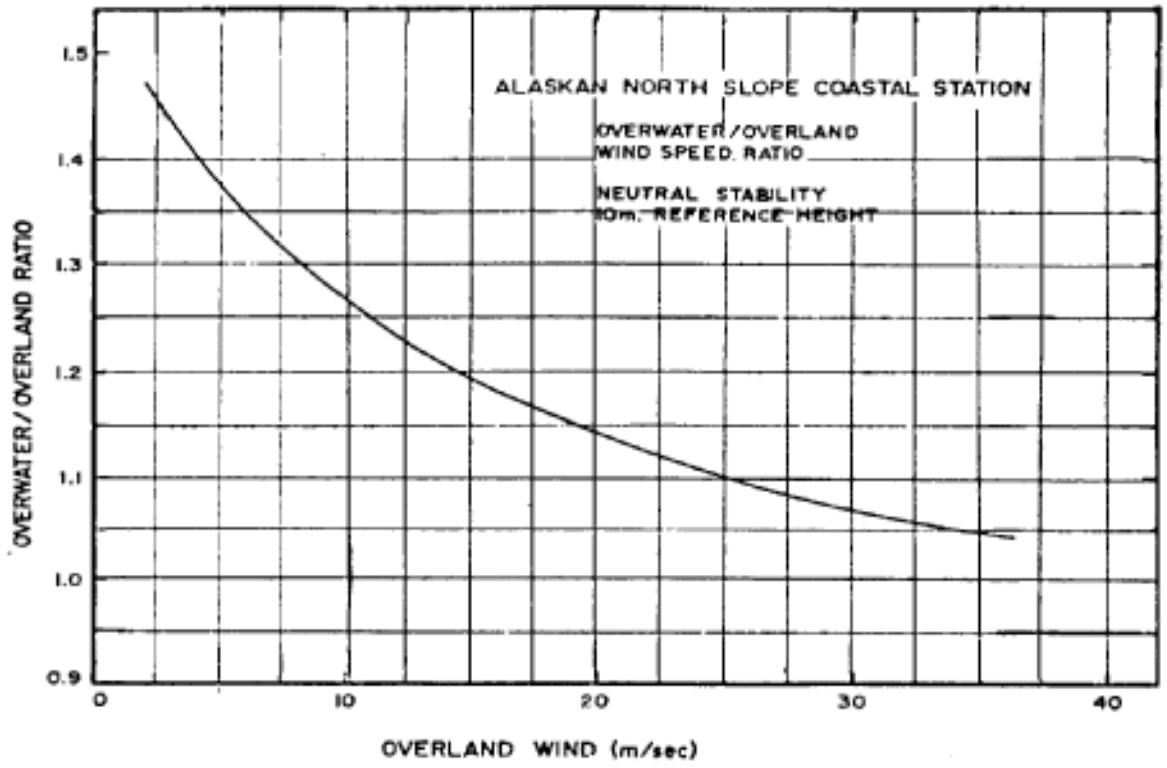

Figure 2. Beaufort Sea overwater-overland wind speed ratio for neutral stability and 10 metre anemometer height.

The area included in the kinematic domain was re-analyzed utilizing all useful additional information available (i.e. rig and ship observations). To ensure a smooth blend along the edges of the nested domain, a selected number of objective grid-point winds were plotted along its border. The usefulness of some of the additional

observations was limited where there was uncertainty about anemometer exposure. It is essential for successful kinematic analysis that all wind speeds are reduced to a common level (e.g. 10 m). Once all the available information was collected, the area of the nested grid was subjected to streamline and isotach analysis. During this process, it becomes apparent that an area north of the Brooks Range, in the Northern Yukon and NE Alaska, extending some distance offshore was affected by a mesoscale funnelling. This effect was outlined by Kozo and Robe (1986), and was displayed by winds up to 60% in excess of the geostrophic wind when the regional flow is parallel to the coast, i.e. easterly or westerly. The above techniques were used in hindcasting the 20 storms listed in Table 2 . The hindcast wind fields were archived in a form of computer files at both Atmospheric Environment Service (AES) and Marine Environmental data Service (MEDS).

The hindcast wind fields were evaluated at a number of locations where sufficient wind measurements were available. The assessment was carried out for all 20 storms. Wind speed and direction, air and surface water temperature records were obtained from all the rigs which were in the study area during each of the storms, The 3-hourly rig or ship observations after being converted to 10m effective neutral winds, were used for the validation of the hindcast wind fields. The concept of the effective wind was introduced by Cardone (1969) to describe the effects of thermal stratification in the marine boundary layer as the wind speed in a boundary layer of a given stratification. The following evaluation methods were applied:

(1) The time series of hindcast wind speed and direction were plotted against the corresponding observed winds at all evaluation sites for the validation storms (not shown here due to space limitation). A quantitative statistical analysis was carried out to provide average evaluation values of the hindcast winds.

Table 2. Twenty Archived Hindcast Storms.

Storm	YYMMDD	Objective Analysis YY/MM/DD/GMT – YY/MM/DD/GMT	Kinematic Analysis YY/MM/DD/GMT – YY/MM/DD/GMT
1	770825	77/08/25/12 – 77/08/28/00	77/08/26/06 – 77/08/28/00
2	770923	77/09/23/12 – 77/09/26/00	77/09/23/12 – 77/09/26/00
3	771006	77/10/06/00 – 77/10/13/00	77/10/09/00 – 77/10/11/00
4	780830	78/08/30/06 – 78/09/04/00	78/08/30/18 – 78/09/02/00
5	780928	78/09/28/00 – 78/10/02/12	78/09/28/18 – 78/10/02/12
6	781006	78/10/06/12 – 78/10/10/12	78/10/07/00 – 78/10/09/18
7	790822	79/08/22/00 – 79/08/25/00	79/08/22/12 – 79/08/24/06
8	790929	79/09/29/12 – 79/10/06/18	79/09/30/12 – 79/10/04/00
9	791023	79/10/23/00 – 79/10/26/12	79/10/23/18 – 79/10/26/12
10	800828	80/08/28/06 – 80/08/30/12	80/08/29/12 – 80/08/30/12
11	800830	80/08/30/00 – 80/09/04/00	80/08/30/06 – 80/09/02/00
12	810801	81/08/01/00 – 81/08/04/12	81/08/02/12 – 81/08/04/12
13	810816	81/08/16/00 – 81/08/18/00	81/08/16/12 – 81/08/17/12
14	810830	81/08/30/00 – 81/09/02/12	81/08/30/00 – 81/09/01/12
15	810927	81/09/27/00 – 81/09/29/00	81/09/27/15 – 81/09/28/18
16	820726	82/07/26/00 – 82/07/28/00	82/07/26/00 – 82/07/27/00
17	820920	82/09/20/00 – 82/09/22/00	82/09/20/12 – 82/09/21/12
18	821018	82/10/18/00 – 82/10/22/00	82/10/19/00 – 82/10/21/18
19	831107	83/11/07/00 – 83/11/10/06	83/11/07/12 – 83/11/09/18
20	850916	85/09/16/00 – 85/09/19/00	85/09/17/06 – 85/09/18/06

(2) Error statistics were calculated for all sites for a given observation period during each storm. The results are summarized in Tables 3a and 3b . The given values show the comparisons of measured and hindcast wind speeds and directions, respectively, in each storm.

(3) Also, Tables 3a and 3b provide the overall error statistics for all Storms. Figures 3a and 3b show scatter plots of hindcast versus observed wind speed and direction, the overall correlation coefficient, and linear regression line.

(4) It was observed that large systematic differences remain between measurement series in a given storm, even where rigs were separated by small distances compared to the so-called synoptic scale over which significant differences should pertain. These differences were found to be comparable to those seen in the comparisons between hindcast and measured winds at any particular measurement location.

7. CONCLUSIONS

For the years 1979 to 1985, the comparative statistics show low errors and good correlations between measured and hindcast values,

During this period increased offshore drilling activity led to a denser observation network and perhaps more importantly greater quality control of the data. This increased availability of measured data enhances the skill of the kinematic analysis and subsequently raises the level of confidence in the model hindcast wind fields. The reduction of wind speed to a common level (10 metres) is made simpler during this period as anemometer heights are more generally known.

Table 3a. Error Statistics of Wind Speed (Knots)

Storm	Date	No. of Points	Average Obs.	Standard Dev.	Average Hindcast	Standard Dev.	Mean Error	Absolute Mean Err.	RMSE	Scatter Index %	Corr. Coeff.
1	25 Aug 77	92	13.12	8.52	12.80	4.83	-0.32	5.73	7.67	58.48	0.452
2	23 Sep 77	101	20.88	7.75	18.49	6.63	-2.40	5.35	6.57	31.49	0.647
3	06 Aug 77	218	14.32	8.73	13.28	6.50	-1.05	6.62	8.98	62.71	0.343
4	30 Aug 78	111	22.16	5.14	17.86	5.08	-4.31	5.06	6.32	28.54	0.589
5	28 Sep 78	91	23.30	7.05	18.35	3.19	-4.95	5.47	7.33	31.45	0.681
6	06 Oct 78	94	25.81	6.46	23.37	5.81	-2.44	3.31	4.56	17.65	0.808
7	22 Aug 79	65	13.15	5.93	13.02	5.44	-0.14	4.29	5.18	39.37	0.588
8	29 Sep 79	177	23.42	6.08	18.51	5.69	-4.91	6.15	7.39	31.53	0.562
9	23 Oct 79	58	25.60	5.16	21.81	6.34	-3.79	4.76	6.65	25.97	0.566
10	28 Aug 80	47	15.43	7.77	12.79	5.94	-2.64	4.81	6.24	40.43	0.690
11	30 Aug 80	79	18.97	7.33	16.80	5.78	-2.18	4.35	5.82	30.65	0.685
12	01 Aug 81	116	19.22	8.45	17.30	8.16	-1.92	3.94	5.19	27.00	0.832
13	16 Aug 81	66	19.26	8.66	18.32	8.48	-0.94	4.12	4.91	25.52	0.842
14	30 Aug 81	107	22.30	5.52	23.17	3.27	0.87	3.47	4.29	19.26	0.650
15	27 Sep 81	66	27.05	4.92	26.35	6.41	-0.70	3.30	4.00	14.78	0.790
16	26 Jul 82	65	17.83	10.34	15.51	7.31	-2.32	5.22	6.77	37.95	0.793
17	20 Sep 82	67	23.45	7.19	20.61	5.40	-2.84	3.97	4.99	21.29	0.824
18	19 Oct 82	50	27.26	12.36	22.62	7.08	-4.64	7.68	9.35	34.30	0.783
19	07 Nov 83	39	18.77	8.27	17.54	7.41	-1.23	3.38	4.19	22.31	0.875
20	16 Sep 85	88	26.36	8.39	22.49	6.85	-3.88	5.53	6.75	25.61	0.755
Overall Average:		1797	20.57	8.77	18.21	7.18	-2.36	5.02	6.61	32.13	0.717

Table 3b. Error Statistics of Wind Direction (°T).

Storm	Date	No. of Points	Mean Error (Bias)*	Absolute Mean Error	RMSE
1	25 Aug 77	92	-9.8	34.3	46.7
2	23 Sep 77	101	12.8	19.4	31.0
3	06 Oct 77	218	11.9	33.4	41.2
4	30 Aug 78	111	17.3	19.4	23.7
5	28 Sep 78	91	6.6	11.8	18.6
6	06 Oct 78	94	10.0	13.9	17.3
7	22 Aug 79	65	21.9	25.6	35.7
8	29 Sep 79	177	13.3	16.5	19.9
9	23 Oct 79	58	9.8	13.9	17.9
10	28 Aug 80	50	-1.4	20.8	25.8
11	30 Aug 80	79	1.2	22.9	34.4
12	01 Aug 81	116	17.2	28.9	40.2
13	16 Aug 81	66	23.1	27.7	39.7
14	30 Aug 81	107	2.2	13.2	15.8
15	27 Sep 81	66	4.2	10.6	13.6
16	26 Jul 82	65	7.7	31.7	41.7
17	20 Sep 82	67	8.8	14.0	17.7
18	19 Oct 82	50	-1.4	18.6	33.7
19	07 Nov 83	39	0.7	21.2	43.6
20	16 Sep 85	88	3.9	19.2	31.6
Overall Average:		1800	9.0°	21.6°	31.4°

*positive bias if clockwise direction negative bias if anticlockwise direction

However, during the years 1977 and 1978 observations were much sparser and information on anemometer height and observation quality unrecorded. The poor comparison statistics for these storms need not necessarily indicate a low level of confidence in the model results. It was necessary during the analysis of these storms to delete observations on a more regular basis due to poor fit to the objective pressure field.

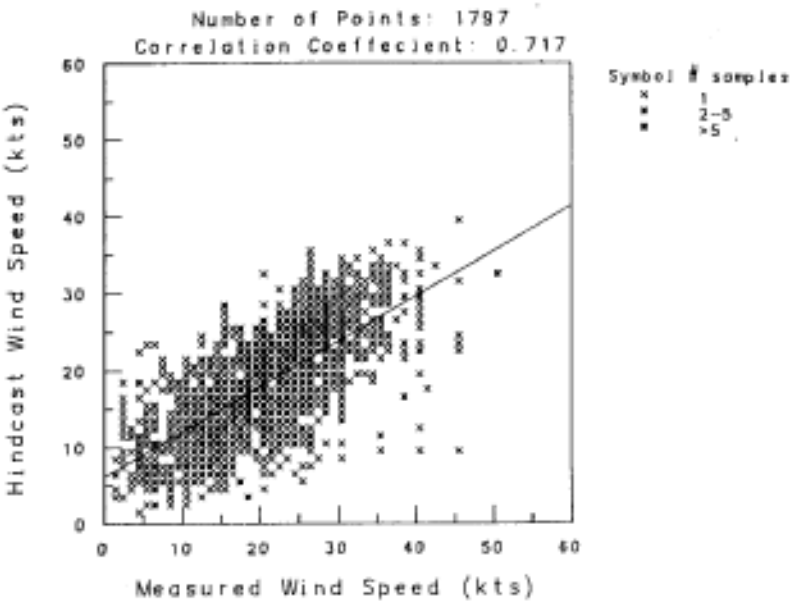

Figure 3a. Hindcast versus observed wind speed for 20 Beaufort Sea storms

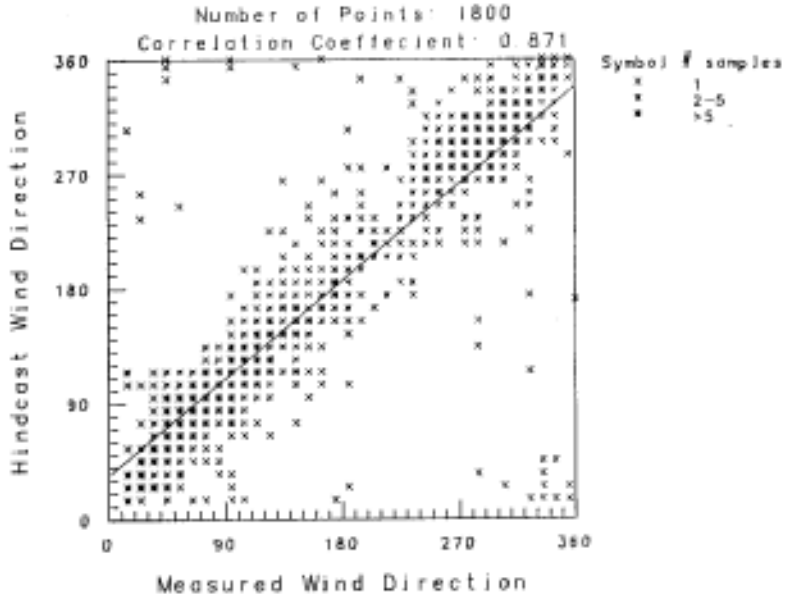

Figure 3b. Hindcast versus observed wind direction for 20 Beaufort Sea storms

REFERENCES

Cardone, V.J. (1969). Specification of the Wind Field Distribution in the Marine Boundary Layer for Wave Forecasting. Report TR-69-1, Geophys. Sci. Lab., New York University. Available from NTIS AD#702-490.

Cardone, V.J., A.J. Broccoli, C.V. Greenwood and J.A. Greenwood. (1980). Error Characteristics of Extratropical Storm Wind Fields Specified from Historical Data. Journal of Petroleum Technology, Vol. 32, pp. 873-880.

Glenn, G. (1986). Storm Selection of Extreme Wave Events in the Beaufort Sea for Applications in Studies of Spectral Hindcasting. NOGAP Project B.8. Marine Environmental Data Service, Department of Fisheries and Oceans, Ottawa, Ontario.

Kozo, T.L. and R.Q. Robe. (1986). Modelling Winds and Open-Water Buoy Drift Along the Eastern Beaufort Sea Coast, Including the Effects of the Brooks Range. Journal of Geophysical Research, Vol. 91, No. C11, pp. 13011-13032, Nov. 15, 1986.

Lalonde, M.E. and J.A. McCulloch. (1975). Ratios of Wind Over Water to That Over Land for the Beaufort Sea. Atmospheric Environment Service, Downsview, Ontario.

Overland, J.E. (1985). Atmospheric Boundary Layer Structure and Drag Coefficients over Sea Ice. Journal of Geophysical Research, Vol. 90, pp. 9029-9049.

Phillips, D.W. and J.G. Irbe. (1977). Lake and Land Ratios of Wind, Temperature and Humidity During IFYGL. CL12-77, Atmospheric Environment Service, Downsview, Ontario.

Resio, D.T. and C.L. Vincent. (1977). A Numerical Hindcast Model for Wave Spectra on Water Bodies with Irregular Shoreline Geometry I. Test of Nondimensional Growth Rates. Miscellaneous Paper H-77-9, Hydraulics Laboratory, U.S. Army Engineer Waterways Experiment Station, Vicksburg, MS.

INTERPRETATION OF WAVE MODEL VALIDATION STATISTIC

H. Günther, W. Rosenthal
GKSS-Forschungszentrum Geesthacht, FRG

0. INTRODUCTION

The North European Storm Study, NESS, is an ongoing joint industry and government project, whose primary objective is to determine a data base for estimating extremal criteria for winds, waves and surge in the entire Northwest European operating area. The study is being conducted by a consortium consisting of the U.K. Met Office, the Norwegian Meteorological Institute, Delft Hydraulics, Danish Hydraulic Institute and GKSS Research Centre. The first phase in the project included the validation of the hindcast models and methodologies to be used in the production phase of the project. This presentation deals with the general problems of an error analysis of spectral wave models exemplified by the validation work within the NESS project.

The hindcast winds for input to the wave model are being constructed by the U.K. Met Office and the Norwegian Meteorological Institute. The wind fields are based on a quasi-geostrophic atmospheric model using archived pressure charts as input or in recent years from numerical products of the U.K. Met Office atmospheric model. This first guess windfield is then improved by objectively blending in platform and ship observations followed by subjective manual analysis by a trained meteorologist.

The HYPAS wave model is a shallow water extension of the HYPA (Hybrid Parametric) model, which is described for example in Swamp (1985) and in "assessment of wave hindcasting methods" (offshore technology report OTH 87 258, 1987). Although results of tests of HYPAS have been published in Bouws et al (A Shallow Water Intercomparison of Three Numerical Wave Prediction Models, SWIM, 1985) and the already mentioned OTH 87 paper (WHIST) and it is in routine use by the German Military Weather Service in a forecast mode, an extensive validation of the model in 20 storm periods was included in the scope of NESS. HYPAS was adapted to a coarse grid, Figure 1 , with a grid spacing of 150 km and fine grid, Figure 2 , with a grid spacing of 30 km. An extensive collection of instrumented wave records for 20 storm periods was gathered from oil industry and government archives. The resultant instrumented data set includes measurements at each of the 49 sites shown in Figure 2 and on average there is measured data for about 12 sites for each of the storm periods. As would be expected the data were collected with several different types of instruments employing various sampling and analysis procedures. Though the quality of the data was checked and overall is considered good, the accuracy of all data cannot be assured. The majority of data was collected at three hour intervals with a sampling period of 20 minutes.

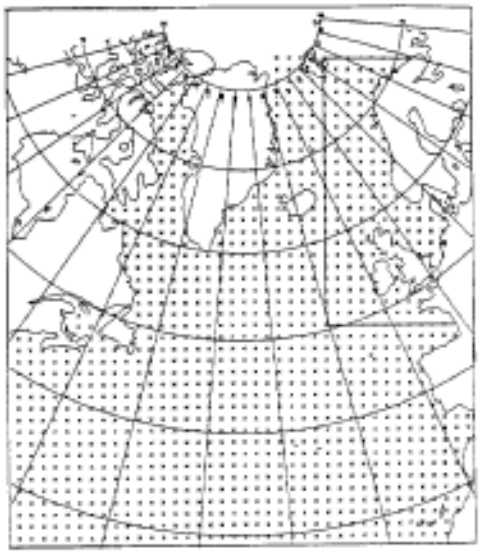

Figure 1. NESS wave model coarse grid area, grid spacing of 150 km. The box around the North European shelf marks the fine grid area (see Figure 2)

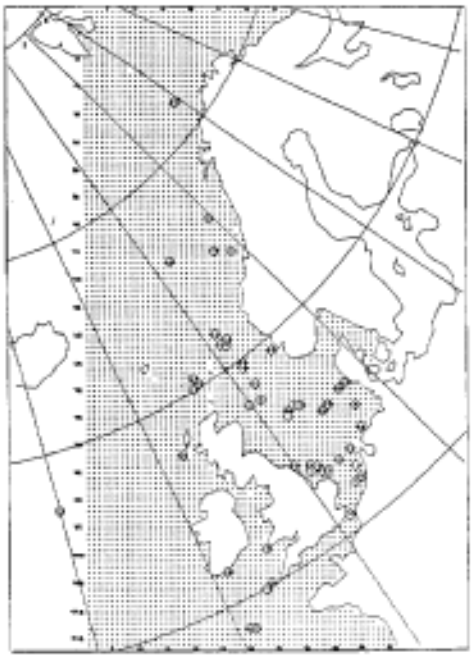

Figure 2. NESS wave model fine grid area, grid spacing of 30 km. Marked by circles are all 49 sides where wave measurements are available.

The primary objective of the validation in NESS is to establish the adequacy of the hindcast procedure in determining the peak storm conditions, which in turn are to be used to estimate long return period events. For this reason comparisons of parameters from the model and instrumental data are made at maxima of significant wave height, H_S, of storms in the storm period. Thresholds for storm peaks were set at 6 m for all areas except the southern North Sea, which was set at 4 m due to the less severe conditions. Since errors in the timing of the model peak is of no consequence to the application for extremes, peaks within nine hours are compared. Although many other parameters are included in the comparison, for example wave period and direction comparisons, this paper will include only the H_S comparisons.

The deviations between measured and modelled wave parameters are influenced by

1. Resolution of the model, inaccuracy of the wind field due to subgrid variability and geophysical sampling errors of the measured data. We estimate the influence of these error sources in section 1 .

2. Since numerical models simulate the expectation values of the wave parameters the local maximum of a modelled time series does not show the variability introduced by the sampling error of a measured time series. Therefore, if the maxima of both time series are compared, the measured maximum is biased high compared with the modelled values. We will give an estimate of this bias in section 2 for a peak event that stays long enough at the same level of H_S to permit several measurements.

3. Another error source are the sampling rates in the model output as well as in the measured wave parameters. To investigate the respective deviations we show computer simulation of comparisons between modelled and measured wave height time series that are sampled at different intervals in section 3 . In this case a peak wave height is assumed for a fixed time with two different growth and decay rates.

1. ESTIMATE OF WAVE MODEL ACCURACY

Before estimating the total scatter for such a peak statistic we emphasize that a numerical wave model does not exhibit the geophysical scatter inevitably inherent in measurements from a finite time series at a fixed location. The numerical model is geared to calculate for given environmental conditions the statistical expectation value, which may have a systematic error.

An estimate of the deviations between measurement and numerical model can be deduced from the analytical expression for ideal orthogonal fetch limited conditions.

The total significant wave height H_s is given by

$$H_s^2 = k \cdot U_{10}^2 \cdot x \qquad (1)$$

where U_{10} = wind speed at 10 m
x = fetch

The coefficient k varies, depending on different sources in the literature, but, as will become clear, this does not influence the result.

If in (1) the expectation values for x and U_{10} are substituted by measured values of one event the equation reads

$$(\hat{H}_s + dH_s^m)^2 = k \cdot (\hat{U}_{10} + dU_{10})^2 \cdot (\hat{x} + dx) \qquad (2)$$

where $d\hat{H}_s^m$ is the model deviation from the expectation value $\hat{H}_s$.

We assume that dU_{10} includes sampling errors from instruments but is mainly caused by inaccuracies in the first guess wind fields from the pressure field analysis or the numerical output of an atmospheric model; dx is assumed to originate from grid resolution of the wave model. If we resolve equation (2) for $\hat{H}_s$ and keep only linear terms in dU_{10} and dx, the relative model error ε_m is quantified as

$$\varepsilon_m = \frac{dH_s^m}{\hat{H}_s} = \frac{1}{2}\left(\frac{dx}{\hat{x}} + \frac{dU_{10}}{\hat{U}_{10}}\right) \qquad (3)$$

Comparing model results with measured values an additional error dHs due to geophysical scatter occurs. If we assume that the model is unbiased, the total relative error ε of the instrument model comparison is given as

$$\varepsilon = \frac{1}{2}\frac{dx}{\hat{x}} + \frac{dU_{10}}{\hat{U}_{10}} - \frac{dH_s}{\hat{H}_s} \qquad (4)$$

The three components in (4) are independent of each other so the total scatter is

$$\sigma = (\sigma^2(H_s) + \sigma^2(U_{10}) + \frac{1}{4}\sigma^2(x))^{1/2}$$

$$= \left(\overline{\left(\frac{dH_s}{\hat{H}_s}\right)^2} + \overline{\left(\frac{dU_{10}}{\hat{U}_{10}}\right)^2} + \frac{1}{4}\overline{\left(\frac{dx}{\hat{x}}\right)^2}\right)^{1/2} \qquad (5)$$

We have to estimate the three contributions in (5). We shall do that for wind speed U_{10} = 20 m/s and a wave height H_s = 6m. The fetch involved for H_s = 6 m is according to (1), x = 274 km.

We estimate the relative accuracy of the wind field to be 12.5 %, that means $\sigma(U_{10})$ = 0.125. The accuracy of the fetch is estimated to be equal to half of the grid distance, in our case 30 km. Since x = 274 km we get $\sigma(x)$ = 0.05. The geophysical sampling variability can be estimated from publications by Günther (1981), Donelan and Pierson (1983) or F. Monaldo (1988) to be of the order of 8 %. The resulting standard deviation of model to instrument comparison is

$$\sigma = \approx 0.15 \text{ or } 15\ \%$$

A reduction of this error is mainly possible by reducing the error in the windfield since this gives the largest contribution.

2. THE BIAS OF THE MEASURED MAXIMUM OF H_s VERSUS THE MODELLED MAXIMUM

A typical time series of a wave buoy for significant wave height H_s is shown in Figure 3 . H_s is derived from wave recordings of 30 min. and in this case with one measurement per 30 minutes. Although the model curve seems to match the data, it is difficult to give a quantitative statement because of the scatter of the measured data. Another, more striking example for data scatter is given in Figure 4 . These data are sampled by ship borne wave recorder and the analysed time series is of 12 min. duration. Again a large data scatter poses a problem for deriving a measure for the model quality. The data variability can be overcome by averaging the measurements. The full line in Figure 4 shows the data when averaged over three hours. The problem of the natural geophysical scatter of surface wave data is treated in Donelan and Pierson (1983) and Gunther (1981). We will use their results subsequently.

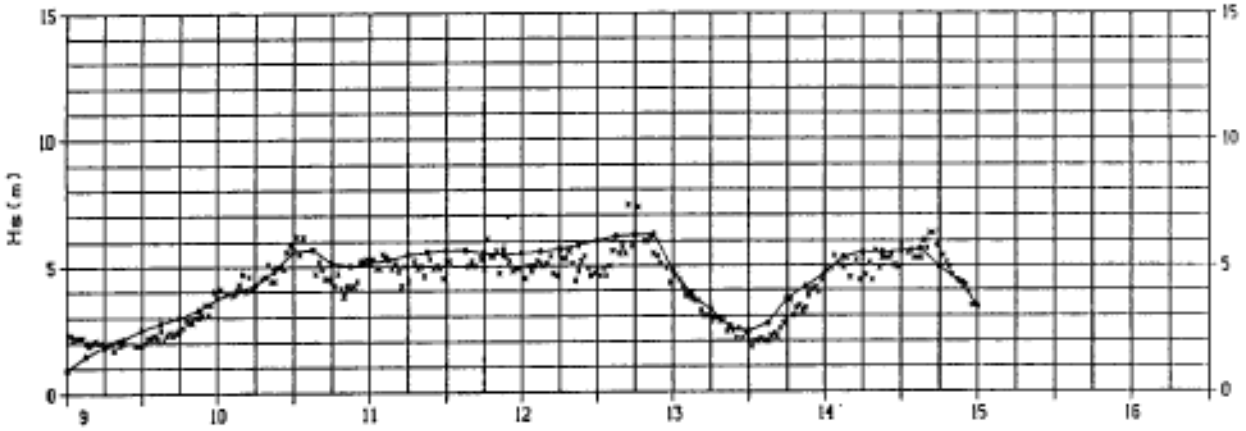

Figure 3. Measured (x) and computed time serie (-o-) of significant wave height at AUK (side 1 in Fig. 2) for NESS storm 31, 86/01/09. - 86/01/15

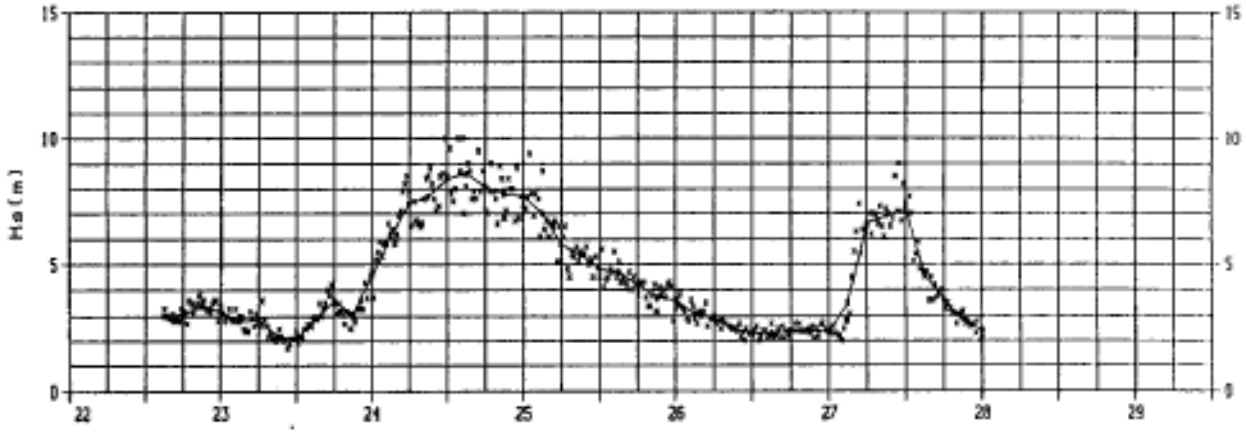

Figure 4. Measured (x) significant wave height at OWS Mike (side 49 in Fig. 2) out of 12 min time series. The full line shows the same data by averaged over 3 hours.

In this section we want to quantify the bias introduced in the model validation statistic when modelled peaks and measured peaks are compared. It has been explained that the numerical model does not exhibit the geophysical scatter inherent in the measurements. Therefore the height of a local maximum of a measured time series is biased high compared to the respective modelled maximum even for an ideal wave model that produces the correct theoretical expectation value at a given time and location.

The duration of a 'peak' seastate depends on the area. e.g. the southern North Sea has much larger durations than other areas. It varies by storm, e.g. Fig. 4 shows a storm peak length of about 18

and 6 hours. Each individual measurement is taken as a realisation of a statistical variable "significant wave height" x_i, i = 1, ...,m. The duration of the seastate is (m-1) Δt, where Δt (normally 3 hours) is the sampling rate. The expectation value for each measurement i is given by F_i. Assuming a the seastate to be a stationary Gaussian process, the statistical variable x_i follows a chi-squared distribution with 2n degrees of freedom:

$$g_i(x) = \frac{1}{\Gamma(n)} \frac{n}{F_i} \left(\frac{x \cdot n}{F_i}\right)^{n-1} e^{-xn/F_i} \qquad (6)$$

We define the statistical variable X = (Maximum of x_i) and in the following we investigate its statistical behaviour. Under the assumption that for all measurements the expectation values are the same (F_i=F i=1 ... m) we can derive the p.d.f for X to be

$$h(x) = \frac{1}{\Gamma(n)} \frac{n \cdot m}{F} \left(\frac{x \cdot n}{F}\right)^{n-1} e^{-xn/F} \left[1 - e^{-xn/F} e^{xn/F}_{n-1} \right]^{m-1} \qquad (7)$$

$\Gamma(n)$ is the gamma function and

$$e^{Y}_{K} = \sum_{j=0}^{K} \frac{1}{\Gamma(j+1)} Y^j \qquad (8)$$

the error function.

Table 1 gives the normalized expectation value E[X]/F for various numbers of m (horizontal axis). Assuming a stationary peak over 3 hours we take m = 2, over 6 hours m = 3, etc. according to a 3 hourly sampling rate. A value of 2n = 100 for the number of degrees of freedom is chosen for the computation of Table 1 , which is equivalent to a scatter index of 10 %, typical for a 20 min wave record. Also given in the table is

$$\text{BIAS[X]} = (E[X]/F - 1)\ 100\ \%$$
$$\text{Standard Deviation [X]} = (VAR[X]/E[X])\ 100\ \% \qquad (9)$$

While the standard deviation decreases with the number of samples, the bias increases to 10 % for just four samples. This effect leads to an "underprediction" of the measured peaks by a model that is calibrated to simulate expectation values of wave height.

Number of measurements m	1	2	3	4	5	6	7	8	9	10	11	12	13	14	15
Standard deviation [x] in %	10.0	8.1	7.3	6.8	6.5	6.2	6.0	5.8	5.7	5.6	5.6	5.5	5.4	5.4	5.3
Normalized expectation value E[x]/F	1.00	1.06	1.09	1.10	1.12	1.13	1.14	1.15	1.15	1.16	1.16	1.17	1.17	1.18	1.18
Bias [x] in %	.0	5.6	8.5	10.5	11.9	13.0	13.9	14.7	15.4	15.9	16.5	16.9	17.4	17.7	18.1

Table 1. Standard deviation, normalized expectation value and bias for n = 100 degrees of freedom of a peak wave height sampled m times during the peak event.

3. INFLUENCE OF SAMPLING RATES ON WAVE VALIDATION

A hypothetical time history of significant wave height is prescribed to represent a 'true' history of H_s. Samples of this true history are taken at intervals of one and three hours to determine the effect of the sample interval length on the accuracy of storm peak estimation. These results are used to determine the sensitivity of the estimated storm peak from model output at intervals of one and three hours. In all examples discussed below a storm with a peak wave height of 8.0 meters is specified. The growth to the peak and the decay following it are assumed to be at the same rate. Tests are made for rates of .2 and 1.0 meters per hour. The period of growth and decay are both six hours. Thus the slow rate of .2m/hour starts and ends with a height of 6.8 m and the fast rate of 1.0 m/hour starts and ends with a height of 2.0m.

A modelled time series is simulated by sampling the true H_s time series at intervals of 1 or 3 hours respectively and finding the maximum of the sample. The phase shift of the model output and the true storm peak was randomly selected for each storm. Ten thousand model time histories with sampling intervals of 1 and 3 hours were constructed for each true storm.

Comparison statistics are presented in the first two lines of Table 2 for true storm histories with growth/decay rates of .2m/hour. (Statistics for one hour sampling are on line one, three hours on line two). The first lines of Table 3 give the same statistics for growth rates 1.0 m/hour. The bias and the measures of scatter increase with increase in sampling interval and for the faster growth rates or narrower storm peaks. The following formulas generalize these results:

$$\text{BIAS} = (R \bullet T)/4. \text{ and RMS} = ((R \bullet T)^2/12.)^{1/2} \qquad (10)$$

where R is the storm growth/decay rate and T is the length of time between measurements.

COMPARISON	MEAN[M]	BIAS[M]	SD[m]	SI[%]
TRUE-MOD 1	8.000	0.050	0.029	0.359
TRUE-MOD 3	8.000	0.150	0.087	1.087
TRUE-INST 1	8.000	-0.710	0.448	5.597
TRUE-INST 3	8.000	-0.253	0.522	6.530
INST 3-MOD 1	8.252	0.302	0.523	6.341
INST 3-MOD 3	8.252	0.403	0.530	6.420

TRUE = SIMULATED STORM PEAK = 8.0 METERS
MOD1 = MODEL STORM PEAK, 1 HOUR SAMPLING
MOD3 = MODEL STORM PEAK, 3 HOUR SAMPLING
INST1 = INSTRUMENT STORM PEAK, 1 HOUR SAMPLING
INST3 = INSTRUMENT STORM PEAK, 3 HOUR SAMPLING
MEAN = MEAN OF STORM PEAKS
BIAS = BIAS OF STORM PEAK ESTIMATES
SD = STANDARD DEVIATION OF STORM PEAK ESTIMATES
SI = SCATTER INDEX = (SD/MEAN) *100

Table 2. Growth/decay is 0.2 meters per hour

COMPARISON	MEAN[M]	BIAS[M]	SD[m]	SI[%]
TRUE-MOD	1.0000	.253	0.144	1.806
TRUE-MOD	38.000	0.752	0.431	5.392
TRUE-INST	18.000	-0.035	0.550	6.881
TRUE-INST	38.000	0.601	0.682	8.522
INST 3-MOD	17.398	-0.348	0.697	9.422
INST 3-MOD	37.398	0.151	0.8051	0.884

Table 3. Growth/decay rate is 1.0 meters per hour (for parameter description see Table 2).

The results indicate that the model storm peaks will be biased low relative to the true peak by a significant amount for sharply peaked storms due to the sampling interval. It should be noted that these results do not include any other source of model error.

As discussed before, all measurements contain the effects of geophysical scatter. To simulate instrumental recordings geophysical scatter was added to each sample of the true history in a simple manner: the error was sampled from a normal distribution and scaled such that approximately 10 percent of the sample errors were greater than ten percent of the wave height, i.e., the error at 1.6 standard deviations was ten percent of the wave height. The mean of the geophysical scatter is zero. As done for the simulated model storm

histories, samples were taken at one and three hour intervals. The phase between the true storm peak and the sampling times was randomly selected, but less than the sampling interval. Ten thousand instrumental time histories with sampling intervals of 1 and 3 hours were constructed for each true storm.

Statistics for these simulations relative to the true storm peak are given in lines 3 and 4 of Tables 2 and 3 . As would be expected the geophysical scatter causes a negative bias and increases the measures of scatter, in comparison with the model statistics in lines one and two, which contain no geophysical scatter. This effect is greatest for the slow growth rate since there is more possibility for the scatter to increase a lower wave height to the maximum of the sample.

In any wave model validation we are faced with the problem that there are no true continuous storm histories for comparison with the model results. The only measure of model accuracy are comparisons with instrumental data, which in our case were primarily available at three hour intervals. Therefore, in our computer simulation, comparisons were made of instrumental data taken at three hour intervals with model data at intervals of one and three hours, with the same restrictions as applied above. Statistics for these comparisons are listed in the last two lines of Tables 2 and 3 . Overall the choice of using a one hour sampling of the wave model output is best since the scatter index is lowest ranging from about six to nine percent, increasing with increase in the storm growth rate. On the other hand the bias for the 1.0 m/hour case is the highest for the one hour model sampling and reaches nearly one half meter. It is instructive to realize that comparing three hourly instrumental data with three hour model output, results in scatter indices of 6.4 to 10.9 percent.

The bias and measures of scatter for the true peak is reduced significantly less when the model output interval is one hour. Over the range of growth rates tested the largest bias and scatter index are .25 m and 1.8 percent, respectively, with the one hour sampling. Maintaining the three hour sampling interval leads on the other hand to a worst case bias of .75 m and a scatter index of 5.4 percent. However, the uncertainty in the instrumental data in describing storm peaks due to the combined influences of geophysical scatter and the three hour sampling interval, overwhelms advantages in sampling the model output more frequently than three hours for validation of wave models.

4. SUMMARY

Possible sources of deviations between measured and modelled wave parameters have been discussed and quantified by simple models. In case of a peak to peak comparison about 15 % scatter and about 10 %

bias are estimated as lower limits of a validation statistic. These numbers were based on typical values for grid resolution, wind field accuracy and geophysical scatter and sampling rates.

Effects of finite water depth have not been considered in this paper. But additional variability from irregularities of the bathymetry and non stationary water depth will increase the above values.

The most significant contributor to bias and scatter in validation of wave models over large areas appear to be in the accuracy of wind field specification. Possible improvements to hindcast wind field specification may be in using instrumental wave data to better specify winds in particular storm development situations. Satellite winds in future may help to resolve this problem by incorporation of more data.

A second contributor to the problem of model validation is the accuracy of instrumental data in defining peak H_s. The problem is having data measured over too short a time periods and too infrequently. Increasing the rather standard observation period from 20 minutes to 30 minutes would increase the number of degrees of freedom from about 100 to 150 and reduce scatter from 10 to 8 percent. While continuous 30 min recordings would be optimal, 30 min recordings every hour would be a significant improvement.

5. ACKNOWLEDGEMENT

We would like to express our thanks to the NESS participants for the permission to use the NESS study results and for their helpful support. We would especially like to thank Dave Szabo for his stimulating remarks and for the permission to include his computer simulations in this presentation.

6. REFERENCES

Donelan, M., Pierson, W. J., 1983: The sampling variability of estimates of spectra of windgenerated gravity waves. J. Geophys. Res. 88, 4381–4392.

Gunther, H., 1981: A parametric surface wave model and the statistics of the prediction parameters. Hamburger Geophys. Einzelschr. 55

Monaldo, F., 1988: Expected differences between buoy and radar altimeter estimates of wind speed and significant wave height and their implications on buoy-altimeter comparisons. J. Geophys. Res. 93 (C3), 2285–2302.

Offshore Technology Report,1987: Assessment of wave hindcasting methods. U.K. Department of Energy OTH 87258, 60 pages and microfiche form.

The SWAMP Group: Allender, J. H., Barnett, T. P., Bertotti, L., Bruinsma, J, Cardone, V. J., Cavaleri, L., Ephraums, J., Golding, B., Greenwood, A., Guddal, J., Gunther, H., Hasselmann, K., Hasselmann, S., Joseph. P., Kawai, S., Komen, G. J., Lawson, L., Linné, H., Long, R. B., Lybanon, M., Mailand, E., Rosenthal, W., Toba, Y., Uji, T., and de Voogt, J. P., 1985:
Sea Wave Modelling Project (SWAMP). An intercomparison study of wind wave prediction models. P.I. In: Ocean Wave Modelling. Plenum Press, New York.

The SWIM group: Bouws, E., Ewing, J. A., Ephraums, J., Francis, P., Gunther, H., Janssen, P. A. E. M., Komen, G. J., Rosenthal, W., de Voogt, W. J. P., 1985,:
Shallow water intercomparison of wave prediction models (SWIM), Quart. J. Roy. Meteorol. Soc. 111, p. 1087-1113.

WAVE-ICE INTERACTION STUDY DURING LIMEX '87

[1]B.M. Eid, [1]C.M. Morton, [2]W.D. Windsor, and [3]V.J. Cardone

[1]MacLaren Plansearch Limited
Halifax, Nova Scotia

[2]C-CORE, Memorial University of Newfoundland
St. John's. Newfoundland

[3]Oceanweather Inc.
Cos Cob. Connecticut

ABSTRACT

During LIMEX '87 field experiment large amounts of data were collected in the Marginal Ice Zone (MIZ) by several research groups to study the dynamics of the southern edge of the Labrador Sea i,e, Ice Field. The aim of this study was to examine wave-ice interaction processes in the MIZ. In situe measurements were made; this included meteorological data, ice characteristics, waves, wave-induced ice motion, and aerial photography. This was supported by SAR overflights.

Ice motion sensor packages were deployed on ice floes to measure wave-induced ice motion at different locations in the MIZ. The limited open water wave measurements were supplemented by spectral wave model hindcast. Ice motion records were analyzed to produce directional wave spectra. A simple one dimensional model describing wave propagation in the MIZ, based on Wadhams exponential decay, was examined using the above field data. Preliminary result are presented,

1. INTRODUCTION

The Labrador Ice Margin Experiment LIMEX'87 was the first major field program of an international effort to study the dynamics of the Marginal Ice Zone (MIZ) of the Labrador Sea ice field. This pilot project took place in the Grand Banks region off the east coast of Newfoundland during the last two weeks of March 1987. LIMEX'87 was the first in a series of experiments to be conducted every two years (LIMEX,89 is currently underway) to address a number of objectives related to the dynamics of sea ice in the MIZ, testing microwave remote sensing techniques, and the development of air-sea-ice models to predict ice/ocean behaviours in this area.

The main objective of this paper is to examine wave-ice interaction processes in the MIZ from the field data obtained during LIMEX,87 field program. Surface observations and measurements were supported by the BIO's research vessel CSS Baffin. Of a particular interest to this study, the wave-induced ice motion was measured using ice motion sensor package developed by C-CORE of Memorial University of

Newfoundland. In addition ice characteristics, aerial photography. meteorological data, and wave buoy measurements were collected during the experiment (MacLaren Plansearach Limited (1988), McNutt et al. (1987)).

Wave-ice interaction is a very complex phenomenon which requires a considerable research efforts before these processes are fully understood. These processes involve wave propagation into the MIZ, reflection at the ice edge, attenuation by both mechanical and frictional processes, refraction, redistribution of spectral energy through non-linear wave-wave interactions, and wave generation within the ice field. This paper provides preliminary results of the study of wave propagation in the MIZ. Throughout the duration of the filed program, waves were essentially onshore and were observed to penetrate into the ice field to distances varied from few hundreds of metres to as far as the entire width of the ice field. This was also observed from SAR images collected by CCRS during the experiment.

The propagation of waves into the MIZ has been the subject of a limited number of studies. In one of the earliest studies, Robin (1963) observed that long period waves can be detected by shipborne wave recorders several kilometers into the ice. In a later study, Wadhams(1975) used a laser profiler and a infrared line scanner to simultaneously image surface waves and ice floe sizes and concentrations over an open drift ice field off the east coast of Newfoundland. More recently, Wadhams (1987) made a series of wave recordings under the ice margin between Greenland and Spitsbergen using an inverted echo sounder mounted on a patrol submarine. As a result of these experiments, the wave energy was found to have an exponential decay with penetration distance, with the rate of decay dependent on the wave frequency. Squire and Moore (1980) studied the wave decay in pack ice in the Bering Sea and found it followed the exponential decay with the decay rate was in general agreement with those found in Wadhams (1975). These studies described only a one dimensional. wave energy decay along the axis of propagation.

Cardone (1980) applied a one-dimensional numerical model to investigate the decay characteristics of typical Bering Sea storm seas in the MIZ. The model included all processes modelled in the two-dimensional deep water model, including propagation and generation, with the addition of the attenuation law of Wadhams (1975) and Squire and Moore (1980), and reductions in the magnitude of the linear and exponential growth rates consistent with reductions in momentum transfer across an interface partially covered with ice. Very recently, Wadhams et al. (1986) studied the effect of the marginal ice zone on ocean directional wave spectrum during the MIZEX-84 experiment in the Greenland Sea. The aim was to study the processes of reflection and refraction of the directional spectra. One of the major

limitations of this work was the limited data regarding prevailing ice conditions and simultaneous wave measurements.

This paper describes the field program carried out to study waves in ice, and reports on conditions encountered during the experiment and presents the results of data analysis.

2. FIELD EXPERIMENT

2.1 Weather and Ice Conditions During The Experiment

A few days before the start of the experiment, winds were predominantly from the west which caused the ice field to extend over to a distance between 100-200km from the coast. On March 13, the wind shifted to northeasterly, and became easterly on March 16, pushing the ice back against the shore. During the principal LIMEX data collection period, March 19-26, the steady easterly to northeasterly winds continued and the ice was further pushed against the shore in a narrow band (approximately 20km) of 10/10th ice (Figure 1). The westward ice drift had resulted in a fully compacted ice cover by March 21 and a formation of a distinct ice edge throughout the experiment period.

The ocean swell striking to the ice edge induces a large bending moment in the ice cover. This causes failure by crushing and abrading the floe perimeters. These failure modes produce a large volume of ground brash. The failing ice consumes a portion of the incident wave energy. This ground brash ice serves to lubricate the contact between the floes. As the failure proceeds, the ice adjacent to the ice edge offers less resistance to bending moments, Then the incident ocean wave field is able to penetrate deeper into the ice cover. The travelling wave attenuates, as it meets still compacted ice floes. The wave energy is absorbed by failing (grinding) solid ice at the floe to floe contacts,Every point into the pack experiences this bending moment, until the wave height is attenuated and the bending stress does not exceed the failure threshold.

The Synthetic Aperture Radar (SAR) imagery, collected by the CCRS Convair 580 Aircraft, on March 21, 23 and 26, displayed the changing nature of the ice cover during the experiment period. The imagery on March 21 showed the ice field compacted to solid ice cover with wave penetration limited to 1-2km of the ice edge. The ice adjacent to the ice edge did not exhibit an evidence of wave penetration. The imagery collected two days later on March 23 showed a distinct shear zone (about 10km from the coast) within the ice cover. East of the transition within the shear zone, there was a clear wave pattern in the ice cover (about 5km). West of the transition, the ice cover maintained enough floe to floe contact strength to absorb the incident wave energy. The SAR imagery collected on March 26 showed the full ice cover penetrated by ocean swell.

2.2 Aerial Photography and Floe Size Distribution Analysis

There were four helicopter flights produced 10 lines of aerial photography. The floe size distributions for the ice edge zone were estimated from the helicopter aerial photographs. Floe size distributions were calculated for selected aerial photograph lines AR #3, AR #5, and AR #10 (on March 23, 25 and 26, respectively), A summary of floe size characteristics for the selected lines is shown in Table 1 . The floe size histograms show the ice cover to be highly broken into small pancake floes. The mean floe size increased as a function of distance from the ice edge. The average floe size varied from 4.3 to 18m with maximum size of about 10 to 50m, respectively. These results provided additional evidence that the incident ocean waves are a major factor in breaking the ice cover of the marginal ice zone into small floes.

Table 1. Summary of Floe Size Distribution Analysis

Date	Location	No. of Floes	Mean(m)	Std. (m)	Maximum (m)
March 23	AR #3 edge	211	4.3	2.1	11
	midpoint	473	4.8	3.2	20
	coast	262	9.9	7.3	37
March 25	AR #5 edge	243	9.8	6.7	34
	2km from edge	115	7.2	5.3	27
	5km from coast	215	10.9	7.3	36
March 26	AR #10 (A) edge	363	5.4	3.4	20
	midpoint	277	7.7	4.7	44
	coast	188	18.0	11.1	51
	AR #10 (B) north end	299	6.7	3.6	23
	at ship	284	7.0	3.7	20
	at south end	284	7.1	3.7	28

Ice thickness measurements were made in the vicinity of the ship on March 20, 21, 23, 25 and 26 (which also coincided with ice motion package deployments). Thickness varied from 50cm to 250cm, with an average of about 140cm (McNutt et al. (1987)).

2.3 Wave-Induced Ice Motion Measurements

Two C-CORE ice motion packages were deployed on ice floes in the marginal ice zone. Both instruments were six degrees-of-freedom motion sensors. The two packages (designated B and C) differed primarily in their measurement of tilt components. Both packages contained three Sundstrand Servo-Accelerometers to measure linear acceleration along

orthogonal axes x,y,z,These sensors have a frequency response error of ±0.1% over the range 0 - 10Hz. Both packages also contained an Endeco Compass to measure magnetic bearing (0-360°). The accuracy of the compass is ±1°, with a resolution of 0.5°. To measure pitch and roll (angular rotation about x and y axes), package B contained a Humphrey Vertical Gyro. The vertical accuracy is ±0.5°, with a maximum linearity error of ±2%. Package C had two Penny & Giles Tilt sensors with a maximum linearity error of ±0.15°. In absolute terms, the computed vertical displacements obtained from LIMEX'87 deployments should be accurate to within ±3cm, The pitch and roll measurements obtained from the gyro in package B should be accurate to within ±0.1°, while those obtained from the tiltmeters in package C should be accurate to within ±1°.

There were 13 deployments of the ice motion packages during LIMEX,87; only eight deployments yielded a useable data of approximately 8 hours on three different days (March 22, 25, 26).

Run I: March 22 (Figure 2)

Deployment 22-1C (using C package) was made at 13:30-15:50 GMT on a small floe in a strip of sea ice of separate floes and a water boundary around all floes, Adjacent floes were not touching or colliding. Floe size in the pack was from 1 to 20m, thickness about 100cm. Two meter swell was visually observed running within the ice cover. The ship moved 500-1000m away from the motion package while recording the data. A waverider (heave) buoy was deployed in the open water adjacent to this strip (at 13:50 GMT) approximately 500m from ice edge. Wind was blowing from N to NNE at 10M/3 (20 knots). Swell travelled in same direction.

Run II: March 25 (Figure 3)

In this test simultaneous measurements were made at the ice edge and progressively into the ice field, This was intended to measure wave penetration into the ice pack. The ice cover was not constrained by land boundaries downwind at this location, Ice concentration was 9+/10 of new to first year ice. Four successful deployments of ice motion packages were accomplished. Deployment 25-1C (15:22 GMT) was on a small floe (<5m) close to the ice edge. The package was left there to collect data over the next six hours while the second package (B) was sequentially placed in the ice pack at approximately 1.5, 2.8 and 4.3km from the edge. These are denoted 25-2B, 3B and 4B respectively. As can be seen from the deployment and recovery positions of the motion packages (Figure 3) the ice was moving southwest throughout the day. The ice conditions along the measurements line showed a heavy pack but with considerable ground or brash ice between floes. The ice conditions changed to heavier floe concentration from stations 2B to

4B. Stations 2B to 4B were relatively on larger ice floes (6-12m) with thickness in the order of 100-150cm. A few hours before the experiment (0600 GMT) there was strong easterly winds (15m/s) shifted to northerly by noon then changed to northeasterly by the end of the day. During the duration of the experiment (1500"2100 GMT) wind speed varied from 10-5 M/3 mainly from N-NE. The field party observed swell penetration to about 5km into the ice pack.

Run III: March 26 (Figure 4)

Three deployments of the ice motion package (26-1B, 2C and 3B) were made at about 0.25, 1.5 and 3nm from ice edge. Only deployments 1B and 3B yielded Usable data. There was land restraint to the west but there was no pressure evident in the ice. The bays to the west were clear of ice. There was high concentration of ground brash between ice floes. The winds were light (5-7m/s) from the NE to E. The propagation of swell in the ice cover was obvious visually. The magnitude of swell did not appear to vary much inside the ice field. SAP image showed the swell to penetrate the entire ice edge with predominant direction from NE. It was also observed that the swell appeared to have more than a single directional components.

3. DATA ANALYSIS AND RESULTS

The standard measurement of wave elevation and slopes normally utilizes a wave buoy whose motion response characteristics are known over the range of wave frequencies in LIMEX 187, motion measurements were made on ice floes within the pack ice. The motion characteristics of the instrumented ice floes were not known, and hence, in general, it was not possible to state how the measured heave, pitch and roll relate to the corresponding wave elevation and slopes.

It is likely that for the predominantly long wavelength waves which penetrate the pack ice, moderately sized ice floes (<10m dia.) would follow the wave surface reasonably closely. In LIMEX 187 the dominant wave periods were greater than 8s (i.e. wave length >100m) and ice floes used were in the order of 5-12m. Thus, the measured floe motions may be assumed equivalent to the local water wave spectrum. This may be true if ice floes were free floating and not constrained in any given direction.

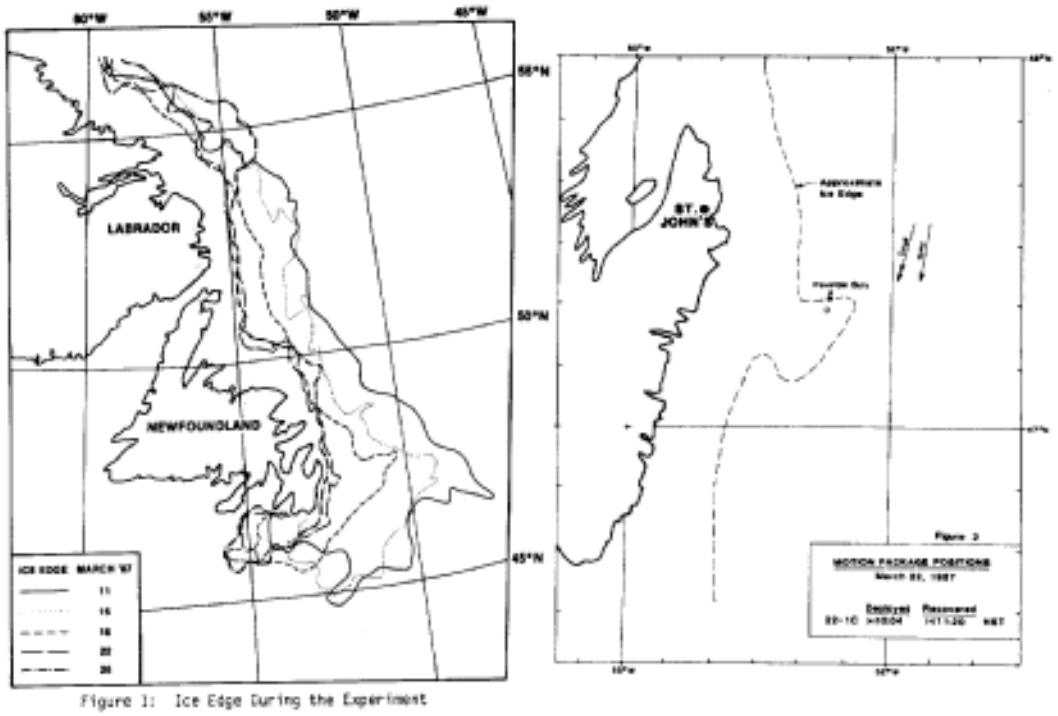

Figure 1: Ice Edge During the Experiment

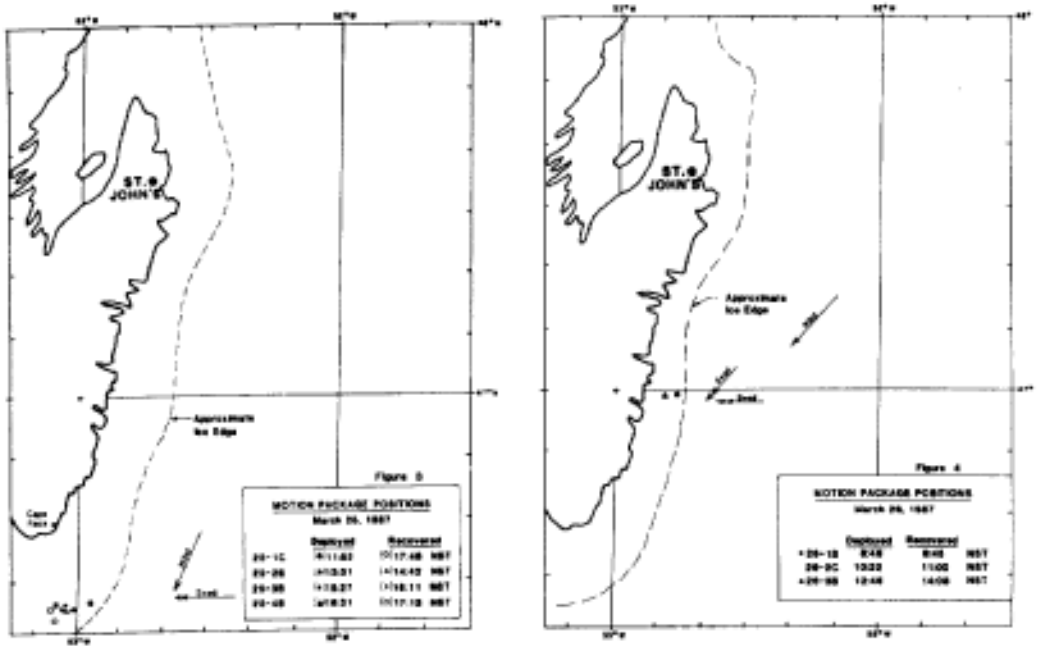

The recorded data by the motion packages were processed and converted into engineering units with reference to geographical coordinates (i,e. north, west and vertical directions). The method of Longuit-Higgins et al. (1963) was used where the convariance C_{ij} and quadrature-spectra Q_{ij} were obtained from correlations involving z(t), $\partial z/\partial x$, $\partial z/\partial y$ (i,j = 1,2,3 respectively).

Similar to the standard waverider buoys each ice motion record was divided into 20 minute blocks, The C-Q spectra (C_{11}, C_{22}, C_{22}, C_{33}, Q_{12}, and Q_{13}) were used to compute the 2-D energy spectra $E(f,\emptyset)$, using the maximum likelihood method of Oltman-Shay and Guza (1984). Since no directional wave measurements were available outside the MIZ, the ODGP spectral wave model was used to hindcast the open water wave fields during the study period. The ODGP results at grid points near the measuring locations were used to provide the open water waves (Figure 5). The results from the ice motion package, ODGP, and waverider buoy are summarized in Table 2 .

Table 2: Summary of Wave/Ice Motion Measurements and Model Predictions

Date	Ice Motion Package					ODGP Hindcast (Offshore)				Waverider Buoy (Thomas 1987)			
	Deployment #	Time (GMT)	Distance from edge	H_s (m)	T_p (s)	G.P.#	Time (GMT)	H_s (m)	T_p (s)	Location from edge	Time (GMT)	H_s (m)	T_p (s)
March 19	19-1B	17:10	no data recovered			3712	18:00	3.0	9.0	-500m**	17:00	2.4	8.0
March 21	20-1B	13:31	no data recovered			3712	18:00	2.8	9.0	500m	16:55	2.4	10.7
March 22	22-1C	13:9	edge*	1.89	9.1	3770	14:00	2.85	8.6	500m	13:50	2.3	9.2
		13:58	edge	1.73	8.0								
March 23	23-1C	13:32	no data recovered			3770	15:00	2.5	7.5	600m	15:30	2.5	9.2
March 25	25-1C	16:04	edge*	1.50	9.1	3741	16:00	1.9	6.3	-	-	-	-
	25-1C	17:13	edge*	1.60	8.7								
	25-2B	17:16	1500m	0.98	8.7	3741	18:00	1.87	6.3				
	25-1C	19:12	edge*	1.69	8.7								
	25-3B	19:05	2800m	0.63	9.5								
	25-1C	20:12	edge*	1.48	10.0	3741	20:00	1.91	8.6				
	25-4B	20:11	4300m	0.27	18.0								
March 26	26-3B	16:23	edge*	2.18	15.0	3741	15:00	2.34	9.7				

* edge = 200-500m from the open water inside the marginal ice zone
** -500m buoy was in open water pool 500m inside the ice edge.

3.1 One-Dimensional Spectra

The deployment 22-1C yielded two spectra. This was compared with the measurements from a waverider buoy which was deployed in the open

water approximately 500m from ice edge. The waverider, the ice motion, and the ODGP spectra are shown in Figure 6 . As shown, a noticeable attenuation of wave energy spectra can be seen, especially in the high frequency side of the spectrum. A reduction in wave height from 2.85 m predicted by ODGP to 2.3 m obtained from the waverider to 1.89-1.73 m from the motion package was found (Table 2).

The deployment 25-1C extended over a period of 5 1/2 hours and produced 15 (20 minute) records. One-dimensional spectra were obtained from the 15 records. Each exhibited prominent primary and secondary peaks. As shown in Table 2 , the significant wave height (H_s) from the 15 spectra did not vary significantly throughout the deployment period with an average of 1.57m,The primary and secondary peak periods were mostly about 9 and 6.5 s, respectively,The ODGP hindcast provided H_s in the order of 1,9 m and peak period about 9.5s. Figure 7a shows the average spectrum from the above records Compared with the hindcast spectrum from ODGP.

Deployments 25-2B, 25-3B and 25-4B were placed at approximately 1.5, 2.8 and 4.3 km from deployment 25-1C which was in the edge 200-300 m from the open water. Figure 7b illustrates the change in the 1-D "wave" energy at various distances into the ice zone versus corresponding spectra from 25-1C.

A comparison of the spectra at various distances into the ice zone indicates a decrease in the spectral energy with penetration into the ice pack with the higher frequency components attenuated much faster by the ice field than the lower frequencies.

On March 26, deployments 26-2C and 26-3B produced two similar, double peak, 1-D spectra, with primary peak period of 15s and secondary period 10.5s. The ODGP spectra indicates a slightly higher wave height and a peak period of 9.7s, The high energy content at 15s period may be explained as a resonant frequency of the ice floe, or a shift in wave energy from 10s to 15s had occurred,

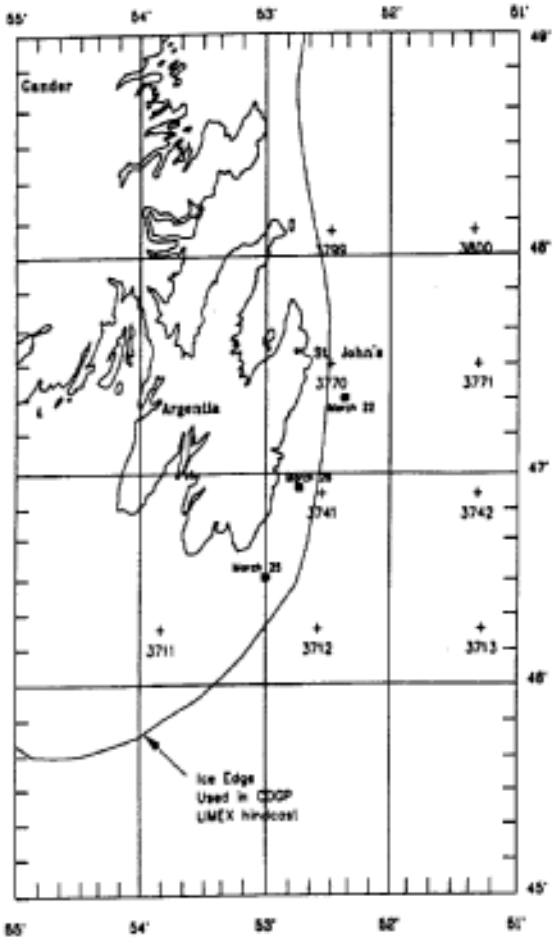

Figure 5: ODGP Model Grid Points Near Experiment Area

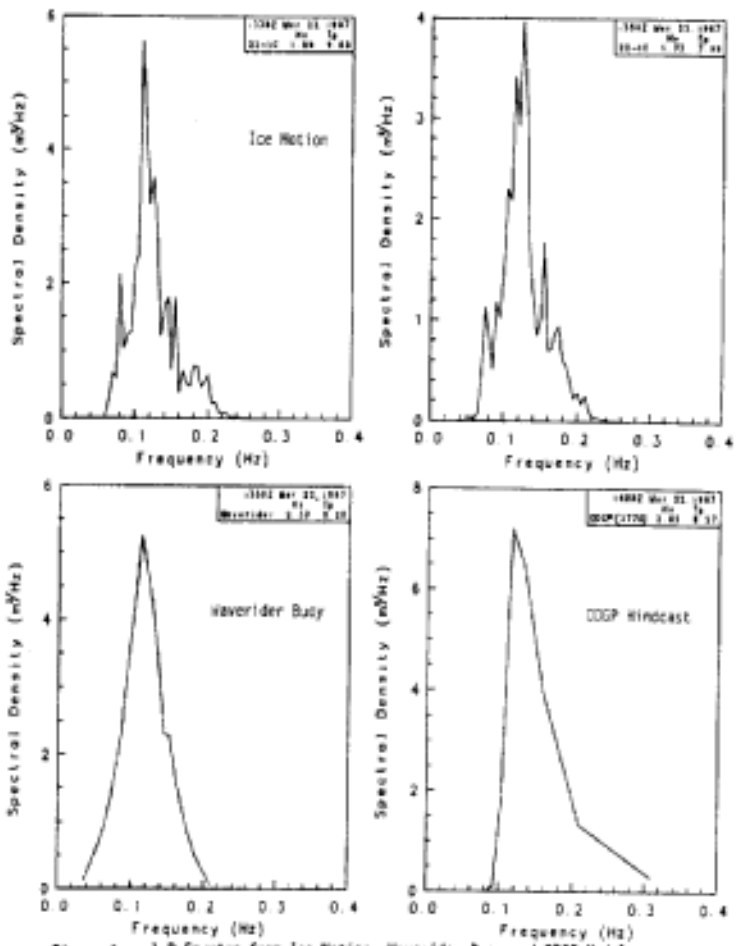

Figure 6 1-D Spectra from Ice Motion, Waverider Buoy and ODGP Model March 22, 1987.

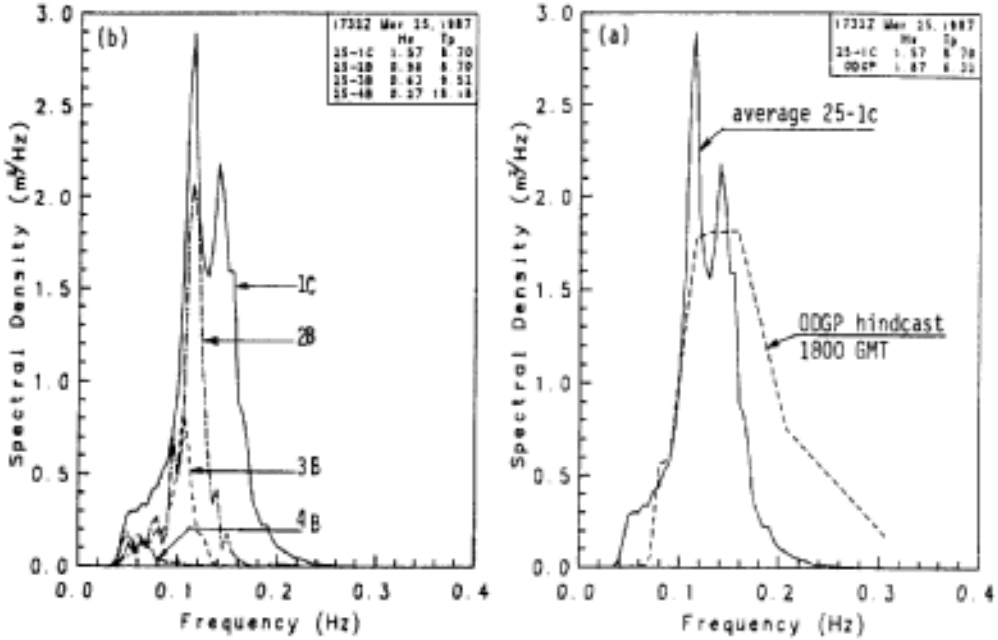

Figure 7: 1-D Spectra for ice motion at edge, 1.5, 2.8 and 4.3 Km

3.2 Wave Attennation in the MIZ

A linear potential theory was used to provide a simple approach to calculate wave attention along the line of propagation of a unidirectional wave. In Wadhams et al. (1986, 1987), the wave energy at a distance x in the ice field can be approximated as:

$$E_f(x) = E_f(o) \exp(-\lambda x)$$

where $E_f(o)$ is the wave energy outside the MIZ and λ is the attenuation coefficient. The attenuation coefficient is dependent on the frequency/wavelength of the incoming wave.

Although the ice package measurements were collected during different time periods, the measurements can still be used to verify Wadhams (1986) one-dimensional attenuation relation, since the duration of each experiment was relatively short during which the sea state did not change significantly. The rate of attenuation was calculated as shown in Figure 8 . The slope of the fitted line is the attenuation coefficient at a given frequency. An example calculation of the attenuation coefficient (at frequency 0.08 and 0.09 Hz) is shown in Figure 8a . The attenuation coefficients were found to be relatively higher than there obtained by Wadhams et al. (1988). Figure 8b shows the attenuation of the wave energy tends to decrease as the frequency decreases, or period increases, with faster decay at high frequencies.

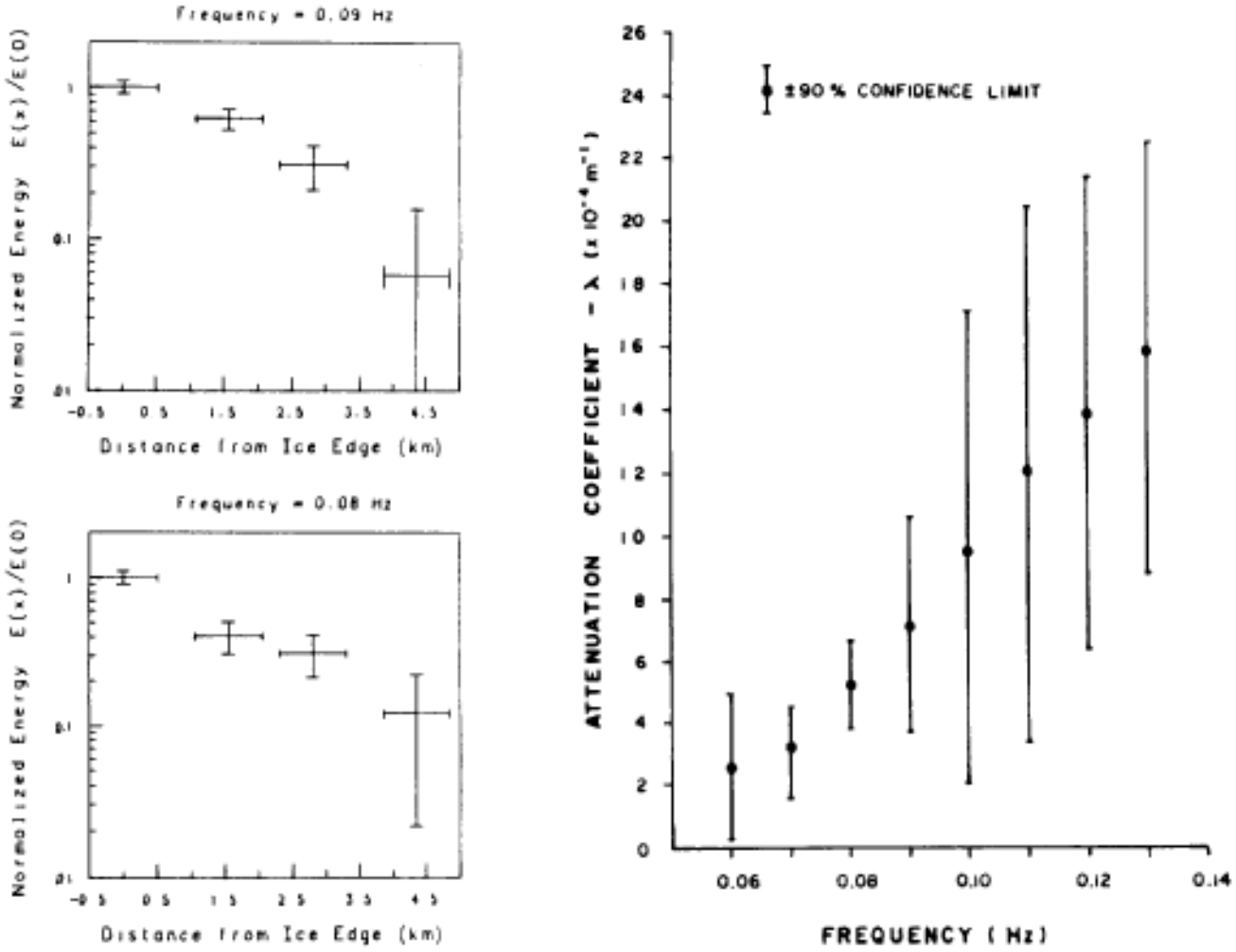

Figure 8: Wave attenuation as function of distance from ice edge and frequency.

3.3 Directional Energy Spectra

The directional spectra obtained from deployment 22-1C and ODGP are shown in Figure 9 . The ice package indicates an average wave direction towards the south-west which agrees with the ODGP spectra. However, the ice package indicates two peaks of energy. The second peak could be due to wave reflection or refraction due to ice pack.

Figures 10 represents selected 2-D spectra from deployments 25-1C, 25-2B, 25-4B, and ODGP, As shown the wave energy was travelling towards the south-west during the deployment. In some 25-1C records another peak travelling towards the north-east was shown which could be due to wave reflection at the ice edge. The 25-4B spectra indicates two peaks; towards north-east, and south-west. The motion towards the south-west agrees with the ODGP and 25-1C record. The northwest peaks could be due to reflection or due to the effect of ice field on floe motion. The change in "wave" frequency indicates a strong attenuation

of the higher frequencies, and perhaps a frequency shift as the waves pass through the ice field, Similar data were obtained from March 26 records,

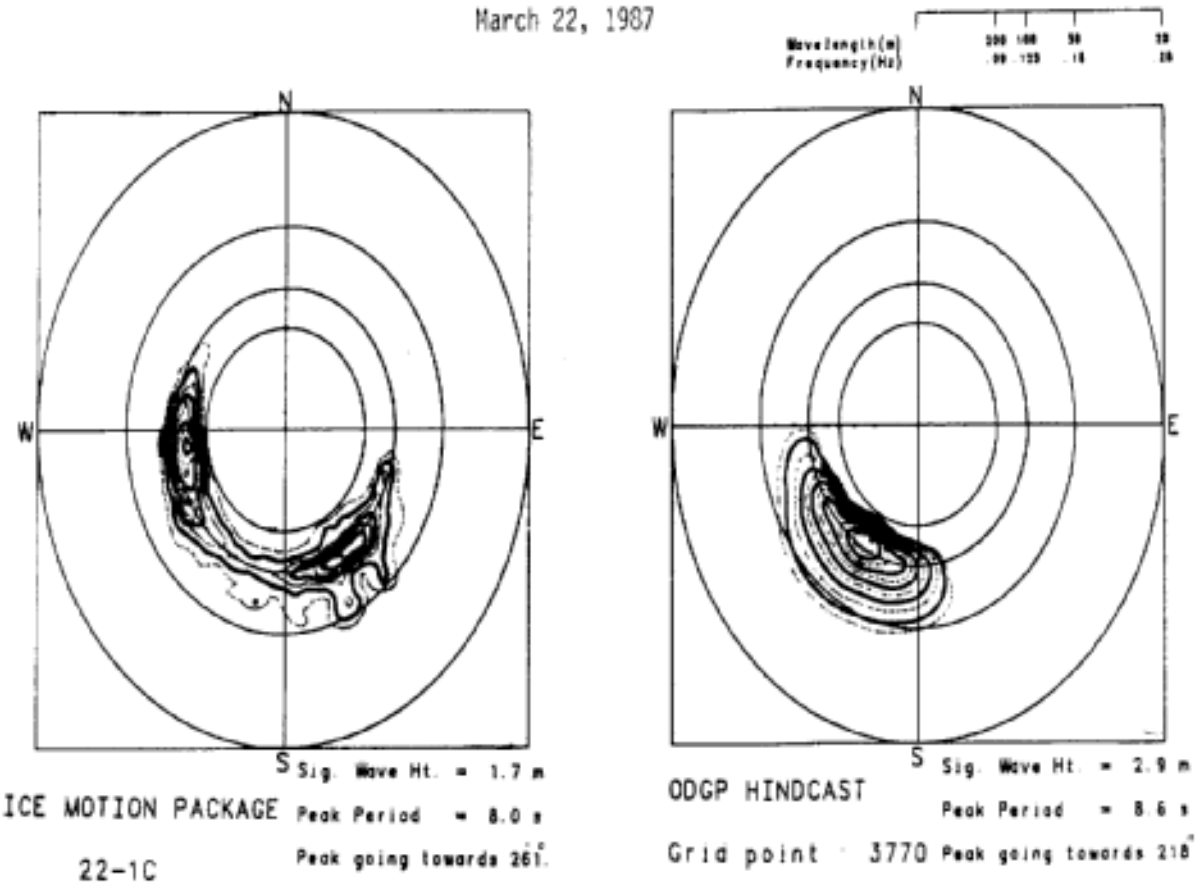

Figure 9

4. DISCUSSION

As seen the directional energy spectra inside the ice zone can be obtained from the ice motion package records. When calculating the directional spectra, the ice motion package was treated as a pitch-roll waverider buoy, with the assumption that the motion of the ice floe would closely follow the wave motion. However, the results from this analysis did not always support the above assumption. In some directional spectral plots, the ice floe motion occurred in a direction where one would expect reflections to be seen. In addition it was observed that ice floe drifted during deployments, and that the ice floe tended to rotate with time, No attempt was made to observe the interaction of the ice floe with other floes. During the deployment, the ice floe may have been subjected to slamming, or wedging between adjacent floes for short periods of time. These factors could greatly affect the analysis results,

Another assumption made during the analysis was that the ice motion package can be used in the same manner as a waverider buoy. Although the heave component has been tested, no attempt was made to test the directional results of the ice motion package in conditions measured by a directional waverider buoy. More tests are needed to determine whether the ice motion package can accurately provide directional spectral information. The dimension of the ice floe is potentially a very important factor in the motion seen by the ice package. Ideally, the ice motion package should be placed in the centre of a motion floe with a uniform thickness and circular in shape. From the oblique photographs of the ice floes used in the deployments, the ice package was not always placed near the center, and the dimensions of some floes were very irregular, These factors could greatly affect the motion measured by the ice package and should be avoided in the next LIMEX 189 experiment.

Another factor influencing the analysis results is the method used to calculate the 2-D spectra from measured parameters. In this study, the maximum likelihood method was chosen even though problems were known to exist with the method.

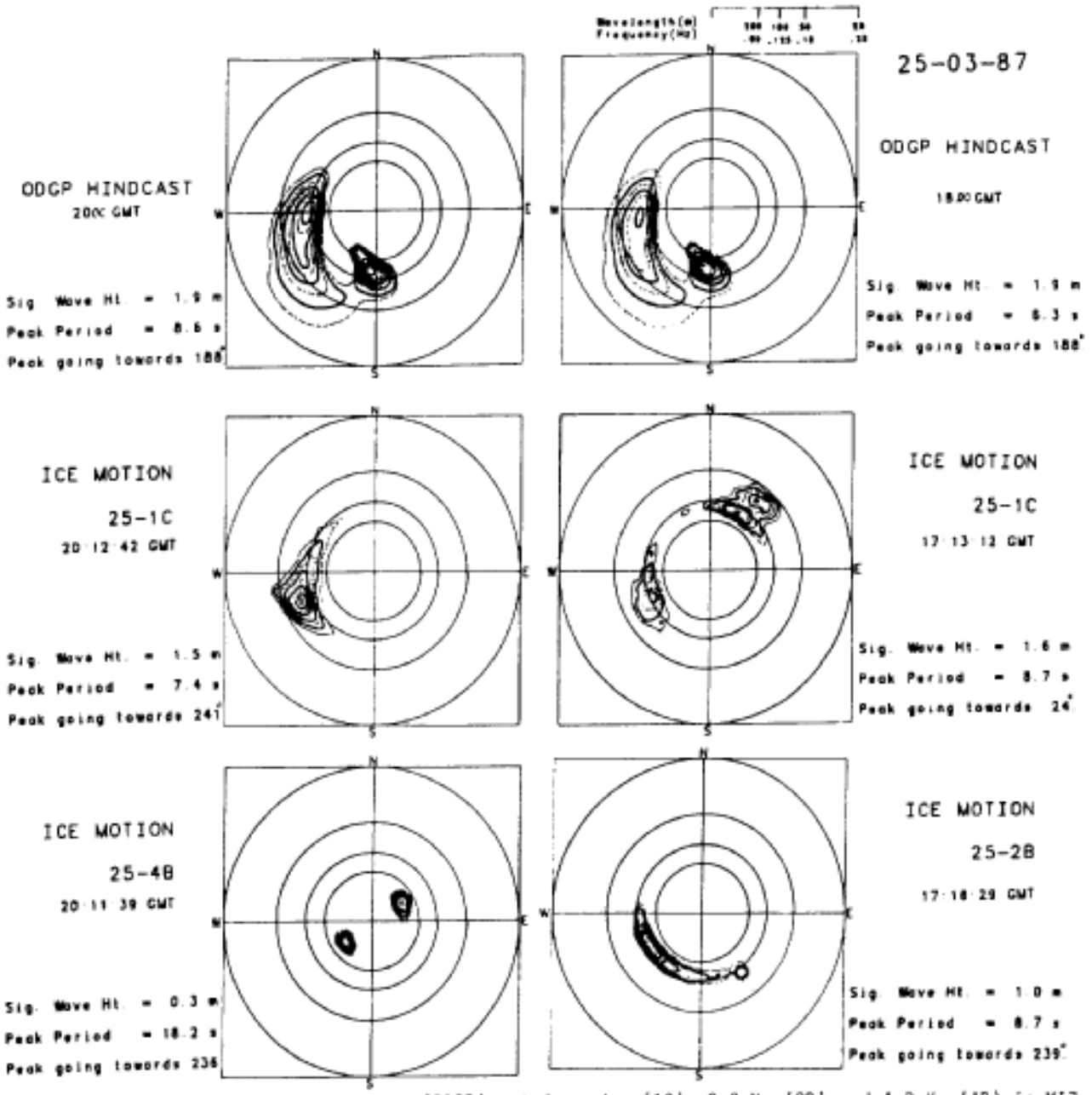

Figure 10: 2-D spectra in open water (ODGP), at ice edge (1C), 2.8 Km (2B) and 4.3 Km (4B) in MIZ

5. CONCLUSIONS

LIMEX'87 Pilot project has demonstrated that the wave-ice interaction is one of the significant environmental processes acting within the ice cover. It also demonstrated that the southern extent of the Labrador ice field is an extremely dynamic environment. The incident ocean waves dissipate most of their energy into the ice at the ice edge. This energy transfer is exhibited in the mechanical action between the ice floes and the grinding of brash ice which lies between the floes, The ice motion measurements show that the penetration of

the ocean waves into ice cover is governed by the size of the incident waves and the ice cover characteristics,

Long period waves and swell can penetrate a significant distance into the ice pack. Attenuation of wave energy is found to follow Wadhams exponential attenuation theory. High frequency components attenuate faster than low frequency components.

ACKNOWLEDGEMENTS This study was a result of an Unsolicited Proposal funded by Supply and Services Canada (DSS UP funds) and contributions from DFO (MEDS and BIO), EMR (CCRS) and PERD. The contribution from these sources are acknowledged with gratitude. The authors are also grateful to the Scientific Authority for this study, Dr. Ron Wilson of MEDS for this support and encouragement.

REFERENCES

Cardone, V., 1980. The Bering Sea Storm Specification Study. Proprietary Report to Exxon Production Resources,

Longuit-Higgins, M.S., D,E, Cartwright and N,D, Smith, 1963. Observations of the directional spectrum of sea waves using the motions of a floating buoy. Ocean Wave spectra, Prentice-Hall, 111-136,

MacLaren Plansearch Limited, 1988, Wave-ice interaction and site-specific wave prediction during LIMEX/LEWEX 187 Plot Project, Report submitted to the Marine Environmental Data Service, March, 1988.

McNutt, L., S. Argus, F, Carsey, B. Holt, J. Crawford, C, Tang, A. Gray and C. Livingstone, 1987, LIMEX 187 Sea Ice and Remote Sensing Data Report. Nov, 1987.

Oltman-Shay, Joan, and R.T, Guza, 1984. A data adaptive ocean wave directional-spectrum estimator for pitch and roll type measurements. J. Physical Oceanography, 14, 1800-1810.

Robin, C.D., 1963, Ocean waves in pack ice, The Polar Record, Vol. 11, No. 72,

Squire, V,A. and S,C, Moore, 1980, Direct measurement of the attenuation of ocean waves by pack ice. Nature, 283, 365-368,

Wadhams, P., 1975, Airborne laser profiling of swell in an open ice field, J. Geophys, Res., 80, 4520-4528,

Wadhams, P., 1978. Wave decay in the marginal ice zone measured from a submarine. Deep Sea Research, 25, 23-40,

Wadhams P., V. Squire, J.A. Ewing and R,W, Pascal, 1986, The effect of the Marginal Ice Zone on the directional wave spectrum of the Ocean, J. of Physical Oceanography, Vol. 16, pp, 358-376,

Wadhams P., V. Squire, D, Goodman, A. Cowan and S. Moore, 1988. The Attenuation rates J.Geophysical Research, Vol. 93, No. C6, of ocean waves in the marginal ice zone. pp. 6799-6818,

AN INTERACTIVE SPECTRAL WAVE FORECASTING TECHNIQUE

W.G. Lumsden

Meteorological and Oceanographic Centre
Halifax, Nova Scotia

1. Introduction

As the result of interactions of a number of individuals at the "First International Workshop On Wave Hindcasting and Forecasting", the Canadian Forces(CF) Meteorological and Oceanographic (METOC) Centre Halifax in co-operation with the Department of Fisheries and Oceans, the Canadian Oil and Gas Lands Administration and the Atmospheric Environment Service (AES) has implemented an interactive spectral wave hindcast/forecasting program. The interactive graphics interface was provided by AES and this interface has been coupled with Cardone's ODGP Spectral Wave Model.

The primary objective of this project, at least from an interdepartmental point of view, is to extend the existing three-year climatology of spectral hindcast data utilizing Cardone's model to a five-year climatology, From a METOC Centre perspective, this program provides the centre with a unique interactive tool which may be exploited in both the oceanographic and meteorological programs.

This paper will describe in rather general terms the interactive graphics interface, some of the implementation problems, the current status of the program and outline the expected future.

2. GRAPHICAL INTERFACE

The Interactive Graphics Editor (INGRED) (de Lorenzis, 1988) is currently running on a Hewlett Packard Series 9000 Model 330CH system. The system is programmed to automatically dial the Canadian Meteorological Centre (CMC) twice daily to access the Objective Analysis data and the Finite Element Model forecast data out to T+48 hrs. Grid point data of pressure and surface temperatures for 8610 points are received and passed to the INGRED system for automatic contouring. The domain for graphical editing is significantly larger than that of the wave model which is shown as Figure 1 , The data capture routine utilizes a Telebit TrailBlazer Plus modem that can achieve data rates of 19,200 baud on a common voice grade circuit.

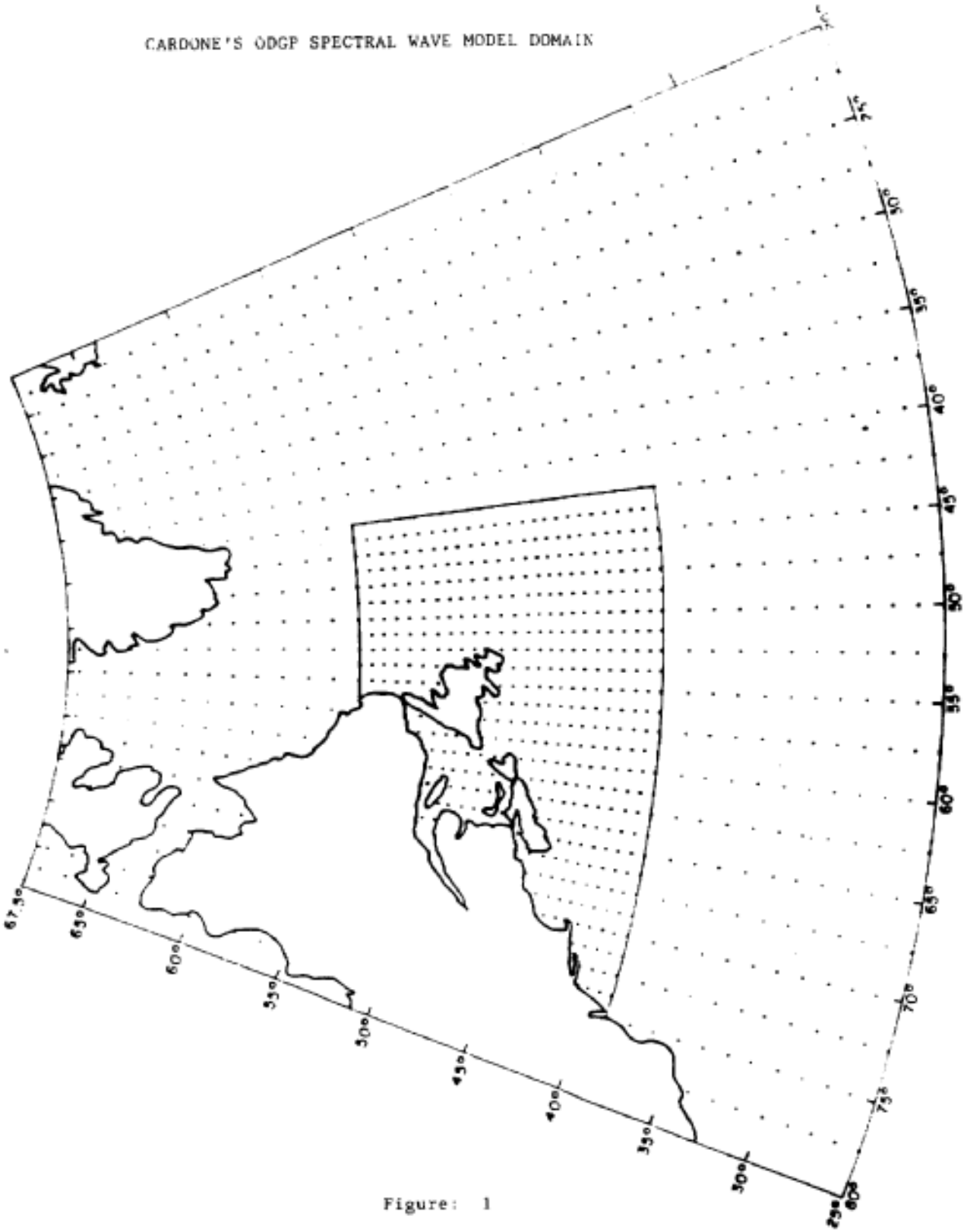
CARDONE'S ODGP SPECTRAL WAVE MODEL DOMAIN
67.5°
65°
60°
55°
50°
45°
40°
35°
30°
25°
60°
65°
70°
75°
80°
85°
90°
95°
100°

Figure: 1

The analyst then can display the objective Analysis fields and compare them with the corresponding subjective analysis produced by the centre and edit accordingly. The INGRED system allows the analyst to edit, delete or draw contours of pressure, temperature and sea surface temperatures. Each of the contours may be labelled or sampled. In addition, the analyst may sample or display specified fields of geostrophic or boundary layer winds. When the analyst is happy that the analysis adequately depicts the surface pressure field and the resulting surface wind regime, the modified analysis is stored and the data may be preprocessed for transfer to the wave model.

The ability to quickly display or sample wind fields is a tremendous feature of this system. When the analyst selects any point the system calculates the perpendicular distance to the closest two, but different, isobars and computes the geostrophic wind. Should one select the boundary layer wind option, then the system utilizes the air-sea temperature difference and calculates the 19.5 metre neutrally stable wind.

Two different methods of preparing the subjectively modified data to the wave model are available. Cardone's original application utilized manual methods of digitizing the pressure contour fields. The contour information was then interpolated to the model grid and the winds were then calculated from the grid point values. The INGRED system can produce pressure information in the same format as that expected by the original spectral wave model. The present hindcast program utilizes this approach.

The second method and the most appealing method to this Centre is to pass calculated wind data into the wave model. The calculation of the boundary layer wind in the INGRED system actually utilizes Cardone's Marine Boundary Layer Model to calculate the 19.5 metre wind. The only major difference is that the INGRED system uses its own method of calculating the geostrophic winds to drive the boundary layer model. Although this method is preferred, the run times on the HP-330 system are still too long and there are still a few minor bugs with respect to the model interface. The primary advantage of using this method is that the wind field can be readily viewed prior to running the actual wave model and re-editing could be an option and since the wind domain is larger than the actual domain of the wave model it is felt that the boundary conditions may be somewhat better.

Cardone's ODGP-OPR real-time wind/wave analysis-forecast system was implemented on the METOC Centre's HP 9000 series model 550 during the May-June 1988 period by MacLaren Plansearch Limited. The actual model implementation went smoothly but unfortunately interfacing the INGRED system, developing automated data capture routines and introducing operational staff to the procedures has been much more time consuming.

The objective here was not to validate the wave model as such since it has been widely accepted, the objective was to implement it on a different host. The early model runs verified that the host conversion was successful.

The model was run during the summer and fall of 1988 utilizing unmodified CMC Objective Analysis data. Twelve hour hindcasts were completed twice daily. Wave model runs were executed in approximately two hours. This clearly indicated to operational staff that the method was acceptable but the long run times precluded operational forecast implementation.

During January 1989 operational staff were introduced to real-time procedures. The CMC objective data is now being modified to be consistent the subjective analyses and ship reports. Early indications from operational staff are mostly positive in nature. The biggest draw back at present is the lack of routines to display the wave output graphically and the ever present cry for hard copy output, A minor bug in the main output file has been discovered thus this program still has a ways to go before the operational hindcast implementation can be determined a success.

3. PROBLEMS ENCOUNTERED

The most significant problem encountered was the lack of good clear documentation. The implementation support was for the most part just that. Learning to adequately sort out the problems associated with interfacing of the INGRED system to the wave model was hampered by a lack of sufficient understanding of each of these systems and having to wade through the source code to fix minor problems.

The Centre could not devote adequate system analyst type support to this project. We seriously under estimated the amount of implementation support required; consequently the time available, after the initial installation to support the programming aspects, was extremely limited,

The development of the automated data capture routines was most interesting but much more time consuming than originally planned. This caused significant slippage in the overall program. At present there are no routines to graphically display the final wave model output, This lack of an adequate output display has not been accepted well by operational staff.

4. FUTURE

The first efforts will be placed on fixing the minor problems in both the graphics system and the wave model output data fields. When this is completed full implementation of the hindcast program

utilizing operational staff on a semi real-time basis will commence. The next step will be to produce adequate documentation on that interim state of the total package. Following this, development of graphical and hard copy output utilities will commenced. The last step in this initial phase will be the interfacing of the INGRED wind field calculations to Cardone's boundary layer model and thence the wave model.

The approach being taken in this hindcast implementation has being well received by operational staff thus it has potential for success in a forecast mode. The current hardware suite will not provide the turn around times required thus more powerful hardware will be required. Bench marking on a number of other systems is planned for the near future and the results of those tests will determine how much further we can go with the limiting funds available.

ACKNOWLEDGEMENT

I would like to thank the following for the excellent efforts they have put forth in making this project happen; Mr. Val Swail AES, Mr. Bruno de Lorenzis AES, Mr, Ron Wilson MEDS, Dr. V.R, Cardone Oceanweather Inc and Dr. B.M. Eid and staff MacLaren Plansearch.

REFERENCES

de Lorenzis, Bruno, 1988: Interactive Graphic Editor Preprint, Fourth International Conference Interactive Information and Processing Systems for Meteorology, Oceanography, and Hydrology American Meteorological Society, 143-145

SEAWEATHER: AN OPERATIONAL, WIND AND WAVE FORECASTING SYSTEM FOR BRITISH COLUMBIA COASTAL WATERS

Donald O. Hodgins and Byron C. Berglund
Seaconsult Marine Research Ltd.
820-1200 West 73rd Avenue
Vancouver, Canada

1. INTRODUCTION

As part of the effort to improve wave forecasting in British Columbia coastal waters, a computerized wave prediction system was developed and tested in the Pacific Weather Centre (PWC) of the Atmospheric Environment Service for a 6-month period from May to the end of October, 1988, This wave prediction system, which incorporated two different spectral wave models, was derived from Seaconsult's Seaweather software package created originally for hindcasting applications. In this paper, we will describe the components of Seaweather adapted for use in the operational forecasting system, and how it was implemented in the weather centre, The results of the system testing, in terms of forecaster acceptance and validation statistics, will then be discussed, leading to our conclusions and recommendations for future systems development.

2. SEAWEATHER SOFTWARE SYSTEM

The Seaweather system comprises a linked set of Fortran computer programs for hindcasting or forecasting marine wind fields and corresponding wave fields. Fig. 1 shows the components in logical order; there are three main levels of input starting with the wind procedures: (1) surface pressure distributions, with information on atmospheric stability, (2) isotach and streamflow lines prepared from a kinematic analysis, and (3) direct wind observations. Pressure, stability and kinematic inputs are specified by contours in digital latitude-longitude format, This information is transformed by software into grid-point 10-m overwater winds on any desired grid spacing on a number ()E different projections, The gradient/geostrophic wind, and atmospheric boundary layer calculations follow conventional practice (e.g. Delage, 1985; Yamada, 1976) , Isotach and streamflow line are interpreted directly into wind vectors through a spatial interpolation procedure,

The third method of directly entering wind observations, or prognosis winds, at a few locations and spatially interpolating them to fill a field, is supported by a mouse driven interactive graphic program that allows data entry, display, edit, and interpolation. The program is used to build up a wind field from few data inputs, display it, modify it and when satisfied, save it for input to the wave prediction step,

This is the method used in the PWC version for forecasting. A branch from this program also allows observed winds to be introduced into a geographical region covered by surface winds calculated through the boundary layer model, and blend the two inputs giving weight to the observed winds near their actual locations and using the pressure-derived winds for areas sparsely covered by observations (e,g. the Beaufort Sea). This facility captures many advantages of the kinematic analysis, with greater speed through the interactive screen graphics. Through these three procedures the final set of wind fields are built up. They are then available for display, input to the wave modules, and archiving.

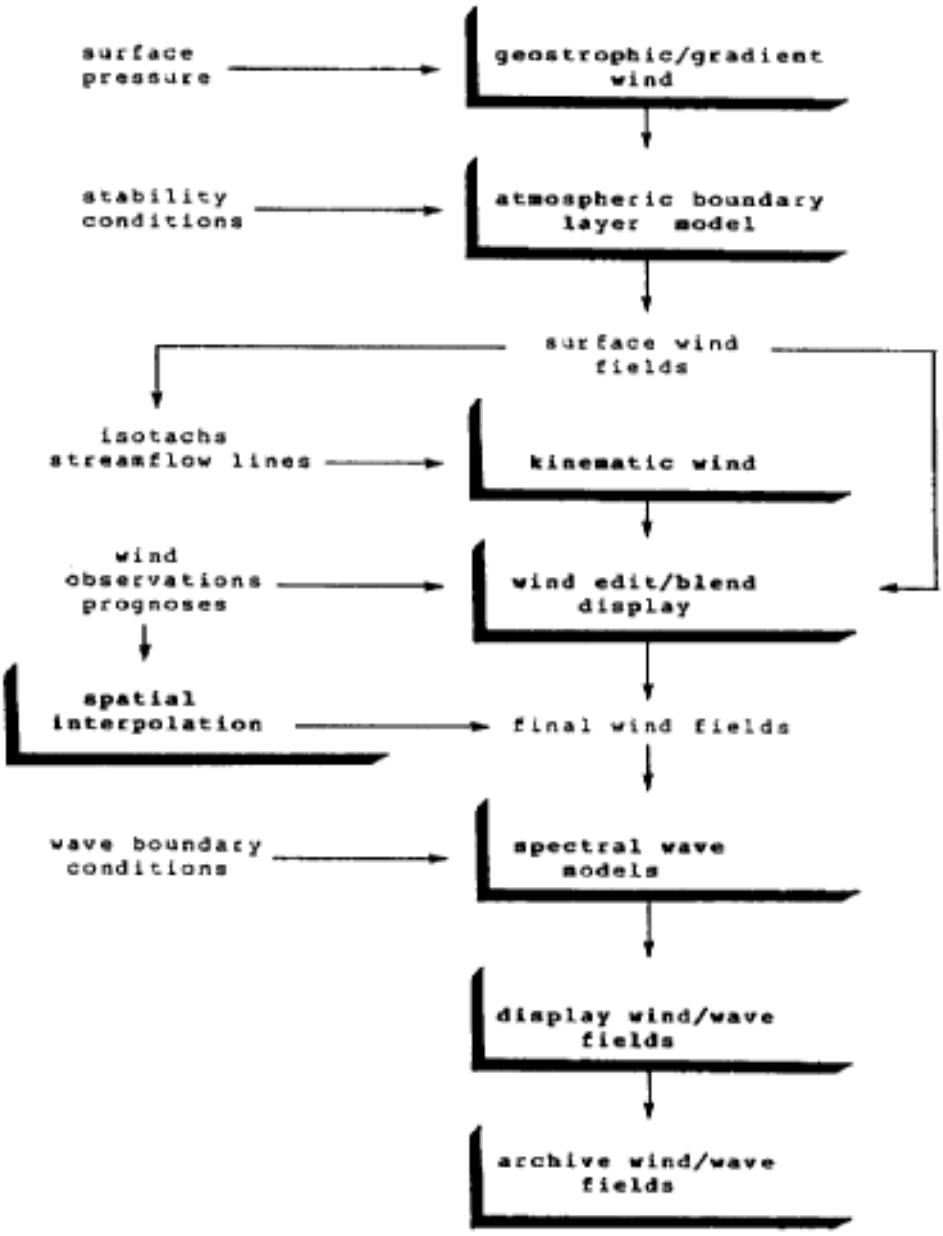

Fig. 1 Seaweather system organization.

For most applications wave boundary data are required in addition to the wind inputs. if the model boundaries are far enough away from the area of interest, and uninfluenced by distant swell, then the boundary input can be set to zero, and any errors so introduced are assumed to be small. in other cases, including the PWC forecasting system, wave data are required along the open sea boundaries. options are included in Seaweather to specify the boundary input as 2-D wave spectra.- or as significant wave height, peak period and direction. This latter

information is transformed to directional spectra using empirical forms.

Three spectral wave models are presently incorporated into the system, The most advanced is the second generation coupled discrete model, WAVAD, developed by Resio (1981, 1987, 1988). It is also described by Hodgins and Nikleva (1986) for hindcasting severe storms along the B,C. coast, The second model, SPECREF, is the first generation discrete propagation code published by Hodgins (1986) and Hodgins and Niwinski (1987), and the third model is the parametric spectral code described by Donelan (1977) and Schwab et al. (1984), denoted here as PARSPEC, Of these, the first two, WAVAD and SPECREF, are fully generalized for shallow water, PARSPEC is usually applied in confined water bodies, such as the Strait of Georgia, where distant swell is not important, and is valid for deep water wave conditions.

To a large extent, tie nature of data available for forecasting in the PWC during 1988 dictated the components included into the operational system, These components are shown in the box in Fig. 1 . Two wave models were applied: SPECREF along the outer coast, and PARSPEC in the Strait of Georgia-Juan de Fuca Strait regions.

3. FORECASTING SYSTEM DESCRIPTION

The operational system was discussed with PWC to determine the best methods of interfacing the facility with procedures and data available to the marine forecaster, The central issue addressed in this work was input of deep water boundary conditions for the coastal wave model, and overwater winds out to 30 hours lead time. Consideration was given to how the offshore forecasts were prepared, the role played by the Canadian Meteorological Centre's (CMC) numerical weather and parametric wave prognosis products, and forecaster time available to interface with a coastal wave modelling system.

3.1 System Concept

The data resources available for deep water wave forecasts included the PWC derived charts, the CMC parametric wave model grid point data, and a second parametric wave forecast issued by the U,S. Weather Service. On-line access to spectral wave model forecasts by the Fleet Numerical Oceanographic Centre(FNOC-Monterey) were not available, and at the time spectral wave model forecasts for the Pacific ocean were not yet available from CMC. Based on forecaster experience, the most suitable source of wave data was judged to be the PWC product. Experience has shown that in some weather systems the CMC output differs substantially from that produced by the local forecaster, and that the local forecast is more reliable,

The situation was similar for overwater winds along the coast, There was no source of automatically generated winds that provides the

reliability of the forecast winds in each marine area that are derived by the marine forecaster. Thus the coastal wave forecasting system concept was one based on two high resolution spectral wave models, applied to the continental shelf and Straits of Georgia/Juan de Fuca respectively, drawing boundary conditions and overwater winds from the PWC forecast products. These prognosis products, developed for a much larger geographical area in the Gulf of Alaska, are in hard copy chart form, coupled with tabular forms for analysis-time data. Thus the focus of hardware and software integration was on a geographical user interface to allow rapid, flexible data entry (winds and boundary waves), with editing capability, and forecast wave data display. The wave models ran transparently to the forecaster on a remote host computer once input data were judged satisfactory for each 30 hour prognosis,

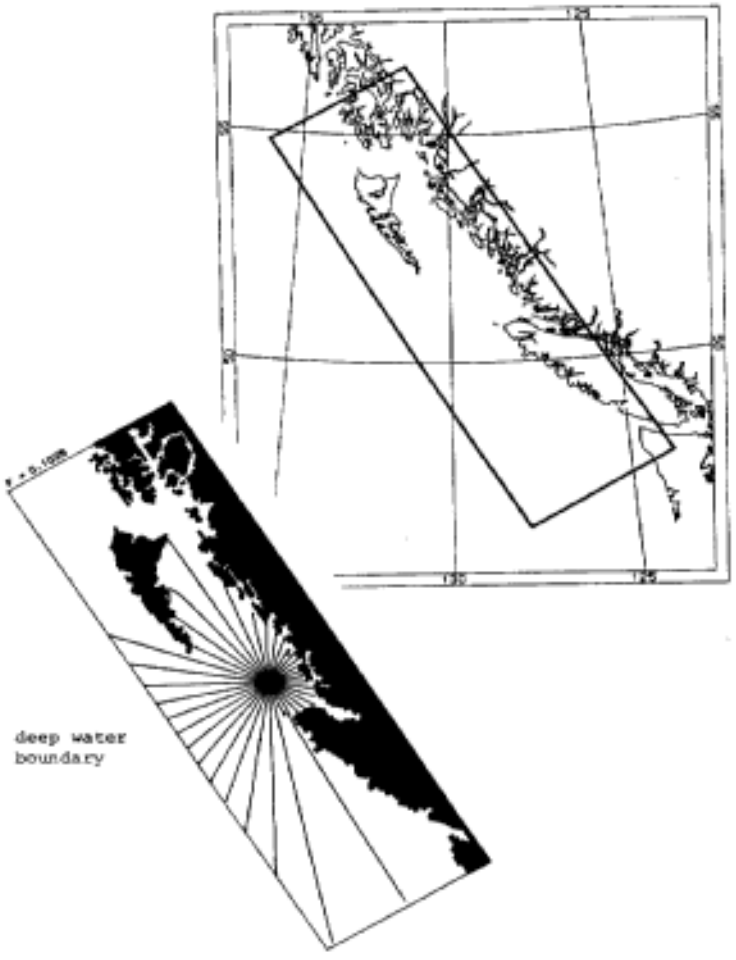

Fig. 2 SPECREF domain on the B.C. coast and a typical 10 s wave ray pattern.

3.2 Wave Models and Data Requirements

Along the outer coast, SPECREF was applied over the area shown in Fig. 2 . It incorporated: (1) high resolution (5 km) of landforms and

bathymetry; (2) shallow water wave transformation (shoaling and refraction); (3) depth dependent wave breaking saturation limit; (4) wind growth. Wave reflection at shorelines, which is a minor factor, and wave-current interactions, were neglected. The model was applied with 32 spectral directions and 16 frequencies. The predicted spectra thus have 512 degrees of freedom, providing good angular resolution for wave direction and clear wind wave and swell discrimination by frequency, Input data requirements were: the directional wave energy spectrum along the deep water boundary, and the overwater 10-m wind inside the model area. These data were required between 0 and +30 hours, Accuracy of the forecasts depends upon the accuracy of these input data, their resolution in time and their resolution in space. This model does not require initial data; the deep water boundary data are transferred into the target output points in each marine forecast area, acted upon by the local wind and shallow water transformation processes.

The Strait of Georgia model, PARSPECF required only wind input. The model was applied on a 4-km grid, matched to that for the tidal currents model for the system (Crean et al., 19 88), This was done to provide a compatible structure for future studies of wave-current interaction. Except for the mouth of Juan de Fuca Strait, these water bodies are surrounded by land and do not require any boundary wave data. in this forecasting system the coastal model and the Strait of Georgia model (which includes Juan de Fuca Strait) were not dynamically coupled,Consequently open ocean swell was not present in the Juan de Fuca predictions.

These input data requirements, derived mainly from hardcopy charts as opposed to grid-point data generated by other models, led to an interactive system emphasizing rapid data entry, rapid and convenient data up-dating/editing and flexibility in how and where geographically wind data were specified, The key specifications for the input and output are discussed in the following sections.

3.3 Methods for Preparing Offshore Wave Data

Discussions during the design phase for this system revealed that forecasters were capable of dealing with combined wave height (Hc) predictions; they were less comfortable with dominant wave directions (D), and did not have procedures for forecasting wave periods (T). Four sets of parameters were considered for input: (i) combined wave height (I parameter); (ii) combined height and dominant wave direction (2 parameters); (iii) separate wind wave and swell heights (2 parameters); and (iv) separate wind wave and swell heights, combined with direction for each (4 parameters). In view of forecaster skills and knowledge, and the time required to maintain input data files, the second-option, Hc and D, was selected. Wave period T was calculated internally using a simple regression equation between Hc and T.

As a result, the methods of deep water wave forecasting for combined height remained the same as those then in place (chart based), Supplementary information on dominant wave direction was, however, required. New procedures, closely coupled to the chart derived height forecasts, were described during training sessions, based on an extension of analysis skills used for wave pattern translation in conjunction with wind, synthesizing information from the CMC progs, analysis charts, and a new storm analogue file prepared for the demonstration project. The deep water wave progs were drawn onto 1:10,000,000 scale charts as wave height contours, The idea behind inputting Hc to the wave model was by specifying the intersection point of each contour on the open boundary, supplemented by direction D, using an interactive graphics program on a colour monitor. This method, which automatically accommodated greater spatial resolution for storm systems (more contours entered at close spacing) and lower resolution of quiet periods (fewer contours at wider spacing), preserved a close correspondence of data entry against a map reference, with the deep water charts.

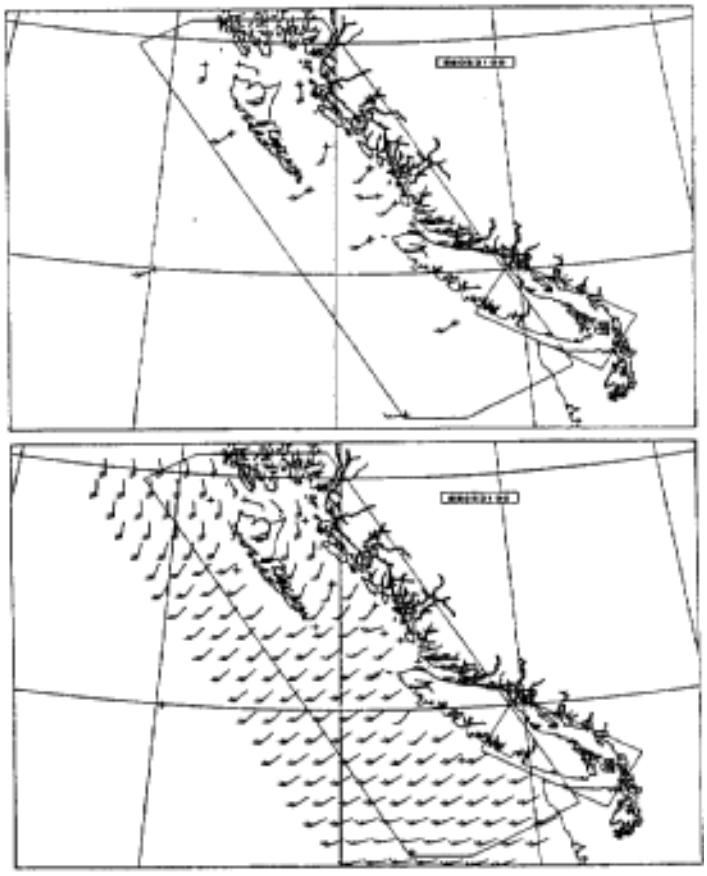

Fig. 3 Computer graphic for displaying wind vectors and interpolated fields.

3.4 Coastal Wind Data

Overwater wind forecasts are routinely prepared for each marine area at 18 hours and 30 hours by the marine forecaster, derived from the weather system analysis. This information provided the basis for specifying winds to both wave models. The user interface software, driven through a series of menus, allowed entry of wind data (direction, speed) at an arbitrary number of locations (Fig. 3) for a specific date and time (the valid time). The forecaster could display and edit the entered data, and interpolate between these data to yield a full vector field (Fig. 3). This field, interpolated yet further to the 5-km grid offshore and the 4-km grid inshore was the basic wind input to both spectral wave models, Linear interpolation between the sequence of valid times, ranging from 0 to 30 hours, completed the input to the wave models.

3.5 Wave Forecast Output

The wave models provided sea state predictions in the form of a screen graphic at the 18 hour and 30 hour prog times. Twenty-two selected output locations (Fig. 4) included 17 points for the marine forecast areas and five sites for validation against buoy measurements, Wave model outputs included combined wave height, dominant wave direction and spectral peak period.

Each wave model created an output file containing these parameters at the points shown in Fig. 4 . This file could be viewed on the screen or printed locally by the forecaster. However, the principal tool for interpreting the combined wave height output was a geographical display portraying Hc and D in a special flag notation. The wave fields were defined by interpolation between output points generated at the 18-h and 30-h prog times (Fig. 5). Recently a colour wave height mapping routine has been added.

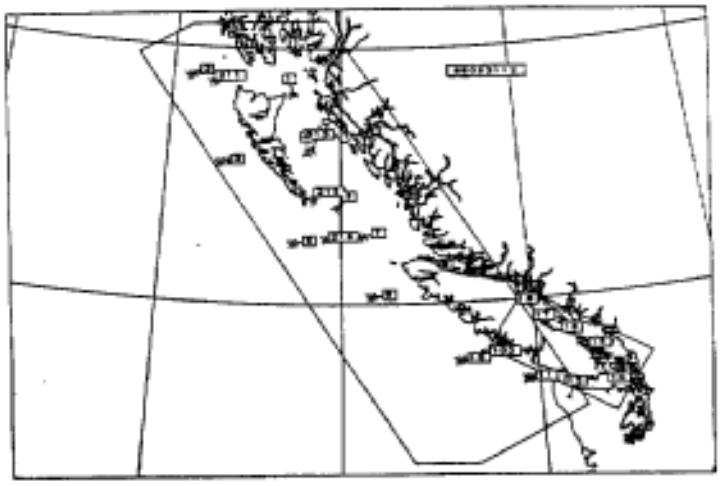

Fig. 4 Output locations for wave predictions.

3.6 Hardware Specifications

The forecasting system consisted of a front-end processor combined with a 19 inch colour graphics monitor, that ran the forecaster interface software coupled over a 2400 baud line to the main processor. The main processor ran the numerical wave models and archived output for later analysis. Hardware specifications are as follows:

Components	Software
Front-end processor	
IBM XT 8088 c/w 8087 coprocessor, 4.8 MHz clock speed 512 Kb RAMF	MS/DOS Metawindows, Fortran
10 Mb hard disk	
NEC Multisync XL colour 19" monitor	
Main processor	
Intel 310 80386 32-bit processor c/w 80387 coprocessor, 16 MHz clock speed,	Xenix O/S, Fortran
12 Mb RAM, 85 Mb hard disk	
Digidata 1600 bpi 9-track tape drive	

The front-end processor was placed at the marine forecast desk, and the wave models were run at a remote site (Seaconsult's office) on the Intel. A dial-up connection to the main computer was made once the wave models were ready to run, or when the models were finished and output data were ready for display.

Fig. 5 Computer graphic for displaying wave height and direction fields for a given valid time.

3.7 System Operation

The concept behind this system was that a set of wind and wave input files would be created for a series of valid times out to 30 hours. When weather systems were evolving rapidly, there would be several files, at perhaps 6 to 8 valid times; when conditions were relatively stable, there would be fewer files created. Once input files were in place, then the wave models were run.

During the next shift the forecaster could build upon the existing files, or create new ones in their place. The idea for updating was that the forecaster could readily view the data already contained in any file for a given valid time using the interactive graphics programs; if it was satisfactory then he exited leaving it unchanged. Otherwise, data at specific

4.0 FORECASTING SYSTEM EVALUATION

4.1 Forecaster Acceptance

The system went into operation in April 1988, and within 2 to 3 shifts, each forecaster could use the software and hardware largely as intended. Small changes to facilitate data entry, and to improve its convenience for users were made through April and May; however, within the first month, all forecasters were using the facility to produce coastal wave forecasts. In this sense, system acceptance was complete and it met its objectives.

The review of the system by the forecasters and our observations showed, however, that there were some limitations. Paramount amongst

these were the time taken to enter wind and wave data digitally, about 40 to 60 minutes, and the uncertainty associated with boundary wave inputs.

During the design phase it was decided to specify winds as spatial fields for a given valid time. The alternative is specification of a 30-h forecast wind time series at a given set of locations (or at selected locations using the coastal map). Experience with the system has shown that some forecasters like the spatial field concept for winds, while others would prefer a time series input. on balance, it now appears that the time series approach is the more desirable of the two, and should be incorporated into an enhanced system as one option for wind entry.

Entry of wave data--heights, periods and directions--along the open boundary presented the greatest difficulty to forecasters. Some problems include: uncertainty in specifying wave direction; uncertainty about wave periods, and a mixed reaction as to whether period should be an input parameter or set automatically in software; uneven skill in specifying direction by different forecasters; time required to manually enter these data, which increases for complex weather systems; and the frustration of being uncertain about the parameter values through unfamiliarity.

This aspect is the weakest part of the present system. Boundary wave data should be supplied from a deep ocean numerical forecast; ideally, one generated with a spectral wave model. It is anticipated that at some point CMC will bring a spectral wave model into service for the Pacific Ocean, although it is not likely to have high enough resolution for B.C. coastal forecasts. Such a model would be suitable to provide wind and wave fields in balance with each other along the deep water boundary of the coastal grid. All work to date in the formulation of SPECREF has had this development in mind.

4.2 Future Developments

The forecasting system described above was installed as a stand-alone facility for the six month demonstration period. Preparing the input for it represented additional work for the forecasters to their normal coastal forecasts, which they continued to prepare using manual techniques. A degree of integration between the new system and conventional practice was achieved only in as much as the manual techniques and associated analysis provided a basis for preparing the computer input for Seaweather.

The conventional practice involves a good deal of hand work in deriving deep water wave conditions. This is presently done on light tables where wave charts are drawn, sometimes superimposed on weather charts for deducing the synoptic coupling and wave pattern evolution.

Future development of the coastal wave forecasting system must be integrated into this process, especially for overwater winds, so that the handwork, which is the final product representing the forecaster's skill and judgement, leads directly to computer derivable information required by the wave models. This integration would accomplish two things: (1) a high degree of acceptance since the additional work to use the wave models is greatly reduced; and (2) a system that uses and builds on the forecaster expertise in the coastal area (as opposed to reverting to a wave forecasting model driven entirely by atmospheric model inputs without forecaster intervention). The latter point was one of the fundamental premises in Seaweather as it evolved.

4.3 Forecasting System Validation

Following the demonstration period, RMS errors and biases were computed using a method equivalent to that followed by PWC. The overall statistical summaries for data from July to October 1988 is presented in Table 1 for the wave model output, and in Table 2 for the PWC manual forecasts. In these tables the columns headed "OBS" and "ANAL" present the mean values of all measured, and analysis chart wave heights, respectively. When a particular buoy did not provide a measurement, then the nearly-equivalent value extracted from the analysis wave chart was used in its place for verification purposes. Thus the data in these two columns are mutually exclusive with respect to time, and are not of equal accuracy. For the latter reason, the RMS errors and biases are summarized for each source of validation data, observed or analyzed, separately.

Comparing these tables shows that the coastal model (SPECREF), with winds and boundary waves entered by the forecasters, is less accurate than manual forecasting at most validation points. The exception is Langara where the model is superior, both in terms of RMS error and bias. At the other locations, the model error ranged up to 1 $ to 2 $ times the forecast error. Both the model and forecast results tend to overpredict actual sea states, averaged over all heights.

The bivariate wave height-error histograms for the 18-h forecasts versus observed wave heights are presented in Tables 3 and 4 for both wave model and PWC predictions respectively. These tables are for the aggregate of all data over the period of July to October. Table 3 shows that the trend to overprediction in the wave model is a feature of low sea states. For large wave heights, this tendency is reversed, with the model underpredicting on average. These characteristics are found in both 18-h and 30-h progs.

Table 1

Validation Statistics For 18 and 30 Hour Forecasts Calculated Using SEAWEATHER

	OBS	ANAL	RMSE9	RMSE10	RMSE11	RMSE12
Langara:	1.91(234)	1.89(13)	0.41(1)	0.12(1)	0.46(52)	0.51(53)
Bonilla:	1.11(207)	0.76(36)	0.88(31)	0.42(31)	1.60(152)	1.69(152)
MEDS buoy #502:	1.26(198)	1.10(48)	1.02(12)	1.20(12)	0.81(139)	0.97(138)
MEDS buoy #503:	2.03(189)	1.77(56)	0.76(18)	1.12(19)	0.92(133)	0.96(131)
Quatsino:	2.51(2)	1.78(228)	0.81(170)	0.94(170)	0.01(1)	0.20(2)
Tofino:	1.43(168)	1.54(76)	1.03(52)	1.13(54)	1.00(125)	1.10(123)
buoy 46204:	1.41(56)	1.57(2)	0.64(2)	0.12(2)	0.75(28)	0.84(26)
Total:			0.86(286)	0.96(289)	1.09(630)	1.18(625)
Inshore:			0.86(286)	0.96(289)	1.09(630)	1.18(625)

	OBS	ANAL	BIAS9	BIAS10	BIAS11	BIAS12
Langara:	1.91(234)	1.89(13)	0.41(1)	0.12(1)	0.01(52)	0.11(53)
Bonilla:	1.11(207)	0.76(36)	0.26(31)	0.19(31)	1.11(152)	1.20(152)
MEDS buoy #502:	1.26(198)	1.10(48)	0.56(12)	0.61(12)	0.20(139)	0.34(138)
MEDS buoy #503:	2.03(189)	1.77(56)	0.03(18)	0.11(19)	-0.26(133)	-0.17(131)
Quatsino:	2.51(2)	1.78(228)	0.44(170)	0.47(170)	-0.01(1)	0.19(2)
Tofino:	1.43(168)	1.54(76)	0.63(52)	0.77(54)	0.66(125)	0.70(123)
buoy 46204:	1.41(56)	1.57(2)	0.64(2)	-0.02(2)	0.00(28)	-0.01(26)
Total:			0.44(286)	0.47(289)	0.39(630)	0.48(625)
Inshore:			0.44(286)	0.47(289)	0.39(630)	0.48(625)

DEFINITIONS

RMSE9 & BIAS9 = rmse & bias of 18HR Seaconsult prog wrt ANAL
RMSE10 & BIAS10 = rmse & bias of 30HR Seaconsult prog wrt ANAL
RMSE11 & BIAS11 = rmse & bias of 18HR Seaconsult prog wrt OBS
RMSE12 & BIAS12 = rmse & bias of 30HR Seaconsult prog wrt OBS

Table 2

Validation Statistics For 18 and 30 Hour Forecasts
Prepared By Pacific Weather Centre

	OBS	ANAL	RMSE5	RMSE6	RMSE7	MSE8
Langara:	1.91(234)	1.89(13)	0.66(13)	0.71(13)	0.57(230)	0.69(231)
Bonilla:	1.11(207)	0.76(36)	0.57(36)	0.27(35)	0.63(203)	0.80(204)
MEDS buoy #502:	1.26(198)	1.10(48)	0.49(48)	0.56(48)	0.63(194)	0.80(193)
MEDS buoy #503:	2.03(189)	1.77(56)	0.51(56)	0.53(56)	0.59(186)	0.74(186)
Quatsino:	2.51(2)	1.78(228)	0.49(226)	0.64(224)	0.65(2)	0.32(2)
Tofino:	1.43(168)	1.54(76)	0.48(74)	0.63(76)	0.48(168)	0.60(164)
buoy 46204:	1.41(56)	1.57(2)	0.16(2)	0.20(2)	0.49(50)	0.58(47)
Total:			0.49(481)	0.60(480)	0.58(1981)	0.72(1977)
Inshore:			0.50(455)	0.60(454)	0.58(1033)	0.73(1027)

	OBS	ANAL	BIAS5	BIAS6	BIAS7	BIAS8
Langara:	1.91(234)	1.89(13)	0.08(13)	-0.25(13)	0.13(230)	0.10(231)
Bonilla:	1.11(207)	0.76(36)	0.10(36)	0.10(35)	0.20(203)	0.26(204)
MEDS buoy #502:	1.26(198)	1.10(48)	0.15(48)	0.17(48)	0.27(194)	0.31(193)
MEDS buoy #503:	2.03(189)	1.77(56)	0.07(56)	0.03(56)	0.00(186)	0.02(186)
Quatsino:	2.51(2)	1.78(228)	0.12(226)	0.12(224)	-0.35(2)	0.10(2)
Tofino:	1.43(168)	1.54(76)	0.13(74)	0.12(76)	0.14(168)	0.18(164)
buoy 46204:	1.41(56)	1.57(2)	0.05(2)	0.00(2)	0.11(50)	0.08(47)
Total:			0.11(481)	0.09(480)	0.18(1981)	0.18(1977)
Inshore:			0.11(455)	0.10(454)	0.15(1033)	0.17(1027)

DEFINITIONS

RMSE5 & BIAS5 = rmse and bias of 18HR forecast wrt ANAL
RMSE6 & BIAS6 = rmse and bias of 30HR forecast wrt ANAL
RMSE7 & BIAS7 = rmse and bias of 18HR forecast wrt OBS
RMSE8 & BIAS8 = rmse and bias of 30HR forecast wrt OBS

These trends are also evident in the PWC forecasts although the scatter (range of error) is reduced from that in the wave model results. The results in these tables indicate that the coastal model proved to be slightly less accurate both in terms of RMS error and bias than the manual forecasting procedures over most of the stations. Prior to model installation at PWC, the numerical wave models were carefully confirmed against standard growth curves. Thus we believe that most of the inaccuracy reflected in these tables results from problems of entering wave data along the boundary, and not to a fundamental problem with model formulation. There were no measured wave data to validate the Strait of Georgia model, which was unfortunate in view of the importance of forecasts in this area for recreational boaters.

5. CONCLUSIONS

Use of forecasting system during the demonstration period led to the following conclusions:

(1) The wave models provide useful data for issuing forecasts, and the concept of using high resolution coastal wave models is

acknowledged as a good one. Further development of a forecasting system is warranted.

(2) The summer demonstration schedule did not, however, provide a good evaluation of the wave models because sea state conditions were too low. Although valuable comments on improvements to the user interface software were obtained, model performance could not be fairly evaluated, especially under severe winter weather conditions.

(3) The Seaweather framework for organizing and displaying input and output data and controlling options is functional and could serve as the basis for the next generation of forecasting system.

(4) The strategy used for entering winds and boundary wave data, while suitable for a limited trial period, is not optimum for an operational system because it is not fully enough integrated with conventional forecasting procedures.

(5) In terms of RMS errors and biases against wave measurements in the outer coastal areas, the conventional wave forecasts tended to be more accurate than wave model predictions. One reason for this may lie in the sensitivity of the wave model to boundary conditions, and the difficulty experienced by forecasters in prescribing these values.

(6) The next generation of coastal wave forecasting system must concentrate development on two aspects:

(a) integration of the wind progs with conventional forecasting procedures to provide gridded wind fields automatically, and

(b) provision of boundary wave data in spectral form from a deep-water wave model driven by either CMC model output, or PWC winds.

The next generation system is envisaged as running on hardware fully contained in the weather centre (forecaster workstation). The premise behind the system concept remains the same as for the demonstration system: that wind and wave forecasts for the coastal marine areas prepared by meteorologists in the PWC are superior to purely numerical progs derived from coarse-resolution atmospheric and ocean wave models. The severe storm hindcast for the B.C. coast described by Hodgins and Nikleva (1986), and the wave prediction sensitivity study reported by Hodgins and Hodgins (1986), strongly supports this premise, and justifies the high degree of man-machine interface.

Table 3

Wave Height Error Versus Wave Height
For the 18 Hour Forecast From SEAWEATHER

Error range (metres)			<1.0	1.1 to 2.0	2.1 to 3.0	3.1 to 4.0	4.1 to 5.0	5.1 to 6.0	6.1 to 7.0	7.1 to 8.0	8.1 to 9.0	9.1 to 10.0	10.1 to 11.0	11.1 to 12.0
	Height range (all range values are in metres).													
4.8	to	5.2	0	0	0	0	0	0	0	0	0	0	0	0
4.3	to	4.7	0	0	0	0	0	0	0	0	0	0	0	0
3.8	to	4.2	2	2	0	0	0	0	0	0	0	0	0	0
3.3	to	3.7	1	4	0	0	0	0	0	0	0	0	0	0
2.8	to	3.2	2	4	1	0	0	0	0	0	0	0	0	0
2.3	to	2.7	6	8	1	0	0	0	0	0	0	0	0	0
1.8	to	2.2	9	9	4	1	0	0	0	0	0	0	0	0
1.3	to	1.7	33	16	3	2	1	0	0	0	0	0	0	0
0.8	to	1.2	30	32	22	3	0	0	0	0	0	0	0	0
0.3	to	0.7	51	51	23	4	1	0	0	0	0	0	0	0
-0.2	to	0.2	62	69	14	2	0	0	0	0	0	0	0	0
-0.3	to	-0.7	34	42	11	4	2	2	0	0	0	0	0	0
-0.8	to	-1.2	1	21	9	4	1	1	0	0	0	0	0	0
-1.3	to	-1.7	0	3	7	7	0	0	0	0	0	0	0	0
-1.8	to	-2.2	0	0	1	1	3	1	0	0	0	0	0	0
-2.3	to	-2.7	0	0	1	1	0	0	0	0	0	0	0	0
-2.8	to	-3.2	0	0	0	0	0	0	0	0	0	0	0	0
-3.3	to	-3.7	0	0	0	0	0	0	0	0	0	0	0	0
-3.8	to	-4.2	0	0	0	0	0	0	0	0	0	0	0	0
-4.3	to	-4.7	0	0	0	0	0	0	0	0	0	0	0	0
-4.8	to	-5.2	0	0	0	0	0	0	0	0	0	0	0	0

Table 4

Wave Height Error Versus Wave Height
For the 18 Hour Forecast From Pacific Weather Centre

Error range (metres)			<1.0	1.1 to 2.0	2.1 to 3.0	3.1 to 4.0	4.1 to 5.0	5.1 to 6.0	6.1 to 7.0	7.1 to 8.0	8.1 to 9.0	9.1 to 10.0	10.1 to 11.0	11.1 to 12.0
	Height range (all range values are in metres).													
4.8	to	5.2	0	0	0	0	0	0	0	0	0	0	0	0
4.3	to	4.7	0	0	0	0	0	0	0	0	0	0	0	0
3.8	to	4.2	0	0	0	0	0	0	0	0	0	0	0	0
3.3	to	3.7	0	0	0	0	0	0	0	0	0	0	0	0
2.8	to	3.2	0	1	0	0	0	0	0	0	0	0	0	0
2.3	to	2.7	0	0	0	1	0	0	0	0	0	0	0	0
1.8	to	2.2	0	7	9	3	0	0	0	0	0	0	0	0
1.3	to	1.7	7	20	19	2	3	0	0	0	0	0	0	0
0.8	to	1.2	38	79	55	16	8	0	0	0	0	0	0	0
0.3	to	0.7	133	268	87	29	7	1	0	0	0	0	0	0
-0.2	to	0.2	230	401	158	45	11	2	0	0	0	0	0	0
-0.3	to	-0.7	13	109	92	34	9	3	2	0	0	0	0	0
-0.8	to	-1.2	0	9	21	20	4	2	0	0	0	0	0	0
-1.3	to	-1.7	0	0	2	7	6	3	1	0	0	0	0	0
-1.8	to	-2.2	0	0	0	1	1	1	0	0	0	0	0	0
-2.3	to	-2.7	0	0	0	0	0	1	0	0	0	0	0	0
-2.8	to	-3.2	0	0	0	0	0	0	0	0	0	0	0	0
-3.3	to	-3.7	0	0	0	0	0	0	0	0	0	0	0	0
-3.8	to	-4.2	0	0	0	0	0	0	0	0	0	0	0	0
-4.3	to	-4.7	0	0	0	0	0	0	0	0	0	0	0	0
-4.8	to	-5.2	0	0	0	0	0	0	0	0	0	0	0	0

6. REFERENCES

Crean, P.B., T.S. Murty and J.A. Stronach, 1988. Numerical Simulation of Oceanographic Processes in the Waters Between Vancouver Island and the Mainland. Oceanogr. Mar. Biol Annu. Rev., 26, 11-42.

Delage, Y., 1985. Surface Turbulent Flux Formulation in Stable Conditions for Atmospheric Models. Monthly Weather Review, 1(3).

Donelan, M.A., 1977. A Simple Numerical Model for Wave and Wind Stress Prediction. Report, National Water Res. Institute, Burlington.

Hodgins, D.O., 1986. Evaluation of Two Shallow Water Spectral Wave Models on Sable Island Bank, Canada. Proceedings of the International Workshop on Wave Hindcasting and Forecasting, Halifax, Nova Scotia. Environmental Studies Revolving Funds, Report Series No. 065, 59-73.

Hodgins, D.O. and S. Hodgins, 1986. Accuracy of Numerical Weather Prediction Winds and Some Consequences for Wave Prediction. Proceedings of the International Workshop on Wave Hindcasting and Forecasting, Halifax, Nova Scotia. Environmental Studies Revolving Funds, Report Series No. 065, 197-208.

Hodgins, D.O. and S. Nikleva, 1986. On the Impact of New Observing Sites on Severe Sea State Warnings for the B.C. Coast. Unpublished Technical Report Prepared For Fisheries & Oceans, Canada, By Seaconsult Marine Research Ltd., Vancouver.

Hodgins, D.O. and C.T. Niwinski, 1987. Prediction of Directional Wave Spectra at Coastal Locations. Proceedings of Coastal & Port Engineering in Developing Countries, Vol. II 2006-2020.

Resio, D.T., 1981. The Estimation of Wind-Wave Generation in a Discrete Spectral Model. J. Phys. Oceaong., 11, 510-525.

Resio, D.T., 1987. Shallow-Water Waves. I Theory. J. Waterway, Port, Coastal and Ocean-Engineering, 113(3), 264-281.

Resio, D.T., 1988. Shallow-Water Waves. II Data Comparisons. J. Waterway, Port,-Coastal, and Ocean Engineering, 114(1), 50-65.

Schwab, J.D., J.R., Bennett and P.C. Liu, 1984. Application of a Simple Numerical wave Prediction Model to Lake Erie, J. Geophys. Res., 89(C3), 3586-3592.

Yamada, T., 1976. On the Similarity Functions A, B, and C of the Planetary Boundary Layer, J. Atmos. Sci., 23, 781-793.

AN OPERATIONAL SPECTRAL WAVE FORECASTING MODEL FOR THE GULF OF MEXICO[1]

Yung Y. Chao

National Meteorological Center, NWS/NMC, NOAA
Washington D.C., U.S.A.

1. INTRODUCTION

Until recently, the NWS has been issuing wave forecast guidance for the Gulf of Mexico using a model developed by the Techniques Development Laboratory (TDL). The model empirically relates the significant wave height and period to wind speed, fetch and duration. The model performance was found to be inadequate in terms of accuracy and consistency of forecasted wave fields. Furthermore, wave forecasts are needed for both the deep (offshore) and shallow (coastal) areas of the Gulf. In each of these areas the dynamics of the wave physics are quite different and the empirical model cannot take these effects into account.

There are two operational global models which also routinely forecast wave conditions for the Gulf. They are the Fleet Numerical Oceanography Center Global Spectral Ocean-Wave Model (GSOWM) and the NOAA Ocean Wave (NOW) model. These models employ dynamical spectral wave forecasting techniques. However, in addition to being global scale models with coarse horizontal resolution, they are only applicable to deep water cases. The edicts of bottom condition on the modification of the wave spectrum are not considered in these models.

In order to improve and extend NMCs wave forecasting capability over the coastal areas of the Gulf of Mexico, a regional spectral ocean wave model, applicable for both deep and shallow waters of the gulf has been implemented recently. Model performance has been evaluated by means of statistical error analysis of the significant wave height forecasts against measurements at NDBC buoys in both deep and shallow water of the gulf. The result of evaluation along with an intercomparison with other deep water wave models forecasts are presented in this paper.

2. WAVE MODEL CHARACTERISTICS

The present model is an adaptation of the model developed by Duffy and Atlas (1984) to the Gulf of Mexico. The essential governing equations and computational procedures follow the model described by Golding (1983). The model solves the energy balance equation of the form

$$\partial E/\partial t = -\nabla \cdot (V\mathbf{E}) - \partial \{(V \cdot \nabla\theta)E\}/\partial\theta + I + D + N \qquad (1)$$

[1] OPC Contribution No.30

where $E(f,\theta)$ is the spectral density of the wave field, V the group velocity and θ is the wave direction, and where I represents energy input from winds, D energy loss due to whitecapping and bottom effects and N the redistribution of energy within the wave spectrum due to conservative nonlinear wave-wave interactions. The equation is solved in four stages in the following order: propagation, refraction, growth and dissipation, and nonlinear interaction.

In computing wave propagation, Golding (1983) used a modified Lax-Wendroff integration scheme while Duffy and Atlas have chosen a two-step, third order scheme suggested by Takaca (1984) to minimize numerical dissipation and dispersion. At grid points adjacent to the coast, this scheme, however, cannot be used because it uses values from two grid points away from the central grid. At these points, simple upstream differencing scheme is used assuming that no waves would be reflected from the shore. The wave refraction effect in shoaling water of varying depth is computed according to Golding (1983). The procedure involves using centered differences to compute the water depth derivatives and using upstream difference to solve the refraction portion of the wave energy equation in flux form.

The growth of waves driven by input surface winds, I, is modelled according to conventional linear and exponential terms representing, respectively, an excitation by turbulence fluctuation in the surface wind and the coupling of existing waves with mean shear flow in the marine boundary layer.

The wave energy dissipation in deep water due to whitecapping is determined according to a formulation involving the entire spectrum as described by Hasselmann (1974). In shallow water, in addition to the calculation of bottom friction loss of wave energy formulated by Collins (1972), a computation of energy low due to bottom percolation proposed by Shemdin et al. (1980) is included in the present model.

The nonlinear wave-wave energy transfer is considered in a parameterized and empirical manner. Firstly, a wind-sea spectrum is defined as that part of a spectrum that is : (1) above 0.8 of the peak frequency and (2) within 90 degrees of direction of wave propagation and wind direction. This wind-sea spectrum is then forced to conform to a modified JONSWAP spectrum based on the assumption that nonlinear interactions will always act to bring the wind-sea spectrum back to the modified JONSWAP-shape spectrum. This modified JONSWAP spectrum incorporates the saturation range in water of arbitrary depth suggested by Thornton (1977) and a cosine square angular spreading function with the original JONSWAP spectrum (Hasselmann et al.,1973).

The peak frequency is determined through an iterative procedure involving empirical equations.

At present, the model has twenty frequency bands ranging from 0.04 to 0.42 Hz and twelve direction bands. The Gulf of Mexico is assumed to be an enclosed ocean basin. Thus incoming waves from the Yucatan Straight and the Straight of Florida are ignored. The grid mesh is 37x27 with a grid interval of 55 km and the computational time step is 30 minutes. The model has been running daily on the NMC Cyber 205 computer generating wave spectra at three hour intervals out to 48 hours. The required wind input at a height of 10 meters above the sea surface is derived from the NMC Regional Analysis and Forecasting System (Holm, 1984). A modified two layers boundary model described by Cardone (1969) incorporates stability effects due to air-sea temperature difference. The wind field forecast is made at six hour intervals.

3. FORECAST PERFORMANCE EVALUATION

Wave data are acquired from buoy measurements in the Gulf of Mexico operated by NOAA Data Buoy Center. The buoy station 42001 on deep water is located at about the center of the Gulf (25.9N, 89.7W), midway between stations 42002 (26.0N, 93.5W) and 42003 (26.ON, 85.9W). The station 42015 (30.1N, 88.2W) is on a water depth of 16 m, 5 nm south of Dauphin Island near Mobil, Alabama. The wave data analyzer (WDA) wave measurement system mounted aboard a deep water buoy, consisting of an axial linear accelerometer, provides spectral estimates with a bandwidth 0.02 Hz and degrees of freedom of 48. The frequency bands range from 0.01 up to a cut-off frequency of 0.39 Hz. The upper and lower bounds of the 90% confidence interval are, respectively, 1.36 and 0.69 of the estimated value. At station 42015 is a pitch-roll directional wave-measuring buoy comprises a data acquisition control and telemetry (DACT) directional wave analyzer (DWA) system. The directional-frequency spectrum has a frequency bandwidth 0.01 Hz with center frequencies ranging from 0.03 to 0.35 Hz and the degree of freedom 24 (Steel and Lang, 1988). The upper and lower bounds of the 90% confidence interval are therefore 1.52 and 0.58, respectively. The wave data and other data such as wind speeds and directions were encoded and relayed to NMC via the Geostationary Operational Environmental Satellite (GOES). The anemometer height is 10 meter above the mean sea level.

The statistical error analysis is performed for the significant wave height forecasts of each model interpolated to the buoy locations at forecast hours : +12 Z, +24 Z, +36 Z and +48 Z using the concurrent buoy measurements as common validation standard. Willmott (1982) has suggested a series of statistical indices which should be calculated since no single index can adequately describe model performance. In this study, the analysis consists of the monthly mean bias error BIAS, correlation coefficient CORR, mean square error MSE as well as its

systematic and unsystematic proportions of magnitudes $(MSE)_s$ and $(MSE)_u$. These indices take the form

$$BIAS = N^{-1}\Sigma(P_i - O_i) \quad (2)$$

$$MSE = N^{1}\Sigma(P_i - O_i)^2 \quad (3)$$

$$(MSE)_s = N^{-1}\Sigma(\hat{P}_i - O_i)^2 \quad (4)$$

$$(MSE)_u = N^{-1}\Sigma(P_i - \hat{P}_i)^2 \quad (5)$$

$$CORR = \left\{\Sigma[(P_i - \bar{P})(O_i - \bar{O})]\right\} / \left\{\Sigma(P_i - \bar{P})^2\Sigma(O_i - \bar{O})^2\right\}^{1/2} \quad (6)$$

where N is the number of data points and $\hat{P}_i = a + bO_i$ in which a and b are the intercept and slope of the least squares regression, respectively, and where $\bar{P}$ and $\bar{O}$ are the means values of model predictions and measurements, respectively.

The *MSE* or its square root (*RMSE*) summarizes the mean difference in the units of *P* and *O*. The *MSE* comprises two parts, i.e.; $MSE = (MSE)_s + (MSE)_u$. For a good model, the systematic difference, from the model should approaches zero while the unsystematic difference approach *MSE*.

Figures 1 shows monthly statistics of the significant wave height forecasts of the present Gulf of Mexico wave model (GMEX) from October 1987 through February 1989 for the projection hour +24Z at deep water location –NDBC 42001. The statics shown in these figures include bias, root mean square error, correlation coefficient and the ratio of systematic root mean square error to total root mean square error. Also shown in Figure 1 are the results of other model forecasts, i.e., NOW model, GSOWM and TDL model.

In comparison with other models, the GMEX model tends to under-predict the significant wave height (SWH) in deep water while the NOW model and GSOWM tend to over-predict SWH. The TDL model also has shown negative bias for most months during the period when it was operative. Monthly root mean square error of the GMEX model is comparable with other models except September 1988. During that month, two hurricanes past through the gulf (Hurricane Florence and Hurricane Gilbert) and the wave height is over-predicted m a result of over-forecast of wind speed by Cardone's boundary layer wind model (1969). This is expected because the model is not designed for hurricane wind prediction. The graph which shows the monthly variation of correlation coefficient indicates that GMEX performs, in general, more consistent with measurements than other models.

The sources of systematic error in the wave height prediction are the result of imperfection in the wave model itself and/or the input wind

from the wind model. Monthly variation of the ratio of systematic root mean square error $(RMSE)_s$, to the total *RMSE* is presented for both wave height and boundary wind predictions. It is of interest to observe that the patterns of their variations are quite similar. It suggests that errors in the wind prediction is a major source that contributes to the error in the wave prediction, at least, in deep water.

Figures 2 shows monthly statistics of the GMEX model significant wave height forecasts for the same time frame and projection hour but in a water depth of 16 m – Buoy 42015.

In contrast to the deep water situation, monthly mean bias fluctuates around zero value ranging between +0.30 and –0.20 meter. the maximum and minimum values of RMSE during 17 months period of time is 0.55 and 0.25 meter and the mean value is 0.35 meter. Error in wind forecast associated with hurricanes Florence and Gilbert during September 1988 does not cause extreme RMSE value as what has happened in deep water situation. This seems to imply that wind is not the only dominant factor affecting coastal wave conditions. It also can be seen from a graph which shows monthly variation of systematic root mean square error of the wave height and wind speed that there is no close similarity in the pattern of fluctuation, i.e., error in wave forecasts is not due to error in wind forecast alone.

4. CONCLUDING REMARKS

The performance of NMC Gulf of Mexico spectral wave forecast model has been evaluated against buoy measurements and other wave forecast models – GSOWM, NOW, and TDL models for the months from October 1987 to February 1989. The model performance evaluation presented in this paper concentrates solely on the the significant wave height forecasts. Three major error statistics, i.e., the monthly bias, root mean square error and the systematic error and a supplementary statistics – correlation coefficient axe used as the evaluation standard. The results show that the GMEX model performs better than other models in deep water except during the erroneous hurricane wind forecast situation. The model performs quite well in coastal areas. Further improvement of the model can be achieved by improving wind forecasts and tuning of certain parameters involved in the model formulation.

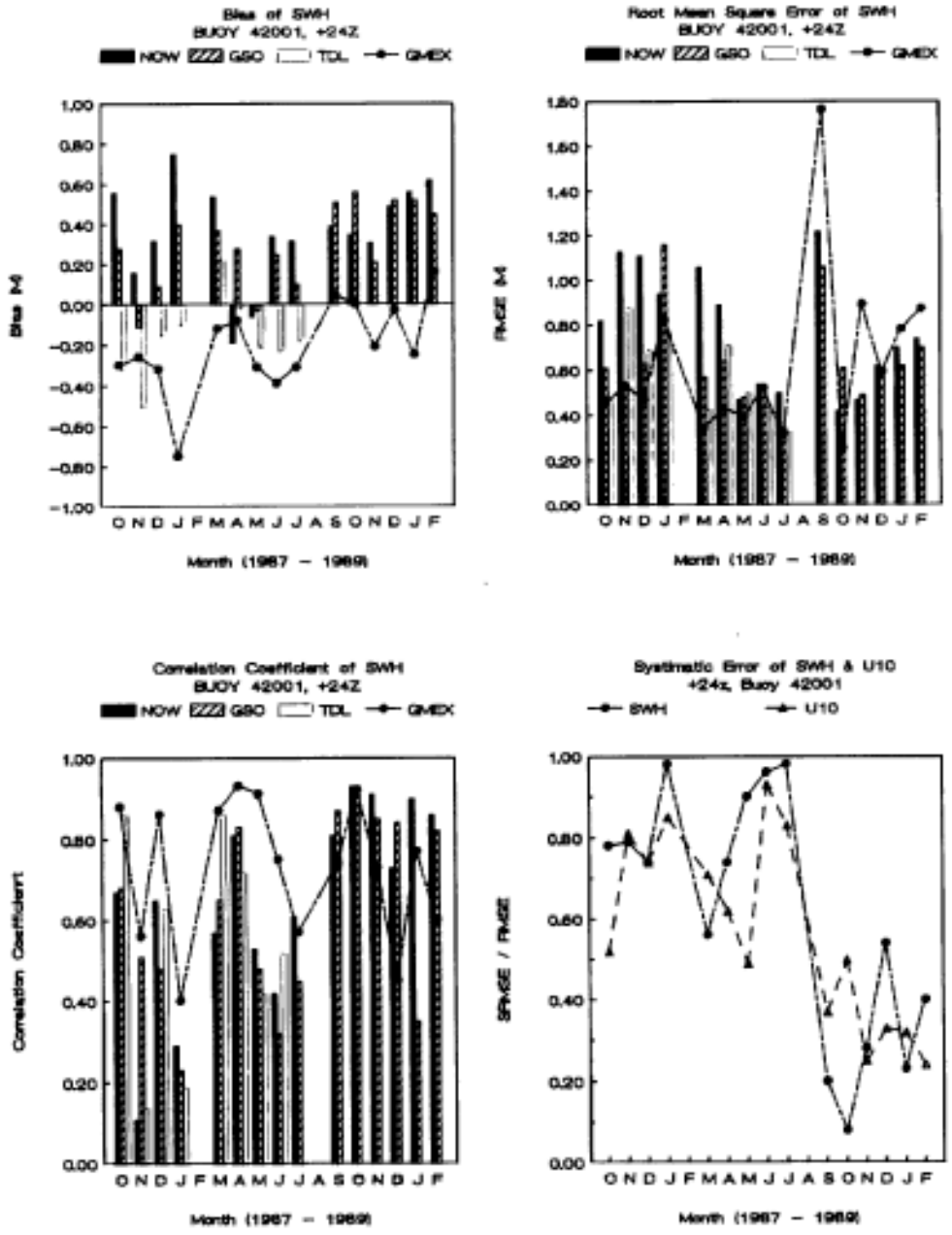

Figure 1: Monthly statistics for +24Z forecasts at a deep water location - Buoy 42001.

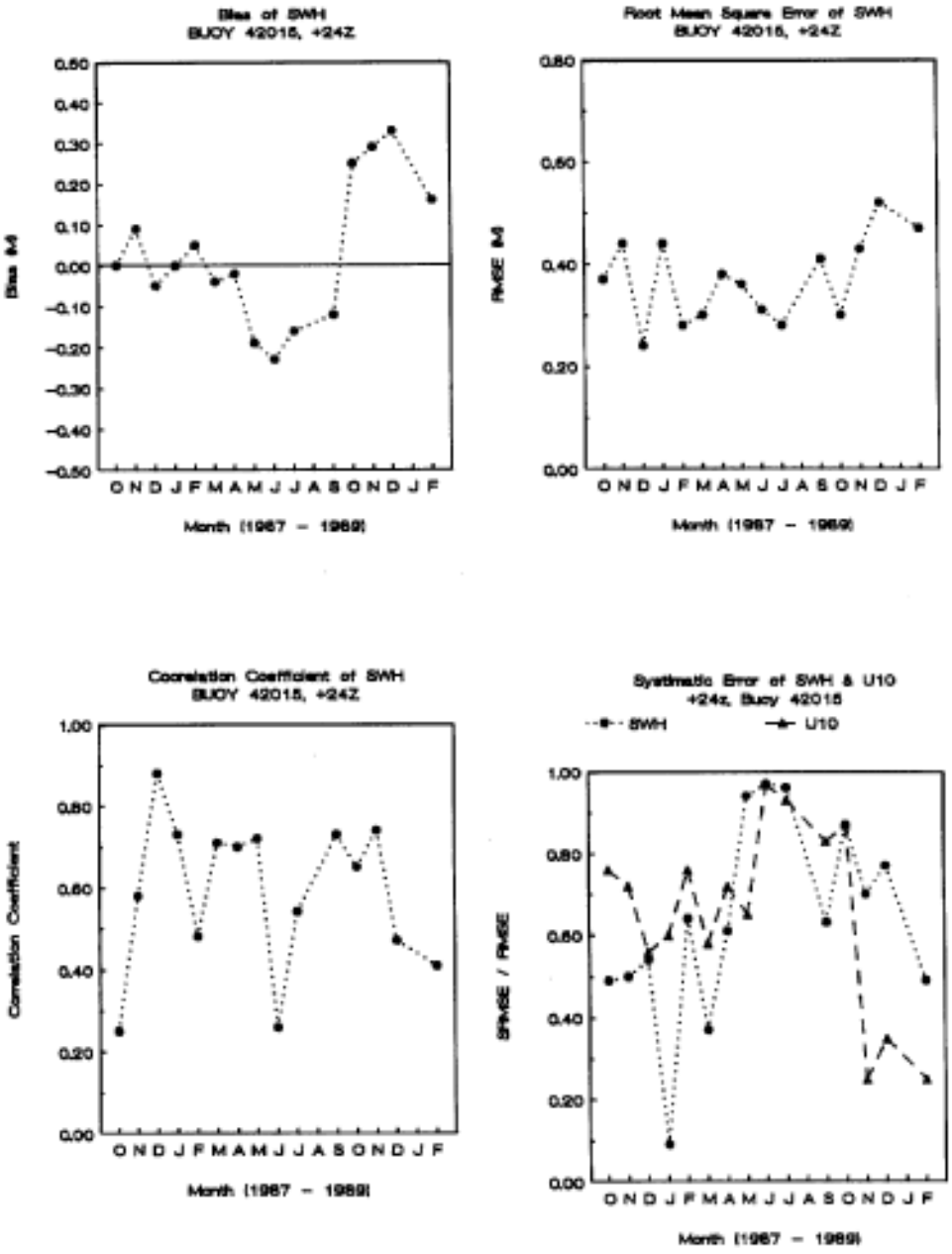

Figure 2: Monthly statistics for +24Z forecasts at a coastal water location - Buoy 42015.

5. REFERENCES

Cardone, V.J., 1969: Specification of the wind field distribution in the marine boundary layer for wave orecasting. Report TR-69-1, Geophys. Sci. Lab., New York University.

Collins., J.I., 1972: Prediction of shallow water spectra. J. Geophys. Res., 77, 2693-2707.

Duffy, D.G., I and R. Atlas, 1984: Surface wind and wave height prediction for the QEII storm using SEASAT scatterometer data. Proceeding of Oceans, September 10-12, 1984, 183-188.

Golding, B.W., 1983: A wave prediction system for real-time sea state forecasting. Q.J.R. Meteorol. Soc., 109, 393-416.

Hasselmann, K., T.P. Barnett, E. Bouws, H. Carlson, D.E. Cartwright, K. Enke, J.A. Ewing, H. Gienapp, D.E. Hasselmann, P. Kruseman, A. Meerburg, P. Müller, D.J. Olbers, K. Richter, W. Sell, and H. Walden, 1973: Measurements of wind-wave growth and swell decay during the Joint North Sea Wave Project (JONSWAP). Dtsch. Hydrogr. Z., Suppl. A8(12).

Hasselmann, K. , 1974: On the spectral dissipation of ocean waves due to whitecapping, Bdy.-Layer Met., 6, 107-127.

Hoke, J.E., 1984: Forecast results for NMC's new regional analysis and forecast system. 10th AMS Conference on Weather Forecasting and Analysis, 6 pp.

Shemdin, O.H., Hsiao, S.V., Carlson, H.E., Hasselmann, K., and Schulze, K., 1980: Mechanisms of wave transformation in finite-depth water. J. Geophys. Res., 85, 5012-5018.

Steele, K.E., and N. Lang, 1988: Samples of NDBC directional wave data. Fourth Conf. Meteo. and Oceano. of the Coastal Zone, Feb. 3-5, Anaheim, Calif., Preprints 50-57.

Takacs, L., 1985: A two-step scheme for the advection equation with minimized dissipation and dispersion errors. Mon. Wea. Rev., 113, 1050-1065.

Thornton, E.B., 1977: Rederivation of the saturation range in the frequency spectrum of wind-generated gravity waves. J. Phys. Ocean., 7, 137.

Willmott, C.J., 1982: Some comments on the evaluation of model performance. Bull. Amer. Metero. Soc., 63(11), 1309-1313.

Preliminary results of the NEDWAM wave model.

H.W. Riepma and E. Bouws

KNMI

De Bilt, Netherlands

Abstract

Presently, at KNMI the wave model GONO runs twice a day to forecast in real time the wave condition in the North Sea. This model may be classified as a second generation wave model of the 'coupled hybrid' type in which windsea and swell are treated separately.

Recently, the WAM group prepared the third generation WAM model which employs todays knowledge of each physical process that contributes to wave growth and dissipation. We implemented a regional version of this model for the North Sea. The new forecasting system was called NEDWAM. In the future we intend to replace GONO by NEDWAM. Before this will actually take place several hindcast runs with NEDWAM must be carried out to verify the new model with field data.

In this paper we present three examples: gale-winds in shallow water with a near balance between wind input and bottom dissipation, a mixed case of windsea and swell, and swell generated in the Norwegian Sea entering the North Sea where light winds occurred. The results are very promising, although some improvements may be necessary.

Introduction

In this paper we will describe some preliminary results that were obtained with a wave model that is candidate to serve as the new operational wave forecast model for KNMI. The work that we have done may be regarded as a test-procedure that needs to be done before the new model can actually be part of the meteorological production process at KNMI.

At present the GONO wave model provides real time operational wave forecasts for the North Sea. This model was developed in the seventies by Sanders (1976). A later version has been described by Janssen et al, (1984). It may be classified as a second-generation wave model of the 'coupled hybrid' type with a parametric windsea and a spectral treatment of swell. In this way the total windsea energy and the dimensionless peak-frequency are functions of U_{10} (where U_{10} is the wind at 10 m height) and the stage of development parameter, which is the ratio of the total windsea energy that is calculated at a certain time and the maximum energy at the given windspeed U_{10}. For the propagation of swell a spectral ray technique is applied for a number of selected "swell points" only. The model runs twice a day to provide

36 hours forecasts, using air-pressure fields produced by the British Meteorological Office which are converted internally to wind speeds.

Our knowledge on the performance of GONO has greatly increased during the past ten years, while at the same time the outstanding reputation of uninterrupted operation was of great benefit to the continuity of the operational service.

On two occasions we had an opportunity to compare GONO directly with other operational wave models. These were the SWAMP (1985) and SWIM (1985) studies during which wave models were compared for idealized and realistic situations. From these studies the strong and weak points became clear while at the same time and perhaps implicitly the existing knowledge about the physics of waves was tested. Thus is was shown for instance that most models contained different non-dimensional duration-limited growth curves especially for extreme wind conditions for which wave forecasts are often most needed. In the case of rapidly changing windfields problems were encountered which originated from the very crude approximations in the energy balance equation.

The WAM development and implementation group WAMDI-G (1988) suggested ways to overcome these problems and prepared the first implementation of what was called a third-generation wave model. This model was called the WAM model. The main improvements dealt with a better parameterization of the non-linear transfer function and the specification of the unknown deep-water dissipation source function. In this way the wave spectrum was computed alone by time integration of the basic spectral evolution equation without any restriction of the spectral shape. For shallow waters, like the southern North Sea, two extensions were provided. These extensions were the finite depth dispersion relation and an additional bottom friction source function. We implemented the shallow water version of the WAM model to do calculations for the North Sea and named the forecasting system NEDWAM.

NEDWAM

The energy balance equation of the NEDWAM model is basically the same as the balance equation of the WAM model with shallow water extensions. The main difference is given by the fact that the equation is written for a stereographic projection in (x,y) coordinates instead of the original spherical coordinates. In this way the 'old' GONO grid with a spatial resolution of 75 km could be kept, see figure 1 . We are however considering an implementation in spherical coordinates as well. If no refraction is taken into account the energy balance equation reads

$$\frac{\partial F}{\partial t} + \vec{c}_g . \nabla F = S \qquad (1)$$

where $\vec{c}_g = \frac{\partial \omega}{\partial k}$ with $\omega = 2\pi f = [gk.\tanh(kD)]^{1/2}$, D=water Depth, F=F(f,,x,y,t) is the spectrum. The source function S is given by

$$S = S_{in} + S_{nl} + S_{ds} + S_{bf} \qquad (2)$$

which represents the wind input as a function of the friction-velocity u_*, the nonlinear source function, deep-water dissipation by white capping, and bottom friction respectively. The detailed descriptions of the source functions are given by WAMDI-G (1988). Work is on its way to improve the parameterizations of S_{bf}. Weber (1989a,b) has tested two theoretical models based upon a draglaw parameterization and an eddy-viscosity model for the turbulent bottom boundary layer. The results of these experiments will be reported elsewhere. Such improvements are important because in some extreme situations the balance is mainly between S_{in} and S_{bf} as we will see below and the simple bottom friction parameterization of WAM may not be adequate.

Implementation

As is well known the performance of a wave model, even a high level third-generation model, is to a high degree dependent on the quality of the wind input. Any improvement in the wind forecast will, without doubt, lead to a better wave forecast. The emphasis for KNMI is on the accurate prediction for the Dutch coast of low-frequency swell entering from the northern North Sea and the Norwegian Sea. To improve on this point a new operational system was designed in 1987 which will be implemented on a CONVEX mini-super computer. In this system an atmospheric limited area model covering north-west Europe and adjacent seas is coupled to several models. Among these are a storm-surge model and the NEDWAM wave model. The atmospheric model has a special boundary layer package which will provide friction velocities to serve as input for NEDWAM. At present however, this feature is not fully operational and we use surface winds instead. Thus the coupling between NEDWAM and the atmospheric model is given by a draglaw formulation according to

$$u_* = U10 \bullet \sqrt{c_D} \qquad (3)$$

where C_D (U_{10}) is based on Charnock's relation as given by Wu (1982), see WAMDI-G (1988).

The first NEDWAM release was developed by Karssen (1987). Some of the early tests were related to the SWIM (1985) study. One of them is reproduced in the next section together with later tests.

Three hindcast tests

We will compare the NEDWAM results with measurements at different positions. These are indicated on the map of figure 1 as Euro, K13 and AUK; Texel lightvessel is situated north of IJmuiden.

a. "Texel-storm", January 1976.

Characteristics:

A north-westerly gale of great intensity and long duration occurred over the North Sea, with wind speeds greater than 25 m/s during 21 hours near the Dutch Frisian Islands. According to Bouws and Komen (1983) the wind input is in near balance with bottom dissipation at the position of the Texel lightvessel.

Results:

We used this storm to check the JONSWAP mean bottom dissipation of the WAM model (see WAMDI-G 1988). Typically the bottom dissipation coefficient Γ is equal to 0.038 m^2s^{-3}. The results obtained with this value are given in figure 2 showing the significant wave height and the mean frequency compared with measurements for Texel lightvessel and Euro. Obviously NEDWAM overestimates the measurements by about 1 to 2 m in terms of H_s.

Better agreement between the model and the measurements may be obtained for Γ equal to 0.067 m^2s^{-3} which is the value proposed by Bouws and Komen (1983). The results for this value of Γ are shown in figure 3 . The implementation of a new value for Γ would be straightforward, however we would like to study the wind input and the bottom dissipation in a more elaborate way before we will actually do this.

b. Swell propagating through the southern North Sea, January 1980.

Characteristics:

In the Norwegian Sea a windsea is generated by a northerly storm around 13 January 1980. During the next days swell propagates into the southern North Sea where light winds occur. The swell dominates the sea state with an exceptionally large amplitude and low peak frequency. The wavelength of the swell is such that in the southern North Sea bottom dissipation dominates over other processes such as transfer by non-linear interactions.

Results:

Again we decided to use this situation as a test for the bottom dissipation with Γ equal to 0.038 m^2s^{-3} which is the mean JONSWAP

value adopted by the WAM group. The results are shown in figure 4 showing the significant wave height Hs and the low frequency wave height $H_{s,10}$ as a function of time for Euro and K13. The upper limit of the low frequencies correspond to a period of 10 seconds.

From figure 4 we observe that NEDWAM predicts the arrival time of the incoming swell and the wave heights H_s and $H_{s,10}$ at Euro in good agreement with the measurements. Also the predicted arrival time at K13 of the incoming swell is in agreement with the measurements. The agreement for H_s and $H_{s,10}$ at K13 is less obvious because NEDWAM at first sight overestimates the measured wave heights. However it is important to note that at K13 the depth locally decreases to approximately 20 m in contrast to the surrounding area where the depth varies between 30 and 40 m. This may result in refraction of waves at a relative small spatial scale giving rise to higher swell amplitudes at K13 which is not taken into account by NEDWAM. Unfortunately we have, as yet, no experimental evidence that refraction is actually taking place at K13.

c: SWIM storm, November 1981.

Characteristics.

The centre of the storm is situated between Norway and the German Bight with northwesterly winds. In the southern North Sea windsea and swell contribute to the wave spectrum. This situation was reported before by SWIM (1985) and Karssen (1987).

Results:

In figure 5 we have included the significant wave height as a function of time for Euro, K13 and Auk calculated by NEDWAM. Also shown are the measured significant wave heights. These results are of special interest because the predictions of the old GONO wave model are given as well, see figure 5 , which enables us to compare the models in some detail. In general the agreement between the models and the measurements is satisfactory. A further comparison is shown in table 1 where the bias and the standard deviation between the models and the measurements are given. The bias is significantly lower for the NEDWAM model, however the standard deviation is more or less the same.

Concluding remarks

From our study we conclude that the present version of the NEDWAM model is ready to operate in an operational environment on a mini-super computer. The time needed to complete a forecast is within the tight time limits that are imposed upon the model in an operational cycle (12 minutes for 30 hour forecast).

As we have shown here, the present version of NEDWAM still needs modifications. Our main concern is the way in which the bottom dissipation is handled. In two tests (SWIM and the swell propagation case) the model behaved satisfactory. From the hindcast of the so-called Texel storm we found indications that the bottom dissipation source function of NEDWAM for an extreme wind sea in shallow water needs further improvement. Our latest results on this subject will be reported during this conference (Weber 1989b).

References

Bouws, E. and G.J. Komen, 1983. On the balance between growth and dissipation in an extreme depth-limited wind-sea in the southern North Sea. J. Phys. Oceanogr. 13 (9), 1653-1658.

Janssen, P.A.E.M., G.J. Komen and W.J.P. de Voogt, 1984. An operational hybrid wave prediction model. J. Geophys. Res. 89 (C3), 3635-3654.

Karssen, B. 1987. Implementation of and first results with the NEDWAM model, a third-generation wave prediction model for the North Sea (in Dutch). KNMI Techn. Rep. TR-102.

Sanders, J.W., 1976. A growth-stage scaling model for the wind -driven sea. D. Hydrogr.Z. 29, 136-161.

The SWAMP Group: J. Allender, T. Barnett, L. Bertotti, J. Bruinsma, V.C. Cardone, L. Cavaleri, J.J. Ephraums, B. Golding, A. Greenwood, J. Guddal, G.J. Komen, L. Lawson, R.B. Long, M. Lybanon, E. Maeland, T. Uji, W.J.P de Voogt, 1985. Ocean Wave Modelling, Plenum Press, New York and London, 256 pp.

The SWIM Group: E. Bouws, J.J. Ephraums, J.A. Ewing, P.E. Francis, He Günther, P.A.E.M. Janssen, G.J. Komen, W. Rosenthal, W.J.P. de Voogt, 1985. A shallow-water intercomparison of three numerical wave prediction models (SWIM). Quart. J.R. Met. Soc. 111, 1087-1112.

The WAMDI-group: S. Hasselmann, K. Hasselmann, E. Bauer, P.A.E.M. Janssen, G.J. Komen, L.Bertotti, P. Lionello, A. Guillaume, V.C. Cardone, J.A. Greenwood, M. Reistad, L. Zambresky and J.A. Ewing, 1988. The WAM Model - a third generation ocean wave prediction model, J. Phys. oceanogr. 18 (12), 1775-1810.

Weber, S.L., 1989a. Eddy viscosity and draglaw models for random wave dissipation. Submitted for publication.

Weber, S.L., 1989b. On bottom friction for random waves during storm conditions. Second International workshop on wave hindcasting and forecasting April, 25-28, 1989, Vancouver, B.C., Canada, Proceedings.

Wu, J. 1982. Wind-stress coefficients over sea surface from breeze to hurricane, J. Geophys. Res. 87, 9704-9706.

position	N $\overline{H}_s$(m) D(m)	Model	bias(m)	σ(m)
Euro	41	GONO	-0.21	0.27
	2.31	NEDWAM	-0.11	0.23
	25			
K13	41	GONO	+0.25	0.45
	3.07	NEDWAM	+0.13	0.43
	25			
Auk	41	GONO	+0.17	0.82
	4.24	NEDWAM	-0.19	0.88
	80			

N = number of points
$\overline{H}_s$ = average of observed significant wave heights
D = water depth
Bias = negative: model too low
positive: model too high
σ = standard deviation

Table 1 Bias and standard deviation of GONO and NEDWAM compared to measurements

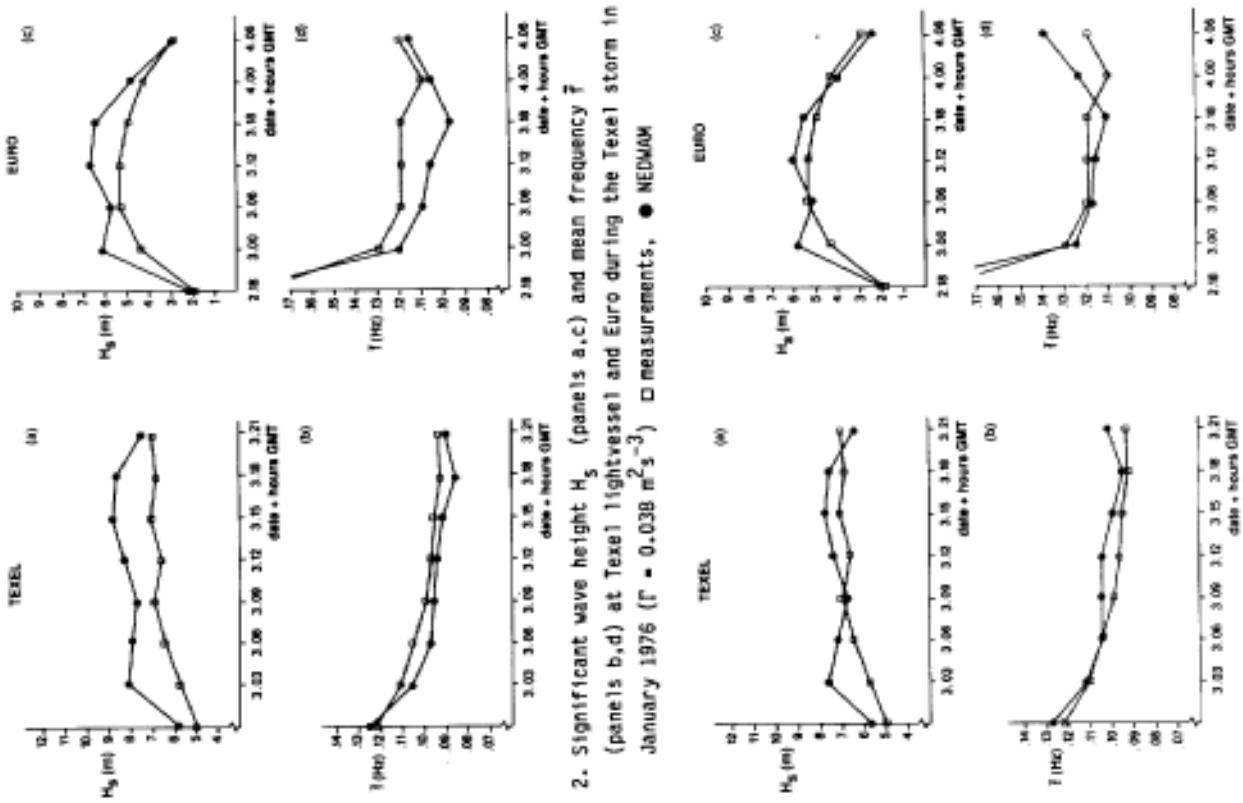

2. Significant wave height H_s (panels a,c) and mean frequency $\bar{f}$ (panels b,d) at Texel lightvessel and Euro during the Texel storm in January 1976 (Γ = 0.038 $m^2 s^{-3}$) □ measurements, ● NEDWAM

3. As figure 2 but for Γ = 0.067 $m^2 s^{-3}$

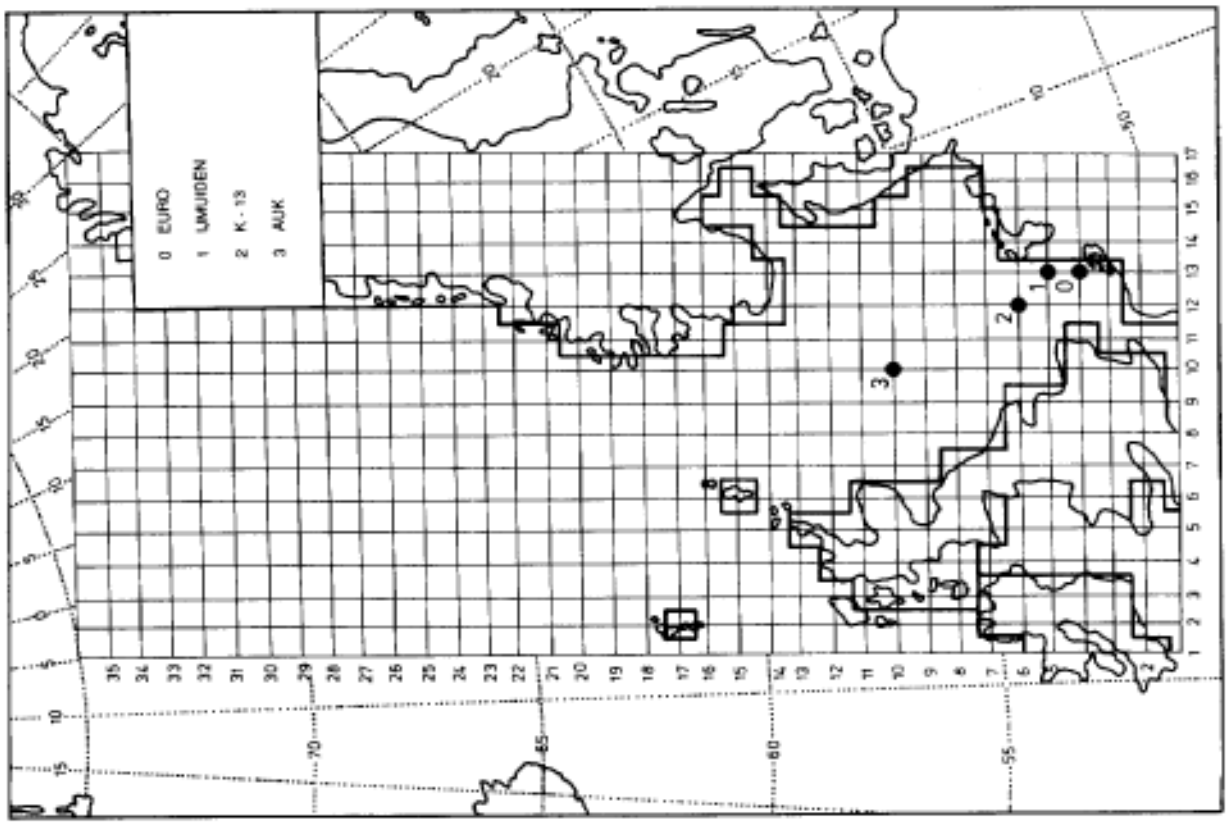

1. The NEDWAM computational grid. (Δx=75 km)

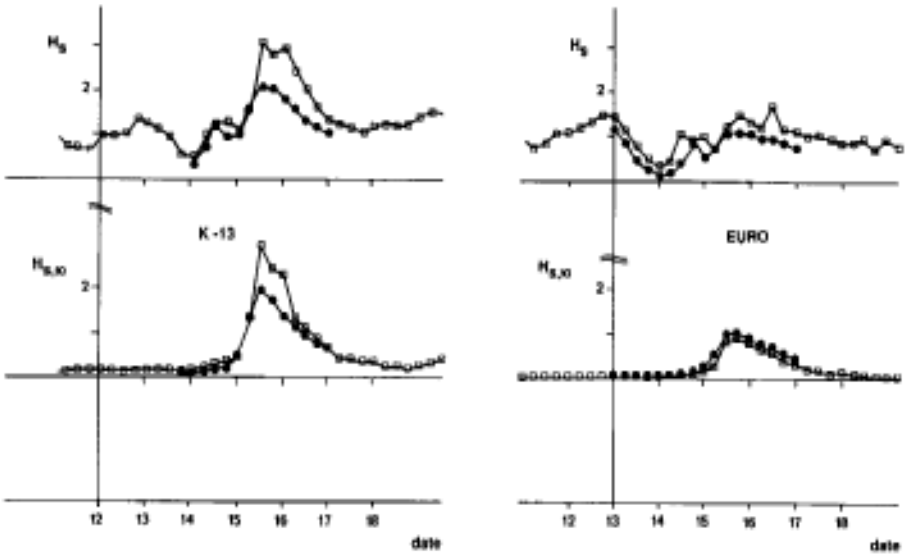

4. Significant wave height H_s and low-frequency wave height H_{s10} at K13 and Euro in January 1980 as a function of time (propagating swell case) □ measurements, ● NEDWAM

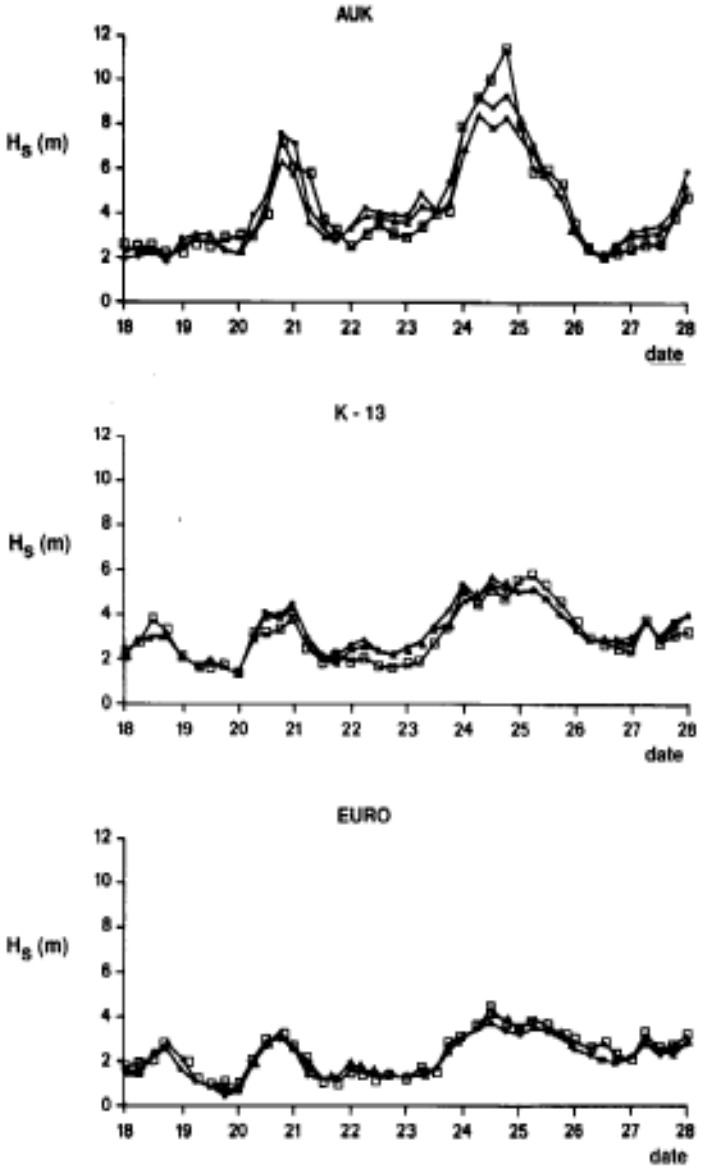

5. Significant wave height H_s at Euro, K13 and Auk as a function of time. Comparison of GONO and NEDWAM in November 1981.
□ meaurements, ▲ NEDWAM, ● GONO

THE USE OF ANALYZED WIND FIELDS FROM THE GREAT LAKES MARINE OBSERVATION NETWORK IN WAVE AND STORM SURGE FORECAST MODELS

David J. Schwab

National Oceanic and Atmospheric Administration
Great Lakes Environmental Research Laboratory
Ann Arbor, Michigan

1. INTRODUCTION

Perhaps the most important ingredient in successful wave and storm surge hindcasting and forecasting is an accurate specification of the wind field. Not only does the accuracy of the forecast wind field limit the accuracy of the wave or storm surge forecast, but when inaccurate hindcast wind fields are used for model calibration and development, serious errors may become built into the model and permanently degrade the accuracy of the model. For this reason, an attempt is made to assess a potentially more accurate technique for analyzing the diverse meteorological data available over and around the Great Lakes into overwater wind fields.

The basic problem of assimilating meteorological data from irregularly spaced observing stations into a continuous representation of the two-dimensional wind field has been addressed quite extensively in the meteorological literature. In this paper, the emphasis is directed toward some of the problems unique to hindcasting and forecasting marine wind fields from a mixture of coastal and offshore observations. Specifically, what is the best way to incorporate the various types of meteorological observations into a consistent analyzed wind field so that the information characterized by the observations is preserved to the highest degree possible without introducing artificial high frequency variations in the analyzed field? How can observations reported at irregular time intervals be used to enhance a synoptic analysis? Are reports from coastal stations representative of overwater conditions, or how can they be used to infer overwater conditions? Can a method be developed that is flexible enough to adapt easily to a constantly changing reporting network? To answer some of these questions, a two step Barnes technique, Barnes (1973), is applied to data from the Great Lakes Marine Observation Network which includes offshore buoys, automated coastal stations, Coast Guard stations, ship reports, and airports. The Barnes technique provides a natural way to incorporate all the data from this type of network and particularly to take advantage of data reported at irregular time intervals.

In the following sections, the characteristics of the Great Lakes Marine Observation Network will be described and analyzed. It will be shown how the characteristics of the network are incorporated into the

analysis scheme and how they affect the ultimate resolution of the interpolated wind field. A brief description of the two step Barnes technique will be presented with emphasis on the natural way in which observations from irregular points in time and space can be incorporated into the scheme and the analytic formulation of the response function that is possible with this technique. The method will be demonstrated on real data from October, 1988 in the Lake Michigan basin. A practical choice must be made for values of the interpolation parameters that minimize the deviations of the interpolated wind field from observed winds while maximizing the accuracy with which observations that were withheld from the analysis can be reproduced. The Lake Michigan data is used to illustrate this point.

2. THE GREAT LAKES MARINE OBSERVATION NETWORK

The National Weather Service collects data from a network of various types of observation stations around the Great Lakes. For the purpose of estimating overwaterwind fields, we adopt an arbitrary definition of 'marine observation station' as a station with sufficient exposure to the lake so as to reflect the influence of the marine boundary layer on the structure of the wind field. This includes Coast Guard Stations which report wind speed, wind direction, and air temperature on a (nominally) two-hourly basis. Coastal Marine Automated Network (CMAN) stations and National Data Buoy Center (NDBC) weather buoys which report on an hourly basis, reports from ships of opportunity at synoptic hours (3-hourly), and a few airports close enough to the lake to be considered 'marine' (see Figure 1).

The station network shown in Figure 1 was analyzed for each lake to determine characteristic interstation spacing. Each lake was covered with a grid of 5 km squares. Then the distance from the center of each square to the nearest observation station was calculated. The mean, median and mode of the distances to the nearest station from all the grid squares in the lake are shown in Table 1 .

Figure 1. Weather observation stations included in objective analysis.

Table 1. Distance in km to nearest meteorological observing station.

Lake	Number of Stations	Distance to nearest station		
		Mean	Median	Mode
Superior	20	38.0	31.4	27.5
Michigan	28	33.9	30.8	37.5
Huron	42	29.6	26.9	32.5
Erie	32	24.9	21.2	17.5
Ontario	20	29.6	26.0	27.5

Assuming that interstation spacing is roughly twice the average distance from a point in the lake to the nearest station, we see that typical interstation spacing varies from about 50 km for Lake Erie to about 75 km for Lake Superior. This means that the network should normally be able to resolve horizontal variations in the wind field with wavelengths greater than 100-150 km. Smaller scale variations will not be resolved and could cause aliasing. Smaller extratropical storm systems that characterize weather patterns in mid-latitudes are roughly 100 km in size, so that variability associated with these systems should be resolved. These figures are used only as a guideline in the interpolation procedure because not all observation stations

report on an hourly basis but ship reports are sometimes available to augment the network.

3. WIND SPEED ADJUSTMENT

For the purposes of wave and storm surge hindcasting and forecasting, a representative overwater wind field at a fixed height above the water surface is usually sufficient to specify the atmospheric forcing function. Adjustments for atmospheric stability may sometimes be required depending on the type of model being used. The Marine Observation Network, however, consists of a mixture of coastal and overwater stations with a variety of measurement heights. In order to make the observations more consistent, all wind speed observations are adjusted to a 10 m height by the profile method described in Schwab (1978). In addition, wind speed reported from coastal stations is modified to be more representative of overwater wind speed. This modification is based on the observation that the histograms of wind speed at overwater stations were found to be quite consistent from lake to lake, but histograms from coastal stations were not and were, in fact, usually quite different than histograms from overwater stations. Several modification schemes based on regressions between wind speed from the coastal station and wind speed from the nearest overwater station were tested. Typical forms for the regression formula are:

$$s_w = a_1 s_c \quad (1)$$

$$s_w = (a_1 + a_2 \Delta T) s_c \quad (2)$$

$$s_w = (a_1 + a_2 \Delta T\ a_3 s_c) s_c \quad (3)$$

$$s_w = (a_1 + a_2 \Delta T) s_c + a_3 + a_4 \Delta T \quad (4)$$

where s_W is the estimated representative overwater wind speed, s_C is the wind speed reported at the coastal station (adjusted for measurement height), ΔT is the air-sea temperature difference, and a_i are regression coefficients. Schwab and Morton (1984) discuss results obtained for Lake Erie with forms similar to (1), (2), and (4). Form (3) is similar to (2) with the addition of a quadratic term in s_C. In this study, it was found that including temperature dependence in the regression always improved correlations between estimated and observed overwater wind speeds, so form (1) was not considered. It was also found that although forms (3) and (4) provided slightly better correlation coefficients and slightly lower mean square errors than form (2), they did so at the expense of distorting the distribution of wind speed, i.e., the modified wind speeds tended to cluster about the mean speed and to show less range in their distribution above and below the mean. Form (2) provided wind speed distributions much closer to observed overwater distributions. An example of the effect of wind speed modification for station 14C is shown in Figure 2 .

4. THE TWO STEP BARNES TECHNIQUE

In order to interpolate meteorological data observed at irregular points in time and space to a regular grid so that it can be used for input into numerical wave and storm surge prediction models, some type of analysis technique must be used. The complexity of the analysis technique should be compatible with the complexity of the observed data, i.e., if observations from only a few stations are available, a best-fit linear variation of wind components in space might be an appropriate method. If more observations can be incorporated into the analysis, spatial weighting techniques can be used. A spatial weighting technique represents the interpolated value of the parameter at a grid point as the weighted sum of observations of the parameter. Weighting functions proportional to some function of distance between the grid point and the observation point are most common. The Barnes

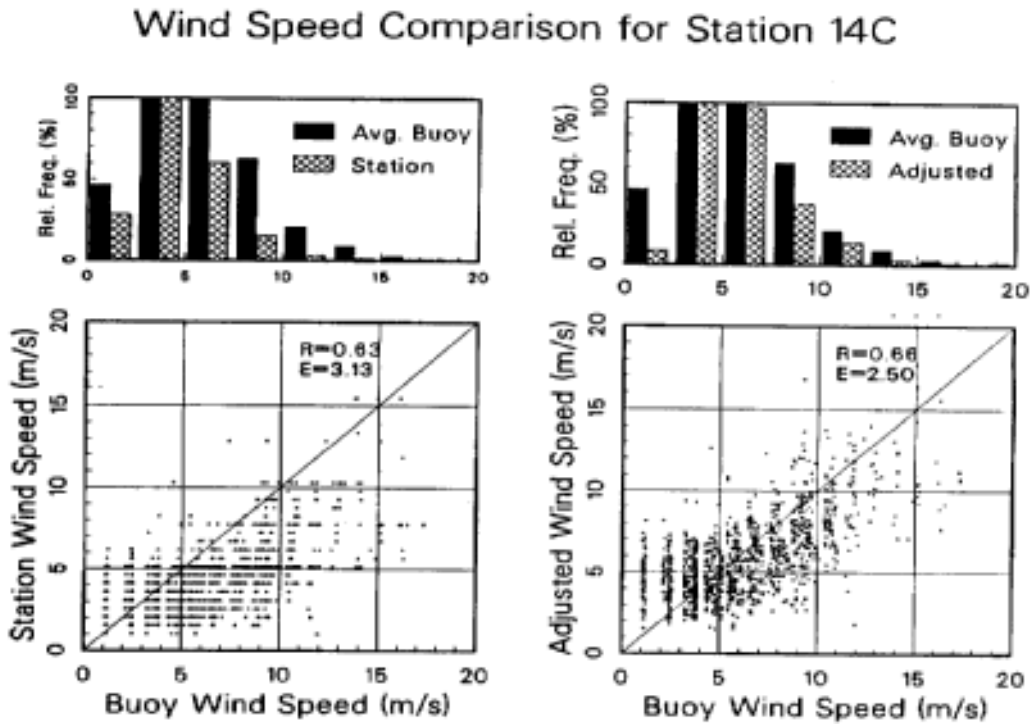

Figure 2. Comparison of coastal station wind speed to buoy wind speed for station 14C and buoy 45002 before modification (left) and after modification (right).

technique uses an exponential spatial weighting function with a decay rate that can be adjusted based on typical interstation separation distance. The weighting function is

$$w_i = \exp - \left(\frac{r_i}{r_0}\right)^2 \qquad (5)$$

where r_i is the distance between the grid point and station i and r_O is the adjustable decay rate. An interpolated value at grid point (x,y), g(x,y), is calculated as the sum of station values times normalized weighting functions, i.e.,

$$g(x,y) = \frac{\sum_{i=1}^{n} w_i f_i}{\sum_{i=1}^{n} w_i} \qquad (6)$$

where n is the number of stations used in the interpolation for this grid point and f_i are the station values. It can be shown, Barnes (1964), that the response function for a single application of this procedure to a sinusoidal spatial disturbance with wavelength λ is

$$D(\lambda) = \exp -\left(\frac{\pi r_0}{\lambda}\right)^2 \qquad (7)$$

where $D(\lambda)$ is the amplitude of the response to a wave of unit magnitude. The sensitivity of this procedure to small scale fluctuations in the wind field is controlled by the choice of r_0. However, the typical interstation spacing distance imposes a lower limit on r_0 to prevent aliasing of wavelengths less than twice the interstation spacing. In practice, since the network (and hence interstation spacing) is generally quite irregular, the choice of r_0 is made empirically using values like those given in Table 1 as guidance.

When the grid point interpolated values are compared to observed values at the stations, a residual value can be determined for each station, i.e.,

$$\Delta g_i = f_i = g_i \qquad (8)$$

Where f_i is the observed value at the station and g_i is the interpolated value. If the station residual values are then interpolated back to the grid points and added to the first pass grid point values

$$g^*(x,y) = g(x,y) + \Delta g(x,y) \qquad (9)$$

the resulting field will more closely match observed station values at the stations and improve the resolution of smaller wavelength features. Such a procedure can then be repeated to match observed values even more closely. If, in the calculation of the interpolated residual values at the grid points, we use a weighting function of the form

$$w_i = \exp - \frac{1}{\gamma}\left(\frac{r_i}{r_0}\right)^2 \qquad (10)$$

where a numerical convergence parameter γ ($0 < \gamma < 1$) has been included, then, according to Koch et al. (1983), for a small enough choice of the parameter γ, only a single iteration of the residual interpolation procedure is required to obtain maximum resolution of resolvable wavelengths. The response function for the two pass technique is

$$D^*(\lambda) = D(1 + D^{\gamma-1} - D^{\gamma}) \qquad (11)$$

where $D(\lambda)$ is given in (7), Barnes (1973). If 0.2 is selected as a practical lower limit for γ, to obtain a 1/e response for the minimum resolvable wavelength (λm) requires $r_0 = 0.72\ \lambda m$, Koch et al. (1983). In the proposed application of the two step Barnes technique to the Great Lakes Network, λm is specified based on the information in Table 1 and r_0 is calculated from this formula.

In order to incorporate observational data reported at irregular time intervals, the weighting function is extended to include time dependence of the data as

$$w_i = \exp -\left(\frac{r_i}{r_0}\right)^2 \exp -\left(\frac{t_i}{t_0}\right)^2 \qquad (12)$$

where t_i is the difference between the time of the observation and the time for which the interpolation is required and t_0 is a characteristic decay time, again related to the characteristics of the observed data.

As a practical matter, observation points more distant from a grid point than some multiple of r_0 or further removed in time than some multiple of t_0 are not considered in the calculation for that grid point. The only problem that these cutoffs might cause would be an insufficient number of stations contributing to the interpolated value at a grid point, so again they are adjusted empirically depending on the network of observational data available.

5. APPLICATION TO LAKE MICHIGAN

Lake Michigan in the month of October, 1988 was chosen as a test case for the interpolation procedure. The two NDBC buoys in the lake had not yet been removed for winter, there were still a representative number of ship reports available, and during October several episodes of large and rapid wind shift occurred. Wind speed, eastward component, northward component, and air temperature were interpolated to a 15 km grid covering the lake at 1 hour intervals for the entire

month. As a test of the method, data from the NDBC buoy in the southern part of the lake (45007) was not used in the analysis and interpolated results for that point were compared to observed values. In addition, residuals at observation stations after the second (correction) pass of the interpolation procedure were calculated to give an indication of how well the interpolation had converged.

Table 2 shows the results of the test interpolations for nine different combinations of γ and λm. The decay constant for time interpolation, t_0, was set at 1 hour. A cutoff distance of $4.5r_0$ was used and a cutoff time of $3t_0$ was used.

Table 2. Results of hourly objective analysis for Lake Michigan Network for October, 1988. Decay constant for time interpolation is 1 hour.

	RMS wind speed deviation at 45007 (ms^{-1})				RMS air temperature deviation at 45007 (°C)			
γ = / λm (km)	0.20	0.35	0.50	0.65	0.20	0.35	0.50	0.65
100	4.17	4.00	3.91	3.87	2.52	2.44	2.39	2.37
150	4.15	3.91	3.83	3.79	2.59	2.44	2.38	2.36
200	4.15	3.88	3.80	3.78	2.60	2.45	2.40	2.39
	Average of hourly RMS wind speed deviations for all other stations (ms^{-1})				Average of hourly RMS temperature deviations for all other stations (°C)			
γ = / λm (km)	0.20	0.35	0.50	0.65	0.20	0.35	0.50	0.65
100	1.01	1.09	1.19	1.28	0.71	0.75	0.80	0.85
150	1.13	1.31	1.47	1.57	0.81	0.90	0.99	1.06
200	1.31	1.53	1.68	1.77	0.93	1.07	1.17	1.25

As can be seen from the table, lower values of γ and λm (less smoothing) tend to provide lower residuals at the observation stations for both wind speed and air temperature, but higher values (more smoothing) give better agreement with observed values at 45007. The deviations at 45007 can be compared to results obtained by using a $1/r^2$ weighting function with station reports from within 15 minutes of the interpolation time. These were 4.20 ms^{-1} for wind speed and 2.82°C for air temperature. During this period, average wind speeds at the stations ranged from 4.35 to 7.48 ms^{-1} with maximum speeds exceeding 20 ms^{-1}.

Another set of tests was carried out with t_0 = 3 hr. Results are shown in Table 3 .

Table 3. Results of hourly objective analysis for Lake Michigan Network for October, 1988. Decay constant for time interpolation is 3 hours. Minimum resolvable wavelength set at λm = 100 km.

RMS wind speed deviation at 45007 (ms^{-1})					RMS air temperature deviation at 45007 (°C)			
γ =	0.20	0.35	0.50	0.65	0.20	0.35	0.50	0.65
3.45	3.23	3.20	3.24	2.92	2.52	2.36	2.28	

Average of hourly RMS wind speed deviations for all other stations (ms^{-1})					Average of hourly RMStemperature deviations for all other stations (C°)			
γ =	0.20	0.35	0.50	0.65	0.20	0.35	0.50	0.65
1.29	1.43	1.54	1.62	0.78	0.88	0.95	1.01	

The longer decay constant for time interpolation improves the agreement at 45007 but increases the residuals at observation stations.

Figure 3 shows four examples of interpolated wind fields and air temperature fields for 22:00 GMT on October 17, 1988. This date and time were chosen because a strong frontal system was just crossing Lake Michigan, resulting in a very complicated wind,pattern, with winds from nearly all points of the compass being reported at some station around the lake. These interpolations used data from all stations, including 45007. In the figure, observed wind vectors are indicated with open arrow heads. Contour lines are drawn in 0.5 ms^{-1} increments for wind speed and 0.5°C increments for air temperature. Values of the interpolation parameters for the four examples were chosen to show representative results for the full tested range of the parameters.

6. DISCUSSION

The very complicated wind pattern used in Figure 3 is not particularly representative of the majority of the data analyzed, but was chosen to most clearly illustrate the effect of various combinations of the interpolation parameters on the analyzed fields.

The interpolated wind field for γ = 0.2, λm = 100km and t_0 = 1 hr (Figure 3a) shows that when the average residual deviation as listed in Table 2 is small (1.01 ms^{-1}), rapid and probably unrealistic shifts in the interpolated wind field can occur. Figure 3b with γ = 0.65, λm = 200 km and t_0 = 1 hr shows the other extreme with a large average residual wind speed deviation of 1.77 ms^{-1} yet a much closer match at 45007 in the test case (3.78 ms^{-1} vs. 4.17 ms^{-1} for the parameters in Figure 3a). Neither of these analyses appear to have the degree of smoothness a human analyst would likely feel was warranted by the observed data. A realistic analysis must then be a compromise between these two extremes, small residual deviations of

interpolated values from observed values at the stations and accurate depiction of interpolated values between observation points. Determination of the optimal compromise remains a subjective question. We hope that by using the analyzed fields for wave and storm surge hindcasts, a more objective determination of optimal parameters can be obtained.

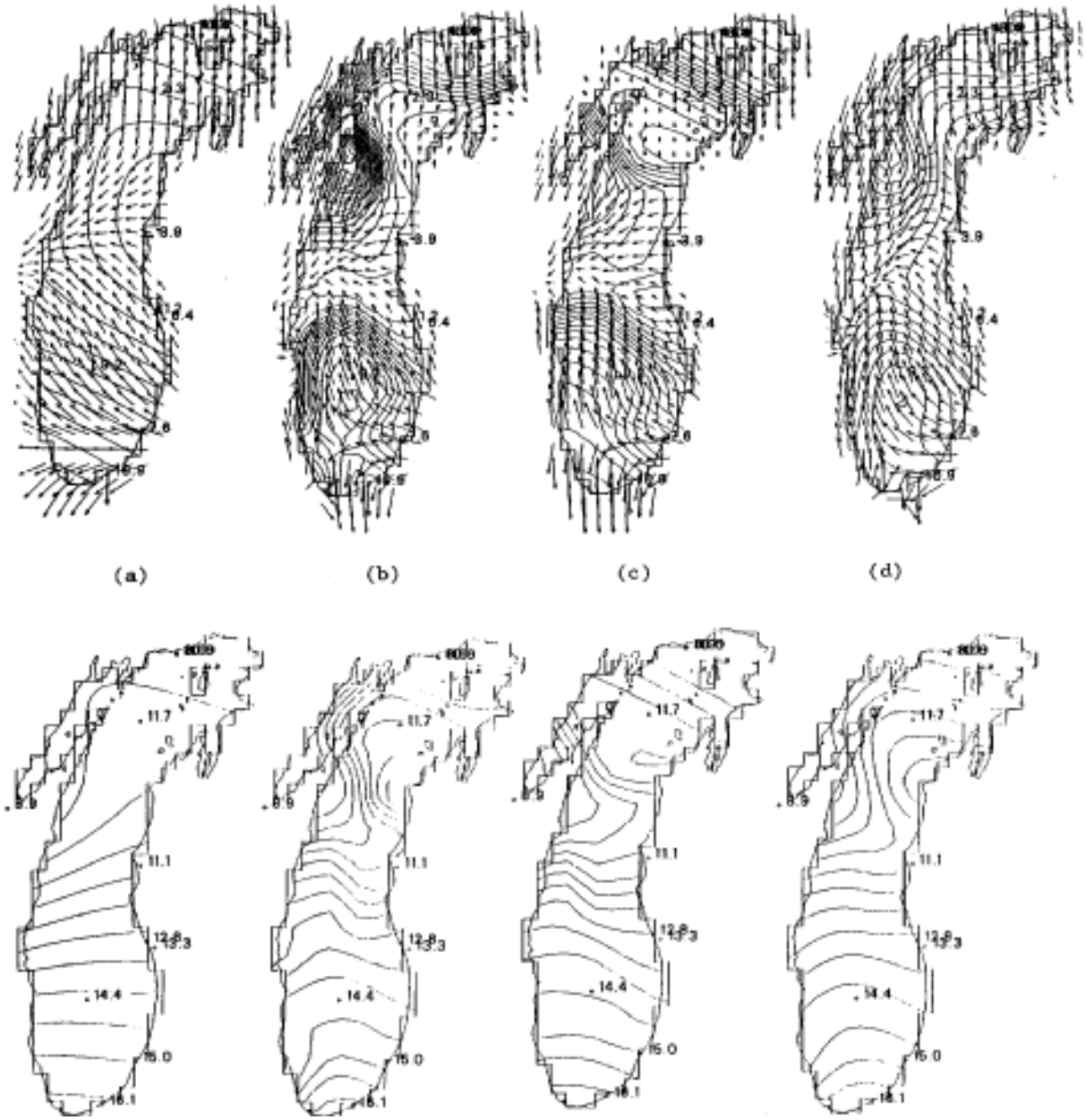

Figure 3. Interpolated wind and air temperature fields for 22:00 GMT October 17, 1988. Observed wind vectors are indicated by open arrowheads. Contour intervals are 0.5 ms^{-1} for wind speed and 0.5 °C for air temperature. Interpolation parameters are: γ=0.2 (a&c), γ=0.65 (b), γ=0.5 (d), λm=100 km (a, c&d), λm=200 km (b), t_0=1 hr (a&b), t_0=3 hr (c&d).

Figures 3b and 3c show interpolated fields using some combinations of the parameters in Table 3 with t_0 - 3 hr. The effect of including data from a wider time window into the interpolation scheme is generally to produce fields that are smoother than the corresponding fields with t_0 - 1 hr. However, Figure 3c shows that for this particular case, a noisier field is produced with the wider time window even though this analysis has a lower value of RMS deviation at 45007 in the test case (3.45 ms^{-1} vs. 4.17 ms^{-1}). The pockets of high wind speed around station 45007 and 0Y2 are evidence of variations in the wind field occurring on a smaller scale than the observation network can resolve. The average station residual values for wind speed, however, are quite a bit higher than for t_0 - 1 hr (1.29 ms^{-1} vs. 1.01 ms^{-1}). The fields for γ = 0.5, λm = 100 km, and t_0 = 3 hr in Figure 3d represent another possible compromise between smoothness and minimum residuals.

The results presented here are the first step in a study to determine whether using the analyzed fields to generate storm surge and wind wave hindcasts will help determine the most accurate interpolation procedure. This work is still in progress, but will consist of using analyzed winds as the forcing function for numerical wave and storm surge forecasting models and comparing the results of the model simulations to observed wave conditions or water level fluctuations for selected cases. The assumption is that the waves and large scale water level fluctuations represent an integrated response to the two-dimensional wind field and may not contain as much variability on smaller space scales as the meteorological parameters themselves. If this is the case, then using wind fields analyzed with different sets of the interpolation parameters or even different interpolation techniques in the wave and storm surge models may be a more objective method of comparing the analyzed wind fields.

7. SUMMARY

A two-step Barnes technique has been applied to the problem of interpolating data from an irregular meteorological observation network to a regular grid for use in numerical forecasting models. The results provide a satisfactory representation of the wind field between observation stations when compared to interpolation with $1/r^2$ weighting. Observations from irregular time intervals can easily be incorporated into the analysis, and the method easily adapts to changes in the reporting network.

Additional plans include:

- Using analyzed wind fields to drive storm surge and wave prediction models and comparing hindcast results to observed water levels and waves. Perhaps this approach will help determine the best compromise values for the interpolation parameters.

- Testing a translational technique to adjust for travel distance of off-interpolation time observations.

- Further investigation of optimum choices of the interpolation parameters γ, λm, and t_0 for different lakes and different time periods.

8. REFERENCES

Barnes, S. L. , 1964: A technique for maximizing details in numerical weather map analysis. J. ARR1, Meteor., 3, 396-409.

Barnes, S. L. , 1973: Mesoscale objective analysis using weighted time-series observations. NOAA Tech. Memo. ERL NSSL-62, National Severe Storms Laboratory, Norman, OK., 60pp. (NTIS COM-73-10781).

Koch, S. E. , desJardins, M. , and P. J. Kocin 1983: An interactive Barnes objective map analysis scheme for use with satellite and conventional data. J. Climate and APP1. Meteor., 22(9), 1487-1503.

Schwab, D. J. p 1978: Simulation and forecasting of Lake Erie storm surges. Mon. Wea. Rev., 106(10), 1476-1487.

Schwab, D. J. , and J. A. Morton, 1984: Estimation of overtake wind speed from overland wind speed: a comparison of three methods. J. Great Lakes Res., 10(1), 68-72.

9. ACKNOWLEDGEMENTS

I would like to thank the staff of the National Weather Service at the Cleveland Forecast Office who designed and implemented the operational marine data collection scheme and who made the data base available to me. This is GLERL Contribution No. 659.

SOME EARLY RESULTS FROM AN EXPERIMENT TO ASSIMILATE GEOSAT ALTIMETER WAVE HEIGHT DATA INTO A GLOBAL WAVE MODEL

P.E. Francis and R.A. Stratton

United Kingdom Meteorological Office,
Bracknell, UK

ABSTRACT

During 1988 the wave modelling group at the UK Meteorological Office has successfully completed a series of experiments in which altimeter wind and wave data from SEASAT were assimilated into a global wave model. A paper reporting this work has been prepared for publication.

Using these proved techniques, the group now intends to extend the work to GEOSAT data, recently available from the United States. These data present many opportunities not available in the SEASAT period. Firstly it is possible to choose an active period in the Northern Hemisphere winter, secondly the number and quality of buoy wave data has markedly increased since 1978, the year of SEASAT. The combination of freedom to choose an active period, and the availability of much buoy data, enables a meaningful independent test of the performance of the wave-model/assimilation-method, During most of the SEASAT period, the few available buoy data were from areas of relative wave inactivity.

Specifically it will be possible to look at an active period in the North East Pacific, using all available data taken from the WMO GTS network. The forcing winds will be taken from the archive of NWP global surface wind fields, maintained at eh UK Meteorological Office since October 1986. An ice edge for the chosen period will be carefully specified from available data.

Results will be presented that illustrate the impact of assimilated wave height data on the global wave model, both by comparison against the assimilated data, and also independently against buoys. The quality of the driving winds will also be discussed.

1. INTRODUCTION

The use of altimeter wave height data in wave models has been discussed by several wave modelling groups in recent publications, eg Francis and Stratton (1989), Esteva (1988), Hasselman et al. (1988), Janssen et al. (1987). It has been generally demonstrated that, given suitable assumptions concerning the translation from significant wave height (derived from the altimeter) to a 2-dimensional spectrum (required by the wave model), the data values in the model can be made to approximate more closely to those measured by the altimeter.

The particular scheme for spectral retrieval used at the United Kingdom Meteorological Office (UKMO) is that developed by Thomas

(1988). This scheme, along with a technique for continuous data assimilation, was used at the UKMO to investigate the impact of SEASAT data on a global wave model run in hindcast mode, Francis and Stratton (1989). This work showed that a significant improvement in modelled wave height was possible, and that the impact of assimilating data was retained in the model for at least 5 days.

One weakness of the SEASAT work was that there were no independent measured wave data against which to check the findings of the experiments. All comparisons were carried out between model values and those from the altimeter data set. The few buoy data available in 1978 were in the Northern Hemisphere, recording unremarkable wave events (the short lifetime of SEASAT was during the northern summer) which were well modelled even without the benefit of the assimilated data.

This present paper reports on the early findings from a similar set of experiments, but with the benefit of the following two major differences, using data from the GEOSAT altimeter.

(a) The period under consideration is during a Northern Hemisphere winter. This allows the testing of the assimilation scheme for a period in which some large wave heights can be expected, in ocean area (North Atlantic, North Pacific) where the performance of Numerical Weather Prediction (NWP) models, including their surface wind field data. Is relatively good, compared for example with the southern oceans.

(b) In this period, and in several areas of the Atlantic and Pacific oceans. there are many 'open sea' buoys giving independent measurements of ground truth, both wave heights and wind speeds. Thus it is possible to test the assimilation process in a more meaningful way, by carrying out a 3-way comparison between model data - buoy data -altimeter data.

The wave model used in this work is that used operationally at the UKMO. Based on an original implementation by Golding (1983), it has been extensively developed in recent years in order to incorporate successive developments in surface wave theory. A series of unpublished technical reports contain details of this work, Ephraums (1986). Thomas and Ephraums (1987), Stratton and Ephraums (1987).

The surface wind fields required for the hindcast runs discussed in this paper were taken from the operational archives of the UKMO. Surface wind fields on a global grid of $1^1/_2^\circ$ x $1^7/_8^\circ$ are routinely archived every 2 hours, extracted from the assimilation stage of the operational NWP system. These fields are available from October 1986 onwards and form a valuable tool for experimentation with wave model hindcasts.

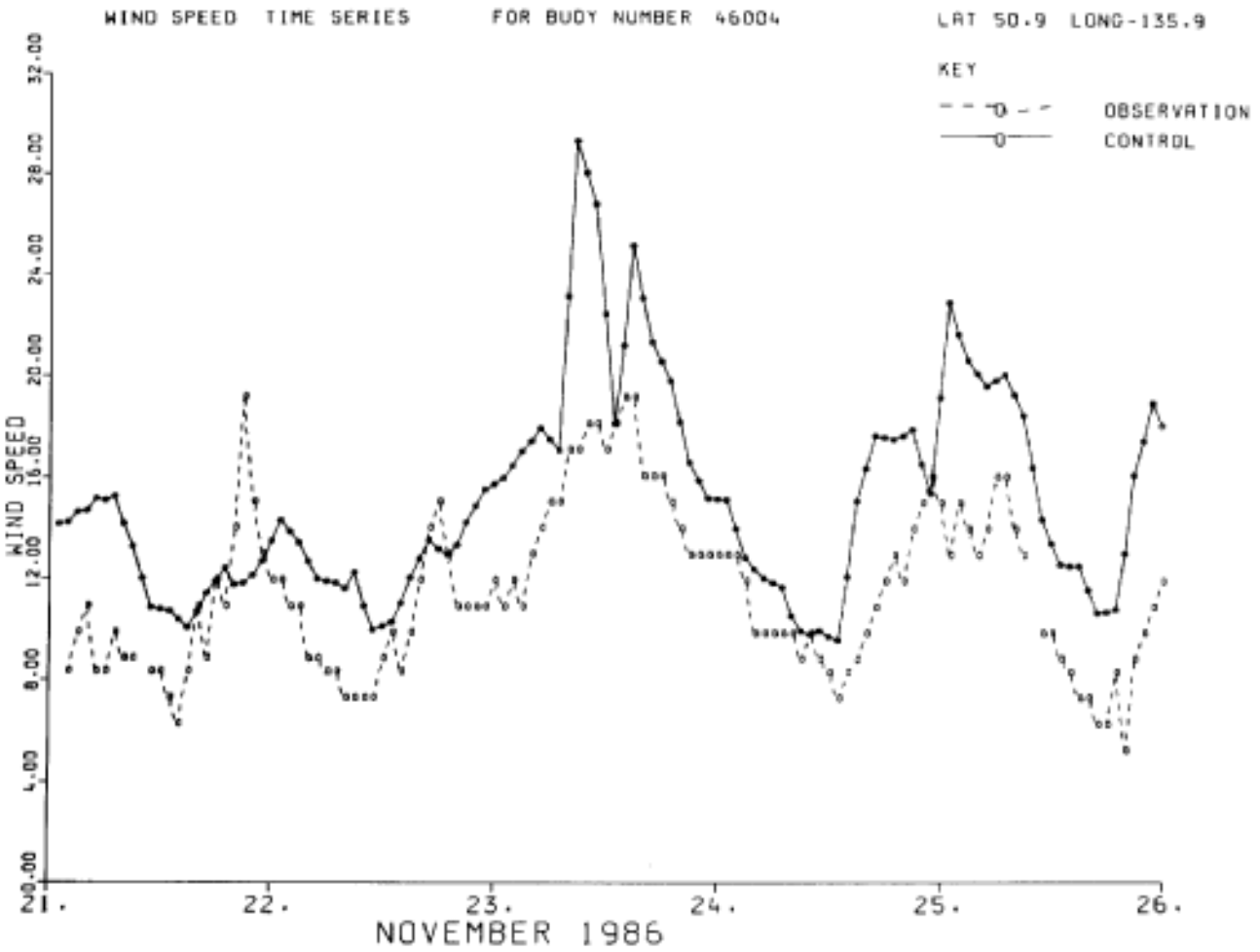

Figure 1. Time series of wind speeds from a buoy at 50.9° N, 135.9° W, along with those of the UKMO NWP model.

2. THE EXPERIMENTS

The wave model was run twice in hindcast mode for the period 00Z 11/11/86 to 00Z 11/12/86. The initial field in both cases was a complete 2-dimensional description of the global wave energy spectrum, taken from the operational archives of the UKMO. A 'spin-up' period was therefore unnecessary. The ice limits for both the Arctic and Antarctic areas were specified as for mid-November 1986, and held fixed during the hindcast runs.

The first hindcast run, the control, was performed as if part of the current operational system. 1-dimensional spectra from every gridpoint were written up for every hour of the period, together with co-located wind speed/direction data.

The second run replicated the first, except for the assimilation of GEOSAT wave height data using the methods mentioned above. Sufficient results were written up to enable a thorough investigation of the impact of assimilated data. For completeness it should be mentioned

that the full retrieval scheme of Thomas (1988) makes use of the altimeter estimate of wind speed, if it is both available and reliable. In the SEASAT experiment an error bar of 10 m/s was applied (ie difference between NWP wind and altimeter wind). This has subsequently been assessed as being too loose a criterion, hence in the present work the error bar has been set at 5 m/s. Altimeter wind estimates which differed by more than this amount from the NWP winds were not used. Some information on wave model RMS error values is required during the data assimilation process. A representative error distribution was deduced by examining a whole month of operationally produced data taken from a northern winter period (February 1988).

The GEOSAT data are taken from the earliest period released after the originally restricted availability. Data from the period 11/11/86 to 11/12/86 are used. At this time the satellite was in a 17 day repeat orbit. The one second averages of significant wave height and sigma zero (back-scattered radar cross-section) were averaged over 20 second periods, corresponding to a spatial scale comparable to that of the model grid. The smoothed sigma-zero values were then translated to equivalent wind speeds at 19.5 m using the Brown retrieval algorithm, Brown et al. (1981). multiplied by an appropriate factor. Data lying on model land or ice points were rejected. The standard deviations of the 20 (maximum) values of wave height and sigma-zero were also-calculated. Any values lying more than two standard deviations from the respective mean value were discarded, and the calculations repeated with the remaining data. A minimum of 3 values was set in order to determine a 'bin' average value.

Several diagnostic outputs were prepared to help in determining the impact of the assimilated data. In addition to the model and altimeter data, a third data set consisting of buoy, weather ship and platform information was composed. These data were taken from the Global Telecommunications System (GTS) of WMO. The buoy data consists of wave height information, plus wind speed measured at a variety of heights, less than 10 m. Platform data consists of measured wind speeds (reduced to a 10 m reference level) plus wave data either from a co-located buoy or an infra-red wave monitor. Ocean weather ship data are essentially made up of visual wave estimates plus measured winds.

As found by Dobson et al. (1987) co-location of satellite passes and fixed ground stations are relatively rare even under a generous assumption of what constitutes a co-temporal, co-spatial event. To avoid these difficulties the method proposed by Francis (1986) has been adopted here, where a numerical model is used as a matrix, by means of which data from different provenances can be compared. Statistics of model-altimeter and model-conventional observation differences are presented. Some time series at distinct locations are also included.

3. WIND DATA

Before assessing the results of the wave modelling experiments it is essential to gain an assessment of the quality of the common wind fields used as forcing functions. Table 1 gives the difference statistics for direct comparison of altimeter wind speed estimates and co-located NWP wind field values.

The wind speed range refers to altimeter measurements, while N denotes the number of comparisons and SD the standard deviation. Values are all metres per second. Differences greater than 10 ms^{-1} have been discounted in order to be more generous than the criterion for use in the spectral retrieval process.

Table 1: Difference statistics (model value minus altimeter value) for wind speed estimates, for the period 00Z 15/11/86 to 00Z 12/12/86

	0-10 ms^{-1}			10-15 ms^{-1}			> 15 ms^{-1}			All speeds		
Lat. band	N	mean	SD	N	mean	SD	N	mean	SD	N	mean	SD
60-20N	13198	0.5	2.6	4414	1.6	3.7	532	-0.7	4.9	18144	0.7	3.0
20N-20S	29885	-0.4	2.2	1621	-0.4	3.5	35	-5.1	4.8	31541	-0.4	2.3
20-60S	33489	-0.4	2.5	11288	-0.2	3.3	474	-2.4	4.0	45251	-0.4	2.7
Global	78835	-0.2	2.4	18543	0.1	3.5	1173	-1.9	4.7	98551	-0.2	2.7

Several points are immediately apparent.

(a) There are marked differences between latitude bands. The model values generally are high compared to the altimeter in latitudes north of 20°N. but low elsewhere.

(b) There are marked differences between observed wind speed ranges. The spread around the mean increases with wind speed, and for the highest speeds (> 15 ms^{-1}) the altimeter values are consistently well above those of the model.

The first point above is probably explained mainly by differences in the quality of the NWP fields. In high northern latitudes the density of observations (even over the sea) is at its highest, and the quality of these modelled products is at its optimum. In more southern latitudes the required pressure gradients are probably not strong enough to give surface winds of equal quality.

The second point demonstrates the well known problem associated with the derivation of wind speed from the altimeter back-scattered radar cross-section. In stronger winds the signal weakens appreciably, making the inversion procedure more likely to error.

Direct comparison of the model winds with measurements from conventional platforms is illustrated in Table 2 , where statistics of differences between model values and buoy values are given.

Table 2: Difference statistics (model value - observation) for wind speed estimates over the period 00Z 15/11/86 to 00Z 12/12/86

Location	Type	Number	Mean (ms^{-1})	Standard Deviation (ms^{-1})
Gulf of Mexico	buoy (4)	2405	-0.6	1.9
US East Coast	buoy (4)	2116	1.1	2.2
US West Coast	buoy (8)	4377	1.1	2.5
European shelf	buoy (2)	1172	1.1	3.0
Total	buoy	10070	0.7	2.5
European shelf	platform	1602	1.5	2.5
Atlantic	OWS (3)	1752	0.2	2.9

Buoy values have not been modified in any way, hence it would be expected that model values should exceed buoy values due to the somewhat higher notional reference level. This is true everywhere except in the Gulf of Mexico where it is suspected that the model boundary layer representation is not adequate. This is confirmed by the values of model-altimeter differences in the region 20-40°N. 80-100°W i.e. a bias of -1.1 ms^{-1} over 276 comparisons.

For comparison purposes the differences between the model and two other classes of observed wind data are also given in Table 2 . Model values appear to be unbiased against ocean weather ship winds, although the scatter is higher. Platform winds (reduced to a 10 m reference level) are understandably lower than model values on average. For completeness it should be noted that the limited amount of European buoy data give a mean difference value comparable to those of US buoys, but with a higher scatter.

Dobson et al. (1987) give a mean of -0.7 ms^{-1} and an SD of 2.2 ms^{-1} as representative figures when comparing overall groupings of buoy and satellite wind speed pairs (at 10 m), up to a distance of 150 km apart. This distance is comparable to the size of a model grid square in mid-latitudes, thus a comparison of difference statistics is meaningful, at least in spatial terms.

Taking all buoys as a reference set, the mean difference between model and buoy values is 0.7 ms^{-1}, the same as between model and altimeter values in the same northern latitude band. The standard deviations for the two comparisons are 2.5 and 3.0 ms^{-1} respectively. Thus the inferred bias between buoy and altimeter data at 19.5 is zero. These figures give much confidence to the wave height differences discussed below since the overall picture of the NWP winds is one of little

overall bias (allowing for reference level differences), and a scatter that is acceptable when it is remembered that both buoy and altimeter measurements have an uncertainty (RMS) of around 1 ms^{-1} (Dobson et al). Although not presented in Table 2 , it is known that the performance of the model over different wind speed ranges, when compared to buoy values, is fairly constant up to 15 ms^{-1} (bias ∽ 0.7 ms^{-1}) and rather more biased low (-1.0 ms^{-1}) at higher wind speeds. A five day time series of model and buoy wind speed values is shown in Fig. 1 . The buoy anemometer is at 6 m, the inferred reference level of the model is at about 20 m.

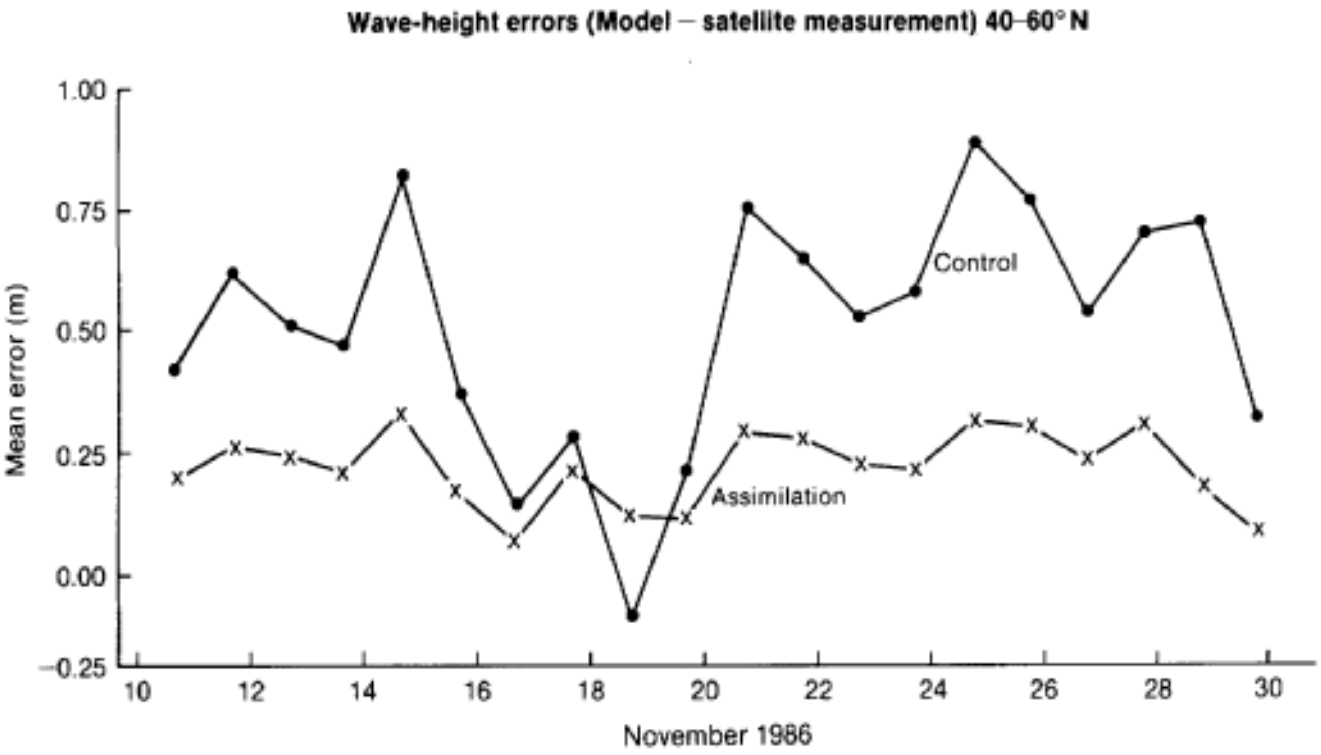

Figure 2. Time series of mean significant wave height difference (model – satellite), averaged over the latitude band 40°–60° N, for both before and after data assimilation.

4. WAVE DATA

Table 3 contains a summary of difference statistics between the model (control run) and altimeter significant wave height values. If the difference was greater than 10 m then that comparison pair was discounted, the assumption being that the altimeter 'bin' estimate had been contaminated. The wave height ranges are as measured by the altimeter. Several immediate conclusions can be drawn from the table.

(a) Wave model - altimeter wave height estimates are virtually unbiased for low waves, with small scatter.

(b) Biases increase with increasing wave height, with the model exceeding the altimeter values in the north, but falling below in the south.

(c) Scatter increases with observed wave height.

(d) Globally the model is unbiased for all wave height ranges.

Table 3: Difference statistics (model control run value minus altimeter value in metres) for significant wave height estimates, for the period 00Z 15/11/86 to 00Z 12/12/86.

	0-3 m			3-6 m			≥ 6 m			All		
Lat. band	N	mean	SD	N	mean	SD	N	mean	SD	N	mean	SD
60-20N	11679	0.3	0.6	6069	0.5	1.0	877	0.8	1.4	18625	0.4	0.8
20N-20S	30429	0.0	0.5	1123	0.4	1.0	27	0.5	2.4	31579	0.0	0.5
20-60S	30883	-0.2	0.6	13965	-0.6	1.0	451	-2.0	1.9	45299	-0.3	0.8
Global	75299	-0.1	0.6	22556	-0.3	1.1	1466	-0.1	2.1	99321	-0.1	0.8

This behaviour of the model wave heights conforms to what would be expected from the NWP winds. Table 1 shows a growing overestimate (compared to the altimeter) of model wind values between the 0 to 10 ms-1 and 10-15 ms-1 speed ranges in northern latitudes, with a large underestimate for strong winds in the south.

The variation of the difference statistics in time is illustrated in Fig. 2 which shows the mean error (model minus altimeter) over the period from 11 to 30 November for the latitude band 40-60°N. Around an overall mean value of 0.6 m, the differences range from -0.1 to +0.9 m.

Table 4: Difference statistics (model assimilation run value minus altimeter value) for significant wave height estimates for the period 00Z 15/11/86 to 00Z 12/12/86.

	0-3 m			3-6 m			≥ 6 m			All		
Lat. band	N	mean	SD	N	mean	SD	N	mean	SD	N	mean	SD
60-20N	11679	0.2	0.4	6069	0.2	0.6	877	0.1	0.9	18625	0.2	0.5
20N-20S	30429	0.2	0.3	1123	0.2	0.6	27	-0.1	2.0	31579	0.2	0.3
20-60S	30883	0.1	0.4	13965	0.0	0.5	451	-0.6	0.9	45299	0.1	0.4
Global	75299	0.2	0.4	22556	0.1	0.6	1466	-0.1	1.0	99321	0.1	0.4

Table 4 contains data equivalent to Table 3 , but with model wave height data taken from the hindcast run which included the assimilation scheme. Major changes in performance are obvious in all latitudes and for all wave height bands. The assimilation scheme is obviously successful in driving the model toward the value of the altimeter, and in retaining the changes when propagated throughout the grid. Overestimates have been reduced, underestimates increased, and the spread of differences decreased accordingly. It is particularly interesting to note that the overall increase of energy in the radiated swell regime (0-3 m) has globally been slight excessive. This may indicate the need to increase the dissipation of swell in the wave model.

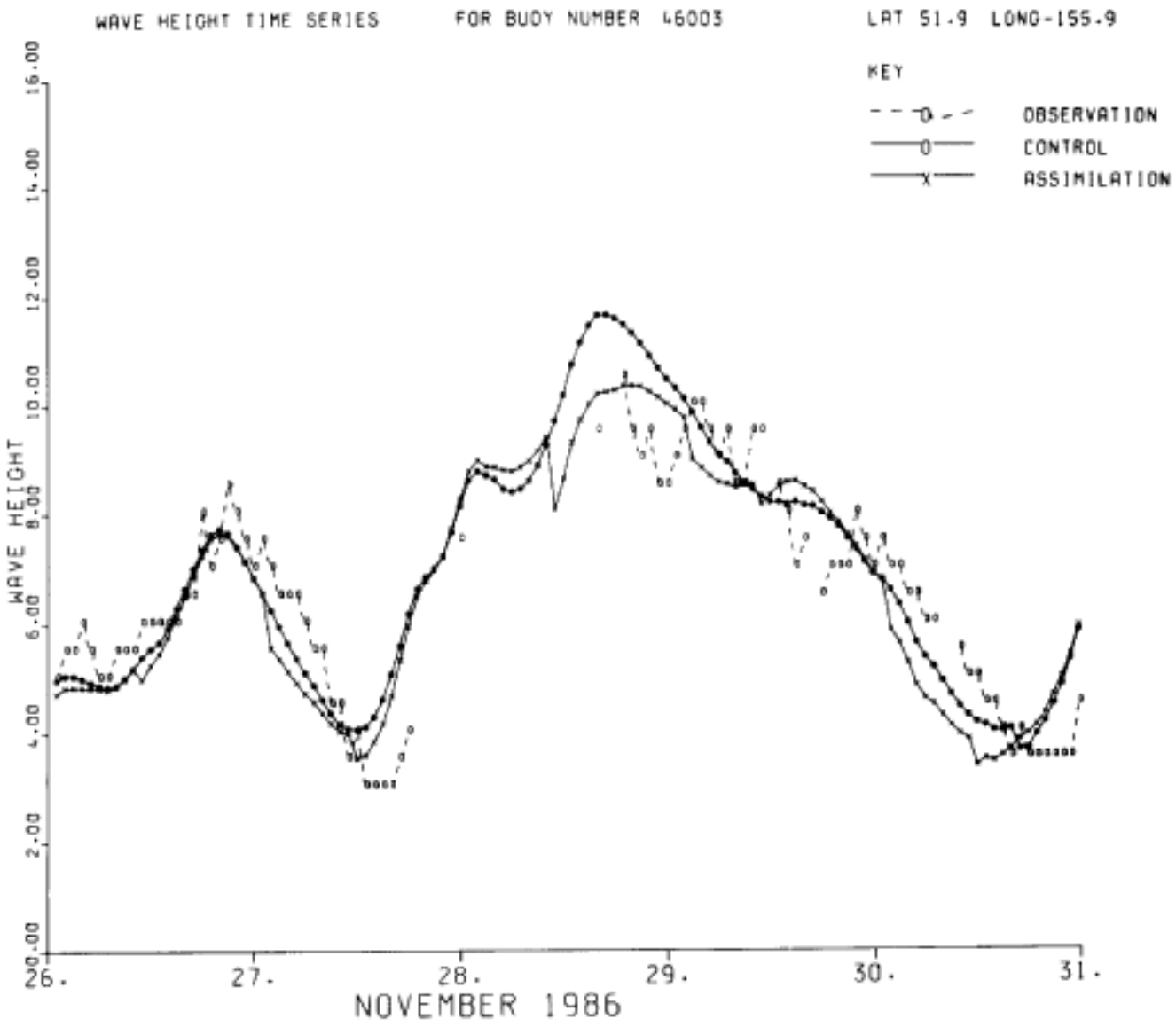

Figure 3. Time series of significant wave heights from a buoy at 51.9° N, 155.9° W, along with those of the UKMO wave model, before and after data assimilation.

Figure 2 illustrates the overall improvement in day to day comparisons between the model and the satellite wave height values. A more even performance is achieved, averaging 0.2 m.

The improvement revealed by comparing Tables 3 and 4 , and illustrated in Fig. 2 could however be illusory if the satellite values were incorrect. In contrast to the SEASAT period, the period studied in this paper does have a large number of independent wave measurements available. Hence a comparison of the model (both with and without assimilated data) with these independent data gives a valuable further perspective.

Table 5: Difference statistics (model control run value - buoy measurement) for significant wave height estimates over the period 00Z 15/11/86 to 00Z 12/12/86

	0-3 m			3-6 m			≥ 6 m			All		
Locations	N	mean	SD	N	mean	SD	N	mean	SD	N	mean	SD
US West coast	699	0.1	0.6	872	-0.2	0.9	361	-0.3	1.5	1932	-0.1	1.0
US East coast	2066	0.1	0.5	331	-0.1	0.8	39	-1.0	1.2	2436	0.1	0.6
Gulf of Mexico	1468	0.0	0.4	14	0.0	1.0	0			1482	0.0	0.4
European Shelf	433	0.4	0.8	1032	0.2	1.0	265	-0.4	1.3	1730	0.1	1.1
Total	4666	0.1	0.5	2249	0.0	1.0	665	-0.4	1.4	7580	0.0	0.8
US Total	4233	0.1	0.5	1217	-0.1	0.9	400	-0.4	1.5	5850	0.0	0.7

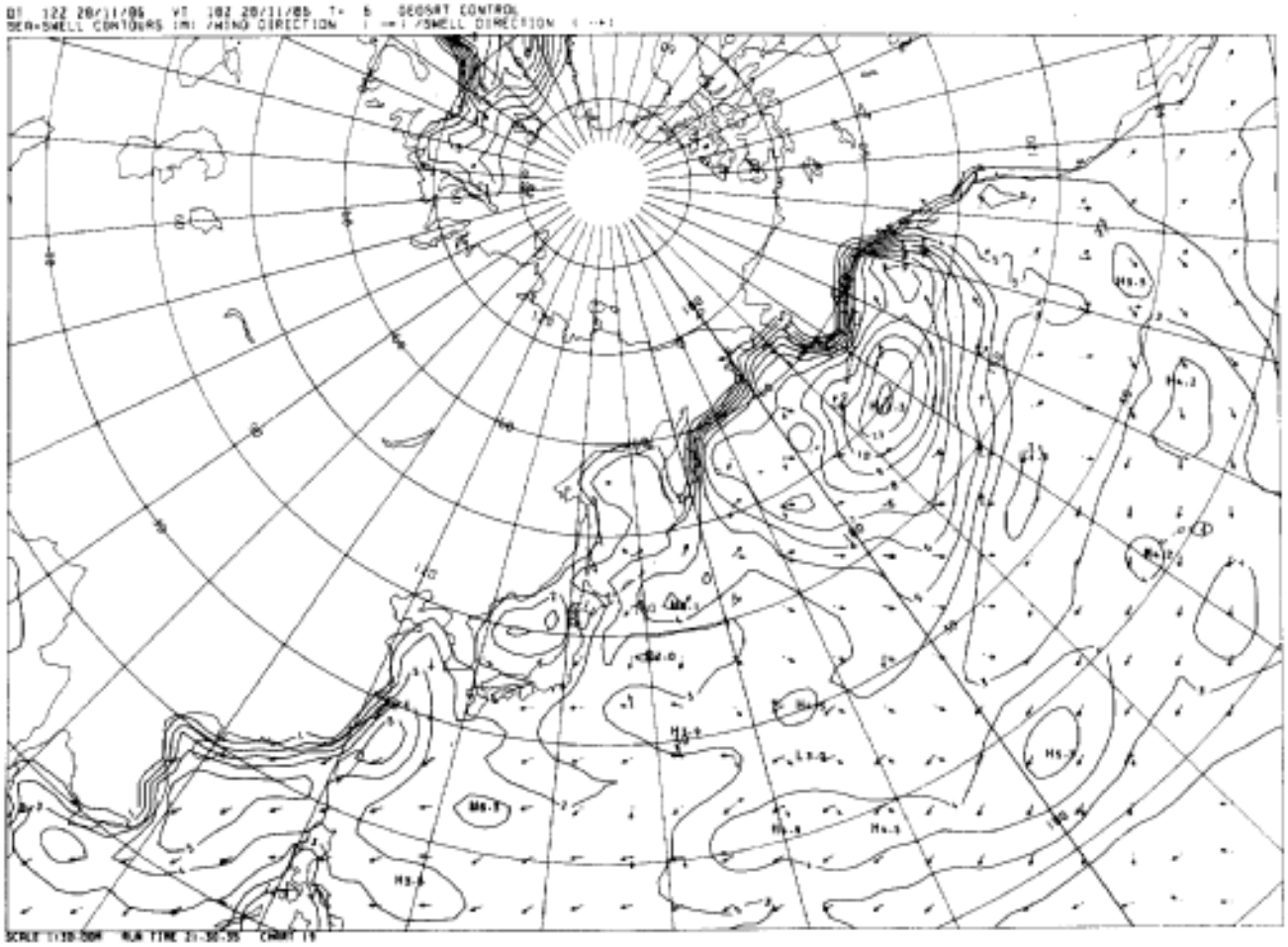

Figure 4(a). Isopleths of significant wave height from the control run of the UKMO wave model 18 UTC 28/11/86.

Table 5 contains a summary of difference statistics between data from the model and a total of 16 buoys, using the 'control' run of the model. Differences between model and buoy of greater than 10 m have been discounted, but only two such events were found. The obvious points to note are as follows

a) Wave model – buoy wave height estimates are almost unbiased when considered over the whole range of measured wave heights. In detail, there are small overestimates by the model at low wave heights, compensated by small underestimates at high wave heights. In the small sample from American East coast buoys there is a larger underestimate by the model for waves greater than 6 m.

b) European buoys are biased higher than the model at low wave heights. US buoys are almost unbiased. The difference is statistically significant, indicating different buoy performances.

c) Scatter increases with increasing wave height.

The overall result of Table 5 for US buoys should be compared to that of the 20–60°N latitude band in Table 3 . The clear inference is that in these latitudes the buoy values are greater than those measured by the satellite.

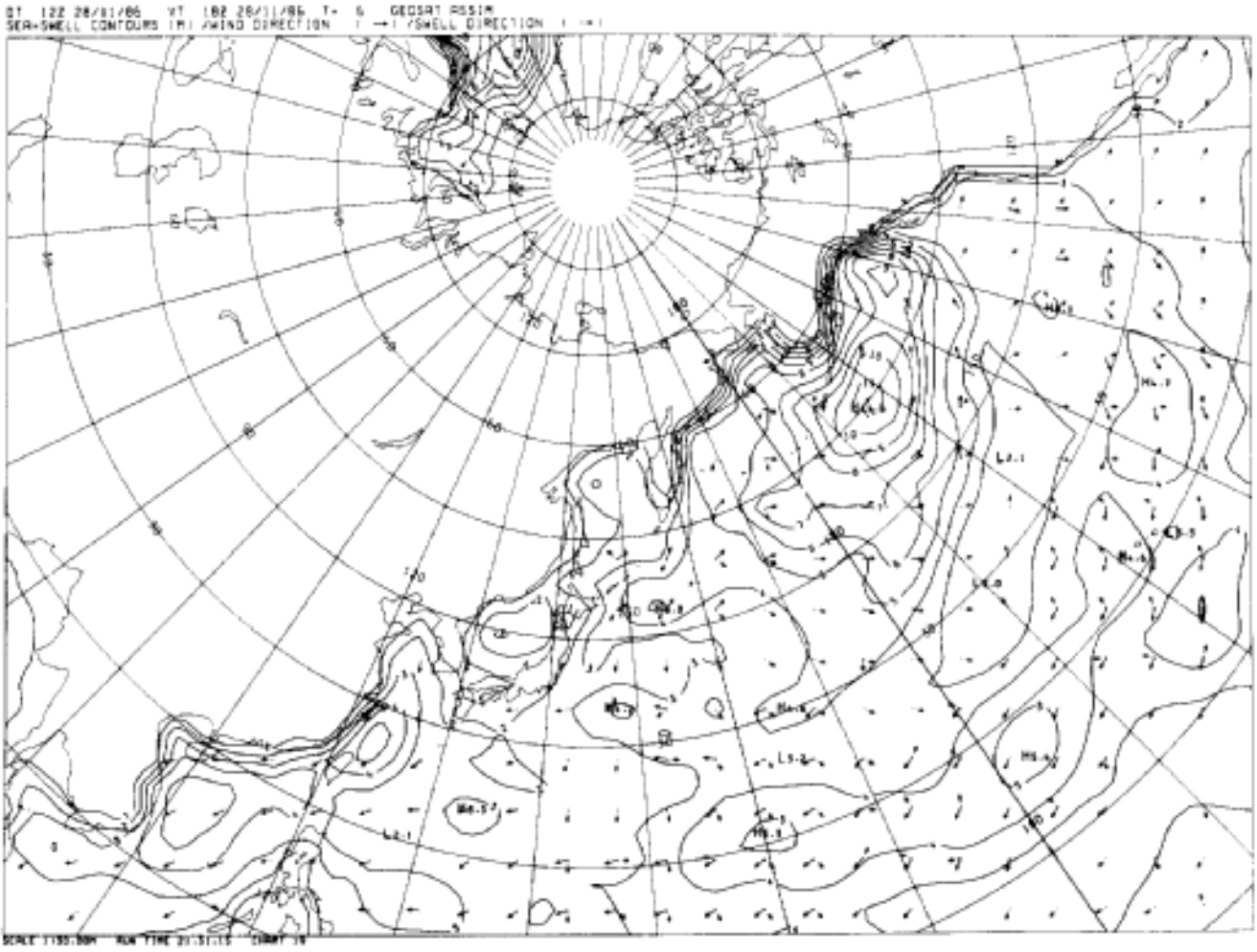

Figure 4(b) Isopleths of significant wave height from the UKMO wave model after assimilation of satellite data. 18 UTC 28/11/86.

This difference is 0.2 m for 0-3 m wave heights increasing to 1.2 m for wave heights greater than 6 m. Since a large sample of data is being used in both comparisons the above difference figures may be taken as indicating a definite bias between buoy and altimeter values. Only a qualitative estimate can be deduced however since the distributions of wave height of the different instruments in the various ranges (0-3, 3-6, ≥ 6 m) are not identical. The difference (buoy-altimeter) for all wave heights is 0.4 m. which matches the difference found by Dobson et al. (1987), where data from 43 buoys were used. Apparently no measurements in excess of 6 m were found in that comparison, hence the information contained in this paper regarding the significant differences in estimates of high wave heights by the different instruments is presently unsupported, although a plot of similar comparisons in a paper by Shuhy et al, (1987) would appear to confirm the trend of increasing bias with height.

Table 6: Difference statistics (model assimilation run value - buoy measurement) for significant wave height estimates over the period 00Z 15/11/86 to 00Z 12/12/86.

	0-3 m			3-6 m			≥ 6 m			All		
Locations	N	mean	SD	N	mean	SD	N	mean	SD	N	mean	SD
US West coast	699	0.2	0.6	872	-0.2	0.8	361	-0.5	1.4	1932	-0.1	0.9
US East coast	2066	0.1	0.5	331	-0.1	0.8	39	-1.2	1.3	2436	0.0	0.6
Gulf of Mexico	1468	0.0	0.4	14	0.0	0.9	0			1482	0.0	0.4
European Shelf	433	0.4	0.7	1032	0.2	0.9	265	-0.4	1.2	1730	0.2	1.0
Total	4666	0.1	0.5	2249	0.0	0.9	665	-0.5	1.3	7580	0.0	0.8

The difference statistics between the wave model, run in assimilation mode, and the buoy measurements are given in Table 6 . On comparison with the results of Table 5 it is apparent that little change has taken place except perhaps in the relative performance of highest wave band considered. The indication here is that model values are even lower than buoy values than in the control run for large wave heights, a result consistent with the findings of the previous paragraph. The minor change in model performance against buoys, after assimilation of satellite data, is at first sight in contradiction to the major change in model performance when assessed against satellite data. The explanation lies in the fact that whereas all model grid points affected by assimilated data are compared with the satellite values, many of the grid points compared with the buoys will not have had a direct assimilation increment, unless within the area of influence of a relatively near satellite overpass. This fact, plus the relative

proximity of buoy locations to land masses, implies that changes, when assessed against buoys, will mainly rely on advected (swell) energy increments, from a restricted range of directions.

A time series of model and buoy wave height data is shown in Fig. 3 , where both control and assimilation model runs are depicted. Near overflights of the satellite occurred on a daily basis during the period shown. On every occasion the impact of the assimilated data was to reduce the model wave height value, sometimes in the order of 1 m.

Although the GTS record is broken near the peak on the 28th, the implication is that the buoy peak value would have been higher than that implied by the earlier altimeter pass. The conclusions of the earlier tabular statistics are clearly confirmed in this example plot, where the impact of assimilated data is to reduce the value calculated by the model.

The structure of a North Pacific wave field is shown in Figures 4(a) and 4(b) , which depict isopleths of significant wave height at 18Z 28/11/86, both before and after data assimilation. The reduction in the peak value in the North East Pacific is clearly noticeable. While the general pattern is unchanged, minor changes in wave height are apparent all over the grid.

5. CONCLUSIONS

It has been demonstrated above, and in the more detailed SEASAT experiment, Francis and Stratton (1989), that wave height data from a satellite altimeter can be successfully assimilated into a numerical wave model.

Independent assessment of the model against buoy data shows that

(a) The model already performs well in simulating Northern hemisphere wave fields, over a wide range of wave heights.

(b) Altimeter wave height estimates are biased against those from buoys, being up to 0.5 m lower for moderate waves (up to 6 m), and in the order of 1.0 m lower for larger waves.

The role of a properly formulated model in extending the possible range of validation experiments for remotely sensed data has been clearly demonstrated. A further investigation into performance of the model in the southern hemisphere is still required, but this awaits an adequate sample of conventional ground truth.

6. REFERENCES

Brown, G.S., Stanley, H.R. and N.A. Roy, 1981: The wind speed measurement capability of spaceborn radar altimeters. IEEE J. Oceanic Engr., OE-6 No. 2

Dobson, E., Monaldo, F., Goldhirsh, J. and J. Wilkerson, 1987: Validation of GEOSAT Altimeter derived wind speeds and significant wave heights using buoy data. John Hopkins University, Applied Physics Laboratory. TECH. DIGEST, 8, No. 2., 222-234.

Ephraums, J.J., 1986: Directional relaxation of the wave energy spectrum in turning winds. Met. Office (Met 0 2b) Tech. Note 105.

Esteva, D.C., 1988: Evaluation of preliminary experiments assimilating SEASAT significant wave height into a spectral wave model. J. Geophys. Res. 93, 14099-14105.

Francis, P.E., 1986: The use of numerical wind and wave models to provide areal and temporal extension to instrument calibration and validation of remotely sensed data. Proceedings of a workshop on ERS-1 wind and wave calibration, Schliersee FRG, 2-6 June 1986 (ESA SP262).

Francis, P.E. and R.A. Stratton, 1989: Some experiments to investigate the assimilation of SEASAT altimeter wave height data into a global wave model. Submitted for publication.
Golding, B., 1983: A wave prediction system for real time sea state forecasting. Quart. J.R. Met. Soc., 109, 393-416.

Hasselman, K., Hasselmann, S., Bauer, E., Bruning, C., Lehner, S., Graber, H. and P. Lionello, 1988: Development of a satellite SAR image spectra and altimeter wave height data assimilation system for ERS-1. Max Planck Institute for Meteorology Report No. 19.

Janssen, P., Lionello, P., Reistad, M. and A. Hollingsworth, 1987: A study of the feasibility of using sea and wind information from the ERS-1 satellite. Part 2: Use of scatterometer and altimeter data in wave modelling and assimilation. ECMWF ESRIN contract report No. 6297/86/HGE-I(SC)

Shuhy, J.L., Grunes, M.R., Uliana, E.A. and L.W. Choy, 1987: Comparison of GEOSAT and ground truth wind and wave observations; preliminary results. Johns Hopkins University Applied Physics Laboratory. TECH DIGEST, 8. No. 2., 219-221.

Stratton, R.A., and J.J. Ephraums, 1987: Great circle turning for the operational wave model. Met. Office (Met 0 2b) Tech. Note 115.

Thomas, J.P. and J.J. Ephraums, 1986: Proposals for new wave model physics. Met Office (Met 0 2b) Tech. Note 107.

Thomas, J.P., 1988: Retrieval of energy spectra from measured data for assimilation into a wave model. Quart. J.R. Met. Soc., 114, 781-800.

WAVE HINDCASTS FORCED BY SCATTEROMETER AND OTHER WIND FIELDS

[1]Peter M. Woiceshyn, [2]Morton G. Wurtele, and [1]Glenn F. Cunningham

[1]Jet Propulsion Laboratory
California Institute of Technology
Pasadena, CA 91109, USA

[2]University of California, Los Angeles
Department of Atmospheric Sciences
Los Angeles, CA 90024, USA

ABSTRACT

Wave hindcasting experiments utilizing scatterometer and other wind fields were conducted in two parts. The first part addressed the testing of the OCTI DWAVE model with diagnostic runs in order to become acquainted with the strengths and limitations of the model. These included time- and fetch-limited wave development experiments, wave propagation experiments with slanting fetch, and the effects of large spatial wind shear.

The second part addressed wave hindcasts with real wind data. These were conducted with the following concurrent data sets in 6-hour time steps: SEASAT scatterometer (SASS) data alone interpolated to grid points; SASS data alone, time-interpolated to produce "synoptic" wind fields; ECMWF operational wind fields for the same synoptic times; and the ECMWF wind fields resulting from the assimilation of SASS data into the operational data set.

The results were highly systematic and consistent, showing that the SASS data alone were sufficient for a viable hindcast, qualitatively and quantitatively competitive with the hindcasts from the ECMWF wind fields. The SASS-only wave fields produced locations and estimates of the highest waves more accurately than both ECMWF-forced fields. However, the SASS-only fields were consistently biased higher than ECMWF-forced and SEASAT altimeter significant wave heights in the low wave regime.

1. INTRODUCTION

The importance of the wind field as the sole input to a wave forecast model raises a number of interesting questions, both for theory and for operations. How is the wind field measured? How is it specified at equally spaced gridpoints? How sensitive is the forecast to differently determined wind fields? How much time has elapsed between the measurement and the wave forecast? Is the wind field input directly from observations, or has it been produced by the assimilation algorithms of a numerical weather prediction (NWP) model? In order to answer such questions it is necessary to have (i) a

creditable wave forecast model, (ii) two or more wind fields independently determined by more than one methodology, and (iii) some reasonably acceptable technique for validation of the forecasts or hindcasts from the input of each of these fields. In this paper we present a study with all of these conditions satisfied. Our chief purpose is to evaluate the waveforecast potential of the wind observations from the scatterometer (SASS) aboard SEASAT, September, 1978, used as direct input to a wave forecast model, without first being assimilated into a numerical prediction model.

2. THE WAVE FORECAST MODEL AND THE FOUR INPUT WIND FIELDS

First, we identify the wave forecast model used in this research, the DWAVE model of Offshore and Coastal Technologies, Inc. (Resio, 1986), which may be described as a second-generation model, and was provided to us by OCTI at the request of one of our sponsors, the Naval Ocean Research and Development Activity, Bay St. Louis, MI. Extensive testing of this model was carried out to assess the strengths and limitations of the OCTI wave model (Woiceshyn *et al.*, 1988), but is not relevant to this paper, which involves only the comparison of hindcasts with the same model using different input wind fields.

Secondly, we identify the wind field data sets. Since there are four such sets from which hindcasts were made, it is necessary that the differences between them be well understood: some of the conclusions derived from the experiments will be based on these differences. Two of these sets consist of SASS data alone, and these will be described first. The JPL-UCLA-AES SASS 15-day record consists of the original SASS data organized in swath cells normal to the sub-track, but with aliases removed (Peteherych et al. , 1984). An interpolation algorithm is applied to these wind vectors to produce gridded data in the nadir gap and between swaths, at 100-km resolution (cover of Aviation Week & Space Technology, March 13, 1989, Vol. 130 (11)). The wind at any given grid point thus represents the value of this variable at a time determined by the times of the SASS observations entering into its interpolation, and this time will therefore be different from the times at other grid points. This wind field is obviously asynoptic, and is so designated.

The second SASS field is produced by a time-interpolation of the asynoptic gridded data at each grid point in such a way as to achieve a fairly good approximation to a synoptic, that is, a simultaneous, wind field, again at 100-km resolution. It should be noted that since the interpolation uses values interpolated from earlier and/or later swaths, the wind value at each grid point contains information earlier and/or later than the synoptic time that labels the field. These fields are called SASS synoptic.

We now turn to the control wind fields. For these we have chosen the 1000-mb synoptic wind fields produced by the European Center for Medium Range Weather Forecasts (ECMWF), as being of the highest quality and resolution available (Anderson *et al.*, 1987). ECMWF graciously provided us with two data sets. The first of these is derived from the standard algorithms of ECMWF, producing a consistent three-dimensional field of atmospheric variables, one of which is the 1000-mb wind field at a resolution of 1.875 degrees latitude/ longitude, and gridded from the spectral format of ECMWF data. The second ECMWF data set was produced by assimilation of all the JPL-UCLA-AES SASS data into the three dimensional system described above. The SASS data was thus allowed to influence the analysis from in situ data in accordance with the algorithmic rules. These two data sets we refer to as ECMWF without SASS, and ECMWF with SASS, respectively. There has been great interest in the impact of high-resolution surface wind data on the analyzed fields of a large numerical forecast model (Anderson *et al.*, 1987) ; we shall see the corresponding impact on wave forecasts.

3. PURPOSE AND ORGANIZATION OF THE HINDCAST EXPERIMENTS

These four data sets, having varying degrees of independence from each other, have been used to make wave hindcasts (that is, forecasts after the fact) in a number of situations, and the results compared. The situations selected fall into two categories: (1) Certain regional scale storms, in particular the famous storm associated with the ocean liner *Queen Elizabeth II* (QEII storm), and typhoons Irma and Judy. Here validation of the hindcasts is qualitative or semi-quantitative, owing to the paucity of reliable in situ wave-height estimates. (2) Along the SEASAT subtrack of certain orbits, altimeter data are available in the geophysical data record, yielding significant wave heights, which may be reliably used for hindcast validation. For these orbits, quantitative comparisons are made extensively, and the statistics derived therefrom are presented.

The thrust of these experiments is the demonstration that by SASS data alone -- either asynoptic or synoptic -- wave hindcasts can be made that are verifiably competitive quantitatively and qualitatively -- that is, in pattern, intuitively assessed -- with hindcasts from surface winds of elaborate numerical weather prediction models. These latter fields are, as noted above, produced only after extensive processing at numerical weather forecast centers. It is thus thought that many operational agencies that have a need for rapidly produced regional wave forecasts will take an interest in this capability.

4. SELECTED REGIONAL HINDCAST EXPERIMENTS

We first present wave hindcasts for a situation of special interest, the so-called QEII storm. Wind and wave fields in the region

of this explosive development -- a "bomb," in meteorological parlance -- were spectacular and thus present severe demands on the accuracy of the input winds and the capability of the wave forecast model. A minimal validating wave field is available from the **Mariner's Weather Log** (James, 1979).

Three wind fields for 11 Sept 1978, 06Z, are presented in Figure 1 , one SASS synoptic, one ECMWF without SASS, and one ECMWF with SASS. Arrows represent wind directions, and isotachs are represented by solid curves at intervals of 2.5 m/s. Maximum wind speeds of about 30 m/s are indicated on all charts, although placement of this maximum varies by several degrees of latitude. SASS winds also locate the storm center somewhat north of its placement by ECMWF. The six-hour wave hindcasts each represented a "spin-up" from five days of wind stress in each data set. Hindcasts were made at six-hourly intervals from 9 Sept 12Z to 12 Sept 06Z. As an example, the hindcast wave fields for the time of the wind fields of Figure 1 , 11 Sept 06Z, are recorded in Figure 2 . The maxima significant wave heights (Hs) of 13, 11, and 14 meters, respectively, are located close to each other, perhaps surprisingly so. We note here that the impact of SASS winds on the ECMWF three-dimensional atmosphere (in the assimilation process) was sufficient to produce an increase of 3 meters in the Hs hindcast. An enlargement of the Hs field in the neighborhood of the region of highest waves is presented in Figure 3 , for convenience. The only validating information available to us is contained in the **Mariner's Weather Log** (James, 1979), as exhibited in Figure 4 as HS contours. The wave heights according to this document were some 31 percent lower than the SASS hindcast; but the source or sources of the data for Figure 4 are not given in James (1979), and, as will be seen from the next section, SASS hindcasts in regions of strong winds do not tend to be biased high.

5. ALONG-TRACK WAVE HINDCASTS, VERIFIED BY SEASAT ALTIMETER

It is obvious that validation is the major problem in a comparison of hindcasts such as the present one. In the case of this study, it was possible to use the geophysical data record of the SEASAT altimeter, which provided significant wave heights at very high resolution along the nadir subtrack. The accuracy of this altimeter was carefully verified against buoy data by Fedor and Brown (1982), with the conclusion that the instrument met the accuracy specifications of 0.5 m or 10 percent, whichever is greater. We have made hindcast validations and comparisons for the period of the JPL/UCLA and the ECMWF data sets, for all those orbits for which the altimeter was in operation -- a total period of three days. The results of this study are as follows.

Since hindcasts were made from the four wind data sets, a convenient method of presentation is to plot the hindcast Hs results along the orbital track, together with the Hs altimeter record. We shall show some selected plots, and then present the overall statistical results. We begin with a relative success for SASS synoptic hindcasting, Rev 1172, shown in Figure 5 . Here we see an altimeter record of a region of almost 10 meter waves at about 40 degrees latitude. The SASS hindcast identifies both location and amplitude of this Hs maximum, whereas the ECMWF hindcasts underestimate and misplace it. However, we note that in the lower latitudes, SASS hindcasting of the two-meter waves is about 100 percent too high. This tendency we see repeatedly in the many such records produced by us. Rev 1166 is another such example (Figures 6a , 6b). SASS hindcasts follow the altimeter curve as the latter increases, but are greatly biased high when Hs falls off in the tropical latitudes. In this case, both ECMWF hindcasts are remarkably good.

The best evidence that these differences between SASS and ECMWF hindcasts is a systematic one lies in the statistics for the entire altimeter-validated record. This is presented in Figure 7 , showing the error (wave model hindcast minus altimeter) as a function of significant wave height, for three of the four wind fields. This presentation deserves careful thought. As noted above, the two SASS wave-hindcast fields are consistently biased high, with a bias of about two meters, for waves of small amplitude, in contrast to the ECMWF fields, which exhibit a positive bias of less than one meter. However, as the wave height increases, the ECMWF hindcasts begin to underestimate the Hs field, and for Hs of six meters or more, the SASS hindcasts are superior to those from the ECMWF wind fields without SASS assimilation. For eight meter waves, the ECMWF without SASS fields lead to mean underestimates of three meters, and error of about 38 percent, whereas the hindcasts from SASS synoptic winds are too low by only about one meter or 11 percent. The frequency distribution of wave heights is relevant here, and this is presented in Figure 8 .

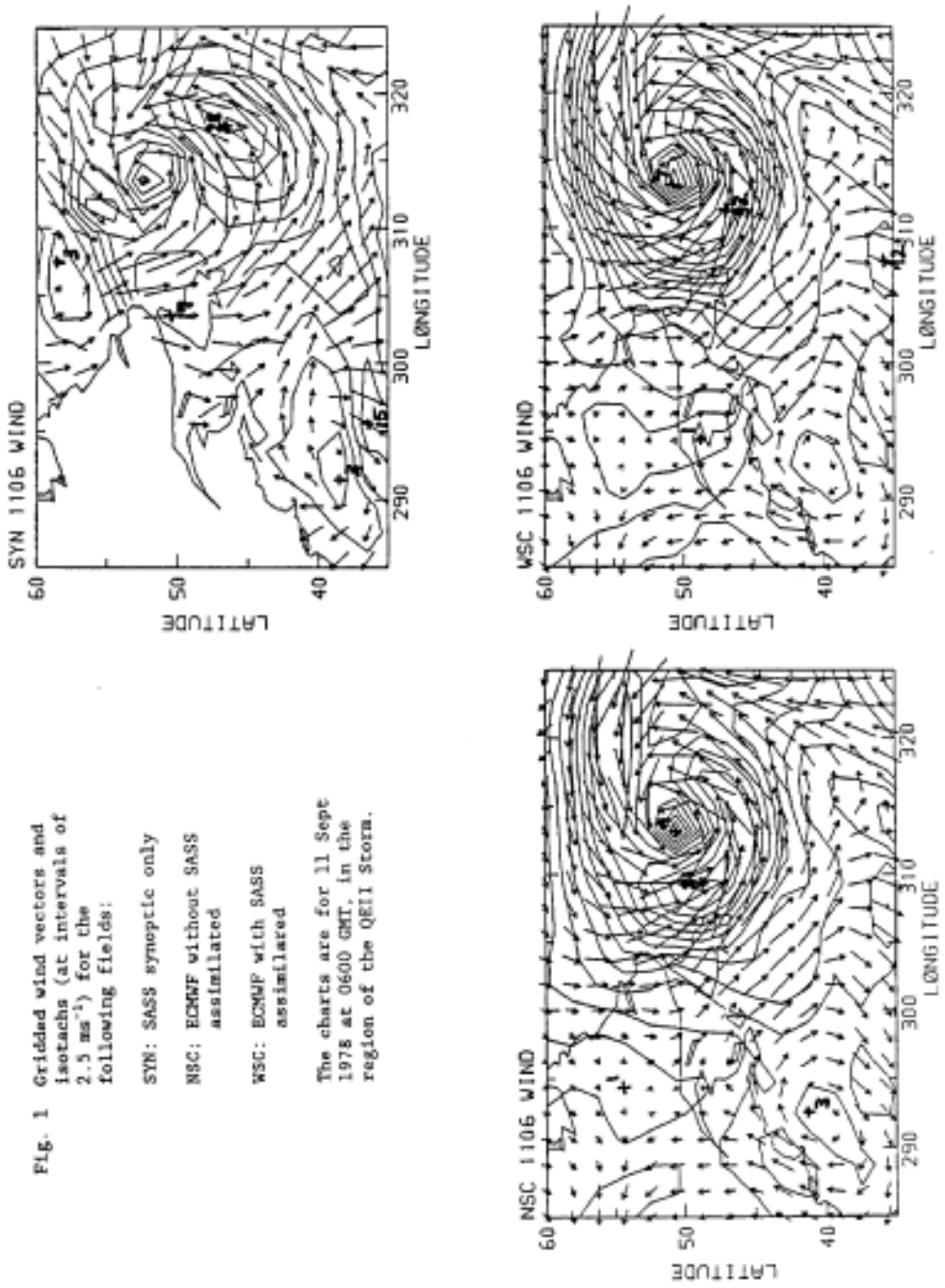

Fig. 1 Gridded wind vectors and isotachs (at intervals of 2.5 ms^{-1}) for the following fields:

SYN: SASS synoptic only

NSC: ECMWF without SASS assimilated

WSC: ECMWF with SASS assimilated

The charts are for 11 Sept 1978 at 0600 GMT, in the region of the QEII Storm.

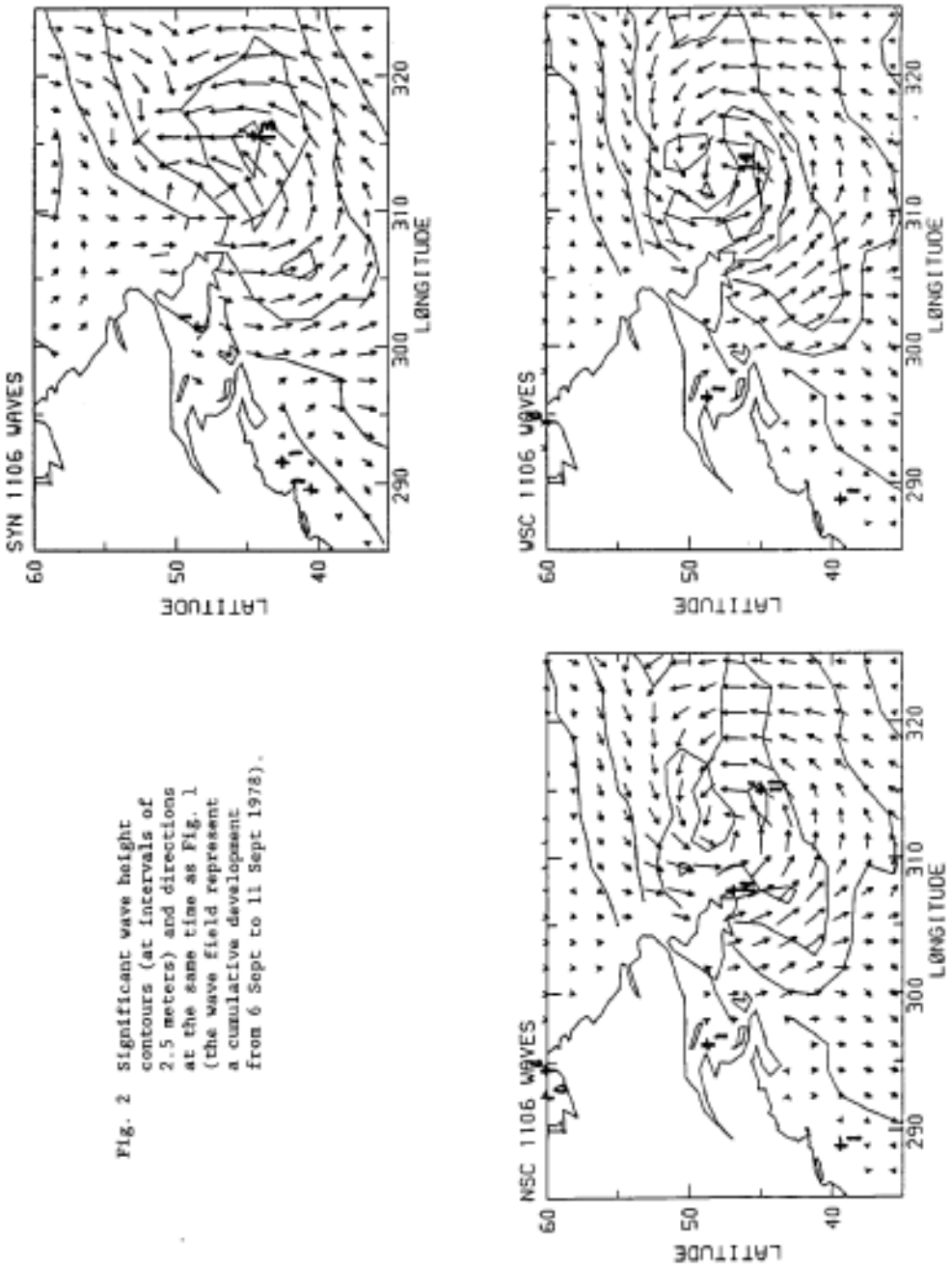

Fig. 2 Significant wave height contours (at intervals of 2.5 meters) and directions at the same time as Fig. 1 (the wave field represent a cumulative development from 6 Sept to 11 Sept 1978).

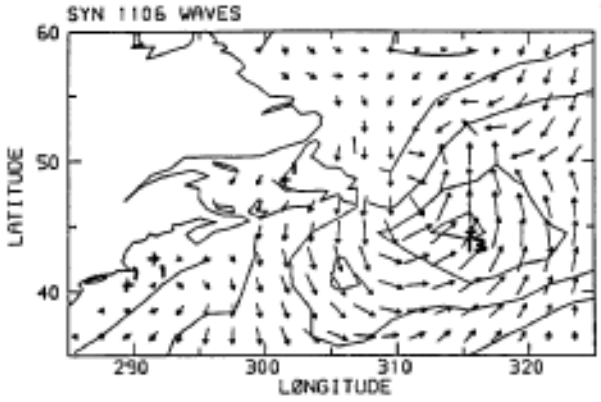

Fig. 3 Enlargement of Fig. 2 panel SYN SASS in the region of maximum significant wave height (Hs).

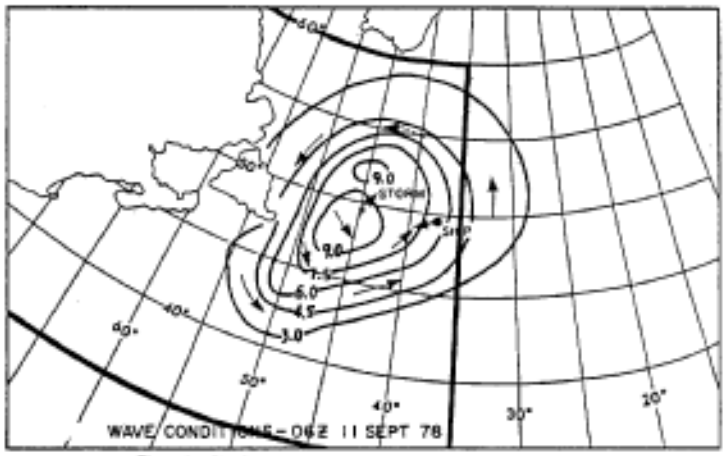

Figure 6.--Significant wave height analysis for 0600 September 11, 1978.

SWH in meters

Fig. 4 Significant wave height analysis for the same time as Fig. 1 (from James, 1979, Mariners Weather Log).

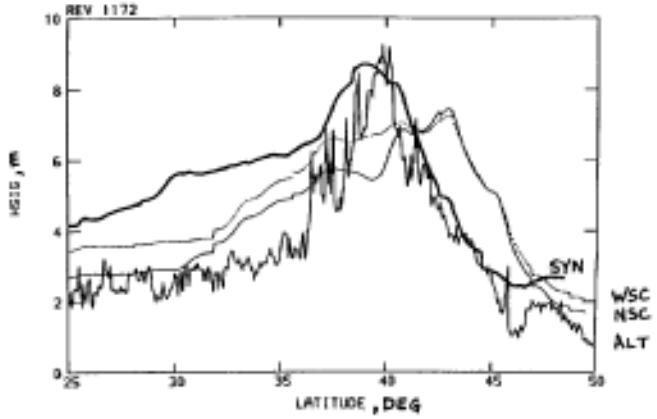

Fig. 5 Significant wave heights as hindcast by SASS synoptic (SYN), ECMWF without SASS (NSC), and ECMWF with SASS (WSC) as verified by SEASAT altimeter (ALT) for SEASAT rev 1172.

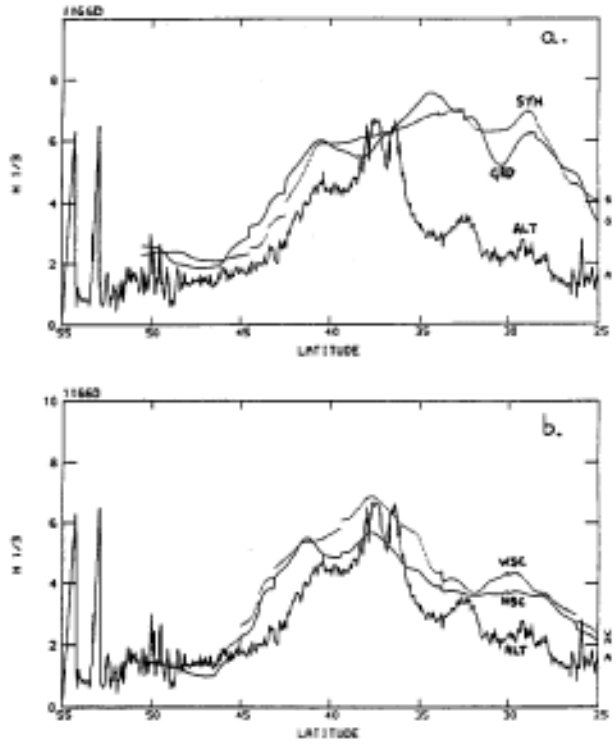

Fig. 6 Panels a) and b) are the same as Fig. 5 but for SEASAT rev 1166.

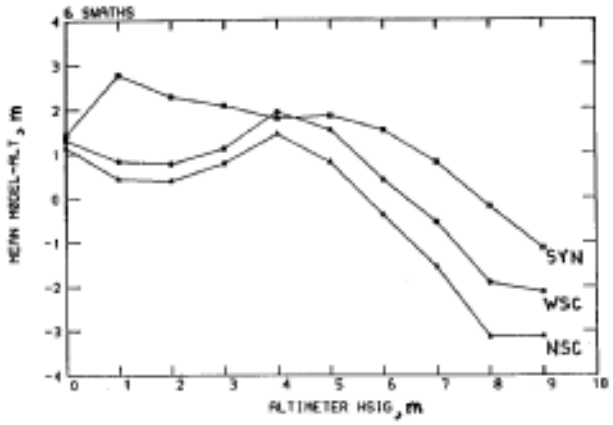

Fig. 7 Mean Hs difference of Hindcast-Altimeter fot 6 sections of data in the western Pacific Ocean.

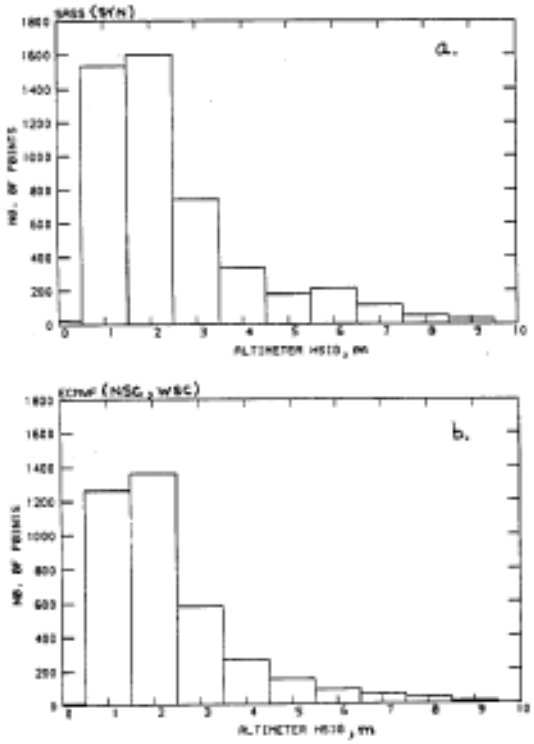

Fig. 8 Panels a) and b) are frequency distributions for data plotted in Fig. 7.

6. DISCUSSION AND CONCLUSIONS

Which of the four wind fields produced the "best" hindcast will depend on the definition of "best." A simple root-mean square comparison would undoubtedly favor the ECMWF hindcasts. However, if greater weight is accorded to the accuracy of hindcasting for larger waves, then the SASS synoptic results might well be determined as superior. Without attempting to determine a definitive criterion, it is safe to assert that **wave hindcasts using SASS data alone constitute a viable competitor to those derived from the most sophisticated weather data processing system**. We further note from this compilation that the introduction of SASS data into ECMWF produces a one-half to one meter change in the hindcast, increasing it over the entire range, and producing a curve about halfway between SASS and ECMWF curves. We also observe that the synoptic SASS fields very slightly improve the hindcasts over those with the asynoptic fields. This may or may not be significant, but the trend is highly consistent.

What can we explain of all this? Since the pattern is similar for all four fields, it seems safe to infer that the high bias for low winds and low bias for high winds is possibly a property of the DWAVE model. This statistical result, highly significant because of the large number of hindcasts, should be valuable information for any wave model revision or construction. However, the consistent failure of SASS winds to hindcast low waves is so pronounced, when compared with results from the other input fields into the same model, that it would seem that there must be a relatively simple explanation. A possible partial explanation may be the tendency for the SASS wind recovery algorithm to overestimate the low wind speeds (Woiceshyn *et al.*, 1986). However, it was found equally that SASS tends to underestimate the high winds, which is not consistent with the hindcast results. Thus some very important questions are posed for wave forecasters as a consequence of this study.

It is also hoped that experiments using control data sets may make possible an interpretation of the hindcast results in such a way as to help to distinguish the contributions to the error fields by the wind inputs from the contributions of the wave model. Once the model is understood, its sensitivity to the input wind fields may make possible feed-back information by which the winds could be corrected. In this way, the wave forecast could become an instrument of quality control on the wind field and on the parameterization of the atmospheric planetary boundary layer.

ACKNOWLEDGEMENTS

We appreciate the assistance and encouragement for this Project from J. Hawkins, R. Pickett, and A. Pressman of NORDA, and R. Kakar, and J. Theon of NASA. In addition, we benefited from discussions with

Drs. P. Janssen (KNMI), D.T. Resio (OCTI), Drs. S. Peteherych and R. Lalbeharry (AES-Canada), D. Boggs (dB Sysytems, Ltd.), and Drs. P. Francis and R. Stratton (UK Met. Office).

We are particularly grateful to ECMWF for the 2 wind data sets used for this work. We also thank Dr. Steven Peteherych and colleagues for helping us jointly produce the two-week dealiased SASS data set used by us to produce the gridded SASS wind fields utilized in this study.

The research described in this paper was performed in part at the Jet Propulsion Laboratory, California Institute of Technology, and was sponsored by the Naval Oceanographic Research and Development Activity and by the National Aeronautics and Space Administration.

REFERENCES

Anderson, D., A. Hollingsworth, S. Uppala, and P. Woiceshyn, 1987: A Study of the feasibilty of using sea and wind information from the ERS-1 Satellite; Part 1: Wind scatterometer data, *ECMWF Contract Report to ESA, ESRIN Contract No. 6297/86/HGEI(SC)*, pp. 121.

Aviation Week & Space Technology, March 13, 1989, 130(11).

Fedor, L. S. , and G. S. Brown, 1982: Wave height and wind speed measurement from SEASAT radar altimeter, *J. Geophys. Res.*, 87, 3254-3260.

James, R.W., 1979: Anatomy of a storm, *Mariners Weather Log*, 23(2),71-75.

Peteherych, S. , M.G. Wurtele, P.M. Woiceshyn, D.H. Boggs, and R. Atlas, 1984: First global analysis of SEASAT scatterometer winds and potential for research, *Proceedings of the URSI Commission F Symposium and Workshop, NASA Conf. Publ. 2303*, 575-587.

Resio, D.T. , 1986: Program DWAVE: Global/regional deep water wave model, OCTI Swamp Group, 1985, *Ocean Wave Modeling*, Plenum Press.

Woiceshyn, P.M., M.G. Wurtele, D. H. Boggs, L.F. McGoldrick, and S. Peteherych, 1986: The necessity for a new parameterization of an empirical model for wind/ocean scatterometry, *J. Geophys. Res.*, 91(C2), 2273-2288.

Woiceshyn, P.M., G.F. Cunningham, and M.G. Wurtele, 1988: Wave Hindcasts with OCTI DWAVE model forced by scatterometer and other wind fields, *JPL Internal Report No. D-5702, Jet Propulsion Lab., Pasadena, CA 91109*, pp 18.

GEOSAT SATELLITE DATA IN COMPARISON TO WAVE MODEL RESULTS AND OCEAN WINDS

A. Behrens and W. Koch

GKSS Research Centre
Geesthacht, Federal Republic of Germany

ABSTRACT

A second generation and a third generation shallow water wave prediction model have been applied to several selected storms in the North European Shelf area. Both models are verified with conventional sea state measurements. The results of the wave models and the driving ocean windfields have been compared with observations recorded by the GEOdesy SATellite (GEOSAT). The considered parameters are significant wave height and wind speed. The well known statistical behaviour of the North European Storm Study wave model results and the corresponding ocean wind fields allow a quality check of the GEOSAT data. In general it is found that the satellite values for significant wave height and the wave model results agree fairly well. In contrast to that the wind speed measurements derived by the radar altimeter are too low in comparison to the ocean winds especially in strong wind situations.

1. INTRODUCTION

In the next few years satellite measurements will provide extensive sea state data sets with the possibility of comprehensive wave model verifications or near real-time assimilation of wave data into models on a global scale. This contribution investigates the reliability of satellite measurements by means of a comparison between an existing GEOSAT data set and the results of two different wave prediction models which are the second generation model HYPAS and the third generation model WAMS. Both are shallow water versions for the North European Shelf area. The driving windfields for the wave prediction models have been received from the United Kingdom Meteorological Office. The GEOdesy SATellite provides significant wave heights and wind speed observations from a radar altimeter.

During the validation phase of the NESS project (NESS: North European Storm Study) all available seastate measurements from weather ships, platforms and data buoys in the North European Shelf area (altogether 49 locations) were collected for 20 selected storm periods between 1978 and 1986. With the aid of that unique data set the second generation wave model HYPAS was calibrated and validated to the conditions of the North European Shelf area and a quantitative error analysis for the 20 storms was produced. Five of the hindcasts were repeated with the third generation wave model WAMS.

A coincidence in time between GEOSAT data and wave model results occur for the two storm periods 1.11.85 - 10.11.85 and 9.01.86 - 15.01.86. For these time periods HYPAS hindcasts as well as WAMS hindcasts are available, so that a detailed comparison for the significant wave height and the driving wind fields can be done.

Section 2 contains a quality consideration of the satellite data together with a description of the applied error removal procedure. The UKMO wind field development is explained in section 3 and a short review on the two wave models used is given in section 4 .

2. THE GEOSAT DATA

GEOSAT was launched in March 1985 and uses a radar altimeter to estimate wind speeds and significant wave heights. The altimeter is a narrow-beam, downward-looking, short-pulse radar that bounces signals off the ocean's surface. Significant wave heights are estimated by measuring the leading-edge slope of the returning pulse. Wind speeds are estimated indirectly. A surface reflection coefficient is calculated from the return pulse magnitude. The satellite was designed to estimate wind speeds within 1.8 m/sec in the range 1 to 18 m/sec and to measure significant wave heights within 10 % for waves greater than 5 m or 0.5 m for waves smaller than 5 m (Pickett, 1986). Whether this accuracy is valid will be checked later on. For further treatment of the GEOSAT data it was necessary to edit the data set to eliminate transmission errors, islands and ice. Additional problems occur in the GEOSAT data set at land/sea boundaries and a permanent data gap at the zero meridian points to an error in the GEOSAT data post processing computer program.

3. THE UKMO WINDFIELDS

Wind speed and direction over the world's oceans are required as input to wave models on all scales. During the NESS validation phase it became obvious that the wave model results depends very sensitively on the forcing windfields. Therefore much work was done by the UKMO to develop high quality windfields. The first guess fields were the archived computer wind fields of an operational running atmospherical model. The next step to improve these fields was to incorporate additional wind information from weather ships and platforms and in a second step the resulting wind fields were checked by an experienced meteorologist. That procedure lead to high quality windfields to perform the NESS wave and storm surge hindcasts.

4. THE DIFFERENT WAVE PREDICTION MODELS

4.1 The HYPAS model

HYPAS is a second generation model which combines the traditional approach of independent calculation of swell energy for each frequency

and direction hand through a ray technique, with a parametrical wind-wave model, using the parameters of the JONSWAP spectrum and the mean wind-sea direction as prognostic variables (Bouws, 1985).

HYPAS runs on a Cartesian 30 km grid with 3922 active seapoints. The geographical extent of the model area is given in Figure 5 and 6 . The directional resolution is 22.5 degrees and the spectrum is devided into 14 frequency bands. At open boundaries HYPAS gets boundary values from a North Atlantic coarse grid model (HYPA deep water version) with a grid spacing of 150 km.

Time series of the significant wave height at two selected locations compared with conventional sea state measurements illustrate the excellent agreement between HYPAS model results and observations. The first one (Figure 1) shows the sea state development during the six days at Ekofisk, a station in the middle of the central North Sea. Figure 2 gives a time series with peaks up to 9 in at Statfjord which is located in the northern North Sea.

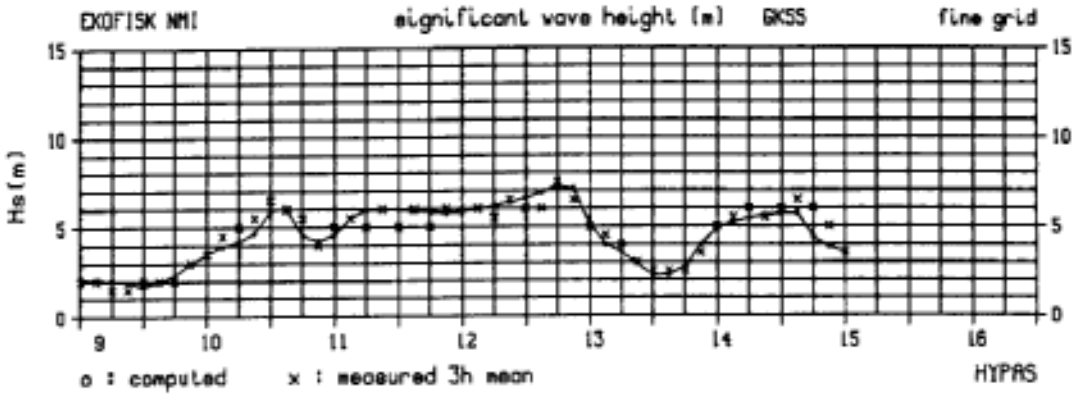

Figure 1: Significant wave heights at Ekofisk (09.01.86 - 15.01.86).

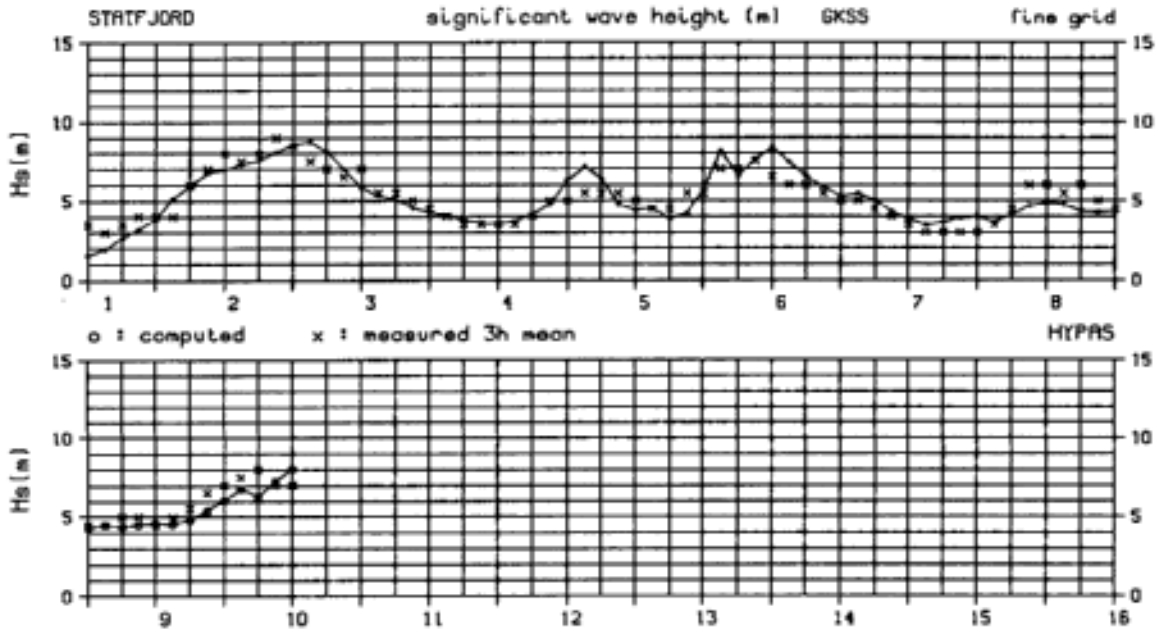

Figure 2: Significant wave heights at Statfjord (01.11.85 - 10.11.85).

4.2 The WAMS model

WAMS is a third generation wave model which integrates the energy balance equation without any restriction on the shape of the spectrum. It contains an efficient method to compute the exact integral expression for the nonlinear wave-wave interaction in the source function.

The model runs on a latitude-longitude grid with a directional resolution of 30 degrees and the spectrum is represented by 25 logarithmically spaced frequencies. A disadvantage of WAMS for our purpose is the missing boundary information at the boundary grid points. A WAMS North Atlantic coarse grid model is not available.

The WAMS results are comparable to the HYPAS values. Corresponding to the HYPAS time series we chose the measured and computed significant wave heights at same stations which are Ekofisk in Figure 3 and Statfjord in Figure 4 . There are only slight differences in the model curves.

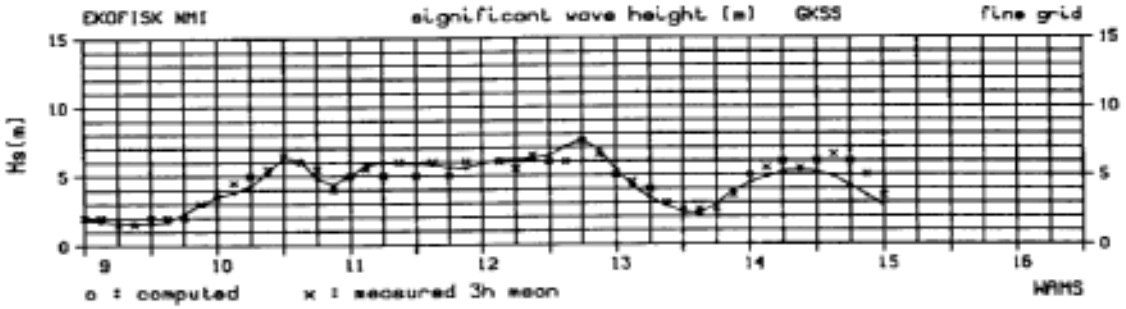

Figure 3: Significant wave heights at Ekofisk (09.01.86 - 15.01.86).

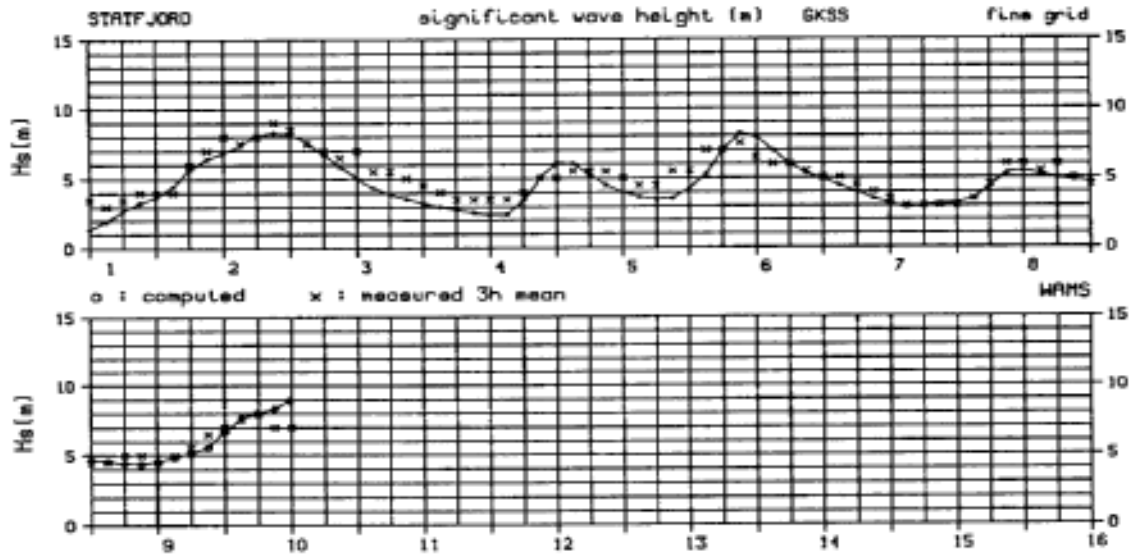

Figure 4: Significant wave heights at Statfjord (01.11.85 - 10.11.85).

5. COMPARISON OF ALTIMETER-DERIVED SIGNIFICANT WAVE HEIGHTS AND WAVE MODEL RESULTS

All 30 satellite passes during the first storm period in the eastern part of the North Atlantic are included in Figure 5 . Figure 6 shows the 40 satellite passes for the second storm. The satellite crosses the region in only a few minutes, so that normally the altimeter measurements are available at times which do not coincide with the three hour schedule of the wave model output (0 h, 3 h, 6 h, 9 h, 12 h, 15 h, 18 h, 21 h). Therefore the observations will be compared with the wave model results of the nearest model output time. The resulting time separations are always less than one and a half hour. The spatial separation of a comparison between altimeter measurement and wave model gridpoint value is less than 15 km corresponding to the wave model grid size of 30 km.

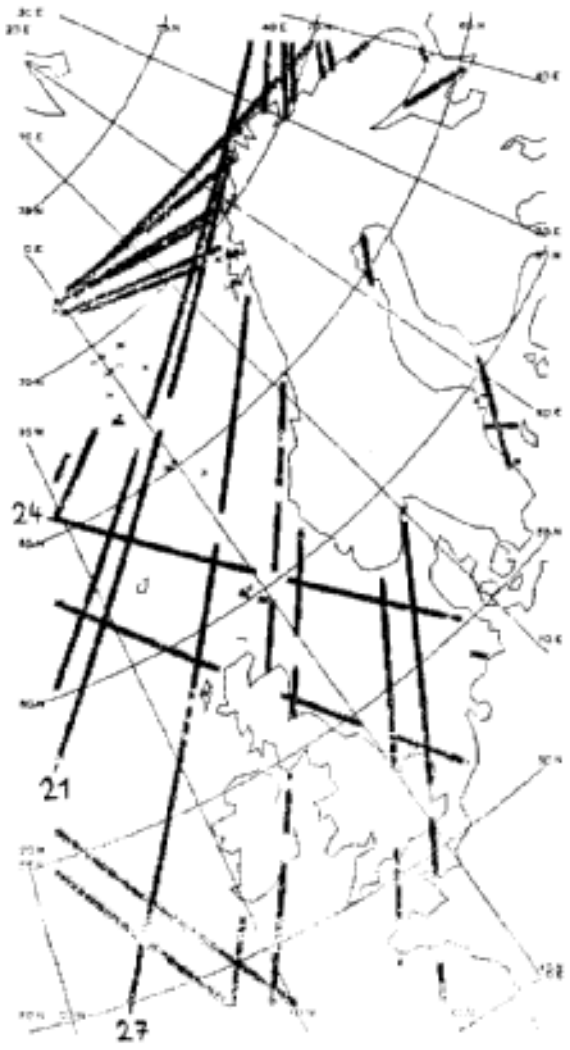

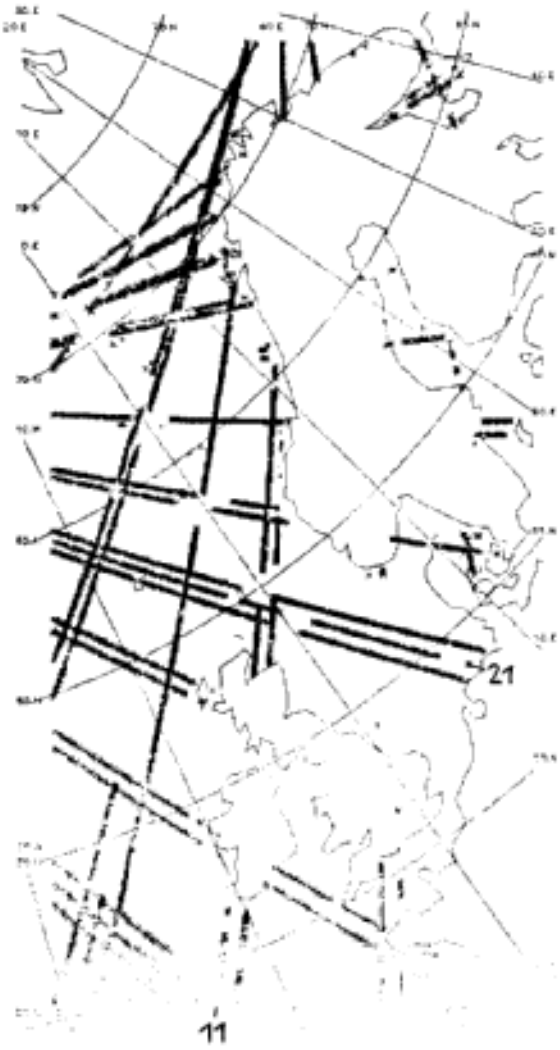

Figure 5: Satellite passes (first storm). Figure 6: Satellite passes (second storm).

The GEOSAT significant wave height measurement accuracy was planned to be 10 % for waves greater than 5 in or 0.5 in for waves less than 5 in. Although after Shuhy (1987) and Dobson (1987) that goal was met it should be emphasized that the significant wave heights in their investigations were for the most part limited to 6 in. Subsequently we show how the altimeter performs under conditions with higher values for the significant wave height as occurred during these storms with peaks up to 16 in.

5.1 GEOSAT data against HYPAS model results

A first example which is representative for waves less than 6 in supports the good agreement between altimeter data and buoy data obtained by Shuhy (1987) and Dobson (1987). Figure 7 displays the altimeter and model wave height comparisons along satellite pass 24

which crosses the central and the northern North Sea on a lateral track. Additionally Figure 8 and 9 show the storm conditions on a longitudinal track along the satellite passes 21 and 27 with higher significant wave heights up to 11.4 in (pass 27). Fortunately we can establish a similar good agreement between altimeter-derived and model wave heights. Significant differences only occur at the boundaries of the model grid where the model values are not as accurate.

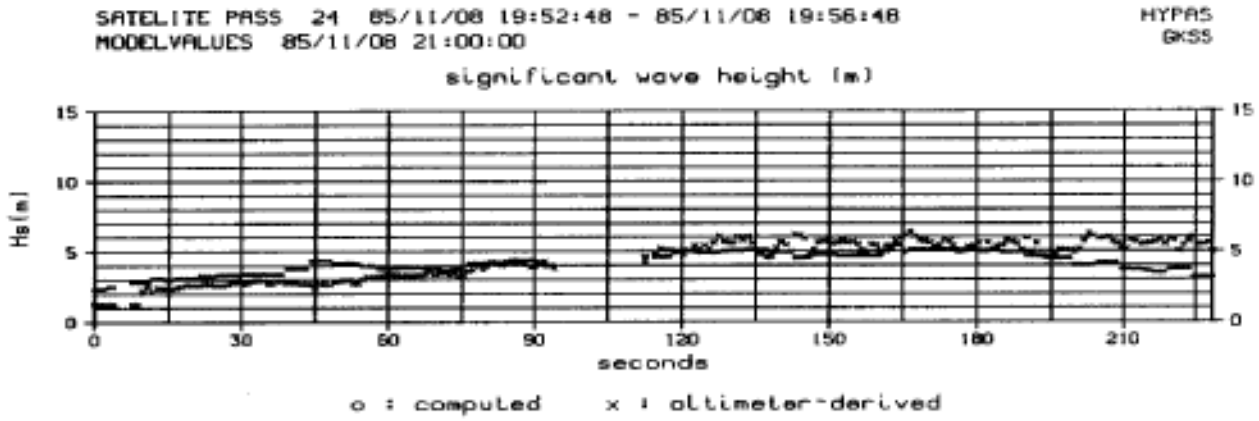

Figure 7: Significant wave heights along satellite pass 24 (first storm)

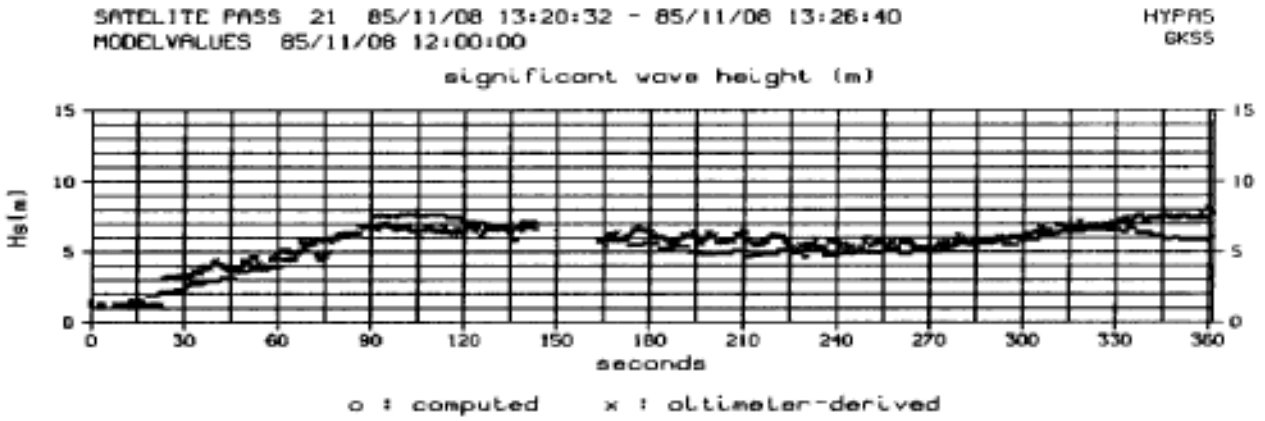

Figure 8: Significant wave heights along satellite pass 21 (first storm)

5.2 GEOSAT data against WAMS model results

A comparison between WAMS significant wave heights and GEOSAT measurements provide similar results. Two further examples in Figure 10 and 11 displaying the GEOSAT passes 21 and 11 of the second storm period illustrate that the satisfactory agreement between altimeter-derived and computed wave heights is also valid under storm conditions. Pass 21 with its extremely high altimeter-derived 16

m-peak crosses the central and northern North Sea on a latitude track and pass 11 covers the Norwegian Sea, the northern North Sea and the southwest approaches on a longitudinal track. Differences at the model grid boundaries between the curves seemed to be greater than in the GEOSAT/HYPA-comparisons. That is due to the missing boundary information from a North Atlantic coarse grid model for the WAMS runs.

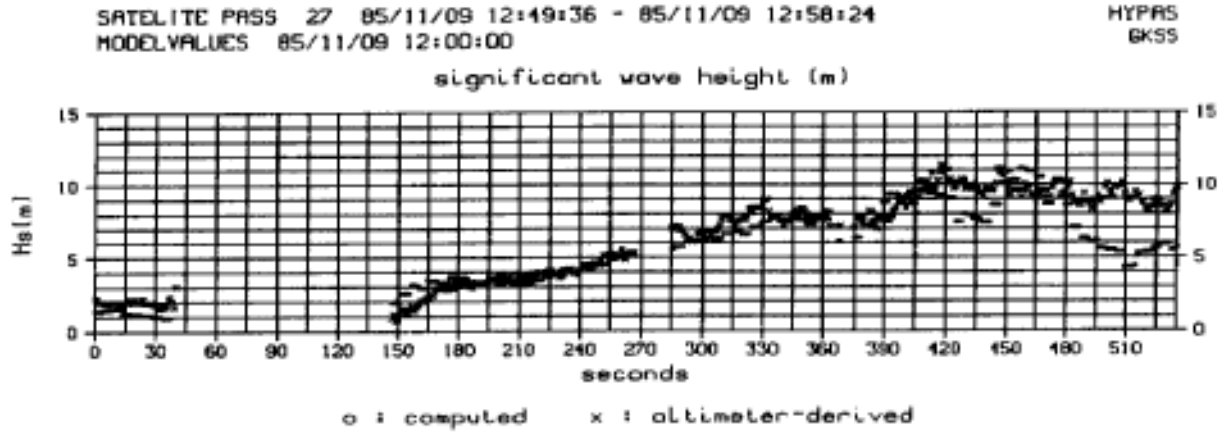

Figure 9: Significant wave heights along satellite pass 27 (first storm)

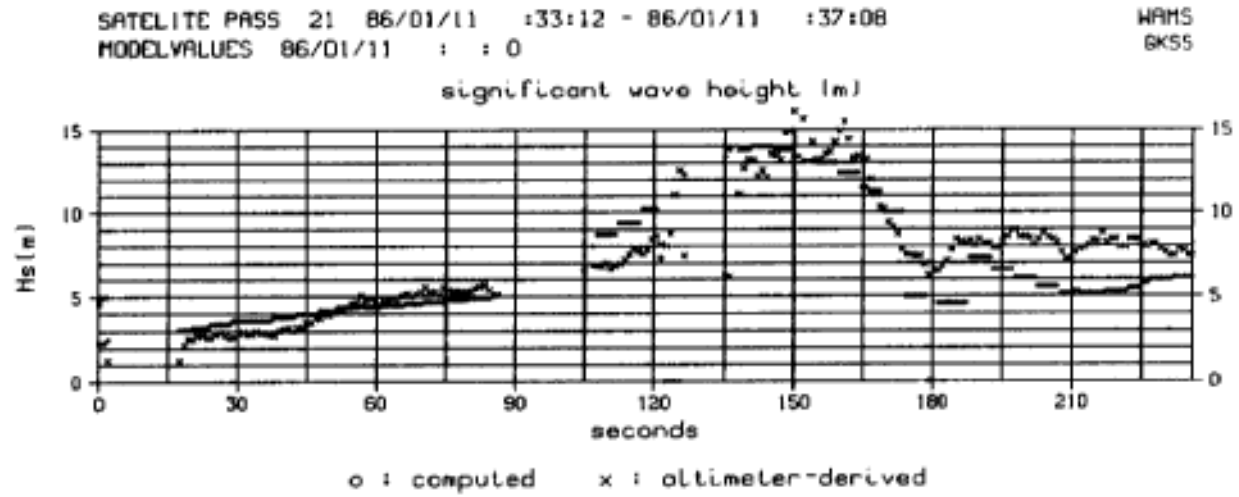

Figure 10: Significant wave heights along satellite pass 21 (second storm).

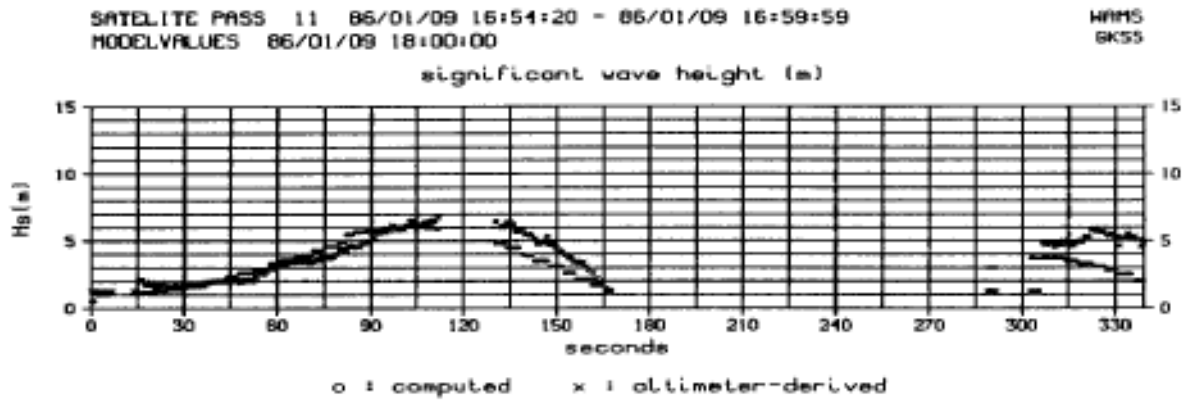

Figure 11: Significant wave heights along satellite pass 11 (second storm).

6. COMPARISON OF GEOSAT AND UKMO WIND SPEEDS

A 1.8 m/sec rms error for the altimeter wind speed measurements is valid for the range 1 to 18 m/sec. Questions remain concerning the performance of the algorithms considered by Dobson (1987) at wind speeds greater than 14 m/sec. The wind speed values during the two storms above were generally very high (up to 30 m/sec), so that we are out of the above mentioned range. Shuhy (1987) found that the wind speeds determined by GEOSAT are lower than his ground-truth data for wind speeds greater than 6 iii/sec. This will be supported by our investigation.

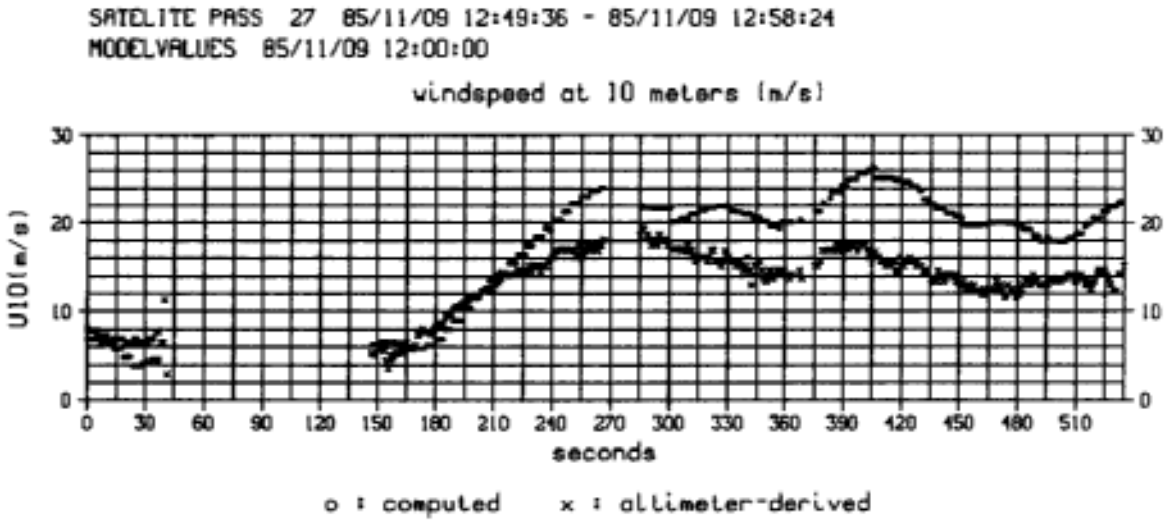

Figure 12: Wind speeds along satellite pass 27 (first storm).

Looking at Figure 12 which shows a comparison between the wind speed observations recorded during satellite pass number 27 and the UKMO wind speed we find out that the measured wind speed in the range 12 to 19 m/sec is obviously much too low (differences occur up to 12

ni/sec). Evidence for the correct UKMO wind is the good agreement with conventional rig anemometer winds. Furthermore it will be supported by the good agreement of the corresponding significant wave heights for the same overflight (Figure 9). Similar conditions are shown in Figure 13 (first storm, pass 21) and 14 (second storm, pass 11), although the differences are smaller (up to 8 m/sec) as in the first example. The corresponding significant wave heights can be seen in Figure 8 (first storm, pass 21) and Figure 10 (second storm, pass 11). Several further examples support the conclusion that the satellite wind speed values are much too low in strong wind situations. In situations with lower wind speeds differences between UKMO wind speeds and altimeter-derived wind speeds will become smaller. The wind speed comparisons we have done generally support the trend that the disagreement increases with increasing wind speed values.

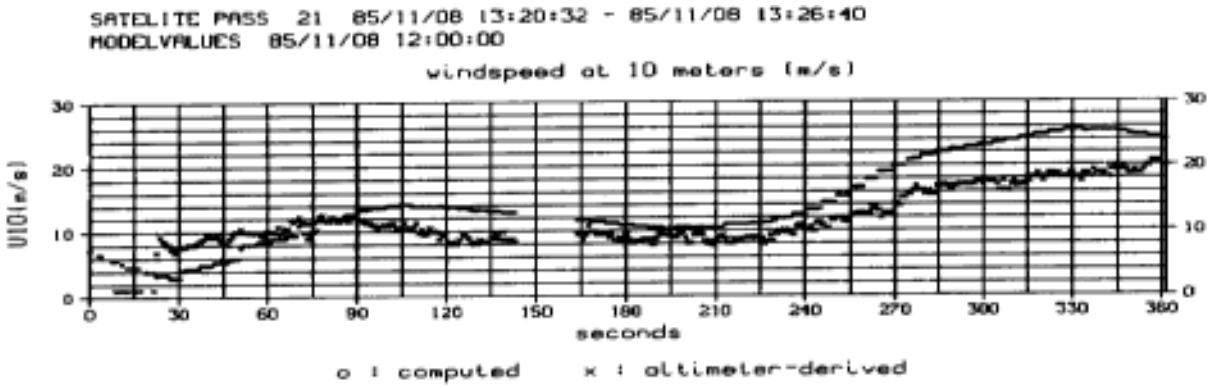

Figure 13: Wind speeds along satellite pass 21 (first storm).

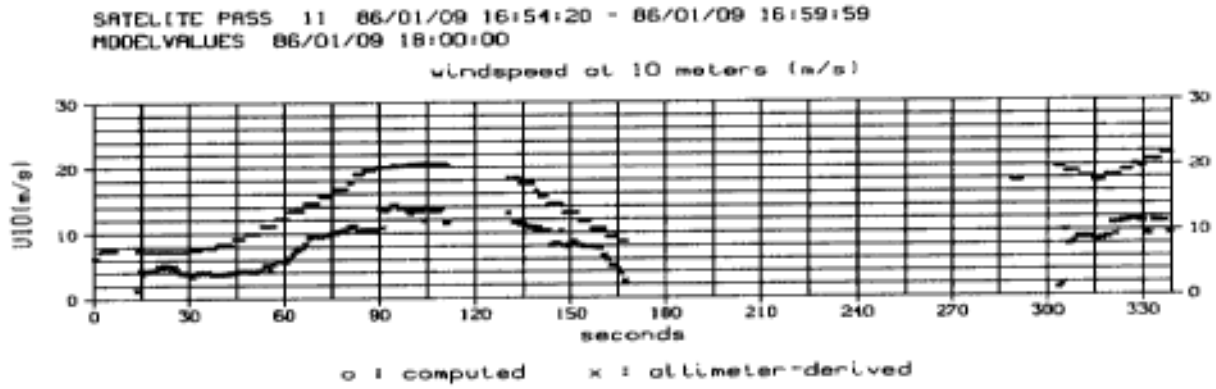

Figure 14: Wind speeds along satellite pass 11 (second storm).

The return pulse magnitudes received by the GEOSAT radar altimeter to estimate wind speeds are generally in harmony with corresponding atmospherical structures. Therefore we assume that the original data

is qualitative good, however the algorithm which is used to extract the wind speeds from the backscattered power may need to be improved.

7. SUMMARY

Fifteen days of altimeter-derived significant wave heights and wind speeds have been compared to wave model results and to wind speeds provided by the UKMO. The Comparisons demonstrate that the agreement between GEOSAT and wave model significant wave heights, Hs, is satisfactory over the whole range of Hs up to 16 m. Therefore we expect that the assimilation of the high quality GEOSAT altimeter-derived significant wave heights into wave prediction models will lead to excellent simulations of natural sea state conditions. Concerning our wind speed comparisons we conclude that for higher wind speeds occurring under storm conditions the GEOSAT altimeter provides wind speed values which are much to low. It must be pointed out that wind speed values exceeding 6 m/sec are not trustworthy without a new reliable calibration,

8. REFERENCES

Bouws, E., J.J. Ephraums, J.A. Ewing, P.E. Francis, H. Günther, P.A.E.M. Janssen, G.J. Komen, W. Rosenthal and W.J.P. de Voogt, 1985: A shallow water intercomparison of three numerical wave prediction models (SWIM). J. R. Met. Soc., 111, 1087-1112.

Cheney, R.E. and L.L. Miller, 1987: Sea level time series in the equatorial Pacific from the GEOSAT radar altimeter. Proceedings of IGARRS'87 Symposium, Ann Arbor, 18-21 May 1987.

Dobson, E., F. Monaldo, J. Goldhirsch and J. Wilkerson, 1987: Validation of GEOSAT altimeter-derived wind speeds and significant wave heights using buoy data. Johns Hopkins APL Technical Digest, Volume 8, No. 2, 222-233.

Haakansson, B., 1987: GEOSAT altimeter measurements of wind speed and wave height in the Baltic proper. SMHI remote sensing notes, No. 13.

Koch, W. and R. Ramseier, 1986: Comparison concept of satellite derived wind and wave data with ground truth. Proceedings of a Workshop on ERS-1 Wind and Wave Calibration, Schliersee, FRG, 2-6 June, 1986 (ESA SP-262).

Monaldo, F., 1988: Expected differences between buoy and radar altimeter estimates of wind speeds and significant wave height and their implications on buoy-altimeter comparisons. J. Geophys. Res., 93(C3),2285-2302.

Pickett, R.L., D.A. Burns and R.D. Broome, 1986: Ocean wind and

wave model comparisons with GEOSAT satellite data. Naval Ocean Research and Development Activity, Report 168.

Shuhy, J.L., M.R. Grunes, E.A. Uliana and L.W. Choy, 1987: Comparison of GEOSAT and ground-truth wind and wave observations: Preliminary results. Johns Hopkins APL Technical Digest, Volume 8, No. 2, 219-221.

ASSIMILATION OF SATELLITE WAVE HEIGHT DATA IN THE INITIALIZATION OF AN AES SPECTRAL OCEAN WAVE PREDICTION MODEL

R.Lalbeharry, M. L. Khandekar, and S. Peteherych
Atmospheric Environment Service (AES)
Downsview, Ontario, Canada

1.0 INTRODUCTION

Operational wave prediction, unlike numerical weather prediction, does not, in general, incorporate the measured wave data to generate the initial sea state, Instead, the initial sea state is derived by spinning up the model from a flat sea up to the forecast start time from some previous time using the observed wind field produced by the atmospheric model. The lack of adequate spatial and temporal distributions of wave data precluded the integration of wave data in wave models, but with the availability of significant wave height data from the GEOSAT satellite and the expected availability from the European Space Agency ERS-1 satellite, scheduled to be launched in 1990, within 3 hours of the satellite observation, there is a growing interest in the problem of assimilation of wave observations in wave models. The inclusion of wave data in ocean wave models is expected to create more accurate initial sea states with the hope of improving ocean wave nowcasting and forecasting given accurate forecast wind specification.

Atmospheric models generally use the model forecast field as their first guess field for correction using the observed field and an appropriate data assimilation technique. In an analogous manner, the hindcast initial wave height field at the start of model forecast run is considered to be the first guess height field which is then modified to introduce the wave observations into the model. The modified height field is then mapped into a two-dimensional (2-D) wave energy spectrum for input to the wave model. The main purpose of this study is to develop a suitable algorithm for integrating the wave data in the specification of the initial wave energy state and to examine the impact of such an assimilation with a view of establishing the general feasibility of using the wave data assimilation system in an operational environment.

2.0 MODEL

The wave model used in this study is the spectral ocean wave model developed by Resio (1981), hereafter referred to as the Resio model, consisting of 16 directional bands spaced at 22.5° intervals measured counter-clockwise from the east and 20 frequency bands from 0.03Hz to 0.22Hz in 0.01Hz increments. The Resio model is a coupled-discrete second generation wave model in which the non-linear wave-wave interaction term is used in a parameterized form. Resio develops a

functional relationship between the equilibrium constant (Phillips constant) and a non-dimensional fetch and obtains an expression for the non-linear source term which involves the square of the wind speed. Further, Resio neglects the linear growth term so that the net source term consists of the exponential growth term and the parameterized non-linear wave-wave interaction term. The model assumes that the waves are already present so that the wave-wave interaction term becomes operative and generates more waves. A local non-propagating parametric model with a moderately high frequency cut-off is incorporated so as to remove excess waves. The boundary between the parametric and the discrete spectral domains of the model is maintained at a fixed point and energy in each domain is conserved independently. More details of the model can be found in Resio (1981). in subsequent studies Resio (1982) has demonstrated the utility of his model for application in the Canadian Atlantic, while Penicka (1986) has amply demonstrated the sensitivity of the Resio model to wind specification. The Resio model is chosen because of its simplicity, minimal computational requirements, and its sensitivity to wind specification.

The Resio wave model uses a 26 x 24 specially design ,%d spherical orthogonal grid (SOG) with a grid spacing of 277.7 km (=2.5° latitude) in each direction. In this grid the axes are curvilinear, allowing east-west grid lines to follow great circle paths and each intersection of grid lines to be orthogonal. The winds are initially specified on a 2.5° latitude x 2.5° longitude grid and the gridded data are interpolated onto the SOG grid by bi-linear interpolation of the four latitude-longitude grid points surrounding each SOG point. Fig. 1 shows the latitude-longitude grid which lies in the area of the Northwest Atlantic ocean bounded by latitudes 30°N and 70°N and by longitudes 20°W and 70°W and the active region of the SOG grid at which winds are derived for input to the Resio model and at which wave parameters are calculated. The first guess wave height field is specified on the SOG grid and is modified by the satellite and buoy measured wave data using an appropriate interpolation scheme. The corrected wave height field is then converted into a 2-D wave energy spectrum to provide the initial sea conditions for a 48-hour wave forecast.

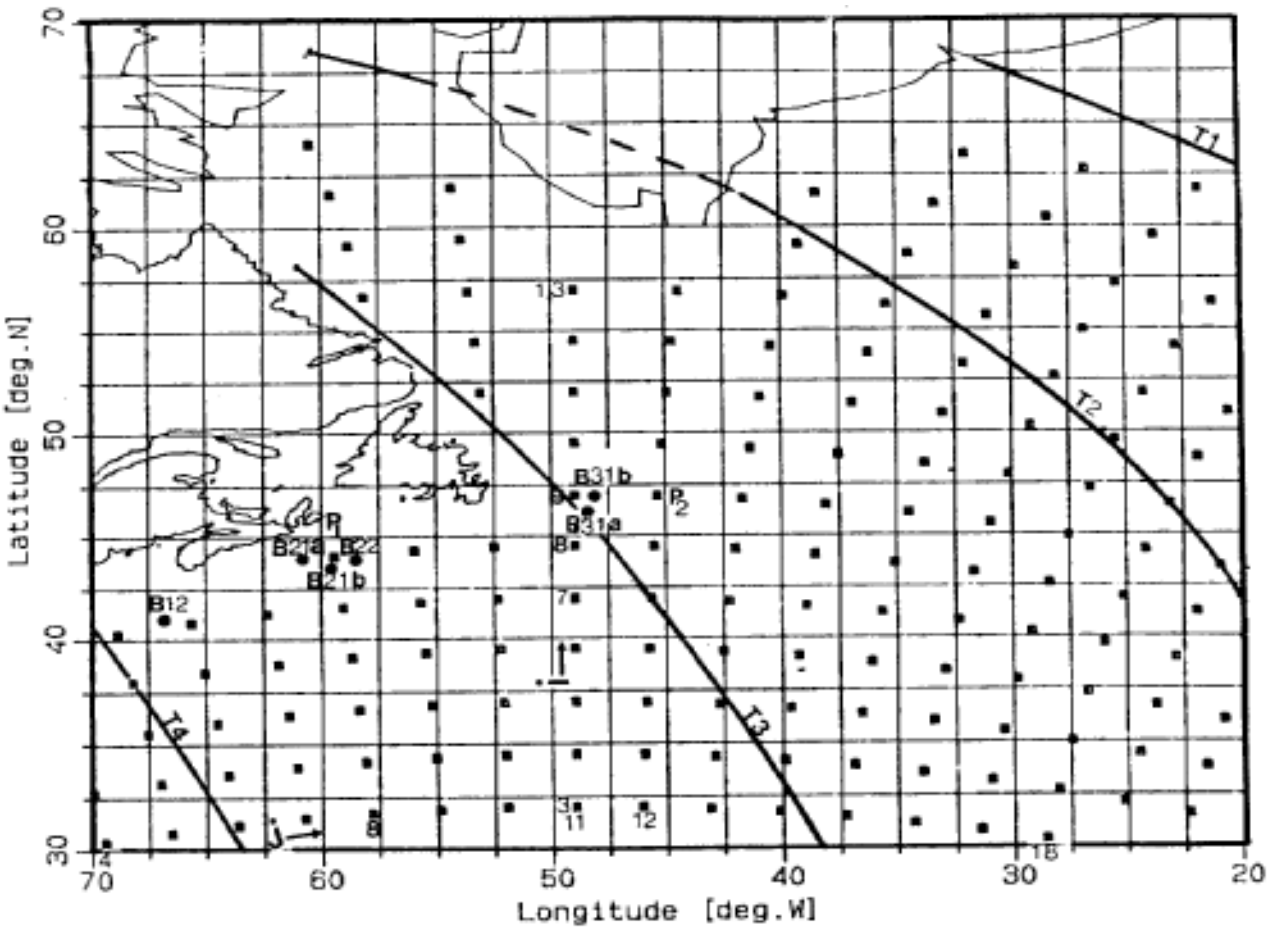

Fig.1: Latitude/longitude grid and the active region of the wave model SOG grid in which the letters "j" identify the column and "i" the row. The wind field at the SOG points (solid squares) are obtained from the wind field specified on the latitude/longitude grid, Buoy sites (solid circles) are identified by the letter "B" and typical GEOSAT satellite tracks marked TI-T4 are shown for the time window of ±3 hours centred at 06Z 16 February 1986.

3.0 WIND AND WAVE DATA

The data sets used in this study are for selected storm periods during the Canadian Atlantic Storms Programme (CASP) field project conducted during January - March 1986. These are:

(i) Operationally produced winds from the Canadian Meteorological Centre (CMC) weather prediction model. The winds are archived on magnetic tape and provided by MacLaren Plansearch (1987).

(ii) GEOSAT satellite and buoy significant wave height (SWH) data.

The CMC winds are given at the 0.998 sigma level which corresponds very closely to the 19.5 m level above the ocean surface. The winds are provided at each grid point on the latitude-longitude grid for

transformation onto the SOG grid every 6 hours from T-12 to T+48 hours where T is CMC model run time 00Z or 12z. No further modifications to the winds, such as stability corrections, are made. The T-12, T-6, and T+0 winds are analysed winds, while the T+6, T+12, ..., T+48 winds are forecast winds. However, the analysed winds at T-6 were not immediately available from the CMC model so that the T+6 prognostic wind field from the 12 hour previous run was substituted instead. The sequence of wind input to the wave model is at 6-hourly intervals corresponding to the regular synoptic weather analysis times. The model time step is 3 hours so that the winds at the intermediate hours are obtained from time interpolation internally in the wave model programme. The T-12 and T-6 winds are used to update the initial wave state with and without wave data assimilation, while the analysed winds at T+O and the forecast winds at T+6, T+12, ..., T+48 are used to drive the wave model in a prediction mode.

The GEOSAT satellite is equipped with a nadir-viewing active microwave radar altimeter operating at 13.5 GHz and emitting electromagnetic pulses at the rate of 1000 per second. The two geophysical parameters of wind speed and SWH are inferred from the altimeter measurements of the signal backscattered by the interacting ocean surface. The wind speed is related to the altimeter-derived normalized radar cross section which decreases as the wind speed increases. The SWH is estimated from the slope of the leading edge of the returned pulse front. wave heights have the effect of stretching out the returned pulse front so that the slope decreases as the wave height increases. The deduced wind speed and SWH are based on 1-second averages of the energy returned from as many as 1000 pulses.

All GEOSAT/buoy wave data in the time window of +3 hours centred at the synoptic map times of 00Z, 06Z, 12Z, and 18Z are considered to be synoptic and are utilized in the assimilation. In the Northwest Atlantic a maximum of up to 4 orbits may be available for inclusion at map time 06Z and occasionally 1 orbit at 18Z, while no orbits are available at 00Z and 12Z. As a result, the model forecast start time is T = 06Z so that in the forecast mode the T+00, T+06, ..., T+48 winds are the forecast winds based on CMC model run at the T-6 hour, while in the hindcast mode the T-06 and T-12 winds are the analysed winds used for updating the initial wave field. Fig.1 shows the locations of the buoy sites and the GEOSAT tracks around 06Z 16 February 1986 during one of the intense observing periods of the CASP experiment.

4.0 WAVE HEIGHT DATA ASSIMILATION SCHEME

The wave model provides the two dimensional wave height energy density, $F(f,\theta)$, at frequency, f, propagating in the direction, θ, at each grid point location at analysis and forecast times and can be expressed in the form

$$F(f,\theta) = S(f)\theta(\theta-\phi) \quad (1)$$

where S(f) is a frequency distribution function and θ is an angular spreading function centred on the local wind direction, ϕ. In discretized form $F(f,\theta)$ is given in frequency-direction bands, from which the wave parameters such as SWH, frequency of spectral peak, and mean wave direction are computed. In terms of the discrete spectrum the total wave energy (sea and swell) for all frequencies and directions is given by

$$E_T = \sum_{i=1}^{N} \sum_{j=1}^{M} F(f_i,\theta_j)\Delta\theta_j\Delta f_i \quad (2)$$

where the subscripts i and j denote respectively the ith and jth frequency and direction bands, N the number of frequency bands, and M the number of directional bands. $\Delta\theta$ is the directional bandwidth given by $2\pi/M$, Δf is the frequency bandwidth which may or may not be the same for each band, and $F(f_i,\theta_j)$ is given in units of $m^2/(rad\ Hz)$. An estimate of the model SWH, H, is obtained from the equation

$$H = 4.0\sqrt{E_T} \quad (3)$$

Wave models predict $F(f_i,\theta_j)$ at each grid point given the initial wave energy state and the forecast winds at the start of the model forecast run. The model generated SWH is then estimated using Eqs. (2) and (3).

Let the subscripts o, m, WS, SW, and T denote respectively the observed/measured, model generated, windsea, swell, and total value of a wave parameter and the subscript A a wave parameter with wave data assimilation. The assumption is made that the model has correctly estimated the ratio of swell energy to total energy. The measured windsea energy of a developing sea is then estimated from the equation:

$$E_{oWS} = E_{oT}(1 - E_{mSW}/E_{mT}) \quad (4)$$

In this formulation the ratio of the model swell energy to the model total energy $0 \le E_{mSW}/E_{mT} \le 1$ and is a more robust ratio than the ratio E_{mSW}/E_{mSW} used by Janssen et al. (1988). E_{oT} is the total measured wave energy obtained by inverting Eq.(3) using GEOSAT and buoy wave data. If E_{oT} is greater than the measured windsea energy, E_{oWS}, then the excess energy is assumed to be the measured swell energy, that is,

$$E_{oWS} = E_{oT} - E_{oWS} \quad (5)$$

From a knowledge of the measured and model generated swell and windsea energies, the windsea and swell scaling factors are given in Eq.(6).

$$C_{WS} = E_{oWS}/E_{mWS} \quad (6)$$

$C_{SW} = E_{oSW}/E_{mSW}$

The full model wave energy spectrum is partitioned into a windsea spectrum, $F_{WS}(f,\theta)$, and a swell spectrum, $F_{SW}(f,\theta)$ from the outset. If $E_{mWS} = 0$, $E_{mSW} = E_{mT}$ and C_{WS} is set to zero. From Eqs. (4) and (5) the measured windsea energy is zero and the measured swell energy is the measured total energy. If $E_{mSW} = 0$, $E_{mWS} = E_{mT}$ and C_{SW} is set to zero, the measured windsea energy is the measured total energy and the measured swell energy is zero. The scaling factor in both these cases becomes EoT/E_{mT}. When both windsea and swell energies are present, separate corrections are made. The spectral components of the windsea spectrum are corrected by multiplying by the factor CWS and those of the swell spectrum corrected by multiplying by factor C_{WS} and those of the swell spectrum by C_{SW}. The shapes of the windsea and swell spectra are preserved and the total modified wave energy, E_{AT}, is now equal to the total measured wave energy E_{oT}. An objective of this study is to modify the wave height field only without modifying the wind field and to assess the impact of the wave data on the wave model in a forecast mode during selected periods of the CASP experiment with a view of subsequent modification of the wind field. Correction of the wave field alone prior to the start of the forecast run may be interpreted as an implicit modification of the past wind field used for updating the initial wave field (see Hasselmann, 1988).

For the forecast run at 06Z 15 February 1986, the model is spun-up from a flat sea for 2 days to create an initial wave energy field called the "restart" field from which the SWH parameter is derived at the SOG grid points. When the restart energy field is not modified by the measured waves to specify the initial sea conditions, the forecast run is termed the "control" run, otherwise, it is termed the "assimilation" run. For a subsequent control run, the restart energy field is updated using the measured wind forcing in the period between the two consecutive model forecast runs.

In the assimilation run, the restart wave height field is designated the first guess field which is then modified by the measured waves using the successive correction method of Cressman (1959). The maximum radius of influence used is 2 grid units (1 grid unit m 277.7 km) and this is reduced to 1.0 for the second scan and to 0.5 for the third scan. Each wave height observation influences only the four grid points surrounding it in the 2nd and 3rd scans. The modified wave height field is termed the measured wave height field which is then mapped into a 2-D wave energy spectrum to provide the measured restart energy field. Grid points not modified by the observations assume values of the first guess wave field. For a subsequent assimilation run, the measured restart field is updated using the same wind forcing as in the control run and the updated field is then modified by the measured wave heights as described

above. Because of the availability of GEOSAT data mainly around 06Z in the area of study, insertion of the observed wave heights is performed only at the model forecast run time once every 24 hours. The preceding procedures are repeated when another period is selected for study.

In the approach of Esteva (1988), the combined swell and sea spectral component is scaled with the ratio E_{oT}/E_{mT} using SWH from the SEASAT altimeter. In the assimilation run, the initial wave height field is corrected using both a replacement technique and a blending technique. The insertion of the wave data is performed at different assimilation frequencies to produce a modified wave field for initializing a 72-hour forecast. The improvements in SWH forecasts are favourable but small. The latter can be partly ascribed to the inadequate global coverage of measured wave data and to the fact that the model is driven by analysed winds rather than forecast winds as in an operational environment. In the approaches of Thomas (1988) and Janssen et al. (1989) both the wind and wave fields are modified during the wave data assimilation cycle. The full wave spectrum is separated into the windsea spectrum and the swell spectrum from the outset. In the absence of any windsea spectrum the spectral components of the swell spectrum are scaled with the ratio E_{oT}/E_{mT}. When both sea and swell are present, the swell spectrum is inflated by the factor E_{oSW}/E_{msw}, while the modified windsea spectrum is constructed from the JONSWAP windsea spectrum. In the work of Thomas estimates of the measured windsea and swell energies are derived from the duration-limited wave growth curve of the model and the measured local wind speed. The JONSWAP windsea spectrum is then modified from a knowledge of these measured parameters. The updated 2-D spectrum is then derived given the wind direction. Janssen et al., on the other hand, obtain estimates of the measured windsea and swell energies from a knowledge of the measured wave height and the ratio of the model swell to windsea energies. Using an iterative procedure the wind field is corrected knowing the the measured windsea wave height and the model wave growth curve. As in Thomas, the JONSWAP windsea spectrum is used to construct a modified 2-D spectrum. The model is then run with the updated wind and wave fields to produce a new first guess wave field. The assimilation procedure is repeated every 6 hours for 24 hours to generate the resultant assimilated wave energy spectrum and an updated wind field consistent with the wave field at the start of the model forecast run. The model is initialized with the wave spectrum described above and is driven by the updated wind field at the start of forecast run and subsequently by the forecast winds. Hasselmann et al. (1988) describe a more comprehensive wind and wave data assimilation system for the ERS-1. However, as a first step in their study, only the wave field is modified, the wind field remains unchanged. The modified wave spectrum is formed by applying a

correction factor to the first guess wave spectrum from a knowledge of the measured wave heights.

5.0 RESULTS AND DISCUSSION

The results presented are based on the heuristic approach of applying correction factors to the windsea and swell spectra separately. The forecast wave heights are interpolated to the locations of the measured data and the wave errors statistics given in Eq.(7) are generated from the wave height differences, $\Delta H = H_{oi} - H_{mi}$ where H_{oi} is the measured height and H_{mi} the model forecast height at the ith observation location.

$$
\begin{aligned}
\text{BIAS} &= 1/N \sum_{i=1}^{N} \Delta H_i \\
\text{RELATIVE BIAS} &= 1/N \sum \Delta H_i / H_{oi} \\
\text{MAE} &= 1/N \sum |\Delta H_i| \\
\text{RMSE} &= [1/N \sum \Delta H_i^2]^{\frac{1}{2}} \\
\text{SI} &= \text{RMSE}/ \bar{H}_o
\end{aligned}
\qquad (7)
$$

where MAE is the mean absolute error, RMSE the root mean square error, SI the scatter index, $\bar{H}_o$, the mean observed wave height and N the total number of observations. The results of the validation of the model forecast wave heights with and without assimilation against the GEOSAT/buoy wave data are given in Tables 1 and 2 .

Table 1 shows comparisons of the wave error statistics for the control and assimilation runs for a 48-hour forecast commencing at 06Z on two consecutive days during the CASP storm period of 15-18 February 1986. The evaluation of the model forecast SWH is made against the measured SWH valid at 00, 12 (when observations are available), 24, and 48 hours from 06Z in each of the runs, utilizing all GEOSAT/buoy wave data within the time window of ±3 hours of 06Z. In the control run, the wave errors show some variability from one verification hour to the next and, in general, tend to degrade as the forecast hour increases. The negative bias implies that in the mean the model SWH is over-predicted, which may be partially due to the CMC wind themselves being over-estimated. For those forecast hours at which the negative bias has nearly the same magnitude as MAE, the model is mostly over-forecasting the SWH along the satellite tracks.

In the assimilation run, the nowcast or the 00-hour forecast SWH is in good agreement with the observed SWH as reflected in the mean

values and at this hour the statistics show significant improvement over the corresponding statistics in the control run. At other forecast hours the wave errors are generally lower than those in the control run and the mean forecast SWH is closer to the measured SWH. The extra information gained through assimilation is, however, lost in about 24 hours into the forecast as the wave errors tend to degrade in a progressive manner to those in the control run. The model still over-predicts the SWH but the biases are lower than those in the control run. This implies that the assimilation run forecast produces better results than the control run forecast. The wave errors for the 16th/06Z run suggest that as the initial wave field is updated and further modified by the observed waves, they degrade more slowly with time and the impact of the data assimilation is still realized after 24 hours into the forecast. The results in Table 2 for only the 16th/06Z run are similar to those in Table 1 when the model forecast SWH is also compared with the observed SWH along the individual satellite tracks denoted by T2 and T3 in Fig.1

Fig.2 gives the one-dimensional plots of the measured and forecast spectral energy densities for the forecast hour T+06 at 12Z 16 February 1986. The measured spectrum is from buoy site B21a with water depth of 40 metres and the forecast spectra in the control and assimilation runs correspond to the SOG grid point P_1(I=8,J=8) nearest to the buoy location. The peak energy in the measured spectrum is in closer agreement with that in the assimilation run spectrum rather than that in the control run spectrum although there is disagreement in the position of the peak frequency. The data assimilation used here modifies the magnitude of the spectral energy but the shape of the spectrum remains unchanged. The shape of the windsea spectrum may be changed through modification of the wind field and windsea energy.

Fig.3 shows plots of the 3-hourly measured SWH and wind speed at buoy site B31a and the 6-hourly forecast wind speed and SWH at the SOG grid point P_2(I=9, J=12) for the 16th/06Z 48-hour forecast run. The winds were mainly from the south-southwest and the SOG point chosen lies somewhat downstream from the buoy site and the GEOSAT track T3 shown in Fig.1 . The forecast peak wind speed is slightly larger than the observed peak wind speed, while the forecast peak SWH precedes the measured peak SWH by about 6 hours. The wave field is modified by the GEOSAT data along track T3 and the corrected wave field propagates towards the SOG point selected. The assimilation run forecast SWH shows improvement over that of the control run when compared with the observed SWH but gradually deteriorates to the control run SWH in about 24 hours into the forecast. In the initial stage of the forecast the extra information gained through wave data assimilation counteracts the effects of wind errors but after about 24 hours the

impact is lost and the wind errors become more dominant. Examination of other grid points and buoys indicates that the impact tends to deteriorate more rapidly when the non-corrected wave field from a region not modified by the measured waves propagates into the neighbouring corrected wave field regions.

Table 1: Daily comparison of control run and assimilation run forecast SWH error statistics valid at 00, 12 (when available), 24, and 48 hour from the wave model run time. The statistics are based on the GEOSAT/buoy observations along all the satellite tracks centred in the time window of ±3 hours at each of the forecast hours during the CASP storm period of 15-18 February 1986. H_o is the observed SWH, H_m the model forecast SWH at the H_o locations, N the total number of data points, and the wave height error $\Delta H = H_o - H_m$.

Run Date/ Time,T		Forecast Hour (T+) Control Run 00	12	24	48	Assimilation Run 00	12	24	48
15/06Z									
	RMSE(m)	1.68	1.69	1.76	1.54	0.31	1.38	1.76	1.50
	MAE(m)	1.35	1.37	1.45	1.34	0.22	1.12	1.36	1.30
	Bias(m)	-0.69	-1.28	-0.48	-1.12	0.00	-0.99	-0.33	-1.07
	Relative Bias	-0.20	-0.28	-0.22	-0.31	-0.00	-0.22	-0.20	-0.30
	SI(%)	43	32	35	33	8	26	35	32
	Mean H_o(m)	3.89	5.27	4.96	4.71	3.89	5.27	4.96	4.71
	Mean H_m(m)	4.58	6.55	5.44	5.83	3.89	6.26	5.29	5.79
	N	1199	480	1043	1256	1199	480	1043	1256
16/06Z									
	RMSE(m)	1.74		1.79	2.37	0.53		1.74	2.27
	MAE(m)	1.46		1.42	2.11	0.32		1.27	1.97
	Bias(m)	-0.32		-1.12	-2.11	-0.01		-0.83	-1.96
	Relative Bias	-0.19		-0.28	-0.52	-0.03		-0.21	-0.48
	SI(%)	35		38	56	11		37	54
	Mean H_o(m)	4.96		4.71	4.21	4.96		4.71	4.21
	Mean H_m(m)	5.28		5.83	6.32	4.96		5.55	6.18
	N								

Table 2: As in Table 1 but the statistics are based on the measured data along the individual satellite tracks denoted by T2 and T3 in Fig.1 and for the model forecast run date/time T at 06Z 16 February 1986.

Along Track		Forecast Hour (T+) Control Run 00	24	48	Assimilation Run 00	24	48
T2							
	RMSE(m)	2.06	0.90	2.60	0.47	0.67	2.48
	MAE	1.76	0.79	2.30	0.33	0.50	2.18
	Bias(m)	-0.50	-0.73	-2.29	+0.02	-0.25	-2.16
	Relative Bias	-0.21	-0.19	-0.52	-0.00	-0.08	-0.49
	SI(%)	33	19	55	7	15	53
	Mean H_o(m)	6.27	4.62	4.71	6.27	4.62	4.71
	Mean H_m(m)	6.77	5.34	7.01	6.25	4.87	6.87
	N	493	418	653	493	418	653
T3							
	RMSE(m)	1.35	1.82	2.54	0.66	1.78	2.54
	MAE(m)	1.18	1.49	2.40	0.32	1.37	2.40
	Bias(m)	-1.06	-0.94	-2.40	-0.01	-0.68	-2.40
	Relative Bias	-0.46	-0.21	-0.57	-0.07	-0.15	-0.57
	SI(%)	41	37	59	20	36	59
	Mean H_o(m)	3.31	4.90	4.29	3.32	4.90	4.29
	Mean H_m(m)	4.38	5.84	6.69	3.33	5.58	6.69
	N	331	627	272	331	627	272

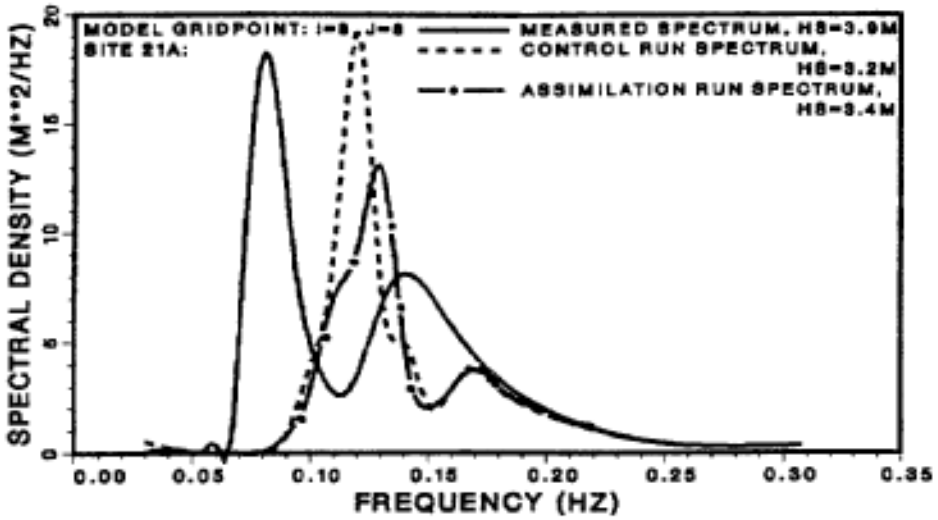

Fig.2: Measured and forecast spectra valid 12Z 16 February 1986. The solid curve is the measured spectrum obtained from buoy B21a. The predicted spectra are for the control run (dash-dotted curve) and the assimilation run (dashed curve) at the SOG grid point (I=8,J=8). HS = significant wave height.

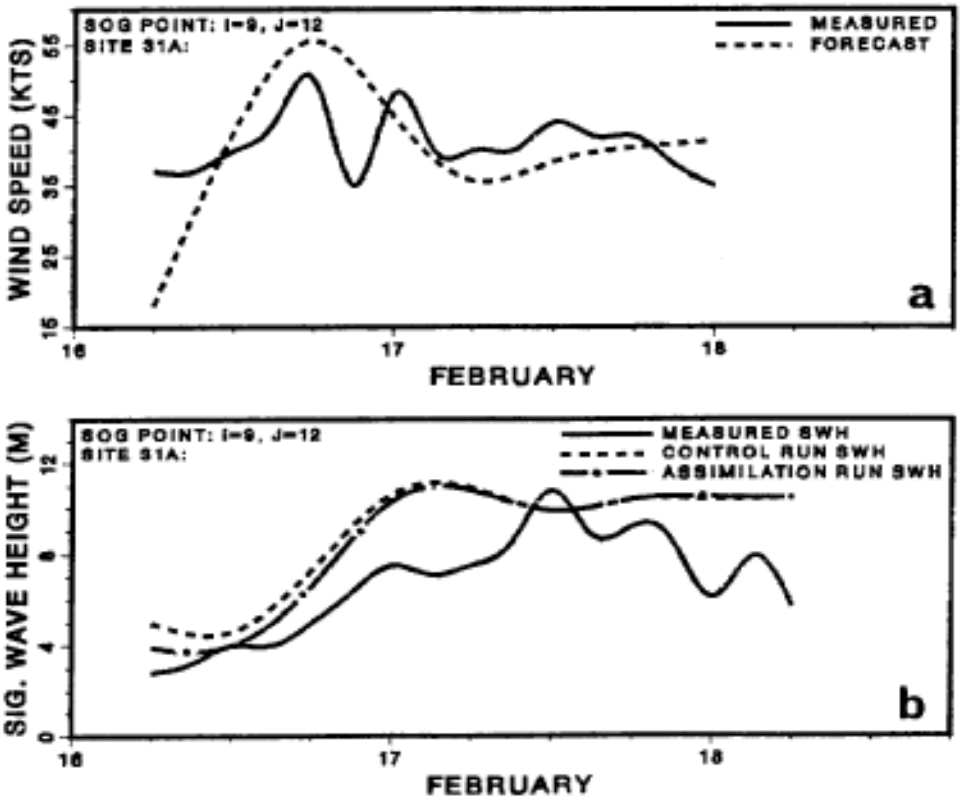

Fig.3: Measured and predicted wind speed and SWH for a 48-hour period beginning at 06Z 16 February 1986. The solid curves are measured values from buoy B31a. The dashed curve in Fig.3a is the forecast wind speed based on CMC model run at 00Z 16 February 1986. In Fig.3b the dashed curve is the assimilation run predicted SWH and the dashed-dotted curve the control run SWH at the SOG grid point (I=9,J=12).

6.0 CONCLUSIONS

The results presented here are preliminary. Although they are restricted to only one storm period during CASP, they do suggest that the incorporation of wave data alone to initialize a spectral wave model in a prediction mode does improve the forecast, in particular, the nowcast and the day one forecast. The extra information gained through data assimilation is lost after about 24 hours into the forecast as the wave forecast degrades to the forecast without data assimilation. The impact also tends to deteriorate more rapidly when the updated region gets contaminated with the non-corrected wave field propagating from an area not influenced by the measured waves. This implies that maximum benefit of wave data assimilation would be realized if the measured waves are allowed to influence the whole grid area. Better spatial and temporal coverages of wave data are, therefore, required for effective data assimilation in order to counteract the effects of the wind errors in at least the day one forecast.

7.0 REFERENCES

Cressman, G. P., 1959: An operational objective analysis system, Mon. Wea. Rev., 87, 367-374.

Esteva, D. C., 1988: Evaluation of preliminary experiments assimilating Seasat significant wave heights into a spectral wave model, J. Geophys. Res., 93, 14099-14105.

Hasselmann, K., S. Hasselmann, E. Bauer, C. Bruning, S. Lehner, H. Graber, and P. Lionello, 1988: Development of a satellite SAR image spectra and altimeter wave height data assimilation system for ERS-1, Max-Planc Institut Report No. 19, a Contract Study Report submitted to the European Space Agency.

MacLaren Plansearch Limited, 1987: Ocean wave models intercomparison study for the duration of the Canadian Atlantic Storms Program Field Project, Final Report submitted to MSRB, Atmospheric Environment Service, Downsview, Ontario, Canada.

Janssen, P., P. Lionello, M. Reistad, and A. Hollingsworth, 1989: Hindcasts and data assimilation studies with the WAM model during the Seasat period, J. Geophys. Res., 94, 973-993.

Penicka, F. X., 1986: Wave hindcast sensitivity, Proceedings of the International Workshop on wave Hindcasting and Forecasting, Halifax, Nova Scotia, September 23-26, 1986. Environmental Studies Revolving Funds, Report Series No. 065, Ottawa, 370pp.

Resio, D. T., 1981: Estimation of wind-wave generation in a discrete spectral model, J. Phys. Oceanogr., 11, 510-525.

------- 1982: An assessment of wave hindcast methodologies in the Scotian Shelf, Grand Banks, and Labrador Sea areas, Can. Contract Rep. Hydrogr. Ocean Sci. 4, 128pp (Available from Department of Fisheries and oceans, Canada).

Thomas, J., 1988: Retrieval of energy spectra from measured data for assimilation into a wave model, Q. J. R. Meteorol. Soc., 114, pp 781-800.

METEOROLOGICAL ASPECTS OF THE DERIVATION OF SURFACE WIND SPEEDS FROM SSM/I BRIGHTNESS TEMPERATURES

A.F. Davies and I.G. Rubinstein

Microwave Group
Institute For Space and Terrestrial Science
York University, North York, Ontario

ABSTRACT

The relevance of various meteorological parameters in the use of SSM/I brightness temperatures for the calculation of winds near the sea surface is discussed. Observational data from buoys, ships, radiosonde observations, and CMC surface and upper air analyses, are correlated with SSM/I brightness temperatures and derived parameters, such as the near sea surface winds. Geostrophic winds, features of frontal analysis from operational charts, the effects of stability, latitudinal variations, convective clouds, observed and derived types, and rates of precipitation, water vapour and cloud amounts are discussed as well as conclusions regarding the quality of the derived wind speeds, as demonstrated by their use in CMC modelling, and in driving wave forecast models.

INTRODUCTION

The use of passive microwave observations for the global monitoring of earth atmospheric (e.g. rain rate) and surface geophysical parameters (such as sea ice cover) dates back to 1972, when 19 GHz (horizontal polarization) data from a radiometer on Nimbus 5 became available. This data set (1972-1976) was supplemented with the measurements from the Scanning Multichannel Microwave Radiometer (SMMR) on SEASAT (June-August, 1978) and Nimbus 7 (October 1978 August 1987). The SMMR was a ten channel radiometer. The measurements of the earth microwave emission were made at five frequencies all having dual polarization. Since June 1987 data from the Special Scanning Microwave Imager (SSM/I) are being used by the scientific community.

Algorithms for the retrieval of the ocean surface wind speed and atmospheric parameters were developed for each one of the sensors. The first retrievals tried to utilize information from all the available channels. Since the resolution of the data is coarser for the larger wavelengths, our research was dedicated mainly to the use of the 37 GHz (0.81 cm wavelength), supplemented by 19 GHz measurements. This channel provided the highest resolution on SMMR. The SSM/I in addition to 19 and 37 GHz provided 85 GHz data. Since the algorithms developed and tested by us were used originally with the SMMR, retrieval parameters were modified, in order to accommodate SSM/I observations.

This paper concentrates on the understanding of the relationship between the measured microwave radiative intensities (Brightness

Temperatures) and the atmospheric and surface conditions at the time of the observations.

In Section 1 we introduce the reader to the physics of the microwave emission and interaction with the atmosphere. The latter sections will concentrate on case studies of various meteorological conditions. The data set from the January-March 1988 was principally used for this project, since during that period of time the weather centres across Canada received near real time wind speed values, derived from SSM/I 37 GHz measurements. The wind speed information was supplemented with colour images of cloud cover, precipitation and water vapour amounts, all estimated from the data set used for the wind speeds. The 19 GHz vertical channel was used to flag the onset of precipitation and for the calculations of the water vapour.

The analysis of the relationships between the observed brightness temperatures and the meteorological conditions space/time coincident with the satellite overpass are used to improve the retrieval of ocean surface and atmospheric parameters. Identification of the onset of precipitation (rain) is a very crucial factor, since parameters used in the algorithms are replaced by a different set, to account for different interacting processes.

1. THEORY

In the absence of scattering, the radiative intensity of the microwave radiation of the earth-atmosphere system (brightness temperature), sensed by a spaceborne sensor can be expressed as:

$$T_B(z,O) = T_{B1}(z,O) + [ET_s + (1-E)T_{B2}]e^{-c}$$

where z is the height of the satellite, E is the effective emissivity, c is the total opacity of the atmosphere along the line of sight and T_s is the surface temperature. The quantities T_{B1} and T_{B2} are, proportional to the upward emission and the downward emission from the atmosphere plus attenuated sky background radiation.

The emissivity of any surface depends on the surface dielectric properties. Water has a large dielectric constant at microwave frequencies. This results in a low emissivity (large reflectivity) for open ocean surfaces. In the absence of the atmosphere the brightness temperature of a surface is a product of its emissivity and the surface physical temperature. Most solid surfaces such as land and some types of sea ice have emissivities in the range of 0.8 to 0.98. The emissivity of the ocean is approximately 0.5, therefore there is a strong contrast between the measurements from the ocean and land or ice covered sea. The low emissivity of the ice free ocean provides good background for monitoring of atmospheric changes.

The emissivity of a calm water surface was calculated by Klein and Swift (1977) and Stogryn (1967) using the dielectric constant of the

water and the Fresnel equations. When the water surface is roughened by wind, its emission and scattering of the microwave radiation becomes more complex. Above certain wind speeds, foam patches are generated on the surface, altering the dielectric properties and therefore the emissivity of the ocean surface. In addition the action of the wind generates capillary waves on the surface, resulting in the roughness of the microwave wavelength scale. Theoretical models of the ocean surface changes induced by wind have to be used in interpreting the spaceborne measurements in terms of the surface wind speeds. Figures 1a and 1b illustrate results of the model (Wentz, 1983) used by the authors in the retrieval algorithms.

This paper concentrates on establishing empirical relationships between the spaceborne measured brightness temperature and the meteorological parameters used by the weather forecasters. The retrieval algorithms were developed using the theoretical and empirical analysis of the changes in the observed brightness temperature.

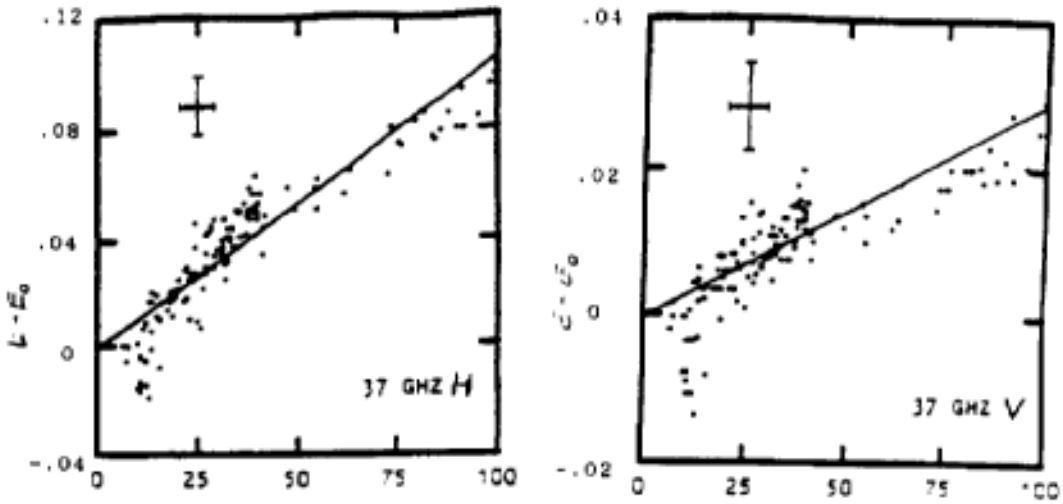

Figure 1a. Figure 1b.

The wind-induced change in sea surface emissivity $E-E_o$. E_o is the calm ocean, clear sky emissivity. (After Wentz, 1983)

The radiance measured by a satellite-borne radiometer is a sum of the attenuated surface emission and the contribution from the atmosphere. The atmospheric influence is partly calculated and partly observed, As a first guess some typical values, obtained from a radiative transfer equations, are used as the input parameters. For the frequencies used in the analysis, water vapour and rain are the main sources of the attenuation. The attenuation of the atmospheric slab is related to its emission, therefore, knowing the attenuation one can determine the brightness temperature of the atmosphere and an estimation of the water vapour and liquid water content. The calculated values for the

atmospheric contribution to the observed radiance at 19 and 37 GHz are used to estimate the total amount of water vapour and liquid water in the atmospheric column. These calculations as well as the estimation of the rain rates are determined by the sensitivities of the frequencies to the changes in the atmospheric conditions. Although algorithms for the evaluation of the ocean surface and the meteorological conditions have been developed, detailed analysis of the changes in the observed brightness temperatures as a function of the changes in the atmospheric condition would increase the reliability of the retrievals, since results Of Such research will be reflected in changes to the algorithms. The theory and experimental results of the microwave interactions with the atmosphere can be found in several good text books. "Microwave Remote Sensing" by Ullaby et. al. (1986) is highly recommended.

2. EMPIRICAL RELATIONSHIPS

2.1 Air Masses and Fronts

The analysis of fronts and their associated air masses is crucial to understand meteorological phenomena, While there is rarely any doubt about their existence, the scarcity of conventional data makes it difficult to place them exactly. SSM/I brightness temperatures can supplement satellite cloud imagery in assisting this function.

In two situations in March, 1988, the relationships of SSM/I brightness temperatures to air masses and fronts were studied. Three hundred observations from orbit 3619, March 2, 1988, 0900Z, were extracted which bracketed and crossed the Arctic cold front. This cold front ran southeastward from a 1000 mb low pressure centre just northeast of Sydney, Nova Scotia (Figs. 2c and 2d).

Similarly, 500 observations from orbit 3842, March 18, 1988, were derived which crossed the Maritime front near a 995 mb low centre located 1200 km West-southwest of Vancouver (Fig. 2b).

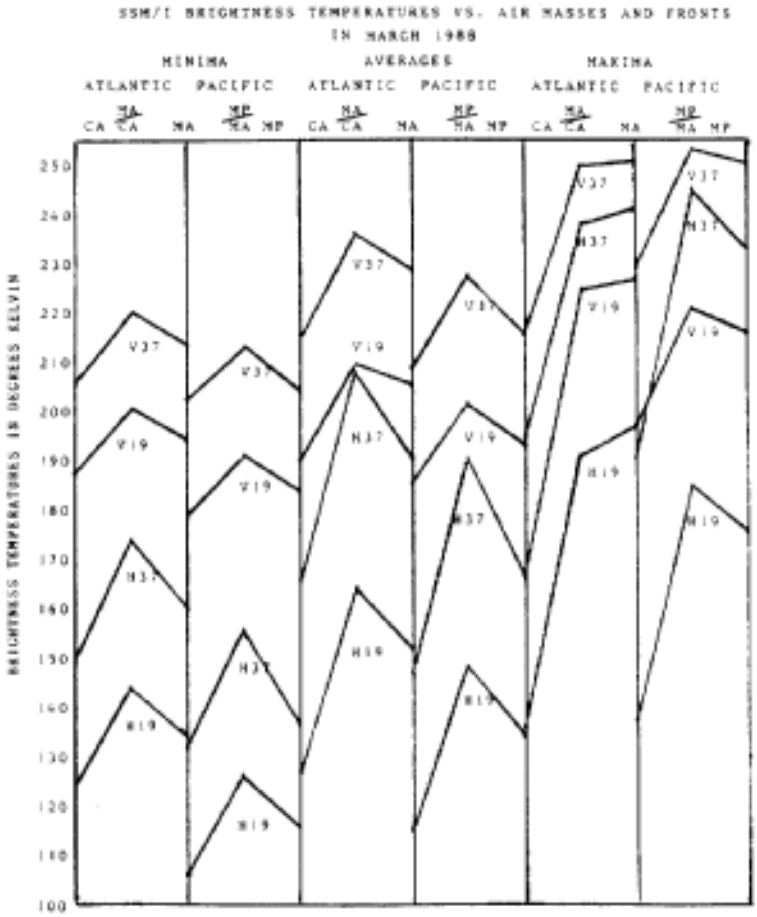

Figure 2a.

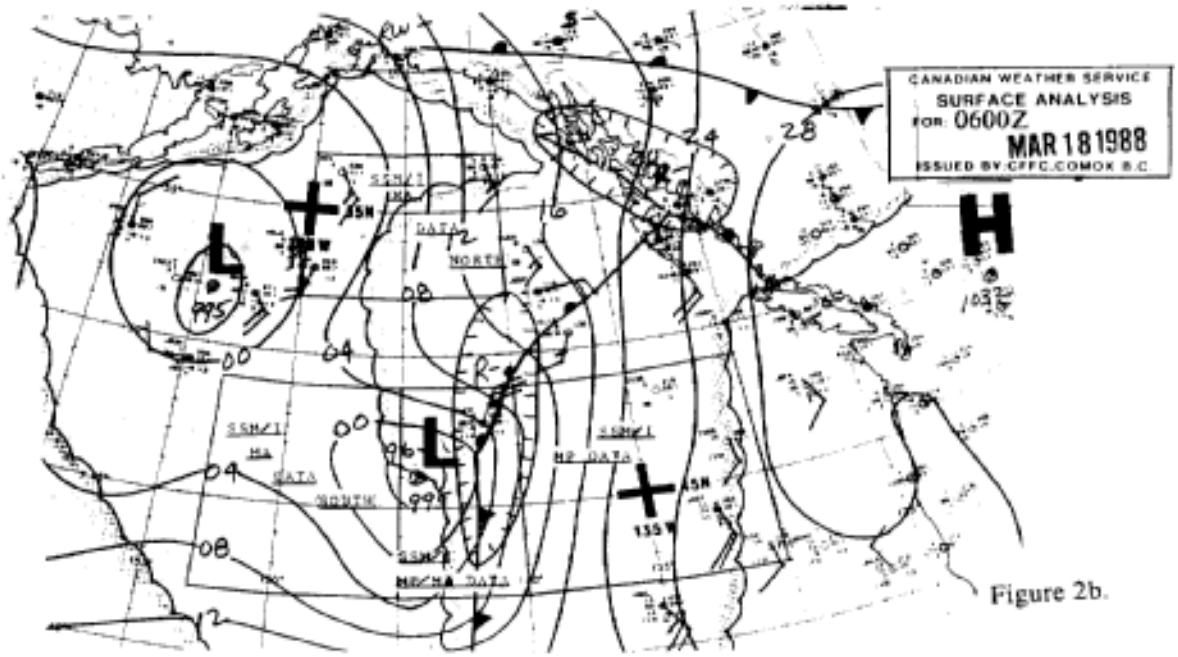

Figure 2b.

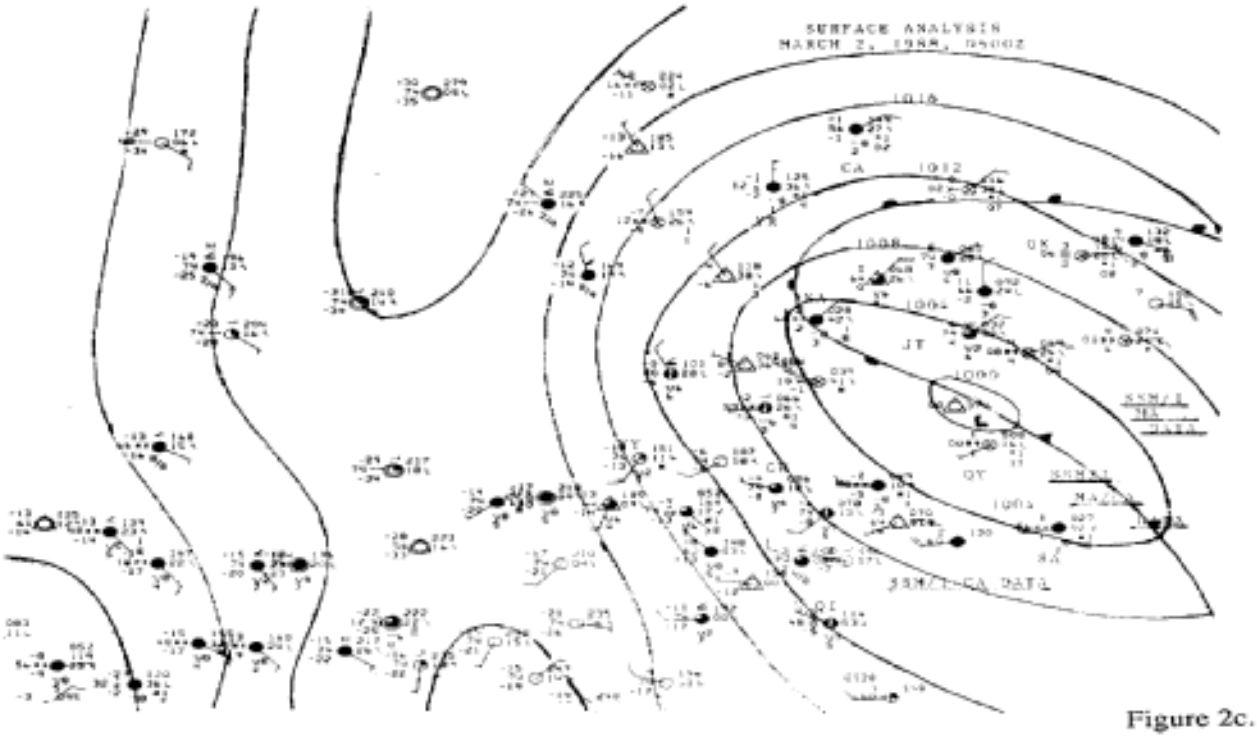

Figure 2c.

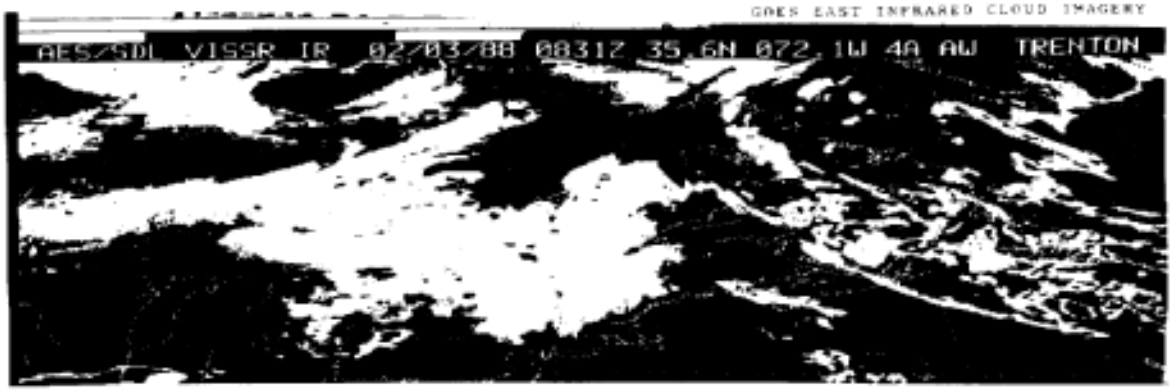

Figure 2d.

Statistical Analysis Results

The results of the statistical analysis may be summarized as follows:

Minimum and average values of the four brightness temperatures, H19, V19, H37 and V37, and with one exception the maximum values also, invariably demonstrated the following characteristics:

- brightness temperatures are higher at the fronts than in the air masses on either side. For minimum values, the excess ranges from 6 to 45 degrees, and, for maximum values, it ranges from 4 to 89 degrees Kelvin greater than on either side. The only exception is that for the Arctic front. The brightness temperatures in the Maritime Arctic air are the same, or a little higher than at the front.

- V37 minimum, average, and maximum values each exceed the same measures of V19 by 19 to 33 degrees Kelvin.

- H37 minimum, average, and maximum values each exceed the same measures of H19 by 25 to 60 degrees Kelvin.

- the standard deviations and ranges for the horizontally polarized brightness temperatures are almost always exactly twice the same measures for the vertically polarized brightness temperatures.

- the warmer valued air masses in the Pacific example each have 19 GHz values of these statistics which are 5 to 20 degrees lower than for the colder Atlantic air masses.

- the same is true for the 37 GHz statistics, except for the frontal maximum values, where the Pacific values are a few degrees higher than the Atlantic values (Fig. 2a).

Practical Implications

Any plotted single SSM/I brightness temperature will identify frontal locations by relative maxima elongated along the frontal position. Since H37 always has the most pronounced relative maximum, it is the preferred choice for this purpose.

The fact that the difference between V37 and V19 values is so consistently in the range of 20 to 33 degrees Kelvin supports the use of these two brightness temperatures in the current operational algorithm.

Where a single general algorithm is used to derive surface wind speeds from the brightness temperatures, frontal positions will coincide with relative maxima in the plotted speeds.

The peaking of the brightness temperatures at the frontal positions is not due to the actual surface winds (which normally are maximum ahead of the front and behind it, but fall to a minimum at the front itself), but is rather due to the concentration of water vapour, liquid water, and heavy precipitation along the fronts. This concentration is in turn due to the ascent maximum produced by low level convergence, lift along the frontal surface, latent heat release, mid-level positive vorticity advection, high level divergence and the tilting and twisting forcing functions which are maximized in cumulonimbus clouds.

The actual surface wind speeds at the frontal location can be derived from those generated by a generalized algorithm, by subtracting a quantity proportional to the brightness temperature excess at the front, for example,

BT(front) – 0.5 [BT(cold air) + BT(warm air)]

This particular approximation reduces H19 and H37 by 15%, and V19 and V37 by 6%, at both the Maritime and Arctic fronts.

The fact that the brightness temperatures in the warmer air masses over the Pacific are lower than those for the colder Atlantic air masses may, with some caution, be attributed to greater attenuation due to higher water vapour content. However, other factors, such as more stable low level temperature lapse rates in the generally southerly flow over the Pacific, than for the unstable flow of cold air over the east coast Gulf stream, would also have to be considered.

2.2 RELATIONSHIPS BETWEEN AIR/SEA INTERFACE AND OTHER METEOROLOGICAL PHENOMENA VERSUS BRIGHTNESS TEMPERATURES

When a single brightness temperature is regressed against a single meteorological parameter, the typical correlation coefficient is about 0.6 to 0.7, so that about 36% to 49% of the variance in the brightness temperature, (or in the meteorological parameter) is explained. The reason for this, as indicated in the theoretical section, is that each brightness temperature is actually a multivariate function of a number of air-sea interface, boundary layer, and free atmospheric variables.

The objective of the particular experiment in this part of the report was to determine which of these influences could be derived by correlating brightness temperatures to conventional operational data such as buoy, ship, and nearby land station reports, and - from cloud imagery, radiosonde data, and CMC surface, 850, 700 and 500 mb analyses.

A 5-day series of simultaneous observations by BUOY M46001 (located at 56N 148W in the Gulf of Alaska), and 7 SSM/I brightness temperatures, provides an illustration of typical relationships between brightness temperatures and various air/sea interface and other meteorological factors.

The Meteorological Situation July 9-13, 1987

During this period, a series of low pressure centres, with central pressures near 1010 mb, moved northeastward towards the Alaskan panhandle, passing about 300 km to the southeast of the buoy. As each low passed, a weak high pressure centre or ridge re-established itself over the buoy. Consequently, there were several cycles from rain to no rain. At 500 mb (about 5600 M) there was a trough of low heights oriented from west to east, just north of the buoy. One 500 mb low centre passed by the buoy on the 11th and another much deeper low approached from the southwest to lie directly over the buoy at the end of the period (Figs. 3a and 3b).

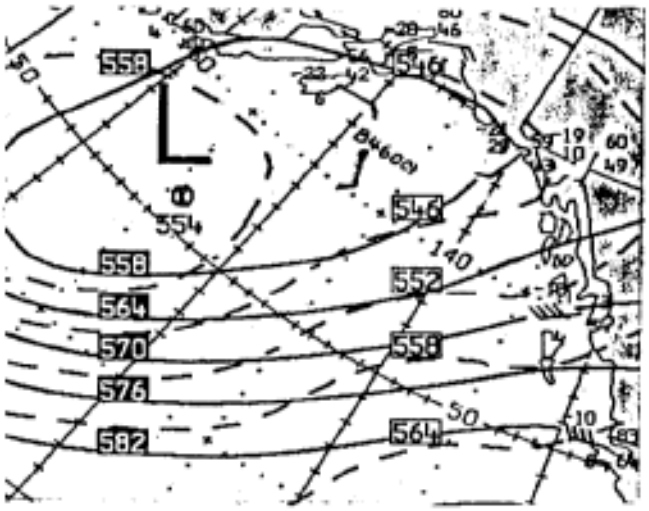

CMC CANADA CWAO 3201
ANAL 500MB/ARCHIVES
VOOZ MON/LUN 87/07/13 05•42

Figure 3a.

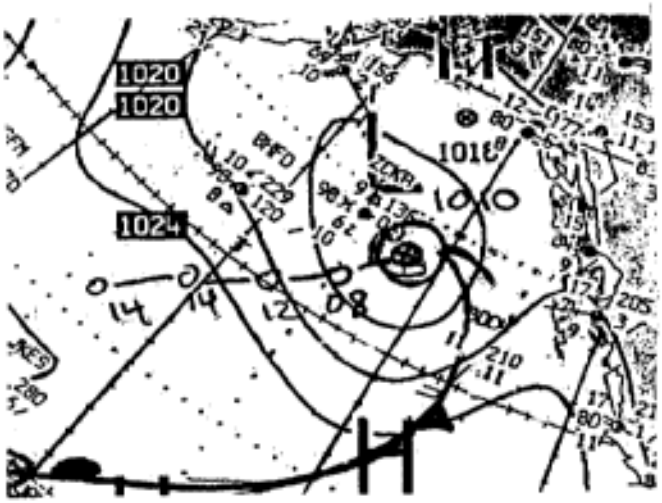

CMC CANADA S81
ANAL SURFACE
VOOZ MON/LUN 87/07/13

Figure 3b.

Relations Between Meteorological Parameters and BT's

About thirty such parameters were regressed against the seven brightness temperatures, V19, H19, V22, V37, H37, V85 and H85, taken singly and then as a group, and the COEFFICIENTS OF DETERMINATION calculated.

In the single regressions, the coefficient of determination is the squared correlation coefficient. For example, a correlation coefficient of 0.8 gives an R-squared value of 0.64. In the multiple regressions, the most conservative measure, namely R-squared (adjusted for degrees of freedom) was used. This is usually about 0.1 to 0.2 less than the original unadjusted figure, but is favoured by most statistical analysts.

SUMMARY OF RESULTS

R-Squared Adjusted Values 0.81 to 0.95

This category included:
(a) rain rate, attributed to Convective development,
(b) total rain rate, and
(c) ascent rates corresponding to a and b.

Corresponding R-Squared For Regressions vs Single BT's

H19 was best, with R-squared from 0.73 to 0.84
V22 was slightly lower at 0.69 to 0.80
H37, V37, and H85 followed with values of 0.44 to 0.67

V85 was lowest at 0.26 to 0.29

Rain rates at the buoy, at the time of the SSM/I observations were determined by interpolation within isopleths of rain rate determined from: 1) rain rates at adjacent low lying land stations; 2) precipitation intensities at nearby ships; 3) satellite cloud imagery; 4) low level stability from buoy air and sea temperatures; 5) calculated mid-tropospheric stability indices; and 6) CMC surface and upper air charts. Ascent rates were then determined from the rain rates and precipitable water calculated from radiosondes, isoplethed and interpolated. Some of the brightness temperatures had good R-squared values when singly regressed against a given brightness temperature, however, in all cases the use of multivariate relationships produced better results, even though the additional brightness temperatures had singly explained relatively low percentages of the variance in the meteorological parameters.

R-Squared Adjusted Values 0.64 to 0.80

This category included:

(a) buoy surface wind speeds,
(b) lifted Convective Index, surface to 500 mb,
(c) Showalter Convective Index, 850 mb to 500 mb,
(d) geostrophic wind speed,
(e) rain rate attributed to Altostratus,
(f) mid-tropospheric ascent calculated from e,

Corresponding R-Squared Values for Single BT's:

H19 was best at 0.41, the H37 at 0.33, H85 at 0.28, V19 at 0.22
V85 was lowest at 0. 16, for Surface Wind Speed

For the other parameters listed above, V22 was best with R-squared values from 0.47 to 0.57. H19 and V19 were slightly lower at 0.37 to 0.50.

These figures illustrate the advantage of using multivariate relationships when correlations between single meteorological parameters and single brightness temperatures are around 0.60 to 0.75 (R-squared = 0.36 to 0.56). Since the brightness temperatures all have different means, while the horizontally and vertically polarized brightness temperatures have very different variances, by combining them 64% to 80% of the variances in the meteorological variables can be explained. This explains the success of the algorithms to derive surface wind speeds and rain rates, etc. The algorithms use at least three brightness temperatures, both horizontally and vertically polarized.

R-Squared (Adjusted) Values 0.49 to 0.63

Buoy air temperatures, wave periods, and fourier maximum amplitude figures fell into this category. The V22 frequencies channel provided the best brightness temperatures, for wave period and the FMXA, with R-squared values of 0.27 to 0.47, while V37, H37 and V19 performed best for air temperatures with R-squared values of 0.20 to 0.26.

These three parameters were given directly by the buoy observations. There is still a definite advantage to using multivariate relationships since they double the amount of variance in the meteorological parameters which is explained by the relationships.

R-Squared (Adjusted) Values of 0.36 to 0.48

Liquid Water, Low Level Stability (Air Temperature-Sea Temperature), and Sea Temperature fell into this category. The V85 was the best single brightness temperature for Liquid Water, with R-squared = 0.30, while V22 performed best for Low Level Stability with 0.45. None of the single brightness temperatures gave an appreciable explanation of the variance in the Sea Temperature.

Total water vapour was an interesting case. The best R-squared value with a single brightness temperature was 0.34 for V37. Although all the other BT's produced values of 0.21 (H19) to 0.29(H85), the multivariate relationship with all seven BT's gave only 0.31. However, V19 and V37 resulted in 0.35, and all the vertically polarized brightness temperatures together gave, as would be expected from the physics, the best result of 0.38. Incidentally, some statisticians feel that the unadjusted R-squared is a better measure, and this gives 0.47 for the vertically polarized BT's, equivalent to a correlation coefficient of 0.69, so the derivation of water vapour from brightness temperatures is certainly viable.

These parameters are in a category where it is not always an advantage to use relationships based on all seven available channels. For example, V22 performs better for Low Level Stability, than the multivariate relationship with all seven channels. On the other hand, the sea surface temperature does benefit from the use of all of the brightness temperatures, as indicated by the R-squared (adjusted) value of 0.36.

R-Squared (Adjusted) Less Than 0.36

In this relatively low surface wind speed data set, the coefficient of determination for multivariate relationships was less than 0.36 for the following meteorological parameters:

Rain rate by extrapolation from an upstream land station, mean sea level pressure, pressure tendency, 500 mb wind direction, position of SSM/I pixel relative to the buoy, thickness from 1000 to 500 mb, 500

mb height, surface air temperature-500 mb temperature, 500 mb windspeed, sea temperature-500 mb dewpoint, 500 mb dewpoint, and 500 mb dewpoint depression.

For the meteorological and air/sea interface parameters in this category, in ten cases the use of the multivariate relationship with all seven channels gave a lower R-squared value than with the single best channel.

General Inference From this July 9-13. 1987 Study

While from a statistical analysis viewpoint it may be expected that multivariate relationships are preferable to simple regressions, optimum results require that the selection of the channels in the relationship is based on the theory of the physics of microwave interaction with the atmosphere, as has been done in the currently used algorithm.

2.3 LATITUDINAL VARIATIONS

Most meteorological parameters vary with latitude, for example the Coriolis force explicitly is a function of latitude (Holton, 1972), and many other meteorological variables contain the Coriolis parameter, explicitly or implicitly. A search through 12000 SSM/I observations on various dates in March, 1988, over the Atlantic, led to the suggestion that the brightness temperatures should be normalized for latitude. In another experiment, it was found that using this principle enabled the use of relationships, derived for Buoy M46001 in the Gulf of Alaska, to be applied to data from Buoy M44004 off the coast of New England. So, in the March 18, 1988, case already described in Section 2.1 , a comparison between two blocks of SSM/I data, centred at 45N and 55N, was made. There was no significant differences in minima and maxima in these two areas, both in Maritime Arctic air, but as was the case in Section 2.1 , maxima were about 20 degrees Kelvin higher at the southern latitudes. This appears to be related to heavier convective development with heavier precipitation at lower latitudes. Further study is needed.

2.4 SSM/I DERIVED WIND SPEEDS IN CMC MODELLING

In a recent report (Ramseier, et al., 1988) it was concluded by CMC researchers that these winds supported the conventional data in the analysis process, added small scale information, and showed potential in capturing developing low pressure system in data sparse areas. Several analyses and prognoses shown there illustrate these benefits.

3. REFERENCES

Anderson, J., 1988: Storm Flight, Chinook, 10(3), 44-50.

Holton, J.R., 1972: An Introduction to Dynamic Meteorology, Academic Press, 1-119

Klein, L.A., and Swift, C.T., 1977: An Improved Model for the Dielectric Constant of Sea Water at Microwave Frequencies, IEEE Trans. Antennas Propag., AP-25, 4965-4980.

Ramseier, R.O., Rubinstein, I.G., and Davies, A.F., 1988: Canadian Meteorological Centre Report, Operational Evaluation of Special Sensor Microwave/Imager by the Atmospheric Environment Service, AP-9.3.

Stogryn, A., 1967: The Apparent Temperature of the Sea at Microwave Frequencies, IEEE Trans. Antennas Propag., AP-15, 278-286.

Ullaby, F.T., Moore, R.K., and Fung, A.K., 1986: Microwave Remote Sensing, Vols. I,II,III, Artech House, Inc.

Wentz, F. J, (1983), Model Function for Ocean Microwave Brightness Temperatures, J. Geophys. Res., 88, pp. 1892-1908

AN OPERATIONAL EVALUATION OF SPECIAL SENSOR MICROWAVE/IMAGER (SSM/I) DATA FROM THE DMSP SATELLITE

E.M. Loder

Maritimes Weather Centre
Atmospheric Environment Service
Bedford, Nova Scotia

1. INTRODUCTION

As part of the overall AES evaluation of the passive microwave data from the U.S. DSMP (Defence Meteorological Satellite Program) satellite, the Maritimes Weather Centre (MWC) did a subjective evaluation of the SSM/I (Special Sensor Microwave/ Imager) surface wind speed data.

During the period from January 21 to March 31, 1988, the MWC received SSM/I-derived surface wind speed data in the form of 1:7.5 M scale facsimile charts from the Canadian Meteorological Centre (CMC). These charts were received approximately 7 to 9 hours after data time. Approximately 10 days later, colour charts of wind speed, rain rate, cloud cover and water vapour, corresponding to the facsimile charts, were received by mail.

The MWC's objectives were to conduct:

1) a comparison of the SSM/I wind speed data with the actual wind field as analyzed in real-time at the MWC;

2) a study of the possible improvement in MWC analyses and forecasts should the SSM/I data be available in real-time.

2. BACKGROUND

The SSM/I is one instrument on board a U.S. DMSP satellite launched in 1987. The SSM/I radiometer receives microwave emissions from the earth's surface and from the intervening atmosphere (PhD, 1987 and NOAA, 1987). Empirical and physical algorithms have been derived which relate the microwave radiation to various meteorological parameters including surface wind speed, rain rate, cloud cover and water vapour over water. In the case of surface wind speed, the challenge is to reduce contamination by atmospheric moisture, as the microwave emissions from the ocean surface are partially screened by the emissions from the water vapour in the atmosphere.

The microwave emissions from the ocean surface increase with the increase in capillary wave action which come about from an increase in wind. The surface wind data derived from the SSM/I are representative of the winds at approximately 1 metre above the surface. The surface

wind which forecasters deal with is the wind at 10 metres above the surface. It is important to recognize this difference in level when assessing the SSM/I wind data as the difference between a 1-m wind and a 10-m wind can be as large as 40 percent. For this evaluation, conversion factors derived by Smith (1981) have been used to adjust the 1-m winds to the 10-m level.

3. EVALUATION APPROACH

The MWC evaluation was mainly a subjective one, in which a comparison of SSM/I wind speed data and the surface wind field as derived from synoptic information (ship reports and surface pressure analyses) was made. The verifying data were studied not only in an effort to compare numbers, but to locate patterns in the SSM/I data which might be potentially useful to an operational forecaster were the data available in real-time. The evaluation considered not only the SSM/I wind speed data but also the precipitation and water vapour information, particularly in terms of the patterns they portrayed.

4. RESULTS

The evaluation results will be presented in three parts. The first part will deal with characteristic over-estimated and under-estimated wind field patterns which were identified. The second part will provide a more detailed comparison which was conducted for Sable Island, the most reliable marine reporting site in our region. Finally, the third part will evaluate the-utility of the SSM/I wind and rain data for locating and identifying synoptic features such as fronts, troughs, strong pressure gradients and areas of organized precipitation.

4.1 SSM/I Wind Characteristics

a) Over-estimated Winds Associated with Rain

In those situations where precipitation was present (as defined by the SSM/I data) it was found that:

- wind speeds were <u>always</u> over-estimated

- there was considerable variability in the ratio of SSM/I wind to actual wind. There was no apparent correlation between the ratio and the speeds being observed (i.e. the ratio was variable in all speed ranges) thus no simple correction factor could be applied to the SSM/I wind to arrive at the actual wind.

- no significant improvement was noted in the over-estimating bias when the wind speed algorithm was changed on March 1.

Table 1 provides some examples of the variability:

DATE	LOCATION	WIND (m s^{-1}) SSM/I (1 m)	ACTUAL
Jan 23 1000Z	41°N 51°W	25	10
Feb 02 2300Z	42°N 68°W	25-30	<10
Feb 03 0900Z	41°N 66°W to 45°N 55°W	25-30	10-13
Feb 06 0900Z	41°N 66°W	20-25	8-13
Feb 10 2200Z	41°N 53°W	20-25	10-15
Feb 29 1000Z	40°N 62°W to 44°N 62°W	20-30	5-10
Mar 01 0900Z	42°N 61°W	15-20	10-15
Mar 05 1000Z	45°N 59°W	20-25	10-15
Mar 13 2200Z	43°N 62°W	20-25	5-10

Table 1: Comparison of SSM/I winds vs. actual winds, showing variability of the overestimation associated with rain.

b) Over-estimated Winds Not Associated with Rain

In those situations where precipitation was not present but cloud amounts and water vapour values were high (as defined by the SSM/I data) it was found that:

- wind speeds were <u>usually</u> over-estimated

- the degree to which the winds were over-estimated was not as great as in the precipitation cases.

Table 2 provides some examples.

DATE	LOCATION	WIND (m s^{-1}) SSM/I	ACTUAL
Jan 27 0900Z	41°N 60°W	20-25	15-20
Jan 30 2300Z	44°N 62°W	15-20	13-18
Feb 15 2200Z	43°N 68°W	15-20	10-15
Feb 21 2200Z	42°N 52°W	20-25	8-13
Feb 26 2200Z	42°N 57°W	25-30	20-25

Table 2: Comparison of SSM/I winds vs. actual winds, showing over-estimation in non-rain situations.

c) Under-estimated Winds

In those situations where precipitation was not present and water vapour values were relatively low (as defined by the SSM/I data) it was found that:

- wind speeds were generally under-estimated but the errors were much lower than errors associated with the over-estimations associated with rain.

- by correcting the SSM/I winds to the 10-m level, much of the under-estimating bias is removed.

Table 3 provides some examples.

DATE	LOCATION	WIND (m s^{-1}) SSM/I (1 m)	SSM/I (10 m)	ACTUAL
Jan 26 2200Z	45°N 57°W	<15	<20	18-23
Jan 29 2300Z	43°N 63°W	<5	<8	5-8
Jan 30 0900Z	41°N 53°W	10-15	13-18	15+
Feb 16 2200Z	42°N 67°W	8-13	10-18	13-20
Feb 17 2200Z	43°N 58°W	10-15	15-20	15-20
Feb 22 1000Z	45°N 58°W	10-15	13-18	15-20

Table 3: Comparison of SSM/I winds vs. actual winds, showing under-estimation in low water vapour situations.

4.2 Sable Island Comparisons

The following table provides a sample of SSM/I winds compared to the reports from the AES observing site on Sable Island. The "raw" SSM/I winds and the SSM/I winds corrected to 10 m are both given. In addition to giving the actual Sable Island winds, adjusted values representative of open-ocean conditions (based on personal communications with J. Walmsley, 1987) are presented.

Date	Winds (m s^{-1}) SSM/I (1 m)	SSM/I (10 m)	Sable (obs)	Sable (adj.)	Situation
Jan 26 1000Z	25	35	13G15	15G18	Rain
Feb 13 0900Z	25-30	35-45	20G25	23G28	Rain
Feb 16 2200Z	25-30	35-45	15G18	18G20	Rain
Feb 21 0900Z	15-20	20-25	3	08	Rain
Mar 01 2300Z	15	20	8	10	Rain
Mar 04 2200Z	15-20	20-28	10	13	Rain
Jan 30 0000Z	<5	8	8	10	No Rain
Feb 22 0000Z	5-10	8-13	15G18	16G23	No Rain
Feb 23 2300Z	10	13-15	13G15	15G18	No Rain
Feb 26 1000Z	<5	8	8	10	No Rain
Mar 05 2200Z	5-10	8-13	15	18	No Rain

Table 4: Comparison of SSM/I winds vs. Sable Island winds in various situations.

From the data in Table 4 , the over-estimating bias in rain situations is clearly evident. It is also evident that the

under-estimating bias in no-rain situations is present, but is less severe.

4.3 General Utility of SSM/I Data

Other than providing additional information on the surface wind field directly, the SSM/I data shows potential usefulness in several other respects:

- The rain-rate data could not be verified objectively, but they appeared to do an excellent job in depicting areas of precipitation, based on general comparisons which were made with the nephanalyses that were done by the operational forecasters using conventional data.

- Warm fronts and cold fronts could often be deduced from the SSM/I patterns. This could lead to an inference of the isobaric field and thus, indirectly, the wind field analysis in data-sparse ocean regions.

- Good rain-rate data upstream from the Maritimes, over the ocean, would undoubtedly improve the MWC analyses and forecasts. The data would be a welcome supplement to the radar coverage which is restricted to within 200 n.mi. of the coast.

- There were cases where the operational analyses of large cloud masses as observed on visible and infrared satellite imagery were misinterpreted as containing extensive areas of organized precipitation. The rain-rate data could be used to refine such analyses.

- Wind speed data did give an indication of the wind maximum that is present in the outflow through the Cabot Strait. Identification of such maxima could be very useful even if the speed data are unreliable.

5. CONCLUSIONS

Based on the evaluation of SSM/I data at the Maritimes Weather Centre between January 21 and March 31, 1988, it is concluded that:

1. The SSM/I wind speed values are seriously influenced by precipitation and/or high water vapour rendering the wind speed data, by themselves, unreliable and inaccurate.

2. The SSM/I water vapour and rain-rate data seem to be quite reliable. They are therefore potentially very useful for analyses of precipitation and clouds and for the detection of certain weather systems.

3. The SSM/I data would be a valuable tool for the operational forecaster if it were available in an operational time frame and in an easily useable format.

6. REFERENCES

NOAA, 1987: Passive Microwave Observing from Environmental Satellites, a Status Report Based on NOAA's June 1-4, 1987, Conference in Williamsburg, Virginia. NOAA Technical Report NESDIS 35, U.S. Department of Commerce, Washington, D.C.

Ph.D. Associates, 1987: Examples of Retrieved Ocean Surface and Atmospheric Parameters from SMMR Observations. Ph.D. and Associates, North York, Ontario.

Smith, S.D., 1981: Factors for Adjustment of Wind Speed Over Water to a 10-metre Height. Bedford Institute of Oceanography Report Series No. BI-R-81-3, Bedford Institute of Oceanography, Dartmouth, N.S.

ON THE TACTICAL PREDICTABILITY OF LARGE WAVES

[1]J. R. Buckley and [2]P. H. LeBlond

[1]Department of Physics
Royal Roads Military College
FMO Victoria, B. C.
Canada, V0S 1B0
[2]Department of Oceanography
University of British Columbia
Vancouver, B. C.
Canada, V6T lW5

1. INTRODUCTION

One of the characteristics of a wind-blown sea is the presence of identifiable sequences of waves with heights exceeding those of their neighbours. These wave groups are readily identified in time-series of sea level taken at any specific location. The statistics of these groups of waves with heights in excess of $H_{1/3}$ (the significant wave height: a convenient threshold) have been studied by a number of authors (Rye, 1974 for example). They have found that wave groups are slightly longer than would be expected from the Rayleigh statistics normally obeyed by wave height distributions. The average group contains two or three waves. High waves thus tend to occur in succession, enhancing their impact on coastal and offshore structures.

There has been continuing debate over the mechanism for wave group formation. While they may arise merely as the chance superposition of random waves, appearing and vanishing as evanescent interference patterns (Longuet-Higgins, 1984), there is theoretical evidence that they may be more permanent, having the properties of envelope solutions which are solutions to a non-linear Schrödinger equation as described by a number of authors (Davey and Stewartson, 1974; Yuen and Lake, 1975; Hui and Hamilton, 1979). These mechanisms need not be mutually exclusive.

Earlier studies by LeBlond et al., 1984a and 1984b, have shown that large waves in this geographical region appear to propagate over distances of up to 17km at the group velocity rather than the phase velocity appropriate for the waves. In these studies, the technique of lagged group correlation analysis was used on data collected from ordinary accelerometer-equipped wave measurement buoys. Wave direction in these studies was inferred from the wind direction.

In this study we examine directional wave data measured at two buoys 2km apart, attempting to show that wave groups exist with greater than random frequency, that there is statistically significant propagation of these wave groups between the buoys, and that the directional

properties of this propagation are in general agreement with theories of envelope solutions.

A better knowledge of the propagation properties of wave groups would contribute to an improved understanding of the low frequency end of the wind wave spectrum, whose relevance to the motion of large floating structures has often been emphasized. The discovery of correlations between wave groups over distances of a kilometre or more might also open up the possibility of a last-ditch warning system announcing the imminent arrival of extraordinarily large waves.

The analysis developed for examining possible wave group correlations is explained in Section 2 . The details of the observational conditions are described in Section 3 . The results are presented in Section 4 . Conclusions are formed in Section 5 .

2. GROUP CORRELATION ANALYSIS

The data used in this study consisted of simultaneous time series of sea-level variations and of two orthogonal slope components from each of two wave buoys. As it was wave groups, containing one or more waves, and not instantaneous sea-level which we wished to correlate between the two stations, we processed each sea-level time series as follows:

The original time series $\eta(t)$ was first rectified by multiplying with itself into $\eta^2(t)$, and the smoothed with a Bartlett filter

$$< \eta^2(t) >= \int_t^{t+2T} f(T,\tau)\eta^2(\tau)d\tau$$

where $f(T,\tau)$ is a triangular function which vanishes for $\tau \times \leq t$ and for $\tau \times \geq 2T$ and equals unity at $\tau = t+T$. Following Funke and Mansard, 1978, T = [peak period of the spectrum] was chosen to make the wave groups explicit. The filtered time series was then decimated by removing 19 of each twenty points. All values below a threshold level of 1.5 times the significant wave height were set to zero. In each block, only a few points stood out as spikes above the threshold; these points tended to cluster in groups.

The correlation process consisted of counting the number of spikes coincident between the two series. Since chance coincidences of course occurred between the two series, we weighed the significance of the measured coincidences against the statistically expected values. The number of spike coincidences expected from two independent time series was calculated using a hypergeometric distribution as is described in Appendix I .

If wave groups do propagate, then there ought to be some time lag in the maximum of coincidences between the buoys. If there is some directionality to group propagation then this time lag ought to be a function of some characteristic direction of the wave field. Accordingly we examined the spike coincidences for a number of time lags between the buoys and for all values of dominant surface wave direction. As individual spikes are generally not independent, we examined correlations over time averages including 1 to 8 adjacent elemental intervals (and hence up to 8 adjacent spikes). To increase the statistical reliability of the results, we combined results of these analyses over all records collected under similar circumstances: i. e. for each time average, we collected results in directional octants.

If the distribution of spikes in a record were purely random then the time intervals between spikes in each record would be distributed according to a Poisson distribution. If large waves occurred in groups then there should be a larger number of occurrences at unit lag than expected from a random distribution (i.e. in a group large waves are adjacent). We calculated the distribution of lags between spikes in each individual record and compared it to a best fit Poisson distribution. The results were summed over all relevant data records to increase the statistical reliability of the result.

3. DATA SOURCES

The data used in this paper arise from the Directional Wave Spectrum Intercomparison Study carried out on the northeast Grand Banks of Newfoundland on the east coast of Canada in the late winter of 1983 (Juszko, 1985). In this experiment, simultaneous directional wave data were collected by two Datawell WAVEC buoys. The instrument locations axe shown in Figure 1 and are listed in Table I . Buoy 248 was located 1.12 nautical miles (2.074km) away from buoy 249 at a bearing of 28° T. These instruments sampled every .78 seconds for 34 minutes (2048 samples).

The primary level of processing of the buoy data was performed by Jusko, (1985). The raw instrumental data were calibrated according to the manufacturer's specifications and directional spectra were calculated according to the algorithm of Longuet-Higgins et al. (1963).

The analysis in this study required that the wave buoys be in a relatively homogeneous wave field. We assured this homogeneity by requiring that the dominant direction of the waves at both buoys agree within 45°. This dominant direction was determined as the direction of wave energy propagation at the peak of the wave spectrum. This selection criterion eliminated all but 438 pairs of records.

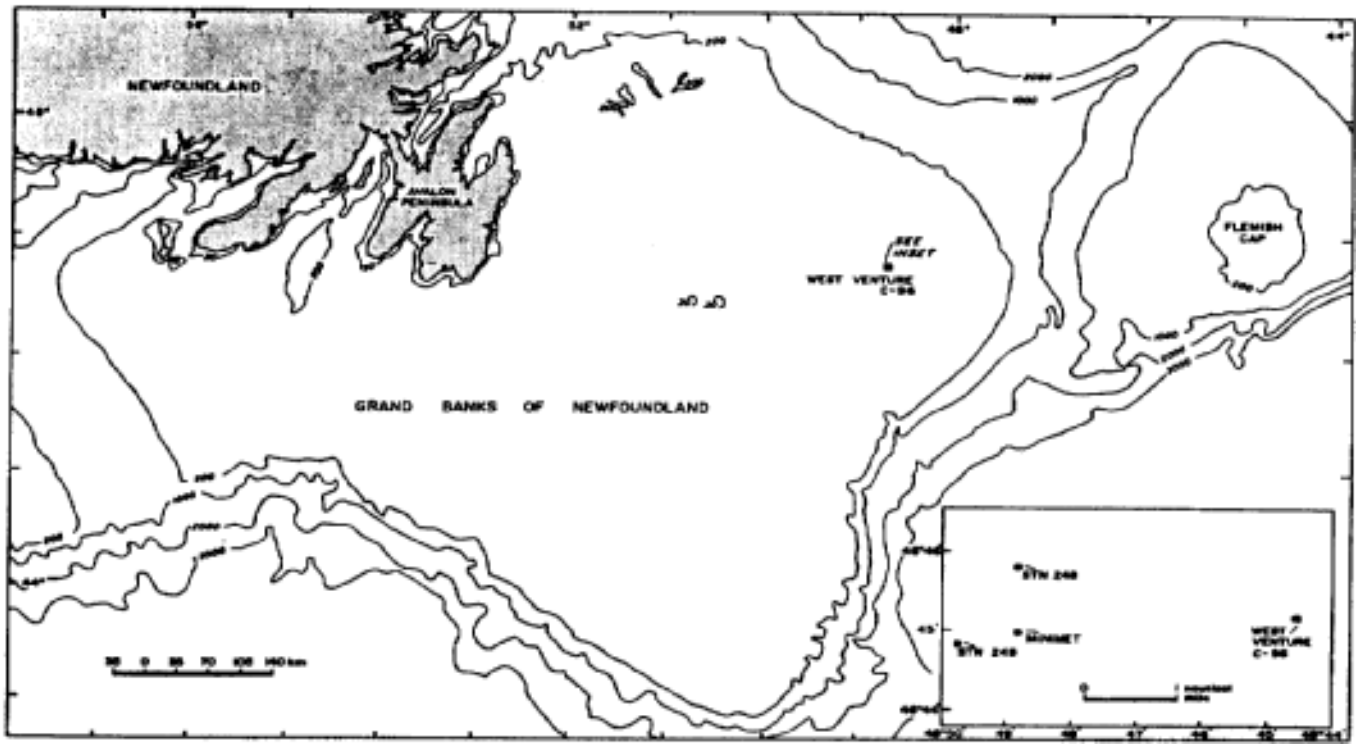

Figure 1: Location of the wave measurement buoys 248 and 249 during the Directional Wave Measurement Study. (From Juszko, 1985).

Table I
Locations of Directional Wave Measurement Buoys

Buoy Number	Lat	Long	Data Return
248	46°45.80'N	48°48.80'W	75%
249	46°44.83'N	48°49.75'W	97%

Since we were interested in the directional distribution of wave group propagation, we divided the data by direction into octants as shown in Table II .

Table II
Directional Distribution of Coincident Wave Data

Quadrant Number	Begin Direction	End Direction	Number of Records
1	185.5°	230.4°	68
2	230.5°	275.4°	67
3	275.5°	320.4°	19
4	320.5°	5.4°	12
5	5.5°	50.4°	104
6	50.5°	95.4°	26
7	95.5°	140.4°	59
8	140.5°	185.4°	83

Data were collected by both buoys from 84/02/14 to 84/04/11. Samples were collected every three hours except during "storm" conditions when data collection was continuous. The definition of "storm" conditions had been established as any time the RMS wave height exceeded 1m. Since the mean significant wave height was 2.5m during the entire measurement period, the data recorders for the buoys operated continuously for much of the time. Consequently over 200 hours of data were collected in simultaneously occurring records from the buoys, in spite of data losses and the poor operation of one of the buoys early in the program.

4. RESULTS AND INTERPRETATION

The plot of spike (i.e. large wave) frequency vs lag in Figure 2 for buoy 248 shows that, for all lags longer than one time unit, the frequency of occurrence of time lag between spikes was in agreement with a Poisson distribution for one degree of freedom. We found 447 occurrences of this one unit lag, when only 155 could be attributed to random chance. Thus large waves occurred together three times more frequently than expected in a fully random sea state. Results from buoy 249 were essentially the same.

5. DISCUSSION AND CONCLUSIONS

The results in the previous section show that groups of waves exist in the Grand Banks region and that they propagate preferentially in the direction of the dominant wind-wave field at the group velocity of those waves. The practical question to be answered now is, given that the above results are true, is it worthwhile trying to predict the occurrence of these waves from some distance, i. e. is it feasible to install a measurement system to provide warning of the imminent arrival of large waves at an offshore facility?

To answer this question we need to look at the number of large waves occurring in the region and the number that would be predicted.

The Rayleigh distribution of wave heights states that:

$$p(H)dH = \frac{2H}{\overline{H^2}} e^{-H^2/\overline{H^2}} dH$$

where $p(H)dH$ is the probability that a wave height is between H and $H + dH$. Using this distribution, the criterion used in this paper for the selection of large waves, $H > 1.5H_{1/3}$ selects the largest 85 waves per thousand. The data showed an approximate average wave period of 8s, so each 34 minute data record contained about 250 waves. Therefore our sample consists of the 21 largest waves in each record, or about 8800 waves in total. The Poisson test showed that about 5% of these waves occurred in non-random groups, as opposed to the 2% expected from random theory.

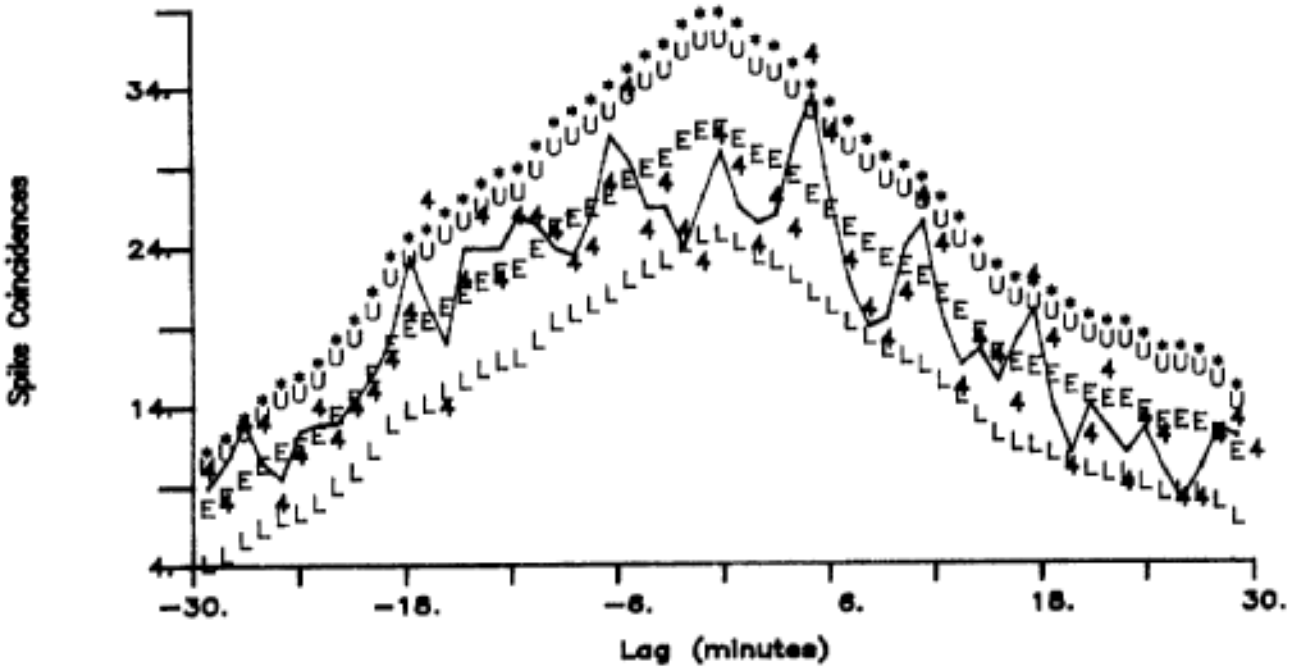

Figure 3: Lagged Coincidence of large waves between buoys 248 and 249 for a dominant wave direction of 208°T.

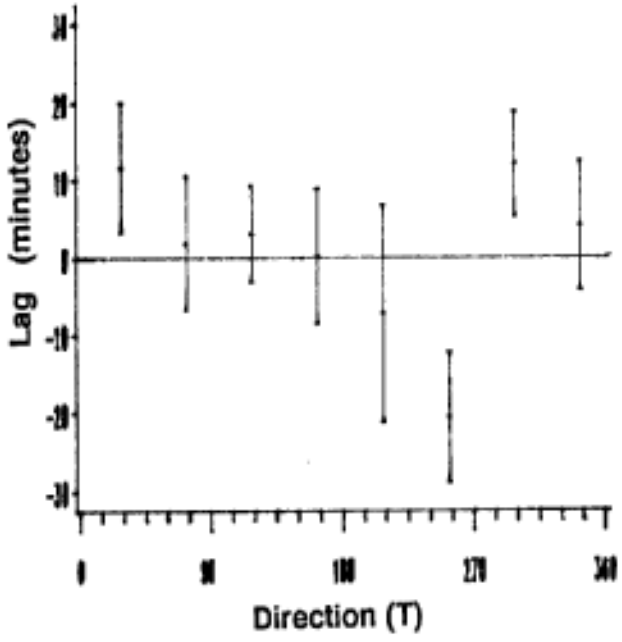

Figure 4: Directional distribution of wave group propagation delays between buoys 248 and 249.

The lagged correlation study showed that these groups tend to propagate in a predictable way, so that, if a group of two or more waves were seen at one location to be propagating in a direction toward another location, it is likely that the group would arrive at the other location with a time delay commensurate with the group velocity of the waves. Therefore a warning system could be devised to tell of the imminent arrival of a group of large waves at an offshore facility. Given the small proportion of large waves that occur in groups however, such a system is likely not economically viable.

6. ACKNOWLEDGEMENTS

This project was funded principally by Petro-Canada on behalf of the Terra Nova Group of Companies and by the National Science and Engineering Research Council. The authors thank these organizations for their support. We also thank B. A. Juszko of Seakem Oceanography Ltd. for providing data and directional spectral analysis from the Directional Wave Spectrum Intercomparison Experiment funded by the Environmental Studies Revolving Fund administered by the Canada Oil and Gas Lands Administration, and Royal Roads Military College for the support in the final stages of the study.

APPENDIX 1 – THE STATISTICS OF SPIKE COINCIDENCES

Each time series was split into N equal sized intervals, where N is chosen as the number of intervals of length T in the time series. Each interval in each time series either contains a "spike" or it does not. The presence of a spike in an interval is indicated by a "1"; the absence , by a "0". Consider that there are n spikes in one series, k in the other. The juxtaposed time series then consist of N objects of four

different types: a number H of (1,1) [a spike both time series] – this is the number of coincidences; a number $n - H$ of (1,0) [a spike in the first, none in the second]; a number $k - H$ of (0,1) [a spike in the second, none in the first] ; and a number $N - H - (n - H) - (k - H) = (N + H) - (n + k)$ of (0,0) [no spikes at all]. For given n, k and N, the probability of H coincidences, assuming that the series are independent of each other, is:

$$p(H) = \frac{\text{number of ways of arranging objects } (0,0),(0,1),(1,0),(1,1)}{\text{total number of configurations of the two series}}$$

which may be written in combinatorial notation as:

$$p(H) = \frac{\binom{N}{(N+H-(n+k)),(k-H),(n-H),H}}{\binom{N}{n}\binom{N}{k}}$$

Using the identities

$$\binom{k_1+k_2+k_3+k_4}{k_1,k_2,k_3,k_4} = \binom{k_1+k_2}{k_1} + \binom{k_1+k_2+k_3}{k_1+k_2} + \binom{k_1+k_2+k_3+k_4}{k_1+k_2+k_3}$$

and

$$\binom{k_1}{k_1-k_2} = \binom{k_1}{k_2}$$

we find

$$p(H) = \frac{\binom{N-n}{k-H}\binom{n}{k}}{\binom{N}{k}} = \frac{\binom{N-k}{n-H}\binom{k}{H}}{\binom{N}{n}}$$

which is the hypergeometric distribution for H, with expectation value and variance given by:

$$E(H) = \sum_H Hp(H) = \frac{kn}{N}$$

$$\sigma^2 = \frac{kn(N-n)(N-k)}{N^2(N-1)}$$

REFERENCES

Davey, A. and K. Stewartson, 1974. On three-dimensional packets of surface waves. Proc. Roy. Sec. A **338** pp 101-110.

Funke, E. R. and E. P. D. Mansard, 1979. "Synthesis of Realistic Sea States in a Laboratory Flume", National Research Council Hydraulics Laboratory Technical Report LTR-HY-66, August, 1979.

Hui, W. H., and J. Hamilton, 1979. Exact solutions of a three -dimensional nonlinear Schrödinger equation applied to gravity waves. J. Fluid Mech. 93, pp 117-133.

Juszko, B. A., 1985. Comparison of Directional Wave Spectra. Environmental Studies Revolving Fund Report 090-17-08. Canada Oil and Gas Lands Administration, Department of Energy, Mines and Resources, Ottawa. 148p.

LeBlond, P.H., D. Cumming and G. Staples. 1984. Searching for long -distance wave group correlations at Hibernia. (abstract only) Atmosphere-Ocean **22**, 8th Congress Issue.

LeBlond, P.H., D. Cumming and J. R. Buckley, 1984. Long Distance

Wave Group Correlations (abstract only). EOS **65**, Annual Fall Meeting Issue.

Longuet-Higgins, M.S., D.E. Cartwright and N. D. Smith. 1963. "Observations of the Directional Spectrum of Sea Waves Using the Motions of a Floating Buoy". In *Ocean Wave Spectra*, Prentice-Hall Inc. Englewood Cliffs, N. J., pp 111-136.

Longuet-Higgins, M. S. 1984. Statistical Properties of Wave Groups in a random sea state. Phil. Trans R. Soc. Lend. A 312, 219-250.

Rye, H., 1974. Wave group formation among storm waves. Proc. 14th Int. Conf on Coastal Engrs. Am. Soc. Civ. Engrs, New York, pp164-183.

Su, M. Y. 1984. Characteristics of Extreme Wave Groups. Proceedings of OCEANS '84, Washington, D. C. pp711-716.

Yuen, H. C. and B. M. Lake, 1975. Nonlinear deep water waves: Theory and experiment. Phys. Fluids 18, 956-60.

BEAUFORT SEA WIND AND WAVE CONDITIONS DURING THE STORM OF SEPTEMBER 16-18, 1985

Donald O. Hodgins and Donald S. Dunbar

Seaconsult Marine Research Ltd.,
Vancouver, B.C.

ABSTRACT

Over a period of 57 hours from September 18th to late on September 18th, 1985, one of the most destructive storms ever witnessed in the Beaufort Sea struck Mackenzie Bay and areas to the west. Kugmallit Bay and points to the east were protected by sea ice. A detailed wind and shallow-water wave hindcast was carried out for this storm using a second generation coupled discrete spectral wave model to define the maximum wave height and duration of large waves at a number of deep- and shallow-water locations. As a first step, the wave model was calibrated against growth relations published in the SWAMP report, and verified against historical wave measurements in the Beaufort Sea for five storms. A new, innovative method for establishing the effective ice edge using AVHRR satellite imagery, in conjunction with conventional ice maps and SAR overflight images, was developed for the September 1985 storm. In this procedure, images form bands 1, 2, and 4 are combined and filtered to yield a nearly-unambiguous ice-water discrimination.

In this paper, the verification results for the wave model are presented and discussed in relation to the difficulties of wind field hindcasting and ice edge specification. Next the use of satellite imagery for ice edge mapping is described and illustrated. This is followed by a discussion of the wave hindcast results, including the very-shallow-water modifications introduced into the model to account for repeated wave breaking. Finally, the sensitivity of predicted wave conditions to horizontal translation of the ice edge during the storm is discussed.

EVALUATION AND REDUCTION OF SYSTEMATIC ERRORS IN LAKE WIND WAVE HINDCASTS

Stephen Clodman

Atmospheric Environment Service
Downsview, Ontario, Canada

1. INTRODUCTION

The parametric lake wind wave model of Schwab et al. (1984) has been effective in routine use in both Canada and the United States. Clodman (1989) found that the constant wind fetch limited situation was dominant, so that if the model was tuned under that assumption, very good results could be obtained even for general cases. However, there are some remaining systematic errors in H. These occur when the wind is rapidly varying in time and also occasionally in other particular conditions. Moreover, there remain substantial systematic errors in the computation of wave period.

In order to reduce these errors it will be necessary not merely to vary model tuning coefficients, but to alter the qualitative form of model forcing equations and spectral functions. This in turn allows some tentative inferences to be drawn about the correct form of these equations and functions.

2. MODEL

We are considering a lake of mesoscale size, such as one of the Great Lakes of North America. We can ignore swell. Assume that the wave energy is a standard function of frequency and of direction. Also assume that deep water wave theory applies. A wave momentum balance is calculated by the model, advancing in time. Significant wave height, a wave period, and a wave direction are derived parametrically as output.

The following is a brief description of the model as used by Schwab et al. (1984) and Clodman (1989). From the wind speed, and the air-water temperature difference, an equivalent 10 m neutral stability wind is computed (Liu and Schwab, 1987). This wind transfers momentum into the moving wave via a drag on the form of the wave. The drag coefficient increases with wave height; this is intended to allow for the increase of wind speed with height near the surface. A model forcing function W governs the rate of wave development with fetch or time, although it does not affect the fully developed height. Schwab et al. use W = 0.028 whereas Clodman recommends an increased value W = 0.07 or 0.08.

The wave energy equation is assumed separable by frequency and direction. The direction part is assumed symmetric. Schwab et al. use

a relatively broad function, i.e., one with a large angular spread of the wave, while Clodman, after discussion, uses a narrower function. The frequency part E(f) of the energy is a JONSWAP form with peak enhancement and with an f^{-5} variation at high frequency.

3. DATA

The data are from U.S. National Data Buoy Center (NDBC) NOMAD type buoys, which measure hourly. The data used here are of the 1982 observing season, 22 March - 8 December, for NDBC buoy 45007 in the middle of southern Lake Michigan (42.7°N, 87.1°W, 150 m depth). Significant wave height H is measured as four times the square root of the variance of the water surface height. Characteristic period P is the inverse of the average energy-weighted frequency. Other relevant measured parameters are wind speed, U, and direction, θ, and the air and water temperatures, T and TW. Atmospheric quantities are sensed at 5 m height. A three hour smoother was applied to H and P values for verification.

Although the model can handle the non-constant case, this study assumes the wind is constant with location since the data buoys are too sparse for a useful spatial analysis. Clodman (1989) concluded that the buoy measured wind speeds were about 10% too low. Therefore these speeds are multiplied by 1.1 before being converted to equivalent 10 m neutral winds for model input.

Verifications are done principally with two sets of data. One of these includes all records at 3-hourly intervals except those which were dropped for missing input or verification data. Sometimes unstable cases (DT = T - TW < 0) were tested separately. The other was restricted to time-constant wind situations with wind speed at least 5 m/s and wind direction from the east, south or west. North winds were not used as they have a large fetch versus azimuth variation for buoy 45007.

Mean buoy values were as follows: There were 1909 cases with the measured mean and standard deviation of 13 being 5.13 ±2.56 m/s. Corresponding values for H were 0.82 ±0.68 m and for P 3.30 ±0.69 s. For the 666 unstable cases mean H was 1.26 m and for the 100 constant wind cases as described mean H was 1.63 m.

4. HEIGHT COMPUTATION

Clodman (1989) tuned the model for optimum computation of H for selected constant wind cases, then showed that results continued to be good for all cases taken together. The form drag run showed in Table 1 gives the results for the model of that study. For buoy 45007 in 1982 with constant wind the average algebraic error is near 0 and the error variance was 0.16 m. The least squares regression line gives

close to a 1:1 relation between computed and measured H. For all cases the result is similar except that the error variance is 0.22 m; the larger error reflecting the broader scope of the cases.

For this study, the measured and model H were subjectively examined hour-by-hour to locate large errors and establish their systematic patterns of occurrence. Some supplementary testing on simple ideal cases was done. First note that really large errors are rare. Of 1909 cases the largest positive (negative) error is +1.18 m (-0.90) with 11 (10) errors greater than +0.7 (-0.7) and 24 (48) greater than +0.5 (-0.5). The median algebraic error is very close to the mean. Hence, for most purposes, the model is sufficiently accurate; however this study will consider if further improvements are possible.

The subjective examination noted the following systematic errors:

- Waves for very stable cases with moderate wind are overestimated; in fact the measured wave may be zero. Probably the air right at the surface is almost stationary and separated from that at anemometer height (5 m). The boundary layer adjustment of the model does not compensate enough for this.

- Decaying waves are sometimes underestimated. This model, since it is parametric nonspectral, does not allow for the fact that low frequency components of the wave energy tend to persist.

- Rapidly turning waves are underestimated. The waves are decayed too much before being built up in the new direction.

- When the model wave height and direction are adjusting to a new wind velocity, the convergence, while a little too fast at first, is excessively slow once the H and θ are close to their final values. This appears to be related to the use of form drag, as discussed below.

Table 1. Summary of model results for data set discussed in text. Model error (algebraic ± standard deviation), correlation between model and observed sets of values, and linear segment least squares fit are shown.

model features		H				P			
		error		regress		error		regress	
drag type	P advec	algeb	stand dev	correl	slope int-cpt	algeb	stand dev	correl	slope int-cpt
all - 1909 cases									
form	no	-0.02	±0.218	0.951	0.99 -0.01	+0.11	±0.488	0.834	1.06 -0.11
mixed	no	0.00	±0.222	0.950	1.00 0.00	+0.13	±0.490	0.836	1.08 -0.13
mixed	decay	0.00	±0.222	0.950	1.00 0.00	+0.18	±0.482	0.850	1.11 -0.20
mixed	yes	0.00	±0.222	0.950	1.00 0.00	+0.24	±0.480	0.856	1.13 -0.19
skin	yes	+0.02	±0.222	0.953	1.02 0.00	+0.24	±0.501	0.854	1.16 -0.29
unstable (DT < 0) - 666 cases									
form	no	-0.06	±0.259	0.957	1.06 -0.14	+0.13	±0.631	0.830	1.22 -0.69
mixed	no	-0.04	±0.265	0.956	1.07 -0.12	+0.15	±0.628	0.837	1.24 -0.74
mixed	yes	-0.04	±0.265	0.956	1.07 -0.12	+0.31	±0.572	0.858	1.22 -0.53
constant wind short fetch (U > 5 m/s) - 100 cases									
form	N	0.01	±0.160	0.975	0.96 +0.08	+0.45	±0.277	0.949	1.17 -0.21

Table 2. Direct comparison of model values. H, P and direction φ(°) shown as algebraic mean difference ± standard deviation from mean comparing the model versions as listed. The correlations between the sets of H and of P values of the two models are also given. Also see Table 1.

models	H			P			φ	
	algeb	± s.d.	corr	algeb	± s.d.	corr	algeb	± s.d.
mixed - form drag	+0.021	±0.052	0.9973	+0.020	±0.091	0.9948	+2.4	± 9.1
skin - mixed drag	+0.012	±0.053	0.9976	+0.002	±0.069	0.9976	+0.4	± 9.8
slope rat - no slope rat	+0.003	±0.016	0.99975	+0.002	±0.054	0.9983	+0.5	±10.4
advect - no advect P	0	±0	1	+0.112	±0.278	0.9526	0	± 0
decay advect - no advect P	0	±0	1	+0.053	±0.199	0.9756	0	± 0

For the purpose of this preliminary study, a simple empirical change is tested on the stability value DT = T – TW, increasing DT when it is large positive to reduce H in stable situations. The new value is DT' – S(DT) DT where S = 1 for DT < 1, S = 5 for DT > 5, and S = DT for 1 < DT < 5 (note all temperatures in Celsius).

To control the decay problem, consider that in decaying situations the wave slope is reduced. This gives less vertical surface for the wave to drag against the wind, hence less drag against the wind and a

reduced decay rate. Therefore the form drag is set proportional to a slope ratio, calculated as shown in the next section.

To improve the final convergence and (in part) the wave turning, a more basic change in the model is called for. Recall that the model use form drag, which assumes that the force on the wave is determined by the impact of the wind on the profile of the wave. Since the wave is moving, the wind velocity is computed relative to the phase velocity. Actually an adjusted phase velocity equal to 1/1.2 times the actual phase velocity is used since the equilibrium phase speed is considered to be 1.2 times the wind speed.

In the form drag used by the model, the forcing is proportional to the square of the difference between the wind velocity and the adjusted phase velocity. It is this fact which causes the convergence towards a new wind velocity to be rapid at first and slow towards the end. If it is noted, however, that the wave field has some spread in direction and phase velocity, it can be seen that the forcing is somewhat larger near equilibrium, perhaps close to a linear proportion of the wind velocity - adjusted phase velocity difference.

Various concepts of wave forcing have been used in modelling, a fact which suggests that the problem has not been conclusively resolved. Several methods appear in the different wave models discussed in SWAMP (1985). One possible version is skin drag. Here the forcing is proportional to the square of the wind velocity rather than to the square of the difference between the wind velocity and the adjusted phase velocity. The friction coefficient here is an increasing function of wave height. A wave dissipation must be incorporated to oppose the wave and allow its height to come in equilibrium with the wind at infinite fetch. Skin drag has been tested, both alone and in combination with form drag, as discussed below.

Several test computations have been carried out to evaluate the various changes discussed here. The results have been evaluated both for their effect on the gross statistics of the model results and for their effect on specific cases. The gross statistical results are shown in Table 1 . The overall result is that the effect of the model changes on H is quite small and ranges from slightly beneficial to neutral. The largest change is the tendency of increased stability to give a negative bias through the reduction of equivalent neutral wind speed.

Table 2 gives a direct comparison between the models themselves. Generally the differences are small, perhaps surprisingly so. The form, mixed and skin drag versions have been tuned to almost the same mean bias. What is even more interesting is that the standard

deviation of the differences are only about 0.05 m. The slope ratio compensation (not shown) has very little effect overall, as tested with mixed drag; its effect with form drag alone would perhaps be greater. The stability increase (not shown) has a little greater effect, mainly in the high positive stability cases, and gives an average bias change of −0.06 m.

In respect to particular error situations, the changes are again neutral to slightly beneficial. The detailed effect of changes is as follows:

- Waves in very stable situations with moderate winds are not overestimated as much if the stability increase adjustment is used. However, for strong wind stable cases, the wave sometimes becomes underestimated.

- The decaying wave situation is usually modelled better by the slope ratio adjustment, but the effect is small.

- Turning winds are a little better modelled by mixed or skin drag than form drag in that the waves are less underestimated. However, a harmful effect is that the waves are overestimated for some high wind situations, especially for north winds (long fetch).

- The convergence in time of the wave to its final value is more satisfactory with mixed or skin drag than with form drag.

5. PERIOD COMPUTATION

The modelled wave period, while good in certain circumstances, is less accurate than the modelled wave height. This is true for a variety of reasons. Since wave height is the most important output, the forcing coefficients and other features of the model are tuned against the data for maximum accuracy and any resulting biases in the period computation remain. The parametric wave model is not very well suited to the evaluation of the period, especially for short periods or for decaying waves. Finally, the verification of the period seems to be affected by certain measurement biases.

Define "peak period" as the inverse of the frequency of maximum energy and "characteristic period" P as the inverse of the energy-weighted mean frequency. As stated above, the energy curve is assumed by the model to follow a peaked JONSWAP form; its equation is

$$E(f) = \alpha\, g^2\, (2\pi)^{-4}\, f^{-5} \exp(-1.25\, f_r)^{-4}\, [3.3^{\exp d}]$$

$$\text{where} \quad d = -(f_r - 1)^2 / 2\beta^2 \qquad (1)$$

$$\text{with} \quad f_r = f/f_p\,, \quad \beta = 0.07\ (f_r < 1) \text{ or } 0.09\ (f_r > 1)$$

Thus the peak period is f_p^{-1}. The characteristic period is less; it is estimated from Eqn (1) as 0.84 f_p^{-1}. The NDBC data gives both the peak and the characteristic period. The difficulties with the peak period are, first, that the period is allowed to take on only certain discrete values which are widely spaced for large periods, and, second, the period is ambiguous for flat-topped or bimodal curve shapes. Therefore Clodman (1989) and this study compute the characteristic period (Schwab et al. (1984) use the peak period).

It is seen from Table 1 that the period computation is very good for the constant strong wind cases but deteriorates somewhat for the more general situation. This is related to the fact that P is computed from the wave momentum assuming constant wind and growing wave. If the wave is decaying, the model is likely to underestimate P substantially.

Computation of small values of P tends to be inaccurate. Very small waves ($H \approx 0.1$ m) tend to be obscured by a slight swell which invalidates the model P. The NDBC wave spectral computation ignores components $f > 0.5$ s^{-1}. To partially correct these problems, a minimum $P = 2.8$ s is imposed on the model before doing the verification.

Larger model P values are better correlated with measurements but do have a positive bias. One reason may be an inaccuracy in the energy equation. Eqn (1) gives a f^{-5} dependence for large f. However, an increasing number of studies, such as Phillips (1985), prefer f^{-4}. If so, the characteristic period/peak period ratio becomes smaller. A preliminary examination of the NDBC measurements shows that this ratio is usually considerably smaller than 0.84. If this were accounted for in the model, the overprediction of the period would be reduced. For complete consistency, a new equation would have to be substituted for (1) leading to substantial changes in the internal computations of the model. It is intended to do a test of revisions in the computation of P later on.

The computation of P is subject to the occasional biases enumerated in the last section. The methods discussed in that section – mixed or skin drag, slope ratio compensation and stability increase – have little effect on accuracy, as can be seen from Tables 1 and 2 .

There is one technique, period advection, which improves accuracy by giving larger P for decaying waves. The premise is that when the wave is not being wind driven its period is conservative and so is advected by the wave group velocity. An advected period is compared to the internal model computed period and the larger of the two is given as output. A partial version of this method gives the advected period as output only if the wave is actually decaying, that is, if the adjusted wave phase speed is greater than the wind speed.

The slope ratio, discussed above, is the ratio of the slope of a calculated non-wind-driven wave to the slope of a wind driven wave. The slope is taken inversely proportional to the wave length for a given H, and the wave length is proportional to the square of P. Thus the slope ratio is the square of the ratio of the internal model computed period to the advected period, if less than 1; otherwise it is set equal to 1.

Although the positive bias is increased by decay advection (Table 1), the error scatter and correlation are considerably improved, especially for the unstable cases (which are usually higher waves). The complete version is more beneficial than the partial version; it reduces the standard deviation of the P error by almost 10% for unstable cases. The complete advection P differs from the no advection P by 0.11 s bias ±0.28 s scatter (Table 2). The effect on individual cases, as briefly examined, was found to be usually beneficial.

6. CONCLUSIONS

The wind wave model of Schwab et al. (1984) as modified by Clodman (1989) has been further examined and tested to reduce biases for specific cases. Generally, wave height hindcasts are already very good, and only marginal improvements are possible in them. Errors in the periods are greater, and leave more room for improvement. Some of that possible improvement has been demonstrated with the use of the advected period.

In addition, this study involves questions of a more basic nature. What are the dominant mechanisms of wave generation and dissipation? What is the most accurate and theoretically consistent way of allowing for measurement height and static stability? These issues have been often examined. Nevertheless, the further study of the relatively simple and clear cut wave field of a lake may yield some clues to their resolution.

REFERENCES

Clodman, S., 1989: Refinement and testing of a lake wind wave model on seasonal data. Atmos.-Ocean., 27(3), in press.

Liu, P. C. and D. J. Schwab, 1987: A comparison of methods for estimating U* from given Uz and air-sea temperature differences. J. Geoph. Res., 92(C6). 6488-6494.

Phillips, O. M., 1985: Spectral and statistical properties of the equilibrium range in wind generated waves. J. Fld. Mech., 156, 505-531.

Schwab, D. J., J. R. Bennett, P. C. Liu and M. A. Donelan, 1984:

Application of a simple numerical wave prediction model to Lake Erie. J. Geoph. Res., 89(C3), 3586-3592.

SWAMP Group, 1985: Ocean wave modeling. Plenum Press, 256 pp.

THE OPERATIONAL WAVE HEIGHT FORECASTING PROGRAM OF THE CANADIAN FORCES FORECAST CENTRE CFB COMOX BC

J.T.Broszkowski and H.W.Murray

Canadian Forces Weather Service
Comox, British Columbia

BACKGROUND:

In September 1983 the Pacific Weather Centre (PWC) extended its marine forecast coverage to 200 nautical miles off the B.C. coast, which introduced two new regions to their Marine Forecast area. For years there had been pressure applied from the Pacific Rim marine community to produce sea state forecasts for the west coast marine areas. With the introduction of the two new marine areas, the High Seas forecasts issued for these areas by San Francisco were ceased, thus leaving a void of sea state forecasts in the Canadian offshore zone. Further pressure to produce open sea forecasts was applied when the Northwest Ocean Services Centre at Seattle assumed responsibility for the U.S. offshore zone for Washington and Oregon.

At that time PWC had insufficient resources to produce quality sea state forecasts and neither could METOC Esquimalt nor CFFC Comox on their own. Pacific Region proposed that a final forecast product be a cooperative effort between the three offices. This program was implemented in December 1984.

To begin with, the actual production of wave height analyses and wave height prognostics was a combined effort between Comox and Esquimalt, with PWC using these products to prepare their sea state bulletins. With the expansion of the PWC to include a new marine forecast desk this cooperative effort was eventually terminated in July 1986.

Meanwhile ongoing discussion on the reconfiguration of west coast resources to provide oceanographic and meteorological products to DND users finally reached fruition. CFB Comox was tasked with the responsibility to provide all meteorological and sea state analyses and forecasts required in support of all military operations (including MARPAC and CFB Comox operations) occurring within the area defined by the Victoria RCC area (all of B.C.) and over the northeast Pacific bounded by 4ON to the south and by 16OW to the west. (Figure 1)

CURRENT PROGRAM:

At the present, analyses are done three times daily; at 0000Z, 0600Z, and 1800Z. Insufficient data at 1200Z precludes analysis of

this chart. All ship and buoy reports of wind and sea state are automatically plotted and subjectively checked. The plot target point has both wind wave and swell information. (Figure 2) The combined wave is calculated, plotted and manually analyzed using a current isobaric surface chart to help determine patterns when data is scarce. The forecast program consists of twice daily prognostics for 18 hours and 30 hours based on 0600Z and 1800Z analyses. (Figures 3 and 4) PWC isobaric progs, with modifications as necessary, are used to determine wind and fetch regimes for the forecasts periods in question. The Bretschneider nomogram is the primary tool for forecasting the wave heights.

The sea state forecasts are broadcast twice daily on a number of HF radio frequencies. The broadcast is available, not only to the Canadian Forces, but to any user with the appropriate weather fax receiver.

VERIFICATION:

A verification program has been in effect for the past two winters, using the October to March period, when the seas are most active. The 18 hour prognosis valid 0000Z the following day is compared against data from five anchored buoys. (I004, I036, I005, I002, I006. See Figure 1) Due to the low number of buoy reports plotted on the wave height analysis chart, an interpolation of wave height was made from the analyzed field for the wave height at the buoy locations. The plotted value of the wave height at the buoy was used when available.

For the past three years numerical guidance has also been provided by the Atmospheric Environment Service in the form of the Parametric Ocean Wave Model. This objective model does not take into account actual wave height observations in the generation of the forecast seas. It uses wind information only. This model was also verified against the actual wave heights and compared with the Comox product.

The statistics generated for verification are listed in Table 1 . The first five lines, under each buoy, gives the number and percentage of forecasts in the categories listed to the left for Comox (YQQ) and for the Parametric Model (CMC) . The categories represent a difference between the forecast sea height and the actual height of: less than one metre, between one and two metres, and so on. The RMS error, the mean absolute error, and the bias were calculated for each comparison. The total statistics follow the same format, and a comparison of whether Comox or CMC produced a closer forecast was done as a summary.

A forecast within one metre is considered excellent and a forecast within two metres is good and acceptable. From the results it can be

seen that both products are well within usable limits, a majority of the time. The forecasts by Comox and CMC were within two metres of the actual value 83% and 72% of the time, respectively. The bias indicates both products tend to underforecast the wave heights.

Comparing the two products, it can be seen that the subjective forecast by Comox does better than CMC's objective model in almost all cases. The RMS error and the mean absolute error are lower for the Comox product. As well, the forecast wave height was closer to the actual value over 50% of the time for Comox. CMC was closer only 35% of the time.

SUMMARY:

The wave height forecasting program is ongoing and will continue to provide forecasts for both military and civilian marine users. Both the subjective forecast by Comox and the numerical guidance provided by CMC produce forecasts that are within acceptable, useable limits. The verification statistics show that the subjective prognostics issued by Comox, using an actual wave height analysis as a starting point and drawing upon the forecaster's experience, provide a more accurate forecast of the sea state than a strictly objective model.

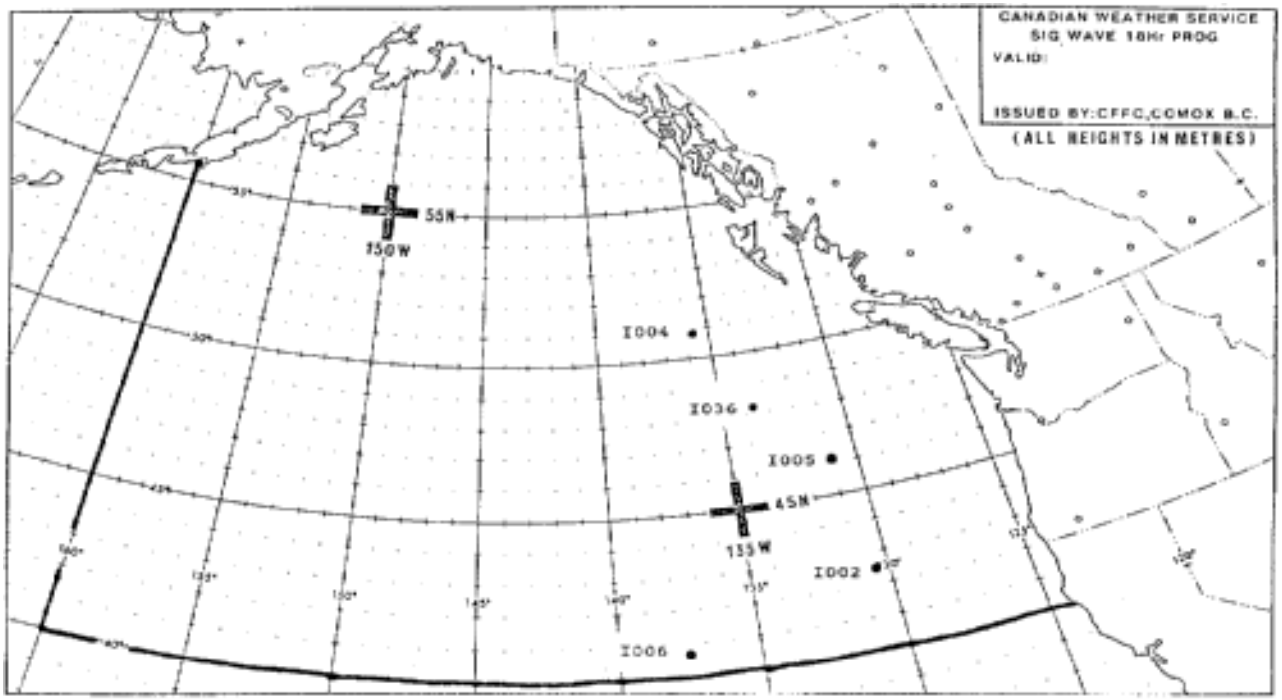

Figure 1. Area of Responsibility and Buoys used in Verification

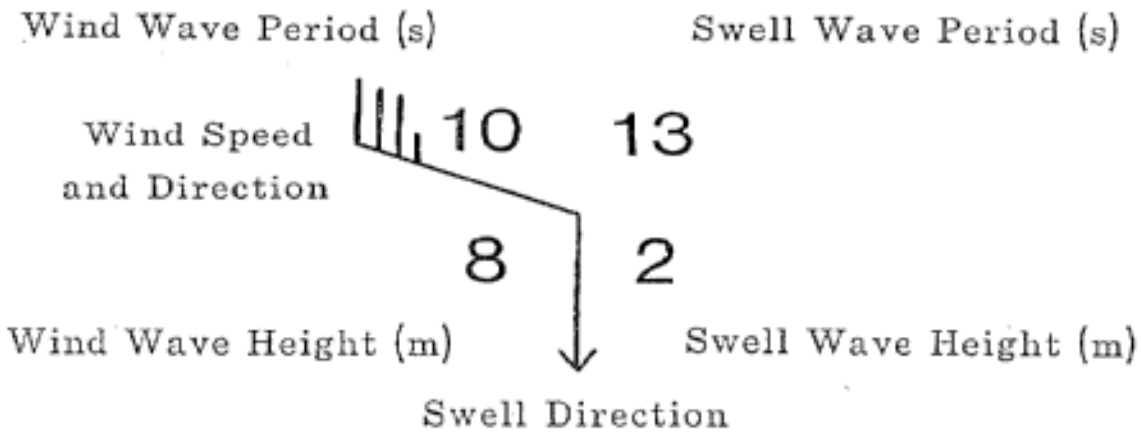

Figure 2. Target Point Plot Model

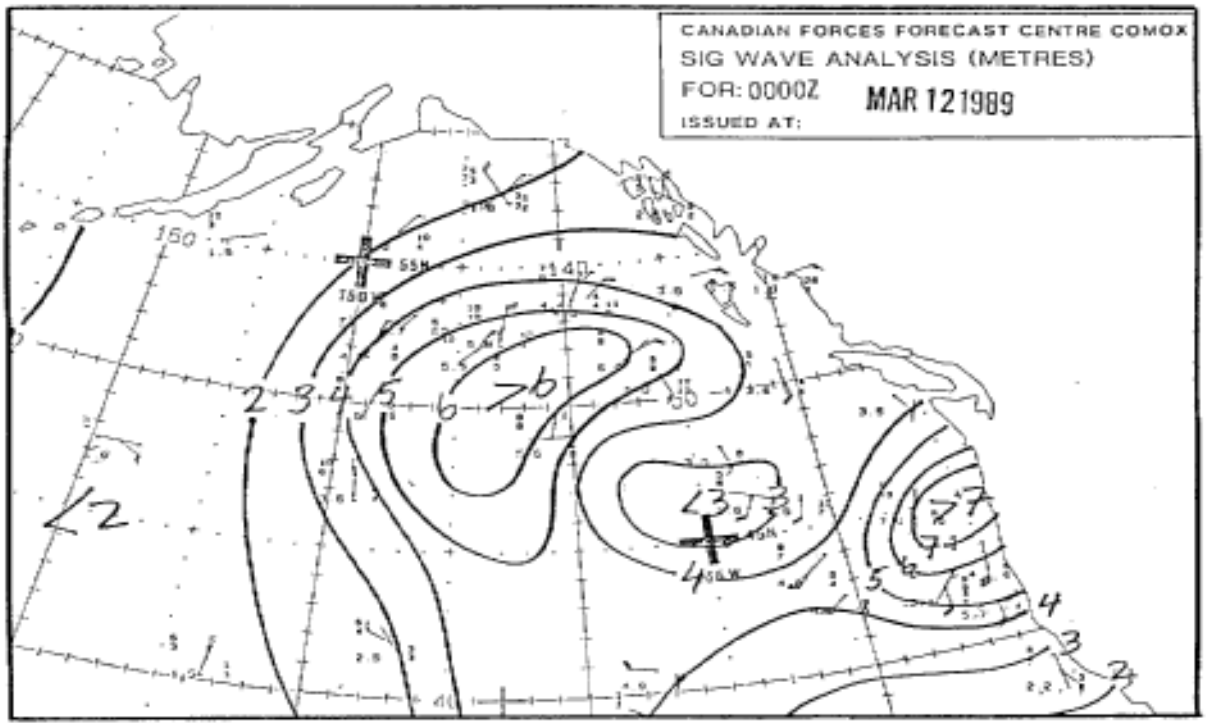

Figure 3. Example Wave Height Analysis

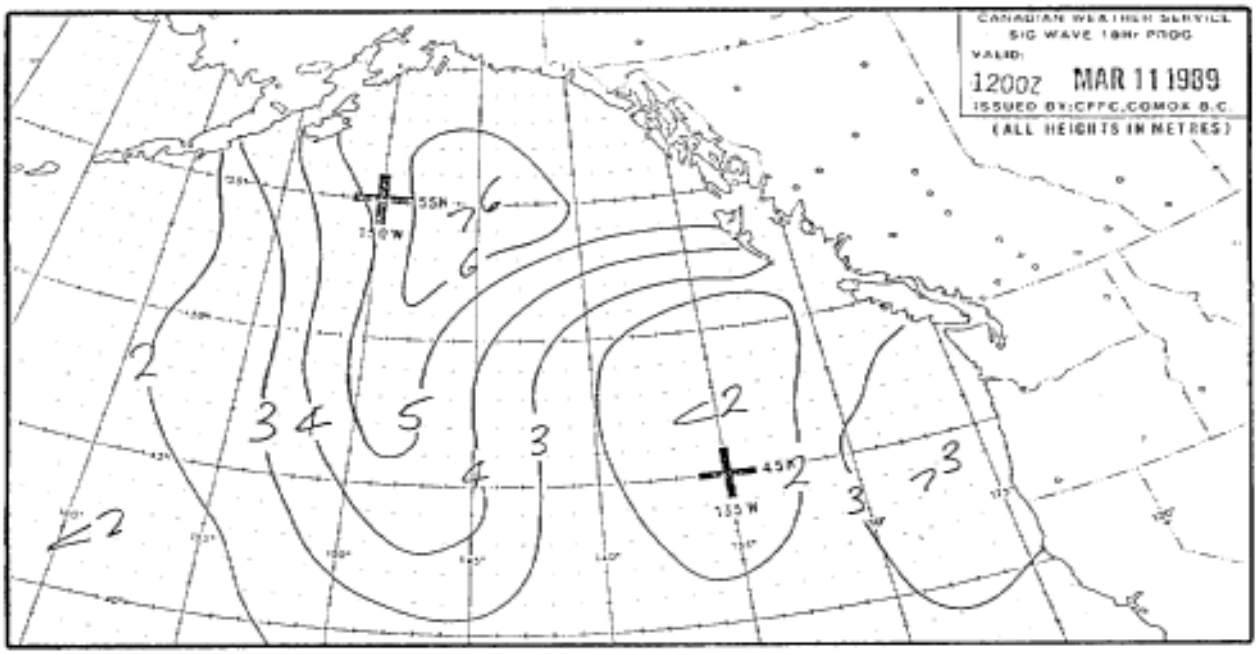

Figure 4. Example Wave Height Prognosis

FORECAST WAVE HEIGHT STATISTICS ON ALL DATA Table 1

	I004 YQQ	I004 CMC	I036 YQQ	I036 CMC	I005 YQQ	I005 CMC
DIFF(1M	139 (51%)	102 (37%)	147 (54%)	112 (41%)	144 (53%)	121 (44%)
1M=(DIFF(2M	85 (31%)	91 (33%)	78 (29%)	86 (32%)	79 (29%)	71 (26%)
2M=(DIFF(4M	43 (16%)	56 (21%)	40 (15%)	60 (22%)	44 (16%)	64 (23%)
4M=(DIFF(6M	5 (2%)	16 (6%)	7 (3%)	11 (4%)	5 (2%)	13 (5%)
6M=(DIFF	1 (0%)	8 (3%)	1 (0%)	4 (1%)	1 (0%)	4 (1%)
RMS =	1.495	2.181	1.555	2.059	1.560	2.099
MN ABS ERR =	1.100	1.593	1.132	1.489	1.135	1.480
BIAS =	-.164	-1.103	-.132	-.969	-.283	-1.155
NUMBER =	273		273		273	

	I002 YQQ	I002 CMC	I006 YQQ	I006 CMC
DIFF(1M	146 (53%)	123 (45%)	162 (59%)	113 (41%)
1M=(DIFF(2M	79 (29%)	77 (28%)	70 (26%)	89 (33%)
2M=(DIFF(4M	45 (16%)	54 (20%)	35 (13%)	53 (19%)
4M=(DIFF(6M	2 (1%)	15 (5%)	5 (2%)	14 (5%)
6M=(DIFF	1 (0%)	4 (1%)	1 (0%)	4 (1%)
RMS =	1.486	1.992	1.401	1.941
MN ABS ERR =	1.070	1.421	1.017	1.431
BIAS =	-.382	-1.207	-.490	-1.105
NUMBER =	273		273	

*** TOTAL STATISTICS ***

	YQQ	CMC
DIFF(1M	738 (54%)	571 (42%)
1M=(DIFF(2M	391 (29%)	414 (30%)
2M=(DIFF(4M	207 (15%)	287 (21%)
4M=(DIFF(6M	24 (2%)	69 (5%)
6M=(DIFF	5 (0%)	24 (2%)
RMS =	1.500	2.056
MN ABS ERR =	1.091	1.483
BIAS =	-.290	-1.108
NUMBER =	1365	

BUOY:	I004	I036	I005	I002	I006	TOTALS
YQQ CLOSER	147(54%)	148(54%)	151(55%)	146(53%)	154(56%)	746(55%)
CMC CLOSER	100(37%)	98(36%)	92(34%)	98(36%)	94(34%)	482(35%)
TIE	26(10%)	27(10%)	30(11%)	29(11%)	25(9%)	137(10%)

OPERATIONAL VIEWPOINTS ON WAVE FORECASTING FOR THE B. C. COAST

Owen S. Lange

Marine Meteorologist
Pacific Weather Centre
Atmospheric Environment Service
Vancouver, B. C.

1. Introduction

The sea state forecasting program at the Pacific Weather Centre in Vancouver, B.C. has now been operating for four years. During this time, the marine forecasters have acquired valuable experience and insight in weather and sea state forecasting for offshore regions. Through this experience, they have become aware of what changes are necessary for further improvements. This paper will also discuss the new challenges of extending the sea state forecast program to the inshore waters.

2. History of Sea State Forecasting for the B. C. Waters

- On October 12, 1984, a severe storm hit the B. C. coastal waters.
- In early 1985 the Le Blond Report, which investigated the marine forecasting program on the West Coast, recommended that sea state forecasts be made available.
- In the Summer of 1985, sea state forecasts began for two offshore areas called Bowie and Explorer.
- Studies were initiated in 1985 to establish support systems for sea state forecasting for the inshore waters.
- During July to October 1988, a computer system was used to test the interface between a computer model and the forecaster in preparation for inshore sea state forecasts.
- In April 1989, sea state forecasts were extended to some of the inner coastal waters.

3. Sea State Forecasting Program at the Pacific Weather Centre

a) Analysis:

An analysis of wave data is made every 6 hours (0000, 0600, 1200, 1800 UTC) for the area shown in Figure 1 . The source of data is primarily from ship reports but also includes information from the deep sea buoys anchored off the coast. Several other buoys located closer to the coast add to the data network. These buoys are marked on Figure 2 . The analysis consists of the combined wave height with no attempt to separate the wind waves and swells.

b) Forecasting:

A forecast wave chart is created twice daily for 18 and 30 hour time periods based on the observed data at 0600 UTC and 1800 UTC. This forecast chart covers about half the area of the analyzed chart. The primary sea state forecasting tools used at the Pacific Weather Centre are as follows:

1. sea state pattern recognition and modelling to an isobaric field on surface prognostic charts
2. Bretschneider nomogram for wind wave generation
3. extrapolation of swell trains
4. decay nomogram for decay of wave trains.

The Parametric model output, which is essentially a computerized Bretschneider wave forecasting procedure, is available twice daily. It is not extensively used since it often over builds the seas too rapidly and, likewise, decays them too quickly.

The information from the forecast wave charts are then translated into a worded forecast for the Bowie and Explorer regions.

c. Forecast Output:

The sea state forecasts for the Bowie and Explorer regions are included within the four regular daily marine forecasts for the B. C. coastal waters. The forecast consists of a worded message such as "Seas one to two metres building to three to four metres Thursday afternoon".

4. Challenges and Potential Solutions

The amount of sea state data that is available varies considerably through the course of the day. The late night reporting time (ie. 1200 UTC or 0400 PST) quite often has no ship observations and if it were not for the network of anchored buoys, there would be no data at all. Making a complete analysis at this time is often no more than a simple extrapolation of the 0600 UTC chart. At other times of the day, when good coverage of sea state data are available, the problem becomes one of deciding which of the data are correct and which need to be disregarded.

Experience has shown that for shorter wave periods the buoy data have lower wave heights than the nearby ship reports. For longer wave periods, the buoy data are higher than the comparative ship reports.

Partial solutions to the data problem might be the use of satellite wave sensing systems or some form of radar.

If spectral wave data were routinely available from the offshore buoys then a better assessment of the wave trains might be possible. This could assist in the overall analysis of the wave patterns. Spectral

data was briefly available at the Pacific Weather Centre in 1988 and was found, through a few hindcasting case studies, to have potential value for the operational forecaster.

A spectral sea state model, based on the Canadian Spectral wind fields, would likely assist in the creation of better sea state forecasts.

5. Inshore Sea State Forecasting

The sea state forecasting program for some of the inshore waters of the B. C. coast has just begun. This program will be reviewed and modified as the marine forecasters adjust to the program and responses are received from the mariners.

a) Regions:

There are three different sea state regimes within the B. C. coastal region as shown on Figure 2 .

1. The offshore waters are beyond the continental shelf and on average have a depth of about 2500m. These waters are open to both wind wave generation and the presence of swells from any part of the Pacific. This region has the least amount of coastal topographical influences.

Forecast for these waters began in 1985.

2. The inner waters: West Coast Charlottes, West Coast Vancouver Island, Queen Charlotte Sound, Central Coast, Hecate Strait and Dixon Entrance have strong topographical influences on both the winds and the seas but can also be affected to varying degrees by Pacific swells. These waters are generally less than 400m deep and are often less than 100m.

Forecast for these water began in April 1989.

3. The last group of marine areas include: Georgia Strait, Juan de Fuca Strait, Queen Charlotte Strait and Johnstone Strait. They are generally bounded by mountains on both sides and have very significant local topographical influences. Except for the western entrance of Juan de Fuca and Queen Charlotte Straits, they are unaffected by Pacific swells. The maximum observed depths in these waters are about 500m in Queen Charlotte Strait, 420m in Georgia Strait and only 275m in Juan de Fuca Strait. Deeper depths are found in some of the adjoining inlets.

Forecasts for these waters will not begin in the near future.

b) Sea State Data over the Inner Waters:

There are several buoys located through the inshore waters which provide sea state data. These buoys are marked on Figure 2 . In

addition, sea state information, based on visual estimates from the land, are available from the coastal lighthouses.

c) Coastal Problems:

Topographical influences play a significant role in the sea conditions of these coastal waters. The wind directions are controlled very strongly by the coastal mountains and have a bias to southeast or northwest through most areas with a more east-west orientation through Dixon Entrance. The winds are often enhanced around headlands and through gaps between islands but are also reduced considerably on the downwind side of islands or promontories. All of these local factors are very difficult to incorporate into computer wind models.

The presence of the land also enhances the effects of tides and currents which, when running counter to the seas, can strongly modify the sea state.

Most areas within this coastal region will be affected by swells from the Pacific Ocean. Dixon Entrance, however, is only open to swells coming directly from the west, and even here the Learmouth Bank tends to dissipate the waves before they reach the coastal section of the area. Hecate Strait is another region with considerable variations within it. The the southern section receives swells from the southwest but this generally does not reach the northern section.

e) Forecast Wording:

The use of the combined sea state is adequate for the offshore waters but this is not the most useful means of describing the seas from the inshore waters. A separation of the seas into wind waves and swell would be better but it would be too cumbersome to issue over radio broadcasts, which are still the main means of disseminating the marine forecast information. The solution to this problem, that the Pacific Weather Centre has adopted, is to provide a combined sea state forecast for the exposed open waters with an additional statement about the swells. The worded forecast then uses the following format: “Seas three to four metres, including southwesterly swell over the southern sections”.

6. Conclusions

The Pacific Weather Centre continues to develop and expand its sea state forecasting program. Sea state forecasts for the offshore waters of Bowie and Explorer began in 1985. In April 1989, sea state forecasts were extended into some of the inshore waters. The need for

more data over the vast Pacific Ocean will continue to be a problem but may be alleviated with satellite data and spectral wave information from the fixed offshore buoys.

The effects of the coastal topography, tides, and strong local currents all have a marked influence on the sea conditions throughout the inshore waters. A very dense network of observations including coastal radar would be necessary to provide an accurate description of the sea state in this region. Coupled with this lack of knowledge about the actual conditions, the format of the sea state forecast prevents a completely detailed description of what is expected to develop. The sea state forecast, which the Pacific Weather Centre provides, is just one other piece of information that the mariners can use to help assess the conditions over the water. The mentioning of swells in the forecast will give the information about the sea conditions which is additional to that which can be surmised from the winds alone.

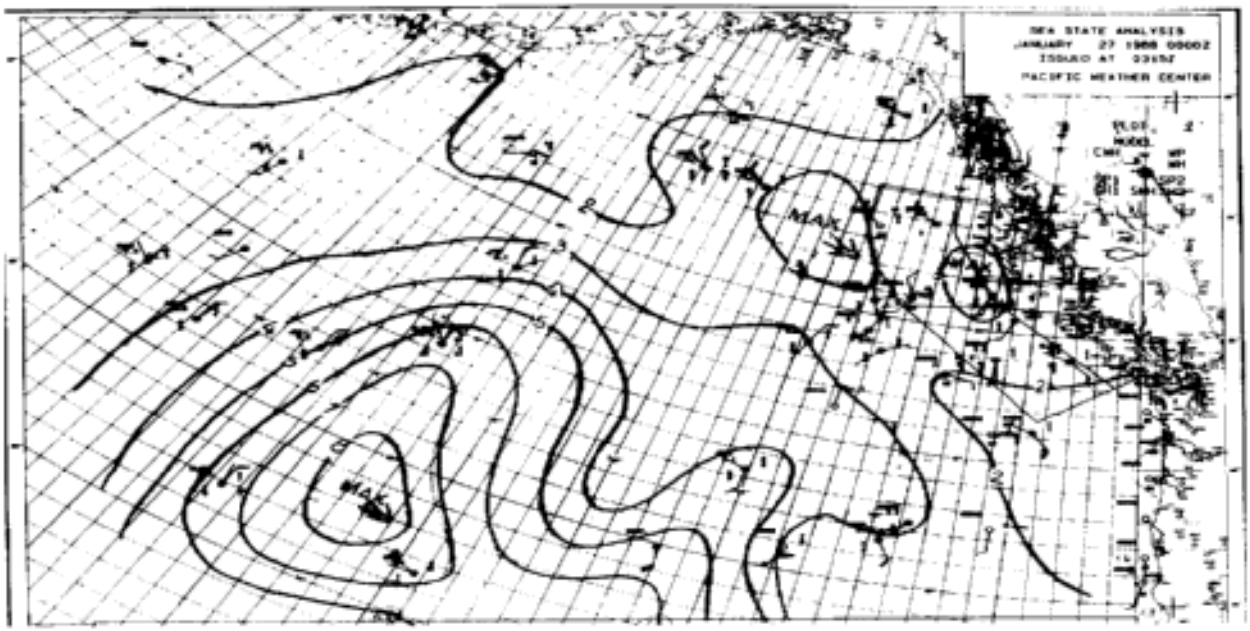

Figure 1 Sea State Analysis Chart

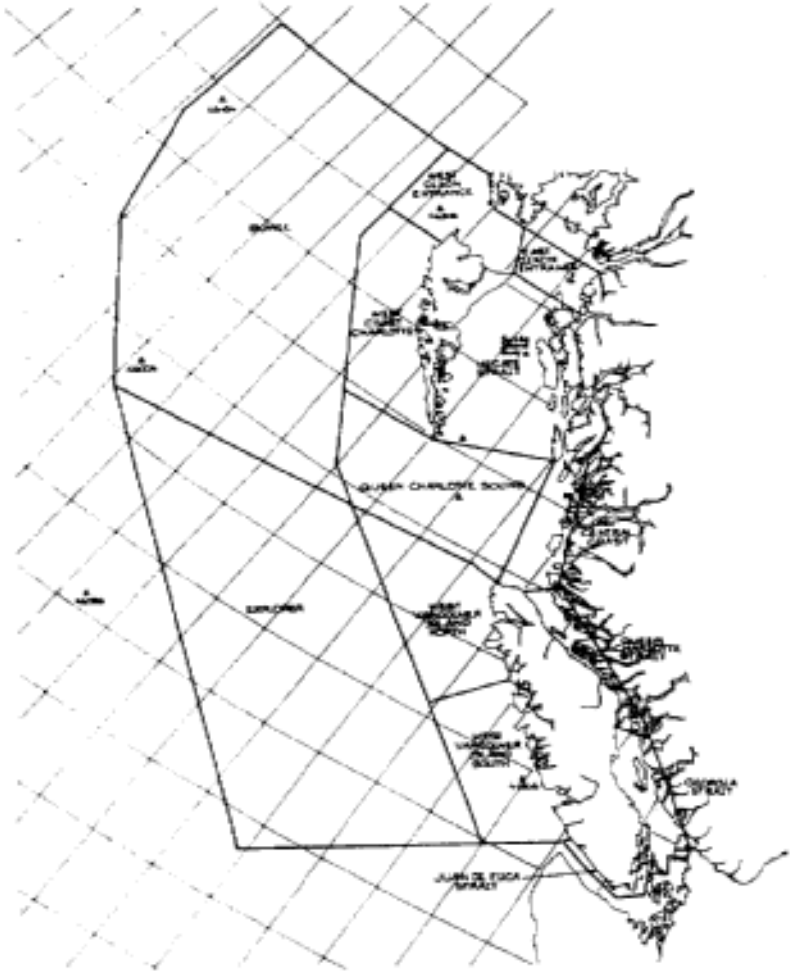

Figure 2 Marine Area Boundaries and Offshore Bouys

TORWAVE: A CALIBRATED PARAMETRIC WAVE MODEL FOR THE TORONTO WATERFRONT, LAKE ONTARIO

[1]Dan McGillivray and [2]Brian Greenwood

[1]The MEP Company
7050 Woodbine Aveue, Suite 100
Markham, Ontario L3R 4G8

[2]Departments of Geography and Geology
Scarborough College, University of Toronto
West Hill, Ontario M1C 1A4

Abstract:

This paper examines the performance of the SMB model before and after calibration in the Toronto area of Lake Ontario. Two calibration procedures are explored: the first involves a re-calculation of the empirical constants in the SMB equations; and the second involves a statistical calibration of the constants in a refined form of the SMB equations. The resulting models, SMB-TOR and TORWAVE respectively, are compared with the original SMB model and the DONELAN model. It is concluded that the performance of the SMB model can be substantially improved for use in fetch restricted waters by the calibration techniques used in the TORWAVE model.

1. INTRODUCTION

Despite the development of sophisticated spectral wave models, the vast majority of coastal engineering studies rely upon simple parametric wave models, like the SMB (Sverdrup-Munk-Bretschneider), for the construction of local deep water wave climates. This is largely due to reasons of practicality, including: past experience and familiarity with the model, availability of both the model and the input data, and simplicity and utility of the output information.

All wave prediction models are based upon semi-empirical formulations derived from prototype environments which are often physically very different from the site of application. Use of these models without calibration often seriously weakens their performance.

The aim of this study is to examine the skill of the SMB model before and after calibration in the Toronto area of Lake Ontario (Fig. 1). Two calibration procedures are explored: the first involves a re-calculation of the empirical constants in the SMB equations; and the second involves a statistical calibration of the constants in a refined form of the SMB equations. The two resulting models, SMB-TOR and TORWAVE respectively, are compared with the original SMB model and the DONELAN model, both of which are endorsed for use in the Toronto Waterfront (e.g. Bishop, 1983) and throughout the Great Lakes.

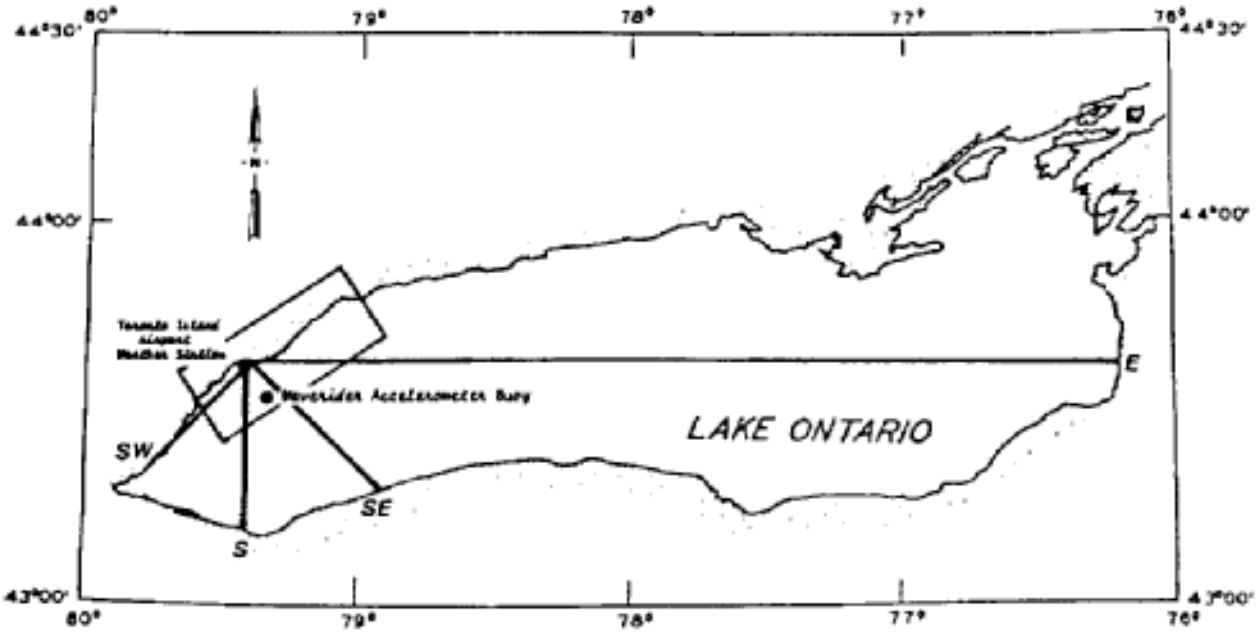

Fig. 1: Toronto Waterfront area and location of wind and wave recording instruments.

2. THE CALIBRATION DATA SET

Calibration of any wave prediction model requires that a comprehensive observed wind/wave data set be assembled. Such a data set was collected in the Toronto area of Lake Ontario as part of the International Field Year on the Great Lakes. The wave data were measured using a non-directional Waverider Accelerometer Buoy which recorded for 20 minutes, at three hour intervals, using a sampling frequency of 1 Hz. The Waverider was located southeast of the Toronto Islands (43.5°N, 79.3°W; Fig. 1) in a water depth of 107.9 m and was in service for approximately one year (March 11, 1972 – April 15, 1973; see MEDS, 1975). This wave data set has been verified through a quality control analysis by Bishop and Donelan (1981) and is considered suitable for the purposes of model calibration.

The wind data were recorded hourly at the Toronto Island Airport Weather Station (43.6°N, 79.4°W; Fig.1). The anemometer was reported to be well exposed and at a height of 11.6 m (Environment Canada, 1982). As illustrated in Figure 1 , winds recorded at this station from the east, southeast, south and southwest, may be defined as 'over-water winds' (Richards and Phillips, 1970) and are therefore used without modification (for alternative see Richards et al., 1966; Resio and Vincent, 1977; Schwab, 1978).

The generation of waves which are large enough to cause significant shoreline erosion or damage to engineering structures (approximately H ≥ 2.0 ft (0.6 m)) requires that wind speed and duration exceed some

minimum value over a constant direction. These conditions are usually associated with the passage of meteorological depressions and are often referred to as 'storm wave events'. Such events are frequently separated by long periods of near zero wave activity; therefore criteria must be established to extract from the wind record those events responsible for wave generation.

According to Hale and Greenwood (1980) no absolute definition of what constitutes a storm wave event exists and the simple meteorological measures used to identify storm magnitude (barometric pressure, maximum hourly wind speed, maximum gust, etc.) are inappropriate in the context of wave prediction. The following criteria are therefore proposed (after Hale and Greenwood, 1980):

(a) Winds must occur within a range of over-water directions affecting wave activity. In the Toronto area this would involve winds from the east, southeast, south and southwest.

(b) Wind speed, defined as the cumulative hourly average during the storm event, must not be less than 19 km h^{-1}. This value was adopted since a wind speed of 19 km h^{-1} will not theoretically generate significant waves greater than 1 m in height or 4 s in period regardless of fetch or duration. A storm event was considered terminated when the cumulative average wind speed fell below 19 km h^{-1}.

(c) The duration of wind speeds equal to or greater than 19 km h^{-1} must not be less than 6 hours. Waves take a certain length of time to develop over any significant fetch length and therefore a single hour of wind, no matter how strong, will not be particularly important unless it is preceded or followed by winds of similar intensity. An arbitrary value of 6 hours was taken as the minimum duration of a storm event.

(d) Wind directional variability must be restricted to fluctuations less than ± 45° from the predominant direction except where fluctuations were for a period of time not exceeding two hours, or the the wind reverted to its original direction (and minimum speed or greater) for a further period of not less than 6 hours within a 7 hour interval. The predominant direction was determined on the basis of the maximum number of hours of wind from a given direction. Where winds blew an equal number of hours from more than one direction the predominant wind was defined by the highest hourly average wind speed.

Application of these criteria to the hourly wind data over the test period (March 11, 1972 - April 15, 1973) resulted in the identification of 74 discrete storm wave events. To verify the procedure, an attempt was made to match these events (defined by wind) with actual wave events (defined as $H_{1/3} \geq 2.0$ ft (0.6 m)) in the MEDS (1975) record.

It should be noted that during the test period, 2258 wave observations were recorded and 941 (29.4% of the total record) were missed, possibly due to instrument failure. No information on wave direction was provided by the Waverider and, because the instrument was positioned at an offshore location, waves could be measured from any compass direction.

The storm event criteria failed to identify 15 observed wave events but each of these were found to occur during periods of strong offshore winds and would not result in waves reaching the Toronto shoreline area. Of the 74 storm wave events identified by the storm event criteria, 15 were found to occur during the missing segments of the wave record. of the remaining 59 events, 6 were found to be questionable for calibration purposes: 5 exhibited wave heights which were constantly low given the recorded wind speeds, suggesting potential instrument malfunction (perhaps due to ice or power loss); and in 1 case, the recorded wave heights were questionably high given the reported wind speeds. Rather than including these uncertain data, the 6 events were eliminated from the calibration data set.

The final calibration wind/wave data set consisted of 264 observations representing 53 storm wave events of various durations and directions: east (30); southeast (1); south (1); and southwest (21). Each 3 hourly observation contained information on the date and hour of storm initiation, the duration of the storm, the average hourly wind speed, the direction of the storm waves (assumed coincident with the wind direction) and the recorded significant wave height ($H_{1/3}$) and peak period (T_p). For the purposes of this study it was assumed that $T_p = T_{1/3}$. This was considered reasonable given the relationship verified experimentally by Goda (1974): $T_{1/3} = \sqrt[4]{4/5\ T_p} \simeq 0.95\ T_p$.

3. THE MODELS

The wave models examined in this study predict monochromatic wave parameters (specifically, significant wave height ($H_{1/3}$), period ($T_{1/3}$) and direction) which represent a very crude approximation of wave conditions in nature, compared for example to directional spectra. Nevertheless, monochromatic wave parameters are considered by some to be more practical for wave climate investigations (e.g. Neu, 1971); furthermore they directly satisfy the input specifications of most available wave transformation models which are used in the analysis of nearshore and surf zone wave climates (McGillivray, 1988). The main problem with parametric wave models is their inability to deal with swell; however in fetch restricted environments, such as Lake Ontario where swell is virtually nonexistent, this problem is not considered serious.

3.1 The SMB Model

Significant wave height and period are determined by the SMB model as a function of wind speed, duration and fetch. The model equations may be expressed as:

$$H_{1/3} = A_1 \, g^{-1} \, U^2 \tanh \left[B_1 \, (gF/U^2)^{m1} \right] \quad (1)$$

$$T_{1/3} = A_2 \, 2\pi/g \, U \tanh \left[B_2 \, (gF/U^2)^{m2} \right] \quad (2)$$

$$t_{min} = 2 \int_0^{F_{min}} \frac{dF}{A_2 \, U \tanh \left[B_2 \, (gF/U^2)^{m2} \right]} \quad (3)$$

where: g is the acceleration due to gravity; U is the wind speed; Fmin is the observed fetch length; t_{min} is the limiting duration and F_{min} is the fetch length corresponding to t_{min}. The globally derived empirical constants are (Bretschneider, 1973):

$A_1 = 0.283$	$B_1 = 0.0125$	$m_1 = 0.042$
$A_2 = 1.2$	$B_2 = 0.077$	$m_2 = 0.25$

Despite the arguments put forward by Resio and Vincent (1979), the effective fetch (Saville, 1954; CERC2 1977) rather than the available fetch lengths were used in this application of the SMB model. This greatly changed the values of F used in the Toronto Waterfront (Table 1).

3.2 The DONELAN Model

Unlike other simple parametric wave models, the DONELAN model does not assume that wind direction (ϕ) and wave direction (ψ) are the same (Donelan, 1980; Donelan et al., 1982). The equations for this model may be written:

$$H_{1/3} = 0.00366 \, g^{-0.62} \, U_c^{1.24} \, F_\psi^{0.38} \quad (4)$$

$$T_p = 0.54 \, g^{-0.77} \, U_c^{0.54} \, F_\psi^{0.23} \quad (5)$$

$$tmin = 30.1 \, g^{-0.23} \, U_c^{-0.54} \, F_\psi^{0.77} \quad (6)$$

where: $U_c = U \cos \theta$ and is the wind speed as a function of the peak wave direction; θ is the angular difference between the primary wind direction (ϕ) and the peak wave direction (ψ); and F is the fetch length in the direction of wave approach. The wave approach direction is calculated by maximizing the term $[(\cos \theta)^{0.54} \, F_\psi^{0.23}]$. Simply stated, the wave direction is biased towards the longest fetch. In the Toronto Waterfront this suggests that winds from the northeast and west may also contribute to the deep water wave regime and southeast winds generate waves from the eastern octant (Table 2).

3.3 The SHB-TOR Model: Calibration of the SMB Equations

Calibration of the SMB equations for the Toronto Waterfront simply involves re-calculating the empirical constants following Bretschneider's (1952) procedure:

(a) Using the effective fetch lengths (Table 1) and Equation 3, the measured wind and wave observations are divided into two groups: the fetch-limited conditions (142 observations) and the duration-limited conditions (122 observations).

(b) Using only the fetch-limited observations, the dimensionless ratios (gF/U^2; C_o/U; $gH_{1/3}/U^2$) are calculated and plotted as shown in Figure 2 . Note that C_o is the deep water wave phase velocity.

(c) The new empirical constants are then determined by computing the best fit line through the data: m_1 and m_2 are given by the slope of the line; A_1 and A_2 are solved for the upper range of the measured wind/wave data set (i.e. where $gF/U^2 = 100{,}000$) and finally B_1 and B_2 are solved at the intercept of the line where $gF/U^2 = 1.0$. The resulting empirical constants for the Toronto Waterfront are:

$A_1 = 0.426$ $B_1 = 0.0132$ $m_1 = 0.376$
$A_2 = 1.74$ $B_2 = 0.0464$ $m_2 = 0.267$

A comparison of these site-specific empirical constants with the universal constants determined by Bretschneider (1973) shows that the values differ by only small amounts. However the SMB-TOR curves agree more closely with the best fit regression lines than do the SMB curves (Fig. 2).

Table 1: Available and effective fetch lengths from the Toronto Island Weather Station, Lake Ontario.

	East	Southeast	South	Southwest
Available Fetch (mi)	160.0	32.8	30.2	21.0
Available Fetch (km)	257.5	52.8	48.6	33.9
Effective Fetch (mi)	66.5	43.5	27.3	18.0
Effective Fetch (km)	107.0	70.0	43.9	29.0

Table 2: F_ψ and θ for the Toronto Waterfront, calculated for the Toronto Island Airport Weather Station.

Wind Direction (ϕ)		Fetch ($F_{(\psi)}$ in km)	Wave Direction (ψ)	($\theta = \lvert\psi-\phi\rvert$)
Northeast	45°	154.7	75°	30°
East	90°	169.7	90°	0°
Southeast	135°	131.2	105°	30°
South	180°	46.3	180°	0°
Southwest	225°	38.7	225°	0°
West	270°	21.7	255°	15°

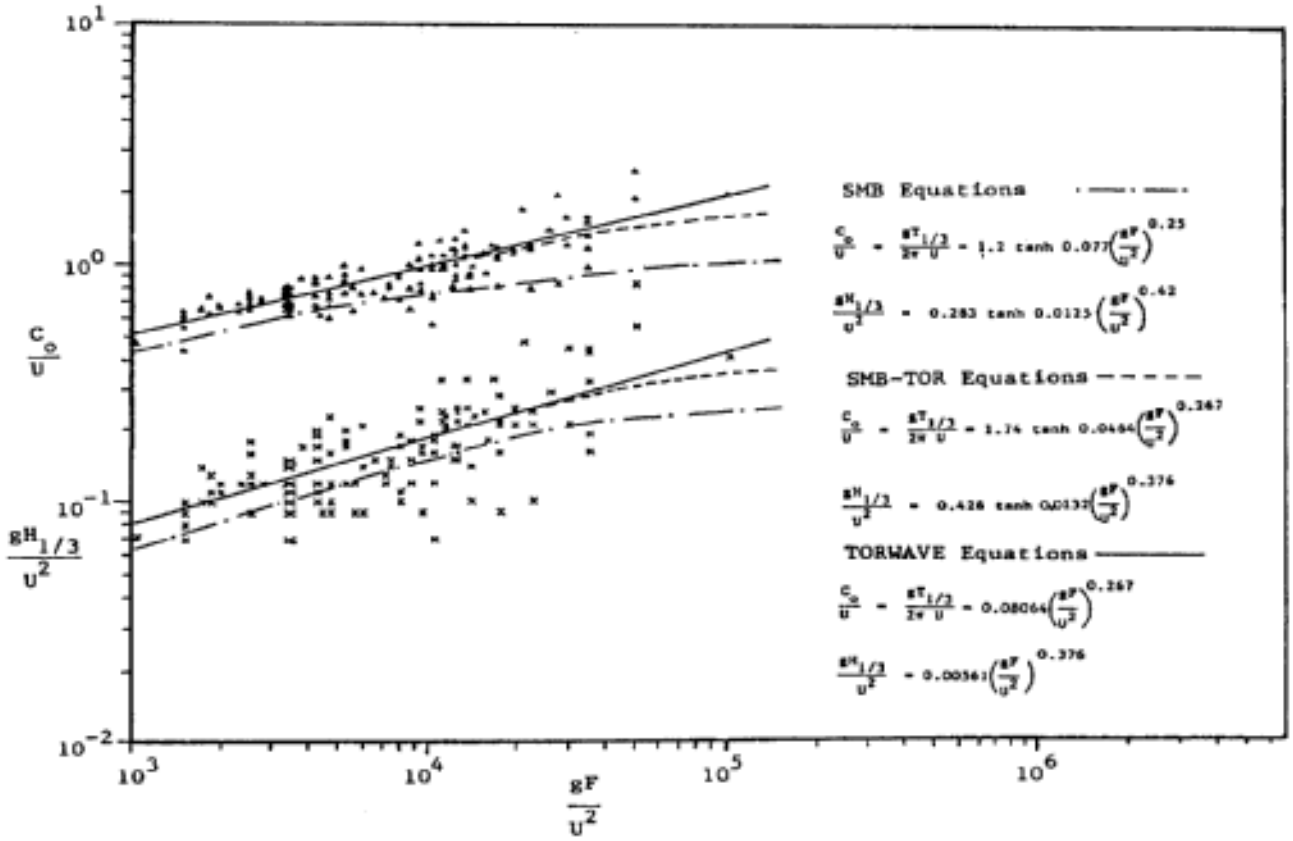

Fig. 2: Empirical relationships between wind speed and fetch and the resulting wave heights (×) and periods (▲) measured in the Toronto Waterfront.

3.4 The TORWAVE Model: Refinement and Calibration of the SMB Equations

Wilson (1963) suggested that the SMB equations could be refined to the form:

$$H_{1/3} = \beta_1 \, g^{-1} \, U^2 \, (gF/U^2)^{m1} \qquad (7)$$

$$T_{1/3} = \beta_2 \, 2\beta/g \, U \, (gF/U^2)^{m2} \qquad (8)$$

where: β_1 and β_2 are empirical constants of proportionality. He noted that equations of this form have not been investigated and may result in improved predictions of wave characteristics. The equation for t_{min} was not described by Wilson (1963) but it would take the form:

$$t_{min} = 2 \int_0^{Fmin} \frac{dF}{\beta_2 U (gF/U^2)^{m2}} \qquad (9)$$

The empirical constants in Equations 7, 8 and 9 were resolved for the Toronto Waterfront by a simple power regression analysis using the fetch-limited observations (Fig. 2):

$\beta_1 = 0.00561$ $m_1 = 0.376$
$\beta_2 = 0.8064$ $m_2 = 0.267$

Note that the TORWAVE equations do not contain the hyperbolic tangent function; therefore no upper limit is defined. These equations are considered to be satisfactory for use within the range $1000 \leq gF/U^2 \leq 100{,}000$ which defines the limits of the calibration data. This assumption is valid in the fetch restricted waters of Lake Ontario but care must be taken in applying the equations in open ocean environments.

4. EVALUATION AND COMPARISON OF MODEL PERFORMANCE

Ideally the skill of each of the wave models should be tested by comparing their predictions against a unique set of wave observations, different from the one used for model calibration. Unfortunately such a data set is not available and the model performance tests had to be limited to those which could be conducted using the original MEDS (1975) wave data.

Recall that the model calibrations were carried out using only the fetch-limited cases, representing 142 of the 264 observations. This allowed the model performance tests to be conducted using two test data sets: (a) the full data set (264 observations) has been used to determine the relative merits of the calibration procedures employed; and (b) the duration-limited cases (122 observations not used for model calibration) have been used to establish which of the four models performed best in the Toronto Waterfront.

4.1 Observed Versus Predicted Wave Characteristics

Analysis of the wave characteristics during a single storm (e.g. Fig. 3) shows that the time span identified by the storm event criteria was reasonable and TORWAVE provided the best estimates. Nevertheless, the duration-limited wave conditions at the beginning of the storm were underestimated by all of the models and the predicted storm waves ended somewhat prematurely. This highlighted several of

the limiting assumptions involved in the wave modelling approach; for example it was assumed that: (a) each storm event began under calm water conditions; (b) waves increased in magnitude as a function of wind speed, duration and effective fetch until a steady-state condition was reached; and (c) the event ended as the winds subsided or significantly changed direction. In reality the water surface is rarely completely calm at the beginning of a storm and wave conditions do not end abruptly as the wind conditions change; although observations indicate that the wave regime in Lake Ontario responds quickly (within a few hours) to changes in the wind regime and swell is rare in this fetch restricted environment. Furthermore, given that the objective of the storm event criteria was to identify wave events greater than or equal to 2.0 ft (0.6 m) it is noted that these limiting assumptions will not seriously impede the performance of the TORWAVE model.

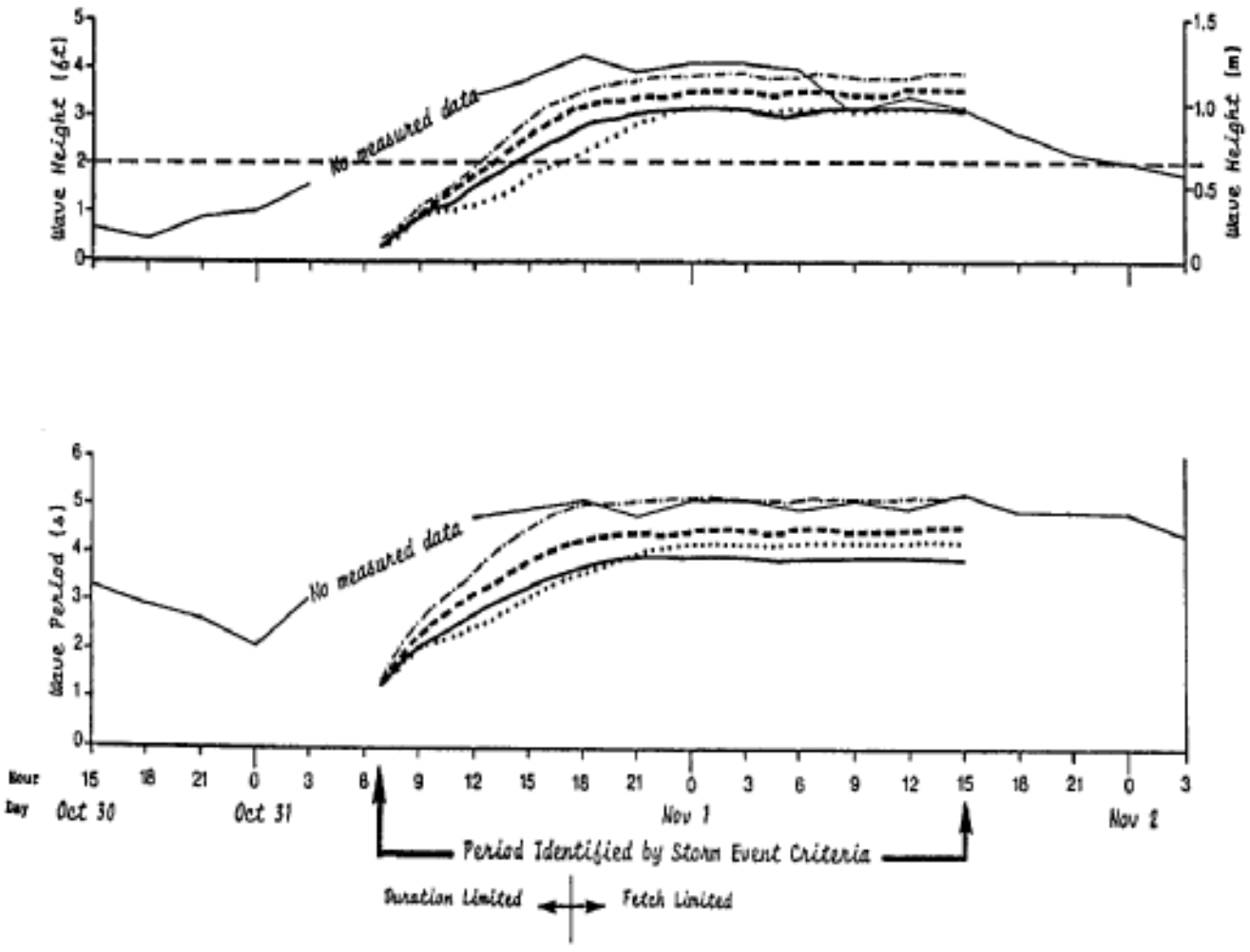

Fig. 3: Comparison of measured and predicted waves during a storm event: EAST - 72·10·31; —— Measured; -·-·- TORWAVE; - - - -SMB-TOR; ——— SMB; ····· DONELAN

Scattergrams of measured versus predicted wave height and period, from each of the wave models, indicate the improved performance of the calibrated models (Figs. 4 and 5). The SMB and DONELAN models are shown to underestimate wave height and period, particularly in the upper range. The SMB results are not consistent with previous studies which report that the model tends to overestimate wave characteristics in the upper range (e.g. CERC, 1977; Brebner and Le Mehaute, 1961; Bishop, 1983). This conflict may be attributed to the fact that the SMB model has been examined in open ocean environments (CERC, 1977) where pressure-derived winds tend to be overestimates of the actual surface winds (e.g. Swail et al., 1984). Furthermore it has been applied in some studies of enclosed water bodies using available rather than effective fetch (Bishop, 1983). Both of these conditions, either together or separately, would lead to overpredictions of the wave characteristics. The results shown for the DONELAN model also conflict with Bishop's (1983) analysis which showed that the predicted wave characteristics correlated favorably with a portion of the Toronto MEDS (1975) data. However, Bishop (1983) carefully screened the wind events to represent only "steady-state" conditions which are fetch-limited; duration-limited conditions were not tested.

As expected, the calibrated models yielded scatterplots of fetch-limited conditions which more closely fit the perfect prediction line (Figs. 4 and 5). However, of greater interest to the verification of the calibrated models is the fact that the duration-limited data followed the same trend. Note that while both the SMB-TOR and TORWAVE predictions of wave height (Fig. 4c and d) appear to be similar in their agreement with the measured data, the TORWAVE predictions of wave period (Fig. 5d) are best overall.

4.2 Model Performance Statistics

The model performance statistics employed in this study are summarized in Table 3 . They were proposed by Willmott (1982) who clearly showed that real significance and statistical significance do not necessarily exhibit a close correspondence. For example, it may be shown that the commonly employed Pearson product-moment correlation coefficient (r) and its square, the coefficient of determination (r^2), are both insufficient and often misleading measures of model accuracy. The value of r reveals only the correlation between the observed and predicted values and r^2 indicates the proportion of variance explained by the model but not necessarily the equality of matched values.

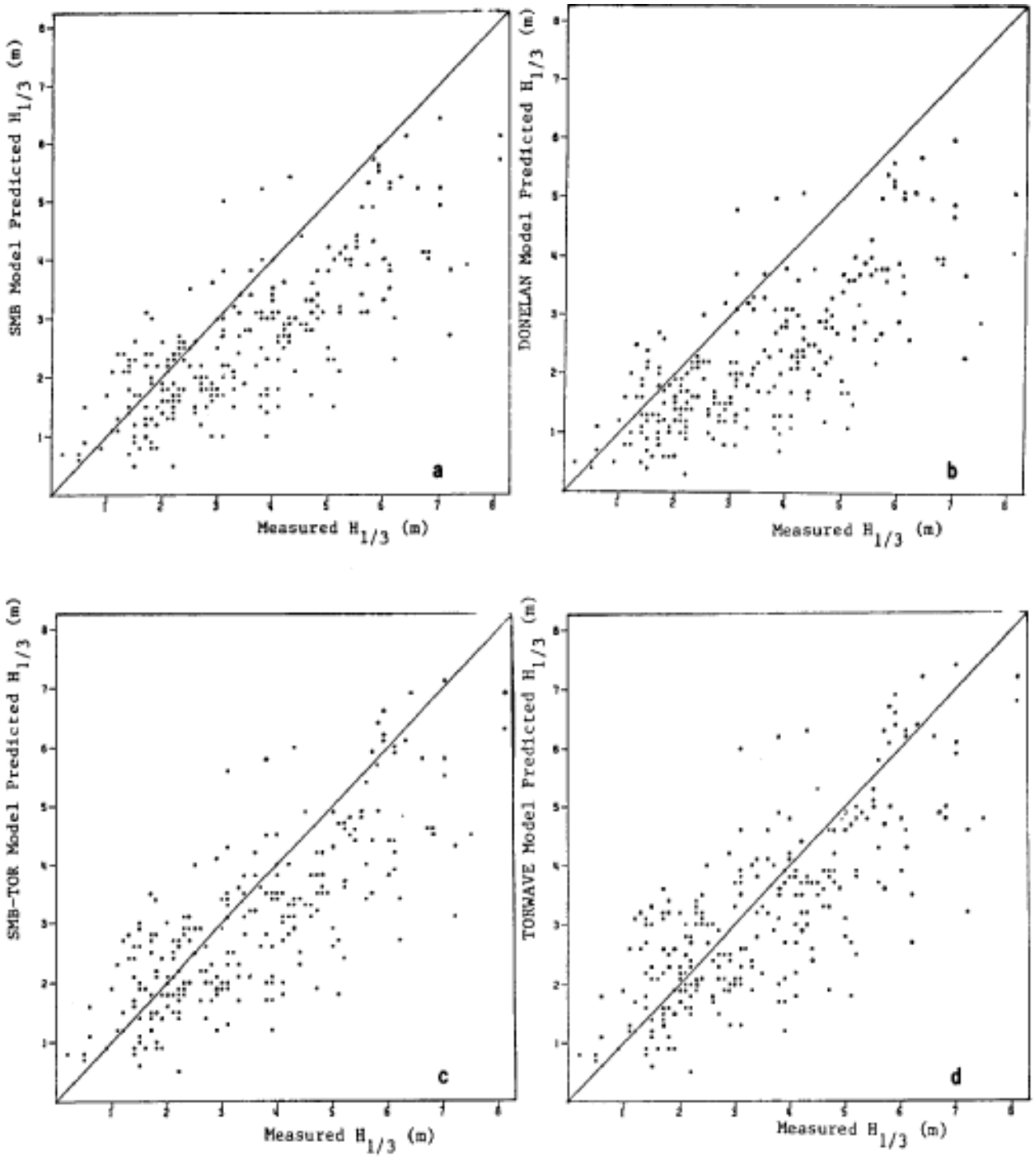

Fig. 4: Scattergrams of measured versus predicted wave height: (a) SMB; (b) DONELAN; (c) SMB-TOR and (d) TORWAVE (• fetch-limited; ◦ duration-limited).

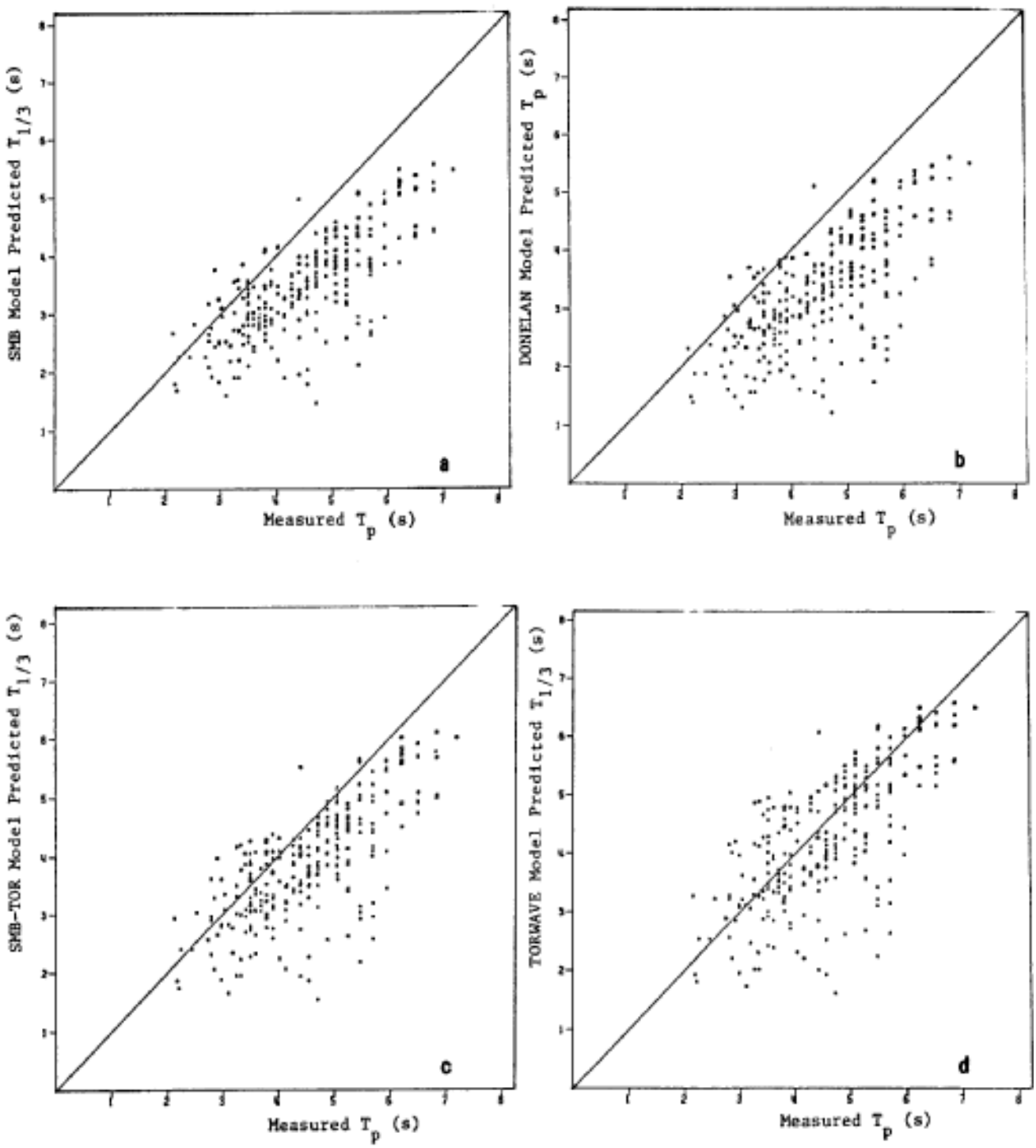

Fig.5: Scattergrams of measured versus predicted wave period: (a) SMB; (b) DONELAN; (c) SMB-TOR and (d) TORWAVE (• fetch-limited; ∘ duration-limited).

Table 3: Statistical measures of model performance (after Willmott, 1982).

I. SUMMARY STATISTICS:

1. Mean Observed: $\bar{O} = N^{-1} \sum_{i=1}^{N} O_i$

2. Mean Predicted: $\bar{P} = N^{-1} \sum_{i=1}^{N} P_i$

3. Standard Deviation (Observed): $S_o = \left[N^{-1} \sum_{i=1}^{N} (O_i - \bar{O})^2 \right]^{1/2}$

4. Standard Deviation (Predicted): $S_p = \left[N^{-1} \sum_{i=1}^{N} (P_i - \bar{P})^2 \right]^{1/2}$

5. Intercept (a) and Slope (b) of the Least Squares Regression: $\hat{P}_i = a + b O_i$

II. DIFFERENCE STATISTICS:

6. Mean Biased Error: $MBE = N^{-1} \sum_{i=1}^{N} (P_i - O_i)$

7. Mean Absolute Error: $MAE = N^{-1} \sum_{i=1}^{N} |P_i - O_i|$

8. Root Mean Square Error: $RMSE = \left[N^{-1} \sum_{i=1}^{N} (P_i - O_i)^2 \right]^{1/2}$

9. Root Mean Square Systematic Error: $RMSE_S = \left[N^{-1} \sum_{i=1}^{N} (\hat{P}_i - O_i)^2 \right]^{1/2}$

10. Root Mean Square Unsystematic Error: $RMSE_U = \left[N^{-1} \sum_{i=1}^{N} (P_i - \hat{P}_i)^2 \right]^{1/2}$

11. Index of Agreement:

$$D = 1 - \left[\sum_{i=1}^{N} (P_i - O_i)^2 \Big/ \sum_{i=1}^{N} (|P_i - \bar{O}| + |O_i - \bar{O}|)^2 \right], \quad 0 \le D \le 1$$

The summary and difference univariate statistics listed on Table 3 are self-explanatory although it is useful to note:

(a) The mean bias error (MBE) simply measures the difference between the mean of the predicted and observed variables.

(b) The mean absolute error (MAE) and root mean square error (RMSE) are among the best overall measures of model skill as they summarize the mean difference between the observed and predicted values; note that MAE is less sensitive to extreme values than RMSE.

(c) Because a model should explain most of the major trends present in the observed record, it is important to know what proportion of the RMSE is systematic ($RMSE_s$) and what proportion is unsystematic ($RMSE_u$). With respect to a 'good' model, $(RMSE_s)^2$ should approach zero while $(RMSE_u)^2$ should approach the RMSE.

(d) The index of agreement (D) provides a measure of the relative size of differences and is intended to be a descriptive measure which is both relative and bounded ($0 \leq D \leq 1$), making it useful for drawing cross-comparisons between models. As the agreement between the observed and predicted values increases, D approaches 1.

The model performance statistics were computed in this study using: the full wave data set representing 264 observations (Table 4); and the duration-limited cases representing the 122 observations not used in model calibration (Table 5). A comparison of Tables 4 and 5 shows a decrease in the level of accuracy of all model predictions for the duration-limited cases. This was not unexpected in the results from the calibrated models, given the re-use of the calibration data. However, because a similar decrease in accuracy is apparent in each of the models tested, it may be suggested that: (a) the wave characteristics in the initial hours of a storm event are not well estimated; and (b) the model tests conducted with the full wave data set (264 observations) are likely indicative of the results one could expect from future tests using a unique wave data set from the Toronto Waterfront area.

The summary statistics (Tables 4 and 5) all indicate that each model tested tends to underestimate the corresponding observed parameters. However, TORWAVE predictions offer the best overall estimates of the observed means and the variability contained in the observed record. Furthermore, while the regression parameters reveal the systematic (linear) underpredictions of each model, they also show that the TORWAVE predictions most closely approach the perfect prediction line ($P_i = O_i$).

The difference statistics reflect the magnitude of the errors involved in the model predictions, and again TORWAVE results are shown to contain the least error (Tables 4 and 5). The RMSE tends to produce a high estimate of the actual average error, particularly when extreme differences occur. Note that the RMSE is least for TORWAVE predictions; it may be seen for example that TORWAVE estimates of wave height are, on average, 0.5 ft (0.15 m) closer to the observed wave heights compared to the DONELAN model predictions.

Table 4: Statistical Measures of Wave Model Performance: Fetch and Duration-Limited Data Set

	Model Performance Measures	Wave Height SMB	DONELAN	SMB-TOR	TORMAVE	Wave Period SMB	DONELAN	SMB-TOR	TORMAVE
Summary Statistics	1) $\bar{O}$	3.4	3.4	3.4	3.4	4.49	4.49	4.49	4.49
	2) $\bar{P}$	2.6	2.3	3.0	3.2	3.46	3.20	3.84	4.23
	3) S_o	1.7	1.7	1.7	1.7	1.05	1.05	1.05	1.05
	4) S_p	1.2	1.2	1.4	1.5	0.83	0.96	0.96	1.11
	5) N	264	264	264	264	264	264	264	264
	6) a	0.7	0.4	0.8	0.9	0.88	0.62	0.90	0.97
	7) b	0.6	0.5	0.6	0.7	0.58	0.64	0.65	0.73
Difference Statistics	8) MBE	-0.8	-1.2	-0.5	-0.3	-1.03	-1.21	-0.66	-0.27
	9) MAE	1.1	1.3	0.9	0.9	1.07	1.23	0.78	0.66
	10) RMSE	1.3	1.6	1.2	1.1	1.26	1.44	1.01	0.90
	11) $RMSE_s$	1.1	1.4	0.8	0.6	1.01	1.26	0.77	0.37
	12) $RMSE_u$	0.8	0.8	0.9	0.9	0.57	0.69	0.67	0.81
	13) D	0.8	0.7	0.9	0.9	0.68	0.65	0.77	0.82
	14) r^2	0.6	0.6	0.6	0.6	0.53	0.49	0.51	0.47

H, b, D, and r^2 are dimensionless; the remaining indices have the units of feet for wave height and seconds for wave period. Significant figures are 2 for wave height and 3 for wave period.
All values of r^2 are significant at $\alpha = 0.05$.

Table 5: Statistical Measures of Wave Model Performance: Duration Limited Data Set

	Model Performance Measures	Wave Height SMB	DONELAN	SMB-TOR	TORMAVE	Wave Period SMB	DONELAN	SMB-TOR	TORMAVE
Summary Statistics	1) $\bar{O}$	2.8	2.8	2.8	2.8	4.23	4.23	4.23	4.23
	2) $\bar{P}$	2.0	1.5	2.3	2.5	3.03	2.69	3.36	3.74
	3) S_o	1.5	1.5	1.5	1.5	1.05	1.05	1.05	1.05
	4) S_p	1.0	0.8	1.1	1.2	0.74	0.74	0.89	1.08
	5) N	122	122	122	122	122	122	122	122
	6) a	0.7	0.6	0.8	0.9	1.19	1.03	1.30	1.46
	7) b	0.5	0.3	0.5	0.5	0.44	0.39	0.49	0.54
Difference Statistics	8) MBE	-0.8	-1.3	-0.5	-0.4	-1.20	-1.53	-0.87	-0.49
	9) MAE	1.0	1.4	0.9	0.9	1.22	1.54	0.98	0.88
	10) RMSE	1.4	1.7	1.2	1.2	1.46	1.77	1.26	1.15
	11) $RMSE_s$	1.2	1.6	0.9	0.8	1.31	1.68	1.01	0.69
	12) $RMSE_u$	0.7	0.6	0.8	0.6	0.58	0.62	0.73	0.92
	13) D	0.7	0.6	0.8	0.8	0.60	0.53	0.66	0.70
	14) r^2	0.3	0.5	0.5	0.5	0.39	0.31	0.33	0.28

H, b, D, and r^2 are dimensionless; the remaining indices have the units of feet for wave height and seconds for wave period. Significant figures are 2 for wave height and 3 for wave period.
All values of r^2 are significant at $\alpha = 0.05$.

Willmott (1982) has suggested that the systematic errors (RMSE.) in model predictions may be substantially reduced through model calibration. The relative merits of the two procedures used to calibrate the SMB model may therefore be examined by evaluating the RMSE, before and after calibration. As shown in Tables 4 and 5 the calibration procedures used in the TORWAVE model appear to be superior to those used in the SMB-TOR model.

It is difficult to distinguish any difference between the index of agreement values (D) for wave height estimates from the SMB-TOR and TORWAVE models. Nevertheless, these measures indicate the successful performance of TORWAVE and the D values for wave period confirm this finding.

5. CONCLUSIONS

The model performance evaluation has shown that the TORWAVE model provides the best estimates of wave height and period. Despite its simplifying assumptions, TORWAVE offers a practical modelling procedure for the construction of deep water wave climates in the Toronto Waterfront area.

It is concluded that the direct application of existing parametric wave models (like the SMB or DONELAN models) without calibration can result in serious underestimates of wave characteristics, particularly in fetch restricted environments. Nevertheless the performance of these models (in this case the SMB) can be substantially improved by calibrating the model for the site of application. It is therefore recommended that where possible, the procedures used in the TORWAVE model should be incorporated into future applications of parametric wave models throughout the Great Lakes.

Acknowledgements

This paper forms part of the research carried out by D. McGillivray under the supervision of B. Greenwood for the degree of Ph.D. at the University of Toronto, supported by operating grants from NSERC. The work was also supported through a National Research Council Postgraduate Scholarship and an Ontario Graduate Scholarship. The authors also wish to acknowledge Mr. Ross Brown for his comments on a very early version of the manuscript and The MEP Company for the unrestricted use of their computer facilities.

References

Bishop, C.T. 1983: Comparison of manual wave prediction models. J. Waterways, Port, Coastal and Ocean Eng., 109(1): 1-17.

Bishop, C.T. and Donelan, M.A. 1981: Verification of 1972 Lake Ontario waverider data. National Water Research Inst., Hydraulics Div. Tech. Note 81-21.

Brebner, A. and Le Mehaute, B. 1961: Wind waves at Cobourg, Lake Ontario. Queen's University, Civil Eng. Rept. No. 19, 44 p.

Bretschneider, C.L. 1952: The generation and decay of wind waves in deep water. Trans. Amer. Geophys. Union 33(3): 381-389.

Bretschneider, C.L. 1973: Prediction of waves and currents. Look Lab/Hawaii, 3(1).

CERC, 1977: Shore Protection Manual. U.S. Army Coastal Eng. Research Center, 3rd edition, 3 volumes.

Donelan, M.A. 1980: Similarity theory applied to the forecasting of wave heights, periods and directions. Proc. Canadian Coastal Conf., April 22-24, Burlington, Ontario, 47-61.

Donelan, M.A., Hamilton, J. and Hui, W.H. 1982: Directional spectra of wind generated waves. National Water Research Inst.,unpubl. rept., Burlington, Ontario.

Environment Canada, 1982: Canadian climate normals 1951-1980. Atmospheric Environment Service, vol. 5 Wind, 212 p.

Goda, Y. 1974: Estimation of wave statistics from spectral information. Proc. Internat. Symp. Ocean Wave Measurement and Analysis, 320-337.

Hale P.B. and Greenwood, B. 1980: Storm wave climatology: A study of the magnitude and frequency of geomorphic proces. In The Coastline of Canada, (ed. S.B. McCann), Geol. Survey of Canada, Paper No. 80-10, 73-88.

McGillivray, D.G. 1988: Modelling Shoreline Stability: Predicting time-averaged rates of longshore sediment transport in the Toronto Waterfront, Lake Ontario, Canada. Ph.D. Thesis, University of Toronto, Toronto, Ontario, 311 p.

MEDS, 1975:Waves recorded off Toronto, Lake Ontario, Stn. 65, March 11, 1972 to April 15, 1973. Marine Environmental Data Service, Environment Canada.

Neu, H.J.A.1971: Wave climate of the Canadian Atlantic coast and continental shelf - 1970. AOL/BIO Rept. 1971-10, 103 p.

Resio, D.T.and Vincent, C.L. 1977: Estimation of winds over the Great Lakes. ASCE, J. Waterway, Port, Coastal and Ocean Div., 103: 265-283.

Resio, D.T. and Vincent, C.L. 1979: A comparison of various numerical wave prediction techniques. ASCE, Proc. 11th Offshore Tech. Conf., OTC Paper 3642, 2471-2481.

Richards, T.L. and Phillips, D.W. 1970: Synthesized winds and wave heights for the Great Lakes. Canadian Dept. of Transport, Met. Branch, Clim. Studies No. 17, 53 p.

Richards, T.L. , Dragert, H. and McIntyre, D.R. 1966: Influence of atmospheric stability and over-water fetch on winds over the lower Great Lakes. Monthly Weather Review, 94(1): 448-453.

Saville, T. Jr. 1954: The effect of fetch of fetch width on wave generation. U.S. Army, BEB, Tech. Memo. 70,

Schwab, D.J. 1978: Simulation and forecasting of Lake Erie storm surges. Monthly Weather Review, 106: 1476-1487.

Swail V.R. , Morstch, L.D. and Carr, D.A. 1984: Intercomparison of marine wind data sets. Canadian Climate Centre, Atmospheric Environment Service, Rept. No. 84-15, 84p.

Willmott, C.J. 1982: Some comments on the evaluation of model performance. Bull. Amer. Met. Soc., 63(11): 1309-1313.

Wilson, W.S. 1963: Deep water wave generation by moving wind systems. Trans. Amer Soc. Civ. Eng., 128(3416): 104-148.

THE APPLICATION OF ENVIRONMENTAL DATA TO OFFSHORE DESIGN

[1]R.F. McKenna, [1]I.J. Jordaan, [1]A.R. Marshall and [2]T. Agnew

[1]Faculty of Engineering and Applied Science
Memorial University of Newfoundland
St. John's, Newfoundland A1B 3X5

[2]Canadian Climate Centre
Atmospheric Environment Service
4905 Dufferin St.
Downsview, Ontario M3H 5T4

ABSTRACT

To satisfy safety criteria, offshore structures must be suitably designed to resist the applied environmental loads. Probabilistic techniques are outlined for determining the return period of rare, occasional and frequent environmental loads. Emphasis is placed on loading events that follow a Poisson distribution, for which the key parameters are the arrival rate and the probability distributions of the extreme environmental events. Where processes are combined, loads are obtained by convolution of the constituent parameter distributions.

Examples illustrating the probabilistic approach are given for the ice loading problem. This involves the definition of critical scenarios based on the seasons and conditions over which they apply. The examples draw on wind and ice cover information contained in data bases supported by AES. Hindcast models were used for determining pack ice drift speed.

1. INTRODUCTION

The Canadian offshore environment is characterised by the presence of wind, waves, sea ice and icebergs. The challenge to the engineer is to design a structure to withstand loads resulting from these processes. Design loads corresponding to a specified level of risk are calculated by probabilistic analyses of the environmental data.

The object of engineering design is to ensure that the design resistance exceeds the applied load by a reasonable margin. Traditionally, this was achieved by a "factor of safety" defined as resistance divided by load, typically in the range from 1.5 to 2.0. Engineering practice has now recognised that it is not in general possible to specify unique values of either load or resistance. The present paper addresses the environmental parameters that influence the probability distribution of loads.

The essential features of ice-structure interactions can be summarised in a set of cases or scenarios for which the parameter inputs and the

calculation of loads are similar. Typical ice load scenarios for the Beaufort Sea are multiyear floes in summer, first year and multiyear floes in winter, and breakoff of landfast ice in the spring. For example, maximum multiyear ice loads in summer can be established from the probability distributions of floe size, ice thickness, ice concentration and ice speed.

The calculation of ice loads is assisted using AES (Atmospheric Environment Service) digital data bases that can be accessed by CRISP (Climate Research for Ice Software Package) and MAST (Marine Statistics Software Package) and DUST (Duration Statistics Package). The data bases contain fundamental ice and meteorological information in standard formats. CRISP deals with ice cover data, snow cover data and temperature data accessed from the NOAA-Navy Joint Ice Center charts coded according to the World Meteorological Standard SIGRID (Sea Ice Grid) and the AES Regional data bases covering the east coast, Hudson Bay and the Canadian arctic (Agnew et al., 1987).

2. PROBABILISTIC MODELLING

One of the refreshing consequences of the probabilistic analysis of loads on offshore structures has been the increased emphasis on modelling, as against data analysis and reduction. No doubt, this has resulted from a shortage of records, and the absence of techniques that are analogous to hindcasting. The result has been that the construction of models, and the reasons and assumptions underlying them, have been given more thought.

The problem is concerned with the maximum of the series of values X_1, X_2, ... Denoting this value as Z, we are interested in

$$Z = \max (X_1, X_2, \ldots, X_i, \ldots) \qquad (1)$$

The values of X are random and have a probability density function (pdf) denoted $f_x(x)$. The distribution of X is called the parent distribution. Since X is random, so is Z. The problem of obtaining the distribution of Z from that of X is essentially one of extremal statistics. The pdf and distribution function of Z are denoted $f_z(z)$ and $F_z(z)$ respectively. This process is illustrated in Figure 1 .

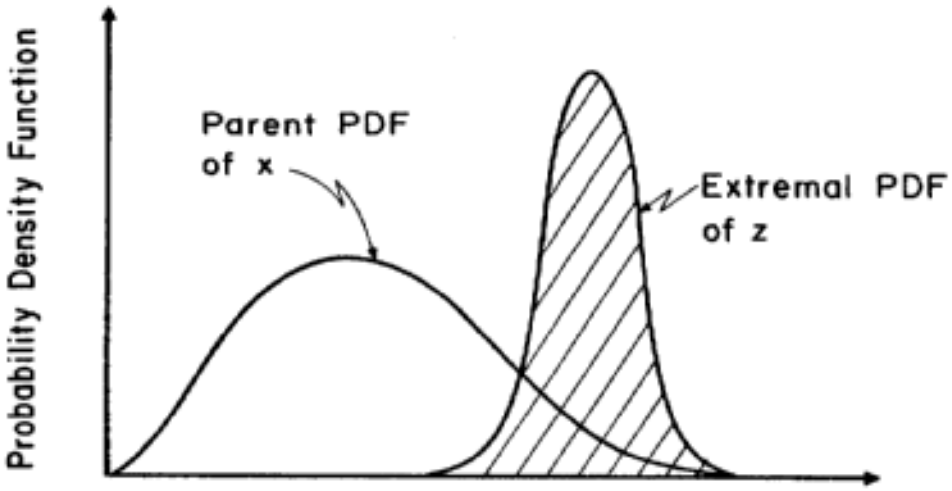

Figure 1. Extremal probability density function

In classical extremal analysis, the number of quantities X_i, say n, in equation (1) is large. This is not generally so in the present context, and it is important to appreciate this fact. The expected number of quantities in equation (1) over the period of one year can be large or small, even less than one (ice islands have a "return period" of more than a thousand years). Therefore the following classification is made (Jordaan, 1988).

Rare events: These are defined so that the probability of occurrence is small enough for the probability of more than one event per year to be neglected, i.e. there will be at most one value in the set (X_1, X_2, ...) of equation (1). The extremal distribution is derived by simple scaling as shown in Figure 2 in which ν = expected number of events in the year ($\nu << 1$). The extremal distributions are characterised by a spike of mass ($1-\nu$) at the origin, and a dif
fuse tail to the right.

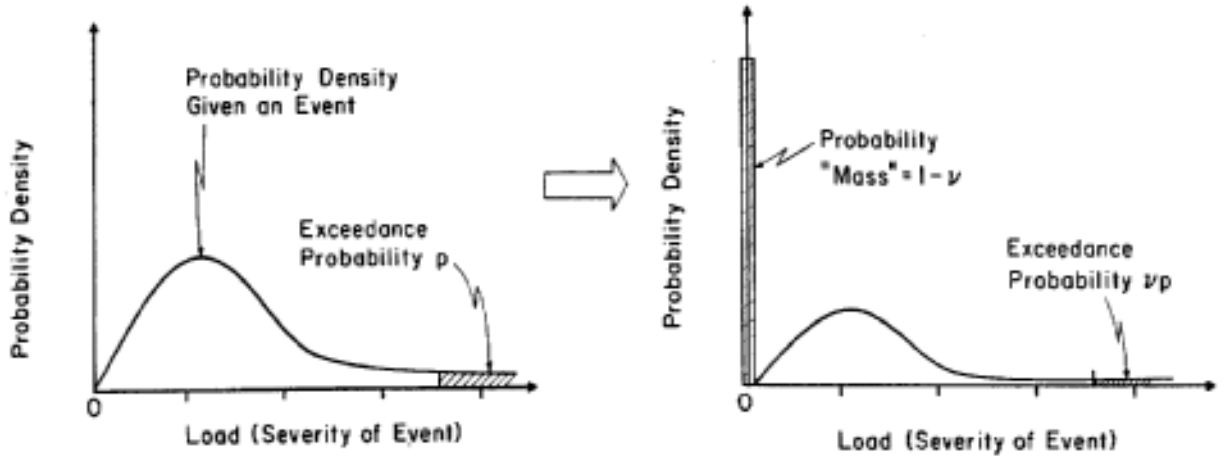

Figure 2. Parent distribution and the distribution of the maximum for rare events

Frequent events: In contrast, the extremal distribution for frequent events is narrow and peaked. If the number of peak quantities X_i in equation (1) is n, then, assuming that the X_i's can be modelled as independent and identically distributed random quantities, the distribution of the extreme Z is

$$F_z(z) - F_x^n(z) \qquad (2)$$

where $F_x(x)$ is the distribution function for x. If n is very large, the distribution of Z tends to the asymptotic extremal distribution

$$F_z(z) = \exp \{ \exp [-\alpha(z-u)] \} \qquad (3)$$

where α and u are parameters of the distribution. There are good mathematical and physical reasons to postulate that the extreme values can be modelled by a distribution function of the form (3). An analogy would be the use of the central limit theorem and the Gaussian distribution in modelling natural averaging processes.

Occasional events: In this case, n is not large and is written as N if it is random. The extremal distribution is given by

$$F_z(z) = \Sigma_{\text{all } n} F_x^n(Z) P_n \qquad (4)$$

where p_n is Pr(N=n). It is convenient to assume that N follows a Poisson distribution

$$pn = e^{-\nu}\nu^n/n! \ , \ n=0,1,2,... \qquad (5)$$

where ν is the expected number of events in the year or time period of interest. Consider events for which X>z. The expected number of arrivals for these will be a proportion of the number ν for all

events. The probability of no quantities X_i being greater than z or all $X_i \leq z$ is just the value of the Poisson distribution (5) with the rate $\nu[1-F_x(z)]$ and with n=0, which substituted into (4) yields

$$F_z(z) = \exp \{ \nu-[1-F_x(z)] \} \quad (6)$$

The necessity to update certain random quantities such as speed or the size of an ice feature conditional on collision with a structure is important (Dunwoody, 1983). Taking the speed V as an example, and letting the symbol C denote the extent of a collision, Bayes' theorem is applied (Jordaan, 1983)

$$p_{v|c}(v|c) = p(C|v)p_v(v)/N \quad (7)$$

where p_v is the generic distribution and N is a normalising constant. Since $p(C|v)$ is proportional to v, the distribution $p_{v|c}$ is different from pv.

3. LOADING SCENARIOS

Rather than trying to anticipate all possible loading situations on an offshore structure, it is more efficient to classify them into a few key scenarios. For the ice load problem, the scenarios depend on the location of the structure and the time of year. Some typical load scenarios are given in Figure 3 . Season boundaries are based on ice concentration criteria and ice thickness information. Distributions of environmental parameters are determined for each season; the season length is a direct input into the expression for arrival rate.

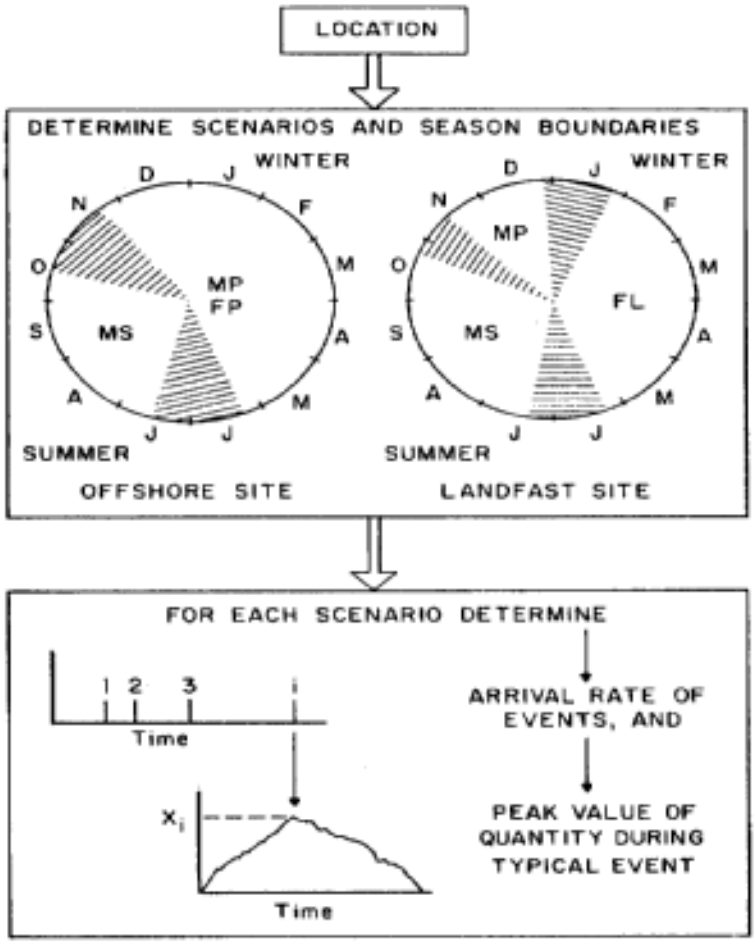

Figure 3. Ice load scenarios according to season - MP: multiyear ice in a first year ice matrix, MS: freely floating multiyear floes, FS: first year pack ice, FL: first year landfast ice

Multiyear floe impacts can occur both in summer and in winter. In both cases the floes can be treated as discrete arrivals, but in winter there is the additional influence of the surrounding pack ice. The important environmental parameters for the multiyear ice scenarios are:

(i) the ice velocity distribution used both for impact speed and arrival rate;

(ii) the season length;

(iii) multiyear ice concentration;

(iv) the floe size distribution, used for impact energy and momentum calculations; and

(v) the ice thickness distribution, not only considering level ice but the dimensions and frequency of ridges.

Maes and Jordaan (1984) and Jordaan et al. (1985) calculated the probability of impact of discrete multiyear floes from the area swept out by their tracks. The number of arrivals in a year is

$$\nu = (\bar{b}+w)\bar{c}\bar{v}t_s/\bar{a} \qquad (8)$$

where the overbars represent mean values and where b is the lateral dimension of floes with pdf $f_B(b)$, v is the ice velocity with pdf $f_v(v)$, c is multiyear ice concentration with pdf $f_c(c)$, a is the floe area with pdf $f_A(a)$, w is the structure width and t_s is the season length of the scenario under consideration. This result assumes mutual stochastic independence between B, C and V, and that the probability distributions of these parameters reflect the changing conditions during the season.

4. HINDCASTING ICE MOTION

Whereas ice concentrations have been well documented historically, a continuous record of ice motion exists only during isolated periods for the nearshore Beaufort Sea. Continuous records of wind exist, enhancing the feasibility of hindcasting pack ice and landfast ice motions. Average ice speed is required for determining arrival rate and extreme values are required for determine impact loads.

Pack ice is motion is primarily wind driven, except in winter when stress is transmitted through the ice pack. The steady state wind-driven drift speed v_{fd} is calculated from the wind speed v_a using boundary layer relations at the air-ice and ice-water interfaces (e.g. McPhee, 1980). When the ice concentration approaches 10/10, ice speed is reduced by a factor $0 \leq \gamma \leq 1$ to account for mechanical resistance

$$v = \gamma v_{fd} \qquad (9)$$

where

$$\gamma = (1-p^*/p)^{0.5} \qquad (10)$$

The parameters p* and p are respectively the maximum resistance of the ice pack and the applied wind load on the ice pack per unit length. This representation is consistent with the approaches of Coon (1980) and Hibler (1979) which assume that the ice cover can only support a rate independent load during the ridging process.

Onshore winds accumulate ice along the landfast ice edge, therefore impeding motion. A model to predict first year and multiyear ice speeds was developed based on local winds. Ice accumulation in this zone was obtained from the onshore component of ice speed from (9) according to the method presented in Figure 4 . One requisite of this

model is ice concentration. In some cases, ice concentration does not necessarily reflect the mechanical behaviour of the ice pack. Particularly during the part of the winter where significant ice growth occurs, the ice thickness and existing flaws also influence ice motion. This emphasises the need for their continuous measurement in future.

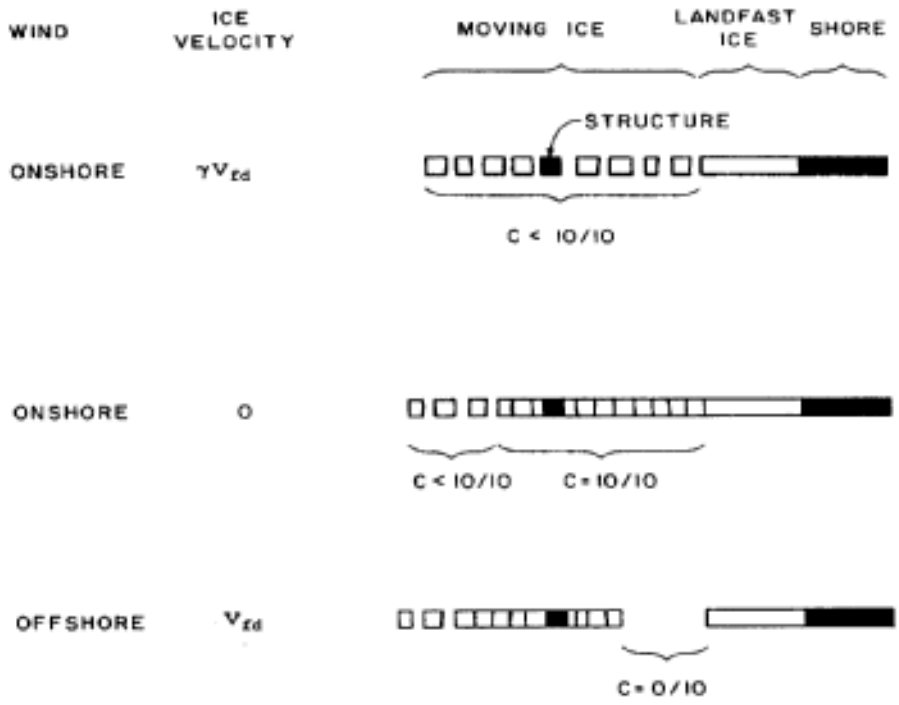

Figure 4. Schematic of nearshore ice drift (c represents ice concentration and ice speed refers to the onshore component)

The example in Figure 5 shows ice speeds hindcast from surface winds at the Amauligak site in the Beaufort Sea (based on equation 9) and observed from buoy data (reported by Marcellus and Morrison, 1982). Differing observation periods and spatial variations in wind and ice motion do not allow a direct comparison of these curves. Since faster floes have a greater chance of impacting the structure, the hindcast distribution was scaled according to the Bayesian updating scheme (7).

Within the landfast zone, the force applied to a structure is a function of the lanfast ice movement rate. Many landfast ice motion events have been observed (e.g. Spedding, 1975). McKenna et al. (1988) used wind as a predictor of these events with some success. Improvements to this approach can be achieved if more information on geometrical features such as grounded ridges and fractures in the landfast ice is available.

It is worth noting that physically based models have potential for providing estimates of joint probability distributions of the various environmental parameters that influence loads on structures.

5. MULTIYEAR ICE LOAD EXAMPLE

The most serious ice load conditions in the Beaufort Sea have been caused by multiyear ice. This was evidenced by the near failure of the Molikpaq structure at Amauligak during the spring of 1986 (Jefferies and Wright, 1988). The above approach for calculating extremal distributions of multiyear ice loads is illustrated using data for the Amauligak site. Amauligak (70.1°N, 133.9°W) lies in the active shear zone of the Beaufort Sea, seldom landfast, and often subject to the encroachment of multiyear pack ice.

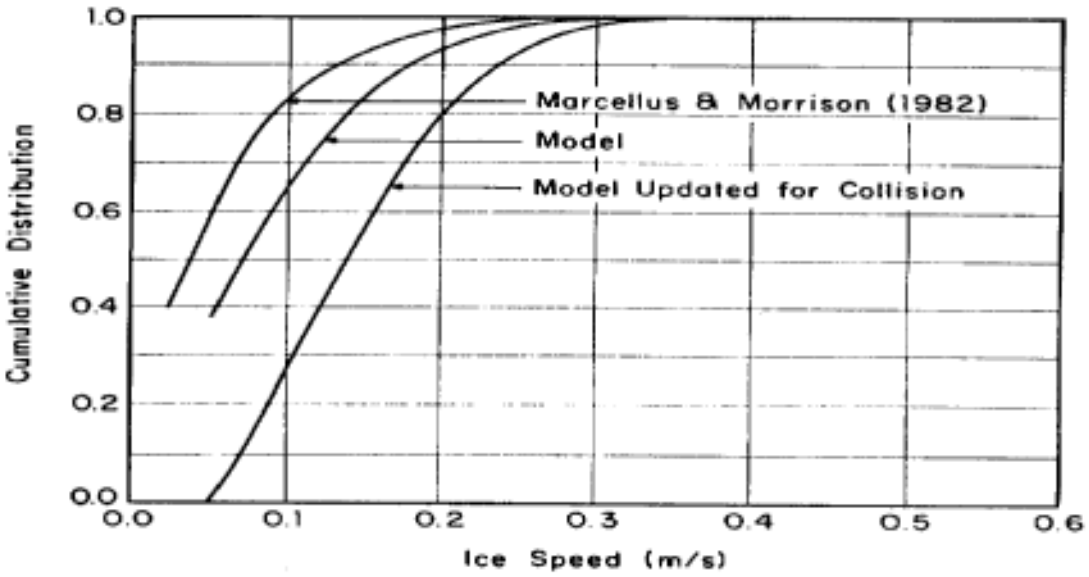

Figure 5. Cumulative distributions of winter ice speed

The force that a freely floating multiyear floe exerts on a structure can be estimated from its initial kinetic energy and the geometry of the contact. This is because most of the energy is dissipated by frictional processes as the ice crushes. The present example is for multiyear floes in summer. Ignoring added mass, the incoming kinetic energy of floes is

$$E_K = 1/2\ \rho a h v^2 \qquad (11)$$

where ρ is the ice density, a is the floe area, h is the ice thickness and v is the floe speed. The distribution of v was calculated using the method outlined in section 4 and the distribution for a was obtained from Spedding (1979). Ice thickness was assumed to have a mean of 3.9m and a standard deviation of 1.6m. The cumulative

distribution for E_K was found from the convolution of the parameter distributions in (11) using a numerical integration approach and is shown in Figure 6 .

The distribution of annual extremes for summer floe impact energy was calculated by modifying the parent distribution in Figure 6 for the expected number of floes at Amauligak. From equation (8) with $\overline{c}$=0.021 (CRISP data base, SIGRID source), $\overline{b}$=100 m, σ_b=150 m (Spedding 1979), $\overline{a}=0.25\pi(\overline{b}^2 + \sigma_b^2)$, $\overline{v}$=0.15 m/s (Figure 6), t_s=128 days (ice concentration and thickness) and w-100 m, the mean number of impacts is ν=273/year. Applying equation (6), the distribution of annual maximum kinetic energy for scenario MS is given in Figure 6 . From this CDF, the 1 in 100 year kinetic energy is 3800 MJ.

6. SUMMARY

The key elements for determining environmental loads on offshore structures are:

(i) To establish a set of scenarios encompassing the critical loading situations and to determine, if necessary, the time period during the year for which they are relevant. This is particularly true for ice loads.

(ii) To calculate the joint probability distributions between relevant environmental parameters for each scenario from available data or by hindcasting.

(iii) To obtain load distributions by appropriate convolution of the constituent environmental parameter distributions for significant loading events.

(iv) To determine the distribution of the maximum load and therefore the design load for the required return period.

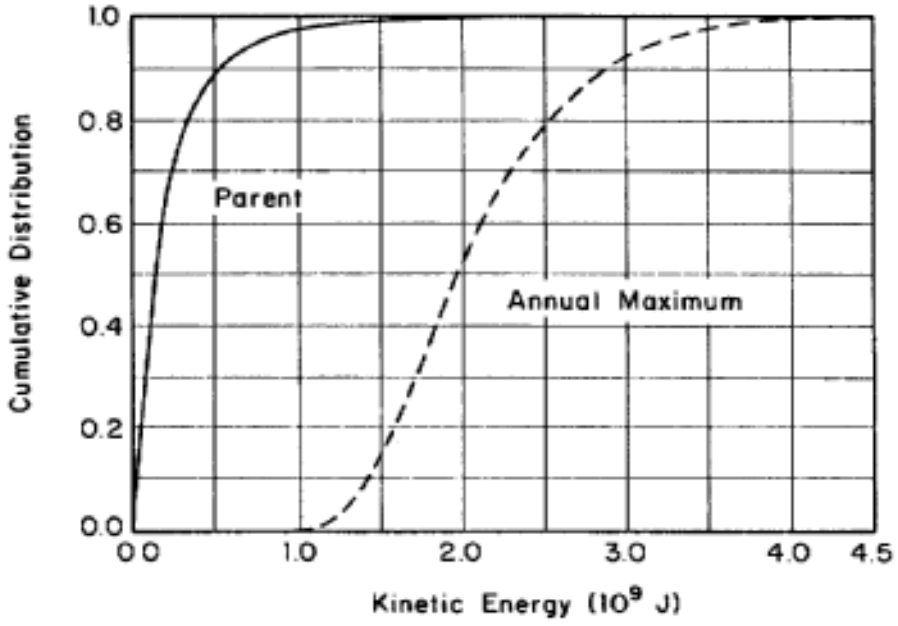

Figure 6. Cumulative distribution of kinetic energy for freely floating multiyear floe impacts at Amauligak during summer

7. REFERENCES

Agnew, T. , B. Maxwell and T. Mathews, 1987: An Ice and Snow Climate Information System, Third International Conference on Interactive Information and Processing Systems for Meteorology, Preprint Volume, American Meteorological Society, 173-177.

Coon, M.D. , 1980: A Review of AIDJEX Modelling, Proceedings of ICSI/AIDJEX Symposium on Sea Ice Processes and Models, University of Washington, 12-27.

Dunwoody, A.B. , 1983: The Design Ice Island for Impact Against an Offshore Structure, Proceedings of Offshore Technology Conference, OTC 4550, Vol. 2, 324-330.

Hibler, W.D. III, 1979: A Dynamic Thermodynamic Sea Ice Model, Journal of Physical oceanography, 9(4), 815-846.

Jefferies, M.G. and W.H. Wright, 1988: Dynamic Response of 'Molikpaq' to Ice-Structure Interaction, Proceedings of OMAE, Houston, Vol. IV, 201-220.

Jordaan, I.J., 1983: Risk Analysis with Applications to Fixed Structures in Ice, Seminar-Workshop on Sea Ice Management, Memorial University of Newfoundland, St. John's, Newfoundland.

Jordaan, I.J., 1988: Safety Levels Implied in Offshore Structural Design Codes: Application to CSA Program for Off shore Structures,

prepared for the Subcommittee on Verification of the Steering Committee CSA Program for Fixed Offshore Structures, 40p.

Jordaan, I.J., S. Lantos and M.A. Nessim, 1985: A Probabilistic Approach to the Estimation of Environmental Driving Forces on Arctic Offshore Structures, Presented at ARCTIC 85, ASCE, San Francisco.

Maes, M.A. and I.J. Jordaan, 1984: Probabilistic Analysis of Iceberg Loads on Offshore Structures, Proceedings of IAHR Symposium on Ice, Hamburg, Vol, II, 175-188.

Marcellus, R.W. and T.B. Morrison, 1982: Ice Design Statistics for the Canadian Beaufort Sea, C.M.E.L. Report No. 1015 prepared for The EIS Partners, 64p.

McKenna, R.F. , A.R. Marshall and I.J. Jordaan, 1988: The Application of AES Environmental Data to Ice Interaction Modelling, Ian Jordaan and Associates Inc. Report to Canadian Climate Centre, Atmospheric Environment Service, 123p.

McPhee, M.G. , 1980: An Analysis of Pack Ice Drift in Summer, Proceedings of ICSI/AIDJEX Symposium on Sea Ice Processes and Models, University of Washington, 62-75.

Spedding, L.G. , 1975: Landfast Ice Movement Mackenzie Delta 1974/75, APOA Project 83, Imperial Oil Limited.

Spedding, L.G., P. McLellan and C. Soares, 1979: Summer Ice Floe Size and Distribution in the Southern Beaufort Sea, Esso Resources Canada, Production Research Division Report IPRT1ME-78.

THE USE OF LONG-TERM SPECTRAL WAVE MODEL HINDCAST DATA FOR ESTIMATIONS OF PROBABLE DOWNTIME FOR FLOATING MOBILE OFFSHORE DRILLING, MINING AND CONSTRUCTION VESSELS

by:

Jerry A. Williams, CCM, & Susan Lally, Accredited Consultant

OCEANROUTES, INC
Sunnyvale, California

OCEANROUTES (CANADA) INC,
Bedford, Nova Scotia, Canada

I. INTRODUCTION

In 1982, the National Climatic Data center completed the conversion of the U.S. Navy Fleet Numerical Oceanography Center (FNOC) Ocean Wave Model (MM) hindcast to a code useable in computer systems other than that used at FNOC; Brines (1982). With the completion of the database, we had for the first time, point specific virtually continuos data for use in environmental analyses. The principal benefit of this time-continuity is the capability to analyze persistence and recurrence of specified wave heights and wind which is necessary for simulations which require a continuous data set; Thompson (1981). In addition to providing standard joint frequency distributions of directional and wave heights, the data can be used to the motion of specific hulls in reaction to the wave spectral. Given the response amplitude operators (R.A.O.'s) of a specific vessel, a downtime simulation can be run to provide an estimate of the percentage of time operating motion limits will be exceeded, thus yielding a "climatology" of motions, as well as winds and waves.

II. DESCRIPTION OF THE DATABASE

The SOWM is a computer model that generates wave data from a wind field; Lazanoff (1975). The model bas been operational at FNOC since December 1974; Gonzales (1974). In an attempt to develop a wave climatology for the northern hemisphere, a special run was made using historical sea level pressure field for the years 1956 through 1975. From this special run, Atlantic data are available from January 8, 1956 through December 30, 1974. Pacific data are available from September 1, 1964 through December 31, 1974. The Pacific set was then extended to February 23, 1977, by adding data from operational model runs. The wind field used to derive the hindcast set are taken from reconstructed historical sea-level pressure analysis, while the operational runs use the wind field available from FNOC's operational six-hour analyses.

The SOWM produces estimates of wave conditions. The data are not observations, however we have found that the data compare well with

values where available. The reasonableness of the data depends on the fundamental restrictions of the model being met; St. Denis (1973).

* The data point is in deep water (water depth twice the wavelength)

* The data point is sufficiently far from land to preclude interference with wave patterns.

* The wind field used to drive the model represents the actual winds.

The SOWM may operate correctly where conditions are violated, but there is no guarantee. In general the SOWM produces an answer that differs from the observation that would have been made at a given point and time.

III. PROCEDURES

A. Development of Joint Frequency Distributions.

1. Tables

In order to provide an easily readable set of wind and wave climatic data at a site or within a small area, a set of joint frequency tables (JFT's) are produced. The spectral data are parameterized to wind speed, wind direction, significant wave height, direction and period and both primary and secondary wave heights, periods and directions. The parameterized data set is then used to drive a suite of statistical programs to develop the JFT's. This set of tables consists of:

1. Tables - (Cont'd)

* Wind Direction versus Wind Speed

* Significant Wave Height versus Total Mean Wave Period

* Significant Wave Height versus Total Wave Direction

B. Calculation of Parameters

Significant Wave Height and Period

Computation of significant wave height and mean wave period is straightforward and is based on the following two formulas: Hoffman (1974, 1979).

$$H_{1/3} = 4\sqrt{M_0} \quad \text{and} \quad \bar{T} = M_0/M_1$$

Where M and M are derived through numerical evaluation of two integrals:

$$M_0 = \int_0^{2\pi} \int S(\omega, \theta) d\omega \, d\theta$$
$$M_1 = \int_0^{2\pi} \int_0^{\infty} \omega S(\omega, \theta) d\omega d\theta$$

In these integrals S(w,) gives the spectral ordinate as a function of wave frequency, and wave direction, .

Wave Direction

Since wave direction is a modular quantity, the calculation of a mean wave direction is difficult since the concept of a mean - a point around which mass is concentrated in a least squared sense - is not well defined in a modular number system. Therefore, heuristic approaches must be used in finding wave direction. The system used in these data is based on locating the maximum of the directional energy spectrum.

$$E(\theta) = \int_0^{\infty} S(\omega, \theta) d\omega$$

It is enhanced through smoothing and averaging.

A discretized energy is used, which gives E(Θ) at 12 equally spaced angles. This spectrum is smoothed by combining energies at adjacent angles in weighted sums, and the maximum is found. The smoothing prevents a swell, which concentrates moderate energy in a narrow directional band, from deciding the wave direction despite the presence of a sea which spreads substantially more energy over a larger directional band.

The direction of maximum smoothed energy is found which defines the basic wave direction. To refine this angle, a return is made to the unsmoothed spectrum and the possible spreading of wave energy into adjacent directions is taken into account. These are averaged into the final result if their energies are at least 70.7% ($1/\sqrt{2}$) that of the energy associated with the energy associated with the maximum.

C. Vessel Motion Simulations

This procedure is sometimes referred to as a downtime simulation; Silveria (1978, 1979). The purpose of the simulation is to estimate the percentage of time that specified threshold values of heave, pitch or roll are exceeded, using a long-term wave climatology. Since most operations require consideration of several different limiting wave heights, we opt to display results as percentage exceedance values for waves at intervals of selected metric or English units.

The database used to drive the simulation is the same as that used to create JFT's. In the simulation, however, the total wave spectra is

used, not simply the parameterized significant wave and total mean period and total wave direction. If the database is not continuous, there are two options for handling missing records. In the first option, the simulation stops and starts when discontinuous records are encountered. In the second option, missing records are zeroed, indicating no wind and a zero wave height. The second option overstates occurrence of a zero wave state, but the distortion can be defined by the difference in calm/zero wave height occurrence in the unadjusted data and in the adjusted (zeroed data) results.

In order to simulate vessel motions, the response amplitude operators (R.A.O.'s) for the specific vessel are input to the program, Rawstron (1978), R.A.O.'s are commonly available as a graph or series of graphs which show the amount of heave, pitch or roll per unit of wave height at various wave periods. These curves are usually developed using test tank results from initial designs. In some cases, the test tank curves are later adjusted using empirical data from experience at sea.

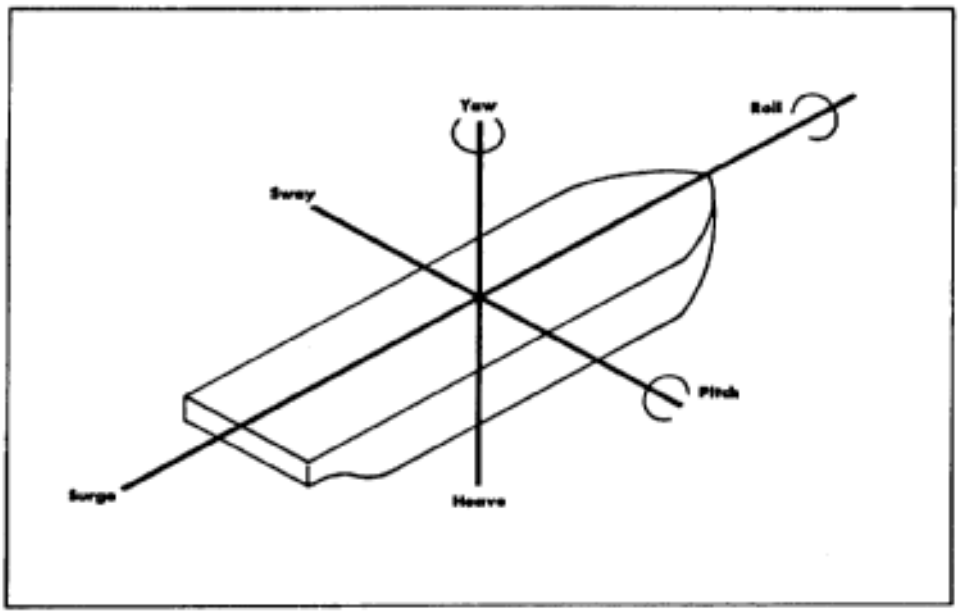

FIGURE 1: VESSEL MOTIONS

The critical axis of motion varies considerably by vessel type; Harris (1972). A ship shape vessel is most likely to exceed motions on the roll axis, while a semi-submersible is most likely to suffer from heave problems, Heavy lift barges can be troubled by heave, pitch and roll. In simulations of construction barge motions, the transfer functions relating to the boom-tip motions are critical. A small amount of heave or roll, translated to the boom-tip, can result in broad movement and difficulty in controlling the lifted load.

A motion simulation can be run for any of these vessel types, with results show as tables of ex for each of the motions, or in sane

cases, only the most likely problem motion. More sophisticated simulations, which couple the motion simulation approach with operational considerations, can be run; ETA Offshore Seminars (1976). A typical application is in a well drilling simulation. In this simulation, each step of a single-well drilling program and the limiting motion for each step is considered. The simulation requires use of the data in time series form. When a limiting motion is exceeded, the program counts time from the initial exceedance to the point where the motions fall within the specified range. The simulations are continued until long-term estimates of actual performance of each function, from arrival at site to completion of well testing and rig removal are made. A program which would take 90 days under ideal weather conditions, may take as long as 120 to 150 days when allowance for heavy weather and excessive vessel motions is made.

A motion simulation for several different drilling vessels may be made using the same database, as a tool for initial vessel selection when there is an option. In that case, the simulation a tool for defining the trade-off between using a smaller or more sensitive rig at a lower day rate, or using a larger or less sensitive, but more expensive rig for the total drilling program.

The environmental consultant may perform the entire simulation program, using data supplied by his client, or the consultant may simply provide the database to the client who then uses his own simulation programs for his operation. This is frequently the case when a drilling vessel owner is hesitant to release response curves for his vessel to an outside company.

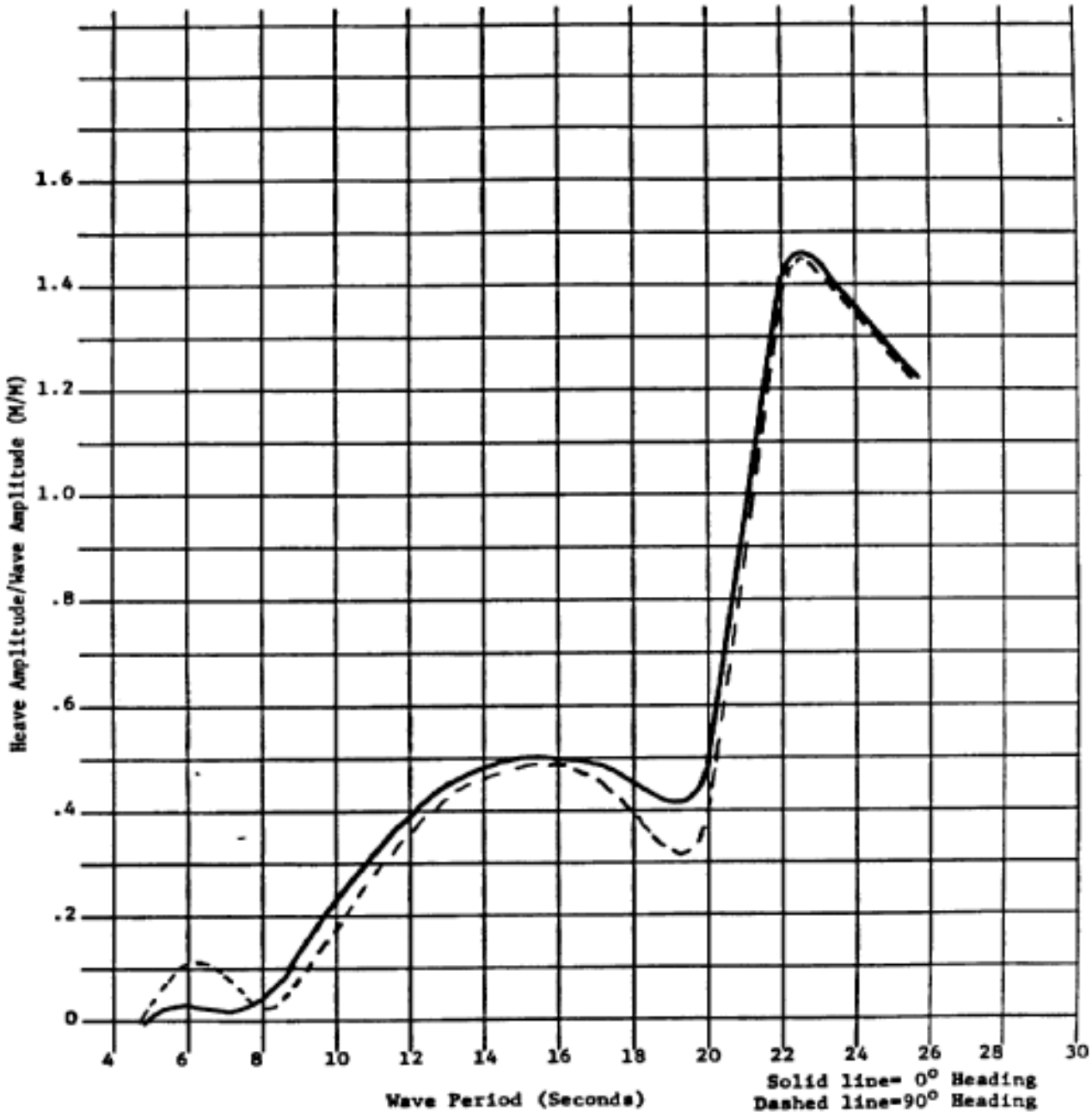

Figure 2: Response amplitude operator graph semi-submersible (with auxiliary columns) used in simulation.

The simulations are normally made for head, beam and quartering conditions. Using the results of the simulation and the JFT's for the site, the operator can reduce the motions by station. In some areas, this best heading will vary from season to season. In areas which experience frequent passage of storms, it may be difficult to select the single best heading, due to the wide distribution of wave

directions. For those sites, the recommended heading is usually based on motions and not simply wave direction.

IV. SIMULATION MODEL

A. General

The simulation model is run using the SOWM hindcast database as input. There are four wave for each each day, at six-hour intervals.

Each entry is tested at 30 degree intervals, from 0 to 90

B. Response Amplitude Operators (RAO's)

The response amplitude operator (RAO) represents the amplitude response of a vessel to a unit amplitude disturbance. Each degree of freedom has its own RAO. Thus, the heave RAO for a particular set of parameters is the deterministic peak-to-peak heave response of the vessel in a given (infinite) wave field of unit amplitude. For example, one-meter amplitude waves of a 15-second period may be impinging on a particular vessel with a given heading from the head (0 degrees relative heading). The heave RAO would then be the peak-to-peak heave in the same units as the wave amplitude, divided by the wave amplitude so as to be a dimensionless quantity, we can write

$$\text{RAO (parameters)} = \frac{\text{Response Amplitude (Parameters)}}{\text{Disturbance Amplitude (Disturbance Parameters)}}$$

The set of parameters referred to is large. The disturbance may be characterized by its period (or frequency) and direction relative to the vessel. The vessel's parameters are such as its hull geometry, mass distribution, draft, skin friction, and so on. Fortunately, for a given vessel these parameters may be assumed constant. Therefore, only the environmental parameters are required, and the equation to

$$\text{RAO (DOF, F, } \Theta) = \frac{\text{Response Amplitude (F, } \Theta)}{\text{Disturbance Amplitude (F, } \Theta)}$$

Where DOF refers to the degrees of freedom (heave, surge, sway, pitch, roll or yaw) F refers to the frequency of the disturbance and linear response, and Θ refers to the relative angle between the ship's centerline axis and the incoming (infinite plane) wave direction.

Figure 2 present RAO graphs for a semi-submersible (with auxiliary columns) which are used as an example.

C. Significant Response Amplitude

The sea state can be conveniently represented by the spectral wave density function $S(F,\Theta)$. Each component of S represents the energy

density in the wave field at frequency F travelling in direction Θ. If we quantize (F,Θ) space into a set of regions (F_i,Θ_j) of size $(\Delta F_i,\Delta\Theta_j)$, the in one of these boxes is

$$E_{ij} = S\ (F_i,\Theta_j) \bullet \Delta F_i \bullet \Delta\Theta_j \qquad (1)$$

E_{ij} is the energy in the wave field with in the range $(F_i - \Delta F_i/z,\ F_i + \Delta F_i/z)$ and moving in directions in the range $(\Theta_j - \Delta\Theta_j/z,\ \Theta_j + \Delta\Theta_j/z)$. The total energy in the wave field is

$$E = \Sigma_{i,j}\ E_{ij} = \Sigma_{i,j}\ S\ (F_i,\Theta_j) \bullet \Delta F_i \bullet \Delta\Theta_j \qquad (2)$$

The significant wave height, H_s is given by

$$H_s = 4\sqrt{\overline{E}} \qquad (3)$$

and other spectral moments may likewise be derived.

With F in HZ and Θ in radians, the units of S are M·M·SEC/RADIAN in the MKS system or FT·FT·SEC/RADIAN in the English system, Energy, E, would then be measured in M·M or FT·FT, respectively, and H_s in meters or feet.

The spectrum is the natural quantity for analysis for reasons; Pierson (1955). In the first place, it allows for the correct recombination of components, since it is their energies and not their amplitudes that add. Secondly, the disturbing wave field is stochastic; the wave spectrum representing the average energy densities as a function of wave frequency and direction, and the derived quantities, such as H_s, expectations of measure values; Phillips (1977).

Due to the stochastic nature of the disturbing field, the response field will also be stochastic in nature and is most appropriately described by its spectrum.

The key to going over to the representation is the observation that the energy is proportional to the square of the amplitude of motion. We may then define a response spectrum

$$S_{RESP}\ (F,\Theta) = K \bullet (\text{RESPONSE AMPLITUDE}\ (f,\Theta))^2 \qquad (4)$$

Where K is some constant factor, and "RESP" refers to the particular degree of freedom under consideration. It then follows that

$$S_{RESP}\ (F,\Theta) = K \bullet [\text{RAO}\ (F,\Theta)]^2 \bullet S\ (F,\Theta) \qquad (5)$$

and the expected significant response amplitude is

$$RESP_s = 4\sqrt{4 \bullet (1/K) \cdot \sum_{i,j} S_{RESP}\ (F_i,\Theta_j)\,\Delta F_i\,\Delta\Theta_j} \qquad (6a)$$

$$RESP_S = 4\sqrt{\sum_{ij} (RAO(F_i,\Theta_j))^2 \, S(F_i,\Theta_j)\,\Delta F_i\,\Delta\Theta_j} \qquad (6b)$$

In equation (6), RESP represents the significant heave, pitch, roll, etc.

The factor of (1/K) in equation (6a) is to get the units right, since it out in equation (6b), it will be omitted whenever we write a version of equation (5).

Equation (5) implicitly assumes the wave spectrum exists in a vessel-defined coordinate system. In general, the wave spectrum's coordinate system is geographic (directions Θ; defined relative to north) and the vessel is at some heading which is not true north. In that case, round Θ to Θ', the nearest of the canonical directions [Θ_j] to Θ, and rewrite equation (5) as

$$S_{RESP}\,(F_i,\Theta_j) = [RAO(F_i,\Theta_j)]\; S(F_i,\Theta_j-\Theta') \qquad (7)$$

and equation (6) as

$$RESP_S = 4\sqrt{\sum_{ij} S_{RESP}(F_i,\Theta_j)\,\Delta F_i\,\Delta\Theta_j} \qquad (8)$$

The simulation spectrum has 16 frequency components and 36 directional components. The frequencies are essentially those used by Fleet Numerical Oceanographic Center (U.S. Navy) and the spectral wave models. They are listed in Table 1 .

There are 36 directional components; the wave energy directions of propagation are every 10° around the compass (as compared to every 30° in the spectral wave models). This scheme makes full use of the resolution available in the driving database.

The wave spectrum may be written as $S(f,\Theta)$. The units are (ft^2•sec/rad). The spectrum is an energy density since the total energy in the spectrum is

$$E = \iint S(f,\theta)\; df d\theta = H_S^2/16$$

S is assumed separable:

$S(f,\Theta) = S(f)\bullet f(\Theta)$

V. RESULTS OF SIMULATION

The results of downtime simulations can be shown as the number of cases when "redline" limits were exceeded, or as a percentage

frequency distribution of exceedance. Figure 3 shows a simple method for indicating results of a simulation, based on heave response exceeding 1.0 meter and 1.5 meters, expressed both as a finite number of records and a percentage of total records. Results may also be shown as a joint frequency distribution (scatter) of heave exceedance versus time for persistence).

VI. ADDITIONAL METHODS OR APPLICATIONS

1. Use of Sea and Swell to Derive Spectra

It is possible, when wave data are not available, to derive wave spectra using sea and swell derived from ship weather observations; Carter (1982). In that approach, angular and frequency spreading are considered and sea (wind waves) are converted to energy densities. Swell are first converted to energy, added to the sea component and converted to energy densities. Although this approach provides realistic results, it may require a synthetic data set to accurately depict expected downtime, as the ship observation data are normally random and discontinuous in both space and time.

2. Predictive Mode

This motion simulation program works well in the predictive mode when analyses and forecasts are available; Hayes (1976). We have successfully used the method to predict heave, pitch and roll for site specific applications out to 72 hours. The method has also been used to advise best and worst headings for a slow moving deep oceanmining vessel, to minimize motion and to avoid worst heading when maneuvering.

VII. SUMMARY

The use of wave model hindcasts, coupled with vessel specific response amplitude operators, provides a sound tool for estimation of probable down time due to excessive motions. The simulation approach can also be used as a viable tool for selecting a floating mobile offshore drilling unit when there is an option of several available rigs. It can be used to evaluate the cost difference between a small, more reactive vessel at a lower day rate, and a larger, less reactive, but more expensive alternative. The technique can also be used in determining the best heading for operations at sea, based on long term past occurrences and probabilities based on the climatological wave data.

In addition to providing a motion based "climatology", the method can be used in the operational mode to predict vessel reactions for motion sensitive operations at a fixed site, or within an area.

VIII. ACKNOWLEDGEMENTS

Our thanks to Dr. David C. Fu and Dr. Cohen for sharing their expertise in computer simulations and to Dr. W.A. Silveria, whose initial interest in real-time applications made operational tests of the method possible. Special thanks to Debbie Coop for typing the manuscript.

IX. REFERENCES

Brines, R.O., 1982. Notes on Grid Point sorting of Synaptic Spectral Ocean Wave Data. National Climatic Data Center, Asheville, NC.

Carter, D.J.T., 1982. Estimation of Wave From Wave Height and Period. I.O.S. Report No. 135. Wormley, Unpublished Manuscript.

ETA Offshore Seminars, Inc. 1976. The Technology of Offshore Drilling, Completion and Production. Tulsa, OK.

Gonzalez, R.E., December 1974, Operational Implementation of an Ocean Wave Spectral (SOWM). Fleet Numerical Weather Central (FNWC), Technical Memorandum No. 28., pp. 13, Monterey, California.

Harris, L.M., 1972. Deepwater Floating Drilling Operations. The Petroleum Publishing Co., Tulsa, OK.

Hayes, J.G., 1976. Operational Wave Forecasting With the Ocean Wave Model. 7th Tech. Exchange Conference, El Paso, Texas.

Hoffman, D., 1974. Analysis of Measured and Calculated Spectra International Symposium on the Dynamics of Marine Vehicles and Structures in Waves. I. Mech. Eng. (UK).

Hoffman, D., 1979. Personal Correspondence with Oceanroutes, Inc.

Lazanoff, S.M., N.M. Stevenson, June 1975. An Evaluation of a Hemispherical Operational Spectral Wave Model. Fleet Numerical Weather Central Tech. Note 75-31 pp, 103, Monterey, California.

Phillips, O.M., 1977. The Dynamics of the Upper Ocean, Cambridge University Press, 2nd Edition.

Pierson, W.J., G. Neumann, and R.W. James, 1955. Practical Methods for Observing and Forecasting Ocean Waves by Means of Wave and Statistics, Publication No. 603, U.S. Navy Hydrographic Office, Washington , D.C.

Rawstron, P. and G. Blight, 1978. Prediction of Weather Downtime for Derrick Barges. Offshore Technology Conference, OTC 3150, Dallas, Texas.

St. Denis, M., 1973. Some Cautions on the Employment of the Spectral Technique to Describe the Waves of the Sea nad the Response Thereto of Oceanic Systems. OTC paper 1819. Houston, Tx.

Silveria, W.A., and H.J. Cohen, 1979. On the Simulation of Ocean-Wave Generation, Propagation and Dissipation by Numerical Spectral Models, and Some Real-Time Engineering Applications. Summer Computer Simulation Conference, Toronto, Canada (July 16-18).

Thompson, E.F., 1981. a Model for the Distribution Function for Significant Wave Height, Coastal Engineering Technical Air No. 81-3. CERC, Fort Belvoir, Va.

TABLE 1. Frequencies, period and bandwidths used in the downtime simulation (similar to SCWM hindcast).

NUMBER	F (HZ)	T (SECONDS)	F (HZ)
1	.25000	4.0	.15259
2	.18200	5.5	.03600
3	.15289	6.5	.02222
4	.13345	7.5	.01667
5	.11678	8.6	.01667
6	.10289	9.7	.01111
7	.09178	10.9	.01111
8	.08344	12.0	.005556
9	.07789	12.8	.005556
10	.07233	13.8	.005556
11	.06677	15.0	.005556
12	.06122	16.3	.005556
13	.05566	18.0	.005556
14	.05011	20.0	.005556
15	.04455	22.4	.005556
16	.03899	25.6	.005556

TABLE 2. Percent Exceedance Tables

Input to simulation considers wave height, wave period, wave direction relative to the vessel and the vessel R.A.O. Output is as a simple percentage exceedance table as shown below:

Percent Exceedance of Heave

Height (m)	Head	Quarter	Beam
1	72	60	22
2	54	38	13
3	38	26	9
4	18	11	3
5	8	5	1
6	4	2	0
7	2	0	0
8	1	0	0
9	.6	0	0
10	.3	0	0
11	.1	0	0
12	*	0	0

* Indicates less than 0.05 occurrence

Table 3. Percent occurrence of heave response downtime for Aker H-3 rig in North Sea Norwegian block 31/6 using a 0° heading (degress true north).

		HEAVE RESPONSE 1 M		HEAVE RESPONSE 1.5 M	
MONTH	TOTAL REC. NO. IN 15 YEARS	NO. OF RECORDS	PERCENTAGE	NO. OF RECORDS	PERCENTAGE
JAN	930	95	10.22	42	4.52
FEB	848	45	5.31	19	2.24
MAR	930	34	3.66	8	0.86
APR	900	28	3.11	12	1.33
MAY	930	2	0.22	0	0
JUN	900	3	0.33	2	0.22
JUL	930	4	0.43	2	0.22
AUG	930	0	0	0	0
SEP	900	27	3.00	11	1.22
OCT	930	55	5.91	19	2.04
NOV	900	67	7.44	33	3.67
DEC	930	98	10.54	41	4.41
TOTAL:	10,958	458	4.18	189	1.72

Improving Global Wave Forecasts Incorporating Altimeter Data

Dinorah C. Esteva

National Oceanic And Atmospheric Administration
National Meteorological Center
Washington, D. C.

Introduction. Because of the lack of global wave observations wave predictions at present are Initialized by driving the ocean surface with a marine boundary layer wind field specified by an atmospheric model. Wave data from satellite borne sensors are now becoming available making it possible for the first time to use these observations in specifying a more accurate initial wave field. The SEASAT satellite mission flown in 1978, generated a 90 day data set of ocean surface winds and wave data from several sensors. The altimeter flown on SEASAT produced collocated estimates of wind speed and significant wave height (SWH). Which have been ground proofed by Fedor and Brown, (Fedor and Brown 1982) among others.

This collocated wind and wave data set has been used in this study to asses the impact on wave forecasts of initializing the operational wave model at the National Meteorological Center (NMC) with what could be termed an analyzed wave field. This model, the NOAA ocean Wave (NOW) model is a second generation spectral wave model similar to the SAIL II model. The model was driven with the NMC analyzed winds fox the corresponding SEASAT period.

Two experiments will be discussed. One experiment generated analyzed wave fields using the altimeter SWH only. The other experiment used both the SWH and the wind speed for generating the analyzed wave field.

Experimental Procedure. The same procedure was followed in the two experiments. A 24 hour hindcast was prepared assimilating data into the model at three hour intervals and the resulting 24 hour field was used as the initial wave field for a 72 hour forecast (Figure 1). The procedure was repeated for 10 consecutive days: 16-26 September, 1978. The model was spun up for 1) days before starting the experiment, and a hindcast was first performed for the 10 days of the experiment. Statistics were computed every three hours between the hindcast SWH and the corresponding SEASAT SWH estimates. These statistics, consisting of bias, root mean square (RMS) difference, and mean absolute difference (MAE), served as a control for assessing the impact of the assimilation through comparison against statistics similarly computed from the 72 hour forecasts.

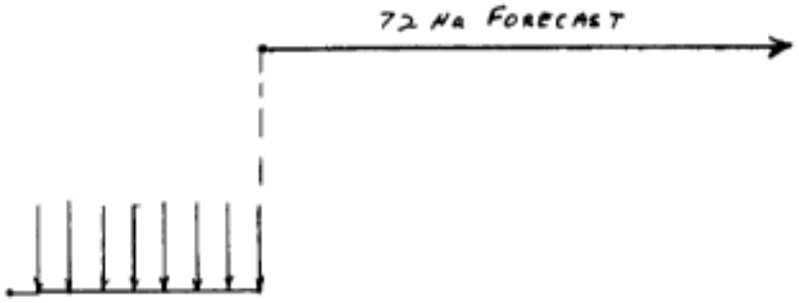

Figure 1. Schematics of the assimilation procedure.

Data were introduced into the 24 hour hindcast by scaling the hindcast spectra. In the first experiment the spectra were scaled uniformly up or down with the factor: $(H_o/H_h)^2$, where H_o is the the SEASAT SWH estimate or observed value, and H_h is the hindcast value. This procedure leaves the distribution of energy in frequency and direction and thus the spectral shape unchanged, while the hindcast SWH is forced to equal the observed value.

In the second experiment the energy in the sea portion of the spectrum was computed using the SEASAT estimate of wind speed. From Hasselmann's expression for non dimensional energy, ε and frequency, ν:

$$\varepsilon = 5.3 \times 10^{-6} \nu^{-10/3} \qquad (1)$$

(Hasselmann 1976), and assuming a constant wind, the dimensional energy, E in the sea portion of the spectrum may be found to be given by (Thomas):

$$E = 5.3 \times 10^{-6} g^{-4/7} U^{15/7} t^{10/7} \qquad (2)$$

where g is the acceleration of gravity, U the wind speed, and t the wind duration. Since t is the same whether the model or the observed winds are used in equation 2, correcting the sea portion of the hindcast spectrum with the ratio $(U_o/U_m)^{2.57}$, where U_m is the model wind, adjusts this portion of the spectrum to what it should be according to the observed wind speed. The remaining energy: $(H_o^2 - H_h^2)$ is used to scale the swell portion of the hindcast spectrum as was done for the total spectrum in the first experiment.

The procedure in the second experiment distinguishes between sea and swell and changes the shape of the spectrum. Sea was considered as that portion of the spectrum with frequencies higher than the Pierson-Moskowitz peak frequency for a fully developed spectrum.

The SEASAT data set and data processing. The SEASAT altimeter produced 1 second averages of SWH and wind speed over a footprint with an approximate radius of 7 K. One second averages between 65°S and 65°N

were edited and gridded as follows. The mean and standard deviation (σ) of the values within 1.5 hours of the model forecasts and within a 2.5 by 2.5 degree square centered at a model grid point were computed. Values differing from the mean by 3σ or more were discarded. The remaining values were averaged and assigned to the corresponding grid point and time. Averages among these based on fewer than three data values and those with a standard deviation greater than 0.5 of the average were also discarded. These gridded SWH were assimilated into the 24 hour hindcasts. When the SEASAT SWH was lower than 0.4 M or differed from the forecast by 0.5 M or less, the forecast was left unchanged. However all available gridded SWH were used when computing statistics.

Table 1 gives the number of gridded SWH values available for the assimilation in the northern and southern hemispheres for each day of the experiment. It is seen that for each 3 hour period the number of values assimilated is a small percentage of the total number of grid points. Yet as will be seen, introducing these few values had an impact on the model forecasts.

Table 1. Number of Gridded SEASAT SWH values available for assimilation for each day of the experiment.

Day in 9/78	Number of SWH values in Hemisphere		Total
	Northern	Southern	
16	166	360	520
17	158	229	387
18	287	512	799
19	268	506	774
20	168	245	413
21	146	295	441
22	154	253	407
23	171	258	429
24	126	302	428
25	143	274	417
26	165	254	419

The NOW model. The Now model is a global deep water model with a 3 hour time step and a 2.5 by 2.5 degree latitude/longitude grid. It produces forecasts every 3 hours to 72 hours from 72.5S to 75.0N.

The model solves the energy transport equation:

$$\frac{\partial F}{\partial t} + Cg\ F = S_{in} + S_{nl}$$

where $F = F(f,\Theta)$ is the two dimensional wave spectrum in frequency, f and direction, Θ. F depends also on location and time. c_g is the group velocity and the terms on the right hand side are the source terms representing the wind input and the non linear wave wave Interactions.

The wind input source term follows the parameterization of Snyder et al. (1981). The nonlinear source term is based on the SAIL II mechanism (Greenwood et al, 1985). A $\cos^3$ law is used for spreading the energy with direction Dissipation in the high frequencies is accomplished by imposing the Pierson-Moskowitz limit for a fully developed spectrum.

The propagation scheme is a downstream interpolation in which each frequency directional band is propagated at group velocity along a great circle. The wind input to the model was the 1000 MB winds reduced to 19.5 m height by means of Cardone's algorithm. (Cardone, 1969)

Results. The bias, root mean square difference (RMS), and mean absolute difference (MAE) were computed from:

$$\text{bias} = N^{-1} \Sigma (H - H_o)$$

$$\text{RMS} = (N^{-1} \Sigma (H - H_o)^2)^{1/2}$$

$$\text{MAE} = N^{-1} \Sigma |(H - H_o)|$$

where H is the model hindcast/forecast, and H_o is the observation.

The bias, RMS and MAE for one of the 10 days are plotted in figures 2 - 4 for the control (C), experiment one (E1) and experiment 2 (E2). Two things are noticeable: one is that after 36 hours into the forecasts, the improvements decrease substantially. This is obviously due to the fact that the model has been updated solely with the forecast wind for these many hours. The second thing is that Introduction of the wind observations increases the improvements. This is better assessed in Figures 5 and 6 where the % improvements in MAE are plotted every six hours for the first 24 hours (day 1 forecasts) and the next 24 hours (day 2 forecasts) for both experiments.

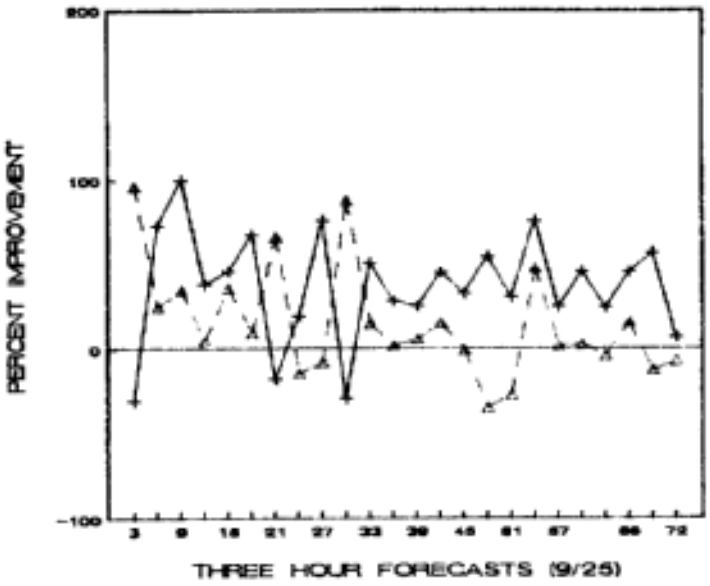

Figure 2. Improvement in bias for a 72 hour forecast. Experiment 1: --Δ--, and experiment 2: --+--.

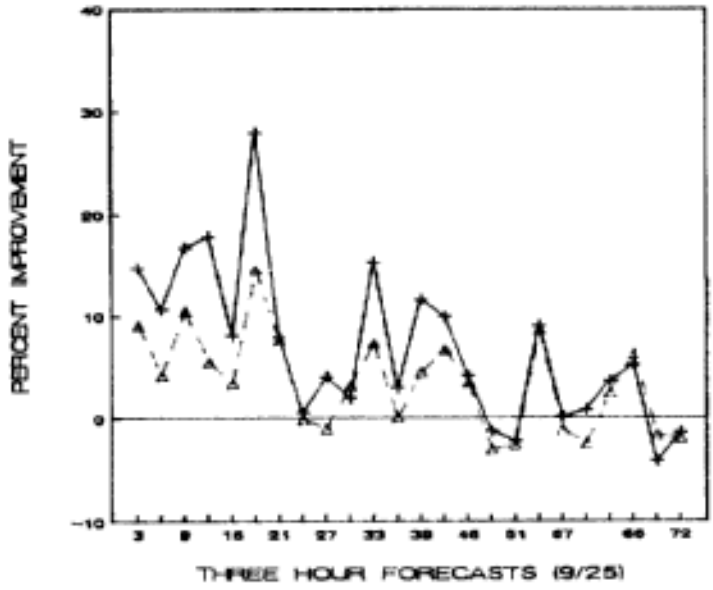

Figure 3. Improvement in RMS for a 72 hour forecast. Same as figure 2.

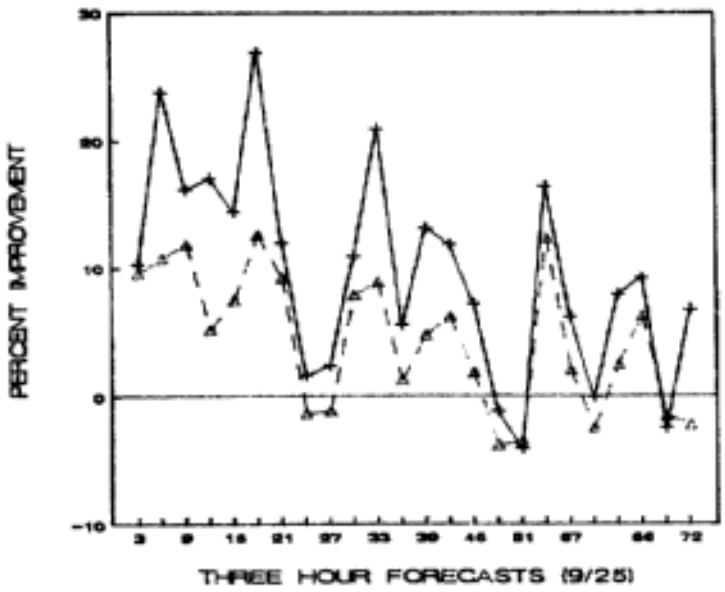

Figure 4. Improvement in MAE for a 72 hour forecast. Same as figure 2.

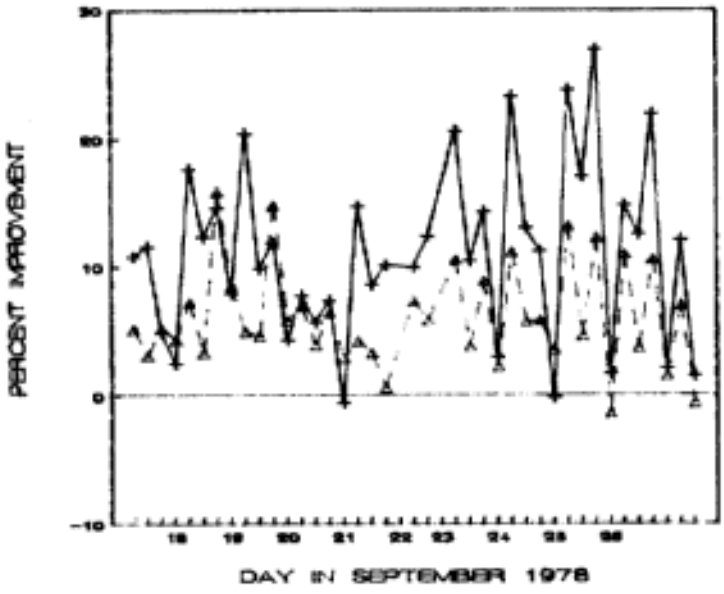

Figure 5. Percent improvement in MAE for day 1 forecasts. Experiment 1: --Δ--, experiment 2: --+--

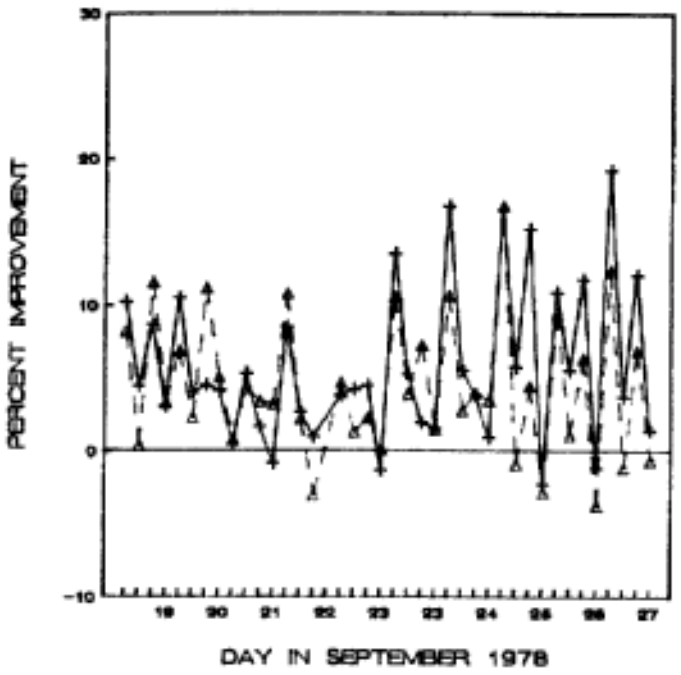

Figure 6. Percent improvement in MAE for day 2 forecasts. Experiment 1: --Δ--, experiment 2: --+--.

Summary. Initializing wave forecasts with analyzed wave fields produced by introducing SWH only improves the model forecasts. When wind observations are also used the average improvements in MAE for the first 24 hour forecasts increase from 7.4 % to 12 %. The increased improvement is believed to be due to differentiation between sea and swell. The improvements decrease with time into the forecast in both cases since observations are no longer updating the wave field.

References.

Cardone, V. J., Specification of the wind distribution in the marine boundary layer for wave forecasting, New York University School of Engineering and Science, Geophysical Science Laboratory TR69-1. December 1969.

Fedor, L.S. and G. S. Brown, Wave height and wind speed measurements from the SEASAT radar altimeter, Journal of Geophysical Research, Vo. 87, No. C5. April 1982.

Greenwood, J.A., V.J. Cardone, and L.M. Larson, Chapter 22, The Swamp Group, 1985, Ocean Wave Modeling, Plenum Press, New York, 256 pp.

Hasselmann, K., D.B. Ross, P.Muller, and W. Sell, A parametric wave prediction model, Journal of Physical Oceanography, Vol 6, No.2, March 1976.

Thomas, J. Personal communication

GLOBAL VALIDATION OF THE NOAA NATIONAL METEOROLOGICAL CENTER OPERATIONAL WAVE MODEL AGAINST GEOSAT DATA

Dinorah G. Esteva

National Meteorological Center,
Washington, D.C.

ABSTRACT

The NOAA National Meteorological Center (NMC) implemented a second generation global spectral model in November, 1984. The model runs daily, producing wave forecasts every 3 hours to 72 hours. Forecasts of significant wave height (SWH) from this model are compared against the GEOSAT satellite altimeter estimates. The GEOSAT altimeter SWH within ±1.5° in latitude and longitude of a model grid point and with ±1.5 hours of the forecast times are averaged and compared against the forecasted SWH. Values of the mean difference (bias), the root mean square (rms) difference, and the mean absolute difference (mad) are computed separately for the northern and southern hemispheres. Data for November and December of 1988 will be presented. Results to date indicate better agreement between the two data sets in the southern hemisphere (rms differences generally less than 1 m), than in the northern hemisphere (rms differences slightly greater than 1 m) regardless of wave height.

MODELING OF WAVES AT THE BELGIAN COAST

[1]D. Van den Eynde, [1]P. Goffart, [2]I. Hermans and [1]B.M. Jamart

[1]Ministry of Public Health and Environment,
Brussels, Belgium

[2]Catholic University of Leuven,
Leuven, Belgium

ABSTRACT

Several models are combined with the aim of forecasting wave spectra at the Belgian coast. These models will serve as a management tool for ship routing towards the Belgian sea harbours through the fairly shallow waters of the southern Bight of the North Sea.

First, the HYPAS model (developed at GKSS Forschungszentrum Geestacht GmbH, West Germany) is applied for a domain covering the entire North Sea. This model has a spatial resolution of 50 x 50 km^2 and is referred to as the "coarse grid model". In order to account for the complex bathymetry in the southern North Sea, a "fine grid model" (of resolution 5 x 5 km^2) is coupled to the coarse grid model through two open ocean boundaries. Sample results from the calculations with the two grids are compared to observations.

Although the shoaling effect is included in the HYPAS model, an additional spectral refraction model is used to take into account the changing direction of wave energy propagation at the lower frequencies. This refraction model is coupled to a tidal flow model in order to take into account the influence of varying water depths. At present, a quasi-stationary approach is implemented. A reverse tracking of the wave rays is carried out in order to determine the modified wave energy density spectra at several points of interest (along the shipping route). The boundary conditions of the refraction model are provided by the fine grid HYPAS model. Preliminary results of the refraction model are also compared to *in-situ* measurements.